Ph.D. Dissertation

Link Level Performance Evaluation and Link Abstraction for LTE/LTE-Advanced Downlink

Author: Albert Serra Pagès

Thesis Advisor: Joan J. Olmos Bonafé

Department of Signal Theory and Communications
Universitat Politècnica de Catalunya

Barcelona, November 2015

A en Gil, a la Queralt i a la Cristina

Acknowledgements

El final de la tesis ha arribat i simplement vull dir que em sento content i feliç. Primer de tot vull agrair al meu director de tesis, en Joan Olmos, la confiança que ha dipositat en mi per a realitzar aquesta tesis, el seu suport incondicional i la seva ajuda tècnica. També vull donar les gràcies a la Silvia Ruiz que em va obrir les portes per poder realitzar la tesis al departament TSC.

En segon lloc vull dedicar el treball fet per aquesta tesis i la paciència que han tingut a la meva família que sense ella no ho hagués pogut aconseguir. També vull agrair als meus pares tot el suport que m'han donat des de sempre.

Finalment deixar escrit que la feina, l'esforç, les ganes d'aprendre i les ganes de gaudir de tot plegat ho dedico a la Cristina, a la Queralt i a en Gil.

Albert Serra
Barcelona, Novembre 2015

Abstract

The LTE/LTE-Advanced standardization activity is an ongoing task to build up a framework for the evolution of the 3GPP radio technologies towards the 4G and beyond. The LTE/LTE-Advanced standard defines an extremely flexible radio interface which is based on OFDM technology with MIMO antenna processing and an all-IP flat network architecture where all the user plane radio functionalities are terminated at the eNodeB. All services are conveyed over packed based shared transport channels. These innovations open important research challenges related to the optimization of the PHY and MAC layers of LTE/LTE-Advanced. The main objectives of this dissertation are the evaluation of the link level performance and the study of link abstraction for LTE/LTE-Advanced DL.

The E-UTRA DL link level simulator which has been built in order to evaluate the LTE/LTE-Advanced DL is a software tool based on OFDM technology with MIMO antenna processing. This simulator contains the MIMO algorithms, the spatial channel models, the modulation and coding schemes and the turbo coding, rate-matching and HARQ processes for LTE/LTE-Advanced. In addition it has been proposed and included in the link level simulator a CEEM channel estimation method and a novel link abstraction method for E-UTRA. The result of this simulator serves to evaluate the MIMO-OFDM LTE/LTE-Advanced link level performance in different environments and create link level LUTs to be used as an input for LTE/LTE-Advanced system level simulators.

Channel estimation is a key aspect for the performance of the physical layer in all MIMO-OFDM systems. In order to obtain realistic performance assessments from the LTE/LTE-Advanced link level simulator, channel estimation errors must be taken into account. Implementing a detailed channel estimation algorithm may lead to long simulation time, in particular for wideband MIMO transmission modes where many channels have to be estimated, and for procedures like Wiener filtering which require matrix multiplications. In this dissertation we propose to simulate channel estimation errors by a Gaussian additive noise error model called CEEM. The noise variance of the model is calibrated as a function of the received SNR for different channel models and Doppler spreads. The model is validated by comparing the BLER curves obtained with the model with the curves obtained when using real channel estimation.

Link abstraction methods are able to predict the BLER in multicarrier wideband systems using AMC techniques under multipath fading. The basic idea is to map the vector of the subcarrier SNRs to a single scalar, the ESNR, which is then used to predict the BLER. This procedure is important during real system operation, since the mobile terminal must report the CQI to the base station, and also for the system level simulators. In order to take into account HARQ, it is also interesting to predict the BLER after one or more IR retransmissions have happened. With IR HARQ there is an additional complexity, since the BLER performance of a given redundancy version (rv) depends on the SNR experienced by the receiver at current rv but also on the SNR of previously received rvs. We propose a novel link abstraction method that can predict the BLER with good accuracy in multipath fading and including the effects of HARQ retransmissions. The proposed method is based on estimating the mutual information between the transmitted bits and the received LLRs. We show that, by working at bit level, the effect of unequal error protection in 16QAM and 64QAM modulations is properly captured without resorting to any set of calibration

constants. We also show how to reduce the set of reference BLER curves when working with multiple MCSs. Finally, we present the simulation results for LTE/LTE-Advanced DL with SISO and 2×2 MIMO assuming perfect channel estimation and SU-MIMO transmission modes.

The simulation of LTE/LTE-Advanced at link level is a hot research topic and it would be useful to define a common set of scenarios for LTE/LTE-Advanced link level simulations with the goal to allow researchers to configure the different simulation tools in a way that the obtained results can be properly compared and simulators become calibrated to a common reference. Researchers working at system level would also benefit from this initiative by having access to well established link level results and LUTs. This dissertation also addresses this task in Chapter 3 by identifying a set of topics, features and parameters to consider when programming the link level simulators. The proposed aspects derive from the experience gained while building the E-UTRA DL link level simulator presented in this dissertation, but since the LTE radio interface is extremely flexible and supports many features, it is difficult to be exhaustive. The aim is to focus on the relevant topics for link level simulator calibration and to discuss the trade-off between simulation complexity and compliance with the standards.

Resum

L'activitat d'estandardització del LTE/LTE-Advanced és una tasca contínua per construir un marc per l'evolució de les tecnologies radio 3GPP cap al 4G i més enllà. L'estàndard LTE/LTE-Advanced defineix una interfície radio extremadament flexible que es basa amb la tecnologia OFDM amb processat d'antena MIMO i una arquitectura de xarxa tota IP a on les funcionalitats radio d'usuari s'acaben a l'eNodeB. Els canals de transport compartits basats en paquets transporten tots els serveis. Aquestes innovacions obren importants reptes de recerca per a la opimització de les capes PHY i MAC del LTE/LTE-Advanced. Els objectius principals d'aquesta tesis són l'avaluació del rendiment a nivell d'enllaç i l'estudi de l'abstracció de l'enllaç pel LTE/LTE-Advanced DL.

El simulador del nivell d'enllaç E-UTRA DL, desenvolupat per a avaluar el LTE/LTE-Advanced DL, és una eina software basada en la tecnologia OFDM amb processat d'antena MIMO. El simulador conté els algoritmes MIMO, els models de canal espaial, els esquemes de modulació i codificació i els processos de turbo coding, rate-matching i HARQ per LTE/LTE-Advanced. A més s'ha proposat i inclòs en el simulador un mètode d'estimació de canal anomenat CEEM i un innovador mètode d'abstracció de l'enllaç per E-UTRA. El resultat d'aquest simulador serveix per avaluar el rendiment a nivell d'enllaç del LTE/LTE-Advanced en diferents entorns i crear LUTs a nivell d'enllaç per ser usades com a entrada de simuladors de sistema del LTE/LTE-Advanced.

L'estimació de canal és un aspecte clau per al rendiment de la capa física en tots els sistemes MIMO-OFDM. Per tal d'obtenir del simulador d'enllaç una avaluació del rendiment realista, l'estimació de canal s'ha de tenir en compte. Implementar un algoritme detallat d'estimació de canal pot portar a temps de simulació molt grans; per exemple, degut a que en el cas de modes de transmissió MIMO de banda ampla s'ha d'estimar molts canals, i els procediments com el filtre de Wiener requereixen multiplicacions matricials. Aquesta tesis proposa simular els errors d'estimació de canal amb un model d'error de soroll additiu Gaussià anomenat CEEM. La variança del soroll del model és calibrada com a funció de la SNR rebuda per diferents models de canal i diferencials Doppler. El model és validat mitjançant la comparació de les corbes de BLER obtingudes amb el model i les corbes obtingudes usant l'estimació de canal real.

Els mètodes d'abstracció de l'enllaç poden predir la BLER en sistemes de banda ampla multi-portadora amb esvaïments multicamí usant tècniques AMC. La idea bàsica és mapejar el vector de SNRs de les subportadores a un valor escalar, l'anomenada ESNR, la qual és usada per a predir la BLER. Aquest procediment és important durant la operació de sistemes reals, ja que el terminal mòbil ha d'informar del seu CQI a l'estació base, i també pels simuladors de sistema. Per tal de tenir en compte HARQ, també és interessant predir la BLER després d'una o més retransmis-sions IR hagin ocorregut. Amb IR HARQ hi ha una complexitat addicional ja que el rendiment de la BLER donada una versió de redundància (rv) depèn de la SNR que té el receptor a la rv actual però també de les SNRs de les rvs prèviament rebudes. Proposem un innovador mètode d'abstracció de l'enllaç que pot predir la BLER amb bona precisió en esvaïments multicamí i que inclouen els efectes de les retransmissions HARQ. El mètode proposat es basa amb l'estimació de la informació mútua entre els bits transmesos i els LLRs rebuts. Es demostra que, treballant a nivell de bit, l'efecte de la protecció d'error desigual en les modulacions 16QAM i 64QAM es captura adequadament sense necessitat de recórrer a constants de calibració. També es demostra

com reduir el conjunt de corbes de BLER de referència quan es treballa amb múltiples MCSs. Finalment, es presenten els resultats de les simulacions per LTE/LTE-Advanced DL fets pels casos SISO i 2×2 MIMO assumint estimació ideal de canal i modes de transmissió SU-MIMO.

La simulació de LTE/LTE-Advanced a nivell d'enllaç és un tema d'investigació d'actualitat i seria útil definir un conjunt d'escenaris comuns per a les simulacions de nivell d'enllaç LTE/LTE-Advanced amb l'objectiu de permetre als investigadors configurar diferents eines de simulació de manera que els resultats obtinguts es puguin comparar adequadament i els simuladors esdevinguin calibrats a una referència comuna. La recerca a nivell de sistema es beneficiarà d'aquesta iniciativa mitjançant l'accés a resultats i LUTs de nivell d'enllaç ben establerts. Aquesta tesis tracta aquesta tasca en el capítol 3 identificant un conjunt de temes, característiques i paràmetres a considerar quan es programa el simulador de nivell d'enllaç. Els aspectes proposats provenen de l'experiència adquirida mentre s'ha desenvolupat el simulador d'enllaç E-UTRA DL en aquesta tesis; de totes maneres donat que la interfície radio del LTE és extremadament flexible i suporta moltes característiques, és molt difícil ser exhaustiu. L'objectiu és centrar-se en els temes més rellevants per la calibració del simulador d'enllaç i analitzar els avantatges i desavantatges entre la complexitat de simulació i la conformitat amb l'estàndard.

Contents

List of Figures

List of Tables

Acronyms

1D *One-Dimensional*

2D *Two-Dimensional*

3G *Third Generation of Mobile Communications Technology*

4G *Fourth Generation of Mobile Communications Technology*

5G *Fifth Generation of Mobile Communications Technology*

3GPP *Third Generation Partnership Project*

16QAM *16-Quadrature Amplitude Modulation*

64QAM *64-Quadrature Amplitude Modulation*

256QAM *256-Quadrature Amplitude Modulation*

ACK *Acknowledgement*

aGW *Access Gateway*

AMC *Adaptive Modulation and Coding*

AP *Antenna Port*

ARQ *Automatic Repeat Request*

AWGN *Additive white Gaussian noise*

BCH *Broadcast Channel*

BER *Bit Error Rate*

BEC *Backward Error Correction*

BICM *Bit-Interleaved Coded Modulation*

binit *binary digit*

BLER *Block Error Rate*

BPSK *Binary Phase-Shift Keying*

BS *Base Station*

CDD *Cyclic Delay Diversity*

cdf *Cumulative density function*

CEEM *Channel Estimation Error Model*

CM *Coded Modulation*

CL *Closed-Loop*

CP *Cyclic Prefix*

CQI *Channel Quality Indicator*

CRC *Cyclic Redundancy Check*

CRS *Cell-specific reference signal*

CSI *Channel State Information*

CSI-RS *CSI reference signal*

CoMP *Coordinated Multipoint*

CTF *Channel Transfer Function*

DFT *Discrete Fourier Transform*

DL *Downlink*

DL-SCH *Downlink Shared Channel*

DM-RS *Demodulation reference signal*

DMC *Discrete Memoryless Channel*

DSL *Digital Subscriber Line*

DVB *Digital Video Broadcasting*

E-UTRA *Evolved UMTS Terrestrial Radio Access*

E-UTRAN *Evolved* UMTS Terrestrial Radio Access Network

Eb/No *Energy per bit to noise power spectral density ratio*

ECR *Effective Code Rate*

ESNR *Effective Signal-to-Noise Ratio*

EESM *Exponential Effective SNR Metric*

EESNR *Exponential ESNR*

eNodeB *evolved NodeB*

eMBMS *evolved Multimedia Broadcast and Multicast Service*

EPC *Evolved Packet Core*

EPDCCH *Enhanced Physical Downlink Control Channel*

EPS *Evolved Packet System*

EPA *Extended Pedestrian A*

EVA *Extended Vehicular A*

ETU *Extended Typical Urban*

EVA70 *EVA channel model and maximum Doppler frequency of 70 Hz*

ETU300 *ETU channel model and maximum Doppler frequency of 300 Hz*

EPA5 *EPA channel model and maximum Doppler frequency of 5 Hz*

EVA5 *EVA channel model and maximum Doppler frequency of 5 Hz*

EVA300 *EVA channel model and maximum Doppler frequency of 300 Hz*

ETU5 *ETU channel model and maximum Doppler frequency of 5 Hz*

ETU70 *ETU channel model and maximum Doppler frequency of 70 Hz*

EPA70 *EPA channel model and maximum Doppler frequency of 70 Hz*

EPA300 *EPA channel model and maximum Doppler frequency of 300 Hz*

FDD *Frequency division duplexing*

FEC *Forward Error Correction*

FFT *Fast Fourier Transform*

FSTD *Frequency-Shift Time Diversity*

GSM *Global System for Mobile Communications*

GWSSUS *Gaussian Wide-Sense Stationary Uncorrelated Scattering*

HARQ *Hybrid ARQ*

HC *High Correlation for MIMO Correlation Matrix*

HSPA *High-Speed Packet Access*

HSPA+ *Evolved HSPA*

HSDPA *High-Speed Downlink Packet Access*

HSUPA *High-Speed Uplink Packet Access*

HetNet *Heterogeneous network*

I-METRA *Intelligent Multi-Element Transmit and Receive Antennas*

ICIC *Inter-cell Interference Coordination*

IDFT *Inverse Discrete Fourier Transform*

IFFT *Inverse Fast Fourier Transform*

iid *Independent and identically distributed*

IMT *International Mobile Telecommunication*

IMT-Advanced *International Mobile Telecommunications-Advanced*

IP *Internet Protocol*

IoT *Internet of Things*

ISI *Inter-symbol interference*

IR *Incremental Redundancy*

ITU *International Telecommunication Union*

L1 *Layer 1: Physical Layer)*

LC *Low Correlation for MIMO Correlation Matrix (Uncorrelated MIMO channel)*

LLR *Log-Likelihood Ratio*

LMMSE *Linear Minimum Mean-Square Error*

LS *Least Squares*

LTE *Long Term Evolution*

LTE-Advanced *LTE Advanced*

LUT *Look-Up Table*

MAC *Medium Access Control*

MAP *Maximum a Posteriori Probability*

MBMS *Multimedia Broadcast and Multicast Service*

MBSFN *MBMS over Single Frequency Networks*

MC *Medium Correlation for MIMO Correlation Matrix*

MCH *Multicast Channel*

MCS *Modulation and Coding Scheme*

MCS i *Modulation and Coding Scheme index i*

MI *Mutual Information*

MIB *Mutual Information at bit level*

MIESM *Mutual Information based exponential SNR Mapping*

MIMO *Multiple-Input Multiple-Output*

3D-MIMO *Three-Dimensional MIMO*

ML *Maximum Likelihood*

MME *Mobility Management Entity*

MMIB *Mean Mutual Information at bit level*

MMSE *Minimum Mean Square Error*

MQAM *Multi-Level Quadrature Amplitude Modulation*

MRC *Maximal Ratio Combining*

MSE *Minimum Square Error*

MU *Multi-User*

MU-MIMO *Multi-User MIMO*

MUX *Multiplexer*

No *Noise power spectral density*

NACK *Negative Acknowledgement*

NLOS *Non-line-of-sight propagation*

NodeB *UMTS Base Transceiver Station*

OFDM *Orthogonal Frequency Division Multiplexing*

OFDMA *Orthogonal Frequency Division Multiple Access*

OL *Open-Loop*

PAPR *Peak-to-Average Power Ratio*

PBCH *Physical Broadcast Channel*

PCCC *Parallel Concatenated Convolutional Code*

PCFICH *Physical Control Format Indicator Channel*

PCH *Paging Channel*

PDCCH *Physical Downlink Control Channel*

E-PDCCH *Enhanced PDCCH*

pdf *Probability density function*

PDP *Power Delay Profile*

PDU *Protocol Data Unit*

PDSCH *Physical Downlink Shared Channel*

PEP *Pairwise Error Probability*

PHY *Physical Layer*

PHICH *Physical Hybrid ARQ Indicator Channel*

PMCH *Physical Multicast Channel*

PMI *Precoding Matrix Indicator*

PRACH *Physical random access channel*

PRB *Physical Resource Block*

PRS *Positioning reference signal*

PSK *Phase-shift keying*

PUCCH *Physical Uplink Control Channel*

PUSCH *Physical Uplink Shared Channel*

QAM *Quadrature Amplitude Modulation*

QPP *Quadratic Permutation Polynomial*

QPSK *Quadrature Phase Shift Keying*

QoS *Quality of Service*

RAN *Radio Access Network*

RACH *Random Access Channel*

RB *Resource Block*

RBIR *Received Bit Information Rate*

RBG *Resource Block Group*

RE *Resource Element*

RF *Radio Frequency*

RLC *Radio Link Control*

RNC *Radio Network Controller*

RRM *Radio Resource Management*

RRC *Radio Resource Control*

RS *Reference Signal*

rv *redundancy version*

rv= x *Redundancy Version x*

rv= 0 *Redundancy Version 0*

rv= 1 *Redundancy Version 1*

rv= 2 *Redundancy Version 2*

rv= 3 *Redundancy Version 3*

Rx *Receiver*

RI *Rank Indicator*

rms *root mean square*

S1 *interface between eNodeB and aGW*

SC-FDMA *Single Carrier-Frequency Division Multiple Access*

SCH *Shared Channel*

SFBC *Space Frequency Block Coding*

SFN *Single Frequency Network*

SIC *Successive Interference Cancellation*

SIMO *Single-Input Multiple-Output*

SISO *Single-Input Single-Output*

SINR *Signal to Interference plus Noise Ratio*

SM *Spatial Multiplexing*

SNR *Signal to Noise Ratio*

STBC *Space Time Block Coding*

SU *Single-User*

SU-MIMO *Single-User MIMO*

SVD *Singular Value Decomposition*

TB *Transport Block*

TBS *Transport Block Size*

TCP/IP *Transmission Control Protocol/Internet Protocol*

TD *Transmit Diversity*

TDD *Time Division Duplex*

TM *Transmission Mode*

TTI *Transmission Time Interval*

Tx *Transmitter*

UBER *Uncoded Bit Error Rate*

UE *User Equipment*

UL *Uplink*

UL-SCH *Uplink Shared Channel*

UPA *Uniform Power Allocation*

UTRA *UMTS Terrestrial Radio Access*

UTRAN *UMTS Terrestrial Radio Access Network*

UMTS *Universal Mobile Telecommunications System*

UPE *User Plane Entity*

VRB *Virtual Resource Block*

VoIP *Voice over IP*

X2 *interface between* evolved NodeBs *(eNodeBs)*

WiMAX *Worldwide Interoperability for Microwave Access*

WCDMA *Wideband Code Division Multiple Access*

WF *Wiener Filter*

ZF *Zero Forcing*

Chapter 1

Introduction

1.1 Motivation and Scope of the Dissertation

Third Generation Partnership Project (3GPP) *Long Term Evolution* (LTE) is the evolution of the *Third Generation of Mobile Communications Technology* (3G), i.e. *Universal Mobile Telecommunications System* (UMTS), towards the *Fourth Generation of Mobile Communications Technology* (4G), that is essentially a 4G mobile broadband system with Internet, voice and other services built on top. The LTE specifications are formally known as the *Evolved UMTS Terrestrial Radio Access* (E-UTRA) and the *Evolved* UMTS Terrestrial Radio Access Network (E-UTRAN) and the initial requirements of LTE are presented in [6]. LTE is designed to increase data rates and cell edge bitrates, improve spectrum efficiency and allow spectrum flexibility. LTE also reduces the radio access network cost and the packet latency, the main restriction for real-time services, such as *Voice over IP* (VoIP) or videoconferences. Furthermore LTE simplifies its network to a flat all-*Internet Protocol* (IP) packet-based network architecture where all the user plane radio functionalities are terminated at the eNodeB.

The LTE standardization activity is an ongoing task to build up a framework for the evolution of the 3GPP radio technologies towards the 4G and beyond. 3GPP started to work on the evolution of the UMTS with the *Radio Access Network* (RAN) evolution workshop in 2004 and the functional freezes of LTE as part of Release 8 and Release 9 were approved in 2008 and 2009, respectively. Therefore, this landmark achievement allowed the operators to realize their early LTE deployment plans. However, the evolution of this technology continued and, in 2010, LTE was enhanced by LTE Release 10, also known as *LTE Advanced* (LTE-Advanced), to meet or exceed the *International Telecommunication Union* (ITU) requirements for *International Mobile Telecommunications-Advanced* (IMT-Advanced) [7].

The key point of LTE is the specification of an extremely flexible radio interface based on *Orthogonal Frequency Division Multiplexing* (OFDM) technology with *Multiple-Input Multiple-Output* (MIMO) antenna processing, where all services are supported on packet based shared transport channels. The application of MIMO-OFDM technologies is one of the most important difference between 3G and 4G and the study of their performance is crucial to maximize network capacity. In order to provide a higher capacity, LTE evolves to LTE-Advanced mainly by increasing the peak data rate, the spectral efficiency and the number of simultaneously active subscribers and improving the usage of MIMO techniques and the performance at cell edges. The starting point of LTE-Advanced is the Release 10, however the LTE/LTE-Advanced technology is continuously enhanced by adding new techniques and improving existing ones. Indeed the enhancements for LTE-Advanced continues on Releases 11 and 12, and nowadays, the evolution of specifications is moving towards *Fifth Generation of Mobile Communications Technology* (5G).

Undoubtedly the LTE and LTE-Advanced innovations open important research challenges related to the optimization and performance assessment of the *Physical Layer* (PHY) and *Medium Access Control* (MAC) layers. The objective of this dissertation is the link level performance evaluation and the link abstraction for LTE and LTE-Advanced. This work requires developing the algorithms and software tools to characterize and evaluate the link level performance of LTE and LTE-Advanced taking into account their key technologies: MIMO-OFDM, Channel Coding, HARQ and *Adaptive Modulation and Coding* (AMC). Particularly *Downlink* (DL) *Single-User MIMO* (SU-MIMO) *Transmission Mode*s (TMs) are evaluated, channel estimation is considered and a link abstraction method is proposed to predict the *Block Error Rate* (BLER) that is used for the link adaptation. This work is split into different partial objectives that are listed below:

- Describe the LTE/LTE-Advanced air interface main features.
- Develop a LTE/LTE-Advanced Link Level Simulator.
- Describe and analyse the signal model and link level processing for transport and physical channels.
- Evaluate and model the channel estimation error for the LTE and LTE-Advanced Reference Signals.
- Evaluate the LTE and LTE-Advanced *Single-Input Single-Output* (SISO) link level performance for *Additive white Gaussian noise* (AWGN) channel as reference case.
- Evaluate the LTE and LTE-Advanced MIMO link level performance with ideal channel estimation.
- Evaluate the LTE and LTE-Advanced MIMO link level performance with imperfect channel estimation.
- Analyse the link adaptation taking into account the AMC schemes and TMs of LTE and LTE-Advanced.
- Propose a novel link abstraction method to predict the BLER with good accuracy in multipath fading and including the effects of HARQ retransmissions.

1.2 Dissertation Outline

This dissertation is divided into seven chapters:

Firstly Chapter 1 corresponds to the introduction describing the motivation, the scope, the outline, the contributions and publications of this dissertation. Chapter 2 presents the background of the LTE/LTE-Advanced Air Interface to understand its main characteristics.

Chapter 3 describes the methodology for developing the LTE/LTE-Advanced link level simulator and the signal models assumed for link level processing of transport and physical channels. Fourthly, Chapter 4 proposes a channel estimation error model to be used in link level simulations and evaluates its performance based on LTE/LTE-Advanced *Reference Signal*s (RSs) distribution.

Chapter 5 evaluates the link level performance results from the point of view of ideal channel estimation and imperfect channel estimation, respectively. Specifically, Section 5.1 presents and validates the AWGN Reference BLER curves for the LTE/LTE-Advanced *Modulation and Coding Schemes* (MCSs) and *Channel Quality Indicators* (CQIs), evaluates the AWGN channel throughput and link adaptation performances and, lastly, shows the MIMO link level performance under ideal channel estimation. In addition, Section 5.3 evaluates the effects of imperfect channel estimation on the MIMO link level performance.

Chapter 6 proposes a novel link abstraction method to predict the BLER with good accuracy in multipath fading and including the effects of HARQ retransmissions. The proposed method is based on estimating the *Mutual Information* (MI) between the transmitted bits and the received *Log-Likelihood Ratios* (LLRs). It is shown that, by working at bit level, the effect of unequal error protection in *16-Quadrature Amplitude Modulation* (16QAM) and *64-Quadrature Amplitude Modulation* (64QAM) modulations is properly captured without resorting to any set of calibration constants. It is also shown how to reduce the set of reference BLER curves when working with multiple MCSs. Lastly the simulation results for LTE/LTE-Advanced DL taking into account SISO and 2×2 MIMO TMs are presented.

Finally, Chapter 7 summarizes the concluding remarks of each chapter of this dissertation and gives the main conclusions and recommendations obtained in this work.

1.3 Dissertation Publications

This Dissertation is focussed on developing a DL link level simulator and evaluating the LTE/LTE-Advanced link level performance. In order to do that, the LTE/LTE-Advanced key technologies are considered and different techniques are implemented such as MIMO processing, MIMO precoding, *Successive Interference Cancellation* (SIC) techniques, link abstraction methods, etc. The work of this dissertation has contributed to the publications listed below.

For the development of a LTE link level simulator:

- Joan Olmos, Albert Serra, Silvia Ruiz, Mario García-lozano, and David Gonzalez. Link Level Simulator for LTE Downlink. In *COST 2100 TD(09)779*, 2009, [8].

For the study of optimum link abstraction methods:

- Joan Olmos, Albert Serra, Silvia Ruiz, Mario García-lozano, and David Gonzalez. Exponential Effective SIR Link Performance Model for LTE Downlink. *COST 2100 TD09)874*, 2009, [9].
- Joan Olmos, Albert Serra, Silvia Ruiz, Mario García-lozano, and David Gonzalez. Exponential Effective SIR Metric for LTE Downlink. *20th IEEE International Symposium On Personal, Indoor and Mobile Radio Communications*, pages 900–904, 2009, [10].
- Joan Olmos, Albert Serra, Mario García-lozano, Silvia Ruiz, and David Pérez Díaz De Cerio. Simulation of LTE IR H-ARQ at System Level Using MIESM Error Prediction. *IC1004 TD(11)02072*, 2011, [11].

- Joan Olmos, Albert Serra, Silvia Ruiz, and Imran Latif. On the Use of Mutual Information at Bit Level for Accurate Link Abstraction in LTE with Incremental Redundancy H-ARQ. In *IC1004 TD(12)05046*, 2012, [12].

For the study of how to model channel estimation error for link level simulations:

- Albert Serra, Joan Olmos, and Maria Lema. Modelling Channel Estimation Error in LTE Link Level Simulations. *IC1004 TD(12)03067*, 2012, [13].

Additionally, the work of this dissertation has contributed to the simulation and study of the LTE system level:

- David González, Silvia Ruiz, Joan Olmos, and Albert Serra. System Level Evaluation of LTE Networks with Semidistributed Intercell Interference Coordination. In *IEEE 20th International Symposium on Personal, Indoor and Mobile Radio Communications*, 2009, [14].
- David Gonzalez, Joan Olmos, Silvia Ruiz, and Albert Serra. Downlink Inter-Cell Interference Coordination and Scheduling for LTE Featuring HARQ over Multipath Fading Channel. pages 1–5, 2009, [15].
- David Gonzalez, Silvia Ruiz, Joan Olmos, and Albert Serra. Link and System Level Simulation of Downlink LTE. In *COST 2100 TD(09)734*, 2009, [16].

Lastly, for the definition of reference scenarios for LTE/LTE-Advanced link level simulations:

- Joan Olmos, Albert Serra, and Silvia Ruiz. On the Definition of Reference Scenarios for LTE-A Link Level Simulations within COST IC1004. In *IC1004 TD(13)06043*, 2013, [17].

Chapter 2

Background for LTE/LTE-Advanced Air Interface

In this chapter, we give the background of the LTE/LTE-Advanced air interface to understand its main characteristics. We start introducing the LTE/LTE-Advanced air interface and the enabling technologies for LTE/LTE-Advanced. Next we give a brief overview of the evolution of the 3GPP technology. We then present the physical layer and the transmission modes of the LTE/LTE-Advanced. Finally, some basic concepts of MI and channel capacity are reviewed and an equivalent binary channel model is introduced and characterized by means on the input-output MI. Furthermore, the MI curves for the LTE modulations are obtained.

2.1 LTE/LTE-Advanced Air Interface Overview

LTE and LTE-Advanced are essentially cellular broadband Internet systems with voice and other multimedia services built on top such as Internet TV, video calls, live streaming and high speed downloads or uploads of any data. In 2004 3GPP started to study the evolution of UMTS to LTE in order to ensure competitiveness and make possible to deliver next generation high quality multimedia services according to the users' expectations [18].

The starting point of LTE was first focused on the feasibility studio described in [1]. The collection of requirements to define the targets for the evolution of the radio-interface and radio-access network architecture is defined in [6]. Basically LTE places high priority on improving the spectral efficiency, increasing the data rate, reducing the latency and reducing cost. In order to fulfil the requirements, the key enablers of LTE are the usage of orthogonal multiple access schemes, adaptive modulation and coding, multi-antenna techniques, HARQ technology and distributed or localized radio resource allocation techniques.

The LTE network architecture is a flat all-IP architecture called *Evolved Packet System* (EPS) which comprises E-UTRAN, the radio access network, and the *Evolved Packet Core* (EPC), the 3GPP core network architecture. A representation of the E-UTRAN architecture is shown in Figure 2.1. E-UTRAN comprises E-UTRA (the air interface of LTE), eNodeBs and *User Equipment*s (UEs). The eNodeBs are interconnected by means of the *interface between eNodeBs* (X2) interface and are also connected by means of the *interface between eNodeB and aGW* (S1) interface to the EPC. In addition radio protocols finish at eNodeB and there is not any centralized radio management entity, i.e, *Radio Network Controller* (RNC) disappears in LTE. In contrast, in *UMTS Terrestrial Radio Access Network* (UTRAN) the RNC controls its *UMTS Base Transceiver Station*s (NodeBs) and the UMTS radio protocols do not finish at NodeBs.

One of the main features of E-UTRAN is that all services, including real-time services, are supported over shared packet channels. This approach allows to achieve increased spectral effi-

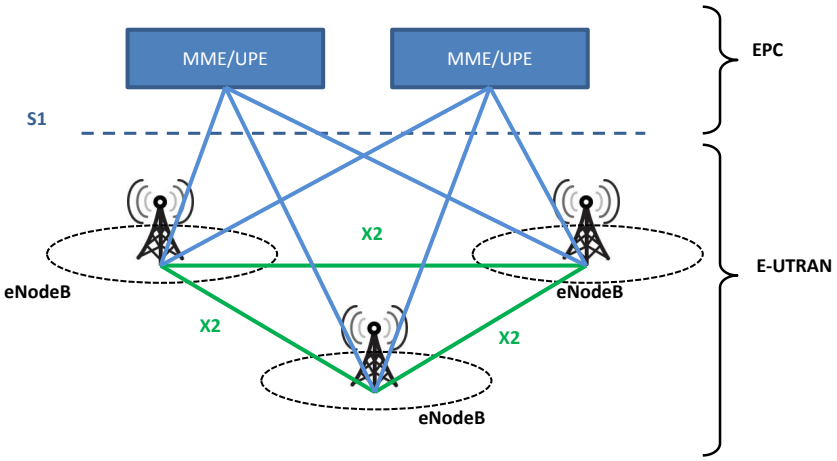

Figure 2.1: E-UTRAN architecture, [1].

ciency, which turns into higher system capacity with respect to UMTS and *High-Speed Packet Access* (HSPA). The use of packet access for all services also leads to better integration among all multimedia services and among wireless and fixed services. Low user-plane latency, defined as the RAN round-trip delay, is important in order to achieve high bitrate for data services. This low latency is partially achieved thanks to the specification of a *Transmission Time Interval* (TTI) of 1 ms and because E-UTRAN is supported through EPC where all the user-plane radio related functionalities are placed at the eNodeBs.

The multiple access schemes used by the radio interface of LTE are *Orthogonal Frequency Division Multiple Access* (OFDMA) in the DL and *Single Carrier-Frequency Division Multiple Access* (SC-FDMA) in the *Uplink* (UL). OFDMA and SC-FDMA share some common features, like the easiness of modulation/demodulation by means of *Fast Fourier Transform* (FFT), the use of a *Cyclic Prefix* (CP) to absorb the channel transient response between consecutive modulation symbols, the possibility of equalization in the frequency domain and easy integration with multiple antenna techniques, i.e., MIMO. Frequency domain equalization is a key issue, since LTE radio-channels can use a bandwidth up to 20 MHz. OFDM shows inherent frequency diversity if a coded block is sent on a set of subcarriers spanning a bandwidth higher that the channel coherence bandwidth. In contrast, SC-FDMA is used in UL because it has a lower *Peak-to-Average Power Ratio* (PAPR) than OFDM and reduces the need for high linearity at the power amplifier of the UE.

Within the OFDMA and SC-FDMA signal AMC is applied with three modulation schemes (*Quadrature Phase Shift Keying* (QPSK), 16QAM and 64QAM) and variable code rate using turbo coding. AMC allows delivering the desired throughput to the users at the cell border while achieving high spectral efficiency for users near the eNodeB. Turbo coding allows near to Shannon performance *Forward Error Correction* (FEC) for high bitrate users. Furthermore, the addition of channel coding and MIMO-OFDM enables several diversity modes to fight spectral nulls due to multipath.

Another key aspect of the LTE radio interface is the use of HARQ with *Incremental Redundancy* (IR) and link adaptation. HARQ is a fast retransmission technique performed at the MAC level and link adaptation is performed via HARQ and AMC. In addition, HARQ helps to achieve a low latency in conjunction with the TTI of 1 ms and smooths the AMC throughput curves, thus allowing less frequent switching between AMC formats. The combination of HARQ, MIMO and 64QAM provides high rate and high spectral efficiency.

MIMO techniques are well integrated into the LTE physical layer from the beginning and play an important role in fulfilling the LTE requirements on increased data rates and improved coverage and capacity. The MIMO schemes standardized for LTE include transmit diversity schemes as well as spatial multiplexing modes. Within the MIMO spatial multiplexing modes, a maximum of four and eight spatial layers can be used for LTE and LTE-Advanced DL, respectively; however, only two independent codewords can be transmitted at the same time. A codeword is a block of turbo encoded bits that is transmitted in one TTI. The eNodeB can use feedback from the UE in order to select a MIMO precoding matrix within a predefined set *Closed-Loop* (CL)-MIMO, or to rely on *Open-Loop* (OL)-MIMO, where a fixed precoding matrix is applied. The precoding matrix can be seen as a set of adaptive complex weights applied at the eNodeB antenna ports aimed to improve the MIMO post-processing signal to noise ratio at the UE.

The LTE and LTE-Advanced standards inherit all the frequency bands defined for UMTS and also cover new bands as defined in [19] and [20]. These bands are divided into *Frequency division duplexing* (FDD) and *Time Division Duplex* (TDD) bands to separate UL and DL traffic. Anyway, this dissertation only considers the DL FDD case using the 2.14 GHz band for the link level performance evaluation. Another feature out of the scope of this dissertation is that LTE-Advanced Release 12 has introduced a higher order modulation: *256-Quadrature Amplitude Modulation* (256QAM).

2.2 Enabling Technologies for LTE/LTE-Advanced

The key features of LTE physical layer are the usage of OFDMA for the DL, SC-FDMA for the UL, MIMO, HARQ and AMC to perform link adaptation. An overview of these enabling technologies for LTE is given below.

2.2.1 OFDM

The OFDM modulation is a frequency-division multiplexing scheme utilized as a digital multi-carrier modulation method that has been used successfully in wire-line access applications, such as *Digital Subscriber Line* (DSL) modems and cable modems, as well as in wireless systems such as *Worldwide Interoperability for Microwave Access* (WiMAX) and *Digital Video Broadcasting* (DVB). OFDM-based transmission is used to overcome the challenges of *Non-line-of-sight propagation* (NLOS) propagation because OFDM is a technology that has been shown to be well suited to the mobile radio environment for high rate and multimedia services [21].

OFDM achieves high data rate and efficiency by using multiple overlapping carrier signals instead of just one carrier. The key advantage of OFDM over single carrier modulation schemes is the equalization in frequency domain due to the ability to subdivide the bandwidth into multiple frequency subcarriers which carry the information streams, are orthogonal to each other and deliver

higher bandwidth efficiency. Therefore OFDM allows higher data throughput even in the face of challenging scenarios such as NLOS links suffering from significant degradation because of multipath conditions. Usually, a guard time is added in each OFDM symbol to combat the channel delay spread. The term delay spread describes the amount of time delay at the receiver from a signal travelling from the transmitter along different paths. The delay induced by multipath can cause a symbol received along a delayed path to interfere with subsequent symbol arriving at the receiver via a more direct path. This effect is referred to as *Inter-symbol interference* (ISI).

The guard time may be divided into a prefix (inserted at the beginning of the useful OFDM symbol and called *Cyclic Prefix* (CP)) and a postfix (inserted at the end of the previous OFDM symbol). The introduction of the CP can eliminate ISI in the time domain as long as the CP duration is longer than the channel delay spread. The CP is typically a repetition of the last samples of data portion of the OFDM block that is appended to the beginning of the data payload and makes the channel appear circular in order to permit low-complexity frequency domain equalization.

OFDM signal generation consists of multiplexing the original data stream into N_c parallel data streams; then and each of the data streams is modulated with a different subcarrier frequency using linear modulation (either *Phase-shift keying* (PSK) or *Quadrature Amplitude Modulation* (QAM)). Then, the resulting signals are transmitted together in the same band. Correspondingly, the receiver consists of N_c parallel receiver paths because of the N_c equally spaced orthogonal subcarriers of OFDM symbol behaves as N_c independent narrowband flat fading channels. In short, OFDM converts the wideband frequency selective fading channel into N_c narrowband flat fading channels thus the equalization can be performed in the frequency domain by a scalar division carrier-wise with the subcarrier related channel coefficients. This fact reduces dramatically the equalization complexity.

The subcarrier pulse used for OFDM transmission is chosen to be rectangular and this has the advantage that the task of pulse forming and modulation can be performed by a simple *Inverse Discrete Fourier Transform* (IDFT) at the transmitter. In practice, the IDFT is implemented very efficiently as an *Inverse Fast Fourier Transform* (IFFT) that keeps the spacing of the subcarriers ortoghonal. Accordingly at the receiver we only need a FFT to reverse this operation but the receiver and the transmitter must be perfectly synchronized. Therefore, according to the theorems of the Fourier Transform, the rectangular pulse shape will lead to a sinc type of spectrum of the subcarriers. Although the subcarriers spectrum overlap, the information transmitted can still be separated because of the orthogonality relation between subcarriers.

Figure 2.3 shows the block diagram of an OFDM based transmission system with one single antenna at the transmitter and one at the receiver. How to characterize a multipath radio channel for OFDM systems is described in [22]. Additionally, how to create the mobile channel models to be used for 3GPP deployment evaluation is explicitly described in [23] where simplifications in order to reduce the computational cost and the complexity of the simulations are presented.

The OFDM modulation accepts several configurations in LTE/LTE-Advanced: the subcarrier spacing can be 15 kHz or 7.5 kHz, this last for *evolved Multimedia Broadcast and Multicast Service* (eMBMS) subcarriers and *Single Frequency Networks* (SFNs). The normal CP duration is about 5 μs but it is also possible to use an extended cyclic prefix of 17 μs (for rural cells) and 33 μs for

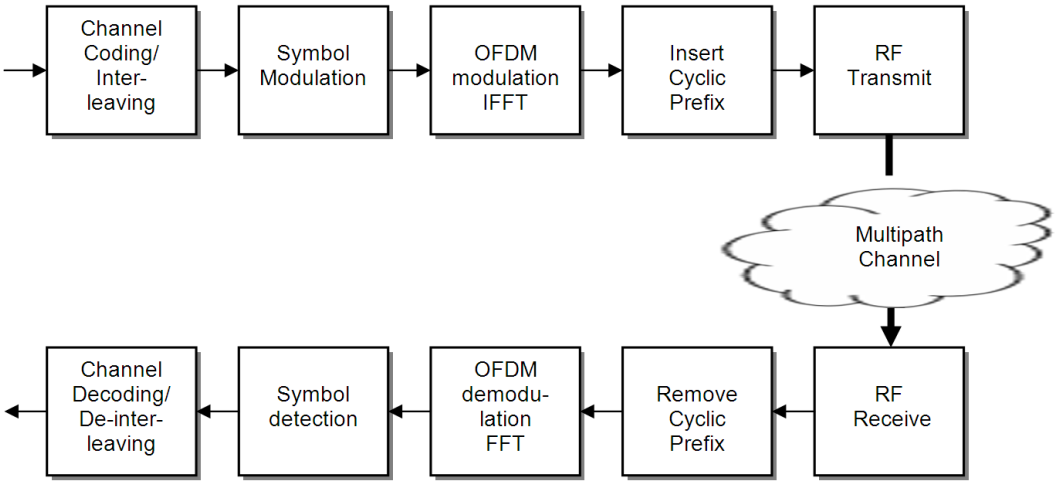

Figure 2.2: Block Diagram of a SISO-OFDM based transmission system

eMBMS. With the normal CP there are 14 OFDM symbols per subframe (1 ms), while for the extended CP there are only 12 OFDM symbols per subframe. The available PHY capacity per subframe depends on the room reserved for control channels and RSs (pilots).

LTE and LTE-Advanced use OFDMA as multiple access scheme for DL because of its robustness to multipath propagation in wideband channels, inherent support for frequency diversity and easiness integration with MIMO antenna schemes. OFDMA applies the same OFDM principles in order to allocate different groups of subcarriers simultaneously to different users. In OFDMA the orthogonality of the subcarriers at the reception depends only on the channel effects, which can be equalized. The time and frequency synchronism is accurate because the OFDMA signal comes from a single transmitter. However, the main disadvantage of OFDMA is its high power peak to average power or PAPR which requires to keep the distortion of the power amplifier bounded.

In contrast to DL, SC-FDMA is used as multiple access scheme for UL. SC-FDMA has lower PAPR than OFDMA and so it does not require a high linear range of the power amplifier, and consequently, the processing complexity and the battery consumption at UE is reduced. Furthermore, SC-FDMA keeps the orthogonality relation between subcarriers of different users, can be equalized in the frequency domain, is compatible with MIMO techniques and allows to use the same time and frequency resource structure than in the DL [24].

2.2.2 MIMO

MIMO is a smart antenna technique based on the use of multiple antennas at both the transmitter and receiver to improve radio link communication performance. MIMO technology is considered in the new wireless communications standards such as 3GPP LTE or WiMAX since it offers significant increases in data throughput and link range without additional bandwidth or transmit power. It achieves this by allowing higher spectral efficiency (more bits per second per hertz of bandwidth) and link reliability or diversity (reduced fading).

The MIMO technique in combination with OFDM has been shown as a good approach for high spectral efficiency wideband systems because OFDM technique simplifies the receiver structure by decoupling frequency selective MIMO channel into a set of parallel flat fading channels. The fading process experienced by each subcarrier is close to frequency flat, and therefore, it can be modeled as a constant complex gain. This consideration allows to obtain the MIMO channel matrix on a subcarrier basis and thus simplify the implementation of a MIMO scheme. The MIMO-OFDM basics are described in [25, 26, 27, 28, 29] and [30]. Figure 2.3 shows the block diagram of a MIMO-OFDM based transmission system where N_{RX} and M_{TX} are the number of antennas at the transmitter and at the receiver, respectively.

MIMO techniques can be divided into *Transmit Diversity* (TD) and *Spatial Multiplexing* (SM) techniques and it depends on the channel condition which MIMO technique to select. TD increases coverage and *Quality of Service* (QoS) because relies on transmitting multiple redundant copies of a data stream to the receiver; while SM increases the spectral efficiency because transmits independent and separately data streams from each of the multiple antennas. Apart from that, MIMO may be used to reduce co-channel interference and provide an array gain, what is called beamforming.

MIMO systems present two modes of operation, OL and CL. While an OL MIMO system only knows the *Channel State Information* (CSI) at the receiver side, CL MIMO systems also know the CSI at the transmitter side which can be used to improve the throughput and reliability of the MIMO system. The estimation of CSI is based on pilot symbols. UEs can report back to the eNodeB the CSI to use for the next transmissions, provided that the channel variation due to mobile speed and environmental changes is slow.

OL MIMO SM can employ different strategies of detection at the receiver side. Those strategies are basically divided into linear detectors, such as *Zero Forcing* (ZF) and *Minimum Mean Square Error* (MMSE), or non-linear detectors, such as *Maximum Likelihood* (ML) or SIC. Examples of OL TD are *Space Time Block Coding* (STBC) and *Space Frequency Block Coding* (SFBC). Here the most known technique is the Alamouti code for the case of 2 antennas at the transmitter [31]. The STBC and SFBC techniques consist on sending the data stream from each of the transmit antennas using certain principles of full or near orthogonal coding. The diversity is obtained by exploiting the fact of independent fading in the multiple antenna links to enhance the *Signal to Noise Ratio* (SNR).

A CL MIMO system has knowledge of the channel at the transmitter. This allows to perform a MIMO precoding at the transmitter based on a precoding weight matrix selected from a set of matrices called "codebook". In particular, the codebook matrix selection is based on the channel estimation performed at the receiver side which then feedbacks the best precoding matrix to maximize the capacity.

2.2.3 HARQ and Channel Coding

The slow fading of the mobile wireless channel can be partially compensated using link adaptation and scheduling techniques. However, the fast fading, the receiver noise and the user interferences cannot be completely corrected and a retransmission technique of erroneous packets is needed. LTE and LTE-Advanced use the HARQ technique which combines FEC, implemented

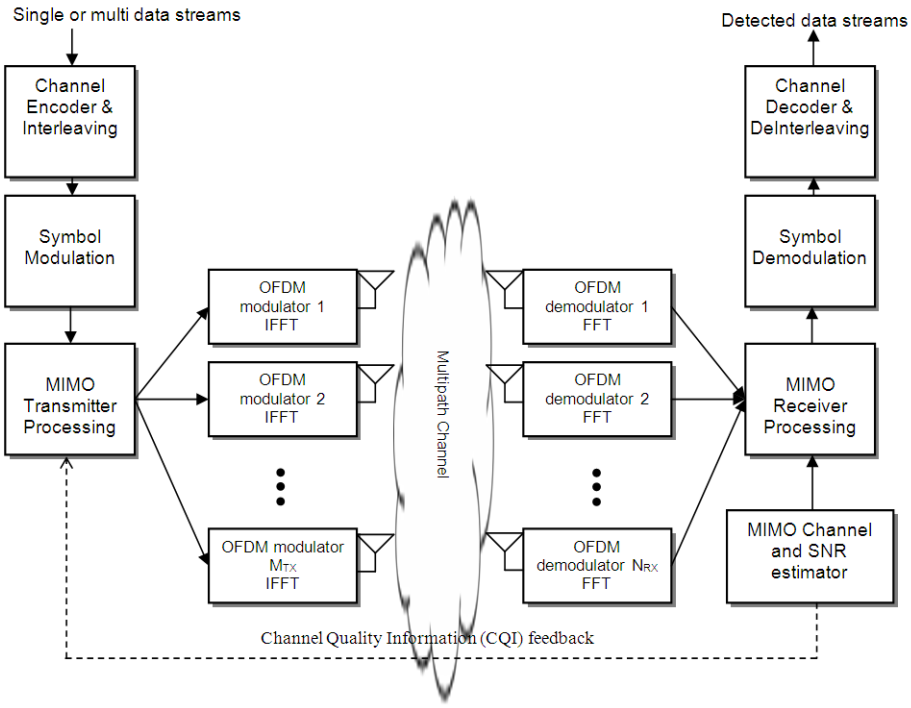

Figure 2.3: Block Diagram of a $N_{RX} \times M_{TX}$ MIMO-OFDM based transmission system

by the Channel Coding, and *Backward Error Correction* (BEC), implemented by the *Automatic Repeat Request* (ARQ) error control. In particular, the retransmissions are performed at MAC level and the retransmitted packets are soft combined at the receiver. This is called HARQ with soft combining [32]. In the case of LTE and LTE-Advanced Turbo Coding and *Cyclic Redundancy Check* (CRC) are used by the FEC and BEC implementation respectively.

In HARQ with soft combining, the erroneously received packet is not discarded and stored in a buffer memory and later combined with the retransmission to obtain a single coded block which is more reliable than its constituents. The process of receiving, storing and combination of retransmissions stops when decoding is successful or a maximum number of retransmissions is reached (4 for LTE and LTE-Advanced). Thus, a retransmission is requested only if the decoding fails. A CRC code is used to detect this event.

The set of information bits to be transmitted in a TTI forms the transport block which is coded to form another set of coded bits called a codeword. The coded bits are divided into systematic and the parity bits, while systematic bits can be used to recover the original information whenever the SNR is high, the parity bits add redundancy. At the first transmission, the systematic bits and only a part of the parity bits are sent. If retransmission is needed, then the same or other coded bits can be sent. There are two main soft combining methods in HARQ:

- **HARQ type I**: HARQ with Chase Combining. Each retransmitted packet is an exact replica of the initial transmission packet and contains the same systematic and parity bits identical to the first transmission. In addition, each received packet is decodable by itself and is combined with previous received packets by applying *Maximal Ratio Combining* (MRC)

which has a multiplying effect on the SNR. Therefore, this method does not introduce redundancy to the transmitted packet, it just increases the received SNR.

- **HARQ type II**: HARQ with Full Incremental Redundancy. This type of HARQ uses an incremental redundancy scheme and, consequently, each retransmitted packet contains additional redundant information that is different from the previous one. This additional redundancy is combined with the previous received packets obtaining a sequence of bits with higher amount of redundancy that increases the probability to decode correctly the received information.

LTE and LTE-Advanced use HARQ type II as retransmission mechanism. Each transmitted packet is characterized by a redundancy version number from 0 to 3, which defines the subset of coded bits in the codeword to be transmitted. The transmitter and receiver know the maximum number of transmissions of the same code block and the redundancy version sequence, such as 0, 1, 2, 3.

HARQ is a stop and wait protocol, i.e, the transmitter must wait to receive an *Acknowledgement* (ACK) or a *Negative Acknowledgement* (NACK) before transmitting next transport block. In addition, a maximum number of active HARQ processes is allowed, for instance 6. Thus a continuous transmission is guaranteed, i.e., the transmitter can be waiting for ACKs or NACKs of six transport blocks at once [24].

The ARQ processing is handled by the MAC layer, while soft combining is handled by the PHY layer. The fact that HARQ with soft combining reduces the effective data rate based on the number of bad packets received, can be seen as an implicit adaptation of the transmission rate to the variation of the channel, i.e, as a complementary mechanism to link adaptation. The main disadvantage of HARQ is that it requires a certain amount of additional memory and processing capacity at the UE.

Channel coding is a method to reduce the BLER at the expense of a reduction of the user information rate (throughput) and to increase reliability combining FEC and ARQ mechanisms. FEC tries to detect the errors and correct them using channel codes. According to the LTE standard [5], the transport channel downstream, called the *Downlink Shared Channel* (DL-SCH), uses Turbo Codes as the channel coding scheme with a mother code rate of 1/3.

2.2.4 Link Adaptation

Link Adaptation is the process by which the eNodeB, assisted by the UE, selects the *Modulation and Coding Scheme* (MCS) that will be used for DL transmission in the next TTI. Link Adaptation aims to adapt the information data rate for each UE to its current channel capacity. In order to achieve link adaptation in the DL the UE reports to the eNodeB the measured DL channel quality in the form of a set of 15 possible *Channel Quality Indicator*s (CQIs); then the eNodeB selects the most appropriate MCS from a set of 28 different formats. The selected MCS is signalled by means of a field of 5 bits (called MCS index) in the *Physical Downlink Control Channel* (PDCCH) preceding the *Physical Downlink Shared Channel* (PDSCH) subframe that carries the DL user plane information. Table 2.1 shows the CQI indices and their interpretations for reporting CQI based on QPSK, 16QAM and 64QAM and Table 2.2 shows the MCS indices to determine the

modulation order and the *Transport Block Size* (TBS) index, [33]. The procedure for the UL is similar; with the difference that the eNodeB is able to measure the UL channel quality based on sounding reference signals sent from the mobile terminal and then command it to use the appropriate MCS.

Table 2.1: 4-bit CQI table based on QPSK, 16QAM and 64QAM

CQI Index	Modulation	Modulation Order	Code Rate x 1024	Efficiency	Code Rate
0	out of range				
1	QPSK	2	78	0.1523	0,076
2	QPSK	2	120	0.2344	0,117
3	QPSK	2	193	0.3770	0,189
4	QPSK	2	308	0.6016	0,301
5	QPSK	2	449	0.8770	0,439
6	QPSK	2	602	11.758	0,588
7	16QAM	4	378	14.766	0,369
8	16QAM	4	490	19.141	0,478
9	16QAM	4	616	24.063	0,602
10	64QAM	6	466	27.305	0,455
11	64QAM	6	567	33.223	0,554
12	64QAM	6	666	39.023	0,65
13	64QAM	6	772	45.234	0,754
14	64QAM	6	873	51.152	0,853
15	64QAM	6	948	55.547	0,926

LTE and LTE-Advanced perform link adaptation via AMC (explicit adaptation) and HARQ (implicit adaptation to errors) in a fast pace (each 2 slots, or 1 ms) providing data quickly and reliably using minimal resources. The addition of AMC and HARQ process allows to minimize the turnaround time and maximize the data throughput of the system. Inside each subcarrier AMC is applied with three modulation schemes (QPSK, 16QAM and 64QAM) and variable code rates to match the modulation and coding rate to the channel conditions that depend on the pathloss, user interferences, the receiver sensitivity, the available transmitter power margin, etc.

The UE measures the DL received signal quality using RSs and reports to the eNodeB the preferred MCS for each codeword. This report is signalled using a CQI index, and summarizes the measured signal quality and also the UE capabilities since the UE is signalling a MCS such that, given current channel conditions, the next codeword can be received with a BLER below 10%. Consequently, in order to produce meaningful CQI feedbacks, a suitable set of BLER vs. channel quality thresholds must be made available to the UE, [34].

In LTE the MCS is constant over all the allocated frequency resources of a particular user, but if two codewords are transmitted simultaneously using MIMO spatial multiplexing, then each codeword can use an independent MCS. For DL SU-MIMO transmission modes, even with OL-MIMO or with a TD scheme, *Precoding Matrix Indicator* (PMI) and *Rank Indicator* (RI) feedback

Table 2.2: Modulation and TBS index table for PDSCH based on QPSK, 16QAM and 64QAM

MCS Index	Modulation	Modulation Order	TBS Index
0	QPSK	2	0
1	QPSK	2	1
2	QPSK	2	2
3	QPSK	2	3
4	QPSK	2	4
5	QPSK	2	5
6	QPSK	2	6
7	QPSK	2	7
8	QPSK	2	8
9	QPSK	2	9
10	16QAM	4	9
11	16QAM	4	10
12	16QAM	4	11
13	16QAM	4	12
14	16QAM	4	13
15	16QAM	4	14
16	16QAM	4	15
17	64QAM	6	15
18	64QAM	6	16
19	64QAM	6	17
20	64QAM	6	18
21	64QAM	6	19
22	64QAM	6	20
23	64QAM	6	21
24	64QAM	6	22
25	64QAM	6	23
26	64QAM	6	24
27	64QAM	6	25
28	64QAM	6	26

from the UE is always needed to perform link adaptation in addition to CQI signalling, [35]. RI refers to the recommended number of layers to be transmitted simultaneously on the same time and frequency resources from the eNodeB to the UE. PMI is applied in CL-MIMO transmission modes. PMI provides the index of the recommended precoder matrix in the codebook for precoding assuming the number of layers indicated by RI.

2.3 3GPP technology evolution

Mobile communication systems have become ubiquitous systems used by everybody, and, in the near future, they will be used to connect machines and other appliances to the Internet in

what is known as "The Internet of Things". Mobile communication technologies are usually split into generations, and, in each stage, wireless technologies have been continuously reaching their limits in terms of capacity because of the growing success of broadband internet, the increasing usage of demanding multimedia services and the non-stop user demand for higher bit rates. In 2000, the specification of the European version of the 3G systems called UMTS was created by a collaboration between groups of telecommunications associations called 3GPP. Since then 3GPP standards have been evolved from UMTS to HSPA, to LTE, to now LTE-Advanced, the *Fourth Generation of Mobile Communications Technology* (4G). Figure 2.4 shows the timeline of the 3GPP technologies evolution. However, the 3GPP evolution will continue in the coming years with further enhancements to LTE-Advanced and getting ready for 5G.

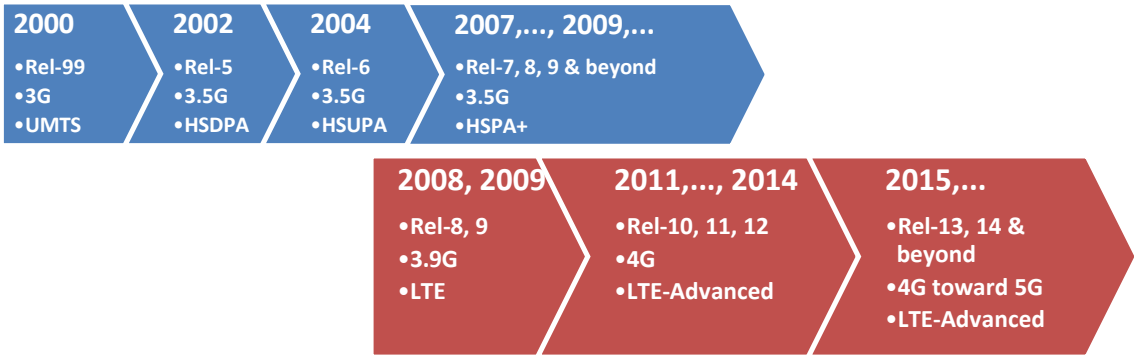

Figure 2.4: 3GPP Technology Evolution

UMTS was the 3G mobile cellular system for networks based on the *Global System for Mobile Communications* (GSM) standard which was specified in 3GPP Release 99. In contrast to GSM standard, UMTS uses *Wideband Code Division Multiple Access* (WCDMA) radio access technology to be more spectrally efficient and a bandwidth of 5 MHz, [36]. Next 3GPP release (Release 4) was the one which introduced the 1.28 Mcps TDD narrowband version of WCDMA, [37]. The next step was to upgrade WCDMA networks (both FDD, and TDD) to HSPA to increase data rates. Firstly Release 5 introduced *High-Speed Downlink Packet Access* (HSDPA) to allow higher downlink bit rates around 10 Mbps, [38]; and then Release 6 introduced *High-Speed Uplink Packet Access* (HSUPA) to enhance UL data rates. The evolution of HSPA, referred to as *Evolved HSPA* (HSPA+), [39], was defined in Releases 7 and 8 in order to further increase bitrates. Release 7 added new features, for instance, higher order modulation schemes (64QAM for DL and 16QAM for UL as well as MIMO (only used in DL)). The combination of MIMO with 64QAM in HSPA+ DL was introduced by Release 8. In addition Release 9 introduced the Dual Carrier HSDPA. Although in the releases after Release 8 HSPA+ keeps evolving, the main work after that has been the specification and evolution of LTE and LTE-Advanced. Table 2.3 shows the evolution of the 3GPP releases per year and the expected maximum channel rate.

The first release of LTE was Release 8 and it was finalized at the end of 2008. The main requirements are basically high spectral efficiency, high peak data rates, reduced latency and flexibility in frequency and bandwidth. Next, in 2009, LTE Release 9 introduced some enhancements and

Table 2.3: Evolution of 3GPP releases

Year	Standard Release	DL Max. Channel Rate	UL Max. Channel Rate	Max. Bandwidth	Radio Technology Novelties
2000	UMTS, Rel 99	384 Kbps	384 Kbps	5 MHz	WCDMA
2001	UMTS, Rel 4				1,28 Mcps TDD
2002	HSPA, Rel 6	14,4 Mbps	5,8 Mbps	5 MHz	HSDPA
2004	HSPA, Rel 7				HSUPA
2007	HSPA+, Rel 7	21 Mbps	11 Mbps	5 MHz	64QAM(DL), 16QAM(UL)
2008	HSPA+, Rel 8	42 Mbps	11 Mbps		MIMO with 64QAM(DL))
2009	HSPA+, Rel 9	84 Mbps	22 Mbps	10 MHz	Dual Carrier-HSDPA
2008	LTE, Rel 8	300 Mbps	75 Mbps	Scalable 1.4, 3, 5,	OFDMA(DL), SC-FDMA(UL)
2009	LTE, Rel 9			10, 15 or 20 MHz	MIMO, up to 64QAM
2011	LTE-Advanced, Rel 10	3 Gbps	1.5 Gbps	Carrier Aggregation	Advanced MIMO
2012	LTE-Advanced, Rel 11			up to 100 MHz (DL)	*Coordinated Multipoint* (CoMP)
2014	LTE-Advanced, Rel 12			up to 40 MHz (UL)	256QAM (DL)

a set of features which were not completed on Release 8. LTE-Advanced is the next step in the development of LTE technology and it is a major enhancement of LTE in order to meet the ITU requirements for IMT-Advanced [7]. The first Release of LTE-Advanced, introduced in 2010, is Release 10 and it is also backward compatible with LTE Release 8. The high level requirements are focussed on increased peak data rate, higher spectral efficiency, increased number of simultaneously active subscribers and improved performance at cell edges. In addition LTE-Advanced introduced new functionalities that are mainly carrier aggregation, enhancements of MIMO techniques and relay nodes. Table 2.4 shows a comparison of evolution of LTE and LTE-Advanced capacity requirements, [6, 5, 40].

Table 2.4: LTE and LTE-Advanced Capacity Requirements Comparison

Parameter		LTE	LTE-Advanced
Scalable Bandwidths		1.4, 3, 5, 10, 15, 20 MHz	20 - 100 MHz (with Carrier Aggregation)
Max Transmission Bandwidth	DL	20 MHz	100 MHz
	UL	20 MHz	40 MHz
Peak Data Rate	DL	100 Mbps	1 Gps
	UL	50 Mbps	500 Mbps
Spectral Efficiency	DL	5 bps/Hz	30 bps/Hz
	UL	2.5 bps/Hz	15 bps/Hz

Mobile communication technologies are coming toward 5G; thus LTE-Advanced is evolving to this milestone by adding new technology components and improving existing ones. The key features of LTE-Advanced Release 10 are carrier aggregation up to 100 MHz of bandwidth, enhanced MIMO techniques supporting SM up to 8 layers for DL and 4 layers for UL (to increase peak data rate), enhanced *Inter-cell Interference Coordination* (ICIC) for heterogeneous network and relaying [41]. Release 11 introduces basically CoMP, a new DL control channel (*Enhanced PDCCH* (E-PDCCH))

and LTE-Advanced enhancements such as enhancements on carrier aggregation and heterogeneous network. Next step is Release 12 whose its functional freeze including stable protocols is planned for March 2015. Release 12 defines new features and improvements. Amongst other novelties, 256QAM and *Three-Dimensional MIMO* (3D-MIMO) are introduced to enhance DL transmission [42, 43, 44]. The use of DL higher order modulation, i.e., 256QAM is found beneficial for small cell scenarios with low mobility [45]. The use of 3D-MIMO is also beneficial as a promising technique in massive MIMO networks to enhance the cellular performance [46].

2.4 Overview of LTE Physical Layer

2.4.1 Radio Interface Protocol Architecture

The LTE access network is simplified and reduced to only the base station eNodeB. The LTE radio interface covers the interface between the *User Equipment* (UE) and the network. The LTE radio interface architecture is composed of the layers 1, 2 and 3. Layer 1 is the physical layer and its specifications are described in the TS 36.200 series [2, 3, 4, 33, 47]. Figure 2.3 shows the E-UTRA radio interface protocol architecture around the physical layer which is presented in [2].

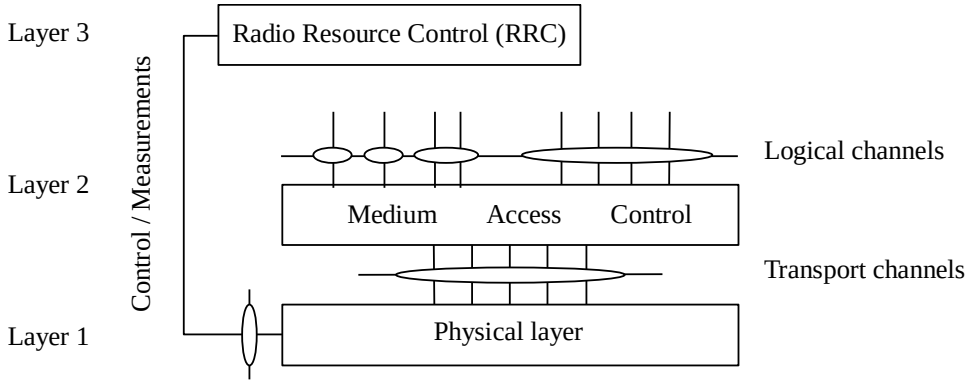

Figure 2.5: Radio interface protocol architecture around the physical layer [2]

The LTE air interface consists of physical channels and physical signals which are defined in [3] and are generated by the LTE physical layer. Physical channels carry data from higher layers including control, scheduling and user payload and physical signals are used for system synchronization, cell identification and radio channel estimation. Figure 2.6 shows the mapping from transport channels to physical channels in E-UTRA [4].

The transport channels are defined in [4] and are generated by the MAC layer. The type of transport channels are *Broadcast Channel* (BCH), DL-SCH, *Paging Channel* (PCH) and *Multicast Channel* (MCH) for DL and *Uplink Shared Channel* (UL-SCH) and *Random Access Channel* (RACH) for UL. The channels used to transport user data or control messages are DL-SCH and UL-SCH.

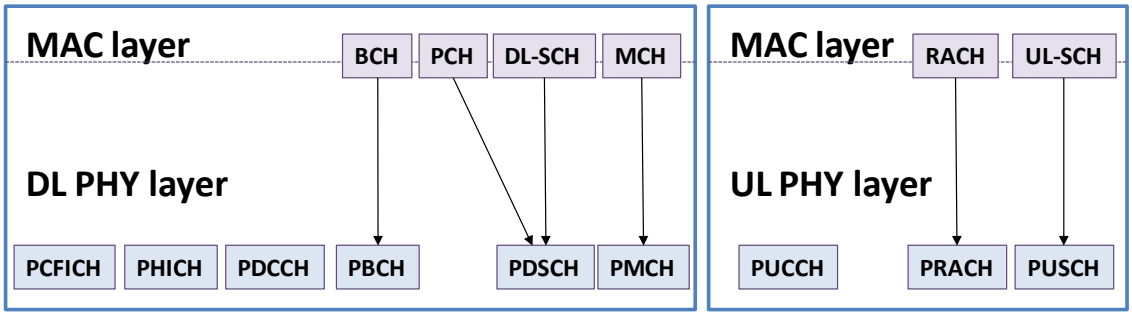

Figure 2.6: LTE mapping from transport to PHY channels

The types of DL physical channels are PDSCH, *Physical Broadcast Channel* (PBCH), *Physical Multicast Channel* (PMCH), *Physical Control Format Indicator Channel* (PCFICH), *Physical Downlink Control Channel* (PDCCH) and *Physical Hybrid ARQ Indicator Channel* (PHICH). The types of uplink physical channels are *Physical random access channel* (PRACH), *Physical Uplink Control Channel* (PUCCH) and *Physical Uplink Shared Channel* (PUSCH). Concerning to physical signals, there are two types of signals, *Reference Signal*s (RSs) and synchronization signals. The physical layer interfaces the MAC of Layer 2 and the *Radio Resource Control* (RRC) of Layer 3. The physical layer offers a transport channel to MAC. A transport channel is characterized by how the information is transferred over the radio interface. MAC offers different logical channels to the *Radio Link Control* (RLC) of Layer 2, where a logical channel is characterized by the type of information transferred. The physical layer performs the following functions in order to enable data transport service:

- LTE physical layer functions applied to transport channels: Error detection on the transport channel and indication to higher layers; FEC encoding/decoding of the transport channel; rate matching of the coded transport channel to physical channels and mapping of the coded transport channel onto physical channels.
- LTE physical layer functions applied to physical channels: Power weighting of physical channels and modulation and demodulation of physical channels.
- Other LTE physical layer functions: HARQ soft-combining; power weighting of physical channels; frequency and time synchronization; radio characteristics measurements and indication to higher layers; MIMO antenna processing; transmit diversity; beamforming and RF processing.

2.4.2 LTE Air Interface Radio Aspects

The LTE air interface supports both FDD and TDD radio access modes to separate uplink and downlink traffic. DL and UL transmissions are organized into radio frames with 10 ms duration. Two radio frame structures are supported: Type 1, applicable to FDD and Type 2, applicable to TDD. Frame structure type 1 (FDD) is applicable to both full duplex and half duplex FDD. The generic radio frame for FDD and TDD has a duration of 10 ms and consists of 20 slots with a slot duration of 0.5 ms. Two consecutive slots form one subframe of length 1 ms that it is the shortest *Transmission Time Interval* (TTI). The E-UTRA OFDMA data channels are shared channels,

i.e., for each TTI a new scheduling decision is taken regarding which users are assigned to which time/frequency resources during this TTI. In addition the TTI duration of 1 ms contributes to minimize the low user-plane latency in order to achieve high bit rate for data services. Focussing on FDD, DL and UL radio transmissions are separated in the frequency domain. Figure 2.7 shows the FDD frame structure.

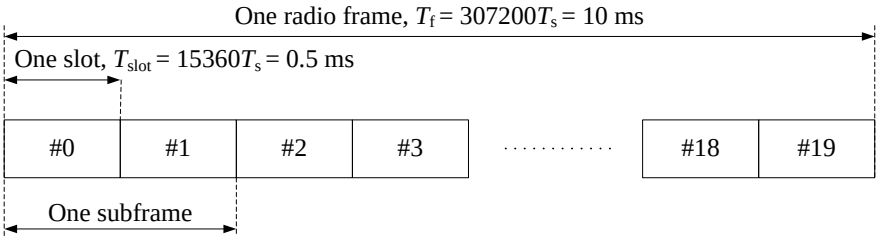

Figure 2.7: FDD frame structure [3]

Different transmission bandwidths are supported from 1.4 MHz to 20 MHz with subcarrier spacing of 15 kHz. A subcarrier spacing of 7.5 kHz has also been specified for the new LTE eMBMS. In both cases, the subcarrier spacing is constant regardless of the channel bandwidth. The smallest amount of resources that can be allocated in the UL or DL is called a *Resource Block* (RB) which spans a bandwidth of 12 subcarriers, i.e, 180 kHz wide. The maximum number of RBs supported by each transmission bandwidth is given in Table 2.5. The supported frequency bands are inherited from UMTS specifications plus new E-UTRA bands for LTE and LTE-Advanced defined in [19] and [20]. In addition, LTE-Advanced introduces carrier aggregation to allow bandwidths of up to 100 MHz for DL and 40 MHz for UL by aggregation of 20 MHz carriers.

Table 2.5: LTE Transmission Bandwidth and Resource Configuration

Channel Bandwidth	1.4 MHz	3 MHz	5 MHz	10 MHz	15 MHz	20 MHz
Number of RBs	6	15	25	50	75	100
Number of occupied subcarriers	72	180	300	600	900	1200
IFFT/FFT Size	128	256	512	1024	1536	2048
Subcarrier Spacing	15kHz / 7.5 kHz					

Each 1 ms subframe (TTI) consists of two 0.5 ms slots, while a slot consists of 6 or 7 OFDM symbols depending on the length of the CP (normal or extended) and the subcarrier spacing. The extended CP is available for use in larger cells and for specific multi-cell broadcast applications. A RB spans either 12 subcarriers with a subcarrier bandwidth of 15 kHz or 24 subcarriers with a subcarrier bandwidth of 7.5 kHz each over a slot duration of 0.5 ms. Table 2.6 shows the possible configurations of physical resource block parameters and Figure 2.8 shows the DL frequency-time resource grid obtained from [3]. Each element of the grid, which is equivalent to one subcarrier during one OFDM symbol period, is called a *Resource Element* (RE). In the case of MIMO

configurations, there is one resource grid defined per antenna port, where each antenna port is defined by its associated RSs.

Table 2.6: Physical RB parameters

Configuration	Number of symbols per slot	Number of subcarriers per RB	Cyclic Prefix length in μs
Normal cyclic prefix Subcarrier spacing = 15 kHz	7	12	5.2 μs for first symbol 4.7 μs for other symbols
Extended cyclic prefix Subcarrier spacing = 15 kHz	6	12	16.7 μs
Extended cyclic prefix Subcarrier spacing = 7.5 kHz	3	24	33.3 μs

One or more RBs can be assigned to a user for a predetermined amount of time. When multiples RBs are assigned to one user, these RBs are mapped to a *Virtual Resource Block* (VRB) in a localized or distributed manner. The frequency and time allocations to map information for a certain user to RBs is determined by the eNodeB scheduler depending on the actual radio channel and transmission traffic. The distributed permutation draws subcarriers pseudorandomly to form a subchannel and it provides frequency diversity and inter-cell interference averaging minimizing the probability of using the same carrier in adjacent sectors or cells. The localized permutation groups a block of contiguous sub-carriers to form a subchannel leaving the door open for the choice of the best conditioned part of the bandwidth.

In LTE/LTE-Advanced, the physical layer is designed to exploit MIMO wireless transceivers, at both the eNodeB and the UE, in order to enhance link robustness and increase data rates compared to SISO channels. The use of MIMO is compulsory and the baseline configuration is 2×2, two transmit antennas at the eNodeB and two receive antennas at the *User Equipment* (UE). Higher-order MIMO configurations are also taken into account; particularly, the 4×2 and 4×4 MIMO (four antennas at transmitter and two or four at receiver, respectively) in E-UTRA Release 8. LTE-Advanced specifications add the MIMO antenna configuration up to 8×8 for DL and 4×4 for UL. Moreover, in Release 12 and beyond advanced MIMO techniques are considered such as 3D-MIMO.

MIMO is integrated as part of E-UTRA physical layer because the requirements on coverage, capacity and data rates make necessary to incorporate new transmission schemes, such as beamforming, TD or SM. TD is primarily intended for common DL channels as it can be difficult to apply other sources of diversity such as retransmission or link adaptation. TD is based on SFBC techniques complemented with *Frequency-Shift Time Diversity* (FSTD) when four transmit antennas are used. On the other hand, SM enables to send independent streams of data simultaneously on the same DL RBs. Data stream can belong to one single user (SU-MIMO) or to different users (*Multi-User MIMO* (MU-MIMO)). SU-MIMO increases the data rate of one user, and, on the other hand, MU-MIMO increases the overall system capacity. The estimated downlink peak rates deemed feasible with E-UTRA are summarized in Table 2.7 with these assumptions: DL, FDD, 64QAM, *rate* = 1 and signal overhead for reference signals and control channel occupying one OFDM symbol). Thus, the usage of MIMO techniques may achieve and even exceed the peak rate requirements outlined in [6, 40].

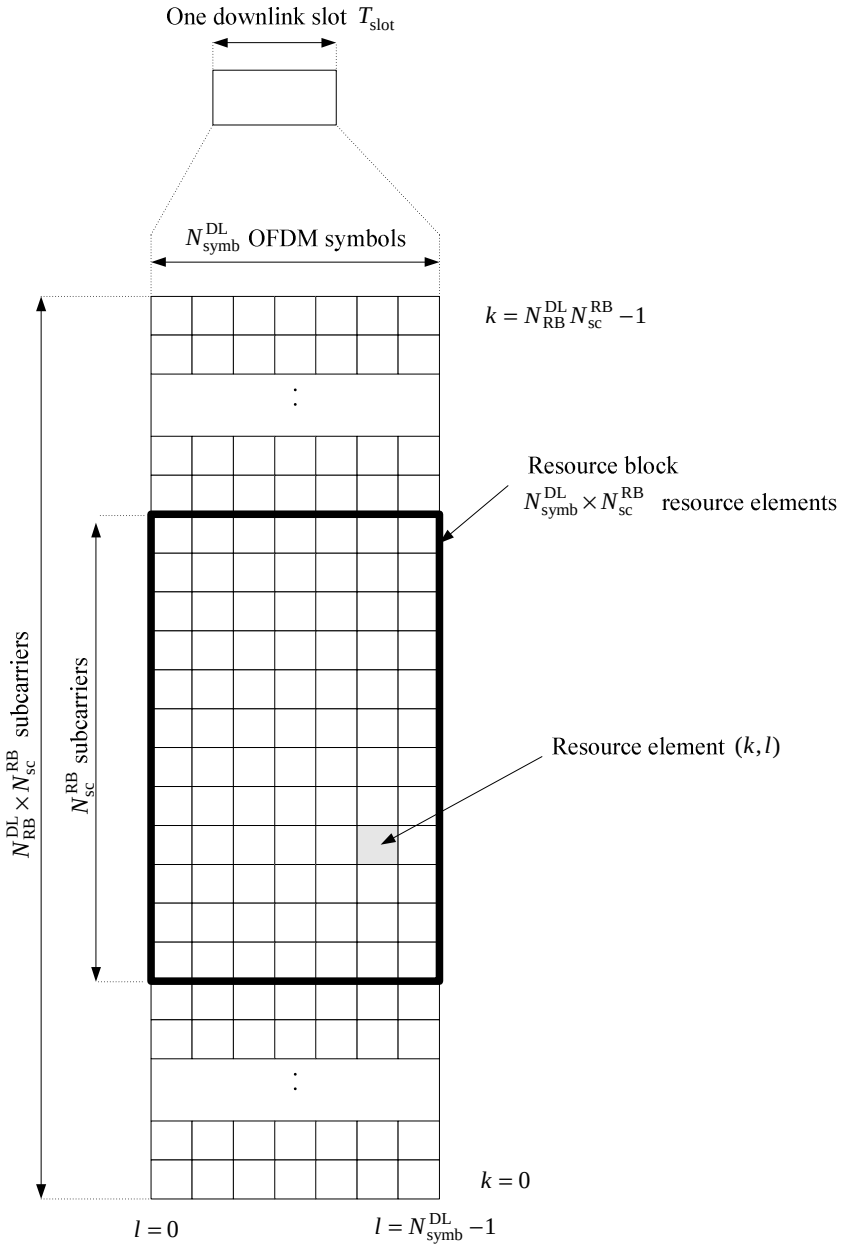

Figure 2.8: DL frequency-time resource grid [3]

2.5 LTE/LTE-Advanced Transmission Modes

MIMO techniques can be configured in different ways to provide a combination of gains in throughput, diversity and beamforming. From the point of view of the CSI the MIMO system can be OL or CL. While OL MIMO systems only have CSI at the receiver, CL MIMO systems also know the CSI at the transmitter and this can be used to improve the throughput and reliability. *Single-User* (SU)-MIMO schemes dedicate all spatial layers to one user, while *Multi-User* (MU)-MIMO schemes allow multiple users to be co-scheduled on the same time and frequency resources.

Table 2.7: DL peak rates for E-UTRA Release 8 and 10 [1, 5]

Units	Peak Spectral Efficiency	Transmission Bandwidth	Peak Data Rate
LTE Requirement	5.0 bps/Hz	20 MHz	100 Mbps
Release 8, 2 layer spatial multiplexing	8.6 bps/Hz	20 MHz	172.8 Mbps
Release 8, 4 layer spatial multiplexing	16.3 bps/Hz	20 MHz	326.4 Mbps
LTE-Advanced Requirement	10.0 bps/Hz	100 MHz	1 Gbps
Release 10, 4 layer spatial multiplexing	16.3 bps/Hz	100 MHz	1.632 Gbps
Release 10, 8 layer spatial multiplexing	30.6 bps/Hz	100 MHz	3.264 Gbps

The set of MIMO schemes to be applied between the eNodeB and the UE for both DL and UL are defined by the LTE/LTE-Advanced TMs. Release 8 supports 7 TMs and allows a maximum of 4 transmit antennas for DL and 1 transmit antenna for UL. The baseline MIMO antenna configuration for Release 8 is 2×2 for DL and 1×2 for UL. LTE-Advanced has increased the number of antennas to 8 transmit antennas for DL, 4 transmit antennas for UL and up to 8 receive antennas. LTE-Advanced Release 11 supports 10 TMs. Therefore MIMO configurations of 8×8 for DL and 4×4 for UL are allowed in LTE-Advanced, and this is one of the key aspects to meet the LTE-Advanced requirements.

The seven Transmission Modes defined in Release 8 are:

- **TM 1: Single antenna port, port 0**
  This mode corresponds to a 1x2 *Single-Input Multiple-Output* (SIMO) configuration, since it only uses 1 transmit antenna and 2 receive antennas. MRC is applied at the receiver to obtain receive diversity gain.

- **TM 2: *Transmit Diversity* (TD)**
  This is the OL Transmit diversity mode for a single user based on SFBC techniques with Alamouti Code at the transmitter complemented with FSTD when 4 transmit antennas are used. It supports 2 or 4 transmit antennas, up to 4 spatial layers and only 1 codeword. MRC combining is used at the receiver.

- **TM 3: Large-delay *Cyclic Delay Diversity* (CDD)**
  This is the OL MIMO SM mode for a single user, and supports 2 or 4 transmit antennas, up to 4 spatial layers and up to 2 codewords. At the receiver side there are at least 2 Rx antennas, so 2×2, 4×2 or 4×4 MIMO configurations are possible. The LTE specifications include a fixed large delay CDD precoding at the eNodeB that consists in transmitting the same OFDM symbols on the same set of subcarriers from multiple antennas with a different delay on each antenna. This creates an artificial multipath that translates into additional frequency diversity, which is then exploited by the turbo code.

- **TM 4: Closed-loop *Spatial Multiplexing* (SM)**
  This is the CL MIMO SM mode for a single user and supports 2 or 4 transmit antennas, up to 4 spatial layers and 1 or 2 codewords. The same MIMO configurations of TM 3 are

possible, i.e., 2×2, 4×2 or 4×4. This mode requires a precoding of the spatial layers based on a codebook, defined by the standard, which is known at both eNodeB and UE. The UE estimates the MIMO channel conditions and feeds back the PMI to the eNodeB.

- **TM 5: MU-MIMO**
  This is the CL MIMO SM mode for multiple users. In the UL the number of simultaneous UEs on the same frequency and time resources is limited by the number of receive antennas at the eNodeB, while in the DL it depends on the precoding techniques available at the eNodeB. With Release 9 up to 4 UEs are supported in the DL (2 UEs in Release 8).

- **TM 6: Closed-loop *Spatial Multiplexing* (SM) using a single layer**
  This mode is a particular case of TM 4 when only one spatial layer is used (rank= 1). The UE feeds back to the eNodeB the best PMI for capacity maximization. This precoding results in certain beamforming gain but, due to the use of a restricted codebook, it does not correspond to the UE-specific beamforming where the beam is directed to the selected UE.

- **TM 7: Beamforming. Single antenna port, UE-specific RS (antenna port 5)**
  This mode is the UE-specific beamforming mode where only one layer is transmitted to one UE and the eNodeB uses a virtual antenna (port 5) to direct the antenna beam to the UE.

LTE Release 9 added the Transmission Mode 8:

- **TM 8: Dual layer beamforming (antenna port 7 and 8)**
  This mode is similar to TM 7 but it specifies a single or a dual layer transmission on antenna ports 7 and 8; therefore this mode allows the eNodeB to dedicate the two layers to one UE (single-user) or two UEs, one layer per user.

LTE Release 10 added the Transmission Mode 9:

- **TM 9: Closed-loop SU-MIMO/MU-MIMO (antenna ports 7 to 14, UE-specific and CSI Reference**
  This mode allows MIMO configurations up to 8×8, dynamic SU-MIMO/MU-MIMO switching and supports the new reference signals introduced by LTE-Advanced: the UE-specific reference signals (*Demodulation reference signal* (DM-RS)) for data demodulation and the *CSI reference signal* (CSI-RS) for downlink channel state information measurement by the UE. The new DM-RSs allow non-codebook based precoding for the CL SU-MIMO/MU-MIMO.

LTE-Advanced Release 11 has introduced the TM 10 which is very similar to TM 9, except that TM 10 allows a UE to be configured with one or more CSI processes per serving cell. Table 2.8 summarizes the LTE/LTE-Advanced Transmission Modes for PDSCH. According to [33] the TD scheme is available in each TM as a fallback mode; so the MIMO configuration can switch from SM to TD or vice-versa depending on the channel conditions.

LTE introduced only one transmission mode for UL, so the TM 1 for PUSCH was the single-antenna port scheme with 1 transmit antenna at the UE and at least 2 receive antennas at the eNodeB (to enable receive diversity). Therefore, the TM 1 does not support SM for a SU-MIMO operation, but MU-MIMO can be used in the UL to enhance system capacity. LTE-Advanced has introduced the TM 2 for PUSCH, which consists on a CL SM MIMO scheme. With this mode up to 4 layers can be transmitted from the same UE and a precoding is applied before transmission to adapt to channel conditions. In the UL there is no transmit diversity fallback mode, so if CL SM is not possible then the system returns to the single-antenna port mode. Table 2.9 summarizes the transmission modes for PUSCH.

Table 2.8: LTE/LTE-Advanced Transmission Modes for PDSCH.

TM	Transmission scheme of PDSCH	Number of Antennas	MIMO Operation	SU/MU MIMO	Releases
1	Single-antenna port, port 0.	1	Open-Loop	SU-MIMO	8, 9, 10, 11
2	TD	2, 4	Open-Loop	SU-MIMO	8, 9, 10, 11
3	Open-loop SM (with large delay CDD Precoding).	2, 4	Open-Loop	SU-MIMO	8, 9, 10, 11
4	Closed-loop SM	2, 4	Closed-Loop	SU-MIMO	8, 9, 10, 11
5	Multi-user MIMO	2, 4	Closed-Loop	MU-MIMO	8, 9, 10, 11
6	Closed-loop SM with a single transmission layer	2, 4	Closed-Loop	SU-MIMO	8, 9, 10, 11
7	Beamforming, Single-antenna port, port 5.	1, 2, 4	Closed-Loop	SU-MIMO	8, 9, 10, 11
8	Dual layer beamforming (antenna ports 7 and 8)	2, 4	Closed-Loop	SU/MU MIMO	9, 10, 11
9	Closed-loop SU/MU-MIMO (antenna ports 7 to 14, UE-specific and CSI Reference Signals)	2, 4, 8	Closed-Loop	SU/MU MIMO	10, 11
10	Closed-loop SU/MU-MIMO (antenna ports 7 to 14, UE-specific and CSI Reference Signals). With one or more CSI processes.	2, 4, 8	Closed-Loop	SU/MU MIMO	11

2.6 Mutual Information and Channel Capacity

2.6.1 DMC Channel Capacity

LTE and LTE-Advanced adopt link adaptation techniques in order to decide dynamically, according to the radio channel conditions, the MCS that maximizes the data rate of the communications link. As described in [48] and [49], from an information theory point of view, the maximum data

Table 2.9: LTE/LTE-Advanced Transmission Modes for PUSCH.

TM	Transmission scheme of PDSCH	Number of Antennas	MIMO Operation	SU/MU MIMO	Releases
1	Single-antenna port scheme	1	Open-Loop	MU-MIMO	8, 9, 10, 11
2	Closed-loop spatial multiplexing scheme	2, 4	Closed-Loop	SU/MU MIMO	10, 11

rate for a reliable communication is called the channel capacity (C). For a *Discrete Memoryless Channel* (DMC) the channel capacity is usually measured in "bits/channel use", i.e. bits per input symbol into the channel, where in this context we call "symbol" to the coded symbols at the output of the encoder (called *binary digit*s (binits) by some authors when the code is binary). For a continuous channel the channel capacity is usually expressed in terms of "bits/dimension" or "bits/s/Hz". Our interest in computing the channel capacity is mainly to have a theoretical bound for the maximum code rate that can be used for a given modulation scheme and SNR or, equivalently, for a given MCS which is the minimum SNR to guarantee error free transmission. Figure 2.9 shows the DMC model of a communications system used to measure the channel capacity.

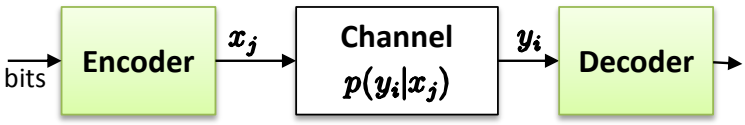

Figure 2.9: DMC model of a communications system

Assuming a DMC with input symbols x_j and output symbols y_i, the channel capacity C is obtained by maximizing the input-output mutual information, $I(X;Y)$, over the set of input symbol probabilities $p(x_i)$ under the constraints $p(x_j) \geq 0$ and $\sum_{j=0}^{q-1} p(x_j) = 1$:

$$C = \max_{p(x_j)} I(X;Y) \tag{2.1}$$

If we call $X = \{x_0, x_1, \ldots, x_{q-1}\}$ to the input alphabet of x_j and $Y = \{y_0, y_1, \ldots, y_{Q-1}\}$ to the output alphabet of y_i then the average mutual information provided by the output Y about the input X can be written as:

$$I(X;Y) = \sum_{j=0}^{q-1} \sum_{i=0}^{Q-1} p(x_j) p(y_i|x_j) \log_2 \frac{p(y_i|x_j)}{p(y_i)} \tag{2.2}$$

where $\log_2 \frac{p(y_i|x_j)}{p(y_i)}$ is the mutual information for an input symbol x_j and an output symbol y_i, $p(y_i|x_j)$ is the transition probability of the channel and $p(y_i)$ is the probability of the output symbol y_i:

$$p(y_i) = \sum_{k=0}^{q-1} p(x_k) p(y_i|x_k) \tag{2.3}$$

2.6.2 Shannon Bound and Channel Capacity

In this section it is shown how to compute the Shannon bound and the channel capacity of *Coded Modulation* (CM) and *Bit-Interleaved Coded Modulation* (BICM). The Shannon Bound is the ultimate limit of channel capacity. According to Shannon formula the maximum data rate for error-free communication over the baseband AWGN channel is given by:

$$\mathrm{C}_{AWGN} = W \cdot \log_2(1 + SNR) \;\; bits/s \tag{2.4}$$

where $W[Hz]$ is the bandwidth of the baseband channel and SNR is the baseband SNR. This expression is also valid for the low-pass equivalent of a *Radio Frequency* (RF) band-pass channel with bandwidth $B = 2W$ and $SNR_{RF} = \gamma$. Since the complex low-pass equivalent channel can be viewed as two independent parallel instances of a real AWGN baseband channel, the channel capacity of the band-pass channel is given by:

$$\mathrm{C}^{RF}_{AWGN} = 2 \cdot \frac{B}{2} \cdot \log_2(1 + \gamma) = B \cdot \log_2(1 + \gamma) \;\; bits/s \tag{2.5}$$

Expression 2.5 stems from the fact that I-Q noise realizations are independent and both the RF signal and noise power are equally split into the I-Q components. If only the in-phase component is used, the Shannon capacity is:

$$\mathrm{C}^{In-phase-only}_{AWGN} = \frac{B}{2} \cdot \log_2(1 + 2 \cdot \gamma) \;\; bits/s \tag{2.6}$$

since the quadrature noise power is not relevant. Taking into account that the maximum sampling rate is $R_S = 2 \cdot W$ *samples/s* for a baseband channel and $R_S = B$ *complex samples/s* for a bandpass channel, the channel capacity in *bits/channel use* is given by:

$$\frac{\mathrm{C}^{\mathrm{RF}}_{\mathrm{AWGN}}}{R_S} = \log_2(1 + \gamma) \;\; bits/channel \;\; use \tag{2.7}$$

Since there is one channel use per second per Hz, expression 2.7 can be interpreted as the maximum possible bandwidth efficiency of any communication system (in $bit/s/Hz$).

Now let's assume that on every "channel use" we send one modulation symbol taken from an alphabet of size M. If modulation symbols are considered independent and equiprobable, the number of binits per modulation symbol is $\log_2 M$, and so the transmission rate in *binits/s* is $R_b = R_S \cdot \log_2 M$. We define the bit energy as $E_b = P_R \cdot T$, where P_R is the RF received power and $R = 1/T$ is the information transmission rate in *bits/s*. The code rate is thus $r = R/R_b$. The RF SNR is:

$$\gamma = P_R/N_0B = E_bR/N_0B = (R/R_S) \cdot (E_b/N_0) = r \cdot \log_2 M \cdot (E_b/N_0) \tag{2.8}$$

where N_0 is the single-sided RF noise power spectral density. Assuming that the MCS achieves the channel capacity, i.e., $R = \mathrm{C}^{RF}_{AWGN}$, the relationship between spectral and energy efficiency for an ideal code and modulation is given by:

$$\frac{E_b}{N_0} = \frac{2^{\frac{R}{B}} - 1}{R/B} \tag{2.9}$$

Since it is impractical to use an ideal MCS and to achieve the Shannon capacity, CM and BICM schemes are used to achieve a channel capacity as close as possible to the Shannon bound. As shown in Figure 2.10, CM and BICM schemes are both formed by an encoder and modulator at the transmitter side and a demodulator and decoder at the receiver side. Both schemes are based on the concatenation of an encoding process and a signal constellation modulator and the main difference is the type of encoder output, non-binary (modulation symbols) for CM and binary for BICM. Additionally, BICM includes interleaving and de-interleaving stages to break the modulator memory for modulations with unequal error protection at bit level.

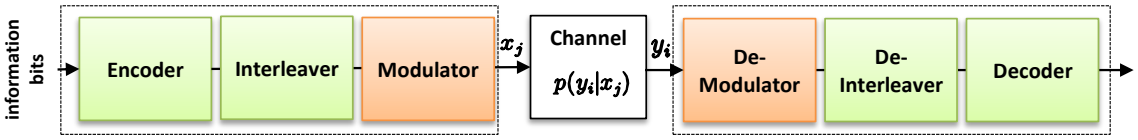

Figure 2.10: Block diagram for CM or BICM transmission scheme

In order to compute the capacity of CM and BICM schemes we assume that the channel can be modeled as a vector channel characterized by a transition *Probability density function* (pdf) $p(y_i|x_j)$ and that the channel state is independent of the channel input.

2.6.2.1 CM Channel Capacity

In order to compute the capacity of a CM scheme we must work at modulation symbol level, i.e. we assume that the demodulator computes the LLR of each received modulation symbol and uses it as the soft information input to the decoder. We assume that the LLR is not quantized. Since the received modulation symbol includes complex additive noise it must be considered a continuous random variable. We wish to compute the MI. The equation 2.2 can be reformulated for continuous random variables as, [34]:

$$MI(x,y) = E_{x,y}\left[\log_2\left(\frac{f_{y|x}(y|x)}{f_y(y)}\right)\right] \tag{2.10}$$

where $E_{x,y}(\cdot)$ means expectation over $\{x,y\}$, $f_{y|x}(y|x)$ is the conditional pdf of $y|x$, and $f_y(y)$ is the pdf of y.

Taking into account that x is a *Multi-Level Quadrature Amplitude Modulation* (MQAM) modulation symbol and y is the received decision variable, $MI(x,y)$ can be rewritten as:

$$MI(x,y) = \frac{1}{M}\sum_{i=1}^{M} E_{y|x_i}\left[\log_2\left(\frac{f_{y|x_i}(y|x_i)}{f_y(y)}\right)\right] \tag{2.11}$$

The LLR at modulation symbol level for a modulation with M states is defined as:

$$LLR_{x_i}(y) = \log_e\left(\frac{p(x_i|y)}{\sum_{k=1;k\neq i}^{M} p(x_k|y)}\right) = \log_e\left(\frac{p(y|x_i)}{Mp(y) - p(y|x_i)}\right) = \log_e\left(\frac{f_{y|x_i}(y|x_i)}{Mf_y(y) - f_{y|x_i}(y|x_i)}\right) \tag{2.12}$$

where $p(y)$ is the probability mass function for discrete-valued y, $p(x_i|y)$ means the probability that state x_i has been transmitted given that the received decision variable is y and $f(\cdot)$ is the pdf. Assuming equal transmission probabilities for all modulation symbols and taking exponentiation on both sides of equation 2.12, the following expression is obtained:

$$\frac{f_{y|x_i}(y|x_i)}{f_y(y)} = \frac{M}{1+e^{-LLR_{x_i}(y)}} \tag{2.13}$$

and the MI at symbol level, equation 2.11, is reformulated as:

$$MI(x,y) = \frac{1}{M}\sum_{i=1}^{M} E_{y|x_i}\left[\log_2\left(\frac{M}{1+e^{-LLR_{x_i}(y)}}\right)\right] \tag{2.14}$$

where $MI(x,y)$ tends to $\log_2 M$ for high SNR since for high SNR the LLRs are much larger than 1. Again, assuming equal transmission probabilities for all modulation symbols and AWGN channel, the $LLR_{x_i}(y)$ becomes:

$$LLR_{x_i}(y) = \ln\left(\frac{e^{-d_i^2/\sigma^2}}{\sum_{k=1;k\neq i}^{M} e^{-d_k^2/\sigma^2}}\right) \tag{2.15}$$

where d_i is the distance from decision variable y to symbol x_i and σ is the noise variance.

There is not a closed expression for the MI, but using equations 2.14 and 2.15 the MI at symbol level can be computed numerically creating high resolution histograms of the symbol level LLRs, then normalize the histograms to get the pdf of the LLRs and finally perform the averaging operation in equation 2.14 by numerical integration. In general, and depending on the modulation scheme and the SNR, the different symbols have different LLR statistics. Figure 2.11 shows the pdf of the LLRs for one of the symbols of the constellation for the LTE modulation schemes.

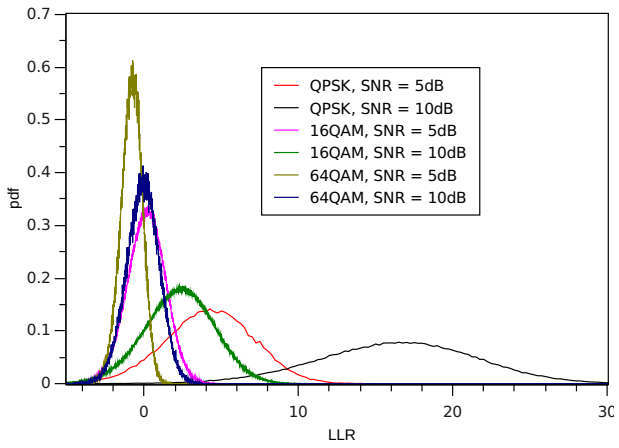

Figure 2.11: pdf of the LLRs for the LTE modulations schemes

The CM capacity in *bit/s/Hz* is equal to the MI. Figure 2.18 shows the capacity for a CM scheme using the LTE modulations in AWGN channel. The curves of MI at symbol level for the LTE modulation schemes, normalized by $\log_2(M)$, are also given in Figure 2.12. The normalized

MI can be interpreted as the fraction of the information carried by a modulation symbol that is preserved after crossing the channel.

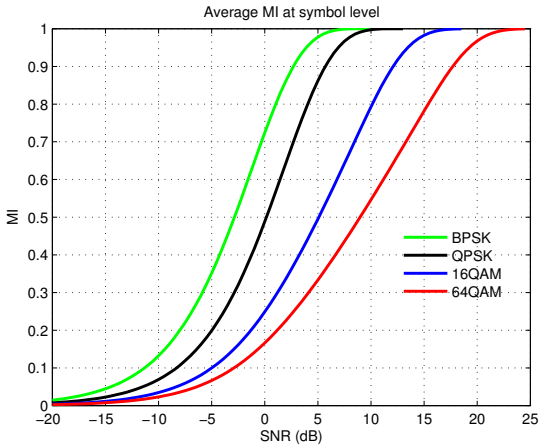

Figure 2.12: $\mathrm{MI}/\log_2(M)$ for the LTE modulation schemes

2.6.2.2 BICM Channel Capacity

In order to compute the capacity for a BICM scheme we consider the channel between the output of the encoder (transmitted binits) and the input of the decoder (LLRs at modulation bit level). It is always possible to characterize such a channel regardless of the applied modulation, the complexity of the radio channel and the processing at the transmitter and at the receiver. This kind of channel has a *hard* input (b) and a *soft* output (z) as depicted in Figure 2.13.

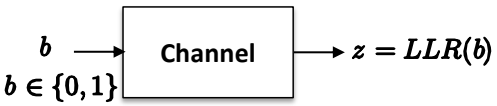

Figure 2.13: Equivalent channel between a transmitted binit and its LLR

This equivalent channel can be properly characterized by using the *Mutual Information at bit level* (MIB) between input and output, $MIB(b,z)$, [12], i.e.:

$$MIB(b,z) = E_{b,z}\left\{\log_2\left(\frac{f_{z|b}(z|b)}{f_z(z)}\right)\right\} = \frac{1}{2}\sum_{i=0,1}\left[\int_{-\infty}^{\infty}\log_2\left(\frac{2}{1+\frac{f_{z|b=\bar{i}}(z|b=\bar{i})}{f_{z|b=i}(z|b=i)}}\right)\cdot f_{z|b=i}(z|b=i)\cdot dz\right] \tag{2.16}$$

where z is equal to $LLR(b)$. Assuming equiprobable binits $f_z(z)$ is given by:

$$f_z(z) = \frac{1}{2}f_{z|b=0}(z|b=0) + \frac{1}{2}f_{z|b=1}(z|b=1) \tag{2.17}$$

By definition the modulation bit level LLR, $LLR(b)$, is the logarithm of the ratio between the probability that the transmitted binit is 0 over the probability that the transmitted binit is 1 based on the knowledge of the received variable of decision y:

$$LLR(b) = \ln\left(\frac{Prob\,(b=0|y)}{Prob\,(b=1|y)}\right)_{|\text{equiprobable binits}} = \ln\left(\frac{Prob\,(y|b=0)}{Prob\,(y|b=1)}\right) \tag{2.18}$$

The computation of equation 2.18 depends on the modulation and on the noise statistics. Again, assuming AWGN channel the modulation bit level LLR is computed as follows:

$$LLR(b) = \ln\left(\frac{\sum_{\forall i: y_i \in S_0} e^{\left(-\frac{|y-y_i|^2}{\sigma^2}\right)}}{\sum_{\forall j: y_j \in S_1} e^{\left(-\frac{|y-y_j|^2}{\sigma^2}\right)}}\right) \tag{2.19}$$

where S_0 is the set of modulation states for which b is at logical zero, S_1 is the set for which b is at logical one and σ^2 is the complex noise variance. From Equations 2.18 and 2.19, it is easy to prove that:

$$\frac{f_{z|b=\bar{i}}(z|b=\bar{i})}{f_{z|b=i}(z|b=i)} = e^{(2\cdot i-1)\cdot LLR(b)} \tag{2.20}$$

Thus, using 2.20 equation 2.16 can be rewritten as:

$$MIB(b,z) = \frac{1}{2}\sum_{i=0,1}\left[\int_{-\infty}^{\infty}\log_2\left(\frac{2}{1+e^{(2\cdot i-1)\cdot LLR(b)}}\right)\cdot f_{z|b=i}(z|b=i)\cdot dz\right] \tag{2.21}$$

In the same way as we did for the LLRs at modulation symbol level, using equations 2.21 and 2.19 the MIB can be computed numerically creating high resolution histograms of the bit level LLRs, then normalize the histograms to get the pdf of the LLRs and finally perform the averaging operation in equation 2.21 by numerical integration.

Finally, the capacity of the BICM scheme is equal to $\log_2(M)$ times the *Mean Mutual Information at bit level* (MMIB), i.e., the average of the MIB over each of the bits channels of the modulation:

$$MMIB = \frac{1}{L}\sum_{j=1}^{L} MIB(b_j, z) \tag{2.22}$$

where $L = \log_2(M)$ and b_j is the bit at position j within the binary word mapping of the modulation symbol.

For 16QAM and 64QAM the different bits within the modulation symbol have different LLR statistics, as shown in Figures 2.14 and 2.15. The curves of MIB and MMIB for the LTE modulation schemes are given in Figure 2.16.

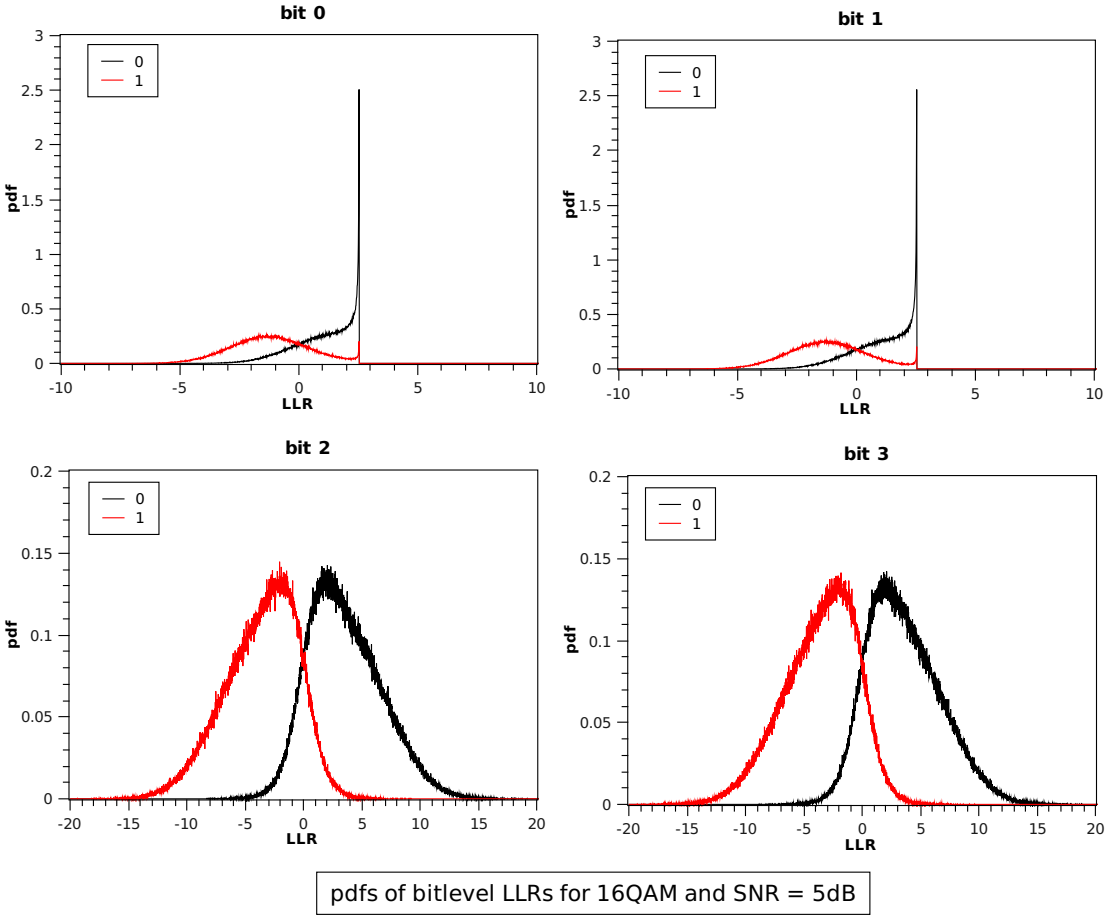

Figure 2.14: pdf of the bit level LLRs for 16QAM and SNR=5 dBs

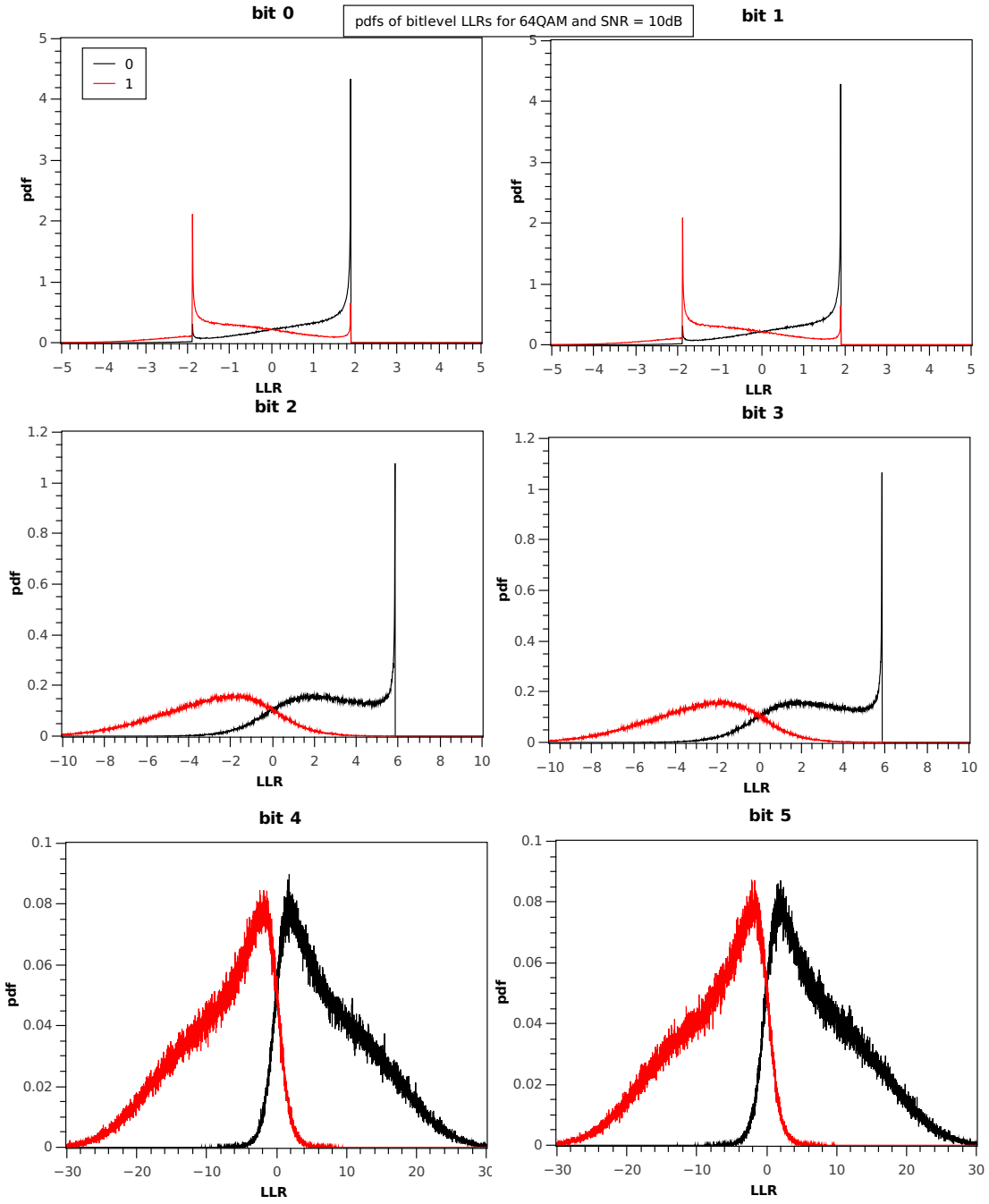

Figure 2.15: pdf of the bit level LLRs for 64QAM and SNR=10 dBs

2.6.3 BICM Capacity of the LTE modulation schemes in AWGN channel

The BICM capacity for the LTE modulation schemes, i.e, *Binary Phase-Shift Keying* (BPSK), QPSK, 16QAM and 64QAM, in AWGN channel has been computed following the procedure described in section 2.6.2.2. Figure 2.18 compares the AWGN capacity of the LTE modulations, with BICM or CM, with the Shannon bound. The obtained results are consistent with the curves previously published in [50].

Figure 2.16 shows the MIB vs. SNR curves, where it can be noticed that 16QAM and 64QAM provide unequal error protection depending on the weight of the bit within the modulation symbol. For instance, in 16QAM the bits that travel in the sign of the in-phase and quadrature (I/Q) components have a higher MIB than those that travel in the absolute value of the I/Q components. A higher MIB means a more reliable LLR and less error probability for a given SNR. Thus, it can be said that 16QAM has two different "bit channels" while 64QAM has three different "bit channels". Also plotted in Figure 2.16 is the MMIB for 16QAM and 64QAM. The MMIB vs. SNR curve is used in the *Mutual Information based exponential SNR Mapping* (MIESM) link abstraction methodology to predict the BLER.

In [51] an approximated closed form expression for the MIB in BPSK is given. The MIB curves for BPSK and QPSK can be well approximated by the function:

$$MIB(\gamma) \approx 1 - e^{-\gamma/\beta} \tag{2.23}$$

where γ is the SNR and β is a suitable constant that depends only on the modulation scheme: $\beta = -1.2$ dB for BPSK and $\beta = 1.8$ dB for QPSK, [51], (see Appendix B). This approximation of MIB curves is depicted in the top right of Figure 2.16. This type of approximation is used in the *Exponential Effective SNR Metric* (EESM) link abstraction method, even for 16QAM and 64QAM (with different values of β), to avoid dealing with the exact MMIB curves.

2.6.4 BICM SNR Threshold

In the previous paragraphs we have seen that the modulation MMIB is equal to the BICM capacity normalized to $\log_2(M)$. Assuming a capacity approaching code, the modulation MMIB can be interpreted as the maximum code rate that can be applied (for a given SNR) in order to obtain an error free transmission in AWGN conditions, [52]. Alternatively, and given a modulation scheme and a code rate r, it is possible to define a SNR threshold γ_0 (called BICM threshold from here on) as the minimum SNR needed to obtain error free transmission when that modulation and code rate are applied. Figure 2.17 shows a representation of this correspondence between MMIB and BICM threshold.

2.6.5 Capacity vs. E_b/N_0

Figure 2.18 shows the capacity vs. SNR of the LTE modulation schemes in AWGN channel. For BPSK and QPSK there is no difference between mutual information at bit or symbol level. For 16QAM and 64QAM and low SNR, the BICM capacity is slightly lower than the CM capacity. This is also in accordance with previously published results, [50]. However, the BICM scheme used in LTE is a very effective scheme that allows to reduce the complexity of the CM scheme in a practical way and almost achieves the CM capacity for 16QAM and 64QAM.

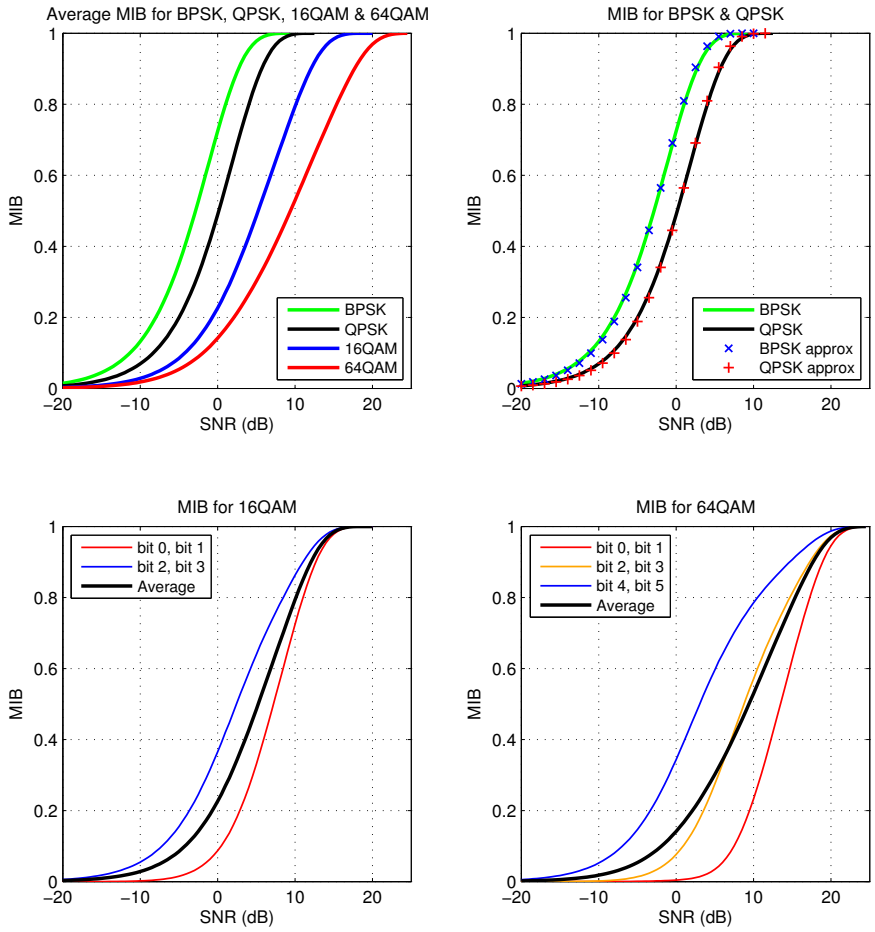

Figure 2.16: MIB for the different "bit channels" of LTE modulations

By interpreting the mutual information as the maximum allowable code rate for error free transmission, and using equation 2.8 we can write that $E_b/N_0 = \gamma/(\log_2 M \cdot f(\gamma))$, where $f(\gamma)$ is the MI/$\log_2(M)$ for CM or the MMIB for BICM. Since $C(\gamma) = \log_2 M \cdot f(\gamma)$ is the capacity vs. γ (as shown in Figure 2.18), the capacity vs. E_b/N_0 can be obtained by plotting $C(\gamma)$ vs. $\gamma/C(\gamma)$. Figure 2.19 shows the capacity vs. E_b/N_0 curves, where it can be seen that the minimum theoretical value of E_b/N_0 for error free transmission with CM is -1.6 dB. However, for BICM and 16QAM and 64QAM this minimum value is increased to -0.7 dB and -0.5 dB, respectively.

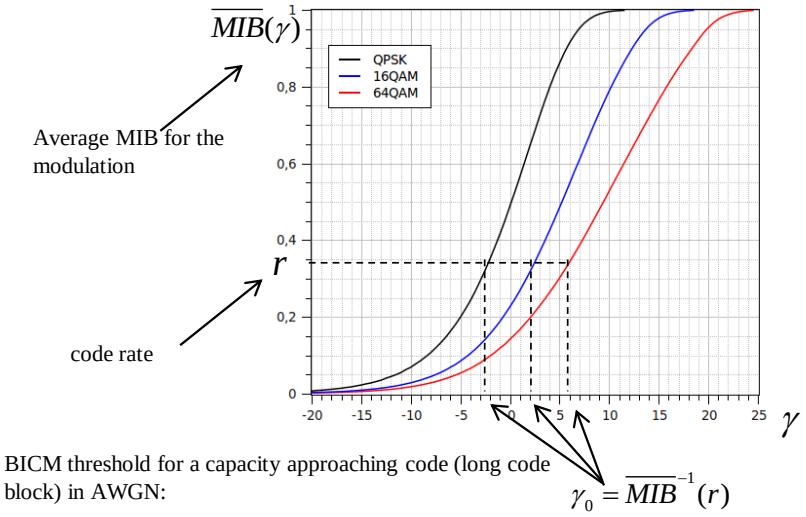

Figure 2.17: MMIB and BICM thresholds for the different LTE modulations

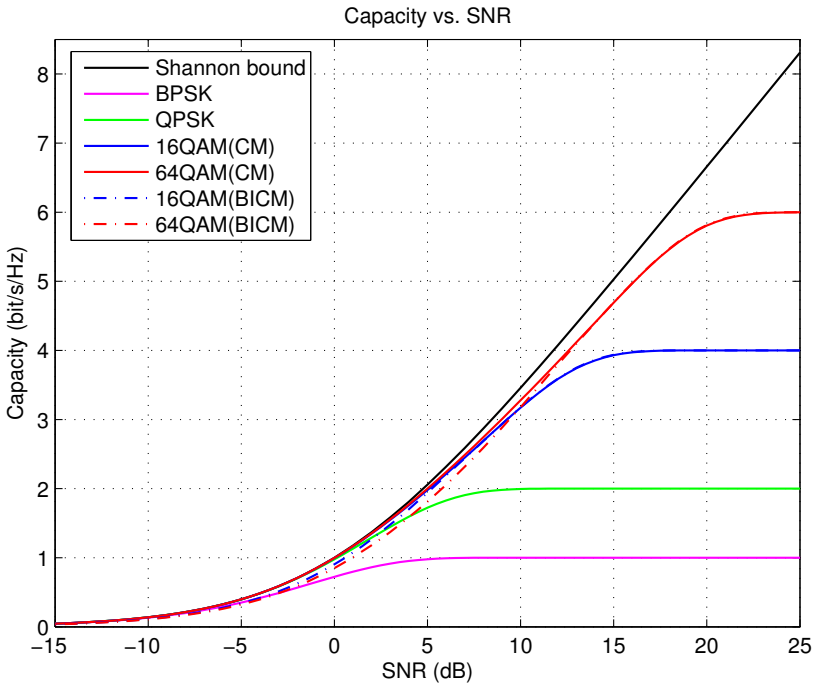

Figure 2.18: Capacity vs. SNR for the different LTE modulations in AWGN channel

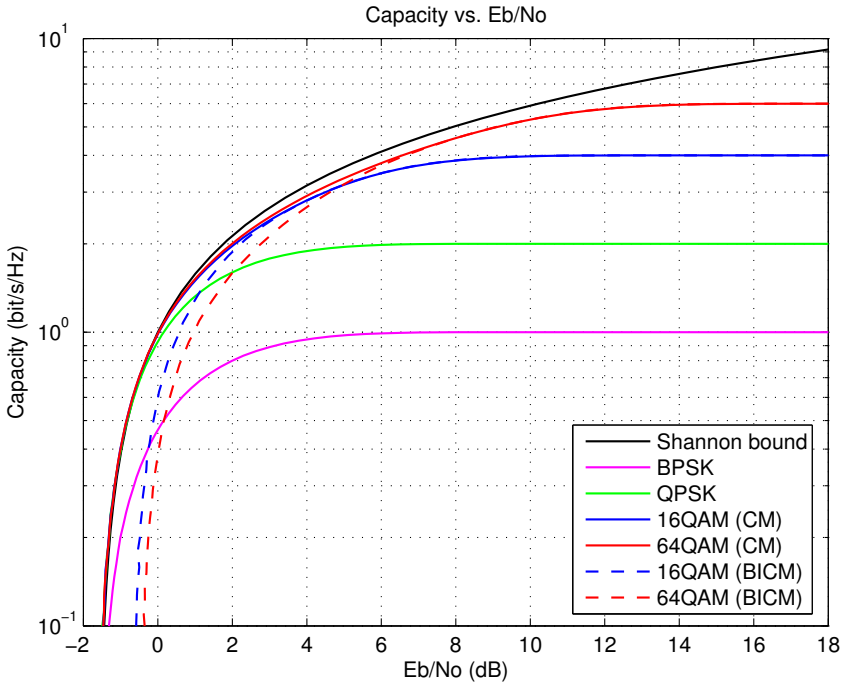

Figure 2.19: Capacity vs. Eb/No for the different LTE modulations in AWGN channel

Chapter 3

Link Level Simulator for E-UTRA

In this chapter, we start defining a common set of scenarios for LTE/LTE-Advanced link level simulations with the goal to identify a set of topics, features and parameters to consider when programming the link level simulators. We then present our link level simulator that is developed by means of ad-hoc C/C++ program based on the E-UTRA physical layer specifications. Next we describe the E-UTRA transport channel processing: first we review how to obtain the transport channel capacity and compute the *Effective Code Rate* (ECR), second we give an overview of the channel coding, rate matching and HARQ processes for LTE and third we analyse the soft demodulation. Finally we present the E-UTRA physical channel processing, we introduce a MIMO channel model for the link level simulator and we describe the MIMO-OFDM processing.

3.1 General aspects for Simulating LTE/LTE-Advanced Link Level

The simulation of mobile communication systems is usually divided in two different instances, i.e., link and system level simulators. The link level simulator simulates a single radio link with full details taking into account all the aspects of the communication involved between the transmitter and the receiver. But the tasks for the link level simulator are too complex to be extended to simulate the whole system. Therefore, the system level simulator takes into account a complete cell deployment and relies on simplified look-up tables generated offline by the link level. However, the border between link and system level, i.e., which tasks are performed at each simulator, depends on the characteristics of the standard and on the simulator designs, making the interface between link and system level simulators more complex.

For example, the modelling of multipath frequency selective fading used to be a link level task, but with the LTE scheduling resolution of 15 kHz (in bandwidth) and 1 ms (in time), multipath fading must be also considered at the system level. The modelling of ARQ is another task that used to be restricted to link level and now (with HARQ) has merged with the system level. The fact that the LTE/LTE-Advanced PHY layer can be configured in many different ways (called TMs) also adds complexity to the link and system level simulators.

The introduction of OFDMA has created the need for link abstraction techniques to predict the transport BLER under frequency selective fading conditions, while the short TTI of 1 ms, which is usually shorter than the channel coherence time, makes short term fading variations almost irrelevant, thus allowing the modelling of the turbo code error performance through AWGN curves. The link abstraction techniques are used to employ link level results in system level simulators and are also necessary for real system operation since the mobile terminal must report the CQI to the base station.

Considering that the link level simulator is a complex project by itself, the first logical step would be to identify which are the objectives and specifications of the project. A few high level

decisions on the scope of the desired results are useful to set research priorities. Among those *bullet points* (which are not mutually exclusive) there are the following features:

A. Simulator configuration

- **A.1** LTE (Releases 8-9), LTE-Advanced (Releases 10-11)
- **A.2** FDD, TDD modes
- **A.3** *Downlink* (DL), *Uplink* (UL)
- **A.4** Unicast, Multicast
- **A.5** Set of supported LTE / LTE-Advanced transmission modes
- **A.6** Simulated bandwidth (contiguous or distributed RBs, Frequency hopping)
- **A.7** MIMO matrix channel simulation: purely stochastic, geometry-based stochastic, measurement campaign traces
- **A.8** Number of antennas
- **A.9** Channel Estimation: Ideal, Pilot-based or based on a *Channel Estimation Error Model* (CEEM)

B. Scope of the desired results

- **B.1** *Uncoded Bit Error Rate* (UBER)
- **B.2** BLER (with coding) in AWGN conditions for SISO mode and single HARQ transmission for the different AMC schemes (reference BLER curves)
- **B.3** BLER and throughput (for relevant transmission modes) under realistic channel conditions (indoor, pedestrian, high speed, etc.) and for different redundancy versions of HARQ (BLER after receiving 1,2,3 or 4 incremental redundancy versions) for the different AMC schemes
- **B.4** Training of link abstraction metrics: EESM, MIESM
- **B.5** Guidelines for transmission mode selection and AMC scheme selection

C. Simulator implementation

- **C.1** Programming language: C++, Matlab, etc.
- **C.2** Open access or closed. Open source or proprietary code

Since the number of aspects to consider is quite high, a prioritization of the most interesting configurations and results is needed. Figure 3.1 illustrates the envisaged main parameters for the Link Level Simulation. Also a sequential implementation of the simulator features, from low to higher complexity, helps to reduce the debugging time by building new features over already tested software blocks.

Following the criteria described in this section, a LTE/LTE-Advanced link level simulator has been developed by means of ad-hoc C/C++ program based on the E-UTRA physical layer specifications. The simulator implements the LTE/LTE-Advanced DL/UL and the FDD mode, although this dissertation is only focussed on the LTE/LTE-Advanced DL. There are two main processing chains to consider at link level:

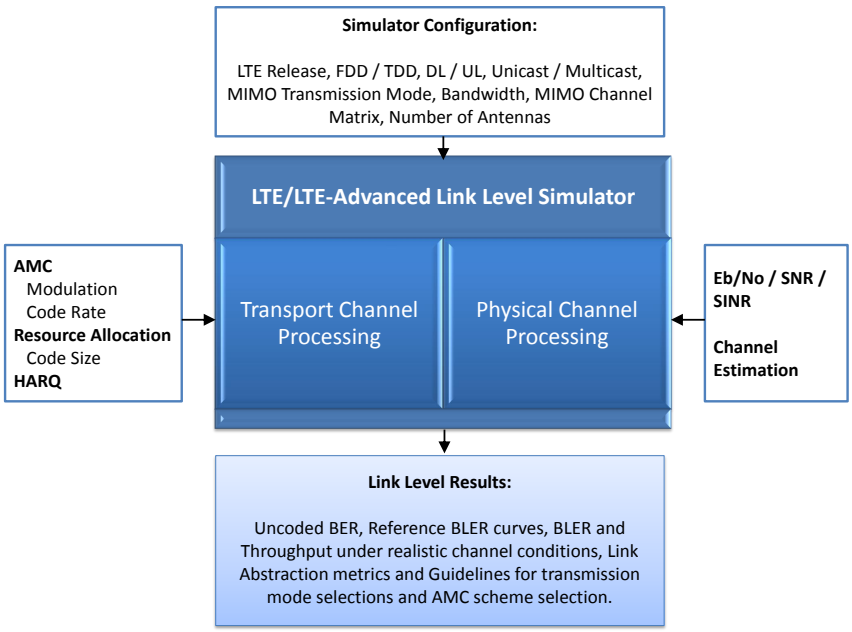

Figure 3.1: Block diagram of the Link Level Simulator inputs/outputs

- The transport channel processing for DL/UL-*Shared Channel* (SCH), [4].
- The physical channel processing for PDSCH/PUSCH, [3],

where the physical channel is the immediate lower layer for the transport channel. Usually only the user plane (PDSCH and PUSCH) is simulated at the link level simulator, but the control plane also must be taken into account, since a fraction of the PHY capacity is reserved for the control channels and this has an impact on the AMC schemes that can be applied for a given allocated bandwidth. Another aspect to consider is the role of the pilot symbols (called RSs in LTE). Pilot symbols must be considered, since they also reduce the available PHY capacity for the user plane (mainly for MIMO modes), and can also be simulated in detail if we need to test realistic channel estimation methods.

Section 3.2 gives an overview of the LTE/LTE-Advanced link level simulator and the details of the transport and physical channel processing are presented in section 3.3 and 3.4 respectively.

3.2 Overview of the LTE/LTE-Advanced Link Level Simulator

The first stage of the link level simulator was presented in [53] and [8]. This link level simulator was developed for LTE-DL and validated against theoretical expression for the *Bit Error Rate* (BER) when possible. The LTE link level simulator encompassed the MIMO algorithms, the OFDM signal, the relevant reference propagation scenarios, the channel modulation and coding schemes, the rate matching and the HARQ process in the communication between the eNodeB and the UE. Initially, ideal channel estimation was assumed and signalling and pilot symbol overhead was not considered. From this point, the link level simulator was extended to the LTE and the LTE-Advanced releases introducing MIMO precoding, CL schemes, SIC techniques, SU-MIMO and

MU-MIMO schemes, practical channel estimation procedures, a channel estimation error model, transport block segmentation, LTE and LTE-Advanced MCSs, different MIMO transmission mode schemes, among others.

The LTE/LTE-Advanced link level simulator is essentially a flexible designed off-line program that can model with accuracy the behaviour of the DL radio interface, in terms of bit and block error and throughput statistics, taking into consideration all the involved environmental parameters. The simulator is subdivided in two processes: the transport channel processing and the physical channel processing; while the physical channel Processing addresses to the MIMO-OFDM physical channel simulation, the transport channel processing carries out the channel coding.

Figure 3.2 shows a block diagram of the main modules of the simulator. Basically at the transmitter (eNodeB); concerning to channel coding, a rate 1/3-turbo encoder with variable code block size that creates three independent streams with systematic and redundant bits which are interleaved and fed to the rate matching and HARQ procedure (up to four IR transmissions per code block are allowed); concerning to physical channel processing, *Multiplexer* (MUX) and MIMO processing and an OFDM physical layer. At the receiver, the inverse operations of the transmitter are performed and ACK/NACK error free transmission is considered for error detection and BLER statistics and link level throughput estimation.

The simulation of the OFDM modulation may be based on *Discrete Fourier Transform* (DFT) or FFT. The advantage of using DFT over FFT is that multipath delays (at the channel simulator) can take any value, while FFT defines a sampling period that must be respected and this forces the channel delays to be integer multiples of the FFT sampling period. Depending on the type of channel simulator, and if perfect time and frequency synchronisation are assumed, it is possible to completely skip the IFFT/FFT stages in the DL link level simulator, since the channel can be simulated in the frequency domain and the receiver noise can also be added to the received signal samples in the frequency domain. The receiver noise becomes correlated after the FFT stage, but since OFDM spectrum accomplishes the Nyquist criterion in the frequency domain, noise samples taken at the subcarrier frequencies become uncorrelated. If IFFT/FFT stages are not simulated then we are assuming that the channel remains constant for the full duration of the OFDM symbols, so that channel variations due to Doppler effect are updated in quantized time steps equivalent to the OFDM symbol duration.

The set of parameters that are considered in the LTE/LTE-Advanced link level simulator presented in this dissertation are the following:

a. The LTE and LTE-Advanced link level simulator configuration

- **a.1** LTE (Releases 8-9), LTE-Advanced (Releases 10-11)
- **a.2** FDD mode
- **a.3** *Downlink* (DL)
- **a.4** Unicast
- **a.5** Set of supported LTE/LTE-Advanced TMs: Single Antenna Port, *Transmit Diversity* (TD), OL MIMO, CL MIMO.
- **a.6** Simulated bandwidth: Customizable (from 1 to 25 RBs), contiguous RBs.

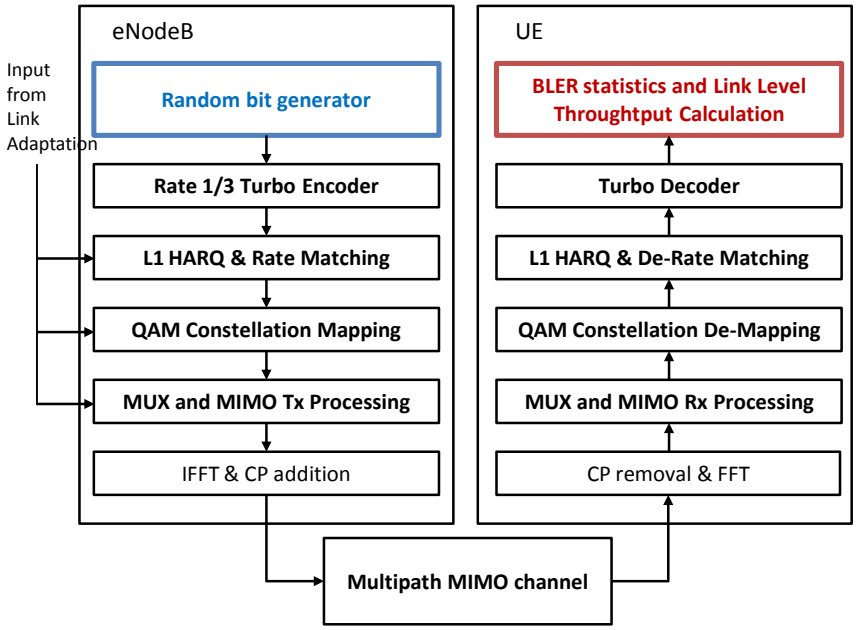

Figure 3.2: Block diagram of the LTE/LTE-Advanced-DL link level simulator

a.7 MIMO matrix channel simulation: purely stochastic

a.8 Number of antennas: up to 4 antennas (1x1, 1x2, 2x2 and 4x4)

a.9 Ideal Channel Estimation and CEEM

b The LTE and LTE-Advanced link level simulator results

b.1 *Uncoded Bit Error Rate* (UBER)

b.2 Reference BLER curves, BLER with coding in AWGN conditions for SISO mode and single HARQ transmission for the different AMC schemes (from *Modulation and Coding Scheme* (MCS) index 0 to 27).

b.3 BLER and throughput (for relevant transmission modes) under ideal and realistic channel conditions (*Extended Pedestrian A* (EPA), *Extended Vehicular A* (EVA) and *Extended Typical Urban* (ETU) Channel Models with configurable maximum doppler frequency) and for different redundancy versions of HARQ (BLER after receiving 1,2,3 or 4 incremental redundancy versions) for the different AMC schemes.

b.4 Training of link abstraction (LA) metrics: EESM and MIESM (also including HARQ).

b.5 Guidelines for transmission mode selection and AMC scheme selection.

c. The LTE and LTE-Advanced link level simulator implementation

c.1 Programming language: C/C++

c.2 Closed access.

Thus, the LTE and LTE-Advanced link level simulator allows to vary all the parameters involved in the simulation configuration in great detail, such as the values of *Signal to Interference plus*

Noise Ratio (SINR) or, equivalently, SNR or *Energy per bit to noise power spectral density ratio* (Eb/No) (where *Noise power spectral density* (No) includes all the sources of noise); the MIMO channel correlation; the MIMO transmit/receive procedures; the channel estimation error model or assuming ideal channel estimation; the modulation, the code size and the channel coding rate; whether or not the HARQ process is enabled; and the resource allocation and bandwidth.

The scope of the desired results for the LTE and LTE-Advanced link level simulator is focused on the performance evaluation of the MIMO-OFDM receive techniques, the computation of the Reference BLER curves for the different LTE and LTE-Advanced AMC schemes, the assessment of the Link Abstraction models to obtain link level *Look-Up Table*s (LUTs) and the guidelines for the transmission mode selection and AMC scheme selection based on the simulated average link level results (an average *Block Error Rate* (BLER) and throughput vs. average SNR).

In summary, the results of the LTE and LTE-Advanced link level simulator allow characterizing the LTE wireless link, creating LUTs to predict the link performance (BLER) for the real system and to map the link level behaviour to a system level simulator and providing guidelines for the LTE and LTE-Advanced transmission mode selection. Moreover, the results based on ideal channel estimation will provide an upper bound on performance and when channel estimation error model is applied, the results will show the degradation due to realistic scenarios and low complexity channel estimation algorithms.

3.3 E-UTRA Transport Channel Processing

In LTE/LTE-Advanced, the MAC layer maps the logical channel to the transport channels outputting the *Protocol Data Unit*s (PDUs), known as transport blocks, to the physical layer, [47]. Thus, the PDSCH carries user data in transport blocks which have a subframe duration of 1 ms (1 TTI). Each transport block is only dedicated to one user and its size is determined as a function of the number of allocated physical channels and the index of the transport block size according to the procedures of [33]. Figure 3.3 depicts the generic block diagram of the transport channel processing at the transmitter side of the link level simulator. The receiving side does the reverse functions in the reverse order, as shown in Figure 3.4.

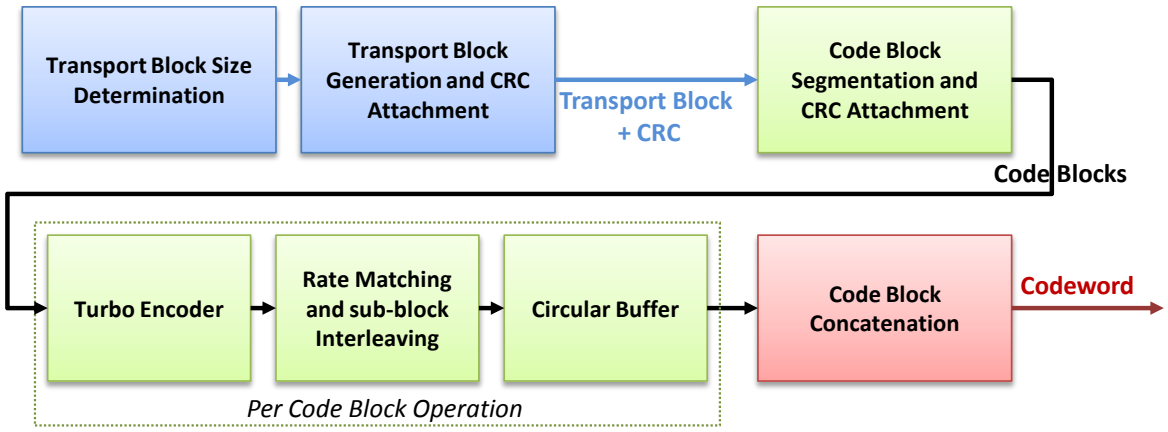

Figure 3.3: Transport channel processing (transmitter side) in LTE link level simulator.

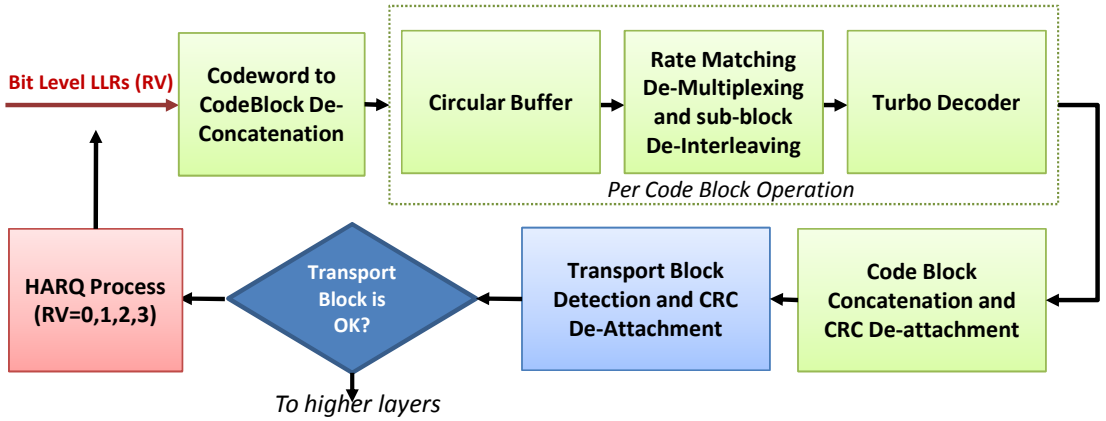

Figure 3.4: Transport channel processing (receiver side) in LTE link level simulator.

The transport channel processing chain starts with an addition of 24 bit CRC to the transport block before turbo encoding. Next the transport channel processing is defined per code block and deals with the transport block segmentation (to fit the maximum systematic block size of the turbo code: 6144 bits). Each code block is processed by Turbo coding, Rate matching (to adapt from the rate 1/3 of the mother code to the desired rate specified by the applied AMC scheme) and sub-block interleaving. The output of each channel coding processing sequence (Code block Segmentation, CRC attachment, Turbo coding, Rate matching and Sub-block interleaving) is stored in the circular buffer where redundancy versions are formed and HARQ processing is managed (4 redundancy versions), as shown in Figure 3.9. Finally coded blocks are concatenated to form the codeword that is sent to the physical channel processing chain in order to be mapped onto the MIMO layers.

The sub-block interleaving process specified by [4] is a main feature to improve the channel coding and is defined as part of the Rate matching process. The Rate matching for turbo coded transport channels consists of three sub-block interleavers for each information bit stream outputted by the Turbo encoder, followed by the bit collection of the whole interleaved bits, the generation of the circular buffer and the performing of the bit selection and pruning. The Sub-block interleaver applies a bit-wise interleaving at the turbo encoder that improves the performance of coded modulation over a Rayleigh fading channel. This technique is called BICM (see section 2.6.2), [50], and is also applied to MIMO-OFDM systems in fast fading scenarios, [54] and [55]. Thus, LTE/LTE-Advanced uses BICM to make possible to approximate the channel characterisation to an independent fast fading channel model that distributes low bit metrics enhancing error correction and increasing capacity.

In LTE/LTE-Advanced a codeword is a transport block after being processed by the chain of Figure 3.3 prior to the codeword to layer mapping. A maximum of two codewords can be transmitted at once using MIMO spatial multiplexing modes. If the number of available MIMO layers is greater than two then parallel transmission is applied to increase the throughput. The most complex block in this processing chain lies in the turbo decoding at the receiver side that uses the soft bit information (LLR) streams from the physical channel receive processing to recover

the transmitted codewords. The *Log-Likelihood Ratio* (LLR) reflects the reliability of the detected complex-valued symbols and, in case of an error occurs, the HARQ process request up to 4 retransmissions of redundancy version.

LTE/LTE-Advanced use an efficient incremental redundancy HARQ mechanism in order to achieve fast error correction at physical layer. This fast error correction is important to avoid the delay due to retransmission at higher layers that could trigger the *Transmission Control Protocol/Internet Protocol* (TCP/IP) congestion detection mechanisms and the associated throughput reduction.

Only for MIMO spatial multiplexing when the rank is greater than 1, two codewords per user may be transmitted. The advantage of transmitting two codewords is that it makes possible to obtain a significant capacity gain by applying *Successive Interference Cancellation* (SIC) techniques at codeword level, [35]. However, if no capacity gain is obtained with two codewords, transmitting only one codeword per user is also possible. Thus, the amount of control signalling is reduced from the point of view of CQI reporting and HARQ ACK/NACK feedback per subframe and user.

3.3.1 Transport Channel Capacity and Effective Code Rate

The DL user data is transmitted through the PDSCH in transport blocks. Thus, the transport channel PDSCH capacity is obtained based on the TBS that must be determined according to the procedures of [33]. The PDSCH capacity (in bits/subframe) is then:

$$C_{PDSCH} = Q_m \cdot N_{RB} \cdot N_L \cdot (12 \cdot (14 - N_{PDCCH}) - N_{RS})\ bits/subframe \tag{3.1}$$

where $Q_m = 2, 4, 6$ bits/symbol is the modulation order, N_{RB} is the number of allocated RBs, N_L is the number of layers available per codeword, N_{PDCCH} is the number of OFDM symbols used for PDCCH and N_{RS} is the number of REs reserved for pilots (per RB) within a subframe. If there are several SM MIMO layers available for the same codeword the PDSCH capacity is increased accordingly. If transmission diversity is applied then we should take $N_L = 1$ in expression 3.1.

In order to compute the *Effective Code Rate* (ECR) which is the key parameter for the Rate matching stage, the next step is to compute the size of the payload (systematic bits) to fit inside the PDSCH capacity (C_{PDSCH}). The PDSCH payload in systematic bits, B, is equal to the size of the *Transport Block* (TB), A, (as derived from table 7.1.7.2.1-1, [33]) plus the size of the additional CRC fields, L.

$$B = A + L \tag{3.2}$$

Due to restrictions in the internal interleaving, the size of the systematic turbo code block cannot be arbitrary; in fact there is a table of valid code block sizes ranging from 40 to 6144 bits, [4]. If the *Transport Block Size* (TBS) is not bigger than 6120 bits then code block fragmentation is not needed. In this case a single CRC of 24 bits (CRC) is added to the TB. If the TBS is greater than 6120 bits then a 24 bit CRC field is appended to the TB and the resulting packet is fragmented into several code blocks of (almost) equal length. Each one of the code block fragments is appended with an additional CRC of 24 bits. This allows the receiver to stop decoding the remaining fragments (if one of them fails to decode) and ask for the transmission of a new HARQ rv. In equation 3.3

B' represents the total amount of systematic bits plus CRC bits where B' depends on the value of C, if the TB is fragmented ($C > 1$) or not fragmented ($C = 1$), [4]:

$$B' = \begin{cases} B & \text{for } C = 1 \text{ and } L = 24\text{bits} \\ B + (C \cdot L) & \text{for } C > 1 \text{ and } L = 24\text{bits} \end{cases} \tag{3.3}$$

where B is the *Transport Block Size* (TBS), L is the size in bit of CRC and $C = \lceil B/(6144 - L) \rceil$ in case of $C > 1$.

Thus, the *Effective Code Rate* (ECR), η_{ECR}, is then:

$$\eta_{ECR} = \frac{B'}{C_{PDSCH}} \tag{3.4}$$

Tables 3.1 and 3.4 show the DL transport block size for an allocated bandwidth of 4 and 25 RBs and SISO mode assuming 8 reserved REs per RB for *Cell-specific reference signal*s (CRSs) in each subframe (1 ms), 1 layer/codeword and normal CP. Tables 3.2 and 3.5 show the DL transport block size for an allocated bandwidth of 4 and 25 RBs and MIMO mode with two antenna ports at the transmitter assuming 16 reserved REs per RB for CRSs in each subframe (1 ms), 2 layers/codeword and normal CP. Lastly, Tables 3.3 and 3.6 show the DL transport block size for an allocated bandwidth of 4 and 25 RBs and MIMO mode with four antenna ports at the transmitter assuming 20 reserved REs per RB for CRSs in each subframe (1 ms), 2 layers/codeword and normal CP.

In these tables the first column is the MCS index I_{MCS}, which is signalled in a 5 bit field within the PDCCH. From that field the UE extracts the modulation order and the TB size (by using tables indexed by the TBS index. Column B' is the PDSCH payload size, column C is the number of fragments and column K_+ is the size of the turbo code block. Columns K_-, C_- and F are set to 0 for the considered cases applying the procedure described by [4] that links this parameters as: $F = C_+ \cdot K_+ + C_- \cdot K_- - B'$ and $C = C_+ + C_-$. The *Effective Code Rate* (ECR) (Column η_{ECR}) is equal to the PDSCH payload over the PDSCH capacity. Notice that for MCS indexes from 0 to 4 the ECR is less than the mother code rate (1/3). In this case all the coded bits are transmitted (no puncturing at all) and the ECR is reduced by bit repetition, that is, some of the coded bits are transmitted more than once within the same rv, thus leading to an energy gain when the receiver combines the LLRs belonging to the same coded bit. Furthermore, notice that the MCS index 28 has been omitted because it has been discarded for the simulations that has been performed in this dissertation since the code rate for this index is too high; for instance, considering SISO mode and normal CP, the code rate for MCS 28 is 0.97 for an allocated bandwidth of 1 and 25 RBs and 0.99 for an allocated bandwidth of 4 RBs.

Additionally, given the ECR and the modulation order it is possible to compute the BICM SNR threshold for a particular AMC format, [17]. The BICM SNR threshold is the minimum SNR that would be required, with that AMC format, to achieve error free transmission with a capacity achieving error correcting code. The BICM threshold is computed by mapping the ECR through the BICM capacity curve of the modulation, see section 2.6.4. As shown in Tables 3.1, 3.2, 3.3, 3.4, 3.5 and 3.6, increasing the I_{MCS} by one leads to a BICM threshold approximately 1 dB higher than the previous format. This is valid except for MCS 10 and 17 where the modulation order is

changed with respect to the previous MCS format and, in these two cases, the space between the BICM thresholds is lower than 0.5 dB.

Table 3.1: Transport block size for 4 RBs, 1 layer/codeword, 8 Reserved REs/RB, Normal CP and 11 PDSCH OFDM symbols per subframe

I_{MCS} MCS index	Mod. Order	TBS index	Pilots [RE]	PDSCH Capacity [bits]	TB Size A [bits]	L [bits]	B [bits]	B' [bits]	C [bits]	C_+ [bits]	K_+ [bits]	C_- [bits]	K_- [bits]	F [bits]	ECR Rate η_{ECR}	BICM Threshold [dB]	Threshold delta [dB]
0	2	0	6	1008	88	24	112	112	1	1	112	0	0	0	0,11	-7,82	
1	2	1	6	1008	144	24	168	168	1	1	168	0	0	0	0,17	-5,89	1,94
2	2	2	6	1008	176	24	200	200	1	1	200	0	0	0	0,20	-5,01	0,87
3	2	3	6	1008	208	24	232	232	1	1	232	0	0	0	0,23	-4,27	0,74
4	2	4	6	1008	256	24	280	280	1	1	280	0	0	0	0,28	-3,28	0,99
5	2	5	6	1008	328	24	352	352	1	1	352	0	0	0	0,35	-2,03	1,25
6	2	6	6	1008	392	24	416	416	1	1	416	0	0	0	0,41	-1,05	0,98
7	2	7	6	1008	472	24	496	496	1	1	496	0	0	0	0,49	0,05	1,10
8	2	8	6	1008	536	24	560	560	1	1	560	0	0	0	0,56	0,87	0,83
9	2	9	6	1008	616	24	640	640	1	1	640	0	0	0	0,63	1,87	1,00
10	4	9	6	2016	616	24	640	640	1	1	640	0	0	0	0,32	2,02	0,15
11	4	10	6	2016	680	24	704	704	1	1	704	0	0	0	0,35	2,64	0,61
12	4	11	6	2016	776	24	800	800	1	1	800	0	0	0	0,40	3,51	0,87
13	4	12	6	2016	904	24	928	928	1	1	928	0	0	0	0,46	4,60	1,09
14	4	13	6	2016	1000	24	1024	1024	1	1	1024	0	0	0	0,51	5,38	0,78
15	4	14	6	2016	1128	24	1152	1152	1	1	1152	0	0	0	0,57	6,40	1,02
16	4	15	6	2016	1224	24	1248	1248	1	1	1248	0	0	0	0,62	7,16	0,76
17	6	15	6	3024	1224	24	1248	1248	1	1	1248	0	0	0	0,41	7,61	0,45
18	6	16	6	3024	1288	24	1312	1312	1	1	1312	0	0	0	0,43	8,06	0,45
19	6	17	6	3024	1416	24	1440	1440	1	1	1440	0	0	0	0,48	8,93	0,87
20	6	18	6	3024	1544	24	1568	1568	1	1	1568	0	0	0	0,52	9,78	0,85
21	6	19	6	3024	1736	24	1760	1760	1	1	1760	0	0	0	0,58	11,03	1,25
22	6	20	6	3024	1864	24	1888	1888	1	1	1888	0	0	0	0,62	11,86	0,82
23	6	21	6	3024	1992	24	2016	2016	1	1	2016	0	0	0	0,67	12,69	0,83
24	6	22	6	3024	2152	24	2176	2176	1	1	2176	0	0	0	0,72	13,74	1,05
25	6	23	6	3024	2280	24	2304	2304	1	1	2304	0	0	0	0,76	14,60	0,86
26	6	24	6	3024	2408	24	2432	2432	1	1	2432	0	0	0	0,80	15,48	0,88
27	6	25	6	3024	2536	24	2560	2560	1	1	2560	0	0	0	0,85	16,40	0,92

Table 3.2: Transport block size for 4 RBs, 1 layer/codeword, 16 Reserved REs/RB, Normal CP and 11 PDSCH OFDM symbols per subframe

I_{MCS} MCS index	Mod. Order	TBS index	Pilots [RE]	PDSCH Capacity [bits]	TB Size A [bits]	L [bits]	B [bits]	B' [bits]	C [bits]	C_+ [bits]	K_+ [bits]	C_- [bits]	K_- [bits]	F [bits]	ECR Rate η_{ECR}	BICM Threshold [dB]	Threshold delta [dB]
0	2	0	12	960	88	24	112	112	1	1	112	0	0	0	0,12	-7,59	
1	2	1	12	960	144	24	168	168	1	1	168	0	0	0	0,18	-5,64	1,95
2	2	2	12	960	176	24	200	200	1	1	200	0	0	0	0,21	-4,77	0,87
3	2	3	12	960	208	24	232	232	1	1	232	0	0	0	0,24	-4,01	0,76
4	2	4	12	960	256	24	280	280	1	1	280	0	0	0	0,29	-3,02	1,00
5	2	5	12	960	328	24	352	352	1	1	352	0	0	0	0,37	-1,75	1,26
6	2	6	12	960	392	24	416	416	1	1	416	0	0	0	0,43	-0,76	1,00
7	2	7	12	960	472	24	496	496	1	1	496	0	0	0	0,52	0,37	1,13
8	2	8	12	960	536	24	560	560	1	1	560	0	0	0	0,58	1,23	0,85
9	2	9	12	960	616	24	640	640	1	1	640	0	0	0	0,67	2,27	1,05
10	4	9	12	1920	616	24	640	640	1	1	640	0	0	0	0,33	2,33	0,06
11	4	10	12	1920	680	24	704	704	1	1	704	0	0	0	0,37	2,96	0,63
12	4	11	12	1920	776	24	800	800	1	1	800	0	0	0	0,42	3,85	0,89
13	4	12	12	1920	904	24	928	928	1	1	928	0	0	0	0,48	4,97	1,12
14	4	13	12	1920	1000	24	1024	1024	1	1	1024	0	0	0	0,53	5,79	0,82
15	4	14	12	1920	1128	24	1152	1152	1	1	1152	0	0	0	0,60	6,86	1,07
16	4	15	12	1920	1224	24	1248	1248	1	1	1248	0	0	0	0,65	7,65	0,80
17	6	15	12	2880	1224	24	1248	1248	1	1	1248	0	0	0	0,43	8,05	0,40
18	6	16	12	2880	1288	24	1312	1312	1	1	1312	0	0	0	0,46	8,51	0,46
19	6	17	12	2880	1416	24	1440	1440	1	1	1440	0	0	0	0,50	9,42	0,91
20	6	18	12	2880	1544	24	1568	1568	1	1	1568	0	0	0	0,54	10,30	0,88
21	6	19	12	2880	1736	24	1760	1760	1	1	1760	0	0	0	0,61	11,60	1,30
22	6	20	12	2880	1864	24	1888	1888	1	1	1888	0	0	0	0,66	12,47	0,87
23	6	21	12	2880	1992	24	2016	2016	1	1	2016	0	0	0	0,70	13,35	0,88
24	6	22	12	2880	2152	24	2176	2176	1	1	2176	0	0	0	0,76	14,47	1,12
25	6	23	12	2880	2280	24	2304	2304	1	1	2304	0	0	0	0,80	15,39	0,92
26	6	24	12	2880	2408	24	2432	2432	1	1	2432	0	0	0	0,84	16,35	0,96
27	6	25	12	2880	2536	24	2560	2560	1	1	2560	0	0	0	0,89	17,40	1,05

Table 3.3: Transport block size for 4 RBs, 2 layers/codeword, 24 Reserved REs/RB, Normal CP and 11 PDSCH OFDM symbols per subframe

I_{MCS} MCS index	Mod. Order	TBS index	Pilots [RE]	PDSCH Capacity [bits]	TB Size A [bits]	L [bits]	B [bits]	B' [bits]	C [bits]	C_+ [bits]	K_+ [bits]	C_- [bits]	K_- [bits]	F [bits]	ECR Rate η_{ECR}	BICM Threshold [dB]	Threshold delta [dB]
0	2	0	16	1856	208	24	232	232	1	1	232	0	0	0	0,13	-7,27	
1	2	1	16	1856	256	24	280	280	1	1	280	0	0	0	0,15	-6,37	0,90
2	2	2	16	1856	328	24	352	352	1	1	352	0	0	0	0,19	-5,24	1,13
3	2	3	16	1856	440	24	464	464	1	1	464	0	0	0	0,25	-3,84	1,41
4	2	4	16	1856	552	24	576	576	1	1	576	0	0	0	0,31	-2,68	1,15
5	2	5	16	1856	680	24	704	704	1	1	704	0	0	0	0,38	-1,55	1,13
6	2	6	16	1856	808	24	832	832	1	1	832	0	0	0	0,45	-0,54	1,01
7	2	7	16	1856	968	24	992	992	1	1	992	0	0	0	0,53	0,60	1,15
8	2	8	16	1856	1096	24	1120	1120	1	1	1120	0	0	0	0,60	1,48	0,88
9	2	9	16	1856	1256	24	1280	1280	1	1	1280	0	0	0	0,69	2,57	1,08
10	4	9	16	3712	1256	24	1280	1280	1	1	1280	0	0	0	0,34	2,56	-0,01
11	4	10	16	3712	1384	24	1408	1408	1	1	1408	0	0	0	0,38	3,19	0,63
12	4	11	16	3712	1608	24	1632	1632	1	1	1632	0	0	0	0,44	4,25	1,06
13	4	12	16	3712	1800	24	1824	1824	1	1	1824	0	0	0	0,49	5,11	0,86
14	4	13	16	3712	2024	24	2048	2048	1	1	2048	0	0	0	0,55	6,08	0,98
15	4	14	16	3712	2280	24	2304	2304	1	1	2304	0	0	0	0,62	7,18	1,10
16	4	15	16	3712	2472	24	2496	2496	1	1	2496	0	0	0	0,67	8,01	0,83
17	6	15	16	5568	2472	24	2496	2496	1	1	2496	0	0	0	0,45	8,36	0,35
18	6	16	16	5568	2600	24	2624	2624	1	1	2624	0	0	0	0,47	8,83	0,47
19	6	17	16	5568	2856	24	2880	2880	1	1	2880	0	0	0	0,52	9,76	0,93
20	6	18	16	5568	3112	24	3136	3136	1	1	3136	0	0	0	0,56	10,67	0,91
21	6	19	16	5568	3496	24	3520	3520	1	1	3520	0	0	0	0,63	12,01	1,35
22	6	20	16	5568	3752	24	3776	3776	1	1	3776	0	0	0	0,68	12,92	0,90
23	6	21	16	5568	4008	24	4032	4032	1	1	4032	0	0	0	0,72	13,83	0,92
24	6	22	16	5568	4264	24	4288	4288	1	1	4288	0	0	0	0,77	14,77	0,94
25	6	23	16	5568	4584	24	4608	4608	1	1	4608	0	0	0	0,83	15,98	1,21
26	6	24	16	5568	4968	24	4992	4992	1	1	4992	0	0	0	0,90	17,60	1,62
27	6	25	16	5568	5160	24	5184	5184	1	1	5184	0	0	0	0,93	18,57	0,97

Table 3.4: Transport block size for 25 RBs, 1 layer/codeword, 8 Reserved REs/RB, Normal CP and 11 PDSCH OFDM symbols per subframe

I_{MCS} MCS index	Mod. Order	TBS index	Pilots [RE]	PDSCH Capacity [bits]	TB Size A [bits]	L [bits]	B [bits]	B' [bits]	C [bits]	C_+ [bits]	K_+ [bits]	C_- [bits]	K_- [bits]	F [bits]	ECR Rate η_{ECR}	BICM Threshold [dB]	Threshold delta [dB]
0	2	0	6	6300	680	24	704	704	1	1	704	0	0	0	0,11	-7,80	
1	2	1	6	6300	904	24	928	928	1	1	928	0	0	0	0,15	-6,48	1,31
2	2	2	6	6300	1096	24	1120	1120	1	1	1120	0	0	0	0,18	-5,56	0,92
3	2	3	6	6300	1416	24	1440	1440	1	1	1440	0	0	0	0,23	-4,30	1,26
4	2	4	6	6300	1800	24	1824	1824	1	1	1824	0	0	0	0,29	-3,06	1,25
5	2	5	6	6300	2216	24	2240	2240	1	1	2240	0	0	0	0,36	-1,93	1,13
6	2	6	6	6300	2600	24	2624	2624	1	1	2624	0	0	0	0,42	-0,99	0,94
7	2	7	6	6300	3112	24	3136	3136	1	1	3136	0	0	0	0,50	0,12	1,12
8	2	8	6	6300	3496	24	3520	3520	1	1	3520	0	0	0	0,56	0,91	0,79
9	2	9	6	6300	4008	24	4032	4032	1	1	4032	0	0	0	0,64	1,94	1,02
10	4	9	6	12600	4008	24	4032	4032	1	1	4032	0	0	0	0,32	2,07	0,14
11	4	10	6	12600	4392	24	4416	4416	1	1	4416	0	0	0	0,35	2,66	0,59
12	4	11	6	12600	4968	24	4992	4992	1	1	4992	0	0	0	0,40	3,49	0,83
13	4	12	6	12600	5736	24	5760	5760	1	1	5760	0	0	0	0,46	4,54	1,05
14	4	13	6	12600	6456	24	6480	6528	2	2	3264	0	3200	0	0,52	5,54	1,00
15	4	14	6	12600	7224	24	7248	7296	2	2	3648	0	3584	0	0,58	6,52	0,98
16	4	15	6	12600	7736	24	7760	7808	2	2	3904	0	3840	0	0,62	7,17	0,65
17	6	15	6	18900	7736	24	7760	7808	2	2	3904	0	3840	0	0,41	7,61	0,45
18	6	16	6	18900	7992	24	8016	8064	2	2	4032	0	3968	0	0,43	7,91	0,29
19	6	17	6	18900	9144	24	9168	9216	2	2	4608	0	4544	0	0,49	9,16	1,26
20	6	18	6	18900	9912	24	9936	9984	2	2	4992	0	4928	0	0,53	9,98	0,81
21	6	19	6	18900	10680	24	10704	10752	2	2	5376	0	5312	0	0,57	10,78	0,80
22	6	20	6	18900	11448	24	11472	11520	2	2	5760	0	5696	0	0,61	11,57	0,79
23	6	21	6	18900	12576	24	12600	12672	3	3	4224	0	4160	0	0,67	12,76	1,19
24	6	22	6	18900	13536	24	13560	13632	3	3	4544	0	4480	0	0,72	13,77	1,01
25	6	23	6	18900	14112	24	14136	14208	3	3	4736	0	4672	0	0,75	14,39	0,62
26	6	24	6	18900	15264	24	15288	15360	3	3	5120	0	5056	0	0,81	15,66	1,27
27	6	25	6	18900	15840	24	15864	15936	3	3	5312	0	5248	0	0,84	16,33	0,67

Table 3.5: Transport block size for 25 RBs, 1 layer/codeword, 16 Reserved REs/RB, Normal CP and 11 PDSCH OFDM symbols per subframe

I_{MCS} MCS index	Mod. Order	TBS index	Pilots [RE]	PDSCH Capacity [bits]	TB Size A [bits]	L [bits]	B [bits]	B' [bits]	C [bits]	C_+ [bits]	K_+ [bits]	C_- [bits]	K_- [bits]	F [bits]	ECR Rate η_{ECR}	BICM Threshold [dB]	Threshold delta [dB]
0	2	0	12	6000	680	24	704	704	1	1	704	0	0	0	0,12	-7,57	
1	2	1	12	6000	904	24	928	928	1	1	928	0	0	0	0,15	-6,25	1,32
2	2	2	12	6000	1096	24	1120	1120	1	1	1120	0	0	0	0,19	-5,32	0,93
3	2	3	12	6000	1416	24	1440	1440	1	1	1440	0	0	0	0,24	-4,05	1,27
4	2	4	12	6000	1800	24	1824	1824	1	1	1824	0	0	0	0,30	-2,80	1,25
5	2	5	12	6000	2216	24	2240	2240	1	1	2240	0	0	0	0,37	-1,65	1,15
6	2	6	12	6000	2600	24	2624	2624	1	1	2624	0	0	0	0,44	-0,70	0,95
7	2	7	12	6000	3112	24	3136	3136	1	1	3136	0	0	0	0,52	0,45	1,15
8	2	8	12	6000	3496	24	3520	3520	1	1	3520	0	0	0	0,59	1,27	0,82
9	2	9	12	6000	4008	24	4032	4032	1	1	4032	0	0	0	0,67	2,34	1,07
10	4	9	12	12000	4008	24	4032	4032	1	1	4032	0	0	0	0,34	2,39	0,04
11	4	10	12	12000	4392	24	4416	4416	1	1	4416	0	0	0	0,37	2,99	0,60
12	4	11	12	12000	4968	24	4992	4992	1	1	4992	0	0	0	0,42	3,84	0,85
13	4	12	12	12000	5736	24	5760	5760	1	1	5760	0	0	0	0,48	4,92	1,08
14	4	13	12	12000	6456	24	6480	6528	2	2	3264	0	3200	0	0,54	5,96	1,04
15	4	14	12	12000	7224	24	7248	7296	2	2	3648	0	3584	0	0,61	6,98	1,02
16	4	15	12	12000	7736	24	7760	7808	2	2	3904	0	3840	0	0,65	7,66	0,68
17	6	15	12	18000	7736	24	7760	7808	2	2	3904	0	3840	0	0,43	8,06	0,39
18	6	16	12	18000	7992	24	8016	8064	2	2	4032	0	3968	0	0,45	8,35	0,30
19	6	17	12	18000	9144	24	9168	9216	2	2	4608	0	4544	0	0,51	9,66	1,30
20	6	18	12	18000	9912	24	9936	9984	2	2	4992	0	4928	0	0,55	10,50	0,84
21	6	19	12	18000	10680	24	10704	10752	2	2	5376	0	5312	0	0,60	11,33	0,84
22	6	20	12	18000	11448	24	11472	11520	2	2	5760	0	5696	0	0,64	12,16	0,83
23	6	21	12	18000	12576	24	12600	12672	3	3	4224	0	4160	0	0,70	13,43	1,26
24	6	22	12	18000	13536	24	13560	13632	3	3	4544	0	4480	0	0,76	14,50	1,08
25	6	23	12	18000	14112	24	14136	14208	3	3	4736	0	4672	0	0,79	15,17	0,66
26	6	24	12	18000	15264	24	15288	15360	3	3	5120	0	5056	0	0,85	16,55	1,39
27	6	25	12	18000	15840	24	15864	15936	3	3	5312	0	5248	0	0,89	17,31	0,76

Table 3.6: Transport block size for 25 RBs, 2 layers/codeword, 24 Reserved REs/RB, Normal CP and 11 PDSCH OFDM symbols per subframe

I_{MCS} MCS index	Mod. Order	TBS index	Pilots [RE]	PDSCH Capacity [bits]	TB Size A [bits]	L [bits]	B [bits]	B' [bits]	C [bits]	C_+ [bits]	K_+ [bits]	C_- [bits]	K_- [bits]	F [bits]	ECR Rate η_{ECR}	BICM Threshold [dB]	Threshold delta [dB]
0	2	0	16	11600	1384	24	1408	1408	1	1	1408	0	0	0	0,12	-7,41	
1	2	1	16	11600	1800	24	1824	1824	1	1	1824	0	0	0	0,16	-6,17	1,24
2	2	2	16	11600	2216	24	2240	2240	1	1	2240	0	0	0	0,19	-5,15	1,02
3	2	3	16	11600	2856	24	2880	2880	1	1	2880	0	0	0	0,25	-3,87	1,28
4	2	4	16	11600	3624	24	3648	3648	1	1	3648	0	0	0	0,31	-2,61	1,26
5	2	5	16	11600	4392	24	4416	4416	1	1	4416	0	0	0	0,38	-1,53	1,08
6	2	6	16	11600	5160	24	5184	5184	1	1	5184	0	0	0	0,45	-0,56	0,97
7	2	7	16	11600	6200	24	6224	6272	2	2	3136	0	3072	0	0,54	0,68	1,25
8	2	8	16	11600	6968	24	6992	7040	2	2	3520	0	3456	0	0,61	1,53	0,84
9	2	9	16	11600	7992	24	8016	8064	2	2	4032	0	3968	0	0,70	2,64	1,11
10	4	9	16	23200	7992	24	8016	8064	2	2	4032	0	3968	0	0,35	2,61	-0,03
11	4	10	16	23200	8760	24	8784	8832	2	2	4416	0	4352	0	0,38	3,22	0,61
12	4	11	16	23200	9912	24	9936	9984	2	2	4992	0	4928	0	0,43	4,09	0,87
13	4	12	16	23200	11448	24	11472	11520	2	2	5760	0	5696	0	0,50	5,19	1,10
14	4	13	16	23200	12960	24	12984	13056	3	3	4352	0	4288	0	0,56	6,26	1,07
15	4	14	16	23200	14112	24	14136	14208	3	3	4736	0	4672	0	0,61	7,05	0,79
16	4	15	16	23200	15264	24	15288	15360	3	3	5120	0	5056	0	0,66	7,84	0,79
17	6	15	16	34800	15264	24	15288	15360	3	3	5120	0	5056	0	0,44	8,21	0,37
18	6	16	16	34800	16416	24	16440	16512	3	3	5504	0	5440	0	0,47	8,90	0,68
19	6	17	16	34800	18336	24	18360	18432	3	3	6144	0	6080	0	0,53	10,01	1,11
20	6	18	16	34800	19848	24	19872	19968	4	4	4992	0	4928	0	0,57	10,87	0,87
21	6	19	16	34800	21384	24	21408	21504	4	4	5376	0	5312	0	0,62	11,73	0,86
22	6	20	16	34800	22920	24	22944	23040	4	4	5760	0	5696	0	0,66	12,60	0,86
23	6	21	16	34800	25456	24	25480	25600	5	5	5120	0	5056	0	0,74	14,06	1,46
24	6	22	16	34800	27376	24	27400	27520	5	5	5504	0	5440	0	0,79	15,20	1,14
25	6	23	16	34800	28336	24	28360	28480	5	5	5696	0	5632	0	0,82	15,78	0,59
26	6	24	16	34800	30576	24	30600	30720	5	5	6144	0	6080	0	0,88	17,25	1,47
27	6	25	16	34800	31704	24	31728	31872	6	6	5312	0	5248	0	0,92	18,12	0,87

3.3.2 Channel Coding, Rate Matching and HARQ Processes

The turbo coding is a forward error correction (or channel coding) technique used for LTE/LTE-Advanced Transport Channels (except for the broadcast channel) to reduce the BLER at the expense of a reduction of the users information rate and increase reliability. Channel coding is a combination of error detection, error correction, rate matching, interleaving and transport channels mapping to physical channels. The output of channel coding processes (coded bits) are stored in a circular buffer where redundancy versions are formed. A rv is the retransmission unit in the hybrid automatic repeat request HARQ and a maximum of 4 rvs is allowed in LTE, where the first one contains the systematic bits and a part of the redundant bits.

3.3.2.1 Turbo Coding

The scheme of the turbo encoder, specified by 3GPP TS 36.212 [4], is a *Parallel Concatenated Convolutional Code* (PCCC) with a coding rate of 1/3, two 8-state constituent encoders and a contention-free *Quadratic Permutation Polynomial* (QPP) turbo code internal interleaver. The turbo encoder performs Trellis termination and before the turbo coding, transport blocks are segmented into byte aligned segments with a maximum information block size of 6144 bits, called code block. The error detection is supported by the use of 24 bit CRC. The result of the rate 1/3 turbo encoder creates three independents streams with systematic and redundant bits. These streams are interleaved and fed to the circular buffer based on rate matching and HARQ procedure.

Figure 3.5 shows the structure of the LTE turbo encoder. c_k is the input sequence to be encoded that corresponds to the systematic bits sequence. c_k is also block-interleaved before it is encoded in the second convolution code constituent to increase the effects of coding diversity, and then, it is called c'_k. The output of a turbo encoder consists of the outputs of each convolutional encoder as well as the original sequence; hence, the overall code is systematic (that is, the information sequence appears at the output). The systematic bits of the second constituent are not sent because they can be obtained in the decoder by interleaving the original sequence sent. Then, the output from the turbo encoder called coded block consists of 3 encoded streams, one with systematic bits, $x_k = c_k$ and two with encoded bits, z_k and z'_k.

The turbo block is ended by a trellis termination and guarantees that the encoder is always at state zero at the end of a turbo block and at the beginning of the next one. During normal operation the bits are transmitted in the following order before multiplexing: x_k, z_k, z'_k that corresponds to a code rate of 1/3. Trellis termination is performed by taking the tail bits from the shift register feedback after all information bits are encoded. The tail bits are padded after the encoding of information bits and the length of the trellis termination sequence is 12. First the three systematic tail bits of the first constituent encoder are padded and they are also encoded and padded. Then the same for the tails bits of the second constituent.

3.3.2.2 Turbo Decoding

At the receiver side, the programming of the turbo decoder is also sensitive to different implementations. The turbo internal interleaving and de-interleaving has been changed with respect to the 3G (*UMTS Terrestrial Radio Access* (UTRA)) specifications. There are different alternatives for soft-input soft-output decoders for the two convolutional codes that are the constituents of the turbo code. The link level simulator presented in this chapter uses *Maximum a Posteriori*

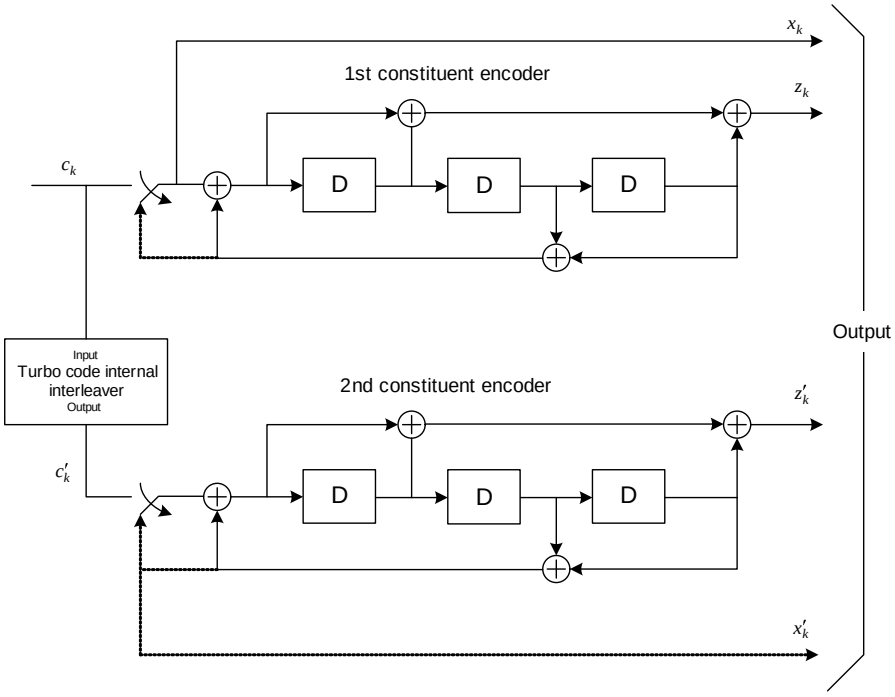

Figure 3.5: Structure of rate 1/3 turbo encoder (dotted lines apply for trellis termination only), [4].

Probability (MAP) algorithm for the decoding of each constituent and a maximum of 8 decoding iterations, [56] and [57]. The number of iterations has an impact on the BLER. Figure 3.6 shows the scheme of the turbo decoder.

For the implementation of the MAP algorithm, the knowledge of the probability of all possible transitions in the trellis, shown in Figure 3.7, is required. The initial conditions to calculate these probabilities starts from the physical channel LLRs conditioned on the transmission of logical level 0 or logical level 1 (how they are obtained is described in section 3.3.3.2). The computation of the LLR of a given bit, c_k, is defined in equation 3.5

$$LLR(c_k) = \ln\left(\frac{Prob\left(c_k = 0|x_k\right)}{Prob\left(c_k = 1|x_k\right)}\right) \tag{3.5}$$

where x_k is the received noisy soft sample of c_k. Then, the LLR can also be written, according to Bayes rule, as equation 3.6:

$$\underset{}{LLR(c_k)} = \underbrace{\ln\left(\frac{Prob(x_k|c_k=0)}{Prob(x_k|c_k=1)}\right)}_{\text{Channel LLR}} + \underbrace{\ln\left(\frac{Prob(c_k=0)}{Prob(c_k=1)}\right)}_{\text{A Priori Information}} \tag{3.6}$$

where the a priori information is different from zero only after the first decoding iteration. The channel LLR can also be decomposed in two additive terms: the intrinsic information and the extrinsic information. The intrinsic information is the LLR that depends only on the noisy sample of the bit x_k, while the extrinsic information is the LLR that depends on the adjacent bits and on

the trellis constraints. Each decoder computes the complete LLR of every bit in every iteration, but to avoid undesirable feedback, only the extrinsic information at the output of each decoder is used as a priori information for the next decoding process. After 8 decoding iterations, a hard decision is taken for every bit based on the sign on the LLR, see equation 3.7. If the LLR is lower than 0, the decoded bit, $\hat{c_k}$, is logical 1, otherwise it is logical 0.

$$\hat{c_k} = \begin{cases} 0, & LLR(c_k) \geq 0 \\ 1, & LLR(c_k) < 0 \end{cases} \tag{3.7}$$

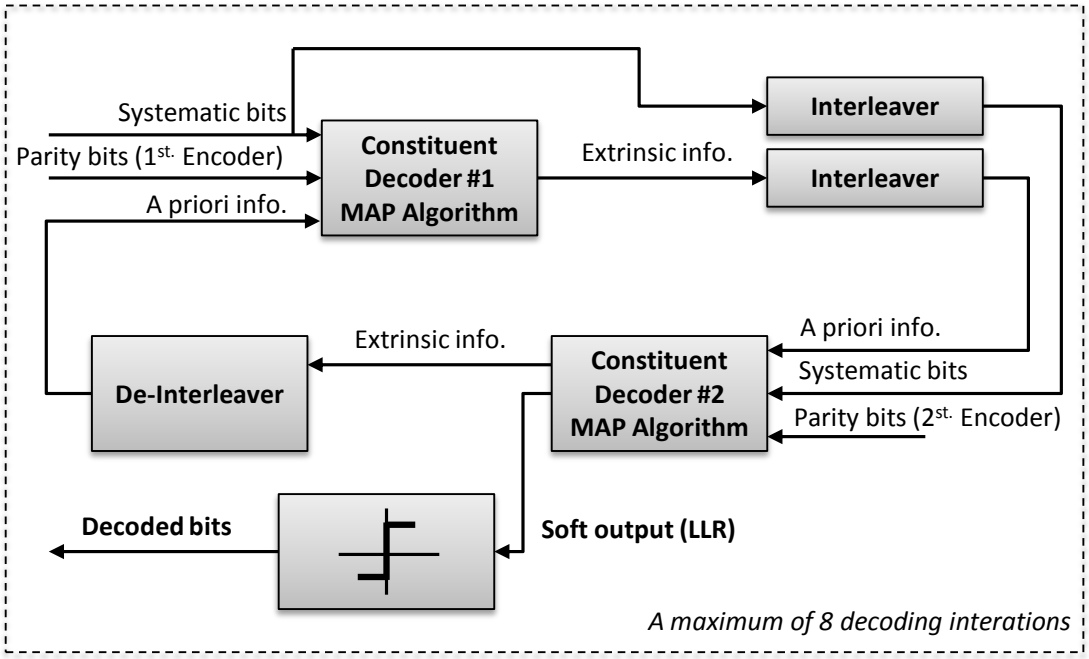

Figure 3.6: Block Diagram of the turbo decoder

3.3.2.3 Rate Matching and HARQ Processes

The implementation of the Rate matching and HARQ are one of the most sensitive pieces within the link level simulator, since small differences in the interpretation of the standards can lead to different results. LTE and LTE-Advanced use IR HARQ. The Rate matching for turbo coded transport channels is performed on the basis of a single coded block. As shown in Figure 3.3, each TB is initially appended with a CRC and, since the turbo encoder admits blocks of information bits with specific sizes and the maximum valid size is 6144 bits, the TB can be fragmented (if necessary) to produce one or several information code blocks not bigger than 6144 bits. If TB fragmentation is applied then each resultant information code block is again appended with an additional CRC.

Figure 3.9 shows a block diagram of the LTE channel coding processing performed on each code block. First the code block is turbo encoded with a mother code rate of 1/3 which outputs three flows of coded bits: systematic, redundancy 1 and redundancy 2. Second, each bit stream

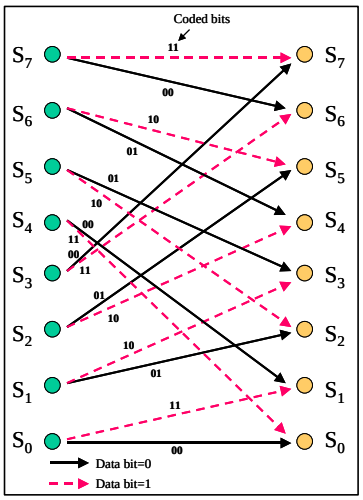

Figure 3.7: Trellis of each 8-state constituent encoders

is interleaved according to the sub-block interleaver defined in [4] and stored in a single buffer. The interleaved systematic turbo-coded bits are stored in the beginning of the buffer contiguously and then interleaved redundant turbo-coded bits of redundancy streams 1 and 2 are stored in an interlaced format. This single buffer is seen as a virtual circular buffer. Since the mother code rate is 1/3, if the size of the information code block to be transmitted is N bits where $40 \leq N \leq 6144$, the size of the circular buffer is $3N + 12$, where 12 bits are used for trellis finalization.

Rate matching is carried out by bit selection and pruning procedure that selects which coded bits will be transmitted at the next subframe to satisfy the desired code rate of operation. Due to the interleaving, reading the circular buffer in an ordered way leads to an appropriate puncturing pattern in the codeword. To produce repetition of the coded bits, the circular buffer (or a portion of it) is transmitted more than once by repeatedly reading it for more than one turn. Figure 3.9 shows a representation of this circular buffer that provides a simple method of generating puncturing patterns with good performance as it is described in [58] and [59].

Figure 3.9 shows how up to 4 different rvs are obtained from the same codeword by reading different sectors of the circular buffer. The depicted situation corresponds to a high code rate (near unity). In this case the first rv= 0 includes almost only systematic bits, while rvs from 1 to 3 are formed by reading subsequent portions of the circular buffer. Notice that each of the rvs is decodable by itself and that each rv partially overlaps with the previous one. The size of the four possible rvs is the same, and it is this size what determines the code rate, since for rate 1/3 (for example) each rv would encompass the full circular buffer, while for rate $< 1/3$ each rv encompasses more than one turn of the circular buffer. So, for rate $< 1/3$ there are at least some coded bits that are transmitted more than once within the same rv, and in general we can say that, after rv= 3 has been received, some coded bits may have been transmitted only once while others may have been transmitted more than once.

Thus, Rate matching is responsible for creating a well designed puncturing pattern of the mother code. It must be implemented exactly as the standard specifies, since the decoding process is

sensitive to the puncturing pattern. Interleaving is always necessary, even for simulations assuming AWGN channel, since the multilevel modulations (mainly 64QAM) have unequal error protection of the coded bits and create a periodic pattern in the reliability of the received LLRs that must be broken by the interleaving (this is the principle of BICM).

Moreover, circular buffer is well suited to IR HARQ operation as different rvs, up to 4, can be specified by simply defining different starting points in circular buffer. HARQ technique is used to control the retransmission of packets, so, if there is no errors in the decoded packet, there is no retransmission. The HARQ process uses the ACK/NACK to detect the error free transmission. In addition to HARQ, E-UTRAN provides ARQ functionalities. The ARQ functionality provides error correction by retransmissions in acknowledged mode at Layer 2 while the HARQ functionality ensures delivery between peer entities at Layer 1.

In order to obtain the HARQ performance, Monte-carlo simulations have been performed for different SNRs to obtain the TB error probability (BLER) performance. The region of interest for BLER results is from 1 to 10^{-2}. The same SNR has been considered for each rv retransmission. The BLERs are computed in the following way taking into account that N_{TB} TBs are transmitted, N_E is the number of erroneous TB detections after the 4 HARQ retransmissions, $N_{cnt}(\text{rv} = x)$ is the number of transmissions performed at rv$= x$ and $N_{err}(\text{rv} = x)$ is the number of erroneous detections after decoding at rv $= x$. Thus, residual BLER is defined as:

$$\text{residual BLER} = \frac{N_E}{N_{TB}} \tag{3.8}$$

the BLER at rv x as:

$$\text{BLER (at } rv = x) = \frac{N_{err}(rv = x)}{N_{cnt}(rv = x)} \tag{3.9}$$

the total number of simulated TTIs to transmit N_{TB} TBs as:

$$N_{TTI} = N_{cnt}(rv = 0) + N_{cnt}(rv = 1) + N_{cnt}(rv = 2) + N_{cnt}(rv = 3) \tag{3.10}$$

the HARQ efficiency as:

$$\eta_{HARQ} = \frac{N_{TB} - N_E}{N_{TTI}} \tag{3.11}$$

and the overall BLER, that is the TTI rate with erroneous TB detections, as:

$$\text{overall BLER} = 1 - \eta_{HARQ} \tag{3.12}$$

For example, Figure 3.8 shows the HARQ performance for MCS 6 in AWGN channel and assuming a bandwidth of 25 RB. A 10% BLER is the point of interest, thus for $rv = 0$ is achieved at around -0.15 dB of SNR, -3.40 dB for $rv = 1$, -5.05 dB for $rv = 2$ and -6.45 dB for $rv = 3$. In addition, the residual BLER matches the BLER at $rv = 3$. Note that the probability of correct decoding is remarkably increased at each incremental redundancy retransmission due to that for every new rv received the LLR are combined before trying to decode the codeword. It has to be noted also that the most remarkable gain is between the first and second rv transmission.

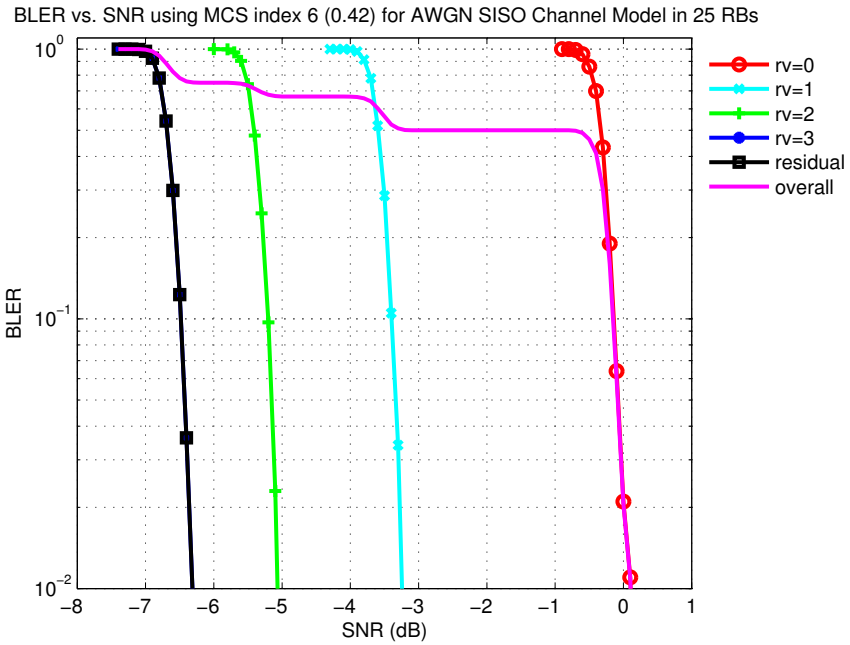

Figure 3.8: BLER curves for MCS 6 with HARQ transmissions rv=0,1,2 and 3 in AWGN channel (assuming a bandwidth of 25 RBs and 8 Reserved REs/(RB and TTI))

3.3.3 Soft Demodulation

LTE/LTE-Advanced is a MIMO-OFDM-BICM system. MIMO provides multiple spatial layers, OFDM divides the frequency band into multiple narrow subchannels and BICM enhances the soft demodulation due to the bit interleaving which distributes the unreliable bit metrics through a bitwise interleaver. At the receiver side, the physical channel processing uses soft demodulation computing the LLR of each coded bit. Then, these LLRs after being de-interleaved are used by the transport channel processing, as shown in Figure 3.4, for soft decoding.

3.3.3.1 BICM System Model

The BICM system model is represented by the block diagram of Figure 3.10 and it consists of an encoder, an interleaver, a multilevel modulation mapper, a stationary finite-memory vector channel with a transition pdf $p_\theta(s|r)$ where θ represents the channel state, a demodulator, a de-interleaver and a decoder. The channel is assumed to be memoryless and θ is assumed to be independent of the channel input. This model can represent AWGN channels (θ = constant) and frequency nonselective slow-fading channels (θ describes the multiplicative fading process) such as the narrowband subchannels of a MIMO-OFDM system, [50].

BICM allows to reduce the complexity of the radio channel to an independent and memoryless equivalent binary channel (DMC) between a transmitted coded bit, $b \in 0, 1$, and the received LLR, z=LLR(b), regardless of the applied modulation and the processing at the transmitter and at the receiver. This is a kind of binary channel with a *hard* input and a *soft* output, as depicted in Figure 2.13. The blocks of the BICM system model involved in this equivalent binary channel are shown in Figure 3.10 with a blue rectangle as background.

3.3.3.2 Simplified Computation of the bit level LLR

The MQAM demodulator at the receiver side computes the bit level LLR to generate soft values as input to the turbo decoder reflecting the reliability of each bit, instead of applying a hard decision on the demodulated bits. The LLR at bit level ($LLR(b)$) is defined by equation 2.18 and computed following equation 2.19 if AWGN channel is assumed. Since equation 2.19 is too complex to evaluate, in particular for high order modulations, $LLR(b)$ is usually approximated by Λ computed as follows, [17]:

$$\Lambda \cong \ln\left(\frac{e^{\left(-\frac{|y-y_0|^2}{\sigma^2}\right)}}{e^{\left(-\frac{|y-y_1|^2}{\sigma^2}\right)}}\right) = \frac{1}{\sigma^2}\left(|y-y_1|^2 - |y-y_0|^2\right) \tag{3.13}$$

where y_0 (respectively y_1) is the modulation state for which the transmitted bit is at logical zero (respectively logical one) that falls nearest to y. The simplification is based on the *max-log* approximation, i.e.: $\ln(e^a + e^b) \approx max(a,b)$. If the noise is not Gaussian, which can happen for example when there is residual interference after equalization, it is possible to take the noise statistics into account in the computation of the LLRs.

Figure 3.11 shows the pdfs of the LLRs at bit level for the LTE modulations in AWGN channel for a fixed SNR. Each SNR value has been selected to achieve approximately the same MIB for all the modulations. The LLRs have been computed based on the exact definition (no max-log approximation) and their pdf has been computed based on the paradigm of Figure 2.13, that is all received bits contribute to the pdf regardless of the weight of the bit within the modulation symbol. This is the reason for the peaks that appear in the plots for 16QAM and 64QAM.

Figure 3.12 shows the statistics of the bit level LLRs for 64QAM when computed based on equations 2.19 or 3.13. In Figure 3.13 it is verified that there is a good agreement between the BLER performance obtained by the aprox and the exact computation of the bit level LLR for rv= 0 in AWGN and *ETU channel model and maximum Doppler frequency of 300 Hz* (ETU300) SISO channels for MCS 0,9,15 and 27 in a bandwidth of 25 RBs with turbo code block size of 704, 4032, 3648 and 5312 bits (see Table 3.4), respectively.

Although the LLRs can take big absolute values (mainly for high SNRs). Figure 3.11 shows that given the range of SNRs of interest, the LLRs can be limited in practice to an absolute value not greater than 10 in the link level simulator. Figure 3.14 shows the region of LLR values for QPSK in AWGN channel for which the pdfs do not overlap contributes to the MI (from equation 2.16) as an integral value. This means the dynamic range of the LLRs can be compressed by limiting their absolute value to the highest value for which the pdfs for $bit = 0$ and $bit = 1$ still overlap. In this way the pdf for the non overlapping region becomes a Dirac delta function that contains the same area as the original pdf and the MI of the channel is preserved. This assumption can also be extended to the rest of the LTE modulations.

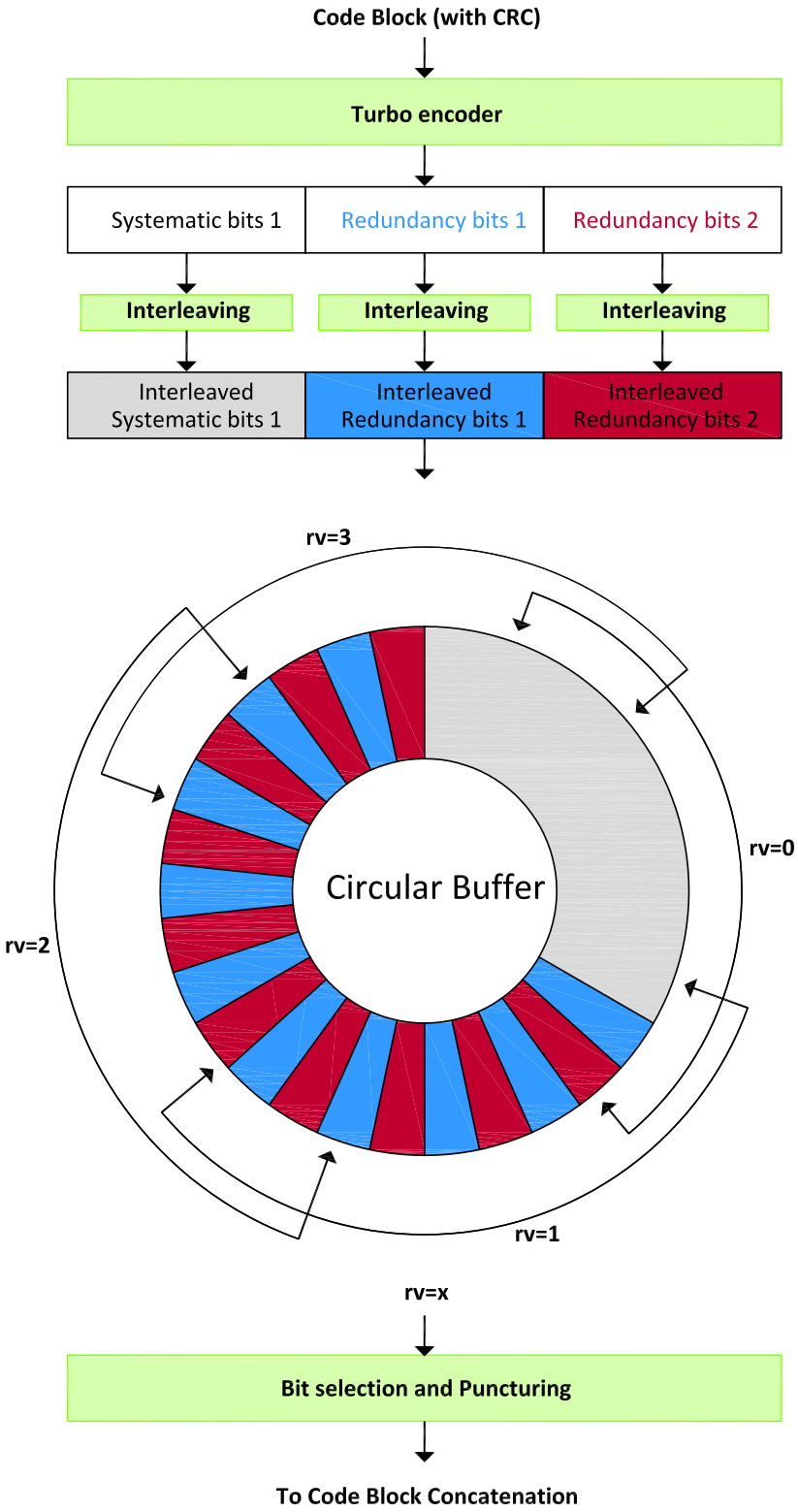

Figure 3.9: LTE/LTE-Advanced Channel Coding Processing and circular buffer reading for different rvs.

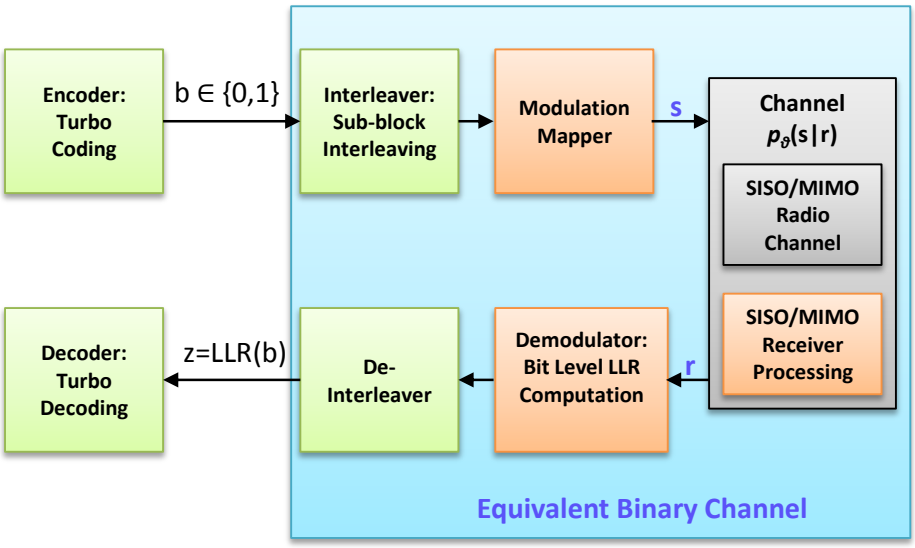

Figure 3.10: Block diagram of BICM transmission/reception

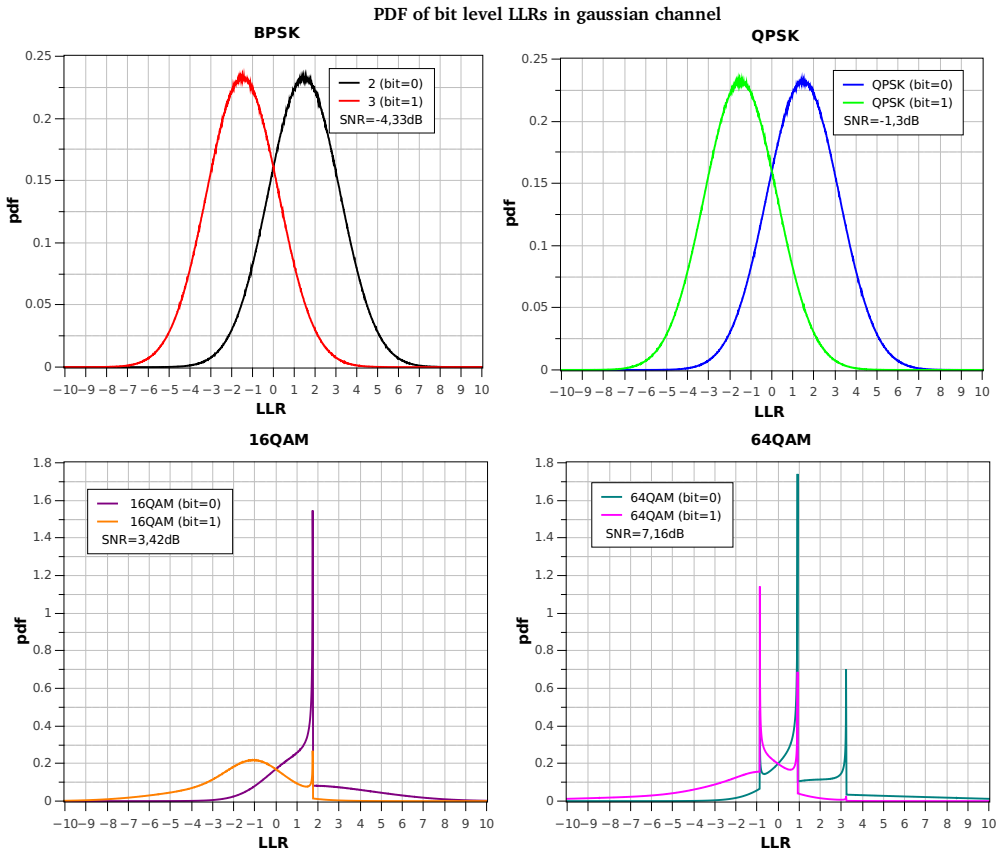

Figure 3.11: pdf of bit level LLRs for the LTE modulations in AWGN channel

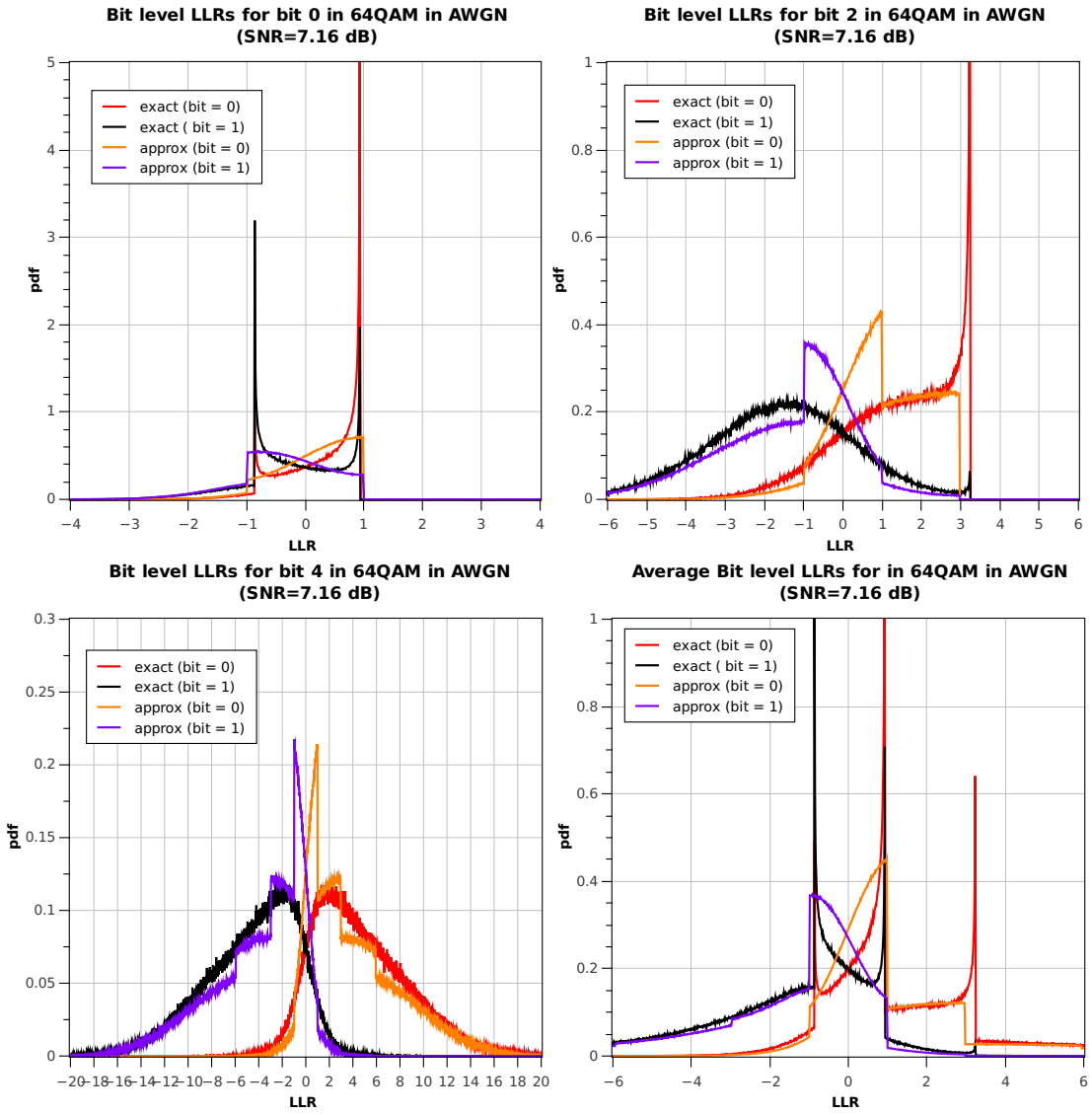

Figure 3.12: Comparison among exact and approximated LLRs for 64QAM and $SNR = 7.16dB$.

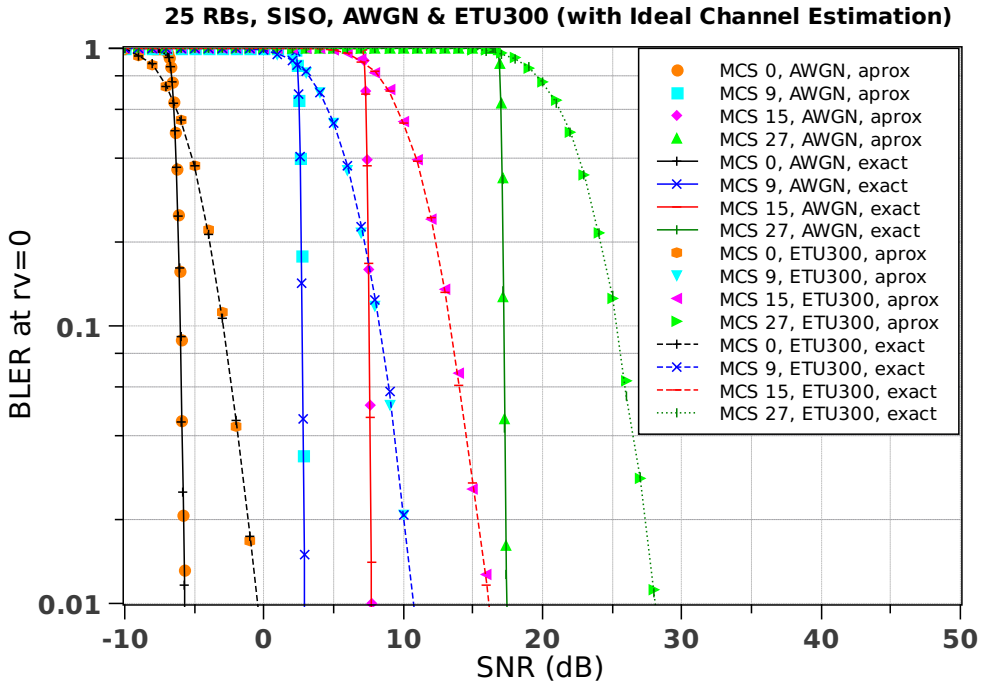

Figure 3.13: BLER curves taking into account the aprox and the exact computation of the bit level LLR in AWGN and ETU300 SISO channels for MCS 0,9,15 and 27 in a bandwidth of 25 RBs

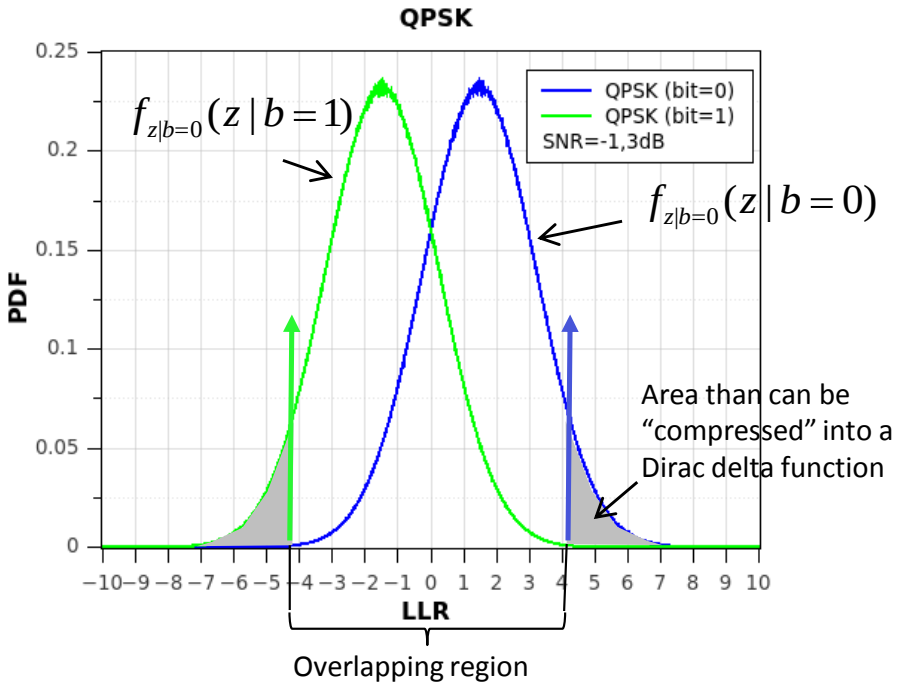

Figure 3.14: Dynamic range of the exact bit level LLRs pdf for QPSK in AWGN channel

3.4 E-UTRA Physical Channel Processing

The physical channel processing is the lowest layer in the link level simulator. Figure 3.15 depicts the physical channel processing for DL and SU-MIMO (for UL is very similar, the main difference is the additional DFT/IDFT blocks that are needed to map/de-map the transmitted signal (SC-FDMA) to the RB assigned to the UE). It takes as input the coded bits of the codewords (1 or 2 codewords) after rate matching and interleaving and processes them according to the selected transmission mode. On the receiving side the LLRs of the coded bits are delivered to the de-interleaver and LLR combiner on the TB processing chain. Notice that if SIC techniques are applied the division between the processing of Physical Channel and Transport Channel is not so sharp, since the already decoded code blocks are sent back to the Physical Channel processing and used to improve the MIMO equalisation.

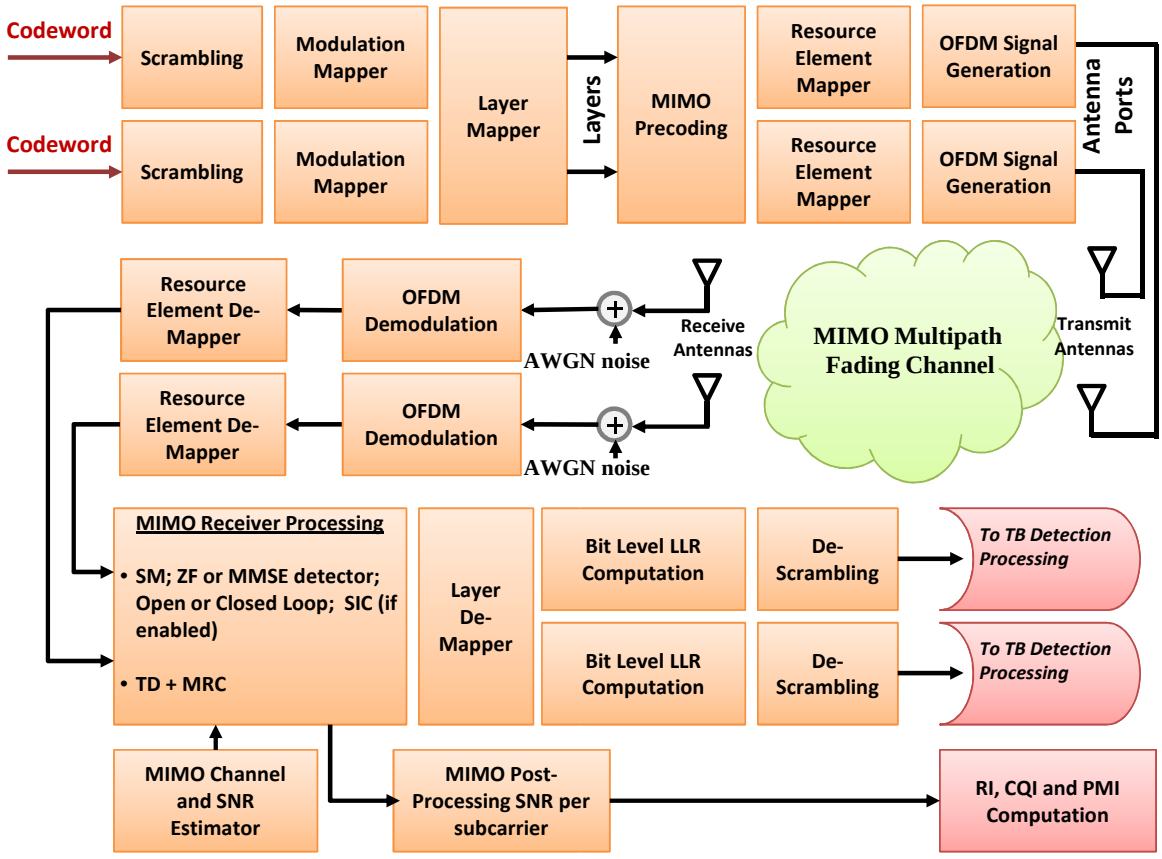

Figure 3.15: Physical channel processing in LTE link level simulator (DL and SU-MIMO).

There are some high level aspects that must be initially specified, like the LTE or LTE-Advanced release, the simulation of FDD/TDD, the simulation of DL or UL and the simulation of an unicast carrier or a broadcast eMBMS carrier. Next high level issue is the simulated LTE/LTE-Advanced transmission mode. In addition to the LTE-Advanced transmission mode, which conditions the full PHY configuration, important parameters to settle down are: simulated carrier frequency and simulated bandwidth. Those parameters have an impact on the channel model that can be applied and on the PHY capacity, which has an influence on the size of the code blocks that can be applied.

In [60] there is a proposal for E-UTRA operating bands for FDD and TDD, as well as deployment scenarios for feasibility study. The RBs are allocated in groups of different sizes depending of the whole system bandwidth. The RBs can be allocated contiguously or scattered in the whole system bandwidth. In the UL, due to the use of SC-FDMA, the RBs are allocated contiguously but a frequency hopping pattern may be applied, on a TTI basis, to increase frequency diversity.

The physical channel processing chain deals with modulated symbols, layers and antenna ports. Firstly, at the transmitter side, the coded bits of each codeword are scrambled with Gold sequences for interference randomization. In second place, the QAM Modulator Mapper generates the complex modulated symbols belonging to either a QPSK, 16QAM or 64QAM constellation, as shown in Figure 3.16, [3]. Next, the complex-valued modulation symbols are mapped onto one or several transmission layers which are precoded for transmission on antenna ports. Then the precoded complex-valued modulation symbols for each antenna port are mapped to resource elements and the complex-valued time-domain OFDM signal for each antenna port is generated. As it has been discussed previously, the simulation of the OFDM modulation is skipped and the link level simulation is performed at the complex-valued frequency-domain. Finally, the link level simulator emulates the MIMO-OFDM transmission/reception through a mobile radio channel model that is described in next section.

The receiver side for the physical channel starts with the inverse processes of the OFDM Signal Generation and Resource Element Mapper in order to map the received signal onto each resource element in the frequency domain. Next the MIMO Receiver Processing is applied in order to detect the transmitted complex-valued symbol and the layer de-mapper reconstructs the received codeword streams (one or two) at symbol level. Finally the Bit Level LLR Computation generates the soft bit information stream for each codeword and, prior to send this bit-level information to the transport block processing for channel decoding, each stream is de-scrambled. Moreover, the receiver has also to estimate the MIMO channel and the instantaneous SNR in order to feedback a CQI to the transmitter.

3.4.1 Simulating the MIMO wideband mobile channel

The simulation of the MIMO multipath channel is one of the key issues in the simulation of the PHY channel. Depending on the desired results and on the simulated LTE transmission modes the channel simulator may introduce different degrees of complexity. The link level simulator presented in this dissertation uses the classical way to simulate the MIMO channel following the procedure outlined in [19], [61], which is a purely stochastic method which uses MIMO correlation matrices, doppler spectra, Rice component parameters and the power delay profile. This method to simulate the MIMO channel was presented and discussed in [62], [63] and [64] and implemented in the *Intelligent Multi-Element Transmit and Receive Antennas* (I-METRA) project, [65]. A more complex method is the one proposed in [66], [67], [68] which takes into account the per-path power azimuth spectrum at the eNodeB and at the UE, so it models the geometry of the scattering in a stochastic way. However, [67] and [68] also propose to apply the simplified stochastic model based on correlation matrices in order to generate channel coefficients.

The implemented channel model basically consists of a power delay profile, with several taps, which depends on the propagation environment (EPA, EVA, ETU),[69], [19] for each path of the MIMO channel. For each propagation path a complex random matrix, with i.i.d. elements is

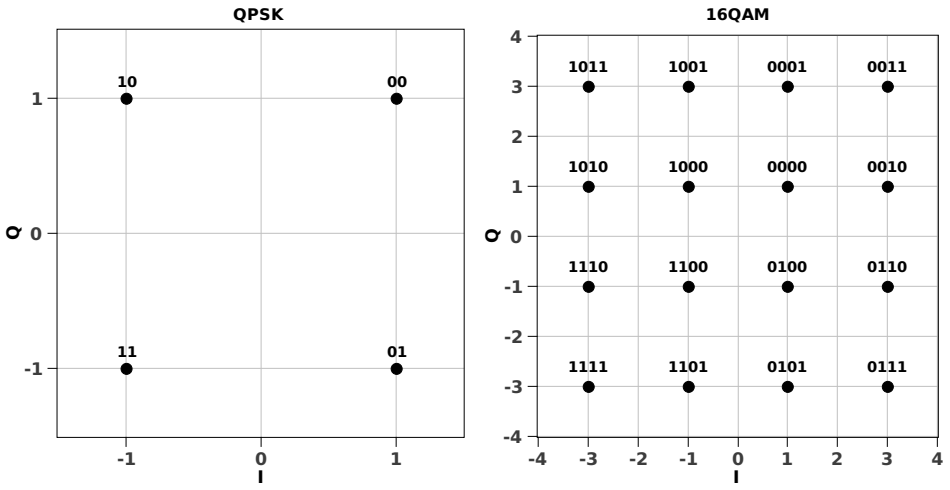

(a) QPSK and 16QAM

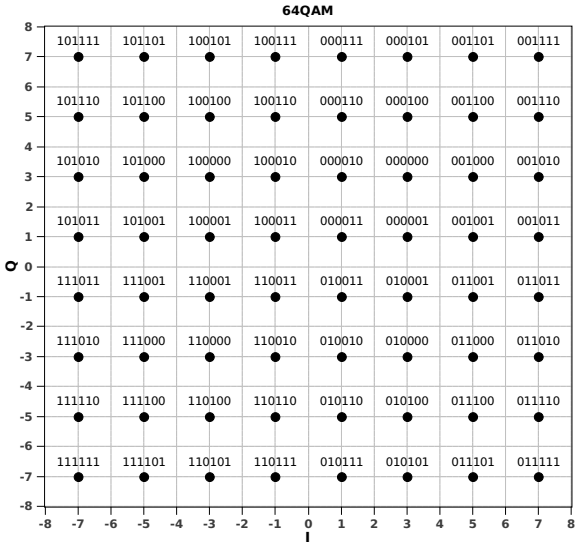

(b) 64QAM

Figure 3.16: Constellations (Not Normalized) of QPSK, 16QAM and 64QAM for LTE/LTE-Advanced [3]

generated. Antenna correlation is introduced by applying Cholesky factorisation to the original i.i.d. elements based on a set of matrices (from [19]) to model low, medium or high correlation. Time variations are simulated by using a classical Doppler spectrum (Jakes) with a maximum Doppler frequency which also depends on the propagation environment.

Given that the TTI in LTE is 1 ms, in slow mobility scenarios it is possible to make the hypothesis that the channel is constant during the transmission of a complete TB. If we also assume that the UE is not scheduled persistently, then the channel realisations in consecutive transmissions can be considered independent. In this case it is not necessary to model the Doppler variations of the channel, and the simulator can generate independent channel snapshots for each TB. This approach is not valid for continuous transmission like, for example, in a broadcast eMBMS carrier.

3.4.1.1 Correlation-based MIMO radio channel stochastic model

The MIMO system depicted in Figure 3.17 is formed by the M_{TX} transmitter antennas and the N_{RX} receiver antennas which define $N_{RX} \times M_{TX}$ spatial channels (subchannels) between the eNodeB and the UE. Each subchannel is a multipath propagation channel based on the *Gaussian Wide-Sense Stationary Uncorrelated Scattering* (GWSSUS) model.

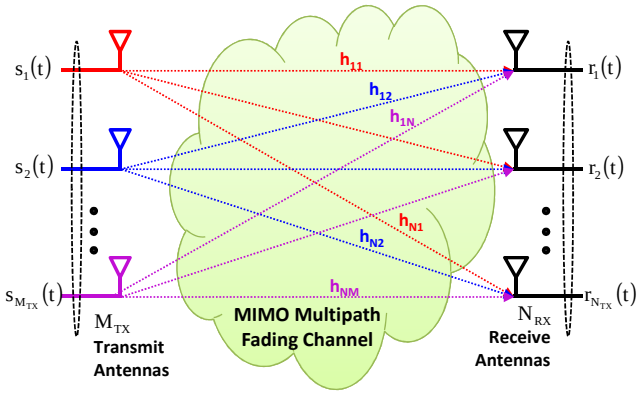

Figure 3.17: MIMO antenna arrays in a scattering environment

The composite MIMO channel response is given by the $N_{RX} \times M_{TX}$ matrix $\mathbf{H}(\tau, t)$ where τ is the *root mean square* (rms) delay spread and t is the channel time variance, Equation 3.14.

$$\mathbf{H}(\tau,t) = \begin{bmatrix} \mathrm{h}_{1,1}(\tau,t) & \mathrm{h}_{1,2}(\tau,t) & \dots & \mathrm{h}_{1,M_{TX}}(\tau,t) \\ \mathrm{h}_{2,1}(\tau,t) & \mathrm{h}_{2,2}(\tau,t) & \dots & \mathrm{h}_{2,M_{TX}}(\tau,t) \\ \vdots & \vdots & \dots & \vdots \\ \mathrm{h}_{N_{RX},1}(\tau,t) & \mathrm{h}_{N_{RX},2}(\tau,t) & \dots & \mathrm{h}_{N_{RX},M_{TX}}(\tau,t) \end{bmatrix} \tag{3.14}$$

Each subchannel is represented by Equation 3.15 that is the time-varying low-pass channel impulse response between the m^{th}, $m = 1, 2, ..., M_{TX}$, transmit antenna and the n^{th}, $n = 1, 2, ..., N_{RX}$, receive antenna denoted as $\mathrm{h}_{n,m}(\tau, t)$, where $\rho_{n,m}(i, t)$ is the complex coefficient of each of the P propagation paths ($i = 1, \cdots, P$) from m^{th} transmitter to the n^{th} receiver antenna at time t to an impulse applied at time $t - \tau_i$. These channel coefficients, $\rho_{n,m}(i, t)$, are zero-mean *Independent and identically distributed* (iid) random complex Gaussian quantities with variance σ_ρ^2 and their amplitudes are shaped in the frequency domain by the Doppler spectrum obtained by classical Jakes low-pass filter. The Doppler spectra depends on the user velocity and the carrier frequency.

$$\mathrm{h}_{n,m}(\tau,t) = \sum_{i=1}^{P} \rho_{n,m}(i,t) \cdot \delta(t - \tau_i) \tag{3.15}$$

The spatial correlation model assumes the correlation between different MIMO subchannels is modelled with the assumption that the correlation among receive antennas is independent from the correlation between transmit antennas, and vice versa. Based on this assumption, the spatial correlation matrix of the MIMO radio channel is the Kronecker product of the spatial correlation matrix at the transmitter and the receiver. The LTE specification enables this model for link level

simulations. The main advantage of this model is its simplicity and analytical tractability, but its main drawback is that it forces both link ends to be separable neglecting the joint spatial structure.

According to [19], the MIMO correlation matrix results from the kronecker product of the correlation matrices seen from the eNodeB and the UE. Equation 3.16 shows the correlation matrix for 1×2 SIMO configuration and Equations 3.17 and 3.18 show the correlations matrices for 2×2 and 4×4 MIMO configuration, respectively. Table 3.7 shows the values of α and β that define different correlation types for *Low Correlation for MIMO Correlation Matrix (Uncorrelated MIMO channel)* (LC), *Medium Correlation for MIMO Correlation Matrix* (MC) and *High Correlation for MIMO Correlation Matrix* (HC). In practice, the low level correlation corresponds to the uncorrelated antennas case. The 4×4 MIMO correlation matrix for medium and high correlation level is adjusted to insure that it is positive semi-definite after round-off to 4 digit precision following Equation 3.19 where $a = 0.00012$ and I_4 is the identity matrix of size 4, [19].

$$\mathbf{R}_{\text{spat}_{1\text{x}2}} = \mathbf{R}_{\text{UE}} = \begin{bmatrix} 1 & \beta \\ \beta^* & 1 \end{bmatrix} \tag{3.16}$$

$$\mathbf{R}_{\text{spat}_{2\text{x}2}} = \mathbf{R}_{\text{eNodeB}} \otimes \mathbf{R}_{\text{UE}} = \begin{bmatrix} 1 & \alpha \\ \alpha^* & 1 \end{bmatrix} \otimes \begin{bmatrix} 1 & \beta \\ \beta^* & 1 \end{bmatrix} = \begin{bmatrix} 1 & \beta & \alpha & \alpha\beta \\ \beta^* & 1 & \alpha\beta^* & \alpha \\ \alpha^* & \alpha^*\beta & 1 & \beta \\ \alpha^*\beta^* & \alpha^* & \beta^* & 1 \end{bmatrix} \tag{3.17}$$

$$\mathbf{R}_{\text{spat}_{4\text{x}4}} = \mathbf{R}_{\text{eNodeB}} \otimes \mathbf{R}_{\text{UE}} = \begin{bmatrix} 1 & \alpha^{\frac{1}{9}} & \alpha^{\frac{4}{9}} & \alpha \\ \alpha^{\frac{1}{9}^*} & 1 & \alpha^{\frac{1}{9}} & \alpha^{\frac{4}{9}} \\ \alpha^{\frac{4}{9}^*} & \alpha^{\frac{1}{9}^*} & 1 & \alpha^{\frac{1}{9}} \\ \alpha^* & \alpha^{\frac{4}{9}^*} & \alpha^{\frac{1}{9}^*} & 1 \end{bmatrix} \otimes \begin{bmatrix} 1 & \beta^{\frac{1}{9}} & \beta^{\frac{4}{9}} & \beta \\ \beta^{\frac{1}{9}^*} & 1 & \beta^{\frac{1}{9}} & \beta^{\frac{4}{9}} \\ \beta^{\frac{4}{9}^*} & \beta^{\frac{1}{9}^*} & 1 & \beta^{\frac{1}{9}} \\ \beta^* & \beta^{\frac{4}{9}^*} & \beta^{\frac{1}{9}^*} & 1 \end{bmatrix} \tag{3.18}$$

$$\mathbf{R}_{\text{spat}_{4\text{x}4}}(\textit{medium or high antenna correlation}) = \left[\mathbf{R}_{\text{spat}_{4\text{x}4}} + aI_4\right]/(1+a) \tag{3.19}$$

Table 3.7: MIMO Correlation Levels

LC		MC		HC	
α	β	α	β	α	β
0	0	0.3	0.9	0.9	0.9

Figure 3.18 shows the flow chart of the practical procedure for the simulation of the proposed correlation-based MIMO radio channel stochastic model with M_{TX} antennas at the eNodeB and N_{RX} antennas at the UE. The generated correlated channel coefficients form the MIMO correlation-based channel matrix $\tilde{\mathbf{H}}(\tau, t)$ as the result of the matrix product of the Cholesky factorization of the $\mathbf{R}_{\text{spat}}$ correlation matrix and the channel vector with GWSSUS subchannels $\mathbf{h}(\tau, t)$ obtained from the MIMO channel matrix $\mathbf{H}(\tau, t)$.

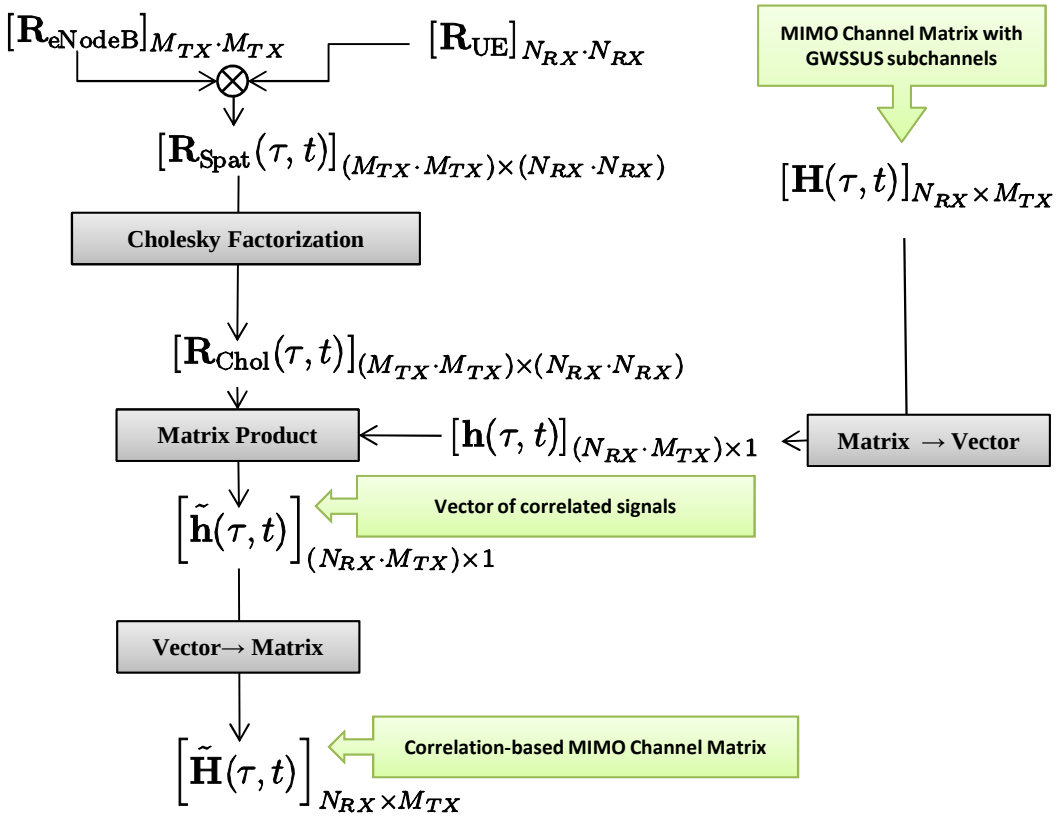

Figure 3.18: Flow chart of the kronecker correlated channel coefficient generation

3.4.2 OFDM system model

In LTE/LTE-Advanced, the subcarrier separation $\Delta f = 1/T = 15$ KHz or 7.5 KHz is considered lower than the coherence bandwidth of the channel. Consequently, when the subcarrier bandwidth is sufficiently narrow, the frequency response across each subcarrier is approximately flat, avoiding the need for complicated time-domain equalization and converting a frequency-selective channel to N narrowband channels, where N is the number of subcarriers. Thus, OFDM divides the frequency band into N narrowband subchannels and it enables to send different sequences of symbols across each subchannel. Each QAM symbol is transmitted over a different subcarrier, and hence, symbol separability at the receiver is ensured by the subcarrier flat fading assumption and the orthogonality property between the different subcarriers.

Figure 3.19 shows the process of the OFDM baseband equivalent signal generation for a SISO-OFDM system which is divided in two parts, the transmitter and the receiver side. The processes of digital to analog conversions and radio frequency are omitted.

At the transmitting part, first of all the input is a $N \cdot log_2(M)$ binary serial data stream where M is the number of symbols of the constellation. The bit rate is $R_b = (N \cdot log_2(M)) \,/\, (T + \tau_L)$ bits/s where T is the duration of the N-points IDFT and τ_L is the duration of the CP. Thus the overall OFDM symbol duration is $T_{cp} = T + \tau_L$ and τ_L is designed to be longer than the channel delay

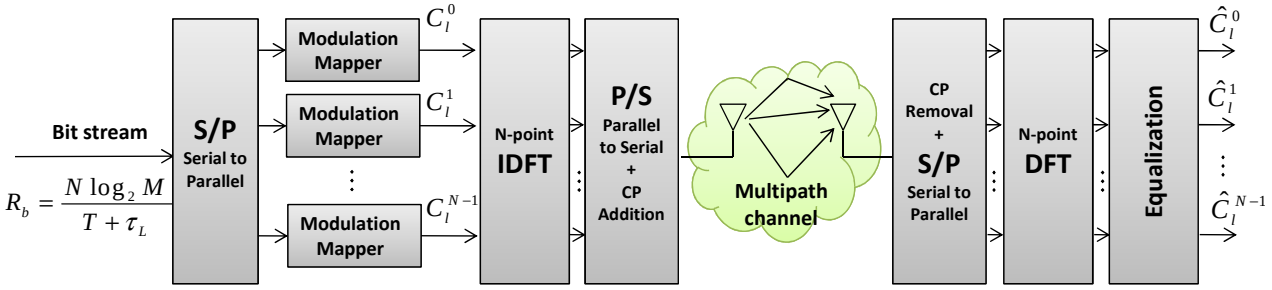

Figure 3.19: Block Diagram of a SISO-OFDM system structure

spread to avoid ISI. Next the input bit stream is divided into N modulated symbols after a serial to parallel converter and a modulation mapper (MQAM in the case of LTE). Next step is to perform the N-point IDFT of the modulated parallel symbols to constitute one OFDM symbol. Then a CP is added by copying the last L samples of one OFDM symbol to the front and then it is converted to a serial sequence to be transmitted.

At the receiver part, the first step is to sample the receive signal, synchronize the initial position of OFDM symbol, remove the CP and convert the serial sampled sequence to N parallel points. Afterwards the data is recovered in the frequency domain by performing the DFT. Finally the channel equalization is performed in the frequency domain to eliminate channel effects and detect the original input sequence.

The OFDM baseband equivalent signal can be expressed as follows:

$$s(t) = \sum_{l=-\infty}^{\infty} \left\{ \sum_{k=0}^{N-1} C_l^k \Phi_k \left(t - lT\right) \right\} \tag{3.20}$$

where C_l^k is the QAM complex symbol at instant l and subcarrier k and $\Phi_k \left(t - lT\right) = rect_T \left(t\right) \cdot e^{j2\pi kt/T}$ where $rect_T \left(t\right)$ is an unit pulse of duration T. Due to there are an integer number of cycles of $\Phi_k \left(t - lT\right)$ in a symbol interval of duration T, the functions expressed by $\Phi_k \left(t - lT\right)$ are orthogonal as shown Equation 3.21.

$$\int_0^T \Phi_k(t)\Phi_q^*(t)dt = \begin{cases} T; & \text{if } q = k \\ 0; & \text{if } q \neq k \end{cases} \tag{3.21}$$

Assuming that the transmitted symbols are uncorrelated and taking into account the equivalent low-pass signal, the OFDM signal spectrum is obtained by superposition of the spectra of the subcarriers which has the form:

$$G_k(f) = \overline{\left|C_l^k\right|^2} T sinc^2(ft - k); (k = 0, 1, \ldots, N-1) \tag{3.22}$$

where $\overline{\left|C_l^k\right|^2}$ is the average power of the QAM symbols and $sinc(x) = sin(\pi x)/(\pi x)$. For instance, Figure 3.20 shows the normalized power spectral density of an OFDM with 32 subcarriers, i.e, $G_k(f)/(\overline{\left|C_l^k\right|^2} T)$ where $f = k \cdot \Delta f$ and $\Delta f = 1/T$ is the subcarrier separation. It can be noticed that although the spectra of the subcarriers are overlapped, at the subcarriers frequencies

$k = 0, 1, \ldots, N-1$ only one subcarrier contributes to the OFDM signal spectrum due to the orthogonality of the subcarriers. The OFDM signal spectrum is almost rectangular and, discarding the small subcarrier spectra tails at the edges of the bandwidth, the occupied bandwidth is N/T.

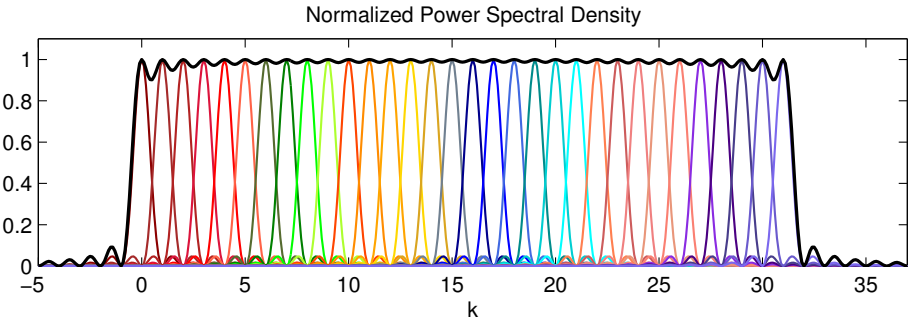

Figure 3.20: Normalized Power Spectral Density of an OFDM signal with 32 subcarriers

The time domain OFDM signal at interval $(lT \leqslant t < (l+1)T)$ is:

$$s_l(t) = \sum_{k=0}^{N-1} C_l^k e^{j2\pi kt/T}; (lT \leqslant t < (l+1)T) \tag{3.23}$$

The digital implementation of $s_l(t)$ sampled at N samples per OFDM symbol of duration T is:

$$s_l(n\frac{T}{N}) = \sum_{k=0}^{N-1} C_l^k e^{j2\pi kn/N}; (0 \leqslant n < N) \tag{3.24}$$

Equation 3.24 is the IDFT of the C_l^k sequence where $K = 0, 1, \cdots, N$. As the IFFT is an efficient computation of the IDFT, the OFDM signal generation is performed optimally by the IFFT.

Assuming ideal channel and no noise at the receiver, the DFT is applied to recover the transmitted OFDM signal as shown in Equation 3.25, where the partial sum of the geometric series and *L'Hôpital's* rule have been applied. In a similar way as in the transmitter, the OFDM signal reception is performed optimally by the FFT.

$$\begin{aligned} \tilde{C_l^k} &= \frac{1}{N}\sum_{n=0}^{N-1} s_l(n\frac{T}{N}) e^{-j2\pi kn/N} = \frac{1}{N}\sum_{n=0}^{N-1}\left(\sum_{i=0}^{N-1} C_l^k e^{j2\pi in/N}\right) e^{-j2\pi kn/N} \\ &= \frac{1}{N}\sum_{i=0}^{N-1} C_l^i \left(\sum_{n=0}^{N-1}\left(e^{j2\pi(i-k)/N}\right)^n\right) = \frac{1}{N}\sum_{i=0}^{N-1} C_l^i \frac{1-e^{j2\pi(i-k)}}{1-e^{j2\pi(i-k)/N}} = C_l^k; (0 \leqslant k < N) \end{aligned} \tag{3.25}$$

Assuming a GWSSUS model for the multipath channel and simplifying Equation 3.15 for the case of SISO, the channel impulse response at time interval $(lT \leqslant t < (l+1)T)$ is as follows:

$$\mathrm{h}_l(t) = \sum_{i=1}^{P} \rho_i \cdot \delta(t - \tau_i) \tag{3.26}$$

where ρ_i is the complex coefficient and τ_i is the channel delay of propagation path i. For a given time interval $(lT \leqslant t < (l+1)T)$ these coefficients can be considered almost constant assuming that the OFDM symbol period is shorter than the channel coherence time. Consequently, the received signal at time interval $(lT \leqslant t < (l+1)T)$ is as follows:

$$\begin{aligned} \mathrm{r}_l(t) = \mathrm{s}_l(t) * \mathrm{h}_l(t) = \left(\sum_{k=0}^{N-1} C_l^k e^{j2\pi kt/T}\right) * \left(\sum_{i=1}^{P} \rho_i \cdot \delta(t-\tau_i)\right) = \sum_{k=0}^{N-1} C_l^k \sum_{i=1}^{P} \rho_i e^{j2\pi k(t-\tau_i)/T} \\ = \sum_{k=0}^{N-1} C_l^k \left(\sum_{i=1}^{P} \rho_i e^{-j2\pi k\tau_i/T}\right) e^{j2\pi kt/T} = \sum_{k=0}^{N-1} C_l^k H_k e^{j2\pi kt/T} \end{aligned} \tag{3.27}$$

where H_k is the channel frequency response at subcarrier k:

$$H_k = H(f)|_{f=k/T} = \left(\sum_{i=1}^{P} \rho_i e^{-j2\pi k\tau_i/T}\right) \tag{3.28}$$

In order to enable the channel equalization in the frequency domain, the received signal must be a circular convolution of the transmitted signal with the channel. To ensure this property, the use of the CP is necessary and its duration must be longer than the channel delay spread. The addition of multipath echoes will create circular convolution within the set of time domain samples to be applied to the DFT as shown in Figure 3.21.

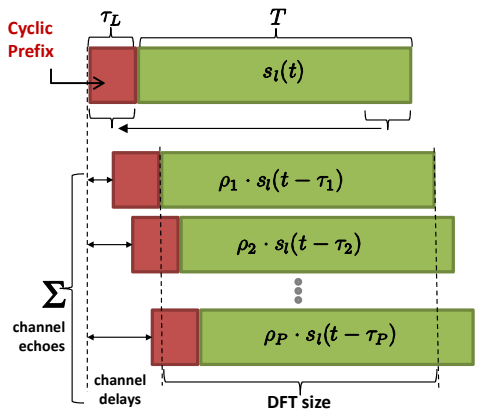

Figure 3.21: CP in OFDM

Considering the channel effects, Equation 3.25 is reformulated as follows:

$$\begin{aligned} D_l^k = \mathrm{DFT}(r_l(n\frac{T}{N})) = \frac{1}{N}\sum_{n=0}^{N-1} r_l(n\frac{T}{N}) e^{-j2\pi kn/N} \\ = \frac{1}{N}\sum_{n=0}^{N-1}\left(\sum_{i=0}^{N-1} C_l^k H_k e^{j2\pi in/N}\right) e^{-j2\pi kn/N} = C_l^k \cdot H_k; (0 \leqslant k < N) \end{aligned} \tag{3.29}$$

Since the channel only produces an amplitude scaling and phase rotation for each subcarrier, the channel equalization may be achieved by multiplying by $H_k^*/|H_k|^2$ the frequency domain samples D_l^k where $(\cdot)^*$ stands for conjugate. This channel equalization technique is known as the ZF one tap equalizer, [70].

3.4.3 MIMO-OFDM system model

A MIMO-OFDM system formed by M_{TX} antennas at the transmitter and N_{RX} antennas at the receiver can be viewed as $\min(M_{TX}, N_{RX})$ SISO-OFDM systems in parallel due to the spatial domain multiplexing. Thus, when OFDM is combined with MIMO, it also transforms the frequency-selective nature of the MIMO wideband mobile channel into $N \times M_{TX} \times N_{RX}$ flat-fading subchannels, which makes possible to use efficient narrowband MIMO techniques to take advantage of the spatial dimensions.

The transmitted signal vector is $\mathbf{s}(t) = \left[\mathrm{s}(t), \quad \ldots, \quad \mathrm{s}_m(t), \quad \ldots \quad \mathrm{s}_{\mathrm{M_{TX}}}(t)\right]^{\mathrm{T}}$, the received signal vector of the MIMO-OFDM system is $\mathbf{r}(t) = \left[\mathrm{r}_1(t), \quad \ldots, \quad \mathrm{r}_n(t), \quad \ldots \quad \mathrm{r}_{\mathrm{N_{RX}}}(t)\right]^{\mathrm{T}}$ and the AWGN noise vector $\mathbf{n}(t) = \left[\mathrm{n}_1(t), \quad \ldots, \quad \mathrm{n}_n(t), \quad \ldots \quad \mathrm{n}_{\mathrm{N_{RX}}}(t)\right]^{\mathrm{T}}$, where $(\cdot)^{\mathrm{T}}$ stands for transpose.

Following the SISO-OFDM system equations from previous subsection but now applied to the MIMO case, the antenna port m transmits $s_m(t)$ for a time interval $lT \leqslant t < (l+1)T$:

$$s_m(t) = \sum_{k=0}^{N-1} C_m^k e^{j2\pi kt/T} \tag{3.30}$$

where C_m^k is the QAM-modulated complex symbol at subcarrier k and transmit antenna port m, N is the number of subcarriers and T is the OFDM symbol duration (the duration of the CP is not considered in T). Thus, the received signal at the antenna n results in:

$$\mathbf{r}(t) = \tilde{\mathbf{H}}(\tau, t) * \mathbf{s}(t) + \mathbf{n}(t) \tag{3.31}$$

where $\tilde{\mathbf{H}}(\tau, t)$ is the MIMO correlation-based channel matrix obtained according to the flow chart of Figure 3.18:

$$\tilde{\mathbf{H}}(\tau, t) = \begin{bmatrix} \tilde{\mathrm{h}}_{1,1}(\tau, t) & \tilde{\mathrm{h}}_{1,2}(\tau, t) & \ldots & \tilde{\mathrm{h}}_{1,M_{TX}}(\tau, t) \\ \tilde{\mathrm{h}}_{2,1}(\tau, t) & \tilde{\mathrm{h}}_{2,2}(\tau, t) & \ldots & \tilde{\mathrm{h}}_{2,M_{TX}}(\tau, t) \\ \vdots & \vdots & \ldots & \vdots \\ \tilde{\mathrm{h}}_{N_{RX},1}(\tau, t) & \tilde{\mathrm{h}}_{N_{RX},2}(\tau, t) & \ldots & \tilde{\mathrm{h}}_{N_{RX},M_{TX}}(\tau, t) \end{bmatrix} \tag{3.32}$$

where $\tilde{\mathrm{h}}_{n,m}(\tau, t)$ denotes the channel between the transmit antenna m and the receive antenna n at time t:

$$\tilde{\mathrm{h}}_{n,m}(\tau, t) = \sum_{i=1}^{P} \tilde{\rho}_{n,m}(i, t) \cdot \delta(t - \tau_i) \tag{3.33}$$

The received signal at antenna n is as follows:

$$\begin{aligned} \mathrm{r}_n(t) &= \left(\sum_{m=1}^{M_{TX}} \tilde{\mathrm{h}}_{n,m}(\tau,t) * \mathrm{s}_m(t)\right) + \mathrm{n}_n(t) \\ &= \left(\sum_{m=1}^{M_{TX}} \left(\sum_{i=1}^{P} \tilde{\rho}_{n,m}^{i} \cdot \delta(t-\tau_i)\right) * \left(\sum_{k=0}^{N-1} C_m^k e^{j2\pi kt/T}\right)\right) + \mathrm{n}_n(t) \\ &= \left(\sum_{m=1}^{M_{TX}} \left(\sum_{k=0}^{N-1} \mathrm{H}_{n,m}^{k} C_m^k e^{j2\pi kt/T}\right)\right) + \mathrm{n}_n(t) \end{aligned} \tag{3.34}$$

where $\mathrm{H}_{n,m}^{k}$ is the frequency response of the channel between the transmit antenna m and the receive antenna n at subcarrier k and the channel coefficient $\tilde{\rho}_{n,m}(i,t)$ at time t is rewritten as $\tilde{\rho}_{n,m}^{i}$:

$$\mathrm{H}_{n,m}^{k} = \mathcal{F}(\tilde{\mathrm{h}}_{n,m}(\tau,t))\big|_{f=\frac{k}{T}} = \left(\sum_{i=1}^{P} \tilde{\rho}_{n,m}^{i} e^{-j2\pi k\tau_i/T}\right) \tag{3.35}$$

When $r_n(t)$ is sampled at N/T samples/s and the FFT is applied, the received signal is moved to the frequency domain:

$$\mathrm{r}_n^k = \mathrm{DFT}(r_n(i\frac{T}{N})); (i=0,\cdots,N-1) = \left(\sum_{m=1}^{M_{TX}} \mathrm{H}_{n,m}^{k} C_m^k\right) + \mathrm{n}_n^k \tag{3.36}$$

The transmitted complex symbols $\mathbf{s}_k$, the detected complex symbols $\mathbf{r}_k$ and the AWGN noise $\mathbf{n}_k$ vectors are expressed in the frequency domain as follows where $(\cdot)^{\mathrm{T}}$ stands for Transpose:

$$\mathbf{s}^k = \begin{bmatrix} C_1^k, & \ldots, & C_m^k, & \ldots & C_{M_{TX}}^k \end{bmatrix}^{\mathrm{T}} \tag{3.37}$$

$$\mathbf{r}^k = \begin{bmatrix} D_1^k, & \ldots, & D_n^k, & \ldots & D_{N_{RX}}^k \end{bmatrix}^{\mathrm{T}} \tag{3.38}$$

$$\mathbf{n}^k = \begin{bmatrix} \mathrm{n}_1^k, & \ldots, & \mathrm{n}_n^k, & \ldots & \mathrm{n}_{N_{RX}}^k \end{bmatrix}^{\mathrm{T}} \tag{3.39}$$

Also in the frequency domain, $\mathbf{H}_k$ is the frequency response of MIMO channel $\tilde{\mathbf{H}}(\tau,t)$ at subcarrier k, which can be written in matrix form:

$$\mathbf{H}_k = \mathcal{F}(\tilde{\mathbf{H}}(\tau,t))\big|_{f=\frac{k}{T}} = \tilde{\mathbf{H}}(f)\big|_{f=\frac{k}{T}} = \begin{bmatrix} \mathrm{H}_{1,1}^{k} & \cdots & \mathrm{H}_{1,M_{TX}}^{k} \\ \vdots & \mathrm{H}_{n,m}^{k} & \vdots \\ \mathrm{H}_{N_{RX},1}^{k} & \cdots & \mathrm{H}_{N_{RX},M_{TX}}^{k} \end{bmatrix} \tag{3.40}$$

Thus, the relation in the frequency domain between the input and the output of the MIMO-OFDM channel can be expressed in the matrix form shown below:

$$\underbrace{\begin{bmatrix} D_1^k \\ \vdots \\ D_n^k \\ \vdots \\ D_{N_{RX}}^k \end{bmatrix}}_{\mathbf{r}_k} = \underbrace{\begin{bmatrix} \mathrm{H}_{1,1}^k & \cdots & \mathrm{H}_{1,m}^k & \cdots & \mathrm{H}_{1,M_{TX}}^k \\ \vdots & \ddots & \vdots & \ddots & \vdots \\ \mathrm{H}_{n,1}^k & \cdots & \mathrm{H}_{n,m}^k & \cdots & \mathrm{H}_{n,M_{TX}}^k \\ \vdots & \ddots & \vdots & \ddots & \vdots \\ \mathrm{H}_{N_{RX},1}^k & \cdots & \mathrm{H}_{N_{RX},m} & \cdots & \mathrm{H}_{N_{RX},M_{TX}}^k \end{bmatrix}}_{\mathbf{H}_k} \underbrace{\begin{bmatrix} C_1^k \\ \vdots \\ C_n^k \\ \vdots \\ C_{M_{TX}}^k \end{bmatrix}}_{\mathbf{s}_k} + \underbrace{\begin{bmatrix} \mathrm{n}_1^k \\ \vdots \\ \mathrm{n}_n^k \\ \vdots \\ \mathrm{n}_{N_{RX}}^k \end{bmatrix}}_{\mathbf{n}_k} \tag{3.41}$$

Figure 3.22 shows what is enclosed inside the MIMO-OFDM system model marked by a grey box. It is equivalent to N narrowband MIMO channels. $C_{m,l}^k$ is the QAM complex symbol transmitted on antenna port m and $D_{n,l}^k$ is the detected complex symbol after OFDM demodulation on receiver antenna port n in OFDM symbol l at subcarrier k.

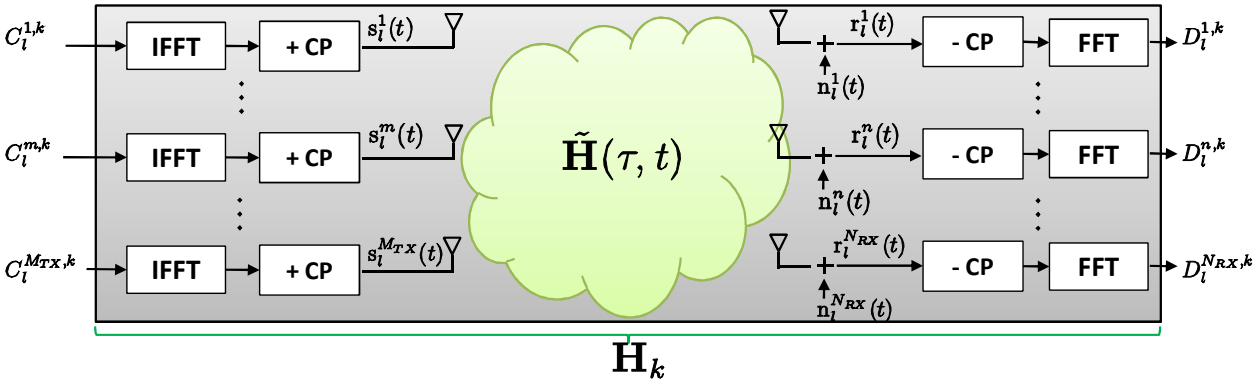

Figure 3.22: Representation of the MIMO-OFDM system model

Using matrix notation, Equation 3.41 can be rewritten as a single carrier MIMO signal model for each subcarrier:

$$\mathbf{r}_k = \mathbf{H}_k \cdot \mathbf{s}_k + \mathbf{n}_k \tag{3.42}$$

The noise added at the receiver side of the MIMO-OFDM system has to be calibrated in order to simulate a given $(E_b/N_0)_k$ for each subcarrier of the OFDM symbol. The noise power in each quadrature branch is denoted as σ_n^2 and for a specific SNR, or equivalently Eb/No, its value depends on the average power of the QAM modulation symbol and the channel *Power Delay Profile* (PDP).

The average power of the MQAM modulation, where M is the number of complex symbols of the constellation and taking into account that the set of MQAM complex symbols is formed by $\pm(2\mathrm{i}-1) \pm j(2\mathrm{i}-1); \mathrm{i} \in \left\{1, \cdots, \frac{\sqrt{M}}{2}\right\}$, equals

$$\overline{|C^k|^2} = \frac{2\sqrt{M}}{M} \sum_{i=1}^{\frac{\sqrt{M}}{2}} |(2\mathrm{i}-1) + j(2\mathrm{i}-1)|^2 = \frac{2}{3}(M-1) = \begin{cases} 2; & \text{QPSK} \\ 10; & \text{16QAM} \\ 42; & \text{64QAM} \end{cases} \tag{3.43}$$

The average power gain of the PDP for each spatial multipath channel is given by Equation 3.44

$$\sigma^2_{PDP} = E\left\{\left(\mathrm{H}^k_{n,m}\right)^2\right\} = \sum_{i=1}^{P} E\left\{\left(\tilde{\rho}^i_{n,m}\right)^2\right\} = \sum_{i=1}^{P} \sigma^2_{\rho} \tag{3.44}$$

Thus, considering the full wideband signal, the long term average SNR is as follows:

$$\mathrm{SNR} = \frac{(1/2)\cdot\overline{|C^k|^2}\cdot\sigma^2_{PDP}\cdot N}{\sigma^2_n} \tag{3.45}$$

Focussing on the narrowband (per subcarrier) average SNR, it is equal to the wideband SNR, however the narrowband noise power must be divided by a factor of N and it results in:

$$\sigma^2_{nb} = \sigma^2_n/N = \frac{(1/2)\cdot\overline{|C^k|^2}\cdot\sigma^2_{PDP}}{\mathrm{SNR}} \tag{3.46}$$

3.4.4 Physical interpretation of full MIMO channel knowledge

A nice and intuitive way to visualize the physical interpretation of a given MIMO channel matrix and the gain of the transmitter channel knowledge is by considering the *Singular Value Decomposition* (SVD) or generalized eigenvalue decomposition of the channel matrix $\mathbf{H}_k$. $\mathrm{SVD}(\mathbf{H}_k) = \mathbf{U}_k\mathbf{D}_k\mathbf{V}^{\mathrm{H}}_k$; where $\mathbf{H}^k$ is the $N_{RX}\times M_{TX}$ complex matrix that models the MIMO channel at subcarrier k, $\mathbf{V}$ is the precoding $M_{TX}\times M_{TX}$ complex unitary matrix, $\mathbf{U}_k$ is the equalization $N_{RX}\times N_{RX}$ complex unitary matrix, $\mathbf{D}_k$ is the $N_{RX}\times M_{TX}$ diagonal matrix of the singular values of $\mathbf{H}_k$ and $(\cdot)^{\mathrm{H}}$ stands for conjugate transpose.

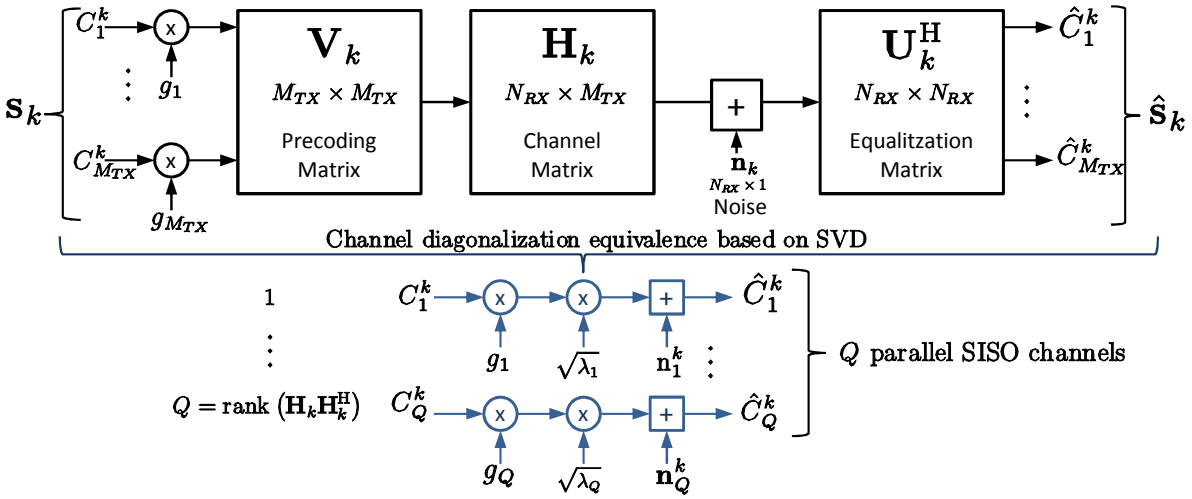

Figure 3.23: Equivalence of the MIMO physical model based on SVD channel decomposition

As shown in Figure 3.23, with linear operations at the transmitter and the receiver, that is, multiplying by $\mathbf{V}_k$ and $\mathbf{U}^{\mathbf{H}}_k$, respectively, the channel can be diagonalized. Therefore, the complex signal precoded transmitted vector is $\mathbf{V}_k\mathbf{s}_k$ and the detected complex vector can be written systematically from the SVD of MIMO channel complex matrix as:

$$\begin{aligned}\hat{\mathbf{s}}_k &= \mathbf{U}_k^{\mathrm{H}}\mathbf{H}_k\mathbf{V}_k\mathbf{s}_k + \mathbf{U}_k^{\mathrm{H}}\mathbf{n}_k = \mathbf{U}_k^{\mathrm{H}}\mathbf{U}_k\mathbf{D}_k\mathbf{V}_k^{\mathrm{H}}\mathbf{V}_k\mathbf{s}_k + \mathbf{U}_k^{\mathrm{H}}\mathbf{n}_k \\ &= \mathbf{I}_{M_{\mathrm{TX}}}\mathbf{D}_k\mathbf{I}_{N_{\mathrm{RX}}}\mathbf{s}_k + \mathbf{U}_k^{\mathrm{H}}\mathbf{n}_k = \mathbf{D}_k\mathbf{s}_k + \mathbf{U}_k^{\mathrm{H}}\mathbf{n}_k\end{aligned} \tag{3.47}$$

where $\mathbf{I}_i$ stands for $i \times i$ identity matrix and $\mathbf{D}_k = \mathrm{diag}\left(\sqrt{\lambda_1}, \ldots, \sqrt{\lambda_m}, \ldots, \sqrt{\lambda_Q}\right)$ has the singular values of the channel matrix $\mathbf{H}_k$ on its diagonal. These singular values are the square roots of the non-zero eigenvalues of $\mathbf{H}_k\mathbf{H}_k^{\mathrm{H}}$ or $\mathbf{H}_k^{\mathrm{H}}\mathbf{H}_k$, where $Q = \mathrm{rank}(\mathbf{H}_k\mathbf{H}_k^{\mathrm{H}})$ and $Q \leqslant \min(M_{TX}, N_{RX})$. Therefore, the MIMO channel can be decomposed into Q parallel SISO channels via SVD as illustrated in Figure 3.23. In the case of $M_{TX} \leq N_{RX}$, then $Q = M_{TX}$ and D_k is as follows:

$$\mathbf{D}_k = \begin{bmatrix} \sqrt{\lambda_1} & 0 & \ldots & 0 \\ 0 & \sqrt{\lambda_2} & \ddots & \vdots \\ \vdots & \ddots & \ddots & 0 \\ 0 & \ldots & 0 & \sqrt{\lambda_{M_{TX}}} \end{bmatrix} \quad \text{where} \quad \sqrt{\lambda_1} \geq \sqrt{\lambda_2} \geq \ldots \geq \sqrt{\lambda_{M_{TX}}} \tag{3.48}$$

SVD diagonalizes the channel and cancels the spatial interference without any matrix inversions or non-linear processing. If the m^{th} stream C_m^k of s_k is always assigned to the same subchannel associated with the m^{th} eigenvalue, the detected m^{th} stream $\tilde{C}_m^k$ is, taking into account g_m as the gain at the transmitter side:

$$\hat{\mathrm{C}}_m^k = \sqrt{\lambda_m} g_m \mathrm{C}_m^k + \mathrm{n}_m^k \qquad (m = 1, \ldots, Q) \tag{3.49}$$

where $\mathbf{U}_k^{\mathrm{H}}\mathbf{n}_k = \begin{bmatrix} \mathrm{n}_1^k & \ldots & \mathrm{n}_m^k & \ldots & \mathrm{n}_{M_{TX}}^k \end{bmatrix}$ and since $\mathbf{U}$ is unitary, $\mathbf{U}_k^{\mathbf{H}}\mathbf{n}_k$ has the same variance as $\mathbf{n}_k$. So the singular value approach does not result in noise enhancement.

The maximum capacity of an $N_{RX} \times M_{TX}$ Rayleigh fading MIMO channel H_k is derived by applying the Shannon formula shown in Equation 2.7. Assuming uncorrelated antennas (i.e. MIMO subchannels coefficients are uncorrelated) and zero-mean iid random complex Gaussian quantities (the subchannel coefficient module follows a Rayleigh statistic), the ergodic MIMO capacity can be calculated as the average value of the capacity for a given average SNR. In addition, the capacity can be written in terms of the non-zero eigenvalues ($\lambda_1 \geq \lambda_2 \geq \ldots \geq \lambda_Q$) of $\mathbf{H}_k\mathbf{H}_k^{\mathrm{H}}$ or $\mathbf{H}_k^{\mathrm{H}}\mathbf{H}_k$, [71], as follows:

$$C = \sum_{m=1}^{Q} \log_2(1 + g_m^2 \lambda_i \gamma) \;\; bits/s/Hz \tag{3.50}$$

where $\gamma = \mathrm{SNR}$ and g_m is the gain at the transmitter applied to the m^{th} non-zero eigenvalue parallel channel.

In other words, the maximum MIMO capacity is achieved by diagonalizing the channel i.e, by applying precoding coefficients at the transmitter and equalization coefficients at the receiver in order to obtain the maximum possible number of parallel orthogonal subchannels. One way to diagonalize the channel and maximize capacity is by using the SVD decomposition and applying the *waterfilling* technique, [71, 24, 72], in order to maximize the capacity on Q parallel subchannels with different optimal power allocation. *Waterfilling* can be applied if the CSI is full known at the transmitter and at the receiver and it consists in allocating more power to subchannels with the

highest gains. From Equation 3.49, it can be observed that the power gain of the m^{th} subchannel is λ_m and the power gain applied by the transmitter is g_m^2 . Assuming all subchannel noise powers to be the same and the SNR of the m^{th} subchannel to be $\text{SNR}_m = \lambda_m \gamma$ $(m = 1, 2, \cdots, Q)$, *waterfilling* allocates more power to the suchannel with higher SNRs where each subchannel is filled up to a common level μ as follows:

$$g_m^2 + \frac{1}{\lambda_m \gamma^2} = \mu \quad \left(\text{if } \frac{1}{\lambda_m \gamma^2} \leq \mu\right) \tag{3.51}$$

$$g_m^2 = 0 \quad \left(\text{if } \frac{1}{\lambda_m \gamma^2} > \mu\right) \tag{3.52}$$

Thus, the subchannel with the maximum eigenvalue (λ_1) receives the largest share of the power. The value of μ must be selected according to the constraint on the total transmitted power is bounded to a predefined value P:

$$\sum_{m=1}^{Q} g_m^2 = P \tag{3.53}$$

On the other hand, if the channel is only known at the receiver side i.e, when CSI is not available at the transmitter side, then *Uniform Power Allocation* (UPA) has to be applied, which consists in allocating uniform power over each transmit antenna where the power gain for all the subchannels is $g_m^2 = \frac{P}{M_{TX}}$, [24]. In this case, the capacity achieved by the UPA technique is slightly lower than the capacity achieved by the *waterfilling* technique since the transmitted power is wasted on the subchannels with null or very small eigenvalues.

Figure 3.24 shows the graph for ergodic capacity vs. SNR for different MIMO systems obtained by averaging 10000 independently generated channels for each value of average SNR. As expected, it can be observed that increasing the number of antennas increases the ergodic capacity. Furthermore, the graph shows that the capacity achieved with full CSI is only higher than the capacity achieved with only CSI at the transmitter for lower SNRs or $M_{TX} > N_{RX}$.

3.4.5 MIMO Receiver Processing

The MIMO processing at the PHY channel is linked to the type of transmission mode which is used. It is on the receiver side and for SM modes where there are many options for the MIMO processing. The BLER and throughput performances of the link level can be heavily influenced by the number of antennas and the implemented MIMO processing. On the transmitter side the mapping from codewords to layers and antenna ports must be specified, as well as AMC and power allocation to the different MIMO layers. For MIMO-SM, the method for selection of the precoding matrix (either within a codebook or unrestricted) must be specified. For SM and for multi-user MIMO modes, the MIMO equalisation technique (ZF, MMSE, ML, SIC, etc.) must be specified. SIC can be applied on a layer basis or on a codeword basis. In this case the CRC of the codeword is verified to ensure that errors are not fed back by the SIC processing.

TD schemes exploit the independent fading in the multiple antenna links to enhance signal diversity by using the spatial dimension to achieve additional redundancy. Thus, TD keeps the data rate equivalent to a SISO channel with the goal to increase robustness. When the redundancy

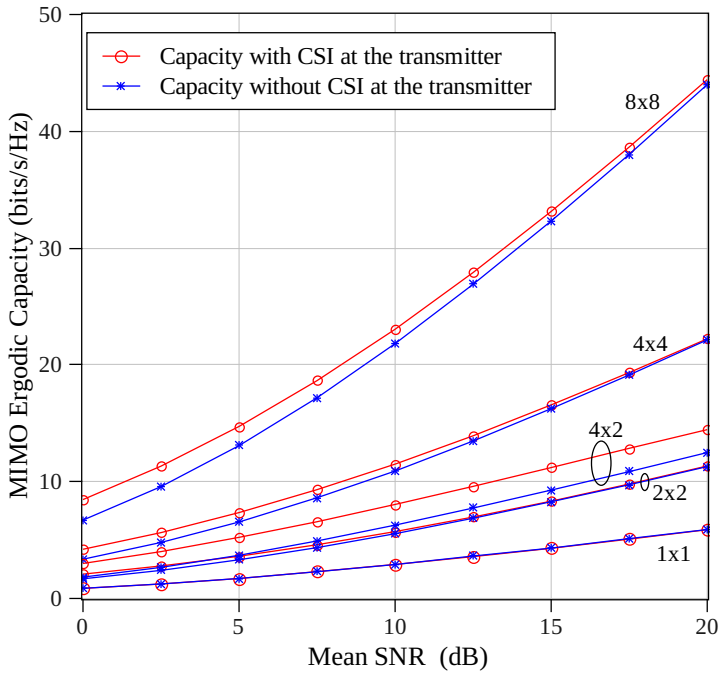

Figure 3.24: MIMO Ergodic capacity with uncorrelated antennas and Rayleigh channel

is generated through coding over the spatial and temporal dimension, the principle is called STBC; and consequently, when coding is applied over the spatial and frequency dimension is called SFBC. That is the case of TD technique defined by LTE.

On the other hand, SM exploits the spatial dimension by transmitting multiple data streams in parallel on different antennas in order to increase the achievable data rate and hence the system capacity. In this case, the number of data streams is equal to the number of transmit antennas M_{TX} and the number of receive antennas N_{RX} is equal or greater than M_{TX}.

MIMO techniques can be performed with or without knowledge of the channel or CSI at the transmitter. The OL techniques assume that the channel is known at the receiver, through pilot symbols or other channel estimation techniques. The CL techniques assume that the channel is known at both sides, the transmitter and the receiver; therefore, a precoding matrix can be applied. These precoding matrices can be based on a codebook or on the SVD decomposition.

The MIMO techniques implemented in the link level simulator presented in this dissertation are the so-called ZF linear detector, the MMSE linear detector and the codeword-SIC receiver for MIMO-SM and SFBC with Alamouti Code and MRC for MIMO-TD.

3.4.5.1 SM Linear Detectors: ZF and MMSE

The optimum MIMO decoding is the ML detection which consists in finding the most likely input vector $\mathbf{s}_k$ via a minimum-distance criterion $\mathbf{s}_k = \arg\min \|\mathbf{r} - \mathbf{H}_k\mathbf{s}_k\|^2$. However, the ML detector is too complex and, since there is not any simple way to compute the ML algorithm, an exhaustive search must be done over all the possible $M^{M_{TX}}$ input vectors, where M is the order of the modulation and M_{TX} the number of transmit antennas. In practice linear detectors are

capable of recovering the transmitted vector by equalizing the MIMO channel and the simplest linear detectors are based on ZF or MMSE processing. These detectors were already presented in [53] as well as in [30, 24, 29].

The baseband equivalent signal MIMO-OFDM model assumes that the bandwidth per subcarrier is so narrow that the channel can be treated as flat-fading per subcarrier as it is described in section 3.4.3. Figure 3.26 shows the MIMO-SM scheme with a linear detector.

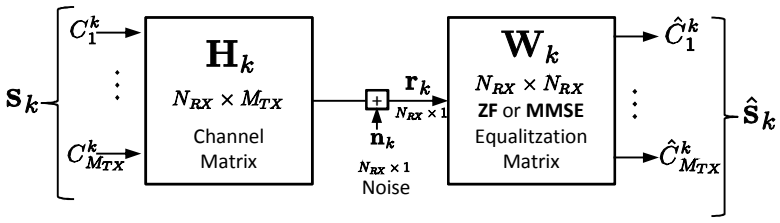

Figure 3.25: Block diagram of the MIMO-SM with Linear detection

The MIMO system consists of M_{TX} transmit antennas and N_{RX} receive antennas and the transmitter sends a M_{TX}-dimensional complex signal vector $\mathbf{s}_k$ for each subcarrier k of an OFDM symbol. Then, the receiver captures a N_{RX}-dimensional complex vector $\mathbf{r}_k$ after adding a AWGN complex noise vector to the received signal. The baseband equivalent signal model is $\mathbf{r}_k = \mathbf{H}_k\mathbf{s}_k + \mathbf{n}_k$ (already given in Equation 3.42) and it describes the relation between $\mathbf{s}_k$ and $\mathbf{r}_k$. $\mathbf{H}_k$ is a $N_{RX} \times M_{TX}$ complex channel matrix at subcarrier k that is assumed constant for the OFDM symbol duration. The vectors $\mathbf{s}_k, \mathbf{r}_k$ and $\mathbf{n}_k$ are expressed in terms of its components as follows:

$$\begin{aligned} \mathbf{s}_k &= \left[C_1^k, \quad C_2^k, \quad \ldots, \quad C_{M_{TX}}^k\right]^{\mathrm{T}} \\ \mathbf{r}_k &= \left[D_1^k, \quad D_2^k, \quad \ldots, \quad D_{N_{RX}}^k\right]^{\mathrm{T}} \\ \mathbf{n}_k &= \left[n_1^k, \quad n_2^k, \quad \ldots, \quad n_{N_{RX}}^k\right]^{\mathrm{T}} \end{aligned} \tag{3.54}$$

The ZF and MMSE linear MIMO detectors are based on an equalization receiver matrix $\mathbf{W}_k$, which is a $M_{TX} \times N_{RX}$ complex matrix that represents the linear processing needed to estimate the signal vector sent $\hat{\mathbf{s}}_k$ for each subcarrier k as follows:

$$\hat{\mathbf{s}}_k = \mathbf{W}_k\mathbf{r}_k; \text{ where } \hat{\mathbf{s}}_k = \left[\hat{C}_1^k, \quad \hat{C}_2^k, \quad \ldots, \quad \hat{C}_{M_{TX}}^k\right]^{\mathrm{T}} \tag{3.55}$$

The ZF detector is a linear MIMO technique which sets the receiver matrix $\mathbf{W}_k$ equal to the inverse of the flat-fading channel matrix $\mathbf{H}_k$ of the subcarrier k when the number of antennas at the receiver is equal to the number of antennas at the transmitter ($M_{TX} = N_{RX}$), or more generally to the pseudoinverse if channel matrix is not square.

$$\mathbf{W}_k^{\mathrm{ZF}} = \left(\mathbf{H}_k^{\mathrm{H}}\mathbf{H}_k\right)^{-1}\mathbf{H}_k^{\mathrm{H}} \tag{3.56}$$

The pseudoinverse exists when M_{TX} is lower than or equal to N_{RX}. Otherwise, if M_{TX} is higher than N_{RX}, the channel matrix is singular, its inverse does not exist and there is no solution for the estimation of the data vector. When the pseudoinverse exists, the ZF detector removes completely

the spatial interference from the transmitted signal $\mathbf{s}_k$ giving an estimated received vector $\hat{\mathbf{s}}_k$ as follows:

$$\hat{\mathbf{s}}_k^{\mathrm{ZF}} = \left(\mathbf{H}_k^{\mathrm{H}}\mathbf{H}_k\right)^{-1}\mathbf{H}_k^{\mathrm{H}}\mathbf{r}_k = \underbrace{\left(\mathbf{H}_k^{\mathrm{H}}\mathbf{H}_k\right)^{-1}\mathbf{H}_k^{\mathrm{H}}\mathbf{H}_k}_{\mathbf{I}_{M_{TX}}}\mathbf{s}_k + \left(\mathbf{H}_k^{\mathrm{H}}\mathbf{H}_k\right)^{-1}\mathbf{H}_k^{\mathrm{H}}\mathbf{n}_k \tag{3.57}$$

where $\mathbf{I}_{M_{TX}}$ is the $M_{TX} \times M_{TX}$ dimensional identity matrix, thus $\mathbf{I}_{M_{TX}}\mathbf{s}_k = \mathbf{s}_k$ and the ZF estimation of $\mathbf{s}_k$ is as follows:

$$\hat{\mathbf{s}}_k^{\mathrm{ZF}} = \mathbf{s}_k + \left(\mathbf{H}_k^{\mathrm{H}}\mathbf{H}_k\right)^{-1}\mathbf{H}_k^{\mathrm{H}}\mathbf{n}_k \tag{3.58}$$

The i^{th} component of $\hat{\mathbf{s}}_k$ denoted by $\hat{C}_i^k$ must be rounded to the nearest constellation point and then all M_{TX} elements of $\hat{\mathbf{s}}_k$ can be demodulated at the receiver.

Since LTE applies channel coding the computation of the post-processing noise variance is needed in order to compute the LLR for the decoding algorithm. A big disadvantage of the ZF detector is that it suffers from noise enhancement, especially for ill conditioned channels. The reason of the noise amplification is that the pseudoinverse inverts the eigenvalues of channel matrix $\mathbf{H}_k$ and the bad spatial subchannels with lower eigenvalues can severely amplify the noise. Thus, the ZF estimation leads to an estimation error vector as follows:

$$e = \hat{\mathbf{s}}_k - \mathbf{s}_k = \left(\mathbf{H}_k^{\mathrm{H}}\mathbf{H}_k\right)^{-1}\mathbf{H}_k^{\mathrm{H}}\mathbf{n}_k \tag{3.59}$$

where $\mathbf{n}_k$ is the complex AWGN noise at subcarrier k. Thus, the covariance matrix of the estimation error is as follows

$$E\left[ee^{\mathrm{H}}\right] = \sigma^2\left(\mathbf{H}_k^{\mathrm{H}}\mathbf{H}_k\right)^{-1} \tag{3.60}$$

where σ^2 is the receiver complex noise power in a subcarrier bandwidth taking into account the baseband equivalent model; consequently the relation between σ^2 and the bandpass noise power σ_{nb}^2 from equation 3.46 is obviously $\sigma^2 = 2\sigma_{nb}^2$.

Thus, the post-processing noise for ZF of the i^{th} spatial component of $\hat{\mathbf{s}}_k$ vector at subcarrier k is $\left(\sigma^2\right)_i^{\mathrm{ZF}} = 2\sigma_{nb}^2\left(\mathbf{H}_k^{\mathrm{H}}\mathbf{H}_k\right)_{i,i}^{-1}$ and, as a result, the ZF post-processing SNR is given by:

$$\mathrm{SNR}_i^{\mathrm{ZF}} = \frac{\overline{\left|C_i^k\right|^2}}{2\sigma_{nb}^2\left(\mathbf{H}_k^{\mathrm{H}}\mathbf{H}_k\right)_{i,i}^{-1}} \tag{3.61}$$

where $\left(\mathbf{H}_k^{\mathrm{H}}\mathbf{H}_k\right)_{i,i}^{-1}$ is the element (i,i) of the diagonal of the matrix $\left(\mathbf{H}_k^{\mathrm{H}}\mathbf{H}_k\right)^{-1}$, $\left|C_i^k\right|^2$ is the transmitted signal average power on antenna port i from Equation 3.43 and σ_{nb}^2 is the receiver bandpass noise power in a subcarrier bandwidth derived from Equation 3.46.

As has been described previously, the soft-decision output at the demodulator is the LLR at bit level, so we apply Equation 3.13 to the ZF linear detector to obtain:

$$\Lambda_{b,i}^{k,ZF} \cong \frac{1}{2\sigma_{nb}^2\left(\mathbf{H}_k^{\mathrm{H}}\mathbf{H}_k\right)_{i,i}^{-1}}\left(\left|\hat{C}_i^k - C_1\right|^2 - \left|\hat{C}_i^k - C_0\right|^2\right) \tag{3.62}$$

where $\Lambda_{b,i}^{k,ZF}$ is the LLR of the b^{th} bit of the i^{th} component of the detected symbol vector $\hat{C}_i^k$, $(b = 1, \cdots, \log_2(M); i = 1, \cdots, M_{TX})$ and C_0 (respectively C_1) is the modulation complex symbol of the set of MQAM complex symbols for which the transmitted bit is at logical zero (respectively logical one) that falls nearest to $\hat{C}_i^k$.

A logical alternative to the ZF receiver is the MMSE, which attempts to strike a balance between spatial-interference suppression and noise enhancement by simply minimizing the distortion by finding the $\mathbf{W}_k$ that minimizes the *Minimum Square Error* (MSE) as follows:

$$\mathbf{W}_k^{\text{MMSE}} = \arg\min_{\mathbf{W}_k} E\left\{\|\mathbf{s}_k - \hat{\mathbf{s}}_k\|^2\right\} = \arg\min_{\mathbf{W}_k} E\left\{\|\mathbf{s}_k - \mathbf{W}_k\mathbf{r}_k\|^2\right\} \tag{3.63}$$

which can be derived following the same notation and using the well-known orthogonality principle as:

$$\mathbf{W}_k^{\text{MMSE}} = \left(\mathbf{H}_k^{\text{H}}\mathbf{H}_k + \frac{2\sigma_{nb}^2}{\left|C_i^k\right|^2}\mathbf{I}_{M_{TX}}\right)^{-1}\mathbf{H}_k^{\text{H}} = \left(\mathbf{H}_k^{\text{H}}\mathbf{H}_k + \gamma\mathbf{I}_{M_{TX}}\right)^{-1}\mathbf{H}_k^{\text{H}} \tag{3.64}$$

where $\gamma = \frac{2\sigma_{nb}^2}{\left|C_i^k\right|^2}$ and $\mathbf{I}_{M_{TX}}$ is the $M_{TX} \times M_{TX}$ identity matrix. γ can be viewed as the inverse of the SNR at subcarrier k without taking into account the power enhancement due to the channel matrix; thus, at high SNRs, the MMSE detector performance converges to the performance of the ZF detector; but at low SNRs, it prevents the worst eigenvalues of the channel matrix from being inverted.

Therefore, the MMSE detection can be rewritten as (see Appendix A.1):

$$\hat{\mathbf{s}}_k^{\text{MMSE}} = \left(\mathbf{H}_k^{\text{H}}\mathbf{H}_k + \gamma\mathbf{I}_{M_{TX}}\right)^{-1}\mathbf{H}_k^{\text{H}}\mathbf{r}_k \tag{3.65}$$

Following the same notation as in the case of ZF but applied to MMSE, the post-processing noise variance of the i^{th} spatial component of $\hat{\mathbf{s}}_k$ vector at subcarrier k is $\left(\sigma^2\right)_i^{\text{MMSE}} = 2\sigma_{nb}^2\left(\mathbf{H}_k^{\text{H}}\mathbf{H}_k + \gamma\mathbf{I}_{M_{TX}}\right)_{i,i}^{-1}$. Thus, at the demodulator output, the LLR at bit level for the MMSE linear detection equals:

$$\Lambda_{b,i}^{k,MMSE} \cong \frac{1}{2\sigma_{nb}^2\left(\mathbf{H}_k^{\text{H}}\mathbf{H}_k + \gamma\mathbf{I}_{M_{TX}}\right)_{i,i}^{-1}}\left(\left|\hat{C}_i^k - C_1\right|^2 - \left|\hat{C}_i^k - C_0\right|^2\right) \tag{3.66}$$

It can be demonstrated that the post-processing SNR of the i^{th} spatial component of $\hat{\mathbf{s}}_k$ vector at subcarrier k for MMSE is, [73]:

$$\text{SNR}_i^{\text{MMSE}} = \frac{\overline{\left|C_i^k\right|^2}}{2\sigma_{nb}^2\left(\mathbf{H}_k^{\text{H}}\mathbf{H}_k + \gamma\mathbf{I}_{M_{TX}}\right)_{i,i}^{-1}} - 1 \tag{3.67}$$

In particular, the definition of a $(M_{TX} + N_{RX}) \times N_{RX}$ extended channel matrix $\mathbf{Z}_k$ and a $(M_{TX} + N_{RX}) \times 1$ extended receive vector $\mathbf{y}_k$, as shown in Equation 3.68, allows Equation 3.42 to be rewritten as $\mathbf{y}_k = \mathbf{Z}_k\mathbf{x}_k + \mathbf{n}'$, [24]:

$$\underbrace{\begin{bmatrix}\mathbf{r}_k \\ \mathbf{0}_{M_{TX}\times 1}\end{bmatrix}}_{\mathbf{y}_k} = \underbrace{\begin{bmatrix}\mathbf{H}_k \\ \sqrt{\gamma}\mathbf{I}_{M_{TX}}\end{bmatrix}}_{\mathbf{Z}_k}\underbrace{\begin{bmatrix}\mathbf{s}_k \\ \mathbf{0}_{M_{TX}\times 1}\end{bmatrix}}_{\mathbf{x}_k} + \underbrace{\begin{bmatrix}\mathbf{n}_k \\ \mathbf{0}_{M_{TX}\times 1}\end{bmatrix}}_{\mathbf{n}'_k} \tag{3.68}$$

Thus, the ZF processing can be applied to $\mathbf{y}_k$ to reach the same result as in Equation 3.65. Equation 3.69 shows this equivalence, and, hence, the MMSE solution can be obtained via the ZF algorithm, already explained above in [29].

$$\begin{aligned}\hat{\mathbf{x}}_k &= \left(\mathbf{Z}_k^{\mathrm{H}}\mathbf{Z}_k\right)^{-1}\mathbf{Z}_k^{\mathrm{H}}\mathbf{y}_k = \\ &= \left(\mathbf{H}_k^{\mathrm{H}}\mathbf{H}_k + \gamma\mathbf{I}_{M_{TX}}\right)^{-1}\begin{bmatrix}\mathbf{H}_k^{\mathrm{H}} & \sqrt{\gamma}\mathbf{I}_{M_{TX}}\end{bmatrix}\begin{bmatrix}\mathbf{r}_k \\ \mathbf{0}\end{bmatrix} = \\ &= \left(\mathbf{H}_k^{\mathrm{H}}\mathbf{H}_k + \gamma\mathbf{I}_{M_{TX}}\right)^{-1}\mathbf{H}_k^{\mathrm{H}}\mathbf{r}_k = \hat{\mathbf{s}}_k^{\mathrm{MMSE}} \qquad (3.69)\end{aligned}$$

where

$$\mathbf{Z}_k^{\mathrm{H}}\mathbf{Z}_k = \begin{bmatrix}\mathbf{H}_k^{\mathrm{H}} & \sqrt{\gamma}\mathbf{I}_{M_{TX}}\end{bmatrix}\begin{bmatrix}\mathbf{H}_k \\ \sqrt{\gamma}\mathbf{I}_{M_{TX}}\end{bmatrix} = \left(\mathbf{H}_k^{\mathrm{H}}\mathbf{H}_k + \gamma\mathbf{I}_{M_{TX}}\right)$$

3.4.5.2 SFBC TD

E-UTRA physical layer employs the transmit diversity technique of SFBC, that is a frequency domain version for multicarrier systems such as OFDM of the well-known STBC. The Alamouti codes [31] are the simplest family of SFBC codes applied to MIMO configurations of 2 antennas at the transmitter and N_{RX} antennas at the receiver. Alamouti codes are rate-1 codes (without rate loss) because of their orthogonality. Therefore, assuming that the channel is perfectly known at the receiver and after a linear receiver processing, there exists a perfect orthogonality between the received symbols and there are two copies of each transmitted symbol at each of the N_{RX} antennas of the receiver.

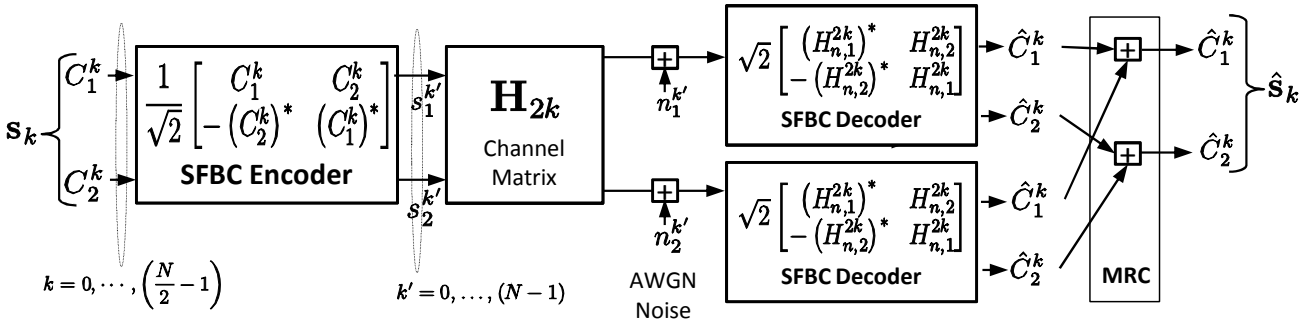

Figure 3.26: Block diagram of the 2×2 MIMO-TD: LTE SFBC with Alamouti Code and MRC

The mapping for the SFBC in E-UTRA physical layer for two transmit antennas is shown in table 3.8, [3]:

Table 3.8: LTE SFBC for 2 antenna ports

subcarrier	antenna 1	antenna 2
$2k$	$\frac{1}{\sqrt{2}}C_1^k$	$\frac{-1}{\sqrt{2}}(C_2^k)^*$
$2k+1$	$\frac{1}{\sqrt{2}}C_2^k$	$\frac{1}{\sqrt{2}}(C_1^k)^*$

After OFDM demodulation, the received vector signal at subcarrier $2k$ is expressed by Equation 3.70:

$$\begin{bmatrix} D_1^{2k} \\ D_2^{2k} \end{bmatrix} = \frac{1}{\sqrt{2}} \begin{bmatrix} H_{1,1}^{2k} & H_{1,2}^{2k} \\ H_{2,1}^{2k} & H_{2,2}^{2k} \end{bmatrix} \begin{bmatrix} C_1^k \\ -\left(C_2^k\right)^* \end{bmatrix} + \begin{bmatrix} n_1^{2k} \\ n_2^{2k} \end{bmatrix} \tag{3.70}$$

and, at subcarrier $2k+1$, it is expressed by Equation 3.71:

$$\begin{bmatrix} D_1^{2k+1} \\ D_2^{2k+1} \end{bmatrix} = \frac{1}{\sqrt{2}} \begin{bmatrix} H_{1,1}^{2k+1} & H_{1,2}^{2k+1} \\ H_{2,1}^{2k+1} & H_{2,2}^{2k+1} \end{bmatrix} \begin{bmatrix} C_2^k \\ \left(C_1^k\right)^* \end{bmatrix} + \begin{bmatrix} n_1^{2k+1} \\ n_2^{2k+1} \end{bmatrix} \tag{3.71}$$

Then, assuming that the channel coefficients are equal in two adjacent subcarriers, i.e., $H_{n,m}^{2k} = H_{n,m}^{2k+1}$, the received signal vector for the k^{th} transmitted signal vector $\mathbf{s}_k = \begin{bmatrix} C_1^k & C_2^k \end{bmatrix}^{\mathrm{T}}$ is expressed by Equation 3.72 as a result of joining Equation 3.70 and 3.71.

$$\begin{bmatrix} D_1^{2k} & D_1^{2k+1} \\ D_2^{2k} & D_2^{2k+1} \end{bmatrix} = \frac{1}{\sqrt{2}} \begin{bmatrix} H_{1,1}^{2k} & H_{1,2}^{2k} \\ H_{2,1}^{2k} & H_{2,2}^{2k} \end{bmatrix} \begin{bmatrix} C_1^k & C_2^k \\ -\left(C_2^k\right)^* & \left(C_1^k\right)^* \end{bmatrix} + \begin{bmatrix} n_1^{2k} & n_1^{2k+1} \\ n_2^{2k} & n_2^{2k+1} \end{bmatrix} \tag{3.72}$$

Equation 3.72 can be expressed as function of the n^{th} receiver antenna as follows:

$$\begin{bmatrix} D_n^{2k} \\ D_n^{2k+1} \end{bmatrix} = \frac{1}{\sqrt{2}} \begin{bmatrix} C_1^k & C_2^k \\ -\left(C_2^k\right)^* & \left(C_1^k\right)^* \end{bmatrix} \begin{bmatrix} H_{n,1}^{2k} \\ H_{n,2}^{2k} \end{bmatrix} + \begin{bmatrix} n_n^{2k} \\ n_n^{2k+1} \end{bmatrix} \tag{3.73}$$

If D_n^{2k+1} is conjugated in equation 3.73, then the received vector at receiver antenna n equals:

$$\begin{bmatrix} D_n^{2k} \\ \left(D_n^{2k+1}\right)^* \end{bmatrix} = \frac{1}{\sqrt{2}} \begin{bmatrix} H_{n,1}^{2k} & -H_{n,2}^{2k} \\ \left(H_{n,2}^{2k}\right)^* & \left(H_{n,1}^{2k}\right)^* \end{bmatrix} \begin{bmatrix} C_1^k \\ \left(C_2^k\right)^* \end{bmatrix} + \begin{bmatrix} n_n^{2k} \\ \left(n_n^{2k+1}\right)^* \end{bmatrix} \tag{3.74}$$

Equation 3.75 is applied to estimate the signal vector sent $\mathbf{s}_k = \begin{bmatrix} C_1^k & C_2^k \end{bmatrix}^{\mathrm{T}}$ for each subcarrier $2k$.

$$\begin{bmatrix} \hat{C}_1^k \\ \left(\hat{C}_2^k\right)^* \end{bmatrix}_n = \sqrt{2} \begin{bmatrix} \left(H_{n,1}^{2k}\right)^* & H_{n,2}^{2k} \\ -\left(H_{n,2}^{2k}\right)^* & H_{n,1}^{2k} \end{bmatrix} \begin{bmatrix} D_n^{2k} \\ \left(D_n^{2k+1}\right)^* \end{bmatrix} \tag{3.75}$$

applying Equation 3.74 to Equation 3.75:

$$\begin{bmatrix} \hat{C}_1^k \\ \left(\hat{C}_2^k\right)^* \end{bmatrix}_n = \begin{bmatrix} \left|H_{n,1}^{2k}\right|^2 + \left|H_{n,2}^{2k}\right|^2 & 0 \\ 0 & \left|H_{n,1}^{2k}\right|^2 + \left|H_{n,2}^{2k}\right|^2 \end{bmatrix} \begin{bmatrix} C_1^k \\ \left(C_2^k\right)^* \end{bmatrix} + \sqrt{2} \begin{bmatrix} \left(H_{n,1}^{2k}\right)^* n_n^{2k} + H_{n,2}^{2k} \left(n_n^{2k+1}\right)^* \\ -\left(H_{n,2}^{2k}\right)^* n_n^{2k} + H_{n,1}^{2k} \left(n_n^{2k+1}\right)^* \end{bmatrix} \tag{3.76}$$

and dividing Equation 3.76 by $\left(\left|H_{n,1}^{2k}\right|^2 + \left|H_{n,2}^{2k}\right|^2\right)$, the estimated signal vector by the MIMO-TD processing at the receiver equals:

$$\begin{bmatrix} \hat{C}_1^k \\ \left(\hat{C}_2^k\right)^* \end{bmatrix}_n = \begin{bmatrix} C_1^k \\ \left(C_2^k\right)^* \end{bmatrix} + \frac{\sqrt{2}}{\left(\left|H_{n,1}^{2k}\right|^2 + \left|H_{n,2}^{2k}\right|^2\right)} \begin{bmatrix} \left(H_{n,1}^{2k}\right)^* n_n^{2k} + H_{n,2}^{2k} \left(n_n^{2k+1}\right)^* \\ -\left(H_{n,2}^{2k}\right)^* n_n^{2k} + H_{n,1}^{2k} \left(n_n^{2k+1}\right)^* \end{bmatrix} \tag{3.77}$$

Thus, the post-processing SNR for TD of the i^{th} spatial component of $\left(\hat{\mathbf{s}}_k^{\mathrm{TD}}\right)_n$ at subcarrier $2k$ and at receive antenna n is as follows:

$$\left(\mathrm{SNR}_i^{\mathrm{TD}}\right)_n = \frac{\left(|H_{n,1}|^2 + |H_{n,2}|^2\right)^2}{2\left(|H_{n,1}|^2 + |H_{n,2}|^2\right)} \frac{|C_i^k|^2}{2\sigma_{nb}^2} = \frac{\left(|H_{n,1}|^2 + |H_{n,2}|^2\right)}{2} \frac{|C_i^k|^2}{2\sigma_{nb}^2} \tag{3.78}$$

and taking the average of Equation 3.78 we obtain as a result the same average SNR of Equation 3.46.

$$\overline{\left(\mathrm{SNR}_i^{\mathrm{TD}}\right)_n} = \frac{2\sigma_{PDP}^2}{2} \frac{\overline{|C_i^k|^2}}{2\sigma_{nb}^2} = \frac{(1/2)\overline{|C_i^k|^2}\sigma_{PDP}^2}{\sigma_{nb}^2} = \mathrm{SNR} \tag{3.79}$$

Then, in order to improve the reliability of the estimation of the detected symbols, MRC is applied between the N_{RX} receiver antennas. Assuming $n = 2$ we obtain Equation 3.80.

$$\begin{bmatrix} \hat{C}_1^k \\ \hat{C}_2^k \end{bmatrix} = \begin{bmatrix} \hat{C}_1^k \\ \hat{C}_2^k \end{bmatrix}_1 + \begin{bmatrix} \hat{C}_1^k \\ \hat{C}_2^k \end{bmatrix}_2 \tag{3.80}$$

As a result of applying MRC, the post-processing SNR equals:

$$\begin{aligned} \mathrm{SNR}_i^{\mathrm{TD+MRC}} &= \frac{\left(|H_{1,1}|^2 + |H_{1,2}|^2 + |H_{2,1}|^2 + |H_{2,2}|^2\right)^2}{2\left(|H_{1,1}|^2 + |H_{1,2}|^2 + |H_{2,1}|^2 + |H_{2,2}|^2\right)} \frac{|C_i^k|^2}{2\sigma_{nb}^2} \\ &= \frac{\left(|H_{1,1}|^2 + |H_{1,2}|^2 + |H_{2,1}|^2 + |H_{2,2}|^2\right)}{2} \frac{|C_i^k|^2}{2\sigma_{nb}^2} \end{aligned} \tag{3.81}$$

And consequently, the MIMO-TD post-processing noise variance applying MRC at the receiver is as follows:

$$\left(\sigma^2\right)_i^{\mathrm{TD+MRC}} = 2\sigma_{nb}^2 \frac{2}{\left(|H_{1,1}|^2 + |H_{1,2}|^2 + |H_{2,1}|^2 + |H_{2,2}|^2\right)} \tag{3.82}$$

where it can be seen that there is a diversity gain if the receiver antennas show uncorrelated fading. Finally, the computation of the LLR at bit level for TD with MRC equals

$$\Lambda_{b,i}^{k,\mathrm{TD+MRC}} \cong \frac{1}{2\sigma_{nb}^2} \frac{\left(|H_{1,1}|^2 + |H_{1,2}|^2 + |H_{2,1}|^2 + |H_{2,2}|^2\right)}{2} \left(\left|\hat{C}_i^k - C_1\right|^2 - \left|\hat{C}_i^k - C_0\right|^2\right) \tag{3.83}$$

3.4.6 SU-MIMO Transmission Schemes

This section gives an overall description of the SU-MIMO transmission schemes for LTE/LTE-Advanced-DL since the performance evaluation of this dissertation is focussed on these schemes.

First some terminology is reviewed related with the transmission schemes in LTE/LTE-Advanced. The transmitted data stream for a given user is carried by a "codeword" which is an independently encoded transport block delivered from MAC to PHY layer and protected by a CRC). In other words, a codeword represents user data after being channel coded before it is mapped onto layers for transmission. One “layer” is one of the independent streams spatially multiplexed and the transmission “rank” is the number of transmitted layers.

Up to two codewords can be transmitted in parallel for MIMO-SM as a function of the channel conditions and the selected transmission mode. If two codewords are used for SU-MIMO SM schemes, both codewords are sent to a single UE. In contrast, for MU-MIMO schemes, each codeword is sent to a different UE. All the RBs carrying the same codeword use the same MCS, even if a codeword is mapped to multiple layers.

As shown in Figure 3.27, the transmission flow consists of the following steps: first the coded bits contained in each codeword are scrambled and the resulting coded bit sequences are mapped to the corresponding QAM modulation symbols. Then the modulation symbols are assigned to one or more layers depending on the transmission mode which is used. The layers can be viewed as the spatial resources of the MIMO and the number of layers used depends partially on the RI feedback from the UE. RI means basically how many layers the UE can discern. Finally the layers are processed by the precoding matrix before being transmitted through the antenna ports. The precoding matrices are defined by LTE specifications, [3].

3.4.6.1 Precoded SM Transmission Scheme

The LTE/LTE-Advanced transmission models for OL-SM and CL-SM use precoding matrices from a codebook defined in [3] to form the precoded transmitted layer. In other words, the MIMO precoding modifies the layer signal $\mathbf{s}_k = \begin{bmatrix} C_1^k & \dots & C_i^k & \dots & C_{N_L}^k \end{bmatrix}^T$ in order to generate the precoded modulated symbols $\mathbf{p}_k = \mathbf{P}_k \mathbf{s}_k$. The precoded modulated symbols from each layer are assigned to the antenna ports to be transmitted. The number of layers is always less than or equal to the number of antenna ports. Thus, both modes of operation can be represented by the same precoding transmission block digram shown in Figure 3.27.

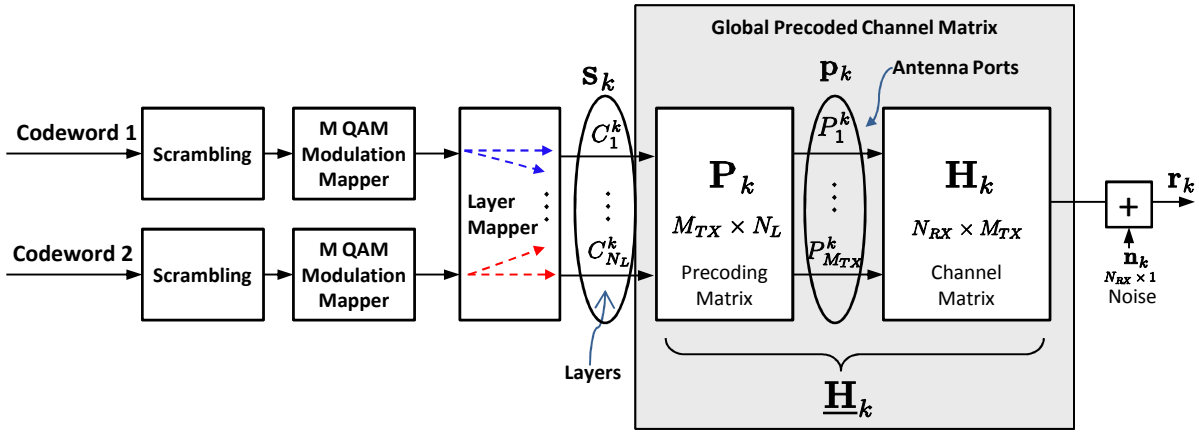

Figure 3.27: Block diagram of the equivalent precoded channel in LTE

The received signal vector is defined as in Equation 3.42 but instead of sending $\mathbf{s}_k$, $\mathbf{p}_k$ is transmitted:

$$\mathbf{r}_k = \mathbf{H}_k \mathbf{p}_k + \mathbf{n}_k \tag{3.84}$$

where $\mathbf{p}_k = \mathbf{P}_k \mathbf{s}_k$ and, consequently, the precoding matrix $\mathbf{P}_k$ and the channel matrix $\mathbf{H}_k$ form a global precoded channel matrix $\underline{\mathbf{H}}_k = \mathbf{H}_k \mathbf{P}_k$:

$$\mathbf{r}_k = \mathbf{H}_k \mathbf{P}_k \mathbf{s}_k + \mathbf{n}_k = \underline{\mathbf{H}}_k \mathbf{s}_k + \mathbf{n}_k \tag{3.85}$$

Thus, precoded SM signal detection, SNR and LLR computation follows the equations from subsection 3.4.5.1 by replacing $\mathbf{H}_k$ with $\underline{\mathbf{H}}_k$.

3.4.6.2 Layer Mapping for SM

Before MIMO precoding, layer mapping is performed in order to map the complex-valued modulation symbols for each of the codewords onto one or several layers. Up to 8 layers are allowed in LTE/LTE-Advanced where Table 3.9 shows the codeword to layer mapping for MIMO-SM in case of one codeword or two codewords in parallel.

Table 3.9: LTE SM for 2 antenna ports

	MIMO SM (2 codewords)		MIMO SM (1 codeword)
	Codeword 1	Codeword 2	Codeword 1
Rank 1			Layer: 1
Rank 2	Layer: 1	Layer: 2	Layers: 1, 2
Rank 3	Layer: 1	Layers: 2, 3	Layers: 1, 2, 3
Rank 4	Layers: 1, 2	Layers: 3, 4	Layers: 1, 2, 3, 4
Rank 5	Layers: 1, 2	Layers: 3, 4, 5	
Rank 6	Layers: 1, 2, 3	Layers: 3, 4, 5	
Rank 7	Layers: 1, 2, 3	Layers: 4, 5, 6, 7	
Rank 8	Layers: 1, 2, 3, 4	Layers: 5, 6, 7, 8	

Focussing on two or four transmit antenna ports, the layer mapping is shown schematically in Figure 3.28. In this case it is assumed that two codewords are spatially multiplexed and mapped onto two and four layers respectively. In addition, a number of layers equal to the number of antenna ports is assumed.

As shown in Figure 3.28, complex-valued modulation symbols $d^{(q)} = d^{(q)}(0), d^{(q)}(1), \ldots, d^{(q)}(M^{(q)}_{\text{symb}} - 1)$ for codewords $q = 1, 2$ are mapped onto two layers $x(i) = \left[x^{(1)}(i) \quad x^{(2)}(i)\right]^T$ or four layers $x(i) = \left[x^{(1)}(i) \quad x^{(2)}(i) \quad x^{(3)}(i) \quad x^{(4)}(i)\right]^T$; where $i = 0, 1, \ldots, M^{layer}_{symb}$, $M^{\text{layer}}_{\text{symb}}$ is the number of modulated symbols per layer and $M^{(\text{q})}_{\text{symb}}$ is the number of modulated symbols for codeword q. Thus, the codeword to layer mapping for two and four transmission layers is shown is Equations 3.86 and 3.93, respectively.

$$\begin{cases} x^{(1)}(i) = d^{(1)}(i) \\ x^{(2)}(i) = d^{(2)}(i) \end{cases} \quad M^{\text{layer}}_{\text{symb}} = M^{(1)}_{\text{symb}} = M^{(2)}_{\text{symb}} \tag{3.86}$$

$$\begin{cases} x^{(1)}(i) = d^{(1)}(2i) \\ x^{(2)}(i) = d^{(1)}(2i+1) \\ x^{(3)}(i) = d^{(2)}(2i) \\ x^{(4)}(i) = d^{(2)}(2i+1) \end{cases} \quad M_{\text{symb}}^{\text{layer}} = M_{\text{symb}}^{(1)}/2 = M_{\text{symb}}^{(2)}/2 \tag{3.87}$$

3.4.6.3 Precoded SM Transmission Scheme for two and four antenna ports

In LTE/LTE-Advanced, the OL-SM precoding consists of a fixed precoding matrix and large-delay CDD precoding at the eNodeB. Large-delay CDD precoding consists in transmitting the same OFDM symbols on the same set of subcarriers from multiple antennas with a different delay on each antenna. This creates an artificial multipath that translates into additional frequency diversity, which is then exploited by the turbo code. This time delay is identical to applying a phase shift in the frequency domain; consequently the CDD precoding can be seen as an additional subcarrier dependent precoding matrix.

In contrast, the CL-SM precoding only consists of a fixed precoding matrix selected from a codebook defined in [3]. Since the UE knows the set of applicable precoding matrices and knows the transfer function of the MIMO channel, it can determine which precoding matrix is most suitable under the current radio conditions. The selection of the precoding matrix is implementation dependant and the preferred precoding matrix index is signalled by the PMI that the UE sends to the eNodeB.

Focussing on two or four transmit antenna ports and the same number of layers that antenna ports, the DFT precoding matrix $\mathbf{U}_{N_L}$ and the matrix $\mathbf{D}(i)_{N_L}$ supporting the large delay CDD are defined in Table 3.10.

Table 3.10: Large delay CDD Precoding Matrices

Number of Layers (N_L)	$\mathbf{U}_{N_L}$	$\mathbf{D}(i)_{N_L}$
2	$\mathbf{U}_2 = \frac{1}{\sqrt{2}}\begin{bmatrix} 1 & 1 \\ 1 & e^{-j2\pi/2} \end{bmatrix}$	$\mathbf{D}(i)_2 = \begin{bmatrix} 1 & 0 \\ 0 & e^{-j2\pi i/2} \end{bmatrix}$
4	$\mathbf{U}_4 = \frac{1}{2}\begin{bmatrix} 1 & 1 & 1 & 1 \\ 1 & e^{-j2\pi/4} & e^{-j4\pi/4} & e^{-j6\pi/4} \\ 1 & e^{-j4\pi/4} & e^{-j8\pi/4} & e^{-j12\pi/4} \\ 1 & e^{-j6\pi/4} & e^{-j12\pi/4} & e^{-j18\pi/4} \end{bmatrix}$	$\mathbf{D}(i)_4 = \begin{bmatrix} 1 & 0 & 0 & 0 \\ 0 & e^{-j2\pi i/4} & 0 & 0 \\ 0 & 0 & e^{-j4\pi i/4} & 0 \\ 0 & 0 & 0 & e^{-j6\pi i/4} \end{bmatrix}$

The codebook for precoding matrix $\mathbf{W}(i)_2$ for transmission on two antenna ports and two layers is defined in Table 3.11. The codebook for precoding matrix $\mathbf{W}(i)_4$ for transmission on four antenna ports and four layers is as follows: The quantity $W_z^{\{s\}}$ denotes the matrix defined by the columns given by the set $\{s\}$ from the expression $W_z = I_4 - 2u_z u_z^{\text{H}}/u_z^{\text{H}} u_z$ where I_4 is the 4×4 identity matrix and the vector u_n is given by Table 3.12.

For OL-SM, the large-delay CDD precoding matrix is defined in LTE specifications as follows:

$$\mathbf{P}(i)_{N_L}^{CDD} = \mathbf{W}(i)_{N_L}\mathbf{D}(i)_{N_L}\mathbf{U}_{N_L} \tag{3.88}$$

Table 3.11: Codebook for transmission on two antenna ports and two layers

Codebook index (z)	$\mathbf{W}_z$
0	$\frac{1}{\sqrt{2}}\begin{bmatrix}1 & 0\\ 0 & 1\end{bmatrix}$
1	$\frac{1}{2}\begin{bmatrix}1 & 1\\ 1 & -1\end{bmatrix}$
2	$\frac{1}{2}\begin{bmatrix}1 & 1\\ j & -j\end{bmatrix}$

Table 3.12: Codebook for transmission on four antenna ports and four layers

Codebook index (z)	u_z	4 layers	$\mathbf{W}_z$
0	$u_0 = \begin{bmatrix}1 & -1 & -1 & -1\end{bmatrix}^{\mathrm{T}}$	$W_0^{\{1234\}}/2$	$\mathbf{W}_0$
1	$u_1 = \begin{bmatrix}1 & -j & 1 & j\end{bmatrix}^{\mathrm{T}}$	$W_1^{\{1234\}}/2$	$\mathbf{W}_1$
2	$u_2 = \begin{bmatrix}1 & 1 & -1 & 1\end{bmatrix}^{\mathrm{T}}$	$W_2^{\{3214\}}/2$	$\mathbf{W}_2$
3	$u_3 = \begin{bmatrix}1 & j & 1 & -j\end{bmatrix}^{\mathrm{T}}$	$W_3^{\{3214\}}/2$	$\mathbf{W}_3$
4	$u_4 = \begin{bmatrix}1 & (-1-j)/\sqrt{2} & -j & (1-j)/\sqrt{2}\end{bmatrix}^{\mathrm{T}}$	$W_4^{\{1234\}}/2$	$\mathbf{W}_4$
5	$u_5 = \begin{bmatrix}1 & (1-j)/\sqrt{2} & j & (-1-j)/\sqrt{2}\end{bmatrix}^{\mathrm{T}}$	$W_5^{\{1234\}}/2$	$\mathbf{W}_5$
6	$u_6 = \begin{bmatrix}1 & (1+j)/\sqrt{2} & -j & (-1+j)/\sqrt{2}\end{bmatrix}^{\mathrm{T}}$	$W_6^{\{1324\}}/2$	$\mathbf{W}_6$
7	$u_7 = \begin{bmatrix}1 & (-1+j)/\sqrt{2} & j & (1+j)/\sqrt{2}\end{bmatrix}^{\mathrm{T}}$	$W_7^{\{1324\}}/2$	$\mathbf{W}_7$
8	$u_8 = \begin{bmatrix}1 & -1 & 1 & 1\end{bmatrix}^{\mathrm{T}}$	$W_8^{\{1234\}}/2$	$\mathbf{W}_8$
9	$u_9 = \begin{bmatrix}1 & -j & -1 & -j\end{bmatrix}^{\mathrm{T}}$	$W_9^{\{1234\}}/2$	$\mathbf{W}_9$
10	$u_{10} = \begin{bmatrix}1 & 1 & 1 & -1\end{bmatrix}^{\mathrm{T}}$	$W_{10}^{\{1324\}}/2$	$\mathbf{W}_{10}$
11	$u_{11} = \begin{bmatrix}1 & j & -1 & j\end{bmatrix}^{\mathrm{T}}$	$W_{11}^{\{1324\}}/2$	$\mathbf{W}_{11}$
12	$u_{12} = \begin{bmatrix}1 & -1 & -1 & 1\end{bmatrix}^{\mathrm{T}}$	$W_{12}^{\{1234\}}/2$	$\mathbf{W}_{12}$
13	$u_{13} = \begin{bmatrix}1 & -1 & 1 & -1\end{bmatrix}^{\mathrm{T}}$	$W_{13}^{\{1324\}}/2$	$\mathbf{W}_{13}$
14	$u_{14} = \begin{bmatrix}1 & 1 & -1 & -1\end{bmatrix}^{\mathrm{T}}$	$W_{14}^{\{3214\}}/2$	$\mathbf{W}_{14}$
15	$u_{15} = \begin{bmatrix}1 & 1 & 1 & 1\end{bmatrix}^{\mathrm{T}}$	$W_{15}^{\{1234\}}/2$	$\mathbf{W}_{15}$

where for two antenna ports and $N_L = 2$ the precoder $\mathbf{W}(i)_{N_L}$ is the precoding matrix corresponding to codebook index 0 in Table 3.11. For four antenna ports and $N_L = 4$ the UE may assume that the eNodeB cyclically assigns different precoders to different transmitted vectors every N_L vectors. In particular, the precoding matrix is selected according to $\mathbf{W}(i)_{N_L} = W_z$, where $z = (\lfloor (i/N_L) \mod 4 \rfloor) + 12$ is the codebook index given by 12,13,14 and 15 in Table 3.12.

For CL-SM, the precoding matrix is defined as follows:

$$\mathbf{P}(i)_{N_L}^{CL} = \mathbf{W}(i)_{N_L} \tag{3.89}$$

where $\mathbf{W}(i)_{N_L}$ is the precoding matrix at transmitted symbol i selected by the UE in order to maximize the link capacity. In other words, the UE should signal to the eNodeB the precoding matrix that would result in a transmission with an *Effective Signal-to-Noise Ratio* (ESNR) following most closely the largest singular values of its estimated channel matrix.

In order to keep limited the total power in the transmit antenna array and to keep the validity of the SNR defined in Equation 3.45, the precoding matrices must be unitary. $\mathbf{U}_{N_L}$ and $\mathbf{D}(i)_{N_L}$ are unitary as accomplish the following property $(\mathbf{U}_{N_L})^{\mathrm{H}}\mathbf{U}_{N_L} = \mathbf{U}_{N_L}(\mathbf{U}_{N_L})^{\mathrm{H}} = \mathbf{I}_{N_L}$ and $(\mathbf{D}(i)_{N_L})^{\mathrm{H}}\mathbf{D}(i)_{N_L} = \mathbf{D}(i)_{N_L}(\mathbf{D}(i)_{N_L})^{\mathrm{H}} = \mathbf{I}_{N_L}$, where $\mathbf{I}_{N_L}$ is the identity matrix of size $N_L \times N_L$. But $\mathbf{W}(i)_{N_L}$ is not unitary and a power scale factor must be considered to convert it to unitary precoding as follows:

$$\begin{gathered}\left(\sqrt{\rho}\mathbf{W}(i)_{N_L}\right)^{\mathrm{H}}\sqrt{\rho}\mathbf{W}(i)_{N_L} = \sqrt{\rho}\mathbf{W}(i)_{N_L}\left(\sqrt{\rho}\mathbf{W}(i)_{N_L}\right)^{\mathrm{H}} = \mathbf{I}_{N_L} \\ \downarrow \\ \rho\left(\mathbf{W}(i)_{N_L}\right)^{\mathrm{H}}\mathbf{W}(i)_{N_L} = \rho\mathbf{W}(i)_{N_L}\left(\mathbf{W}(i)_{N_L}\right)^{\mathrm{H}} = \mathbf{I}_{N_L}\end{gathered} \tag{3.90}$$

where ρ is equal to the number of transmit antennas (M_{TX}) if the number of transmit antennas is the same than the number of spatially multiplexed layers. Thus for two transmit antennas $\rho = 2$ and for four transmit antennas $\rho = 4$.

Thus the precoding matrix $\mathbf{P}_k$ defined in Equation 3.85 is as follows:

For OL-SM,

$$\mathbf{P}_k = \sqrt{\rho}\mathbf{P}(i)_{N_L}^{CDD} = \sqrt{\rho}\mathbf{W}(i)_{N_L}\mathbf{D}(i)_{N_L}\mathbf{U}_{N_L} \tag{3.91}$$

For CL-SM,

$$\mathbf{P}_k = \sqrt{\rho}\mathbf{P}(i)_{N_L}^{CL} = \sqrt{\rho}\mathbf{W}(i)_{N_L} \tag{3.92}$$

where the i^{th} complex-valued modulation symbol of each transmitted layer is mapped onto k^{th} subcarrier.

3.4.6.4 TD Transmission Scheme

The LTE/LTE-Advanced specifications define only the TD precoding operation for two and four antenna ports combined with a specific layer mapping for TD according to [3]. For TD, the layer mapping for two antenna ports is as follows:

$$\begin{cases} x^{(1)}(i) = d^{(1)}(2i) \\ x^{(2)}(i) = d^{(1)}(2i+1) \\ \text{where } M_{\text{symb}}^{\text{layer}} = M_{\text{symb}}^{(1)}/2 \end{cases} \tag{3.93}$$

and for four antenna ports it is as follows:

$$\begin{cases} \begin{gathered} x^{(1)}(i) = d^{(1)}(4i) \\ x^{(2)}(i) = d^{(1)}(4i+1) \\ x^{(3)}(i) = d^{(1)}(4i+2) \\ x^{(4)}(i) = d^{(1)}(4i+3) \\ \text{where} \end{gathered} \\ M_{\text{symb}}^{\text{layer}} = \begin{cases} M_{\text{symb}}^{(1)}/4; \text{ if } M_{\text{symb}}^{(1)} \mod 4 = 0 \\ \left(M_{\text{symb}}^{(1)}+2\right)/4; \text{ if } M_{\text{symb}}^{(1)} \mod 4 \neq 0 \end{cases} \\ \text{if } M_{\text{symb}}^{(1)} \mod 4 \neq 0 \text{ two null symbols shall be appended to } d^{(1)}(M_{\text{symb}}^{(1)}-1) \end{cases} \tag{3.94}$$

In TD, there is only one codeword, thus it is a rank-1 transmission, and the number of layers is equal to the number of antenna ports used for transmission of the physical channel. In addition, as shown in Equations 3.93 and 3.94, the size of each layer in symbols is half of the codeword size for two antenna ports and a approximately one fourth of the codeword size for four antenna ports.

The TD transmission scheme for two layers is pure Alamouti SFBC and the symbols transmitted from the two antenna ports are mapped onto each pair of adjacent subcarriers (it is described in section 3.4.5.2). while a combination of FSTD with SFBC is employed for the TD transmission scheme for four layers. FSTD schemes basically transmit symbols from each antenna on a different set of subcarriers.

The TD transmission scheme for four layers can be viewed as a combination of two single SFBC schemes with Alamouti code in parallel mapped to independent subcarriers on non-consecutive antenna ports 0, 2 and 1,3, respectively. The reason for distributing the two SFBCs in an interlaced way is related to the fact that the first two cell-specific antenna ports have a higher reference signal density than the two last and interlacing ensures a more balanced decoding performance. The output of this TD precoder for four antennas ports is illustrated in Table 3.13 and Figure 3.29 shows a representation of the codeword to layer mapping after applying SFBC.

Table 3.13: LTE SFBC for 4 antenna ports

subcarrier	antenna 1	antenna 2	antenna 3	antenna 4
$4k$	$\frac{1}{\sqrt{2}}C_1^k$	0	$\frac{-1}{\sqrt{2}}\left(C_2^k\right)^*$	0
$4k+1$	$\frac{1}{\sqrt{2}}C_2^k$	0	$\frac{1}{\sqrt{2}}\left(C_1^k\right)^*$	0
$4k+2$	0	$\frac{1}{\sqrt{2}}C_3^k$	0	$\frac{-1}{\sqrt{2}}\left(C_4^k\right)^* k$
$4k+3$	0	$\frac{1}{\sqrt{2}}C_4^k$	0	$\frac{1}{\sqrt{2}}\left(C_3^k\right)^*$

The fact that TD transmission scheme for four antenna ports is composed of two independent SFBCs for two antenna ports makes easier the receiver implementation at the UE due to the fact that symbol detection can be performed in parallel for both schemes. Thus, the equations for SFBCs for two antenna ports described in subsection 3.4.5.2 can be applied and the received signal vector is as follows:

$$\begin{bmatrix} D_1^{4k} & D_1^{4k+1} & D_1^{4k+2} & D_1^{4k+3} \\ D_2^{4k} & D_2^{4k+1} & D_2^{4k+2} & D_2^{4k+3} \\ D_3^{4k} & D_3^{4k+1} & D_3^{4k+2} & D_3^{4k+3} \\ D_4^{4k} & D_4^{4k+1} & D_4^{4k+2} & D_4^{4k+3} \end{bmatrix} = \frac{1}{\sqrt{2}} \begin{bmatrix} H_{1,1}^{4k} & H_{1,2}^{4k} & H_{1,3}^{4k} & H_{1,4}^{4k} \\ H_{2,1}^{4k} & H_{2,2}^{4k} & H_{2,3}^{4k} & H_{2,4}^{4k} \\ H_{3,1}^{4k} & H_{3,2}^{4k} & H_{3,3}^{4k} & H_{3,4}^{4k} \\ H_{4,1}^{4k} & H_{4,2}^{4k} & H_{4,3}^{4k} & H_{4,4}^{4k} \end{bmatrix} \begin{bmatrix} C_1^k & C_2^k & 0 & 0 \\ 0 & 0 & C_3^k & C_4^k \\ -\left(C_2^k\right)^* & \left(C_1^k\right)^* & 0 & 0 \\ 0 & 0 & -\left(C_4^k\right)^* & \left(C_3^k\right)^* \end{bmatrix} + \begin{bmatrix} n_1^{4k} & n_1^{4k+1} & n_1^{4k+2} & n_1^{4k+3} \\ n_2^{4k} & n_2^{4k+1} & n_2^{4k+2} & n_2^{4k+3} \\ n_3^{4k} & n_3^{4k+1} & n_3^{4k+2} & n_3^{4k+3} \\ n_4^{4k} & n_4^{4k+1} & n_4^{4k+2} & n_4^{4k+3} \end{bmatrix} \tag{3.95}$$

Thus, assuming that channel coefficients are equal for two adjacent subcarriers, i.e., $H_{n,m}^{4k} = H_{n,m}^{4k+1}$ and $H_{n,m}^{4k+2} = H_{n,m}^{4k+3}$, the space frequency block decoding after OFDM demodulation is expressed in equations 3.96 and 3.97 per each receiver branch n :

$$\begin{bmatrix} \hat{C}_1^k \\ \left(\hat{C}_3^k\right)^* \end{bmatrix}_n = \begin{bmatrix} \left|H_{n,1}^{4k}\right|^2 + \left|H_{n,3}^{4k}\right|^2 & 0 \\ 0 & \left|H_{n,1}^{4k}\right|^2 + \left|H_{n,3}^{4k}\right|^2 \end{bmatrix} \begin{bmatrix} C_1^k \\ \left(C_3^k\right)^* \end{bmatrix} + \sqrt{2} \begin{bmatrix} \left(H_{n,1}^{4k}\right)^* n_n^{4k} + H_{n,3}^{4k} \left(n_n^{4k+1}\right)^* \\ -\left(H_{n,3}^{4k}\right)^* n_n^{4k} + H_{n,1}^{4k} \left(n_n^{4k+1}\right)^* \end{bmatrix} \tag{3.96}$$

and

$$\begin{bmatrix} \hat{C}_2^k \\ \left(\hat{C}_4^k\right)^* \end{bmatrix}_n = \begin{bmatrix} \left|H_{n,2}^{4k+2}\right|^2 + \left|H_{n,4}^{4k+2}\right|^2 & 0 \\ 0 & \left|H_{n,2}^{4k+2}\right|^2 + \left|H_{n,4}^{4k+2}\right|^2 \end{bmatrix} \begin{bmatrix} C_2^k \\ \left(C_4^k\right)^* \end{bmatrix} + \sqrt{2} \begin{bmatrix} \left(H_{n,2}^{4k+2}\right)^* n_n^{4k+2} + H_{n,4}^{4k+2} \left(n_n^{4k+3}\right)^* \\ -\left(H_{n,4}^{4k+2}\right)^* n_n^{4k+2} + H_{n,2}^{4k} \left(n_n^{4k+3}\right)^* \end{bmatrix} \tag{3.97}$$

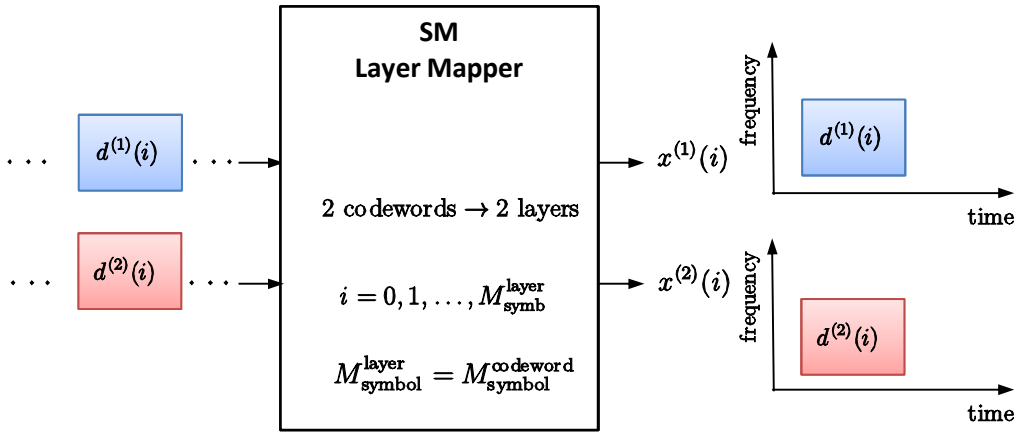

(a) Codeword to layer mapping scheme for SM and 2 layers

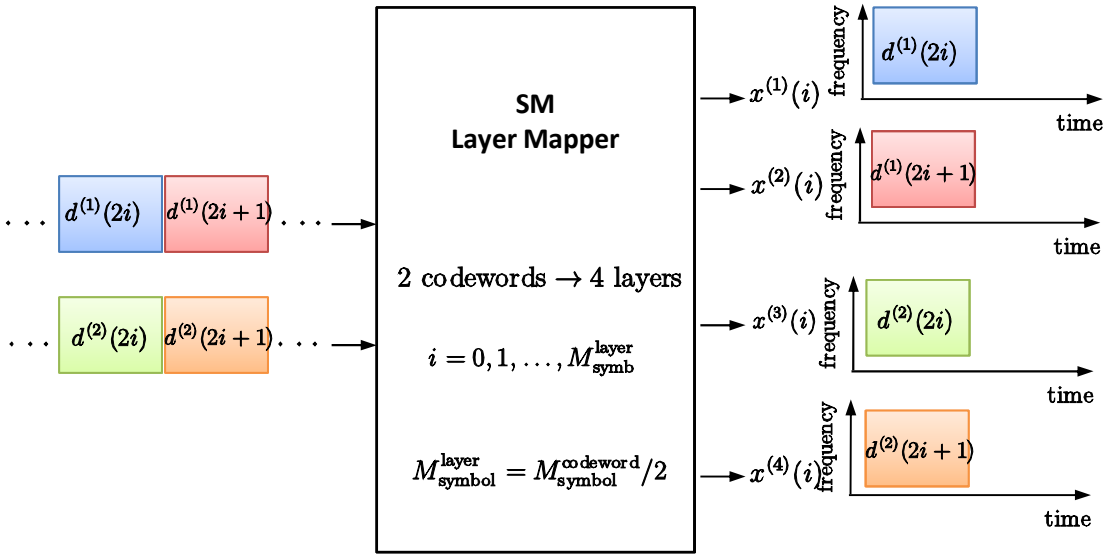

(b) Codeword to layer mapping scheme for SM and 4 layers

Figure 3.28: Codeword to layer mapping scheme for SM and 2 layers (a) and 4 layers (b).

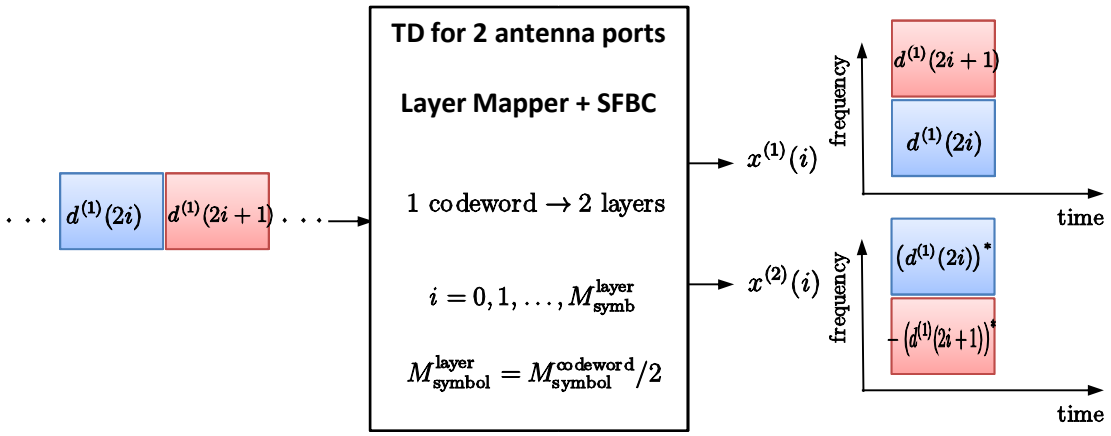

(a) Codeword to layer mapping scheme for TD and 2 layers

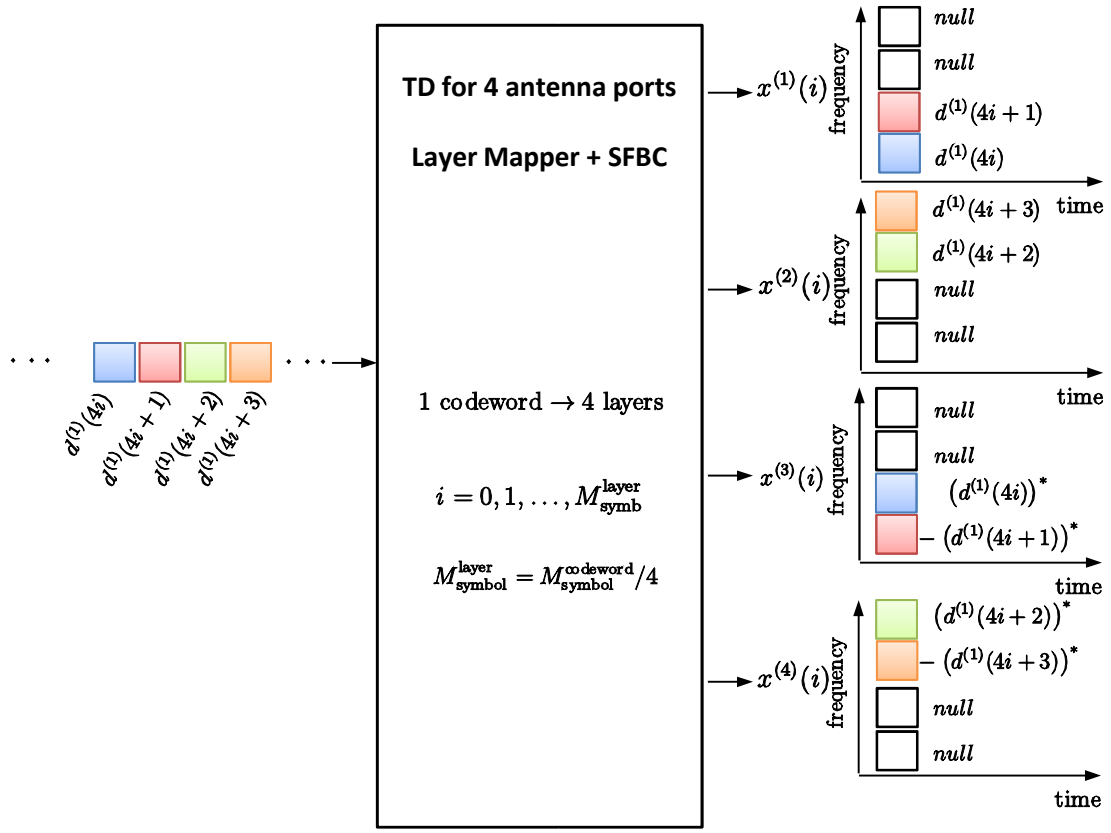

(b) Codeword to layer mapping scheme for TD and 4 layers

Figure 3.29: Codeword to layer mapping scheme for SM and 2 layers (a) and 4 layers (b)

3.4.7 MIMO-SIC Receiver

The basic idea of a SIC receiver is that it can detect and decode the codewords of the received data streams in such a way that if a codeword is successfully decoded, then the decoded data of this codeword is re-encoded, re-modulated and cancelled from the originally received signal in order to reduce the interference for the remaining data streams and try to detect and decode again. [74] describes different types of SIC receivers at symbol level (symbol-SIC) or at codeword level (codeword-SIC) In symbol-SIC, the interference cancellation is done independently at each subcarrier on modulated-symbol level, whereas in codeword-SIC the detection is done on codeword level and the interference contribution is subtracted after decoding and re-encoding of the codeword. Furthermore, as described in [75], in the SIC processing it may happen that a data stream is correctly decoded after a certain number of HARQ transmissions. In this case, the interference cancellation cannot only be performed in the current TTI, but also in previous TTIs if there are other remaining undecoded data streams.

The link level simulator presented in this work implements a codeword-SIC over MIMO MMSE linear receiver and takes also into account the HARQ operation. The block diagram of the codeword-SIC receiver is shown in Figure 3.30 where MIMO processing and interference cancellation are performed independently at each subcarrier. Two codewords are spatially multiplexed and the codeword-SIC algorithm is only employed after the correct decoding of one of the two codewords. Therefore, the advantage of codeword SIC receiver is that interference cancellation cannot introduce errors that propagate through the detection process in contrast to symbol-SIC operating on undecoded data streams.

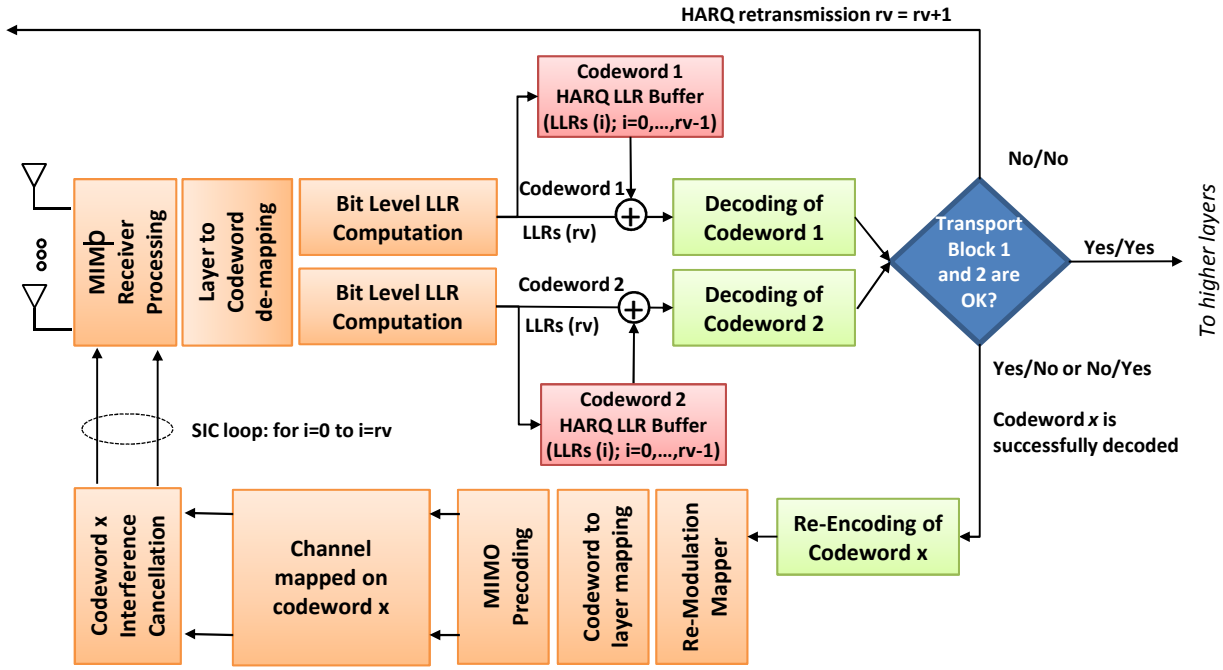

Figure 3.30: Block diagram of a Codeword-SIC receiver

In the following the codeword-SIC algorithm is described for a 2×2 and 4×4 MIMO system. We begin by using Equation 3.41 to write the 2×2 and 4×4 MIMO-OFDM system models at subcarrier k as follows, respectively:

$$\underbrace{\begin{bmatrix} D_1^k \\ D_2^k \end{bmatrix}}_{\mathbf{r}_k} = \underbrace{\begin{bmatrix} \mathrm{H}_{1,1}^k & \mathrm{H}_{1,2}^k \\ \mathrm{H}_{2,1}^k & \mathrm{H}_{2,2}^k \end{bmatrix}}_{\mathbf{H}_k} \underbrace{\begin{bmatrix} C_1^k \\ C_2^k \end{bmatrix}}_{\mathbf{s}_k} + \underbrace{\begin{bmatrix} \mathrm{n}_1^k \\ \mathrm{n}_2^k \end{bmatrix}}_{\mathbf{n}_k} \tag{3.98}$$

$$\underbrace{\begin{bmatrix} D_1^k \\ D_2^k \\ D_3^k \\ D_4^k \end{bmatrix}}_{\mathbf{r}_k} = \underbrace{\begin{bmatrix} \mathrm{H}_{1,1}^k & \mathrm{H}_{1,2}^k & \mathrm{H}_{1,3}^k & \mathrm{H}_{1,4}^k \\ \mathrm{H}_{2,1}^k & \mathrm{H}_{2,2}^k & \mathrm{H}_{2,3}^k & \mathrm{H}_{2,4}^k \\ \mathrm{H}_{3,1}^k & \mathrm{H}_{3,2}^k & \mathrm{H}_{3,3}^k & \mathrm{H}_{3,4}^k \\ \mathrm{H}_{4,1}^k & \mathrm{H}_{4,2}^k & \mathrm{H}_{4,3}^k & \mathrm{H}_{4,4}^k \end{bmatrix}}_{\mathbf{H}_k} \underbrace{\begin{bmatrix} C_1^k \\ C_2^k \\ C_3^k \\ C_4^k \end{bmatrix}}_{\mathbf{s}_k} + \underbrace{\begin{bmatrix} \mathrm{n}_1^k \\ \mathrm{n}_2^k \\ \mathrm{n}_3^k \\ \mathrm{n}_4^k \end{bmatrix}}_{\mathbf{n}_k} \tag{3.99}$$

Equations 3.99 and 3.98 can be rewritten as follows:

$$\mathbf{r}_k = \begin{bmatrix} \mathbf{h}_{(k,1)} & \mathbf{h}_{(k,2)} \end{bmatrix} \begin{bmatrix} C_1^k \\ C_2^k \end{bmatrix} + \mathbf{n}_k \tag{3.100}$$

$$\mathbf{r}_k = \begin{bmatrix} \mathbf{h}_{(k,1)} & \mathbf{h}_{(k,2)} & \mathbf{h}_{(k,3)} & \mathbf{h}_{(k,4)} \end{bmatrix} \begin{bmatrix} C_1^k \\ C_2^k \\ C_3^k \\ C_4^k \end{bmatrix} + \mathbf{n}_k \tag{3.101}$$

Next, it is assumed that the codeword x is successfully decoded and the codeword $\bar{x}$ is not correctly decoded, where $x \in \{1, 2\}$ and if $x = 1$ then $\bar{x} = 2$ and, vice versa, if $x = 2$ then $\bar{x} = 1$. Thus, the interference cancellation for a 2×2 MIMO-SM scheme where two codewords are mapped onto two layers is formulated as follows:

$$\mathbf{r}_k^{(\mathrm{sic})} = \mathbf{r}_k - \mathbf{h}_{(k,x)} C_x^k = \mathbf{h}_{(k,\bar{x})} C_{\bar{x}}^k + \mathbf{n}_k \tag{3.102}$$

and the interference cancellation for a 4×4 MIMO-SM scheme where two codewords are mapped onto four layers is formulated as follows:

$$\begin{aligned} \mathbf{r}_k^{(\mathrm{sic})} &= \mathbf{r}_k - \mathbf{h}_{(k,2x-1)} C_{(2x-1)}^k - \mathbf{h}_{(k,2x)} C_{2x}^k \\ &= \begin{bmatrix} \mathbf{h}_{(k,2\bar{x}-1)} & \mathbf{h}_{(k,2\bar{x})} \end{bmatrix} \begin{bmatrix} C_{(2\bar{x}-1)}^k \\ C_{2\bar{x}}^k \end{bmatrix} + \mathbf{n}_k = \mathbf{H}_{(k,\bar{x})} \mathbf{s}_{(k,\bar{x})} + \mathbf{n}_k \end{aligned} \tag{3.103}$$

As a result, the reformulated MIMO-SIC processing to decode the second codeword by using the MMSE receiver (as described in section 3.4.5.1) for the 2×2 antenna configuration is as follows:

$$\hat{C}_{\bar{x}}^k = \mathbf{W}_k^{\mathrm{MMSE}} \mathbf{r}_k^{(\mathrm{sic})} = \left(\mathbf{h}_{(k,\bar{x})}^{\mathrm{H}} \mathbf{h}_{(k,\bar{x})} + \gamma \right)^{-1} \mathbf{h}_{(k,\bar{x})}^{\mathrm{H}} \mathbf{r}_k^{(\mathrm{sic})} \tag{3.104}$$

and for the 4×4 antenna configuration is

$$\hat{\mathbf{s}}_{(k,\bar{x})} = \mathbf{W}_k^{\mathrm{MMSE}} \mathbf{r}_k^{(\mathrm{sic})} = \left(\mathbf{H}_{(k,\bar{x})}^{\mathrm{H}} \mathbf{H}_{(k,\bar{x})} + \gamma \mathbf{I}_2 \right)^{-1} \mathbf{H}_{(k,\bar{x})}^{\mathrm{H}} \mathbf{r}_k^{(\mathrm{sic})} \tag{3.105}$$

To summarize, the codeword-SIC algorithm steps are listed in Algorithm 3.1.

Algorithm 3.1 Codeword-SIC algorithm

1. Detection and decoding process is performed for each of the codewords as the receiver would do if codeword-SIC was not used.

   (a) MIMO detection follows the MMSE linear receiver processing described in subsection 3.4.5.1 taking into account the global precoded channel matrix described in subsection 3.4.6.1 in order to compute the bit level LLRs of each codeword

   (b) Soft decoding and HARQ retransmissions follows the processing described in subsection 3.3.2

2. After decoding each codeword the decoded TBs are obtained and the receiver can, by checking the CRC, know whether the TBs have been correctly received or a retransmission is required, thus the next conditions are checked:

   (a) If the CRCs of the two TBs are correct, then they are passed to higher layers.

   (b) Otherwise, if only one of the two TBs is successfully decoded, then the SIC processing is employed as described in next step 3

   (c) On the contrary, if both TBs are not correctly decoded, then an HARQ retransmission is required.

3. The correct TB is re-encoded to rebuild the codeword and then it is re-mapped to precoded complex symbols after applying the modulation mapper, the codeword to layer mapping and the MIMO precoding. In this case, as the channel is estimated at the receiver, the channel corresponding to the antennas on which the correct codeword has been mapped is applied to the precoded complex symbols in order to reconstruct the received signal due to the transmission of the correct codeword. Finally, the interference created by the correct codeword is cancelled from the signal received during the transmission of the second codeword which was not successfully decoded.

4. The interference cancellation and the MIMO-SIC processing are performed.

   (a) The interference cancellation is performed by cancelling the correct codeword from the received signal at all subcarriers using Equations 3.102 and 3.103 if 2×2 and 4×4 MIMO configurations are considered.

   (b) Next, the MIMO-SIC processing is performed at all subcarriers by employing Equations 3.104 and 3.105

5. Moreover, in order to optimize the codeword-SIC receiver for HARQ operation the LLRs in the current TTI are written to an additional buffer and, then, decoding is performed based on the combined LLRs from this additional buffer and the HARQ buffer with the LLRs from previous transmissions. In addition, the LLRs at each retransmission are recomputed taking also into account the enhancement due to the interference cancellation.

The performance of this SIC algorithm with HARQ has been evaluated by link level simulations taking into account the simulator parameters listed in Table 5.4. In particular, the assumed simulation conditions are: ETU300 channel model, ideal channel estimation, a bandwidth of 4 RBs, OL MIMO-SM with large delay CDD precoding, CL MIMO-SM with CL(k) precoding, HARQ retransmissions with the same SNR for each rv and MCS 6.

In Figures 3.31, 3.32, 3.33 and 3.34, "Retransmission Percentage" stands for the percentage of transmissions where at least one of the two transmitted codewords are not properly decoded and HARQ retransmissions are required. "Codeword Successfully Decoded Percentage" stands for the percentage of transmissions where both transmitted codewords are properly decoded regardless of SIC being in use or not. "SIC Percentage" stands for the percentage of transmissions where the codeword-SIC is used only because one of the codewords is properly decoded. Finally, "Codeword successfully decoded using SIC" stands for the success percentage when codeword-SIC is applied.

Figure 3.31 and 3.32 shows that in OL MIMO-SM with CDD precoding the "SIC percentage" is low and only when the mean SNR is around -4 dB presents a slight usage for uncorrelated MIMO antennas (2×2LC and 4×4LC). In the case of highly correlated antennas, for 2×2HC the "SIC percentage" is also low and it is only used between -4 and 6 dB of mean SNR. Notice that it is only used at rv= 0 for a mean SNR of 6 dB and 2×2HC and for a mean SNR of -4 dB and 4×4LC. On the other hand, 4×4HC MIMO configuration degrades significantly the success ratio of decoding, so the use of SIC expands to the whole range of SNRs and for an SNR of 26 dB, it is performed only at rv= 0. In any case, when SIC is applied, the success percentage is high, more than 50% for -4 dB of SNR and almost 100% for 6 dB of SNR.

Figure 3.33 and Figure 3.34 shows that in CL MIMO-SM with CL(k) precoding the "SIC percentage" presents a higher usage with respect to OL mainly due to the non-priority codeword. As has been described, CL(k) precoding is designed to maximize the post-processing SNR of the priority codeword, thus, the non-priority codewords presents a poorer post-processing SNR. For low antenna correlation, codeword-SIC is applied between -4 dB to 6 dB of mean SNR and for high antenna correlation, it is used in the whole range of SNRs. If SIC is applied, the success percentage is high, almost 100% if the overall SNR taking into account HARQ retransmission is enough. Therefore, codeword-SIC combined with HARQ contributes to reduce the need of requesting the next HARQ retransmission.

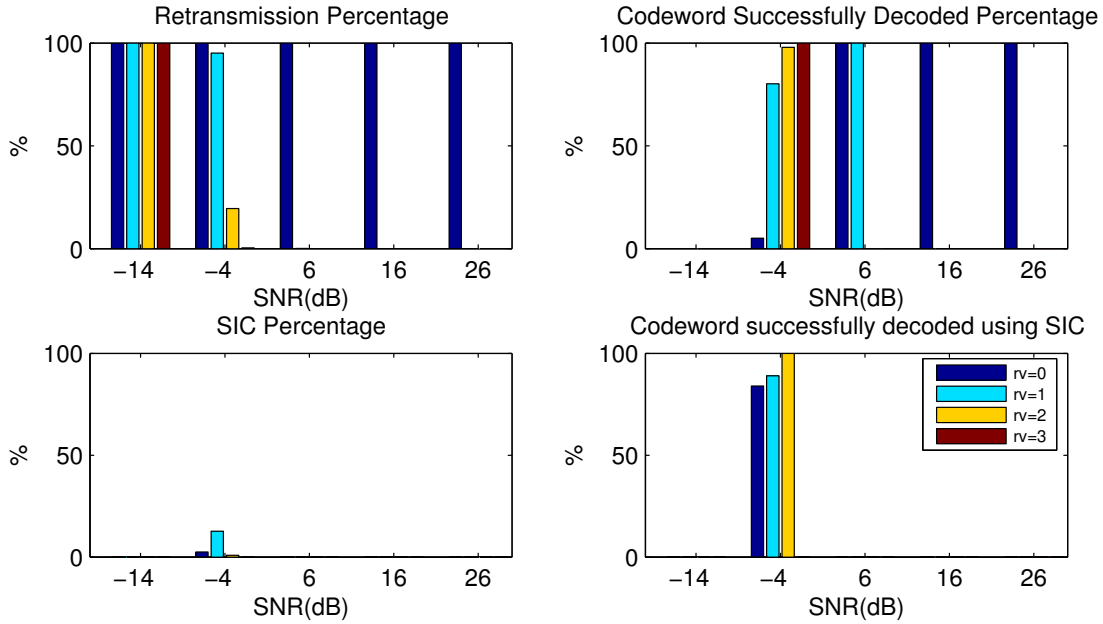

(a) 2×2LC, MCS 6, OL with CDD Precoding

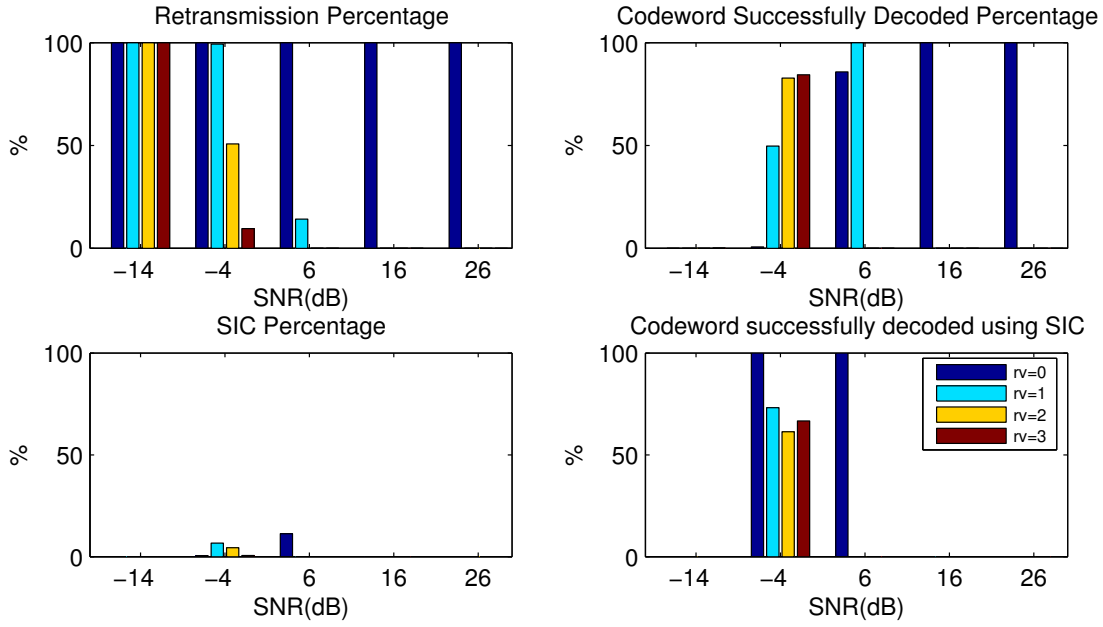

(b) 2×2 HC and MCS 6, OL with CDD Precoding

Figure 3.31: Codeword-SIC performance with HARQ for MCS 6, 2×2 MIMO with CDD Precoding

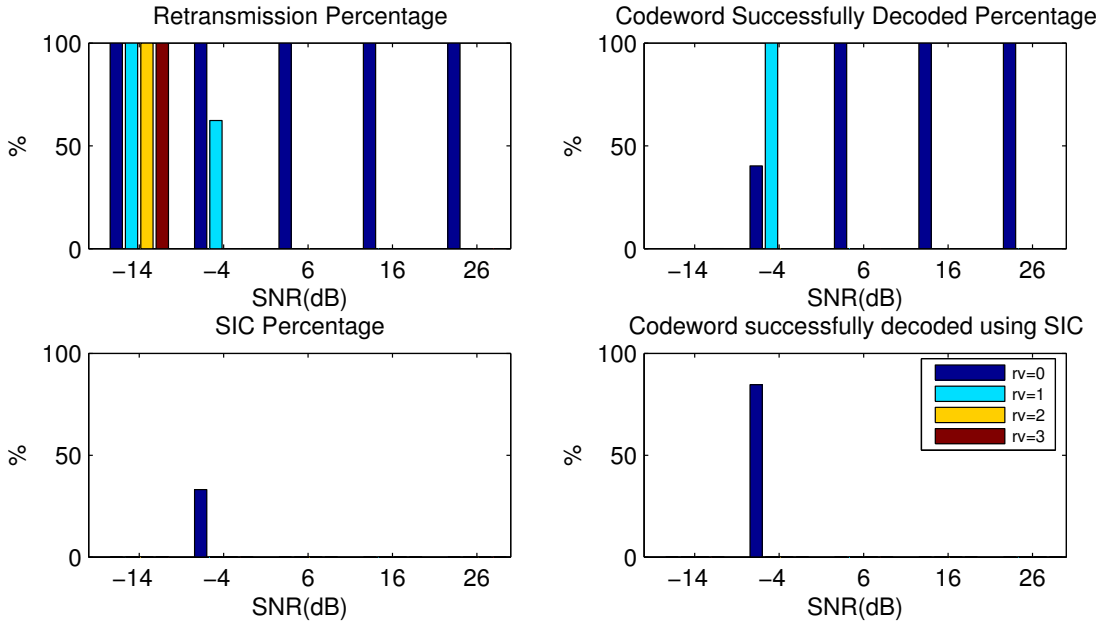

(a) 4×4 LC, MCS 6, OL with CDD Precoding

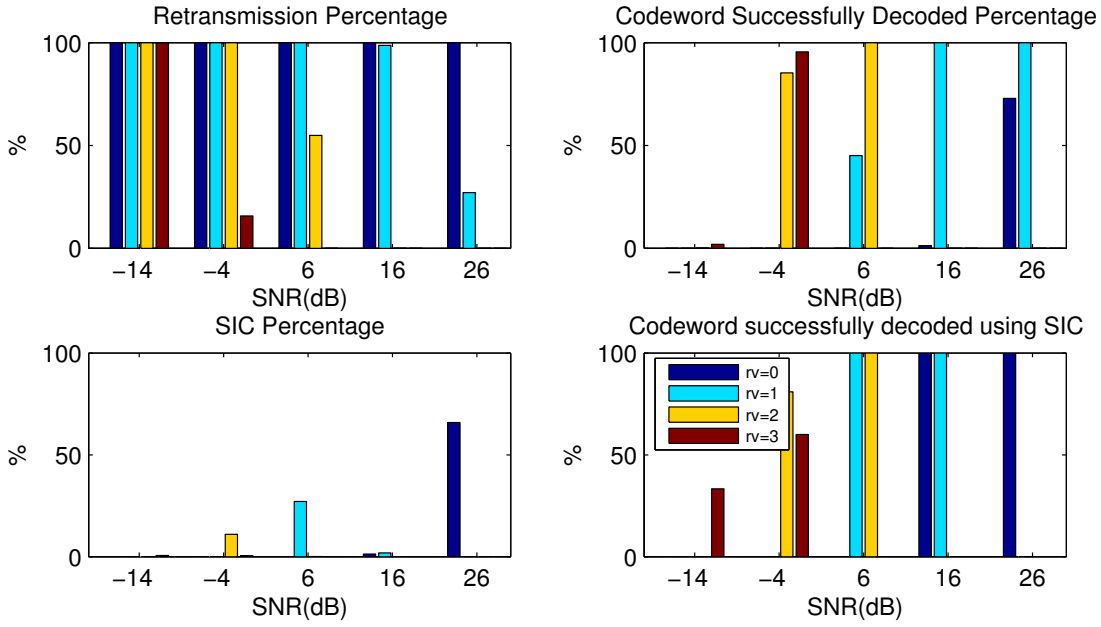

(b) 4×4 HC, MCS 6, OL with CDD Precoding

Figure 3.32: Codeword-SIC performance with HARQ for MCS 6, 4×4 MIMO with CDD Precoding

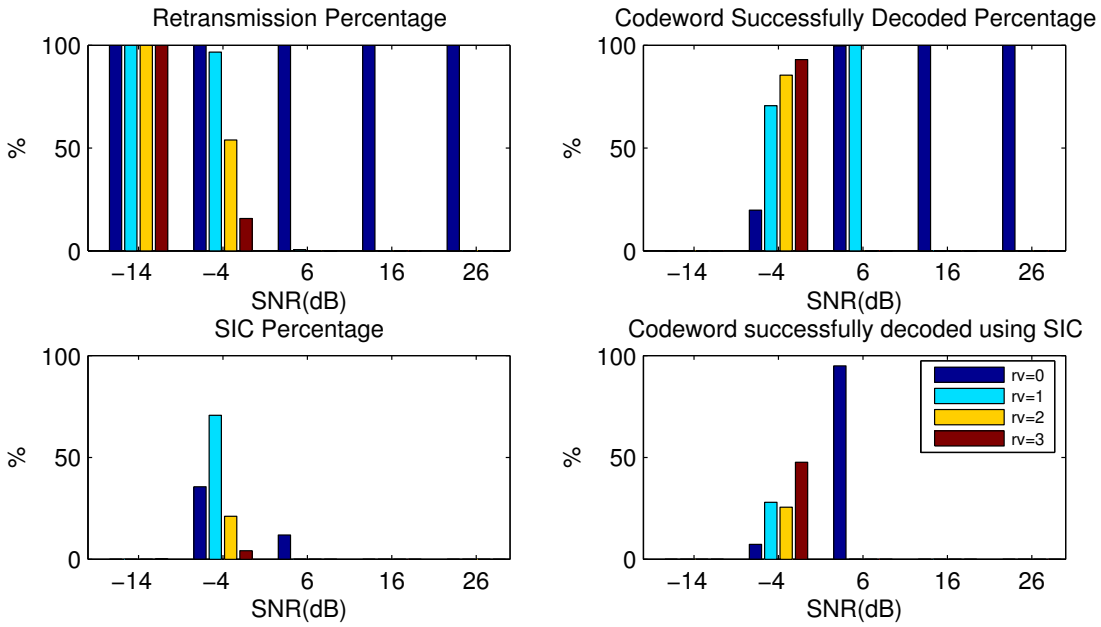

(a) 2 × 2 LC, MCS 6, CL with CL(k) Precoding

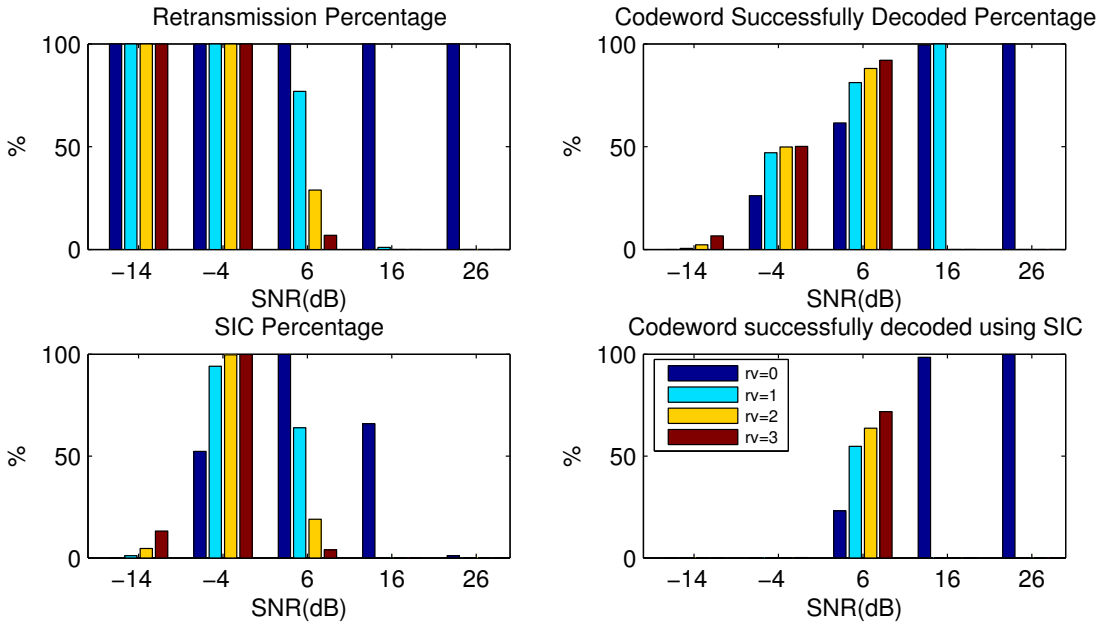

(b) 2 × 2 HC, MCS 6, CL with CL(k) Precoding

Figure 3.33: Codeword-SIC performance with HARQ for MCS 6, 2×2 MIMO with CL(k) Precoding

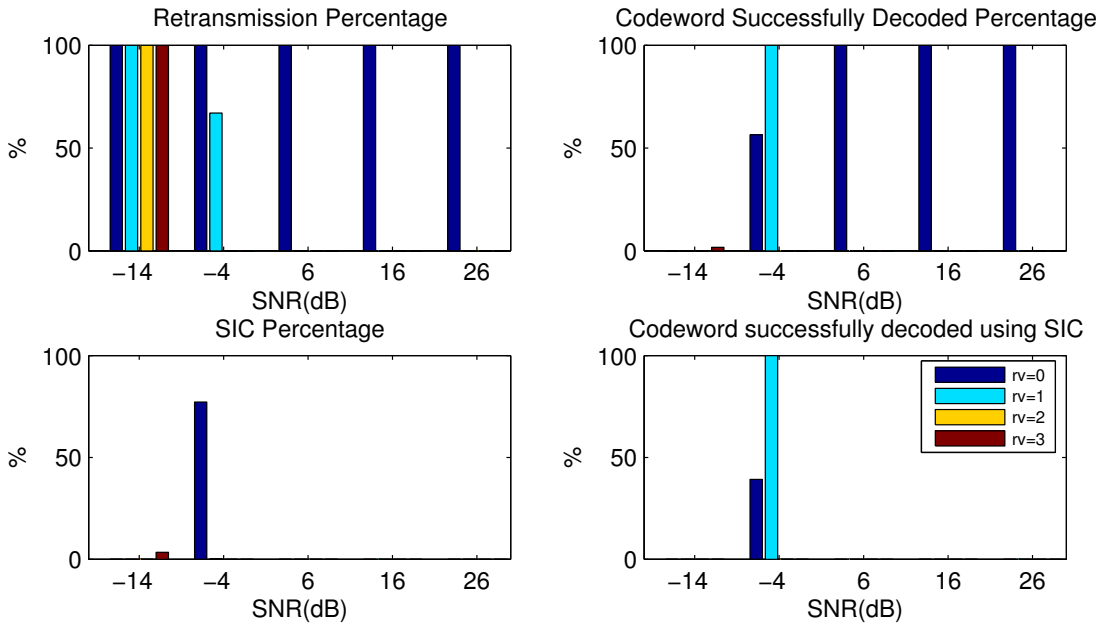

(a) 4×4 LC, MCS 6, CL with CL(k) Precoding

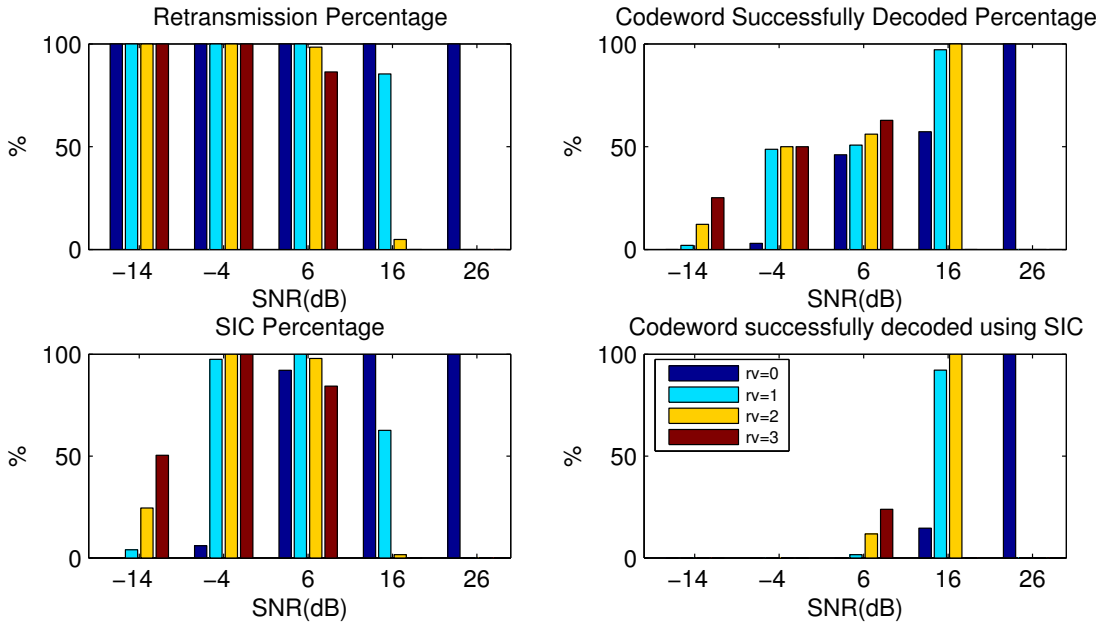

(b) 4×4 HC, MCS 6, CL with CL(k) Precoding

Figure 3.34: Codeword-SIC performance with HARQ for MCS 6, 4×4 MIMO with CL(k) Precoding

Chapter 4

Channel Estimation Error Model

In this chapter, we propose to simulate channel estimation errors by a Gaussian additive noise error model. This channel estimation error model, called CEEM, is used to obtain realistic performance assessments from the LTE/LTE-Advanced link level simulator. We start introducing the E-UTRA reference signals and their mapping. Next we describe the system model and we discuss practical channel estimation methods. We then evaluate the channel estimation procedure based on CRSs and we show the channel estimation error curves as a function of the received SNR for different channel models and Doppler spreads that have been obtained with our link level simulator. The model is validated by comparing the BLER curves obtained with the model with the curves obtained when using real channel estimation. Finally we show the impact of channel estimation errors on the LTE DL BLER performance.

4.1 Introduction

Channel estimation is a key aspect for the performance of the physical layer in all MIMO-OFDM systems, like LTE and LTE-Advanced. Its goal is to obtain an accurate estimate of the current channel matrix suitable for the MIMO processing at the receiver side. Since the channel is time variant and frequency selective a different channel matrix must be estimated for every subcarrier and symbol interval. To support channel estimation the transmitter includes pilot symbols that are densely scattered, in time and frequency domain, among the data symbols. In LTE the pilot symbols are called *Reference Signal*s (RSs) and transmissions from the different MIMO antennas are orthogonal, which allows performing separate channel estimation for each element of the channel matrix. Channel estimation usually involves a *Least Squares* (LS) estimation followed by averaging and interpolation in time/frequency. These procedures, combined with impairments like noise and fast channel variations due to Doppler spread, lead to channel estimation errors which have an important impact on the performance of MIMO-OFDM systems. Those errors must be taken into account in the link level simulator for a realistic performance assessment.

Since implementing a detailed channel estimation algorithm may lead to long simulation time, in particular for wideband MIMO transmission modes where many channels have to be estimated and for procedures like Wiener filtering which require matrix multiplications, in this chapter it is proposed to simulate channel estimation errors by a Gaussian additive noise error model, which is called *Channel Estimation Error Model* (CEEM), with a variance that reflects the accuracy obtained in the channel estimation. The noise variance of the model is calibrated as a function of the received SNR for different channel models and Doppler spreads. Finally, the model is validated by comparing the BLER curves obtained with the model with the curves obtained when using real channel estimation.

4.2 E-UTRA Reference Signals

LTE and LTE-Advanced systems make use of pilot signals, known as RSs, for DL and UL channel estimation and channel state information feedback. Focusing on the RS evolution according to 3GPP standardization in [3], while the UL RSs basically follows the same design in both LTE (Release 8/9) and LTE-Advanced specifications (Release 10 and beyond), the DL RSs have evolved, mainly by separating the demodulation RSs and the channel state information RSs. The evolution of RSs from LTE to LTE-Advanced is analysed in [76] where their underlying design principles are examined. Tables 4.1 and 4.2 show the applicable reference signals in each 3GPP Release.

The Release 8 LTE defines three types of downlink RSs: CRSs, associated with non-*MBMS over Single Frequency Networks* (MBSFN) transmission; MBSFN RSs, associated with MBSFN transmission; and UE-specific RSs. Then Release 9 LTE adds another type a DL RSs: *Positioning reference signal*s (PRSs). The evolution to Release 10 LTE-Advanced adds a fifth type: CSI-RSs; and the last Release of LTE-Advanced, Release 11, splits UE-specific RSs in two types, UE-specific RSs, associated with PDSCH, and *Demodulation reference signal* (DM-RS) associated with *Enhanced Physical Downlink Control Channel* (EPDCCH), both referred as DM-RS.

In Release 8/9, DL channel estimation is mainly based on CRS which are used for coherent data demodulation and feedback calculation. Although CRS are also taken into account for backward compatibility with transmission modes that use them, in LTE-Advanced Release 10/11 new DL RSs are defined: DM-RS for demodulation and CSI-RS for CSI measurement and CSI feedback.

Table 4.1: DL Reference Signals in the 3GPP standards.

DL RS	Rel. 8	Rel. 9	Rel. 10	Rel. 11
CRS	✓	✓	✓	✓
MBSFN RS	✓	✓	✓	✓
UE-specific RS (DM-RS)	✓	✓	✓	
PRS		✓	✓	✓
CSI-RS			✓	✓
UE-specific RS (DM-RS)				
associated with PDSCH				✓
Demodulation RSs (DM-RS)				
associated with EPDCCH				✓

Regarding UL RSs, both LTE and LTE-Advanced support two types: Demodulation RS and Sounding RS. While Demodulation RS are associated with transmission of PUSCH or PUCCH and are used for channel estimation to allow coherent data demodulation, Sounding RS are not associated with transmission of PUSCH or PUCCH and are used by the eNodeB to estimate the UL channel quality of the UE for enabling UL frequency-selective scheduling and link adaptation. The difference between UL RS in Release 8/9 and Release 10/11 is the extension of Demodulation RS and Sounding RS to enable UL SU-MIMO in order to take into account multi-layer transmission.

Table 4.2: UL Reference Signals in the 3GPP standards.

UL RS	Rel. 8	Rel. 9	Rel. 10	Rel. 11
Demodulation RS	✓	✓	✓	✓
Sounding RS	✓	✓	✓	✓

4.3 Mapping of DL Reference Signals

Figure 4.1 shows the mapping of the CRS on the DL frequency-time grid for 1 RB and 1 TTI assuming normal CP, [3]. CRSs are transmitted in all DL subframes and all the RBs on *Antenna Port* (AP) 0,1,2 and 3. In Figure 4.1 CRSs are marked in different colours for each antenna and for 1, 2 and 4 antennas at the transmitter side.

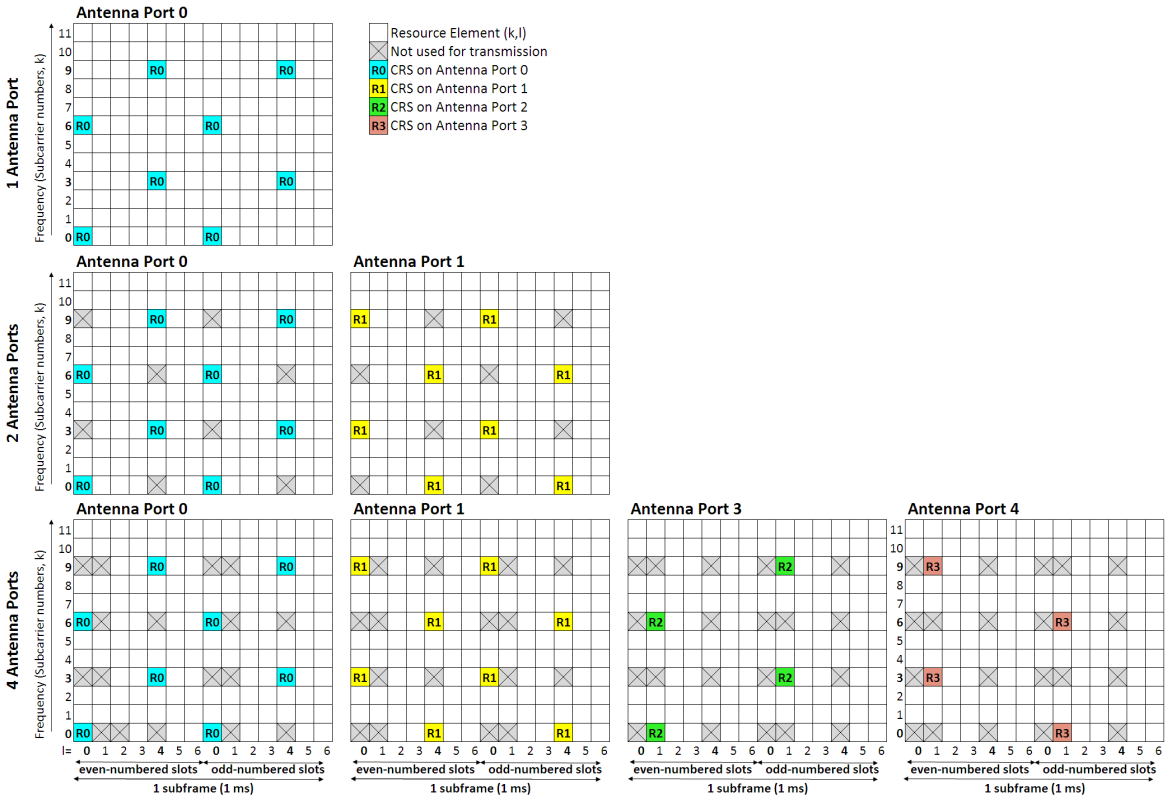

Figure 4.1: CRS mapping on the DL frequency-time grid in a subframe (normal CP) for 1, 2 and 4 antenna ports (where Antenna Port in this figure stands for AP)

The CRS, which are common for all the cell users, are always QPSK modulated according to the expression:

$$r_{l,n} = \frac{1}{\sqrt{2}}\left[1 - 2 \cdot c(2m)\right] + j\frac{1}{\sqrt{2}}\left[1 - 2 \cdot c(2m+1)\right] \tag{4.1}$$

where m is the RS index, l is the symbol number within the slot and n is the slot number within the frame. The sequence $c(i)$ is a Gold sequence of length 31 that carries also the LTE cell

identity. Notice that having one RS every 0.5 ms allows for a Nyquist channel sampling rate even for the Doppler present on high speed train propagation conditions. Also the RS separation of 3 subcarriers guarantees that, for the maximum delay spread of 5 s (the LTE cyclic prefix duration), the frequency selective fading for consecutive RS shows a 50% decorrelation. In principle, the power allocated to each pilot symbol is equal to the mean power of the transmitted data symbol constellation, although it can be boosted up to a maximum of 6 dB above the data symbol power. When MIMO transmission modes are applied, each transmitting antenna sends an independent pilot while all others are silent (see Figure 4.1), thus avoiding interference among pilots form different antennas.

In LTE the bandwidth is dynamically allocated to users in blocks of RBs. Depending on the allocated bandwidth, the LTE terminal has to track the channel variations on a possibly large frequency-time grid area. Since the time and frequency selectivity of the channel are closely related to the propagation environment and vehicle speed, the channel estimation methodology must adapt to the conditions prevailing at every moment.

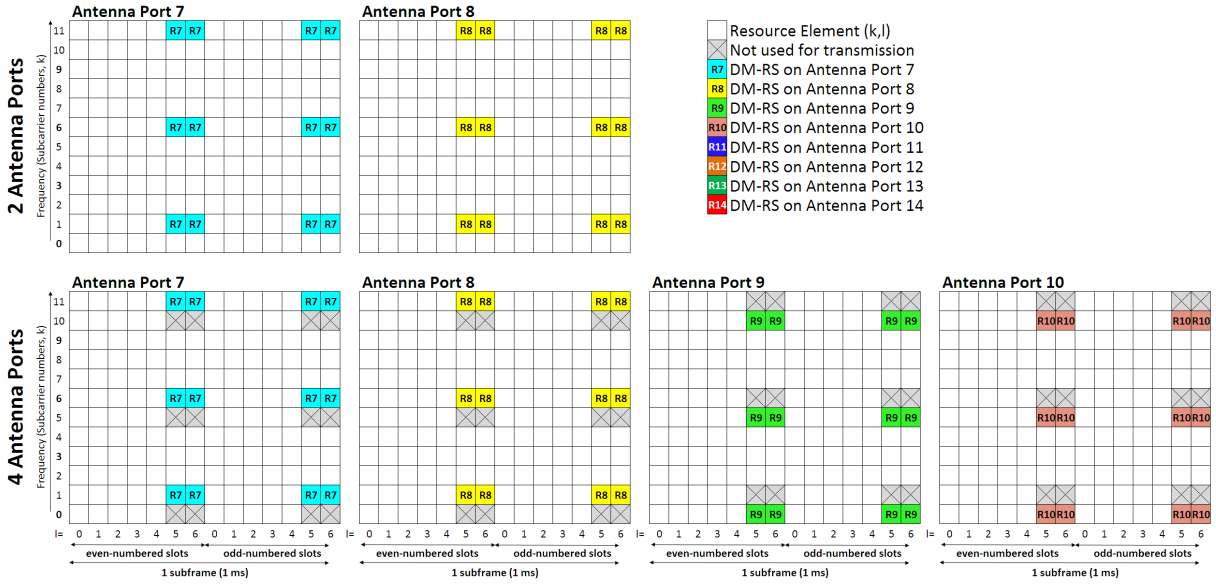

Figure 4.2: DM-RS mapping on the DL frequency-time grid in a subframe (normal CP) for 2 and 4 antenna transmission

UE employs CRSs to estimate the LTE DL channel, i.e., from the eNodeB to its location. Only one CRS is transmitted for each AP and they are introduced after precoding due to the CSI feedback calculation. UE will estimate how the radio channel alters the received signal via CRS and this estimation is used for CSI feedback calculation and, together with the knowledge of the codebook index of the employed precoding matrix, coherent data demodulation. Therefore, UEs must receive precoding information from eNodeB and, in order to maintain a reasonable overhead, non-codebook based precoding is not allowed in LTE . This restriction makes the codebook based precoding be the limiting factor in the system performance of MU-MIMO transmission as it is reported in [77] and [78].

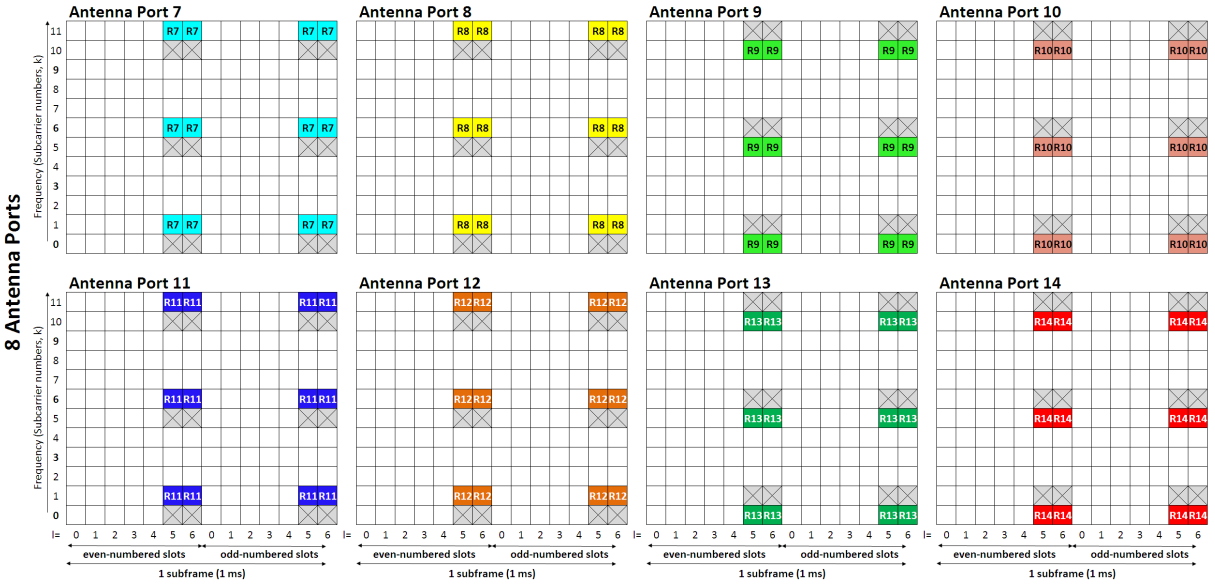

Figure 4.3: DM-RS mapping on the DL frequency-time grid in a subframe (normal CP) for 8 antenna transmission

In order to overcome the drawbacks of CRS, LTE-Advanced proposes an enhanced RS design that distinguishes two type of RSs according to their purpose, DM-RS for coherent data demodulation and CSI-RS for CSI feedback. An overall description of the new RS features in LTE-Advanced and a general comparison between DM-RS and CSI-RS is given in [79] and [80]. While DM-RS are added before precoding and are user specific, CSI-RS are added after precoding and are shared by all users. Thus, the knowledge of the received DM-RS will provide information about the combined influence of radio channel and precoding, enabling coherent data demodulation and also CSI feedback to support dynamic rank adaptation when resources are allocated to UE. Then the knowledge of the received CSI-RS will provide channel state information enabling CSI estimation for multiple cells, which is is useful for multicell cooperative transmission schemes.

The LTE-Advanced RS design enhances the MIMO transmission schemes to meet the IMT-Advanced requirements [7] by allowing non-codebook based precoding useful for SU-MIMO and MU-MIMO and for supporting up to eight antenna single user transmissions with a reasonable RS overhead. Moreover, both DM-RS and CSI-RS transmissions from the different MIMO antennas are also orthogonal like CRS.

The LTE-Advanced mapping of UE-specific (DM-RS) and normal CP for 2 and 4 antenna transmission is shown in Figure 4.2 and in Figure 4.3 for 8 antenna transmission. In contrast, the density of CSI-RS is significantly lower than DM-RS as observed in Figures 4.4 and 4.5 where the mapping of CSI-RS and normal CP is shown, for 2 and 4 antenna transmission and for 8 antenna transmission, respectively.

Table 4.3 shows the overhead due to CRS, DM-RS and CSI-RS (in percentage) in one subframe and for a given number of APs. The overhead is the number of reserved REs for RSs versus the total number of REs. It can be observed that CRS density compared to DM-RS density is

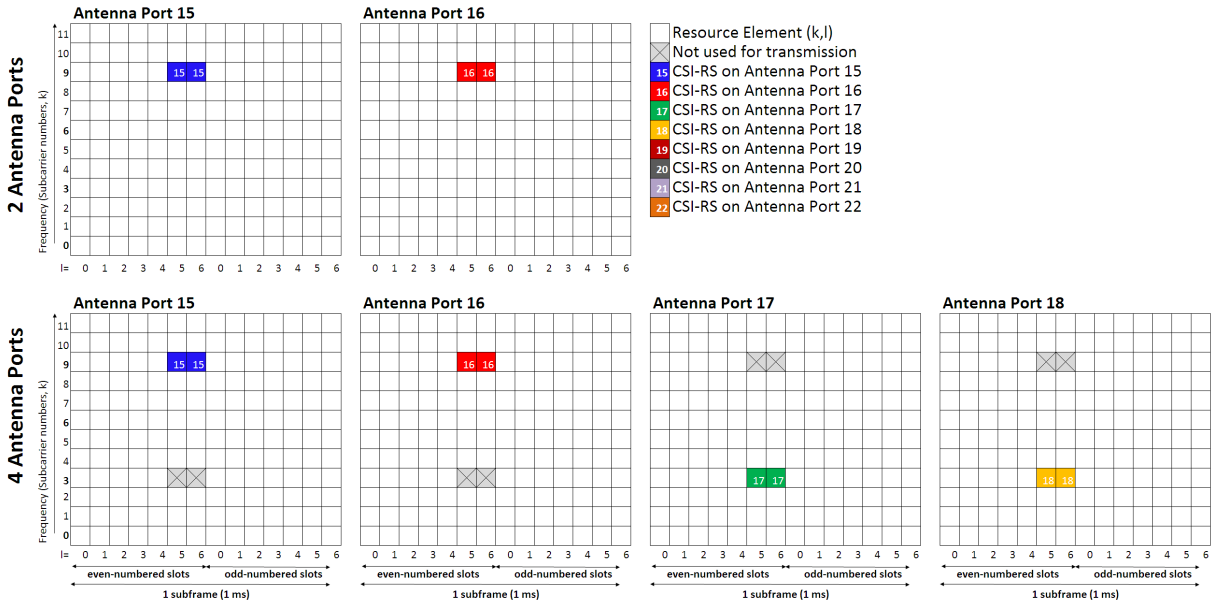

Figure 4.4: CSI mapping on the DL frequency-time grid in a subframe (normal CP) for 2 and 4 antenna transmission

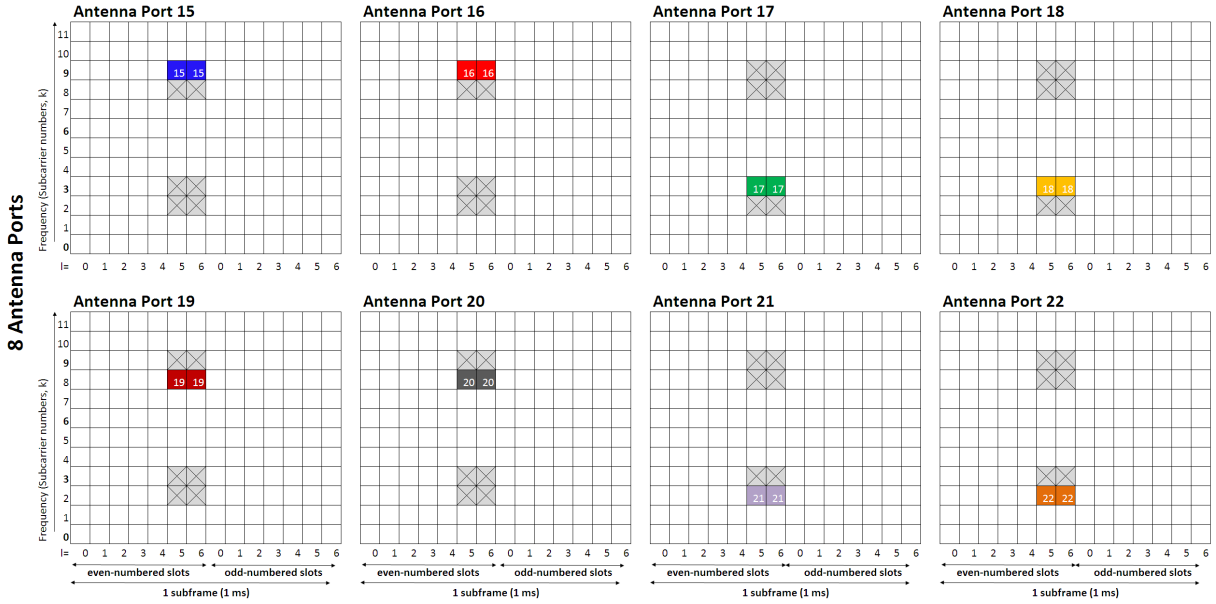

Figure 4.5: CSI mapping on the DL frequency-time grid in a subframe (normal CP) for 8 antenna transmission

the same for 4 antenna transmission, higher for 2 antenna transmission and lower for 1 antenna transmission; but CRS is not possible for 8 antenna transmission.

Table 4.3: Overhead due to RSs in percentage (%).

Reference	Number of *Antenna Ports* (APs)			
Signal	1	2	4	8
CRS	4.76	9.52	14.29	-
DM-RS	7.14	7.14	14.29	14.29
CSI-RS	1.19	1.19	2.38	4.76

4.4 System Model

In LTE each AP has a unique set of locations within a subframe to map pilot signals and no other antenna transmits data nor pilots at these locations in time and frequency domain. This feature makes pilot transmission from different antennas to be orthogonal and allows MIMO channel estimation. Moreover, this orthogonality between pilots in multi-antenna configurations inherently means that each pilot channel can be treated as a SISO channel. Therefore, for the purpose of channel estimation, and since pilot transmissions from different antennas are orthogonal, a SISO-OFDM system model is considered. The received OFDM pilot vector, at one of the receiver antennas, can be written as:

$$\mathbf{Y} = \begin{pmatrix} C_1 & 0 & \dots & 0 \\ 0 & C_2 & \dots & 0 \\ \vdots & \vdots & \dots & 0 \\ 0 & 0 & \dots & C_{N_p} \end{pmatrix} \cdot \mathbf{H} + \mathbf{n} = \mathbf{C} \cdot \mathbf{H} + \mathbf{n} \tag{4.2}$$

where N_p is the number of pilots that fit in the allocated bandwidth, that is $N_p = 2N_{RB}$ for CRSs, where N_{RB} is the number of allocated RBs. $\mathbf{C}$ is a $(N_p \times N_p)$ diagonal matrix that contains the complex pilot symbols, $\mathbf{H}$ is a $(N_p \times 1)$ complex vector that contains the channel frequency response at the pilot subcarriers and $\mathbf{n}$ is a $(N_p \times 1)$ complex Gaussian noise vector with covariance matrix $\sigma^2 \mathbf{I}_{N_p}$.

For the channel estimation error evaluation, it is considered the procedure proposed in section *Post FFT equalisation* of annex F of [81] and it is also tested an enhancement which uses Wiener filtering in the frequency domain. The proposed baseline channel estimation procedure is to obtain a LS estimate of the channel by dividing $\mathbf{Y}$ by the known pilots:

$$\hat{\mathbf{H}}_{LS} = \mathbf{C}^{-1}\mathbf{Y} = \mathbf{H} + \mathbf{C}^{-1}\mathbf{n} \tag{4.3}$$

If the $(N_p \times N_p)$ covariance matrix of the channel is denoted as $\mathbf{R}_{\mathrm{H}} = \overline{\mathbf{H}\mathbf{H}^{\mathrm{H}}}$, then all the diagonal elements of $\mathbf{R}_{\mathrm{H}}$ are equal to the average channel gain, denoted as G. From expression (4.3) it is clear that the LS method overestimates the average channel power gain by a factor:

$$\Delta G = \frac{G + \frac{\sigma^2}{B}}{G} = 1 + \frac{1}{\gamma} \tag{4.4}$$

where $B = |C_1|^2 = \cdots = \left|C_{N_p}\right|^2$ and $\gamma = G \cdot B/\sigma^2$ is the SNR of the received pilots. The factor G can be important at very low SNR. Assuming that γ is known, to compensate for this a modified estimator is used defined as, [82]:

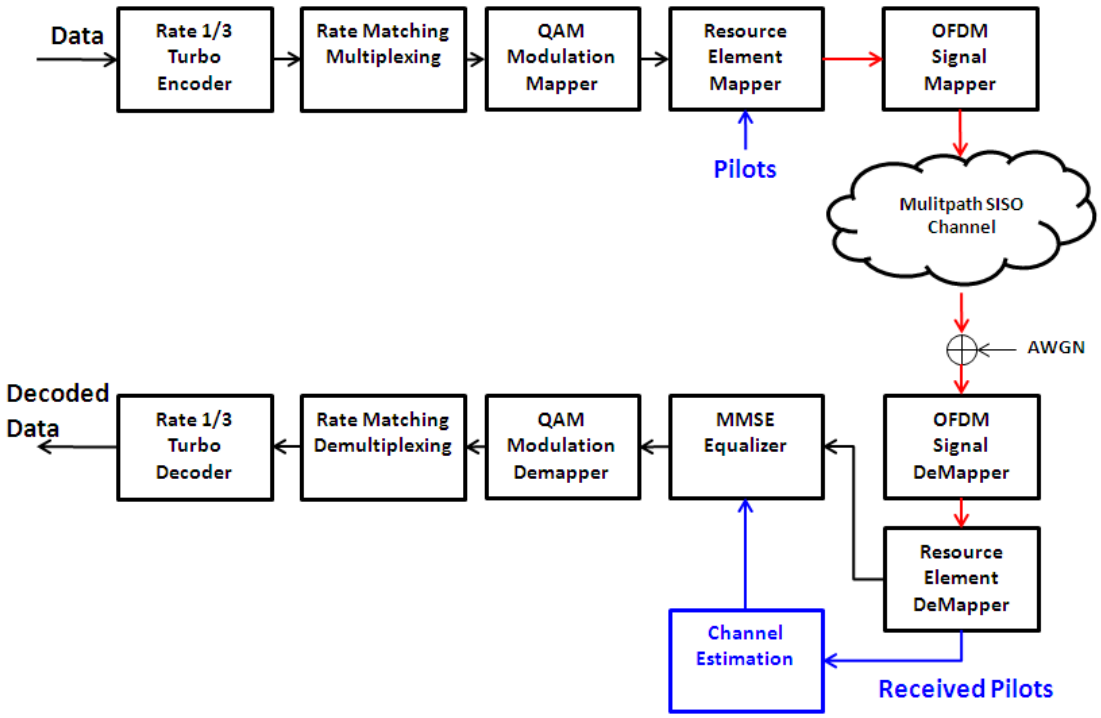

Figure 4.6: Block Diagram of the considered SISO-OFDM system model for channel estimation evaluation based on pilot transmissions

$$\hat{\mathbf{H}} = \frac{1}{\sqrt{\Delta G}} \cdot \hat{\mathbf{H}}_{LS} = \frac{1}{\sqrt{\Delta G}} \cdot \mathbf{H} + \frac{1}{\sqrt{\Delta G}} \cdot \mathbf{C}^{-1}\mathbf{n} \tag{4.5}$$

According to (4.5) the average power gain of $\hat{H}$ is equal to G for all γ. If $\varepsilon = (1+\gamma)^{-1/2}$ is defined, then $\Delta G = \left(1-\varepsilon^2\right)^{-1}$ and expression (4.5) can be rewritten as:

$$\hat{\mathbf{H}} = \sqrt{1-\varepsilon^2} \cdot \mathbf{H} + \varepsilon \cdot \mathbf{N} \tag{4.6}$$

where $\mathbf{N}$ is a normalized noise vector with covariance matrix:

$$\mathbf{R}_{\mathrm{N}} = \overline{\mathbf{N}\mathbf{N}^{\mathrm{H}}} = \frac{1-\varepsilon^2}{\varepsilon}\mathbf{C}^{-1}\overline{\mathbf{n}\mathbf{n}^{\mathrm{H}}}(\mathbf{C}^{\mathrm{H}})^{-1} = \frac{\gamma\sigma^2}{B}\mathbf{I}_{N_p} = G \cdot \mathbf{I}_{N_p} \tag{4.7}$$

Therefore, the estimated channel gain can be split into a useful contribution with variance $(1-\varepsilon^2)G$ and a noise contribution with variance $\varepsilon^2 G$. The parameter ε, which depends on the SNR of the received pilots, is always within the range $[0,1]$ and is a measure of how accurate the channel estimation is.

Although the previous expressions have been derived considering noise as the only source of degradation, provided that G is known, expression (4.6) can be used to assess the performance of different channel estimation methods by obtaining an estimate of ε from many realisations of $\mathbf{H}$ and $\hat{\mathbf{H}}$:

$$\hat{\varepsilon} = \sqrt{1 - \left(1 - \frac{\overline{\left|\hat{\mathbf{H}} - \mathbf{H}\right|^2}}{2N_p \cdot G}\right)^2} \tag{4.8}$$

where $|\mathbf{H}|$ means vector norm. The purpose of expression (4.8) is to assess the channel estimation accuracy when there are additional sources of error, like channel averaging and interpolation, and/or there are sources of improvement, like Wiener filtering for example. By creating look-up tables of $\hat{\varepsilon}$ for different combinations of SNR, channel estimation methodology and propagation conditions, expression (4.6) suggests that channel estimation errors can be simulated, in the LTE link level simulator, by weighting $\mathbf{H}$ with $\sqrt{1-\varepsilon^2}$ and adding a random complex Gaussian noise with a variance $\varepsilon^2 G$.

In an OFDM system, a channel estimation procedure based on a two-dimensional *Linear Minimum Mean-Square Error* (LMMSE) computation would give best results [83]. Usually two-dimensional LMMSE is too complex and practical implementations must use simplified algorithms, as recommended in [79] in order to make channel estimators implementable. A possible simplification is to perform LS estimation on the REs containing pilots, as explained before, and then interpolate separately in time and frequency domains. If the SNR and the frequency domain channel correlations can be estimated, then Wiener filtering in the frequency domain only (one-dimensional LMMSE) is an efficient solution to reduce the channel estimation error of LS estimator, [84]. The LMMSE estimator in the frequency domain is, [85, 86, 87]:

$$\hat{\mathbf{H}}_{\mathrm{w}} = \mathbf{R}_{\mathrm{h}} \left[\mathbf{R}_{\mathrm{H}} + \frac{\sigma^2}{B}\mathbf{I}_{N_p}\right]^{-1} \cdot \hat{\mathbf{H}}_{LS} \tag{4.9}$$

where $\mathbf{R}_{\mathrm{h}} = \overline{\mathbf{h}\mathbf{H}^{\mathrm{H}}}$ is the $(12N_{RB} \times N_p)$ correlation matrix of the $(12N_{RB} \times 1)$ full channel response vector $\mathbf{h}$ with $\mathbf{H}$ (The detailed formulation of the LMMSE estimator in the frequency domain is given in Appendix A.2).

4.5 Computation of the CEEM post-processing noise

4.5.1 Narrowband CEEM system model

The computation of the post-processing noise considering the proposed CEEM is described herein. The channel estimation error is denoted as $\mathbf{N}$ which it is a normalized noise matrix to have the same covariance matrix as the true channel matrix $\mathbf{H}_k$, i.e., $\mathbf{R}_N = \overline{\mathbf{N}\mathbf{N}^{\mathrm{H}}} = G\mathbf{I}_{N_{RX}} = \sigma^2_{PDP}\mathbf{I}_{N_{RX}}$. From Equation 4.6, the estimated MIMO channel matrix in the frequency domain at subcarrier k is given by:

$$\hat{\mathbf{H}}_k = \sqrt{1-\varepsilon^2}\mathbf{H}_k + \varepsilon\mathbf{N} \tag{4.10}$$

which can be also written as:

$$\hat{\mathbf{H}}_k = \begin{bmatrix} \hat{\mathrm{H}}^k_{1,1} & \cdots & \hat{\mathrm{H}}^k_{1,M_{TX}} \\ \vdots & \hat{\mathrm{H}}^k_{n,m} & \vdots \\ \hat{\mathrm{H}}^k_{N_{RX},1} & \cdots & \hat{\mathrm{H}}^k_{N_{RX},M_{TX}} \end{bmatrix} = \\ = \sqrt{1-\varepsilon^2} \begin{bmatrix} \mathrm{H}^k_{1,1} & \cdots & \mathrm{H}^k_{1,M_{TX}} \\ \vdots & \mathrm{H}^k_{n,m} & \vdots \\ \mathrm{H}^k_{N_{RX},1} & \cdots & \mathrm{H}^k_{N_{RX},M_{TX}} \end{bmatrix} + \varepsilon \begin{bmatrix} \mathrm{N}^k_{1,1} & \cdots & \mathrm{N}^k_{1,M_{TX}} \\ \vdots & \mathrm{N}^k_{n,m} & \vdots \\ \mathrm{N}^k_{N_{RX},1} & \cdots & \mathrm{N}^k_{N_{RX},M_{TX}} \end{bmatrix} \tag{4.11}$$

where the portion of the correct channel matrix $\mathbf{H}_k$ is scaled to keep the covariance of the estimated channel and the covariance of the true channel matrix to be identical and where the scalar $\varepsilon \in [0,1]$ configures how accurate the channel estimation is. If $\varepsilon = 0$, then it indicates perfect channel estimation; otherwise, if $\varepsilon > 0$, then the estimation error increases with ε.

4.5.2 SISO CEEM post-processing noise

The complex baseband equivalent model of the received signal at the subcarrier k, given in Equation 3.42, is particularized for SISO-OFDM case as follows:

$$r_k = H^k_{1,1} s_k + n_k = H_k s_k + n_k \tag{4.12}$$

where s_k is the transmitted symbol, r_k is the received signal, H_k is the complex channel gain and n_k is the AWGN noise complex value. Thus, from Equation 4.11, the estimated channel and the true channel are related as follows:

$$\hat{H}_k = \sqrt{1-\varepsilon^2} H_k + \varepsilon N \tag{4.13}$$

so the true channel can be written as:

$$H_k = \frac{\hat{H}_k - \varepsilon N}{\sqrt{1-\varepsilon^2}} \tag{4.14}$$

The SISO receiver performs the frequency equalization at each subcarrier, to detect the transmitted signal, by taking into account the estimated channel as follows:

$$\hat{s}_k = \sqrt{1-\varepsilon^2} \frac{\hat{H}^*_k}{|\hat{H}_k|^2} r_k = \sqrt{1-\varepsilon^2} \frac{\hat{H}^*_k}{|\hat{H}_k|^2} \left(\frac{\hat{H}_k - \varepsilon N}{\sqrt{1-\varepsilon^2}} s_k + n_k \right) = \\ = s_k - \frac{\hat{H}^*_k}{|\hat{H}_k|^2} \varepsilon N s_k + \sqrt{1-\varepsilon^2} \frac{\hat{H}^*_k}{|\hat{H}_k|^2} n_k \tag{4.15}$$

the estimation error is given by

$$e = \hat{s}_k - s_k = \sqrt{1-\varepsilon^2} \frac{\hat{H}^*_k}{|\hat{H}_k|^2} n_k - \frac{\hat{H}^*_k}{|\hat{H}_k|^2} \varepsilon N s_k \tag{4.16}$$

the complex baseband post-processing noise power is

$$E[|\varepsilon|^2] = \left(1-\varepsilon^2\right) \frac{\sigma^2}{|\hat{H}_k|^2} + \frac{\varepsilon^2 G \overline{|C^k|^2}}{|\hat{H}_k|^2} \tag{4.17}$$

and, consequently, the CEEM bandpass post-processing noise variance is given by

$$\sigma^2_{\text{CEEM}} = \frac{E[|\varepsilon|^2]}{2} = \frac{1}{|\hat{H}_k|^2}\left(\left(1-\varepsilon^2\right)\sigma^2_{nb} + \varepsilon^2\frac{\overline{|C^k|^2}}{2}\sigma^2_{PDP}\right) \tag{4.18}$$

where is divided in two contributions, the AWGN receiver noise: $(1-\varepsilon^2)\sigma^2_{nb}$, and the contribution due to the channel estimation error: $\varepsilon^2\frac{\overline{|C^k|^2}}{2}\sigma^2_{PDP}$. So σ^2_{CEEM} can be rewritten as

$$\sigma^2_{\text{CEEM}} = \kappa\left(\left(1-\varepsilon^2\right)\sigma^2_{nb} + \varepsilon^2\frac{\overline{|C^k|^2}}{2}\sigma^2_{PDP}\right) \tag{4.19}$$

where $\kappa = \frac{1}{|\hat{H}_k|^2}$ is the noise gain factor, the average channel gain is $G = \sigma^2_{PDP}$ and the average transmitted symbol power is $\overline{|s_k|^2} = \overline{|C^k|^2}$. As a result, the CEEM post-processing SNR for the SISO case is given by:

$$\text{SNR} = \frac{\overline{|C^k|^2}}{2\sigma^2_{\text{CEEM}}} \tag{4.20}$$

Finally, at the receiver, the LLR at bit level is computed based on Equation 3.62 as follows:

$$\Lambda^k_b \cong \frac{1}{2\sigma^2_{\text{CEEM}}}\left(\left|\hat{C}^k - C_1\right|^2 - \left|\hat{C}^k - C_0\right|^2\right) \tag{4.21}$$

where Λ^k_b is the LLR of the b^{th} bit of the detected symbol $\hat{s}^k$, $b = 1, \cdots, \log_2(M)$ and C_0 (respectively C_1) is the modulation complex symbol of the set of MQAM complex symbols for which the transmitted bit is at logical zero (respectively logical one) that falls nearest to $\hat{s}_k = \hat{C}^k$.

4.5.3 MIMO CEEM post-processing noise

For the MIMO-OFDM case it can be shown that the computation of the post-processing SNR and the LLR at bit level can follow the same expressions as for SISO case taking into account the noise enhancement factor due to the MIMO processing at the receiver. Equation 4.10 can be rewritten as:

$$\mathbf{H}_k = \frac{\hat{\mathbf{H}}_k - \varepsilon\mathbf{N}}{\sqrt{1-\varepsilon^2}} \tag{4.22}$$

the MIMO-SM processing performed by the receiver is reformulated based on Equation 3.55 and taking into account the CEEM as:

$$\hat{\mathbf{s}}_k = \sqrt{1-\varepsilon^2}\hat{\mathbf{W}}_k\mathbf{r}_k \tag{4.23}$$

where $\hat{\mathbf{W}}_k$ is the linear receiver matrix based on the MIMO channel estimation: for ZF it is $\hat{\mathbf{W}}^{\text{ZF}}_k = \left(\hat{\mathbf{H}}^{\text{H}}_k\hat{\mathbf{H}}_k\right)^{-1}\hat{\mathbf{H}}^{\text{H}}_k$ and for MMSE it is $\hat{\mathbf{W}}^{\text{MMSE}}_k = \left(\hat{\mathbf{H}}^{\text{H}}_k\hat{\mathbf{H}}_k + \gamma\mathbf{I}_{M_{TX}}\right)^{-1}\hat{\mathbf{H}}^{\text{H}}_k$. Since $\mathbf{r}_k = \mathbf{H}_k\mathbf{s}_k + \mathbf{n}_k$, Equation 4.23 is rewritten as:

$$\hat{\mathbf{s}}_k = \hat{\mathbf{W}}_k\hat{\mathbf{H}}_k\mathbf{s}_k \underbrace{-\varepsilon\hat{\mathbf{W}}_k\mathbf{N}_k\mathbf{s}_k + \sqrt{1-\varepsilon^2}\hat{\mathbf{W}}_k\mathbf{n}_k}_{\text{post-processing noise}} \tag{4.24}$$

As it is assumed uncorrelated noise in each MIMO receiver branch as well as uncorrelated CEEM noise in each MIMO subchannel; the MIMO-SM post-processing noise power of the i^{th} spatial component at subcarrier k for ZF receiver is as follows:

$$\left(\sigma^2_{\text{CEEM}}\right)_i = \left(\hat{\mathbf{H}}_k^{\text{H}}\hat{\mathbf{H}}_k\right)^{-1}_{i,i}\left(\left(1-\varepsilon^2\right)\sigma^2_{nb} + \varepsilon^2\frac{\overline{|C^k|^2}}{2}\sigma^2_{PDP}\right) \tag{4.25}$$

and for MMSE receiver

$$\left(\sigma^2_{\text{CEEM}}\right)_i = \left(\hat{\mathbf{H}}_k^{\text{H}}\hat{\mathbf{H}}_k + \gamma\mathbf{I}_{M_{TX}}\right)^{-1}_{i,i}\left(\left(1-\varepsilon^2\right)\sigma^2_{nb} + \varepsilon^2\frac{\overline{|C^k|^2}}{2}\sigma^2_{PDP}\right) \tag{4.26}$$

where $(\mathbf{A})^{-1}_{i,i}$ is the element (i,i) of the diagonal of the matrix $(\mathbf{A})^{-1}$.

The CEEM post-processing SNR for MIMO-SM is given by:

$$\text{SNR}_i^{\text{CEEM}} = \frac{\overline{|C_i^k|^2}}{2\left(\sigma^2_{\text{CEEM}}\right)_i} \tag{4.27}$$

and, for MIMO-SM and taking Equations 3.62 and 3.66 as reference, the LLR at bit level considering the effect of the CEEM is rewritten as:

$$\Lambda_{b,i}^{k,CEEM} \cong \frac{1}{2\left(\sigma^2_{\text{CEEM}}\right)_i}\left(\left|\hat{C}_i^k - C_1\right|^2 - \left|\hat{C}_i^k - C_0\right|^2\right) \tag{4.28}$$

In the same way, for MIMO-TD plus MRC, the computation of the CEEM post-processing SNR and LLR at bit level follows the same expressions as in the case of MIMO-SM but with a different value of $\left(\sigma^2_{\text{CEEM}}\right)_i$ which is, according to Equation 3.82:

$$\left(\sigma^2_{\text{CEEM}}\right)_i^{\text{TD+MRC}} = \frac{2}{\left(|H_{1,1}|^2 + |H_{1,2}|^2 + |H_{2,1}|^2 + |H_{2,2}|^2\right)}\left(\left(1-\varepsilon^2\right)\sigma^2_{nb} + \varepsilon^2\frac{\overline{|C^k|^2}}{2}\sigma^2_{PDP}\right) \tag{4.29}$$

4.6 Practical Channel Estimation Procedures

In this section, the practical channel estimation procedures are explained based on the two considered types of channel estimators, LS and one-dimensional LMMSE (Wiener filtering). In order to gain an initial insight on the channel estimation performance of LS and Wiener filtering estimators, a short GNU Octave script has been written to test frequency-domain only channel estimation. It is assumed a simple two-ray channel response of the form: $H(f) = 1 + b \cdot e^{-j2\pi f\tau}$, where τ is a constant and b is a complex Gaussian random variable with unity variance. The average channel gain for this case is equal to 2, so $G = 2$. Many independent channel realisations are generated to compute $\hat{\varepsilon}$, using (4.8), for different combinations of SNR, channel estimation methodology and τ. The simulated bandwidth is 1 RB (180 kHz), so 4 subcarriers contain pilots within 1 slot, although a maximum of 2 pilots is allowed within a single OFDM symbol interval.

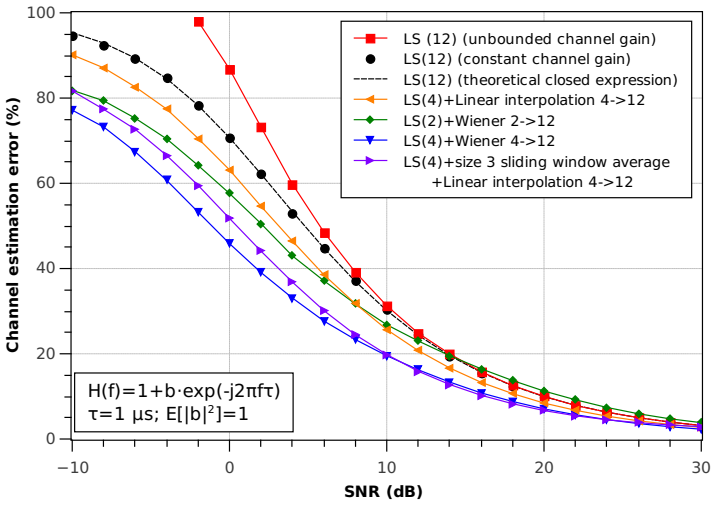

Figure 4.7: Channel estimation error for a two-ray model and $\tau = 1\,\mu s$

Figure 4.7 shows the channel estimation error in percentage for $\tau = 1\,\mu s$. In Figure 4.7 the notation LS(N_p) means that, among the 12 simulated subcarriers, N_p pilot symbols have been considered. Taking as a reference the LS(12) estimator with constant channel gain (black dots), it is seen that the LS(12) estimator with unbounded channel gain has bad performance at very low SNR. Since the coherence bandwidth of this channel is wider than the pilot subcarrier separation, the frequency response becomes oversampled by the pilots and then linear interpolation in frequency domain acts as a low pass filtering processing that reduces noise variance. For that reason the LS(4) estimator followed by linear interpolation slightly outperforms LS(12) estimator in this case. It can be seen that the Wiener filter, when fed with the right channel correlation matrices and SNR, is able to outperform LS(12) even if only 2 pilots per RB are available. Finally, LS(4) followed by a size 3 sliding window averaging plus linear interpolation in frequency domain outperforms LS(4) plus linear interpolation. This is due to the noise reduction effect of the averaging in conjunction with the high coherence bandwidth of this channel. Figure 4.8 shows the same results for $\tau = 5\,\mu s$. In this case the coherence bandwidth is 5 times narrower and so linear interpolation and averaging lead to irreducible floors in the estimation error. In these results it has not been considered any time averaging stage, and so the channel estimation error is high for all the studied procedures, which suggests that sliding window time domain averaging should be applied to reduce noise when possible.

To include the time domain, the channel estimation procedure of annex F of [81] with some enhancements is used. The step by step proposed algorithm is:

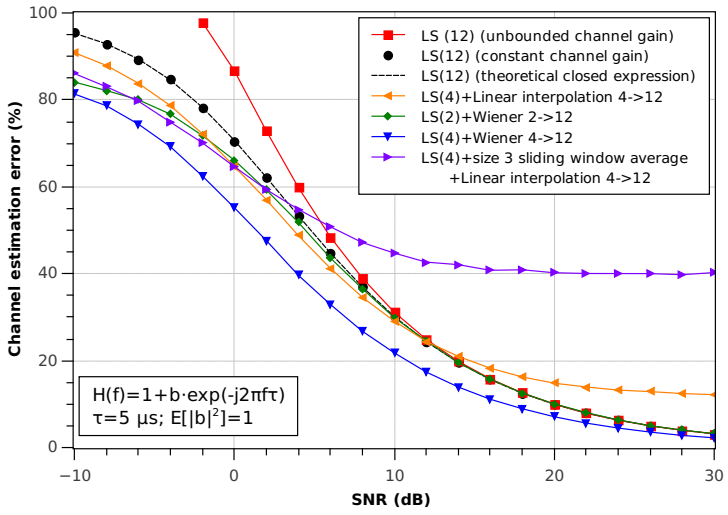

Figure 4.8: Channel estimation error for a two-ray model and $\tau = 5\,\mu s$

Algorithm 4.1 Proposed Channel Estimation Procedure

1. Compute the LS channel estimates at the pilot REs on the DL frequency-time grid shown in Figure 4.1 according to equation 4.3. This creates a set of LS estimates of the channel sampled at the pilot REs.

2. Optionally, perform a sliding window time averaging of the LS estimates at each RS subcarrier to reduce unwanted noise. The window size spans an odd number of pilot REs, so that the resulting average is assigned to the RE at the centre of the window. A maximum window size of 9 TTIs (17 pilots) is considered. A window size of 1 TTI means no time averaging at all.

3. Perform linear interpolation in time domain at each RS subcarrier of the time-averaged LS estimates to estimate the channel for all REs of the RS subcarriers.

4. Optionally, perform averaging in frequency domain of the time-averaged RS subcarriers with a sliding window. The size of the window is an odd number of RS subcarriers in order to ensure that there is a RS at the centre of the window. For RS subcarriers at or near the edge of the allocated RBs the window size is reduced accordingly to annex F of [81]. A window size of 1 RS subcarrier means no frequency averaging at all.

5. (a) Perform linear interpolation in the frequency domain to estimate the channel at each RE from the averaged LS estimates at RS subcarriers.

   (b) Alternatively, instead of linear interpolation, apply Wiener filtering in the frequency domain.

The Wiener filter is applied according to expression (4.9) and with some simplifying assumptions:

- Perfect synchronization.
- Perfect estimation of SNR.
- Perfect estimation of the covariance matrices of the channel, i.e., perfect estimation of the power delay profile of the channel.
- In order to reduce the computation complexity, Wiener filtering is applied on a RB basis, i.e., the correlation matrix of the channel $\mathbf{R}_{\mathrm{h}}$ has dimensions (12×4), as proposed in [88] and [89],

Figure 4.9 shows graphically the REs involved in each step of the proposed channel estimation algorithm for a 1 RB allocation in frequency domain and a 3 TTI sliding window.

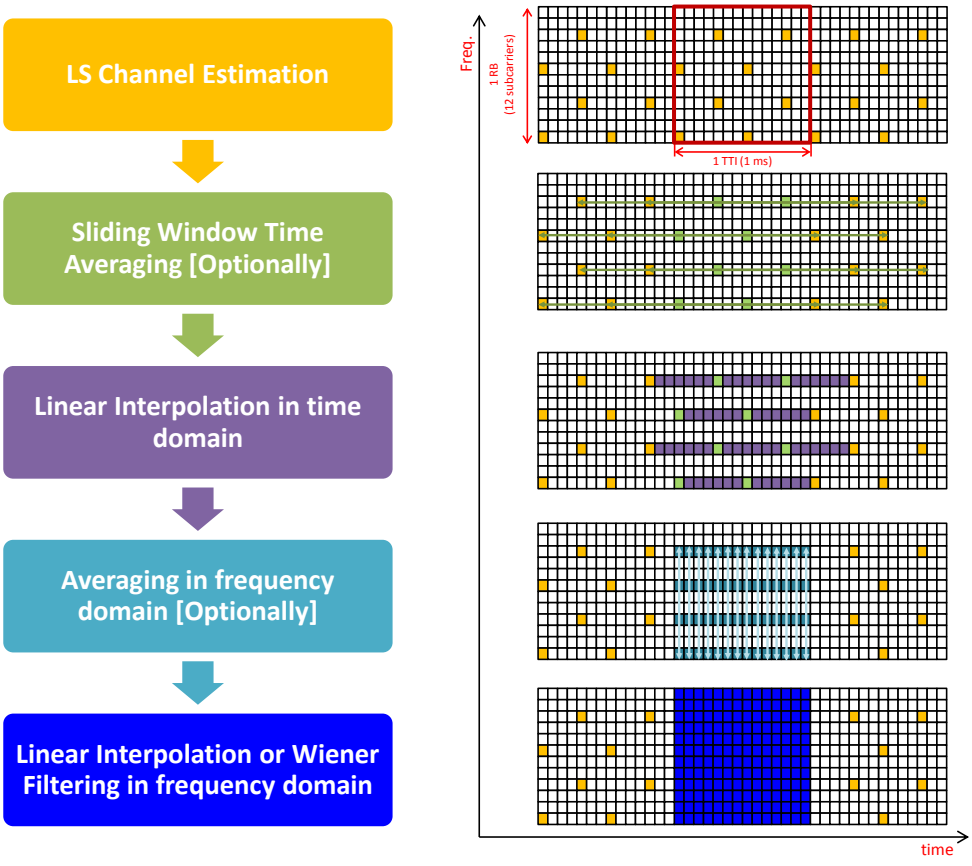

Figure 4.9: Coloured graphical representation of the REs involved in the practical channel estimation procedure.

4.7 Performance Evaluation of Channel Estimation based on CRSs

In order to evaluate the channel estimation performance based on CRS on a more realistic scenario taking into account the power delay profiles of E-UTRA channel models shown in Table A.1

and the time and frequency domain full processing already explained in this chapter, simulations are carried out using the LTE link level simulator presented in chapter 3. In order to obtain these results, the proposed channel estimation algorithm has been programmed in the simulator.

Table 4.4: E-UTRA channel models

E-UTRA Channel Model [19]	**Maximum Doppler Frequency** (f_d)	**Delay Spread (r.m.s)** (σ_s)	50% **Coherence Bandwidth** ($\approx 1/5\sigma_s$) [90]	50% **Coherence Time** ($\approx 0.423/f_d$) [90]
EPA5	5 Hz	45 ns	4444 KHz	84.6 ms
EVA70	70 Hz	357 ns	560 KHz	6.0 ms
ETU300	300 Hz	991 ns	202 KHz	1.4 ms

The acronyms used in the legends of the next figures to refer to the different algorithm combinations are listed in Table 4.5. The legend "LS (all pilots)" means that all RE are considered RS and the LS estimation is performed on all the REs without any time or frequency averaging.

Table 4.5: Meaning of the acronyms in figure legends

Acronym	**Description**
LS	LS estimation
SVT	Sliding window average, of size V TTIs, in time domain
LT	Linear interpolation in time domain
SQF	Sliding window average, of size Q pilots, in frequency domain
LF	Linear interpolation in frequency domain
WF(C)	Wiener filtering in frequency domain where C is the number of subcarriers considered for Wiener filtering matrix
BP	Pilot power boost of P dB

4.7.1 Finding optimal parameters for practical channel estimation procedures

The objective is to find an optimal configuration for the proposed algorithm 4.1 establishing a trade-off between the channel estimation error minimization and the channel estimation procedure complexity. As it was demonstrated in [91], pilot-based channel estimation in OFDM systems presents a two dimensional grid in time and frequency domain with some known elements that correspond to pilots while the rest have to be estimated. The optimum channel estimator should consider *Two-Dimensional* (2D) filters but they do not present a good trade-off between performance and complexity. Therefore, the channel estimation procedure is divided in two *One-Dimensional* (1D) processing, in time and frequency domain. The proposed algorithm 4.1 follows this rule of separable filters and also considers two channel estimators, LS, Equation 4.5, and 1D-LMMSE, Equation 4.9.

In case of using the LS channel estimator, linear interpolation in the frequency domain is performed in step 5a of algorithm 4.1. If 1D-LMMSE is used, Wiener filtering, step 5b, is applied in

the frequency domain taking into account the size of the sliding window in number of pilots; thus Equation 4.9 is rewritten as follows:

$$\hat{\mathbf{H}}_{\mathrm{W}} = \mathbf{R}_{\mathrm{h}} \left[\mathbf{R}_{\mathrm{H}} + \frac{\sigma^2}{V_p \cdot Q \cdot B} \mathbf{I}_{N_p} \right]^{-1} \cdot \hat{\mathbf{H}}_{LS} \tag{4.30}$$

where V_p is the size in pilots of the sliding window in time domain (SVT) and V is the size in number of TTIs. Therefore $V_p = v \cdot \mathrm{V}$ where v is the number of estimated pilots per TTI. Q is the size in pilots of the sliding window in frequency domain (SQF). The reason to consider these factors in the Wiener filtering equation is that performing a sliding window average enhances the signal-to-noise ratio of the estimates proportionally to the window size. But sliding window averaging also makes channel estimates be low-pass filtered and, as result, it can degrade them in case that the sliding window size is greater than the channel coherence time in the time domain and/or the channel coherence bandwidth in the frequency domain.

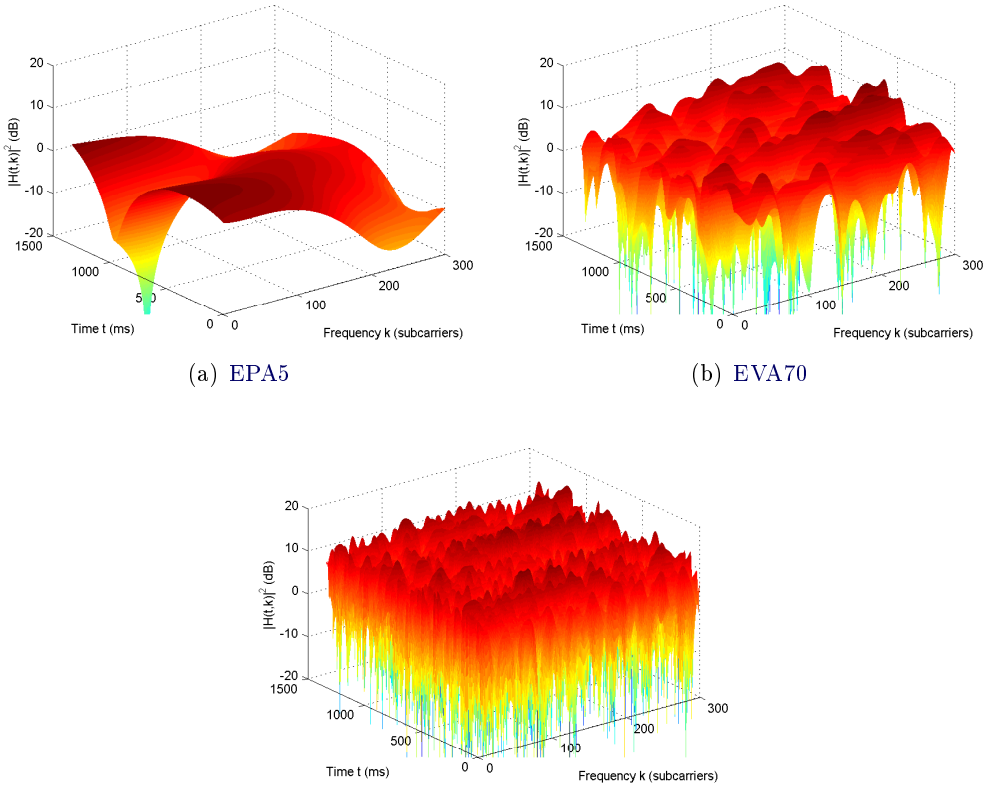

(a) EPA5 (b) EVA70

(c) ETU300

Figure 4.10: Example of CTF $|H(t,f)|^2\,(dB)$ over time for different channel models: (a) EPA5, (b) EVA70 and (c) ETU300

According to annex F of [81], OFDM demodulator performs 140 FFTs, one for each OFDM symbol comprising the full 10 ms frame, that is 10 subframes or 140 OFDM symbols. Therefore, the maximum sliding window size in time is 10 ms. Moreover, the moving average in frequency domain is defined by a sliding window of a maximum size of 19 subcarriers. So taking into account

not to exceed the maximum settings for averaging sliding windows, the channel error performance for *EPA channel model and maximum Doppler frequency of 5 Hz* (EPA5), *EVA channel model and maximum Doppler frequency of 70 Hz* (EVA70) and ETU300 channels have been analysed. Figure 4.10 shows an example of the *Channel Transfer Function* (CTF) over time for these channel models.

For example, Figure 4.11 and 4.12 show snapshots of channel estimation performance in time domain (10 TTIs) for EPA5 and ETU300, respectively, and SNR= 10 dB. In the case of Wiener filter, it is performed linear interpolation using the LMMSE estimates to obtain the remaining channel coefficients in time domain. In addition, notice that for EPA5, averaging in time domain decreases substantially the channel estimation error. Figure 4.13 shows snapshots of CTF estimation performance in frequency domain (4 RBs) for ETU300 and SNR= 10 dB. Notice that Wiener filtering improves significantly the results compared to LS estimate.

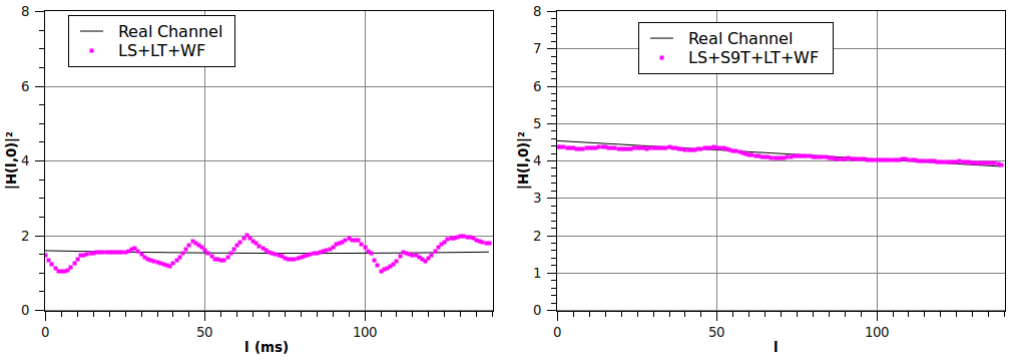

Figure 4.11: Channel estimation performance snapshots of $|H(l,k)|^2$ (dB) for EPA5 in time domain (where k is the subcarrier index and l is the index in time domain) and SNR= 10 dB

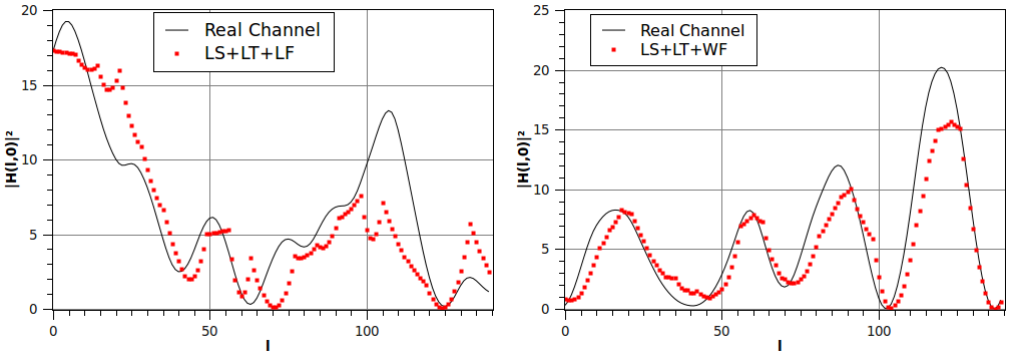

Figure 4.12: Channel estimation performance snapshots of $|H(l,k)|^2$ (dB) for ETU300 in time domain (where k is the subcarrier index and l is the index in time domain) and SNR= 10 dB

Figures 4.14, 4.15 and 4.16 show the channel estimation error (in percentage) for different channel estimation algorithms and EPA5, EVA70 and ETU300 channel models, respectively. It can be

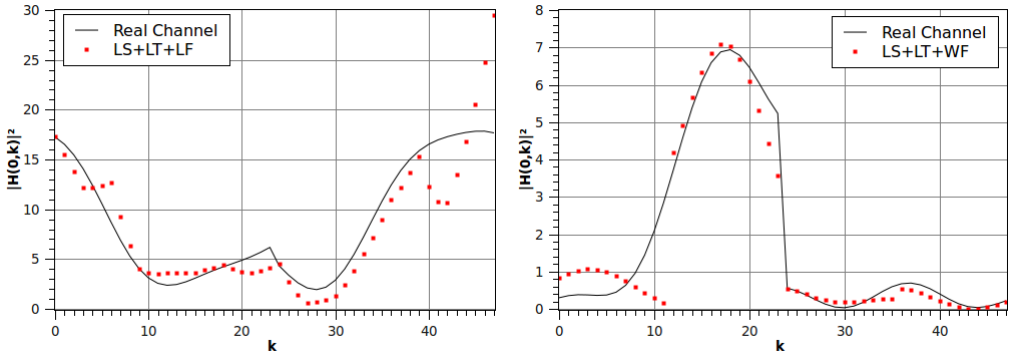

Figure 4.13: Channel estimation performance snapshots of $|H(l,k)|^2$ (dB) for ETU300 in frequency domain (where k is the subcarrier index and l is the index in time domain) and SNR= 10 dB

observed that the optimum estimators are the following:

- **LS+S9T+LT+WF(48)** for EPA5
- **LS+S3T+LT+WF(48)** for EVA70
- **LS+LT+WF(48)** for ETU300

Concerning to the optimum averaging window size in the time domain, it is 9 for EPA5, 3 for EVA70 and 1 for ETU300; consequently, this parameter is related to the channel coherence time shown in Table A.1 and the time window size must be carefully chosen in order to not span more than the channel coherence time. Notice that averaging in the time domain improves substantially the estimation error performance at low SNRs for EPA5 and EVA70, but its effects at high SNRs are not significant compared to no averaging.

Averaging in the frequency domain introduces a large error floor for the LS channel estimator case compared to no averaging for medium and high SNRs. For the Wiener filtering case averaging in the frequency domain is not necessary for EPA5 and EVA70 channel model, since it does not improve the performances of the not averaged case. Averaging in frequency domain is also not useful for ETU300 channel model, since it introduces a large error floor. Therefore, averaging in frequency domain is not recommended for any scenario.

Even the low complexity Wiener filtering implemented in the frequency domain improves significantly the results compared to linear interpolation for any type of channel, but it must be kept in mind that perfect SNR and power delay profile estimation are assumed.

4.7.2 Analysis of the Wiener Filtering Performance

Wiener Filtering is an efficient method for channel estimation that allows to obtain better performance, compared to using only LS channel estimator and linear interpolation in time and frequency domain, as it has been assessed in this section. Ideally 2D Wiener filter is the optimal channel estimator, [83], but two concatenated 1D Wiener filters reduce the channel estimator complexity and its performance is similar to 2D Wiener filtering, [83, 91]. The proposed channel estimation

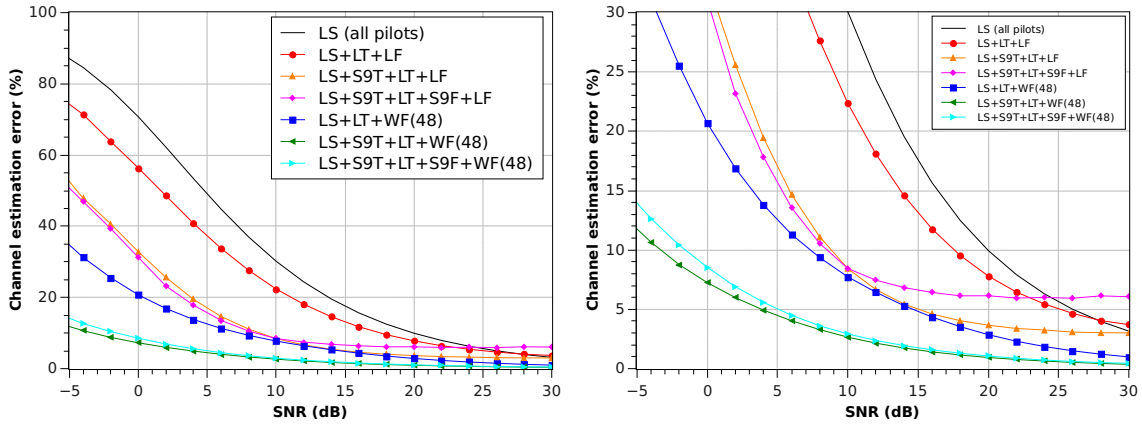

Figure 4.14: Channel estimation error for EPA5 channel model. The figure on the right hand side shows a zoom of the range between 0 an 30% of the channel estimation error.

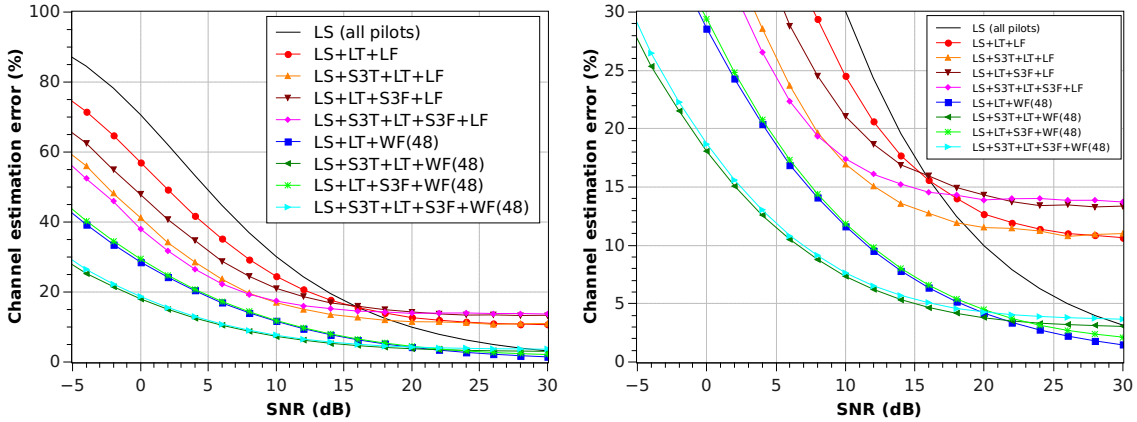

Figure 4.15: Channel estimation error for EVA70 channel model. The figure on the right hand side shows a zoom of the range between 0 an 30% of the channel estimation error.

procedure takes into account Wiener filtering in the frequency domain and linear interpolation in time domain instead of 1D wiener filtering in order to reduce channel estimation complexity.

The order of two concatenated filters, first in the frequency domain and then in the time domain, or vice-versa, is arbitrary due to the linearity of this method. Annex F of [81] propose first processing in time domain and then in frequency domain; but, for instance, [83, 89] proposes the reverse order, first in frequency domain and then in time domain. In this section we discuss the trade-off between channel estimator complexity and performance.

Along with assessing channel estimation performance, its computation complexity must also be analysed. The 1D Wiener filtering according to expression (4.9) requires knowledge of the channel frequency correlation, to compute the covariance matrices, and the SNR which also have to be estimated. The 1D Wiener filtering matrix is fixed during the time interval in which the channel frequency correlation and the SNR do not vary. This period of time depends on the actual coherence time of the channel, so the receiver must follow the evolution of these values

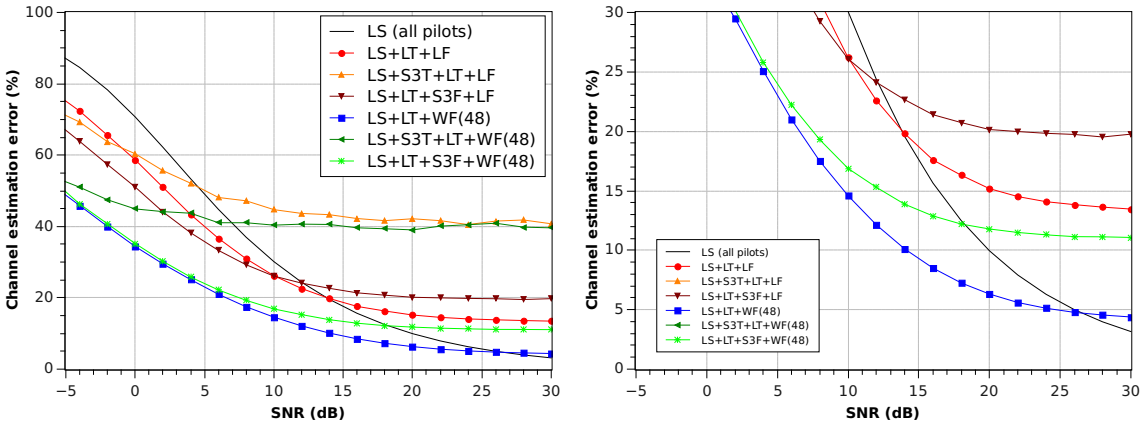

Figure 4.16: Channel estimation error for ETU300 channel model. The figure on the right hand side shows a zoom of the range between 0 an 30% of the channel estimation error.

and recompute the 1D Wiener filtering matrix for a reliable estimation. From this point of view, changing the 1D Wiener filtering matrix only when it is necessary reduces the computational cost of the channel estimation procedure. However, a reduced dimension of the 1D Wiener filtering matrix is necessary in order to minimize the computational cost of this operation as described below.

Wiener filtering in the frequency domain (Equation 4.30) requires one matrix inversion and a matrix multiplication and is divided in two steps: first, the estimated 1D Wiener filtering matrix computation that depends on the channel frequency correlation and SNR, expression (4.31), and second the matrix multiplication, Equation (4.32). The matrix multiplication is performed for each channel estimation computation, but the matrix inversion is performed only when channel frequency correlation and/or SNR vary significantly.

$$\hat{\mathbf{R}}_{\mathrm{W}} = \mathbf{R}_{\mathrm{h}} \left[\mathbf{R}_{\mathrm{H}} + \frac{\sigma^2}{V_p \cdot Q \cdot B} \mathbf{I}_{N_p} \right]^{-1} \tag{4.31}$$

where $\hat{\mathbf{R}}_{\mathrm{w}}$ is the $(12N_{RB} \times N_p)$ 1D Wiener filtering matrix in the frequency domain.

$$\hat{\mathbf{H}}_{\mathrm{W}} = \hat{\mathbf{R}}_{\mathrm{W}} \cdot \hat{\mathbf{H}}_{LS} \tag{4.32}$$

where $\hat{\mathbf{H}}_{LS}$ is the $(N_p \times 1)$ LS channel estimation vector and $\hat{\mathbf{H}}_{\mathrm{W}}$ is the Wiener filtered channel estimation vector.

The complexity for a $(n \times n)$ matrix inversion is $O(n^3)$ without optimization and for a matrix multiplication of $(n \times m)$ matrix and $(m \times p)$ matrix is $O(nmp)$. In order to reduce matrix inversion and multiplication complexity, the allocated bandwidth $N_{RB}{}'$ can be divided into P non-overlapping bins and each part is Wiener filtered independently. In addition, given a channel model, the Wiener filtering matrix for each bin is the same since it only depends on the separation between frequencies within the allocated bandwidth. So $N_{RB} = \frac{N_{RB}{}'}{P}$, the size of the 1D Wiener filtering matrix is $(12N_{RB} \times N_p)$ and the expression (4.32) computation is reduced to P matrix multiplications of a $(12N_{RB} \times N_p)$ matrix by a $(N_p \times 1)$ vector. In [92] this simplification of

Wiener filtering, by partitioning the channel vector into small subvectors and decompositing the channel autocorrelation matrix by non-overlap or overlap technique is proposed.

Thus, P must be chosen taking into account a trade-off between complexity and performance. Since the most correlated subcarriers are within the coherence bandwidth among adjacent frequencies of the channel, the 1D Wiener filtering matrix can be reduced to span less than 4 RBs if EVA or ETU coherence bandwidth is considered (EPA coherence bandwidth is too large to be considered as a whole). In [89] it is proposed to use the nearest six pilot symbols for Wiener filtering matrix that span a bandwidth of 3 RBs, i.e., 36 subcarriers.

Figures 4.17, 4.18 and 4.19 show the channel estimation error performance for EPA5, EVA70 and ETU300 channel models, respectively, taking into account different 1D Wiener filtering sizes. Moreover, there are also considered two options for the practical channel estimation procedure: the one proposed in algorithm 4.1, i.e., first applying linear interpolation in the time domain (step 4) and then Wiener filtering in the frequency domain (step 5); or reversing the order of these steps. In these Figures, WF(C) represents the Wiener filtering matrix in the frequency domain, $\hat{\mathbf{H}}_{\mathrm{W}}$, spanning $C = 12N_{RB}$ subcarriers. Depending on whether the linear interpolation in the time domain is applied before or after Wiener filtering in the frequency domain, the number of estimated pilots per RB is different, 4 or 2, respectively, according to DL frequency-time grid for AP 0 or 1 shown in Figure 4.1. Therefore, the size of $\hat{\mathbf{H}}_{\mathrm{W}}$ matrix is $C \times N_p$, where $N_P = 4N_{RB}$ or $N_P = 2N_{RB}$.

The channel estimator LS+SVT+LT+WF(C) applies linear interpolation of received and averaged pilots before Wiener filtering in the frequency domain. To denote the same operations in reverse order we use LS+SVT+WF(C)+LT. Then, in order to evaluate the impact of the $(C \times N_p)$ Wiener filtering matrix, it is considered that $\hat{\mathbf{H}}_{\mathrm{W}}$ spans a bandwidth of 36, 48 and 300 subcarriers. Thus, according to the optimum channel estimators presented in previous subsection, the evaluated channel estimators are:

For EPA5 channel model,

- LS+S9T+LT+WF(C)
- LS+S9T+WF(C)+LT

For EVA70 channel model,

- LS+S3T+LT+WF(C)
- LS+S3T+WF(C)+LT

And for ETU300 channel model,

- LS+LT+WF(C)
- LS+WF(C)+LT

For EPA5 channel model the LS+S9T+LT+WF(C) channel estimator achieves better channel estimation error performance than the LS+S9T+WF(C)+LT for all cases, i.e. for C equal to 36, 48 and 300 subcarriers. At a SNR of 5 dB, the gain introduced by the LS+S9T+LT+WF(C) with respect to the LS+S9T+WF(C)+LT is about 2 dB. Then, the UBER performance for all channel estimators taking into account C equal to 36 and 300 subcarriers is almost identical. Therefore, the LS+S9T+LT+WF(36) channel estimator is proposed as a trade-off between performance and complexity.

For EVA70 channel model the LS+S3T+LT+WF(C) channel estimator achieves better channel estimation error performance than the LS+S3T+WF(C)+LT for all cases, i.e. for C equal to 36, 48 and 300 subcarriers. At a SNR of 5 dB, the gain introduced by the LS+S3T+LT+WF(C) with respect to the LS+S3T+WF(C)+LT is also about 2 dB. This result is similar to the EPA5 channel model case, but instead of a sliding window average of size 9 TTIs, the applied size is 3 TTIs. Then, the UBER performance for channel estimators taking into account C equal to 36 and 300 subcarriers is also almost identical, only a degradation of 1 dB with respect to ideal channel estimation is observed at an SNR of 2 dB. Therefore, the LS+S3T+LT+WF(36) channel estimator is proposed as a trade-off between performance and complexity.

For ETU300 channel model and low and medium SNR, the LS+LT+WF(C) channel estimator achieves better channel estimation error performance than the LS+WF(C)+LT for all cases, i.e. for C equal to 36, 48 and 300 subcarriers. At high SNR the LS+WF(C)+LT channel estimator obtains the best results because the LS+LT+WF(C) introduces an error floor; but this result is significant only for the case of 300 subcarriers case since where this effect is observed for SNR above 15 dB. The other two cases, the error floor introduced by LS+LT+WF(48) and LS+LT+WF(36) are observed for SNR above 22 and 23 dB, respectively. At a SNR of 5 dB, the gain introduced by the LS+LT+WF(C) with respect to the LS+WF(C)+LT is about 3 dB. The UBER performance of the LS+LT+WF(36) channel estimator is degraded compared to the LS+WF(300)+LT about 2 dB at high SNR and 1.5 dB at low and medium SNR. But the low complexity of the channel estimator is prioritized and only 36 subcarriers are considered, so the proposed channel estimator is the LS+LT+WF(36) since its UBER presents 1 dB of gain with respect to LS+WF(36)+LT for low and medium SNR.

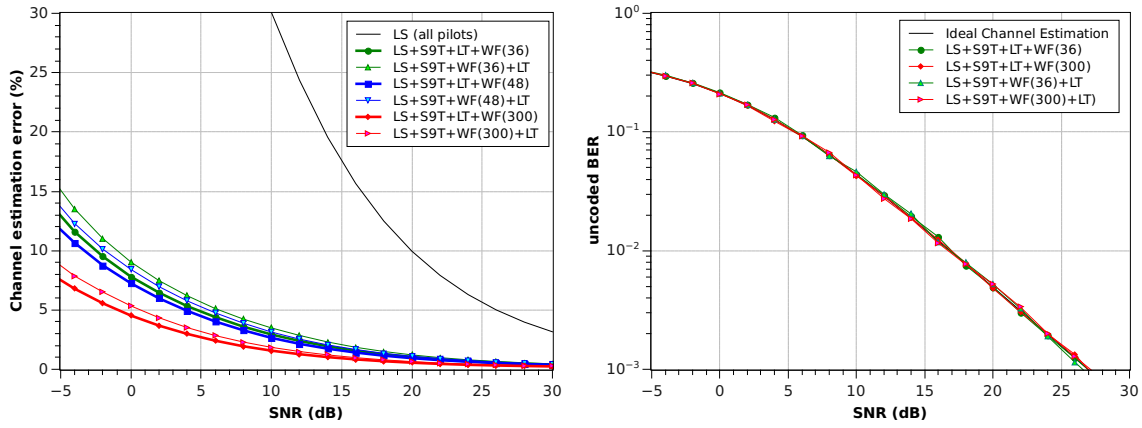

Figure 4.17: Channel estimation error for different channel estimation procedures and the UBER obtained for QPSK modulation with EPA5 channel model

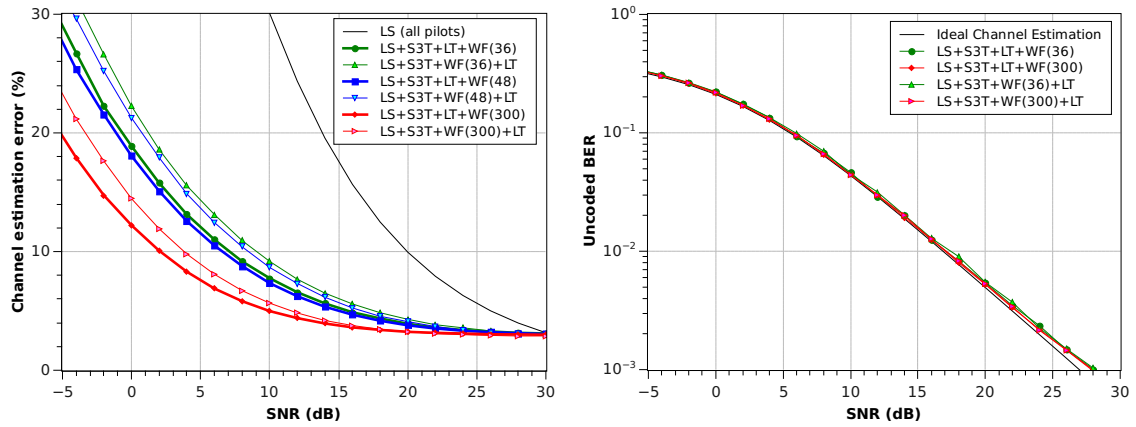

Figure 4.18: Channel estimation error for different channel estimation procedures and the UBER obtained for QPSK modulation with EVA70 channel model

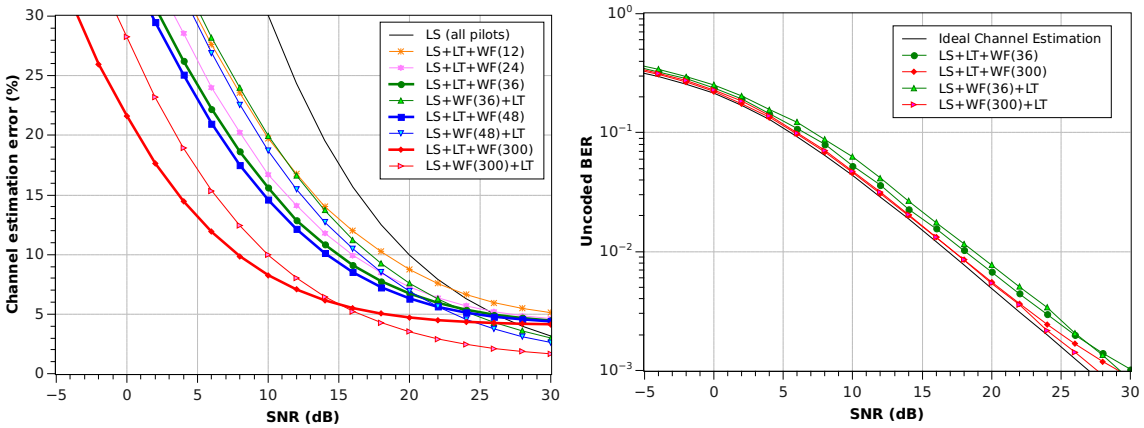

Figure 4.19: Channel estimation error for different channel estimation procedures and the UBER obtained for QPSK modulation with ETU300 channel model

4.7.3 Effect of imperfect knowledge of channel statistics on the Wiener Filter

In case of imperfect knowledge of channel statistics on the Wiener Filter, it will affect to the channel estimation error performance. Figures 4.20, 4.21 and 4.22 show the channel estimation error and UBER performance for EPA5, EVA70 and ETU300 channel models under perfect and imperfect channel statistics estimation, respectively.

The channel estimator LS+S9T+LT+WF(36) is proposed for EPA5 channel model when perfect channel statistics estimation is assumed. In this section we compute the channel estimation performance of that estimator assuming wrong channel statistics (i.e. *EVA channel model and maximum Doppler frequency of 5 Hz* (EVA5) or *ETU channel model and maximum Doppler frequency of 5 Hz* (ETU5) instead of the right one (EPA5), i.e:

- LS+S9T+LT+WF(36)[EVA]

- LS+S9T+LT+WF(36)[ETU]

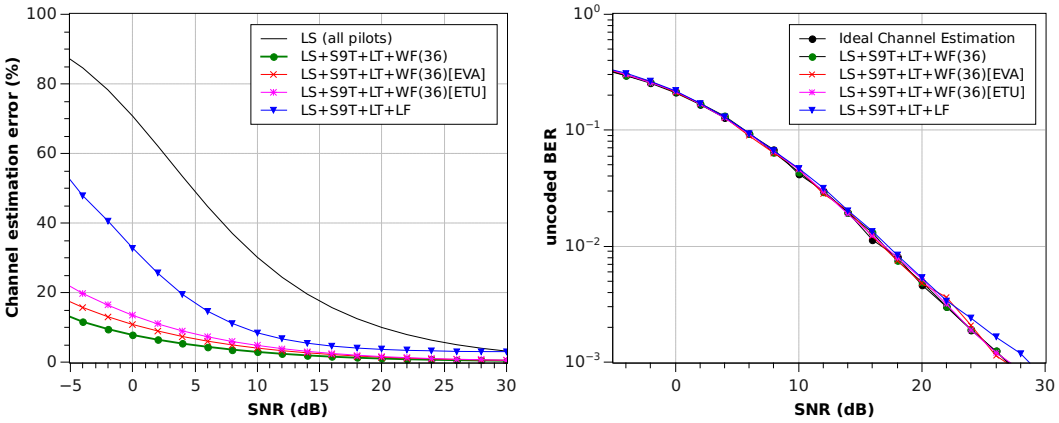

Figure 4.20: Channel estimation error for EPA5 with perfect and imperfect wiener filter channel matrix estimation and UBER obtained for QPSK modulation

In Figure 4.20 it is observed a small degradation in the channel estimation error performance when imperfect channel statistics is assumed, but there is no significant degradation in the UBER performance.

The channel estimator LS+S3T+LT+WF(36) is proposed for EVA70 channel model when perfect channel statistics estimation is assumed. Next we compute the channel estimation performance of that estimator assuming wrong channel statistics (i.e. *EPA channel model and maximum Doppler frequency of 70 Hz* (EPA70) or *ETU channel model and maximum Doppler frequency of 70 Hz* (ETU70) instead of the right one (EVA70), i.e:

- LS+S3T+LT+WF(36)[EPA]
- LS+S3T+LT+WF(36)[ETU]

Figure 4.21 shows a large degradation in the channel estimation error performance when EPA channel statistics are assumed, but there is no significant degradation when ETU channel statistics are assumed due to the fact that ETU channel frequency correlation is more similar to EVA channel frequency correlation than to EPA. Consequently, the UBER performance is practically identical if the true channel statistics or ETU channel statistics are assumed, but in the case of assuming EPA channel statistics, an error floor is introduced at high SNR.

The channel estimator LS+LT+WF(36) is proposed for ETU300 channel model where perfect channel statistics estimation is assumed. Here we compute the channel estimation performance of that estimator assuming wrong channel statistics (i.e. *EPA channel model and maximum Doppler frequency of 300 Hz* (EPA300) or *EVA channel model and maximum Doppler frequency of 300 Hz* (EVA300)) instead of the right one (ETU300), i.e:

- LS+LT+WF(36)[EPA]
- LS+LT+WF(36)[EVA]

Figure 4.22 shows a medium degradation in the channel estimation error performance when EVA channel statistics are assumed due to the fact that ETU frequency correlation changes faster than EVA frequency correlation; but if EPA channel statistics are assumed, then a high degradation in the channel estimation error performance is observed due to the fact that EPA frequency correlation is almost constant in the frequency domain which is not true for the ETU channel. For those reasons, assuming imperfect channel statistics, an error floor in the UBER performance is introduced; the error is large for EVA channel statistics and even larger for EPA channel statistics.

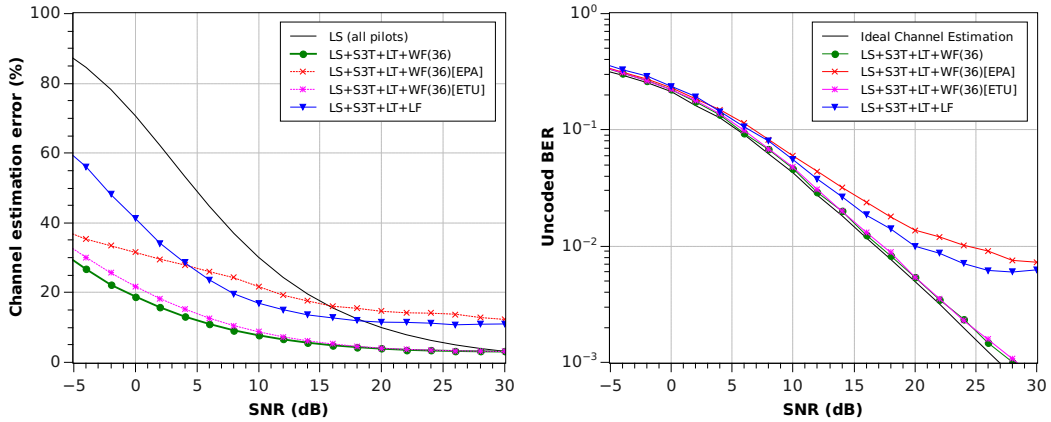

Figure 4.21: Channel estimation error for EVA70 with perfect and imperfect wiener filter channel matrix estimation and UBER obtained for QPSK modulation

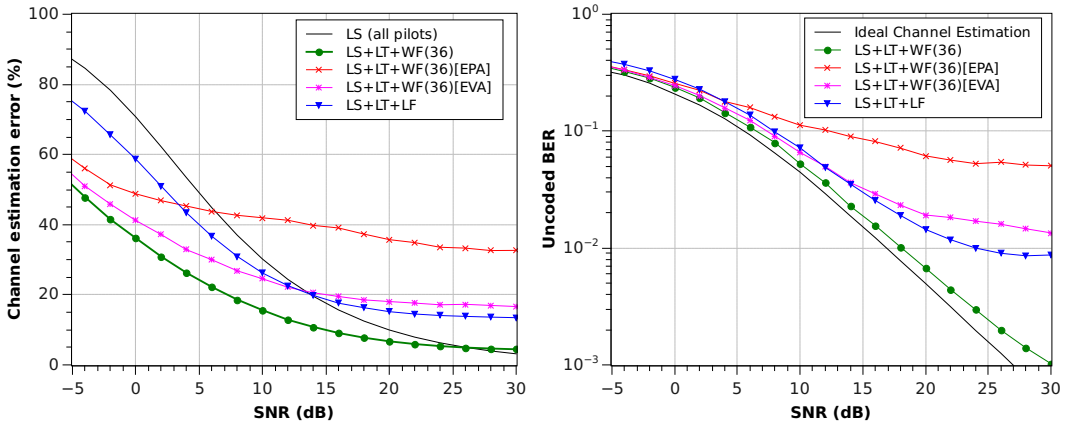

Figure 4.22: Channel estimation error for ETU300 with perfect and imperfect wiener filter channel matrix estimation and UBER obtained for QPSK modulation

4.7.4 Channel Estimation Error for LTE Practical Channel Estimation Procedures

The channel estimation error LUTs for different combinations of SNR, AP pilots and channel models are shown in Figure 4.23. They have been created based on the optimum channel estimators proposed in this chapter which are listed below:

- LS+S9T+LT+WF(36) for EPA5
- LS+S3T+LT+WF(36) for EVA70
- LS+LT+WF(36) for ETU300

Figure 4.23 shows the channel estimation error LUTs according to CRS pilot density represented in Figure 4.1, that is eight pilots per TTI and RB for APs 0 and 1 and four pilots per TTI and RB for APs 2 and 3. As it can be observed, the channel estimation error performance is better if APs 0 and 1 pilots are used instead of APs 2 and 3. The reason for this result is that CRS pilot density for APs 2 and 3 is half of the density for APs 0 and 1, so the channel estimation error decreases if more pilots are used. Thus, channel estimation error performance for APs 2 and 3 introduces a degradation not higher than 2 dB at a SNR of 10 dB for EPA5 and EVA70 channel models, but this degradation is about 11 dB for ETU300 channel model since a large error floor, about 15 %, is introduced by channel estimation based on APs 2 or 3 pilots.

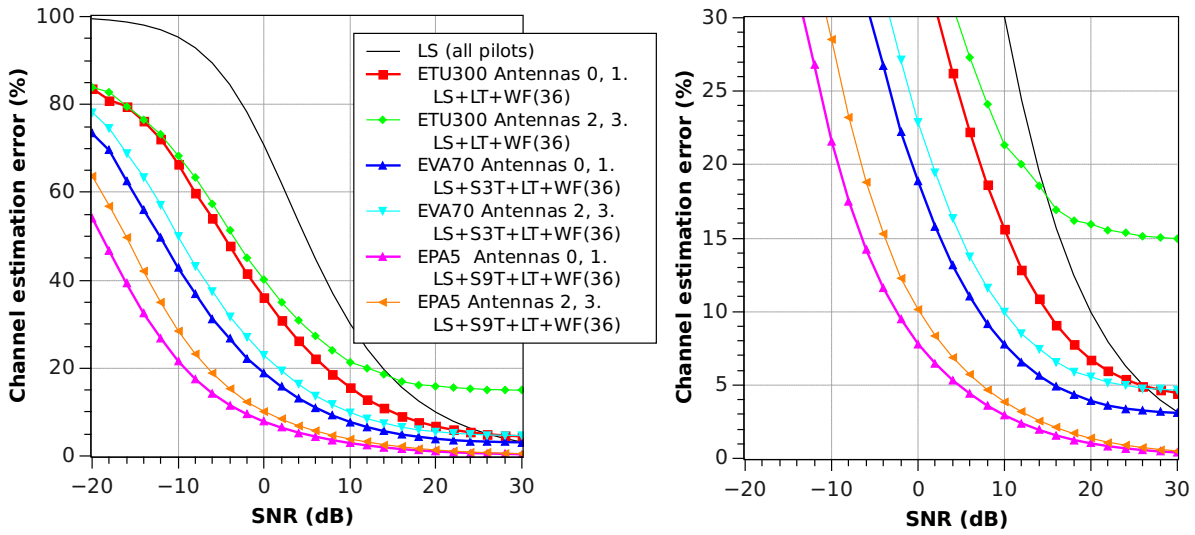

Figure 4.23: Channel estimation error LUTs for EPA5, EVA70 and ETU300 channel models and APs 0,1,2 and 3 (where APs are labelled as Antennas in the legend of this figure)

4.8 Impact of Channel Estimation Error on LTE DL BLER Performance

In order to evaluate the impact of channel estimation error on link level performance, the E-UTRA link level simulator presented in this dissertation has been enhanced by programming the detailed channel estimation algorithm explained in section 4.6 as well as the Gaussian channel estimation error model called CEEM (Equation 4.6). Table 4.6 lists the parameters used in the link level simulations.

Figure 4.24 compares the UBER performance for a QPSK transmission through an ETU300 channel under ideal channel estimation with the LS+LT+WF imperfect channel estimator and

Table 4.6: LTE DL link level simulator parameters.

Parameter	Value
Carrier frequency	2.14 GHz
Sub-carrier spacing	15 kHz
Number of sub-carriers per RB	12
Number of allocated RBs	4
TTI length	1 ms
Number of OFDM symbols per TTI	14 (11 PDSCH + 3 PDCCH)
Channel model	EPA5, EVA70 and ETU300, [19]
Channel Coding	Turbo code basic rate 1/3
Rate Matching and HARQ	According to [4]. Max 4 IR transmissions
AMC formats	MCS 6 (0.44), 12 (0.43), 17 (0.43) and 27 (0.89) (code rate in parenthesis)
Channel estimation	Ideal channel estimation, pilot-based channel estimation and CEEM
Antenna scheme	SISO

with the same estimator with a pilot power boost of 6 dB. A small gain of approximately 0.7 dB can be observed on the UBER when using a pilot power boost of 6 dB. For low and medium SNR, the UBER with real channel estimation is close to the UBER with ideal channel estimation, but for high SNR the UBER with imperfect channel estimation degrades 2 dB with respect to the ideal case.

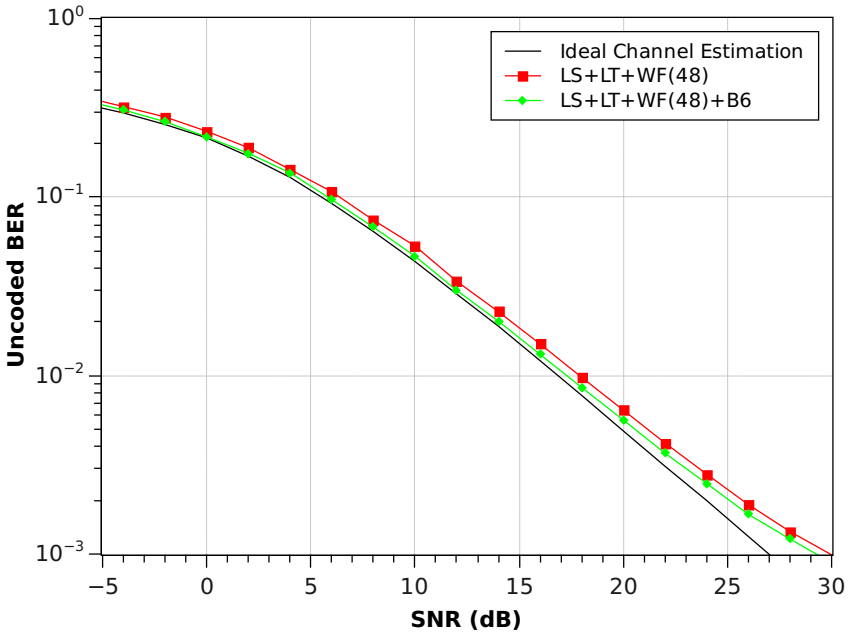

Figure 4.24: UBER for QPSK modulation, with ETU300 channel model

In order to validate the proposed channel estimation error model, a channel estimation error LUT has been created assuming the best estimator algorithm for each channel model in accordance

to Figure 4.23. The LUTs are then fed into the link level simulator to compare the BLER at first transmission (redundancy version rv= 0 of the HARQ procedure) for ideal channel estimation, pilot-based channel estimation and CEEM. Figure 4.25 shows the BLER (at rv= 0) vs. mean SNR curves for MCS 6 (QPSK + turbo code with rate 0.44) in EPA5, EVA70 and ETU300 channels, respectively. Also, these figures prove the validity of the proposed CEEM, which allows the simulation of the LTE link level without processing the RS. It can be verified that when Wiener filtering is used, the pilot power boost is not necessary, since without it a performance near to the ideal estimation case is obtained mainly for EPA5 and EVA70 channel. For ETU300 an appreciable improvement can be observed due to pilot power boost. It is conjectured that pilot power boost would be even more relevant in this environment if non-ideal power delay profile estimation is considered. The BLER curves for ETU300 show a steeper slope than the curves for EPA5 and EVA70 due to the frequency diversity effect of the error correcting code jointly with the increased frequency selectivity of fading. In EPA5 conditions the system would probably apply CDD or Alamouti's space-time diversity, which have not been considered here.

The BLER curves of Figure 4.25 are used to validate the proposed model but do not represent the LTE DL throughput performance, since it is assumed that the same MCS index is applied in a wide range of SNR, which is not the real situation. In practice the MCS index is switched upwards or downwards, on a TTI basis, whenever the BLER for rv= 0 departs from a target of 10%. What can be deduced from those plots is that, by using the worst estimator (red BLER curves), where Wiener filtering is not used, a mean SNR of about 10 dB is needed to use MCS index 6 in any of the scenarios, and then the SISO DL throughput would be close to $2 \cdot 0.9 \cdot 0.44 \cdot 11/14 = 0.62$ bit/s/Hz. But in this case, if a pilot power boost of 6 dB is used, then BLER performance (magenta BLER curves) matches approximately the BLER curves when Wiener filtering is used without power boost, obtaining roughly the same SNR at a BLER of 10% and at 1% there is a degradation not higher than 1 dB.

Figure 4.26 shows the BLER at rv= 0 for MCS 6 (QPSK and code rate 0.44), MCS 12 (16QAM and code rate 0.43), MCS 17 (64QAM and code rate 0.43) and MCS 64 (64QAM and code rate 0.89) in ETU300 comparing ideal channel estimation, pilot-based channel estimation and the proposed channel estimation error model. The estimator considered here is LS+LT+WF (the best for ETU300). The BLER curves show a degradation not higher than 1.5 dB due to imperfect channel estimation except for the MCS 27 case which presents a degradation between ideal and pilot-based channel estimation around 4 dB at a BLER of 10%. But the BLER error floor obtained by the proposed channel estimation error model at high SNR is above 10% leading to differ slightly for SNR higher than 25 dB.

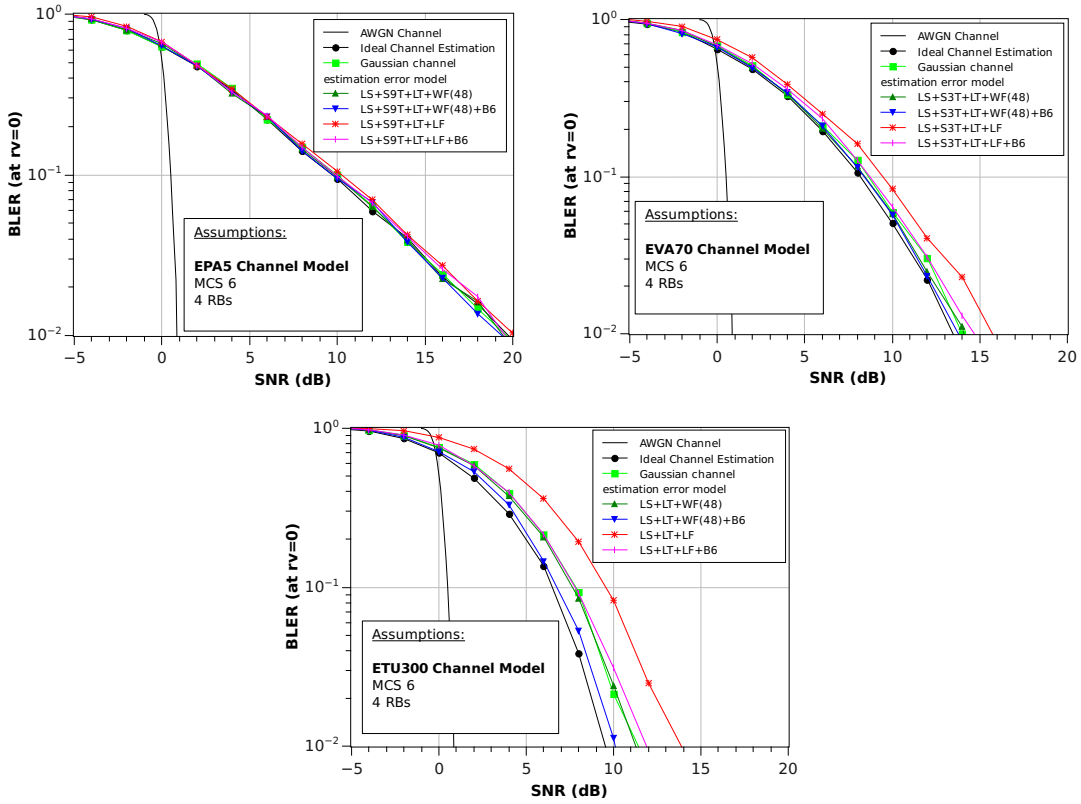

Figure 4.25: BLER (at rv= 0) for EPA5, EVA70 and ETU300 channel models and MCS 6 in a bandwidth of 4 RBs

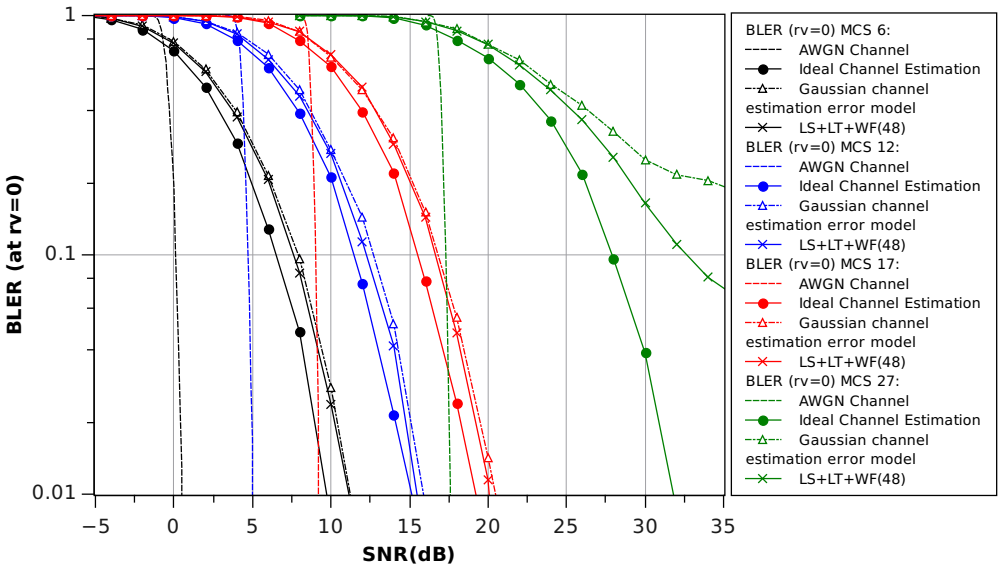

Figure 4.26: BLER (at rv= 0) for MCS 6, 12, 17 and 27 with ETU300, a bandwidth of 4 RBs and either ideal channel estimation or the proposed channel estimation model

Next, the MCS 27 case is analysed for the three considered channel models, EPA5, EVA70 and ETU300, in terms of the following parameters:

- BLER (at rv= 0) comparison of ideal channel Estimation, pilot-based channel estimator and CEEM.
- Channel estimation error comparison of pilot-based channel estimator and CEEM.
- *Cumulative density function* (cdf) of real part of error vector (EV) for pilot-based channel estimator and CEEM at 30 dB of mean SNR.

Figure 4.27 shows how the BLER (at rv= 0) and channel estimation error curves of the pilot-based channel estimator and CEEM match to each other. In contrast to EPA5 channel model, CEEM presents a slight difference compared to the BLER curve of the pilot-based channel estimation for SNR higher than 26 dB and 23 dB for EVA70 and ETU300, respectively. This small difference is about 1.5 dB at 30 dB of SNR for EVA70 and about 2 dB for ETU300 as it is observed in Figures 4.28 and 4.29, respectively. In any case, the channel estimation error curves match for these channel models.

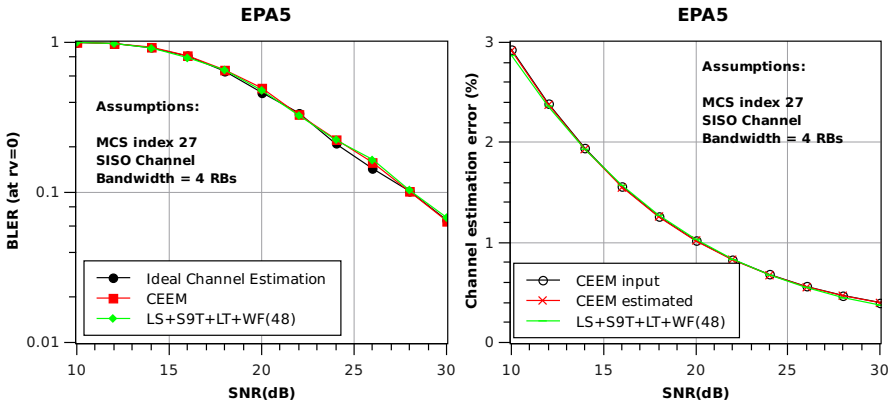

Figure 4.27: BLER (at rv= 0) and channel estimation error comparison between pilot-based channel estimator and CEEM for EPA5 channel model

In addition, Figure 4.30 shows the cdf of the real part of EV that is $Re(EV) = Re(\mathbf{s_d} - \mathbf{s})$ where s_d is the detected symbol and s is the transmitted symbol. The obtained results show that the cdf of the pilot-based channel estimator is also Gaussian and matches the cdf of the CEEM cdf for EPA5, EVA70 and ETU300. Thus, for all the analysed cases, it can be concluded that CEEM is validated for a SNR range between -20 dB and 30 dB.

Finally, the Gaussian channel estimation error model (CEEM) is evaluated taking into account HARQ in a bandwidth of 25 RBs. It has been considered the highest modulation and coding scheme, MCS 27 (64QAM and code rate 0.85, based on [33]), with the same transmission power at each redundancy version. The BLER curves are shown in Figure 4.31 and it can be observed, in addition to the coding gain due to the larger code length in a bandwidth of 25 RBs with respect to the previous case of 4 RBs, that the HARQ process reduces the difference between the Gaussian

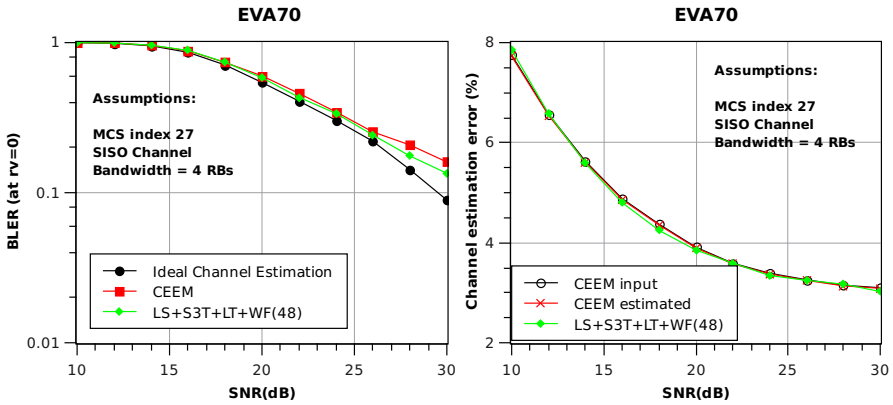

Figure 4.28: BLER (at rv= 0) and channel estimation error comparison between pilot-based channel estimator and CEEM for EVA70 channel model.

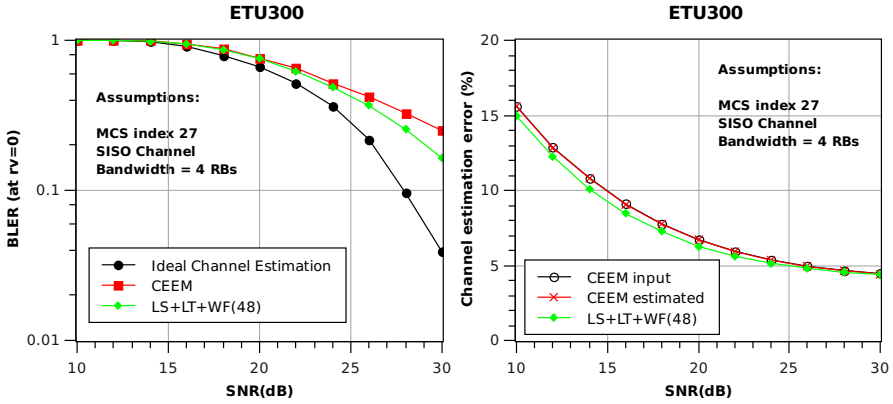

Figure 4.29: BLER (at rv= 0) and channel estimation error comparison between pilot-based channel estimator and CEEM for ETU300 channel model

channel estimation error model and the ideal channel estimation from 4 dB for rv= 0 at a BLER of 10% to around 1 dB for the rest of redundancy versions.

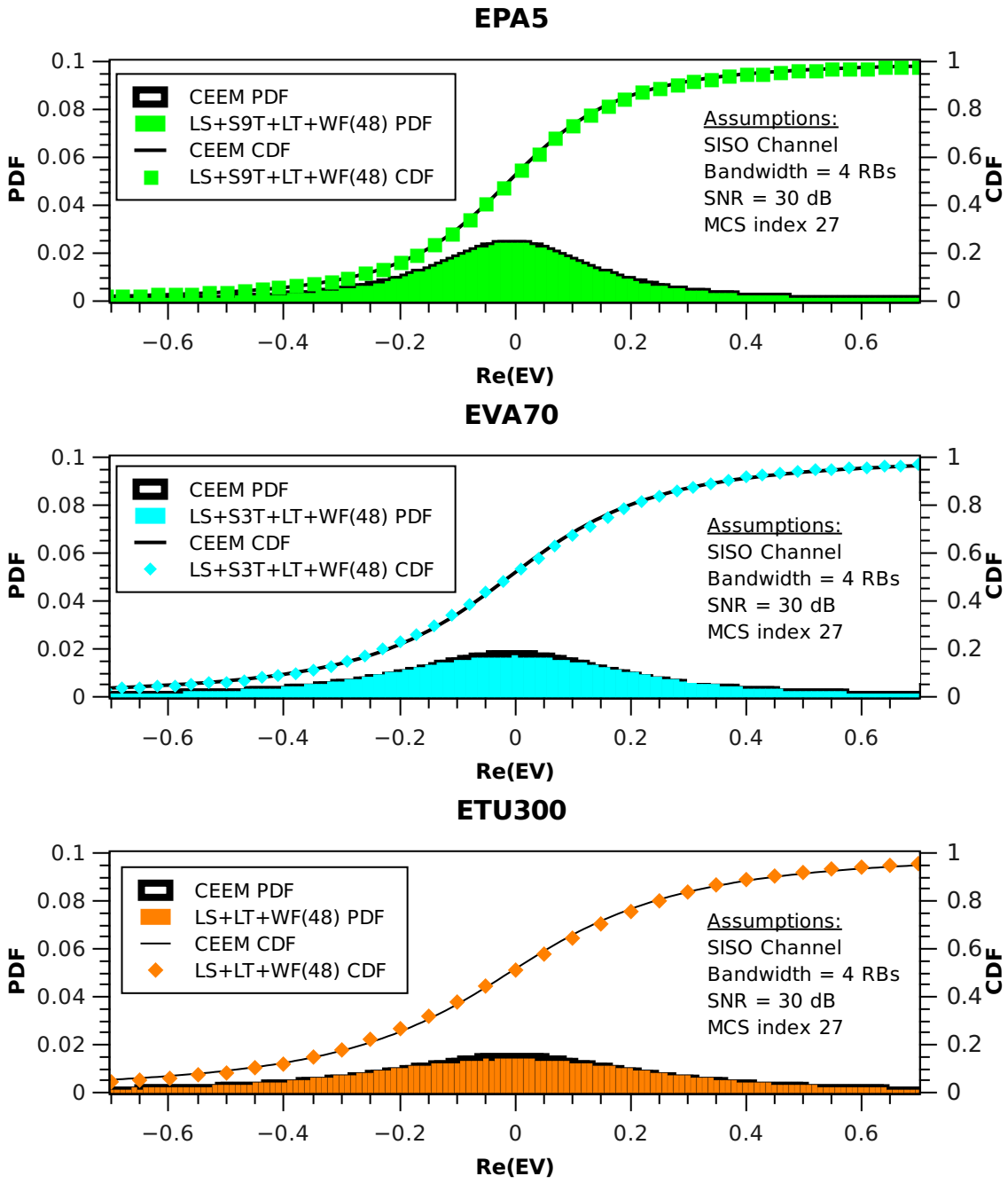

Figure 4.30: cdf and pdf of real part of error vector (EV) for pilot-based channel estimator and CEEM at 30 dB of SNR for EPA5, EVA70 and ETU300.

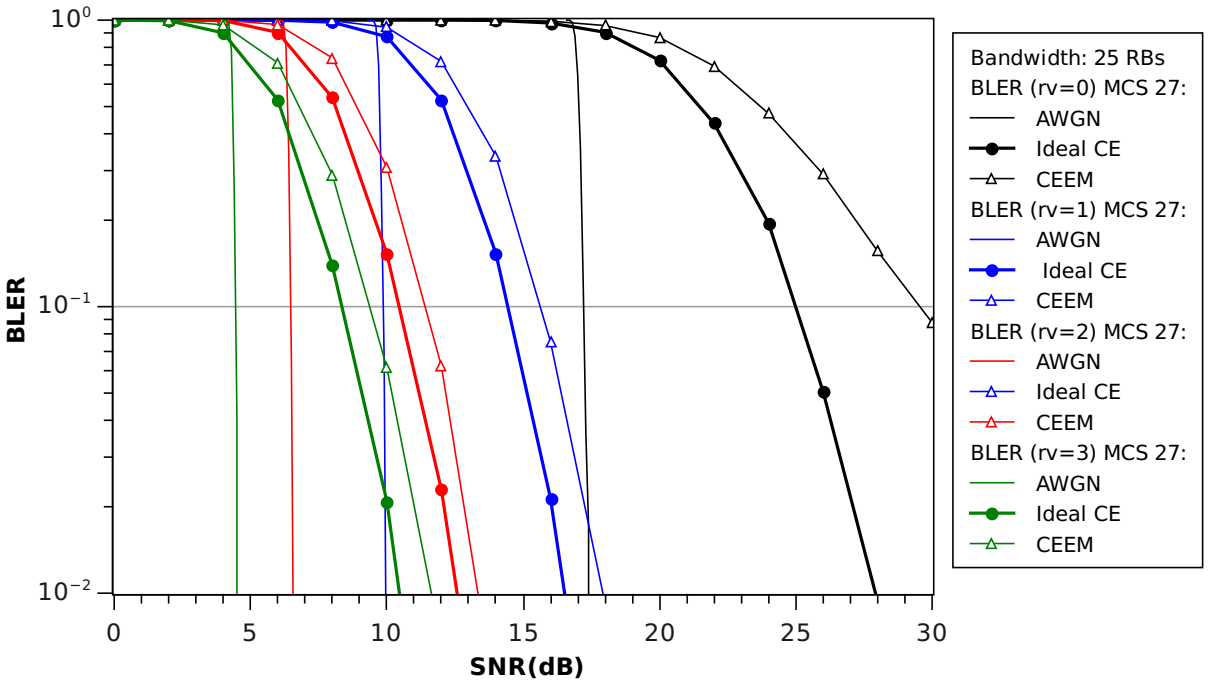

Figure 4.31: BLER (at rv= $0, 1, 2, 3$) vs. mean SNR for MCS 27 with ETU300 and a bandwidth of 25 RBs for ideal channel estimation and CEEM

Chapter 5

E-UTRA DL Link Level Performance

In this chapter, we first provide the E-UTRA DL link level performance in a static non-fading AWGN channel for the AMC schemes of LTE/LTE-Advanced and this is compared to the Shannon capacity of a SISO system. Next, we examine the E-UTRA DL link level performance results of LTE/LTE-Advanced in different 3GPP multipath fading channels for various MIMO configurations with low, medium and high antenna correlations (LC, MC and HC) considering the ideal condition of perfect channel estimation. These results show the benefits of applying different MIMO techniques, such as OL and CL MIMO-SM techniques, precoding techniques, MIMO-TD and ZF/MMSE receivers. Furthermore, we examine link level results for the non-linear receiver structure called codeword-SIC which is proposed in section 3.4.7 and the performance results are compared in order to highlight the benefits and drawbacks of each MIMO technique. Finally, we obtain the E-UTRA DL link average throughput from the link level results taking into account non-perfect channel estimation which is modelled by the proposed CEEM and these results are compared to perfect channel estimation.

5.1 AWGN Link Level Performance

The LTE performances are commonly assessed by means of both link level and system level simulators, where the first one is able to model a single link with high detail and the second one models a cell deployment as a whole, including *Radio Resource Management* (RRM) and scheduling algorithms. In order to obtain results within a reasonable time, system level simulators work on LUTs provided by link level simulators. This mapping from link level to system level simulator typically adopts the form of AWGN BLER vs. ESNR tables for the different possible MCS formats plus a link abstraction model to compute the ESNR of a given user at a given TTI. The ESNR is thus a single scalar that summarizes the information capacity limitations due to the applied modulation and code rate, plus the effects of all channel impairments experienced by a given TB transmitted inside one or more RBs, i.e.: propagation losses, shadowing fading, frequency selective fading and thermal plus interference noise power. Therefore, in order to implement AMC, system level simulation needs an accurate prediction of link level performance in terms of BLER and, for this reason, AWGN link level simulation is required.

The AWGN link level performance is used to determine the SINR thresholds for AMC and to estimate the BLER in a fading channel based on the actual channel ESNR and the selected MCS value. In section 5.1.1 we provide the obtained reference BLER curves in AWGN channel for all CQI and MCS formats, SISO configuration and for certain range of SNR values. The horizontal line at BLER= 10% which is drawn over the BLER reference curves defines the set of SINR thresholds to compare with the current channel ESNR and select the highest CQI and MCS values compatible with a BLER< 10%.

The Shannon capacity is the theoretical maximum information transfer rate that no real communication system can exceed given the SNR and bandwidth constraints. How close a real communication system comes to this bound can be used as a measure of its efficiency. Thus, in section section 5.1.2, we provide the AWGN link level performance relative to Shannon capacity which can be used as benchmark to understand the inherent limitations of the LTE/LTE-Advanced radio link.

Link adaptation aims to adapt the information data rate for each UE to its current channel capacity. In order to achieve link adaptation in the DL the UE reports to the eNodeB the measured DL channel quality in the form of a set of 15 possible CQIs; then the eNodeB selects the most appropriate MCS form a set of 28 different formats. The link adaptation strategy in terms of AMC based on the AWGN link level performance and the actual channel ESNR is provided in section 5.1.3.

5.1.1 BLER performance

In this section, we provide the basic AWGN link level performance in terms of BLER for each CQI and MCS scheme of LTE/LTE-Advanced. In order to obtain the reference BLER curves for all CQI and MCS values, simulations in AWGN channel were performed using the LTE link level simulator in SISO mode. These results validate the simulator against previously published results in the literature, [34, 11]. The simulated SNR is described in section 3.4.3 where it is shown that the subcarrier average SNR is equal to select the wideband average SNR.

5.1.1.1 Reference BLER curves for the LTE CQIs

The CQI is the LTE feedback reported by the UE to eNodeB which indicates the modulation and code rate that allows to demodulate and decode the transmitted DL data with a maximum BLER of 10% conditioned to the actual channel conditions. Based on this CQI, the eNodeB uses link adaptation to the optimum MCS.

The modulation and coding rate for each CQI are shown in Table 2.1 which is specified in [33]. A finite set of valid turbo code block sizes which range from 40 bits to 6144 bits is defined in [4]. Figure 5.1 shows the AWGN BLER curves of the LTE CQIs without HARQ (i.e. at rv= 0) for a bandwidth of 1 and 25 physical RBs. The set of reference BLER curves is dependent on the bandwidth allocated to the UE, since the more physical RBs are available the higher is the turbo code block size that can be applied. It can be noticed that the BLER curves are spaced by 2 dB approximately and that the curves for 25 RBs show a steeper slope due to the larger code block sizes.

Table 5.1 and Figure 5.2 show the SNR needed for a BLER performance of 10% at rv= 0 in SISO AWGN channel for each CQI in a bandwidth of 1, 4 and 25 RBs. The BLER = 10% defines the set of SNR thresholds to compare with the current channel ESNR and select the highest CQI compatible with a BLER< 10%.

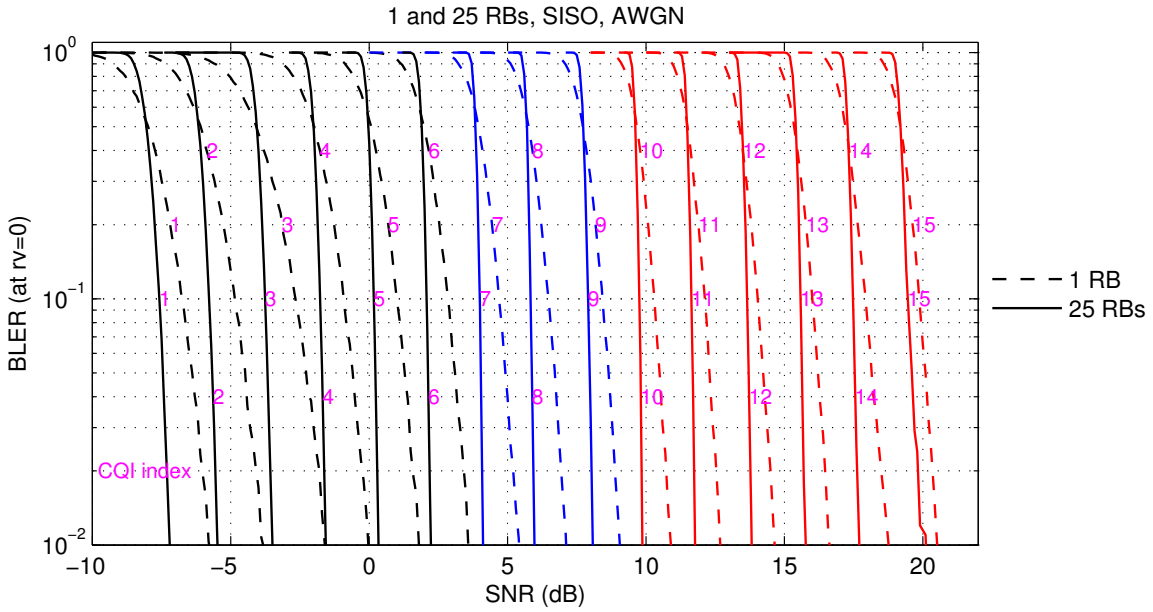

Figure 5.1: AWGN BLER curves of the LTE CQIs without HARQ

Table 5.1: SNR needed for BLER=10% at rv= 0 in SISO AWGN channel for the LTE CQIs

CQI index	Mod.	Mod. Order Q_m	Code Rate	Number of allocated RBs 1 RB $SNR_{10\%}$	4 RBs $SNR_{10\%}$	25 RBs $SNR_{10\%}$
1	QPSK	2	0.076	-6.76	-6.93	-7.58
2	QPSK	2	0.117	-4.85	-5.21	-5.78
3	QPSK	2	0.189	-2.66	-3.31	-3.76
4	QPSK	2	0.301	-0.92	-1.45	-1.77
5	QPSK	2	0.439	1.00	0.48	0.17
6	QPSK	2	0.588	2.85	2.35	2.07
7	16QAM	4	0.369	4.69	4.23	3.99
8	16QAM	4	0.478	6.48	6.06	5.83
9	16QAM	4	0.602	8.43	8.03	7.91
10	64QAM	6	0.455	10.31	9.86	9.76
11	64QAM	6	0.554	12.13	11.75	11.64
12	64QAM	6	0.650	14.03	13.64	13.65
13	64QAM	6	0.754	16.01	15.54	15.58
14	64QAM	6	0.853	17.93	17.47	17.48
15	64QAM	6	0.926	19.87	19.39	19.46

5.1.1.2 Reference BLER curves for the LTE MCSs

Figures 5.4 and 5.5 show the AWGN reference BLER curves for rv= 0 for all MCS formats in a bandwidth of 4 and 25 RBs, respectively. A single antenna at the transmitter side is also assumed, thus each codeword is mapped onto one single layer and 8 reserved REs per RB and TTI

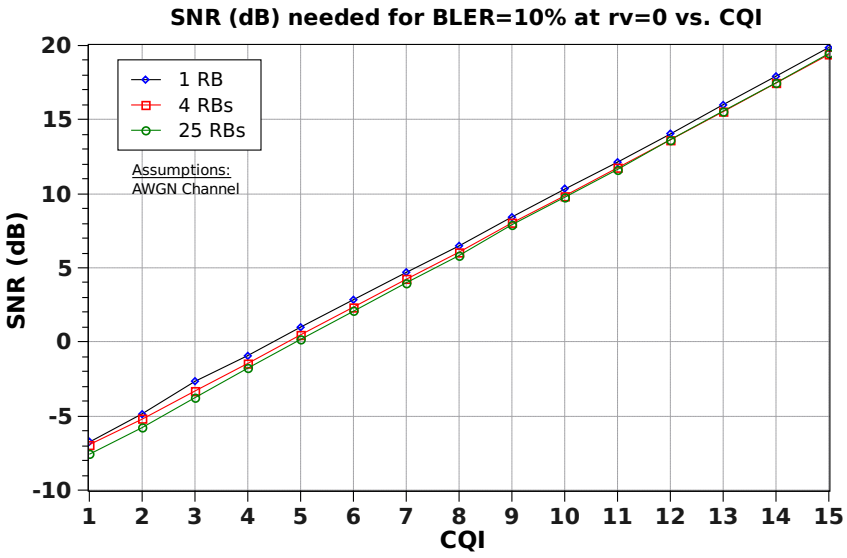

Figure 5.2: SNR needed for BLER=10% at rv= 0 in SISO AWGN channel for the LTE CQIs

are used for pilot signals. Table 5.2 shows the modulation order and the ECR (see Equation 3.4) of the channel encoder for each MCS format. The allocated bandwidth determines the number of OFDM subcarriers available for transmission, and thus the size of the code block that can be transmitted in a single TTI for a given MCS index. The bigger the code block size the steeper is the slope of the reference BLER curves. The shape of the curves is very similar, since they are almost parallel, and once the modulation is fixed it is the ECR what determines the SNR needed for a given BLER target. In addition, it can be noticed that the curves are regularly spaced in intervals of approximately 1 dB, except for MCS 10 and 17 where the space with respect to the next BLER curve is about 0.5 dB. Table 5.2 and Figure 5.3 show the SNR needed for a BLER performance of 10% at rv= 0 in SISO AWGN channel for each MCS in a bandwidth of 1, 4 and 25 RBs.

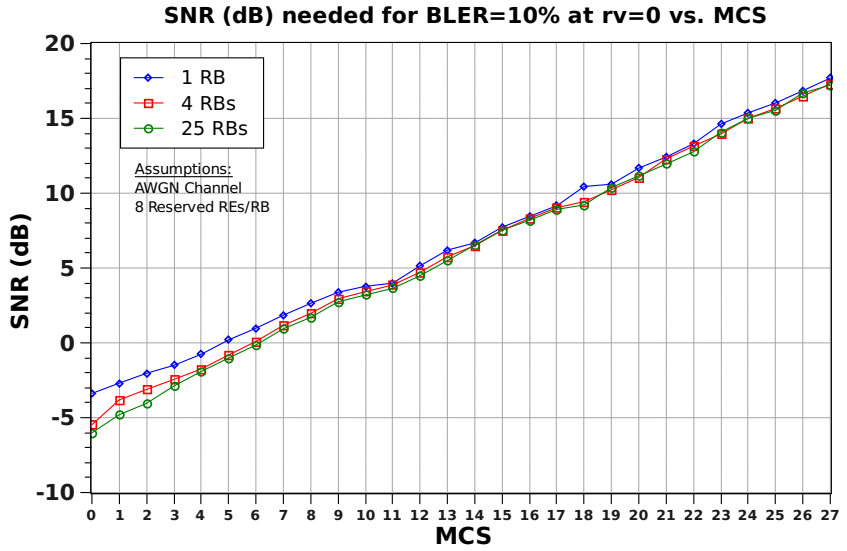

Figure 5.3: SNR needed for BLER=10% at rv= 0 in SISO AWGN channel for the LTE MCSs

Table 5.2: SNR needed for BLER=10% at rv= 0 in SISO AWGN channel for the LTE MCSs

MCS		Mod.	Number of allocated RBs					
		Order	1 RB		4 RBs		25 RBs	
index	Mod.	Q_m	η_{ECR}	$SNR_{10\%}$	η_{ECR}	$SNR_{10\%}$	η_{ECR}	$SNR_{10\%}$
0	QPSK	2	0.16	-3.38	0.11	-5.47	0.11	-6.01
1	QPSK	2	0.19	-2.69	0.17	-3.81	0.15	-4.80
2	QPSK	2	0.22	-2.03	0.20	-3.11	0.18	-4.04
3	QPSK	2	0.25	-1.50	0.23	-2.44	0.23	-2.88
4	QPSK	2	0.32	-0.76	0.28	-1.74	0.29	-1.91
5	QPSK	2	0.38	0.20	0.35	-0.81	0.36	-1.01
6	QPSK	2	0.44	0.98	0.41	0.10	0.42	-0.14
7	QPSK	2	0.51	1.85	0.49	1.17	0.50	0.94
8	QPSK	2	0.57	2.64	0.56	1.97	0.56	1.70
9	QPSK	2	0.63	3.38	0.63	2.95	0.64	2.74
10	16QAM	4	0.32	3.78	0.32	3.42	0.32	3.20
11	16QAM	4	0.33	3.99	0.35	3.87	0.35	3.64
12	16QAM	4	0.40	5.15	0.40	4.72	0.40	4.49
13	16QAM	4	0.46	6.20	0.46	5.76	0.46	5.50
14	16QAM	4	0.49	6.68	0.51	6.49	0.52	6.54
15	16QAM	4	0.56	7.73	0.57	7.52	0.58	7.53
16	16QAM	4	0.60	8.45	0.62	8.32	0.62	8.19
17	64QAM	6	0.40	9.16	0.41	9.03	0.41	8.92
18	64QAM	6	0.47	10.45	0.43	9.44	0.43	9.22
19	64QAM	6	0.48	10.60	0.48	10.23	0.49	10.38
20	64QAM	6	0.53	11.68	0.52	11.06	0.53	11.16
21	64QAM	6	0.57	12.42	0.58	12.30	0.57	11.95
22	64QAM	6	0.61	13.31	0.62	13.15	0.61	12.77
23	64QAM	6	0.68	14.62	0.67	13.96	0.67	14.08
24	64QAM	6	0.72	15.37	0.72	15.01	0.72	15.01
25	64QAM	6	0.76	16.03	0.76	15.66	0.75	15.54
26	64QAM	6	0.80	16.85	0.80	16.49	0.81	16.70
27	64QAM	6	0.85	17.69	0.85	17.31	0.84	17.22

Figures 5.6 and 5.7 show the AWGN reference BLER curves for rv= 1 for all MCS formats in a bandwidth of 4 and 25 RBs, respectively. After the second HARQ transmission (i.e. at rv= 1), the effective code rate is halved with respect to the code rate for rv= 0. It can be verified that this leads to a shift of 3 dB in the reference BLER curves for rv= 1 (vs. the same curves for rv= 0) for $0 \leq$ MCS index ≤ 4. This is because for a code rate $\leq 1/3$ the whole codeword is already transmitted for rv= 0; then for rv= 1 the effective code rate is increased by simply repeating again the whole codeword, which is equivalent to doubling the SNR. On the other hand, for a high code rate (e.g. code rate = 0.89 in MCS index 27), a very important gain of about 8 dB is obtained by halving the effective code rate at rv= 1. This is because for rv= 0 practically only systematic bits are sent and so there is a very limited error correction capability, while for rv= 1 many redundant bits are sent which suddenly provides much better error correction by using the combined LLRs.

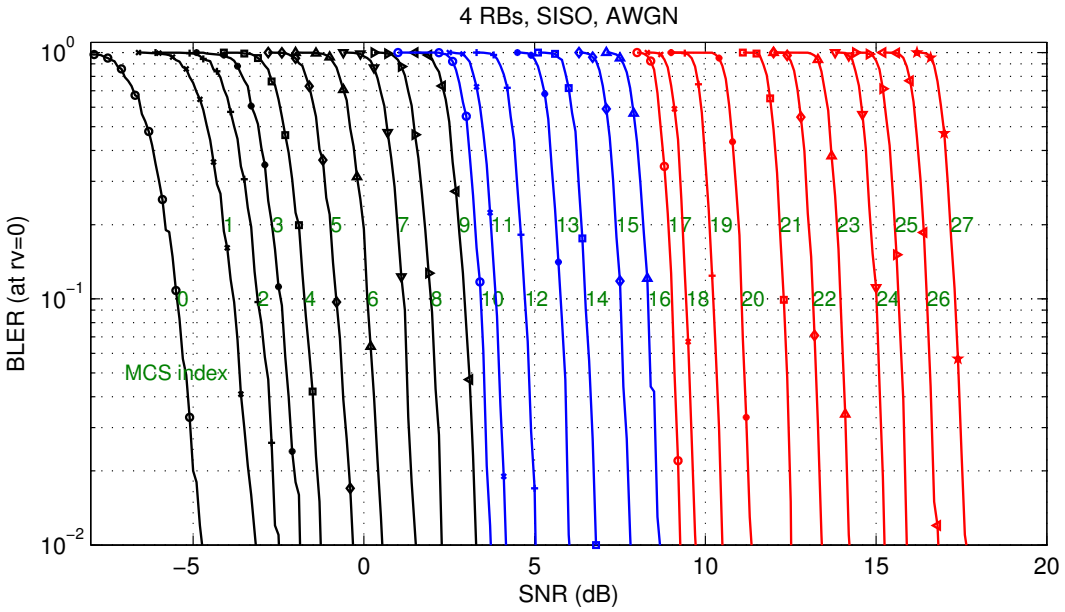

Figure 5.4: LTE DL AWGN Reference BLER (rv= 0) for all MCS formats (4 RBs)

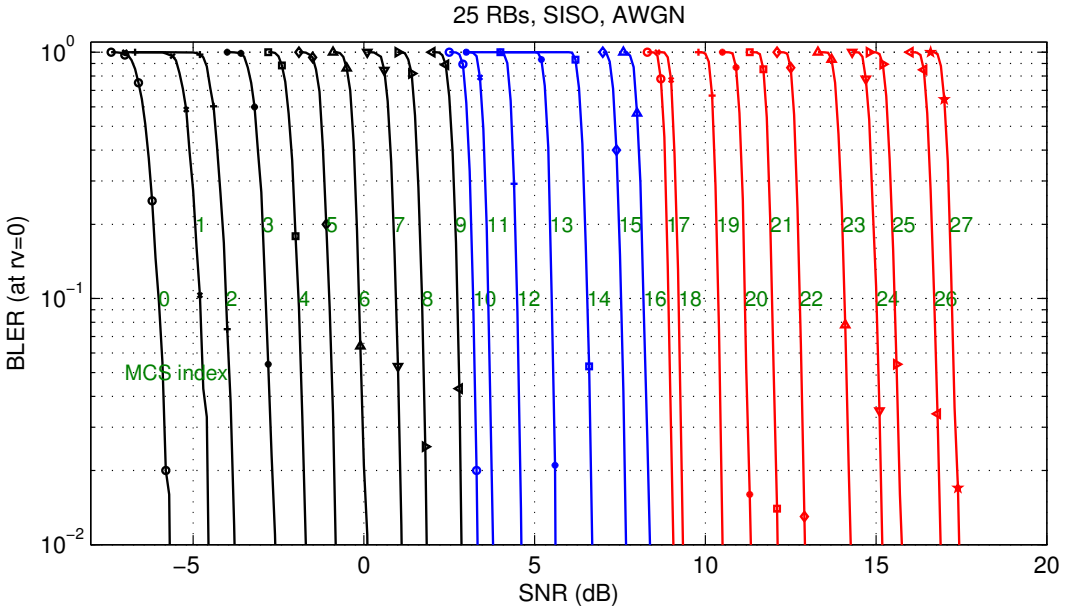

Figure 5.5: LTE DL AWGN Reference BLER (rv= 0) for all MCS formats (25 RBs)

Figures 5.8 and 5.9 show the AWGN reference BLER curves for rv= 2 and Figures 5.10 and 5.11 show the AWGN reference BLER curves for rv= 3 for all MCS formats in a bandwidth of 4 and 25 RBs, respectively. Lastly, Figure 5.12 plots the reference BLER curves for rv $= 0, 1, 2, 3$ for MCS indexes 9, 16 and 27 for a bandwidth of 25 RBs in AWGN SISO channel. In Figure 5.12 the SNR gain due to the effective code rate reduction is clearly visible for the MCSs with the highest code rate for each modulation scheme, but these curves assume equal SNR per rv, which is not

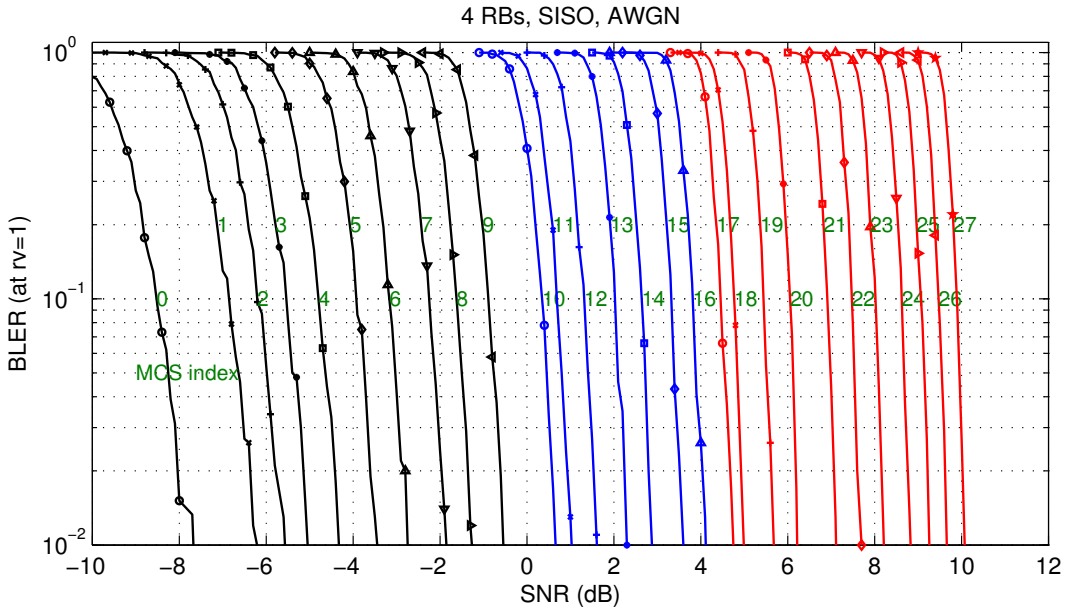

Figure 5.6: LTE DL AWGN Reference BLER (rv= 1) for all MCS formats (4 RBs)

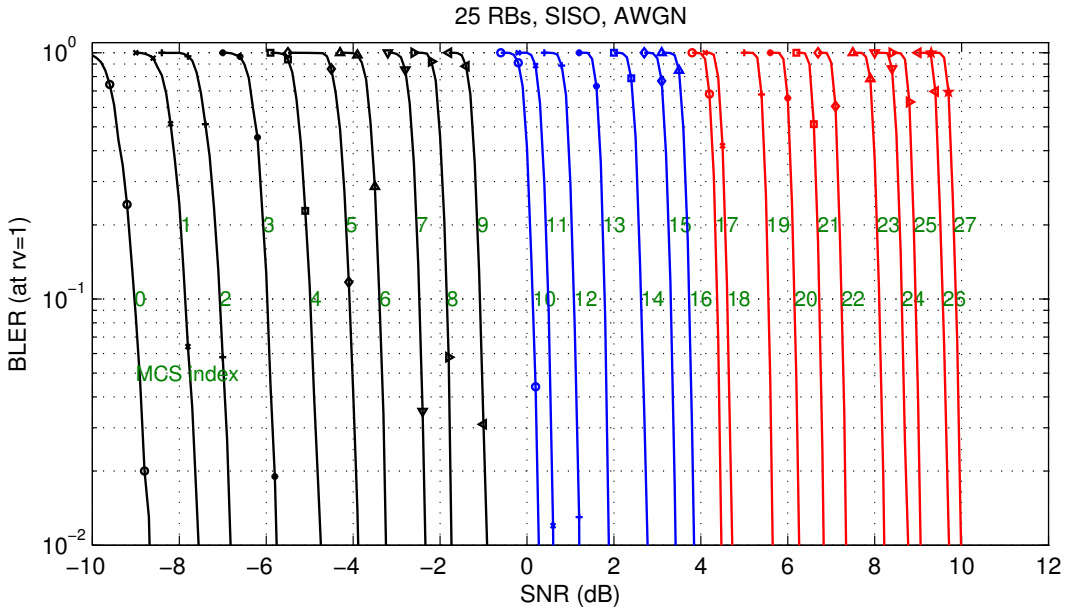

Figure 5.7: LTE DL AWGN Reference BLER (rv= 1) for all MCS formats (25 RBs)

necessarily the real situation.

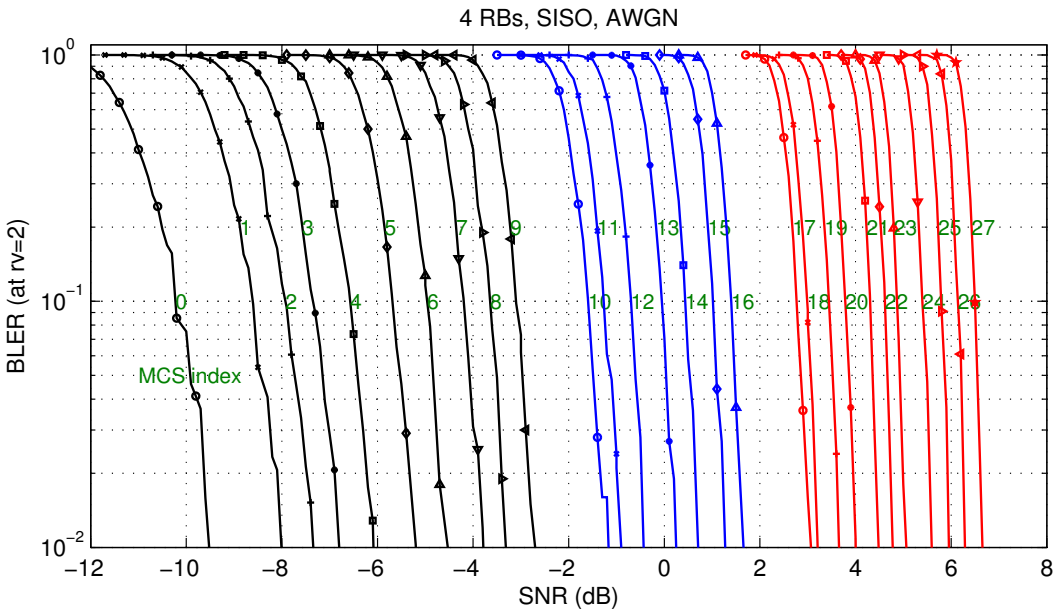

Figure 5.8: LTE DL AWGN Reference BLER (rv= 2) for all MCS formats (4 RBs)

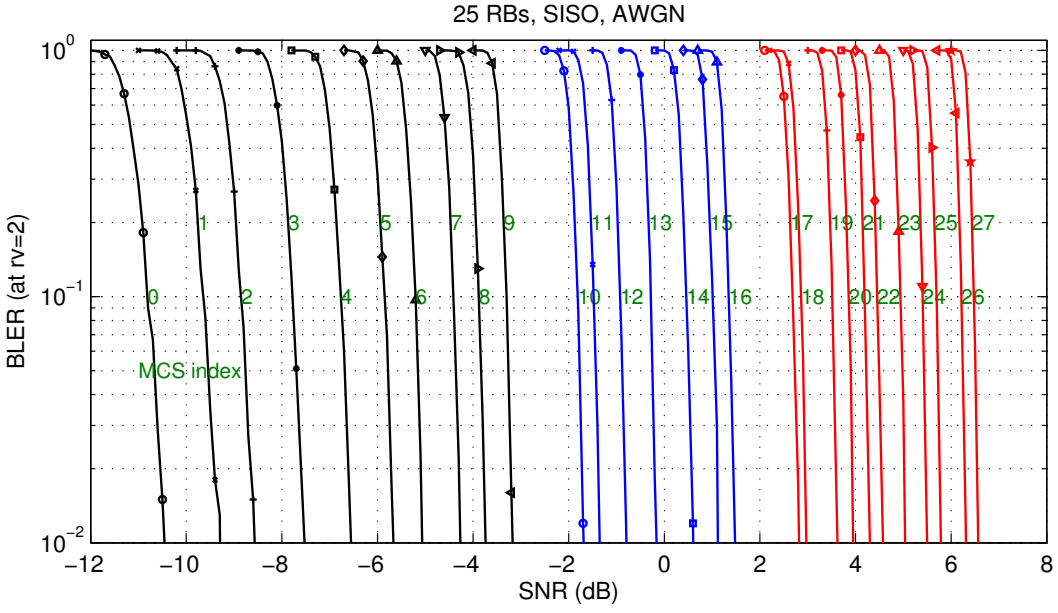

Figure 5.9: LTE DL AWGN Reference BLER (rv= 2) for all MCS formats (25 RBs)

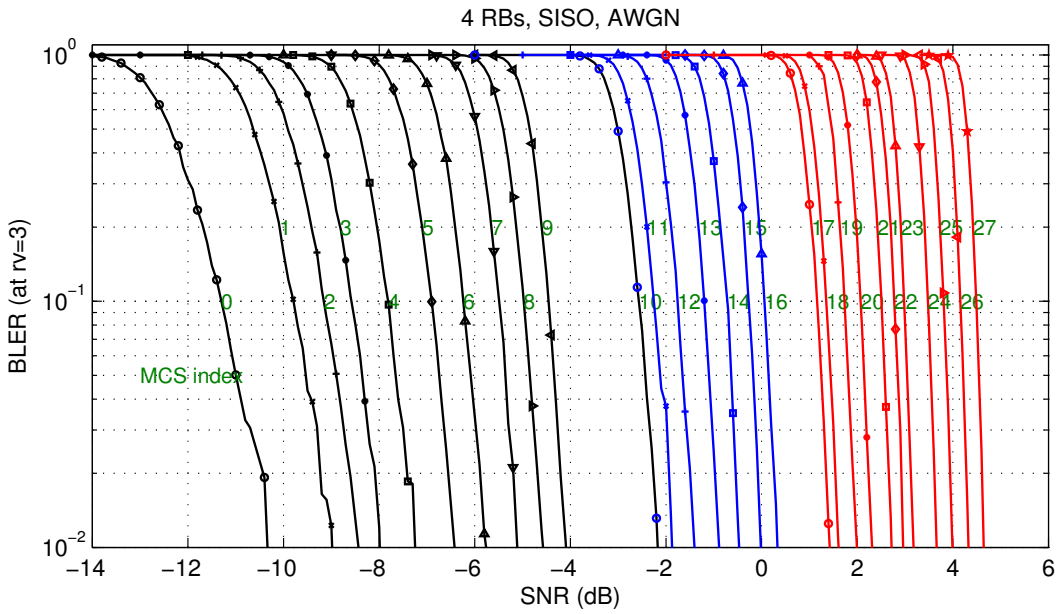

Figure 5.10: LTE DL AWGN Reference BLER (rv= 3) for all MCS formats (4 RBs)

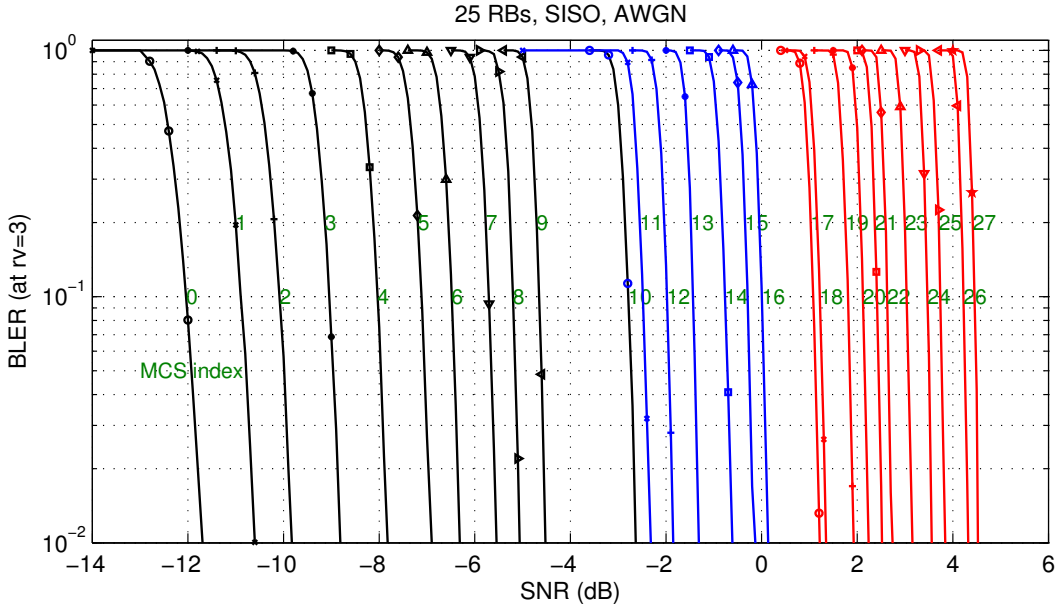

Figure 5.11: LTE DL AWGN Reference BLER (rv= 3) for all MCS formats (25 RBs)

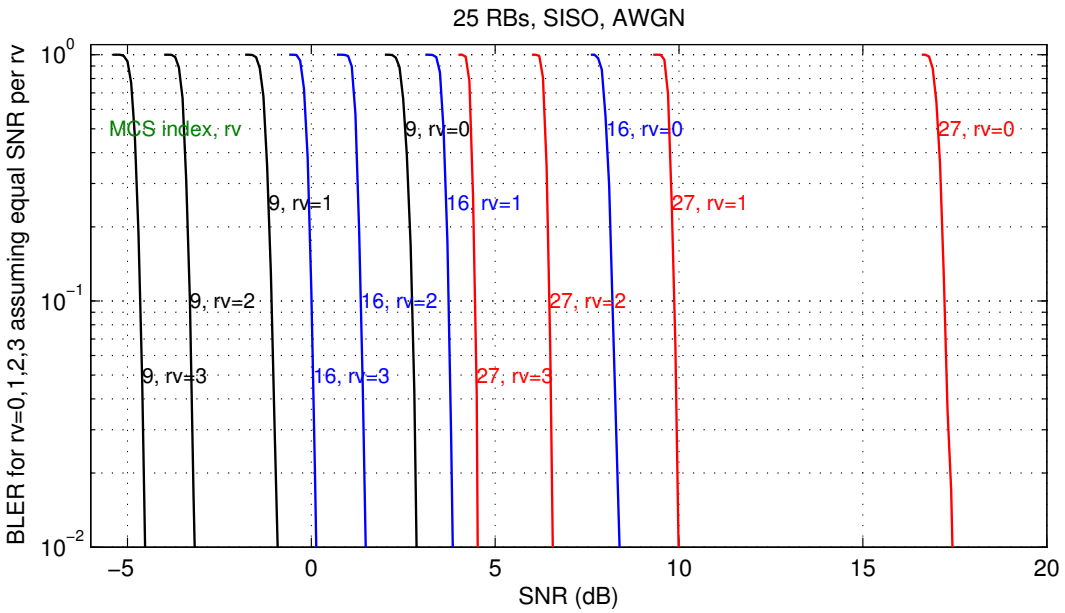

Figure 5.12: AWGN BLER for the different rvs (assuming equal SNR per rv) for MCS index 9, 16 and 27 (25 RBs)

5.1.2 Capacity and Net Throughput

In LTE, AMC has to ensure a BLER value smaller than 10% at rv= 0. The SNR at a BLER of 10% ($SNR_{10\%}$) can thus be obtained from the AWGN reference BLER curves at rv= 0. Figures 5.13 and 5.14 plot the $SNR_{10\%}$ values and the BICM thresholds over the BLER vs. SNR curves with circle, triangle and square marks, respectively, for QPSK, 16QAM and 64QAM modulation schemes for a bandwidth of 4 and 25 RBs, respectively. These values are used to compute the capacity and the net throughput.

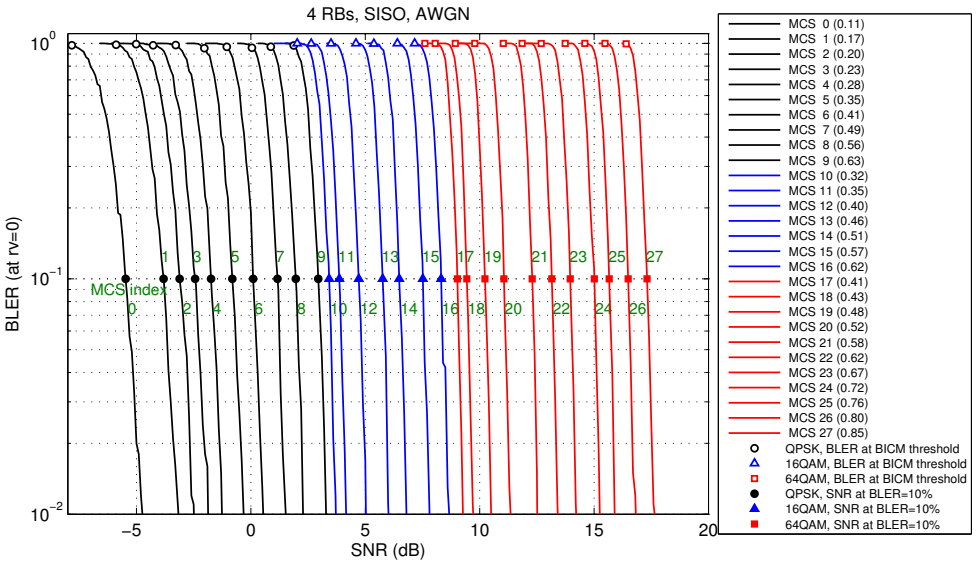

Figure 5.13: BLER curves at rv=0 and BICM SNR thresholds for all MCS indexes in AWGN channel in a bandwidth of 4 RBs

Figure 5.15 shows the SNR needed to achieve a target BLER of 10% for rv= 0 in AWGN channel in a bandwidth of 1, 4 and 25 RBs. It can be verified that increasing the MCS index by one increases the SNR target by about 1 dB, in accordance with the shift between the BICM thresholds of approximately 1 dB as shown in Tables 3.1 and 3.4.

The BLER curves are used to obtain the spectral efficiency per transmitted coded bit by computing $(1-BLER)\cdot r$, where r is the effective code rate that corresponds to the conveyed information (in bits) per received coded bit (or LLR). The MI curves shown in Figure 2.16 represents the capacity of the LTE modulation coding schemes with BICM. This capacity can be interpreted as the code rate necessary (assuming an ideal code) to achieve a BLER of zero for a given SNR called the BICM threshold. The Shannon capacity is the theoretical maximum information transfer rate of the channel for a given SNR. As a result, Figure 5.16 summarizes the SISO link level performance in AWGN channel from an information transfer point of view for all the MCS formats in a bandwidth of 4 RBs and 25 RBs taking into account 8 REs per RB for pilot signals. The circle (QPSK), triangle (16QAM) and rhomb (64QAM) marks placed over the modulation capacity curves relate the effective code rate to the BICM SNR threshold for each MCS format (identified by the numbers near the marks). Those points are the absolute capacity limits of the different formats from an information theory point of view.

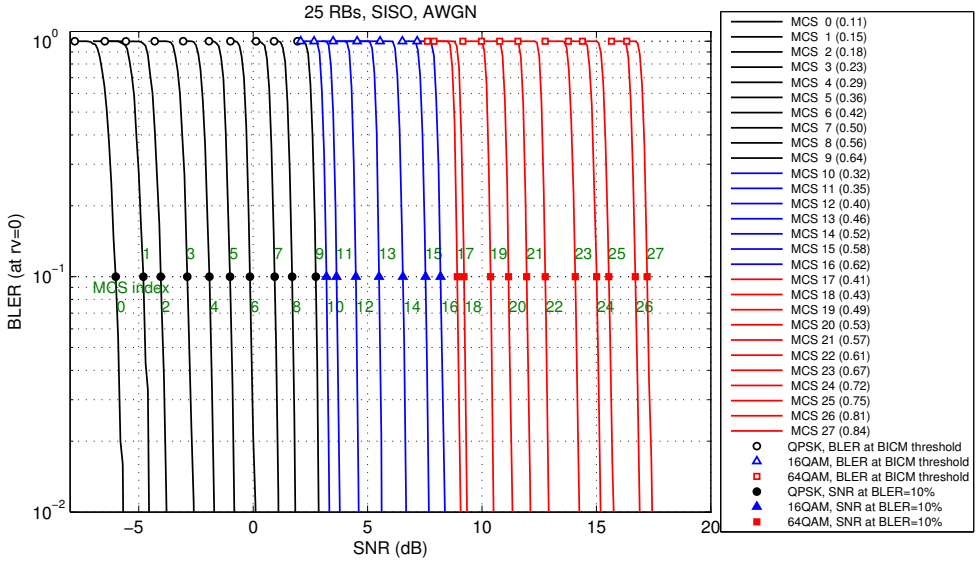

Figure 5.14: BLER curves at rv=0 and BICM SNR thresholds for all MCS indexes in AWGN channel in a bandwidth of 25 RBs

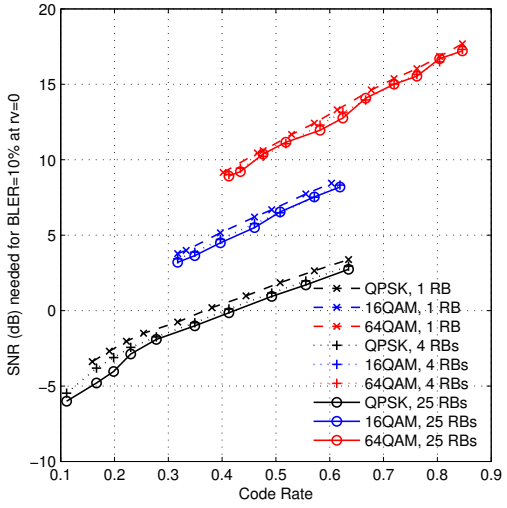

Figure 5.15: SNR (dB) needed to achieve BLER= 10% at rv= 0 for AWGN Channel and 8 Reserved REs/RB

In Figure 5.16, the square (QPSK), asterisk (16QAM) and star (64QAM) marks relate the net throughput (net transferred information rate in bits/LLR) to the SNR threshold for a BLER of 10% ($SNR_{10\%}$) obtained from the results shown in Figures 5.13 and 5.14. Notice that for MCS formats 0 to 4, which imply bit repetition, a single coded bit may give rise to the reception of several LLRs. The net throughput at $SNR_{10\%}$ is 90% of the effective code rate of the MCS format. For MCS 9 in a bandwidth of 4 RBs, for example, the coordinates of the circle mark are $(1.87, 0.63)$ since the BICM threshold is 1.87 dB and the effective code rate is 0.63. The coordinates of the plus and square marks are $(2.95, 0.567)$ because for the $SNR_{10\%}$ of 2.95 dB the net throughput is

$0.9 \cdot 0.63 = 0.567$ bits/LLR.

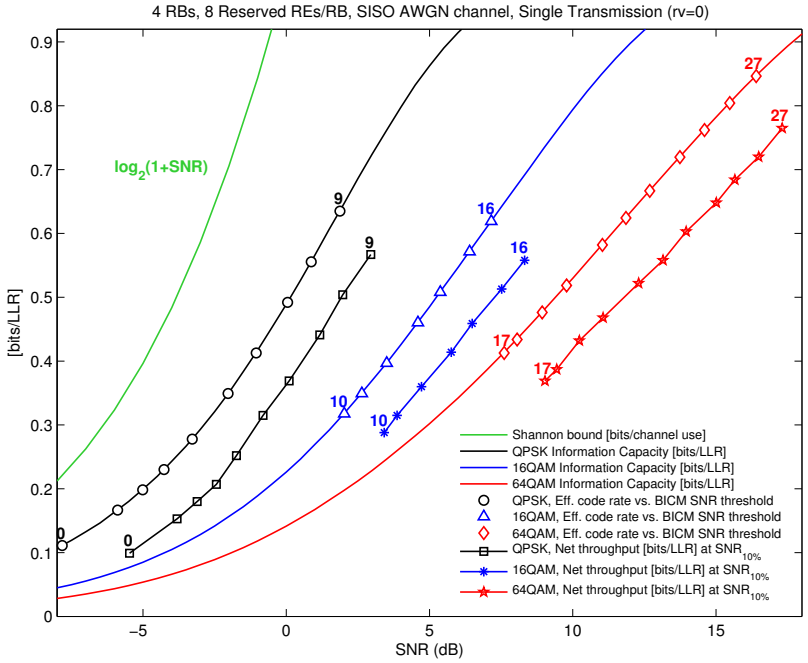

(a) 4 RBs

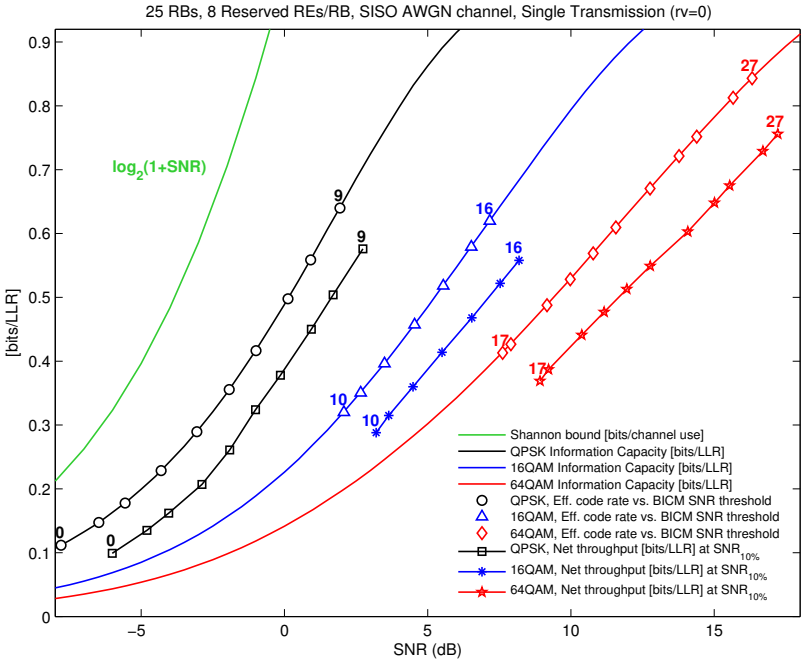

(b) 25 RBs

Figure 5.16: Capacity and net throughput for all MCS indexes (6 REs/RB) in AWGN channel.

5.1.3 E-UTRA AMC Spectral Efficiency for Link Adaptation

The spectral efficiency is a measure of how efficiently the channel is utilized by the physical layer and it can be improved by using radio resource management techniques. Link adaptation is one of them and it is performed via AMC. One of the parameters to be configured by the AMC at the eNodeB is the MCS to be used for DL transmission. The CQI is the LTE feedback reported by the UE to eNodeB which indicates the modulation and code rate that allows to demodulate and decode the transmitted DL data with a maximum BLER of 10% conditioned to the actual channel conditions. Based on this CQI, the eNodeB uses link adaptation to select the optimum MCS.

The spectral efficiency for the LTE DL link adaptation can be related to the link level performance in SISO AWGN channel by means of the ESNR. Hence, the spectral efficiency for SISO mode is calculated as follows:

$$C = Q_m \cdot r \cdot (1 - \text{BLER}(ESNR)) = C_{max} \cdot (1 - \text{BLER}_{\text{AWGN}}(ESNR, r)) \ \text{[bit/s/Hz]} \tag{5.1}$$

where Q_m is the modulation order and r is the code rate. For QPSK, 16QAM and 64QAM, Q_m is 2, 4 and 6 *bits/symbol* respectively. The code rate of the selected MCS, $r = \eta_{ECR}$, is defined in Equation 3.4. BLER $(ESNR)$ is the BLER for the ESNR of the actual multistate channel that can be predicted by $\text{BLER}_{\text{AWGN}}(ESNR, \eta_{ECR})$ as described in section 6.3.4 using the reference BLER curve and η_{ECR} for the selected MCS. The maximum spectral efficiency which can be achieved in the case of an error-free communication is $C_{max} = Q_m \cdot r$.

Figure 5.17 shows the spectral efficiencies vs. SNR in AWGN channel without HARQ for each CQI index. The considered code block size is the maximum that fits in a bandwidth of 4 RBs. It can be observed that, in order to keep maximum spectral efficiency, the CQI must be changed when the SNR increases or decreases by a few dB, about 2 dB.

UE feedbacks the best CQI index that maximizes the spectral efficiency according to the actual channel state as follows:

$$\text{CQI} = \arg\max_{\text{CQI}} (Q_m \cdot r \cdot (1 - \text{BLER}_{\text{AWGN}}(ESNR, \eta_{ECR}))) \tag{5.2}$$

where r is the code rate and Q_m is the modulation order both given by the CQI index tabulated in Table 5.1. Assuming AWGN channel, the SNR is the same for all subcarriers, thus ESNR=SNR.

As the code rate (r) of the reported CQI is known, the eNodeB can estimate the ESNR of the actual channel assuming $\text{BLER}_{\text{AWGN}}(ESNR, r) = 0.1$. Thus, given an ESNR, the code rate and the modulation order reported by the CQI, the eNodeB selects the best MCS that maximizes the spectral efficiency as follows:

$$\text{MCS} = \arg\max_{\text{MCS}} (Q_m \cdot \eta_{ECR} \cdot (1 - \text{BLER}_{\text{AWGN}}(ESNR, \eta_{ECR}))) \tag{5.3}$$

where η_{ECR} is the ECR of the MCS and $\text{BLER}_{\text{AWGN}}(ESNR, \eta_{ECR}) \leq 0.1$. Tables 5.1 and 5.2 show the SNR needed for a BLER performance of 10% in SISO AWGN channel for each CQI and MCS, respectively. It is assumed a bandwidth of 1, 4 and 25 RBs, one layer per codeword, 11 PDSCH OFDM symbols per subframe and 8 reserved RE per RB are considered to compute the ECR for each MCS.

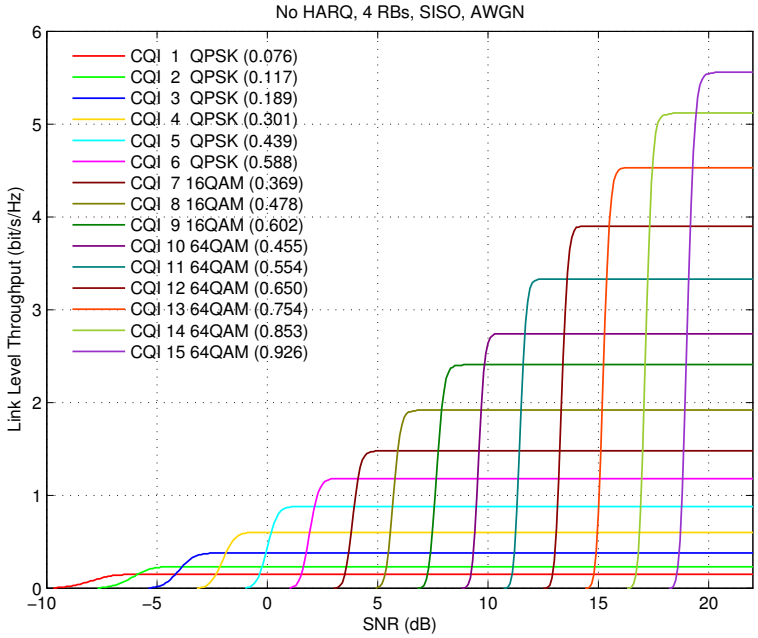

Figure 5.17: AWGN SISO channel.

Figure 5.18 shows the spectral efficiencies vs. SNR in AWGN channel without HARQ for each MCS. It is considered the code rate and code size that result from the mapping of one codeword onto one layer with only one transmit antenna, a bandwidth of 4 RBs and 8 reserved REs per RB. It can be observed that, in order to keep maximum spectral efficiency, the MCS must be changed when the SNR increases or decreases by a few dB (usually less than 1 dB). In comparison, Figure 5.19 shows the spectral efficiencies vs. SNR in AWGN channel with HARQ and assuming the same SNR for each retransmission. It can be observed that now, since HARQ has smoothed the curves, it is possible to keep nearly the optimum throughput without frequent changes in the MCS format.

Figure 5.20 shows the bound of the maximum spectral efficiency for each modulation. It can be observed that the SNR gap between the curves of the Shannon capacity and the maximum spectral efficiency achieved by the link adaptation (i.e. selecting the best MCS) is around 2.5 dB taking into account a useful SNR range from -5 dB to 17.5 dB.

The spectral efficiency curves can be used to determine the AMC thresholds for link adaptation to achieve the maximum spectral efficiency. Table 5.3 shows the BICM thresholds and AMC thresholds in AWGN channel for each MCS and considering a bandwidth of 1, 4 and 25 RBs. Finally, Figures 5.21, 5.22 and 5.23 show graphically the AMC thresholds for each MCS (numbers in black) vs. the AMC thresholds for each CQI (numbers in colour).

Table 5.3: BICM thresholds and AMC thresholds in SISO AWGN channel (1 layer/codeword, 8 Reserved REs/RB and 11 PDSCH OFDM symbols per subframe)

		25 RBs			4 RBs			1 RB		
MCS	Mod. Order	ECR	BICM	AMC	ECR	BICM	AMC	ECR	BICM	AMC
index	Q_m	η_{ECR}	Thr.	Thr.	η_{ECR}	Thr.	Thr.	η_{ECR}	Thr.	Thr.
0	2	0,112	-7,80		0,111	-7,82		0,159	-6,12	
1	2	0,147	-6,48	-4,97	0,167	-5,89	-4,36	0,190	-5,22	-3,20
2	2	0,178	-5,56	-4,10	0,198	-5,01	-3,26	0,222	-4,45	-2,42
3	2	0,229	-4,30	-2,98	0,230	-4,27	-2,58	0,254	-3,76	-1,99
4	2	0,290	-3,06	-2,02	0,278	-3,28	-1,88	0,317	-2,56	-1,26
5	2	0,356	-1,93	-1,09	0,349	-2,03	-0,99	0,381	-1,53	-0,08
6	2	0,417	-0,99	-0,17	0,413	-1,05	0,04	0,444	-0,60	0,83
7	2	0,498	0,12	0,89	0,492	0,05	1,04	0,508	0,26	1,64
8	2	0,559	0,91	1,70	0,556	0,87	1,93	0,571	1,08	2,52
9	2	0,640	1,94	2,73	0,635	1,87	2,90	0,635	1,87	3,35
10	4	0,320	2,07	3,50	0,317	2,02	3,90	0,317	2,02	4,90
11	4	0,350	2,66	3,67	0,349	2,64	3,89	0,333	2,33	3,99
12	4	0,396	3,49	4,49	0,397	3,51	4,68	0,397	3,51	4,94
13	4	0,457	4,54	5,49	0,460	4,60	5,71	0,460	4,60	6,03
14	4	0,518	5,54	6,54	0,508	5,38	6,50	0,492	5,12	6,79
15	4	0,579	6,52	7,54	0,571	6,40	7,51	0,556	6,15	7,70
16	4	0,620	7,17	8,24	0,619	7,16	8,36	0,603	6,91	8,48
17	6	0,413	7,61	9,30	0,413	7,61	9,60	0,402	7,38	10,30
18	6	0,427	7,91	9,29	0,434	8,06	9,54	0,466	8,72	10,36
19	6	0,488	9,16	10,38	0,476	8,93	10,26	0,476	8,93	10,75
20	6	0,528	9,98	11,19	0,519	9,78	11,08	0,529	9,99	11,67
21	6	0,569	10,78	11,99	0,582	11,03	12,29	0,571	10,83	12,55
22	6	0,610	11,57	12,80	0,624	11,86	13,21	0,614	11,65	13,41
23	6	0,670	12,76	14,09	0,667	12,69	14,02	0,677	12,90	14,64
24	6	0,721	13,77	15,05	0,720	13,74	15,06	0,720	13,74	15,54
25	6	0,752	14,39	15,63	0,762	14,60	15,76	0,762	14,60	16,18
26	6	0,813	15,66	16,74	0,804	15,48	16,58	0,804	15,48	17,02
27	6	0,843	16,33	17,30	0,847	16,40	17,42	0,847	16,40	17,91

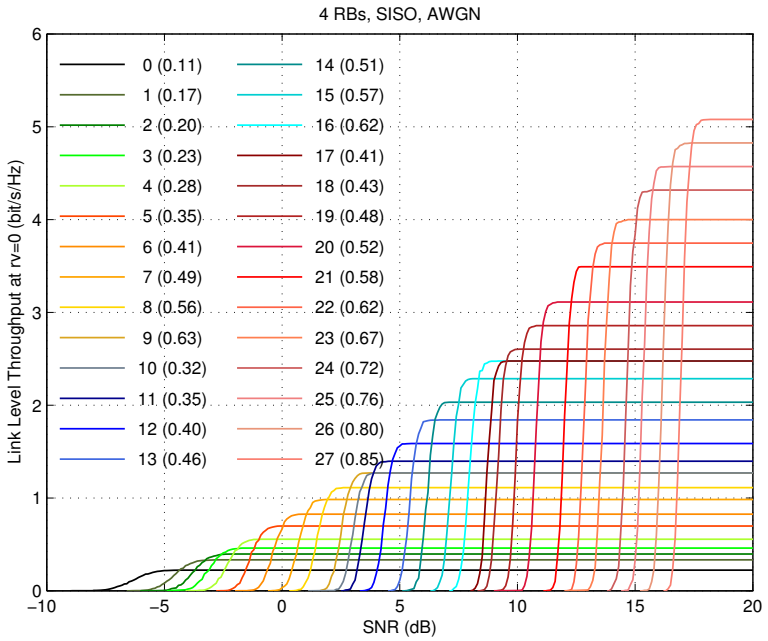

Figure 5.18: Spectral Efficiency for the LTE MCSs in SISO AWGN channel without HARQ (1 codeword mapped onto 1 layer, 1 transmit antenna, a bandwidth of 4 RBs and 8 reserved REs per RB)

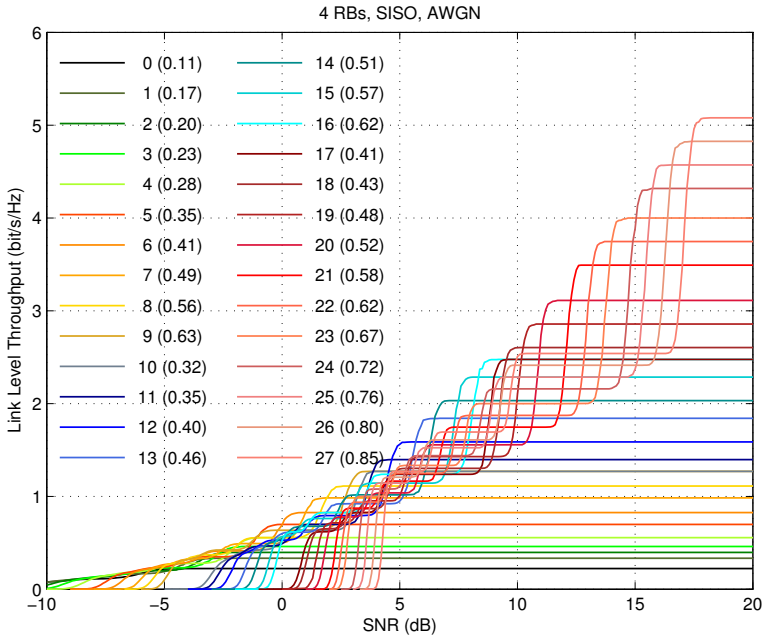

Figure 5.19: Spectral Efficiency for the LTE MCSs in SISO AWGN channel with HARQ (1 codeword mapped onto 1 layer, 1 transmit antenna, a bandwidth of 4 RBs and 8 reserved REs per RB)

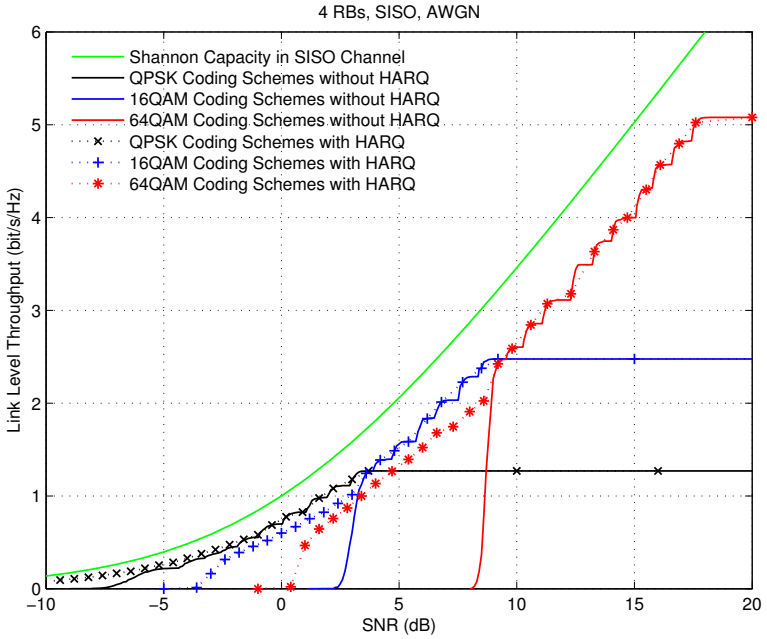

Figure 5.20: Spectral Efficiency for the LTE modulation schemes at rv=0 (4 RBs and 8 reserved REs/RB) in AWGN SISO channel

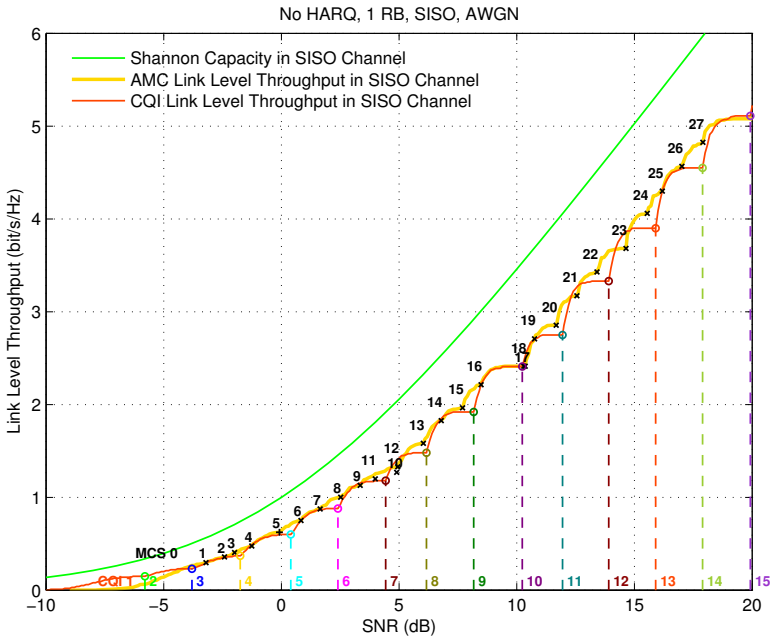

Figure 5.21: AMC thresholds for each MCS (numbers in black) and each CQI (numbers in colour) in AWGN SISO channel for 1 RB without HARQ (at rv= 0)

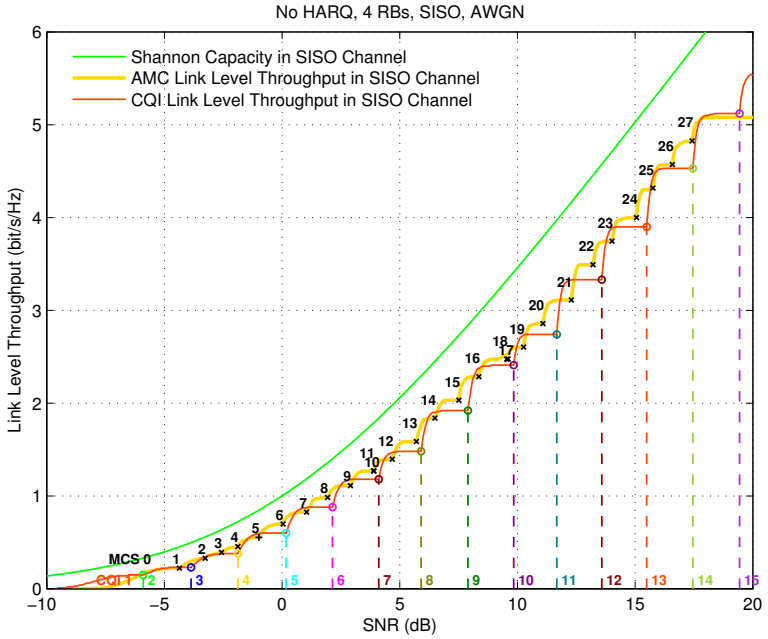

Figure 5.22: AMC thresholds for each MCS (numbers in black) and each CQI (numbers in colour) in AWGN SISO channel for 4 RBs without HARQ (at rv= 0)

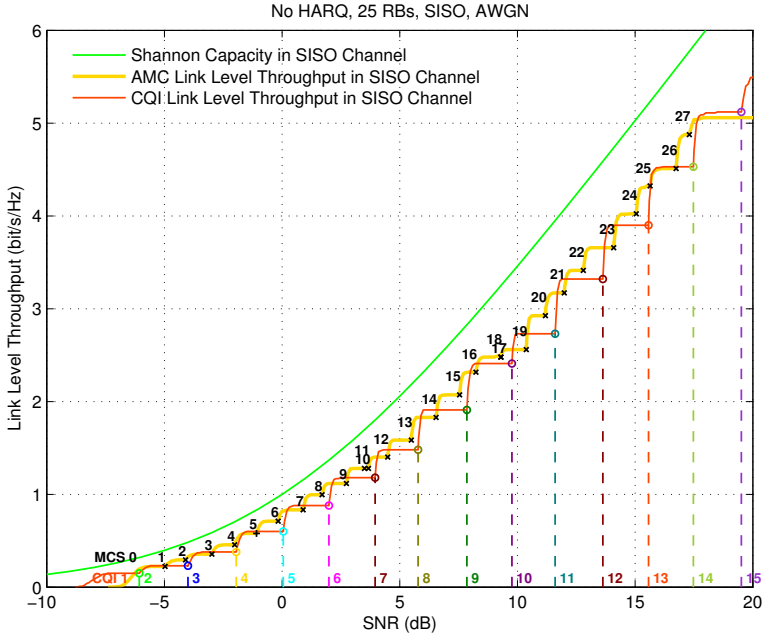

Figure 5.23: AMC thresholds for each MCS (numbers in black) and each CQI (numbers in colour) in AWGN SISO channel for 25 RBs without HARQ (at rv= 0)

5.2 Performance Evaluation of the different MIMO techniques

In this section, the LTE DL simulation results for the study of the performance of the different MIMO techniques described in Chapter 3 are presented. This study is based on the link level simulation carried out considering ideal channel estimation, i.e, the channel is perfectly known at each subcarrier. The 2×2 and 4×4 MIMO configurations with LC, MC and HC as well as the ETU channel model with 300 Hz maximum doppler frequency (ETU300), [19], have been considered.

The MIMO-SM detectors are ZF and MMSE with/without codeword-SIC and, for MIMO-TD, the Alamouti detector is used (see section 3.4.5). The codeword-to-layer mapping for MIMO-TD and MIMO-SM is shown graphically in Figures 3.29 and 3.28, respectively. The precoding schemes for MIMO-TD and MIMO-SM are described in sections 3.4.6.3 and 3.4.6.4, respectively. The performance of SISO and 1×2 SIMO is also shown for the sake of comparison. The SISO and SIMO detector which has been considered is the ZF one tap equalizer. In the case of SIMO configuration, MRC of all antenna branches is also applied. Table 5.4 summarizes the set of LTE DL link level simulator parameters which have been used for the simulations presented in this section.

Table 5.4: LTE DL link level simulator parameters

Parameter	**Value**
Carrier Frequency	2.14 GHz
Sub-carrier spacing	15 kHz
Number of sub-carriers per RB	12
Number of allocated RBs	4
TTI length	1 ms
Number of OFDM symbols per TTI	14 (11 PDSCH + 3 PDCCH)
Channel Model	AWGN and ETU300 [19]
Channel Coding	Turbo code basic rate 1/3
Rate Matching and HARQ	According to [4] Maximum of 4 IR transmissions
AMC formats	According to [33] MCS 0, 6, 12, 17, 27
Channel estimation	Ideal Channel Estimation
Antenna scheme	SISO and MIMO: 1×2, 2×2 and 4×4 for SU-MIMO configuration
MIMO Correlation	According to [19] LC, MC and HC
SISO Detector	ZF one tap equalizer
MIMO Detector	ZF, MMSE, Alamouti Detector

We assume ETU300 channel model and the ideal case of perfect channel estimation for the performance comparison of the proposed detectors for MIMO-SM. Although these assumptions are not a real case, the reason to consider ETU300 is that the simulation time, which comprises a certain number of channel coherence time intervals, is reduced because the ETU300 coherence

time is much lower than the EVA70 or EPA5 coherence time. Furthermore, working with ideal channel estimation leads to the ETU300 simulation results to be likely extrapolated to EVA70 and EPA5.

Since the goal is to evaluate the link level performance of the MIMO detector and not the gain due to turbo code size nor the performance of the HARQ processes, a bandwidth allocation of 4 RBs and rv= 0 have been set for a single user. The E-UTRA turbo code block size and the code rate are obtained as described in section 3.3.1. Table 5.5 shows the modulation and the code rate of the MCS indexes which have been used for the simulations presented in this section.

Table 5.5: Modulation and code rates of the MCS indexes used for the simulations

		Number of transmit antennas		
		1	2	4
MCS index	Modulation	Code rate	Code rate	Code rate
MCS 0	QPSK	0.11	0.12	0.13
MCS 6	QPSK	0.41	0.43	0.45
MCS 12	16QAM	0.40	0.42	0.44
MCS 17	64QAM	0.41	0.43	0.45
MCS 27	64QAM	0.85	0.89	0.93

Table 5.6 shows the acronyms used in the legends of the next figures to refer to the different combinations of the parameters of the different transmission modes which are listed below:

- Single Antenna Port, port 0, LTE DL TM 1: 1×2 SIMO configuration, ZF one tap equalizer and order 2 MRC at the receiver and only one transmitted codeword.
- MIMO-TD, LTE DL TM 2: 2×2 or 4×4 MIMO with SFBC (based on Alamouti Scheme) at the transmitter side and MRC at the receiver side and only one transmitted codeword.
- OL MIMO-SM, LTE DL TM 3: Large Delay CDD Precoding, with/without codeword-SIC and two transmitted codewords.
- CL MIMO-SM, LTE DL TM 4: Codebook-based precoding, with/without codeword-SIC and two transmitted codewords.
- CL MIMO-SM with SVD-based precoding, UPA at the transmitter side and two transmitted codewords.

Table 5.6: Meaning of the acronyms in figure legends

Acronym	Description
$N_{RX} \times M_{TX} cC$	N_{RX} receive antennas, M_{TX} transmit antennas and cC is the MIMO correlation level (LC, MC, HC)
CDD	OL with Large Delay CDD Precoding
CL(k)	CL with Codebook-based precoding per subcarrier
CL(1)	CL with Codebook-based precoding per Resource Block
SVD(UPA)	CL with SVD-based precoding and UPA
TD	TD
MRC	MRC at the receiver
SIC	codeword-SIC
c1	Codeword 1 in case of SM with two codewords
c2	Codeword 2 in case of SM with two codewords
Ideal C. E.	Ideal Channel Estimation

5.2.1 MIMO-TD

Figure 5.24 shows the BLER (at rv= 0) vs. mean SNR curves for MIMO-TD mode under ideal channel estimation. In LTE/LTE-Advanced, Alamouti scheme is applied in the frequency domain and, at least, two antennas at the UE are used to implement an order 2 MRC receiver diversity scheme. The TD precoding with two or four antenna ports is defined in [3] (see section 3.4.5.2) and only one codeword is transmitted. 2×2 and 4×4 MIMO modes have been considered under different antenna correlations, MCS formats 0, 12 and 27, ETU300 and EVA70 channel models and a bandwidth of 4 RBs. As a reference, the BLER performance of the LTE DL TM 1 and the SISO case are also depicted in Figure 5.24. The scheme for TM 1 consists of a single transmission antenna port and 2 receive antennas where order 2 MRC is applied. We observe that the baseline 1×2 SIMO antenna configuration always outperforms the SISO performance by a SNR gain higher than 4 dB for LC and 3 dB for MC and HC. For instance, focussing on a BLER of 10% and ETU300 channel model, the gain is 4.5 dB for MCS 0, 5 dB for MCS 12 and 7 dB for MCS 27 for LC. In contrast, the SNR gain is only 3 dB for MCS 0, 3.5 dB for MCS 12 and 5 dB for MCS 27 for correlated antennas (Notice that 1×2 SIMO with MC and HC achieves approximately the same BLER performance).

The 2×2 MIMO-TD configuration outperforms the 1×2 for LC and MC, but there is no noticeable difference for HC. This gain is due to the TD gain introduced by the Alamouti scheme. Focussing on MIMO configurations, the 4×4 MIMO-TD configuration outperforms the 2×2 for MCS 0 and 12. The reception for MIMO-TD assumes that the channel does not change between the two consecutive subcarriers where the SFBC is done (see section 3.4.5.2), and for the extreme case represented by MCS 27 and ETU300 channel model, this assumption leads to a BLER error floor at high SNR with the exception of LC case. In particular, for 2×2 and 4×4, MCS 27 and ETU300, a BLER (at rv= 0) of 10% cannot be achieved with MC and HC. In contrast, when EVA70 channel model is considered, the channel for two consecutive subcarriers is likely to be quite similar; thus, the BLER error floor is not appreciable below 30 dB of SNR.

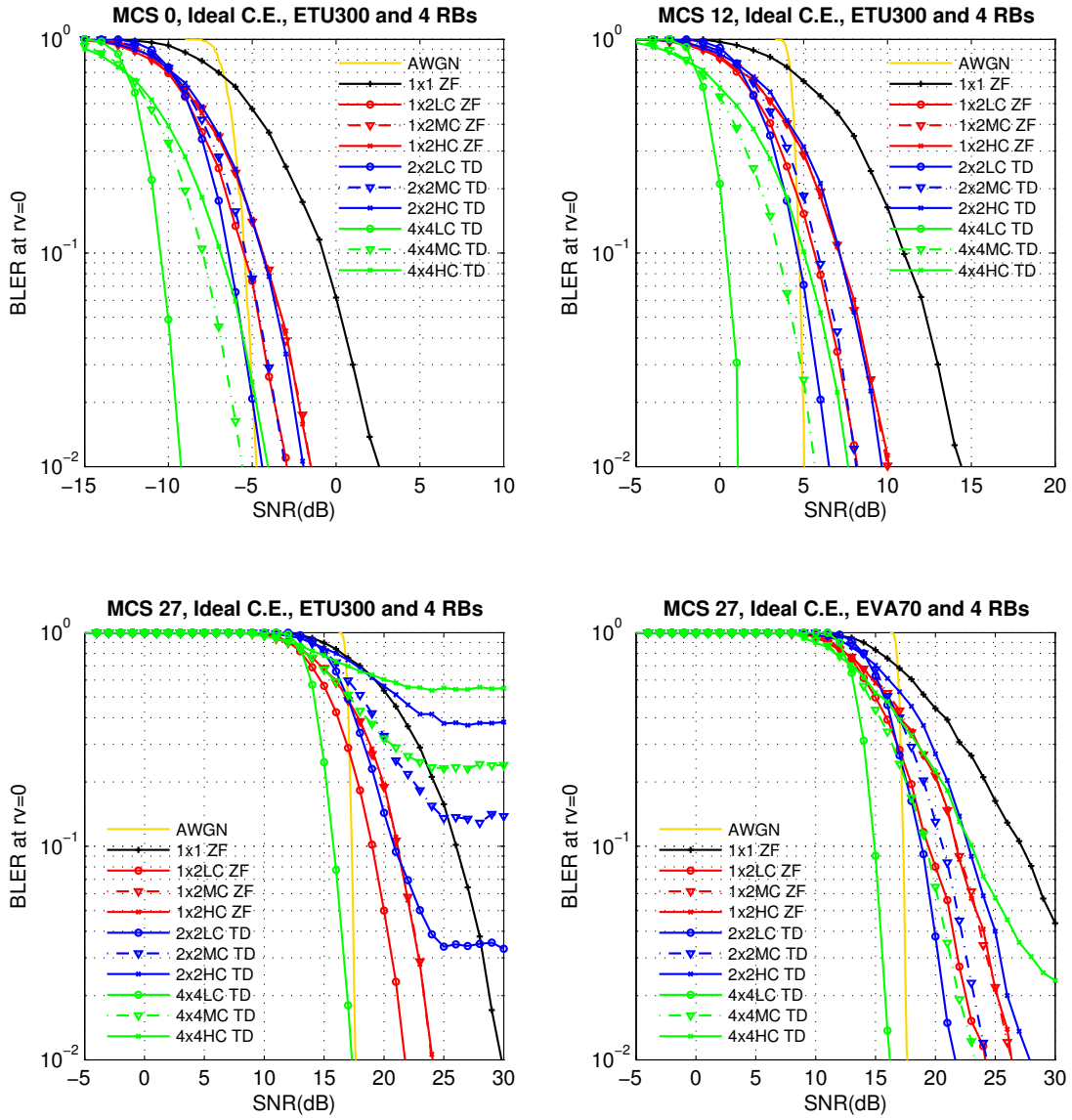

Figure 5.24: BLER (at rv= 0) vs. mean SNR for 2×2 and 4×4 MIMO-TD with MCS 0, 12 and 27 in ETU300 and MCS 27 in EVA70 with Ideal Channel Estimation in a bandwidth of 4 RBs

Note, however, that we have assumed the ideal case of perfect channel estimation; thus, although this is an unlikely case, we can observe the maximum achievable gain for 4×4 MIMO-TD respect to the rest of the cases depicted in Figure 5.24. This is due to the whole gain due to the transmit and receive diversity. Finally, for the obtained MIMO-TD simulation results, Table 5.7 shows the mean SNR needed for a BLER (at rv= 0) of 10% where "x" denotes that the BLER of 10% is not achievable.

Table 5.7: SNR needed for a BLER (at rv= 0) of 10% for MIMO-TD in a bandwidth of 4 RBs and Ideal Channel Estimation

MIMO	TM	ETU300 MCS 0	ETU300 MCS 12	ETU300 MCS 27	EVA70 MCS 27
1x1	**SISO**	-0.77	10.98	26.03	27.21
1x2LC	**port 0**	-5.51	5.64	19.03	19.41
1x2MC	**port 0**	-4.35	7.12	21.10	21.78
1x2HC	**port 0**	-4.37	7.12	21.14	21.74
2x2LC	**TD**	-6.43	4.62	20.86	18.85
2x2MC	**TD**	-5.38	5.84	x	20.60
2x2HC	**TD**	-4.42	7.14	x	22.75
4x4LC	**TD**	-10.48	0.39	15.78	14.92
4x4MC	**TD**	-7.94	3.48	x	19.23
4x4HC	**TD**	-6.88	5.02	x	23.04

5.2.2 MIMO-SM

5.2.2.1 ZF and MMSE Receivers

The low-complexity MIMO detectors which have been taken into account for OL MIMO-SM are the ZF and MMSE receivers (they are described in section 3.4.5.1). The ZF and MMSE link level performance is evaluated considering ideal channel estimation. In addition, it has been considered the LTE large delay CDD precoding at the transmitter side which corresponds to the LTE-DL TM 3. Figures 5.25 and 5.26 show the evaluation of the ZF and MMSE detectors for MCS 6 and 17 for low and high antenna correlation in ETU300 channel model and a bandwidth of 4 RBs, respectively. In particular, it can be observed that the MMSE detector outperforms the ZF detector.

For MCS 6 and 2×2LC, 2×2HC and 4×4LC, the two multiplexed codewords (c1 and c2) achieve the same mean BLER performance. For 4 × 4HC, at a high SNR, about 28 dB, the codewords can be detected using MMSE recevier. In addition, for 4 × 4HC and MCS 17, the high antenna correlation eliminates the opportunity of spatial demultiplexing at the receiver. For MCS 6 and 2 × 2LC and 2 × 2HC, the MMSE receiver outperforms the ZF detector regardless of whether or not CDD precoding is used. On the other hand, for MCS 17 and 2 × 2LC and 2 × 2HC, CDD precoding improves the BLER performance regardless of whether ZF or MMSE are used.

We can observe in Figure 5.25 that considering perfect channel estimation and low antenna correlation, the 2 × 2 MIMO-SM with ZF detector without precoding and the SISO detection achieve the same BLER performance. In Figures 5.25 and 5.26 we observe that, for low antenna correlation, the MMSE link level performance gain compared to SISO at a BLER (at rv= 0) of 10% is around 2 dB and 0.4 dB for 2 × 2LC and MCS 6 and 17, respectively. It is around 7 dB and 2.5 dB for 4 × 4LC and MCS 6 and 17. Notice that theses gains results from the ideal case of perfect channel estimation and each MIMO antenna transmits with the same power than the case of only one antenna (SISO). Furthermore, for the case of four antennas at the transmitter, the code length is about twice respect to the SISO case since one codeword is mapped onto two

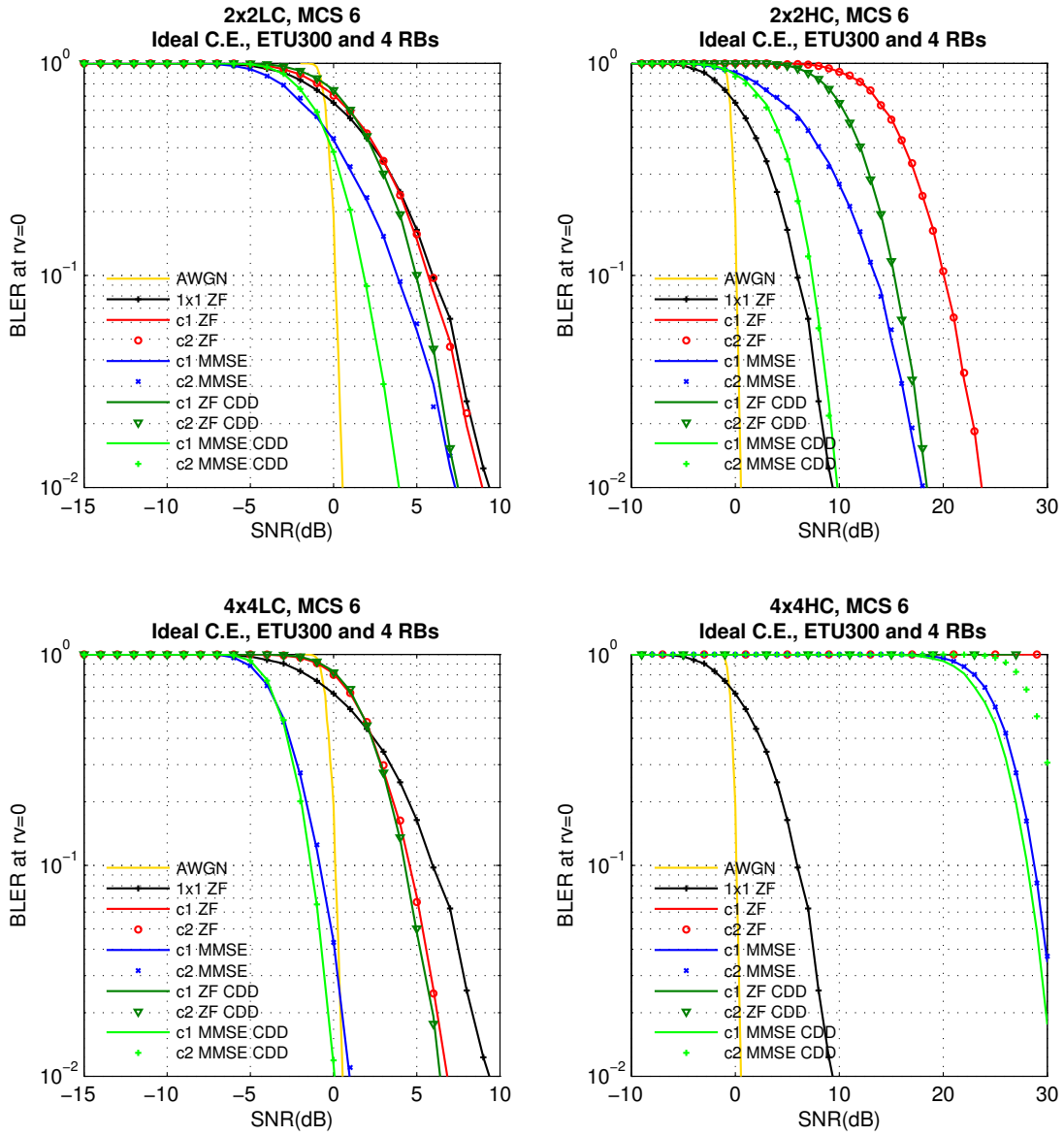

Figure 5.25: BLER (at rv= 0) vs. mean SNR for 2×2 and 4×4 OL MIMO-SM. MCS 6 in ETU300 with Ideal Channel Estimation in a bandwidth of 4 RBs. Antenna correlation LC (on the left) and HC (on the right). ZF vs. MMSE detector, CDD precoding vs. no precoding.

layers. On the other hand, for the high antenna correlation case, the MMSE with CDD precoding link level performance is worst compared to the SISO case.

The use of CDD precoding enhances the link level performance with respect to no precoding at the transmitter side. The MMSE with CDD precoding link level performance compared to no precoding is around 2 dB for MCS 6 and 2×2LC, around 1 dB for MCS 17 and 2×2LC and around 0.5 dB for MCS 6 and 4×4LC.

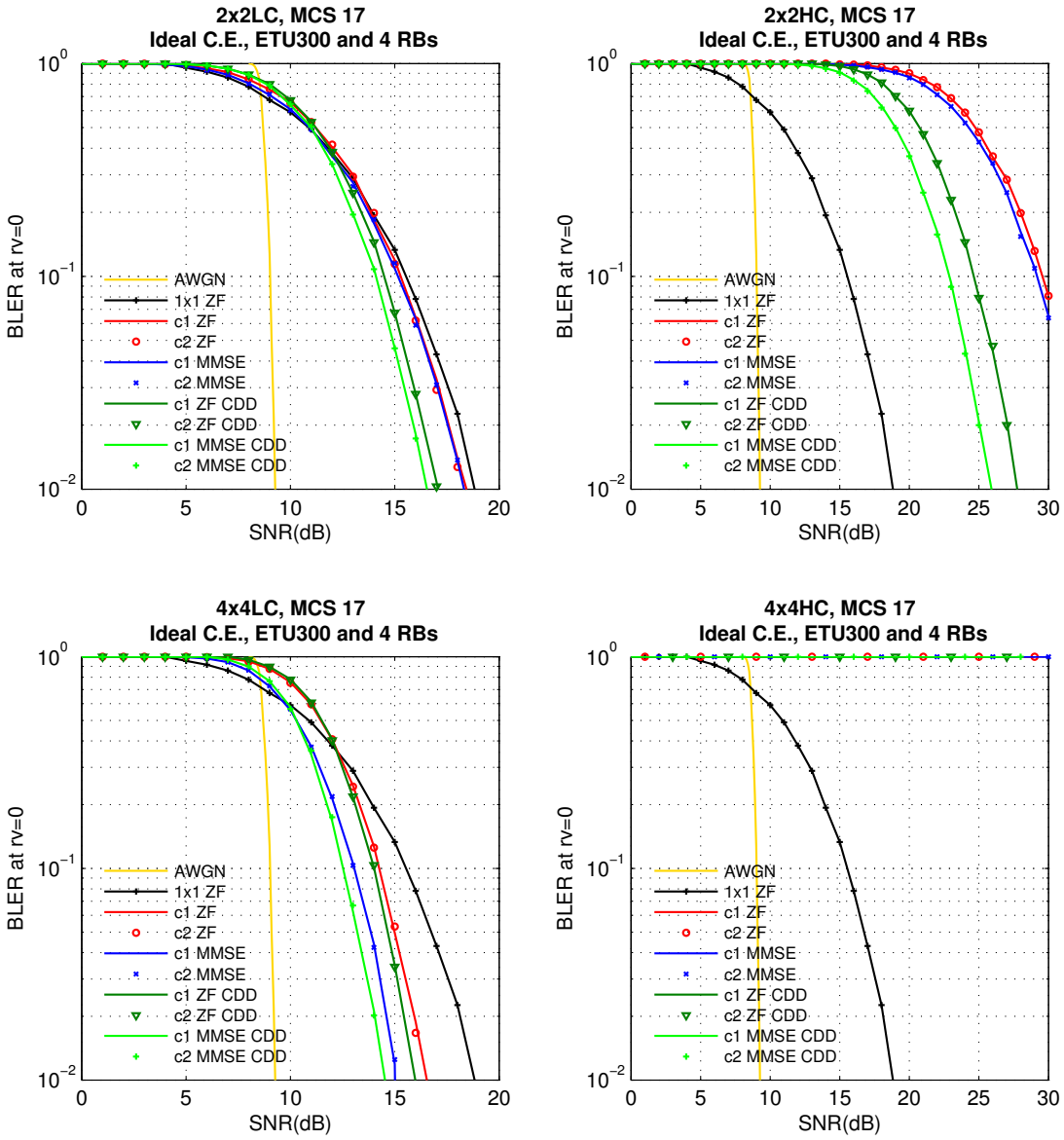

Figure 5.26: BLER (at rv= 0) vs. mean SNR for 2×2 and 4×4 OL MIMO-SM. MCS 17 in ETU300 with Ideal Channel Estimation in a bandwidth of 4 RBs. Antenna correlation LC (on the left) and HC (on the right). ZF vs. MMSE detector, CDD precoding vs. no precoding.

To sum up, the MMSE detector achieves better link level performance compared to the ZF receiver regardless of the antenna correlation. For OL MIMO-SM, the MMSE detector combined with CDD precoding at the transmitter enhances the link level performance. For the obtained simulation results of OL MIMO-SM: ZF vs. MMSE, Table 5.8 shows the mean SNR needed for a BLER (at rv= 0) of 10% where "x" denotes that the BLER of 10% is not achievable.

Table 5.8: SNR needed for a BLER (at rv= 0) of 10% for MIMO-SM: ZF vs. MMSE in a bandwidth of 4 RBs and Ideal Channel Estimation

MIMO	TM	ETU300 MCS 6 codeword 1	ETU300 MCS 6 codeword 2	ETU300 MCS 17 codeword 1	ETU300 MCS 17 codeword 2
1x1	SISO	5.95		15.54	
2x2LC	**ZF**	5.68	5.94	15.28	15.22
2x2LC	**MMSE**	3.81	3.86	15.15	15.21
2x2LC	**ZF CDD**	4.96	5.00	14.49	14.48
2x2LC	**MMSE CDD**	1.82	1.86	14.10	14.09
2x2HC	**ZF**	20.04	20.09	29.56	29.57
2x2HC	**MMSE**	13.44	13.39	29.18	29.16
2x2HC	**ZF CDD**	15.27	15.24	24.63	24.61
2x2HC	**MMSE CDD**	7.37	7.26	22.88	22.80
4x4LC	**ZF**	4.57	4.55	14.25	14.26
4x4LC	**MMSE**	-0.83	-0.79	13.06	13.04
4x4LC	**ZF CDD**	4.28	4.31	14.01	14.03
4x4LC	**MMSE CDD**	-1.36	-1.38	12.52	12.58
4x4HC	**ZF**	x	x	x	x
4x4HC	**MMSE**	28.75	28.71	x	x
4x4HC	**ZF CDD**	x	x	x	x
4x4HC	**MMSE CDD**	28.08	x	x	x

5.2.2.2 CL MIMO-SM

The CL MIMO-SM link level performance is evaluated considering ideal channel estimation, two transmitted codewords (c1 and c2), the MMSE detector, 2×2 and 4×4 MIMO under low and high antenna correlation in ETU300 channel model, and a bandwidth of 4 RBs. The CL precoding is based on the LTE codebook-based precoding defined in [3] as described in section 3.4.6.1, which corresponds to the CL precoding for the LTE-DL TM 4. Since ideal channel estimation is assumed, the channel is known for each subcarrier; consequently, for all CL MIMO simulations we have assumed a perfect precoding matrix selection that the best codebook-based precoding is selected for each subcarrier (what is labelled as CL(k) hereafter). So the CL(k) implemented in the link level simulator selects the best precoding matrix which maximizes the post-processing SNR for codeword c1 at each subcarrier k. For comparison evaluation, it has also been simulated the CL precoding based on SVD using UPA at the transmitter side (what is labelled as SVD(UPA) hereafter). Figures 5.27 and 5.28 show the CL(k) vs. SVD(UPA) BLER (at rv= 0) performance for MCS 6 and 17, respectively, where it can be observed the better c1 BLER performance compared to the c2 BLER performance because of the c1 priority. This is due to the beamforming gain that receives the priority codeword (c1) from the CL precoding (CL(k), SVD(UPA)) .

For 2×2LC and MCS 6, the CL(k) BLER performance of codeword c1 is about 2 dB better and the SVD(UPA) BLER performance of codeword c1 is about 4.5 dB better than the CDD precoding

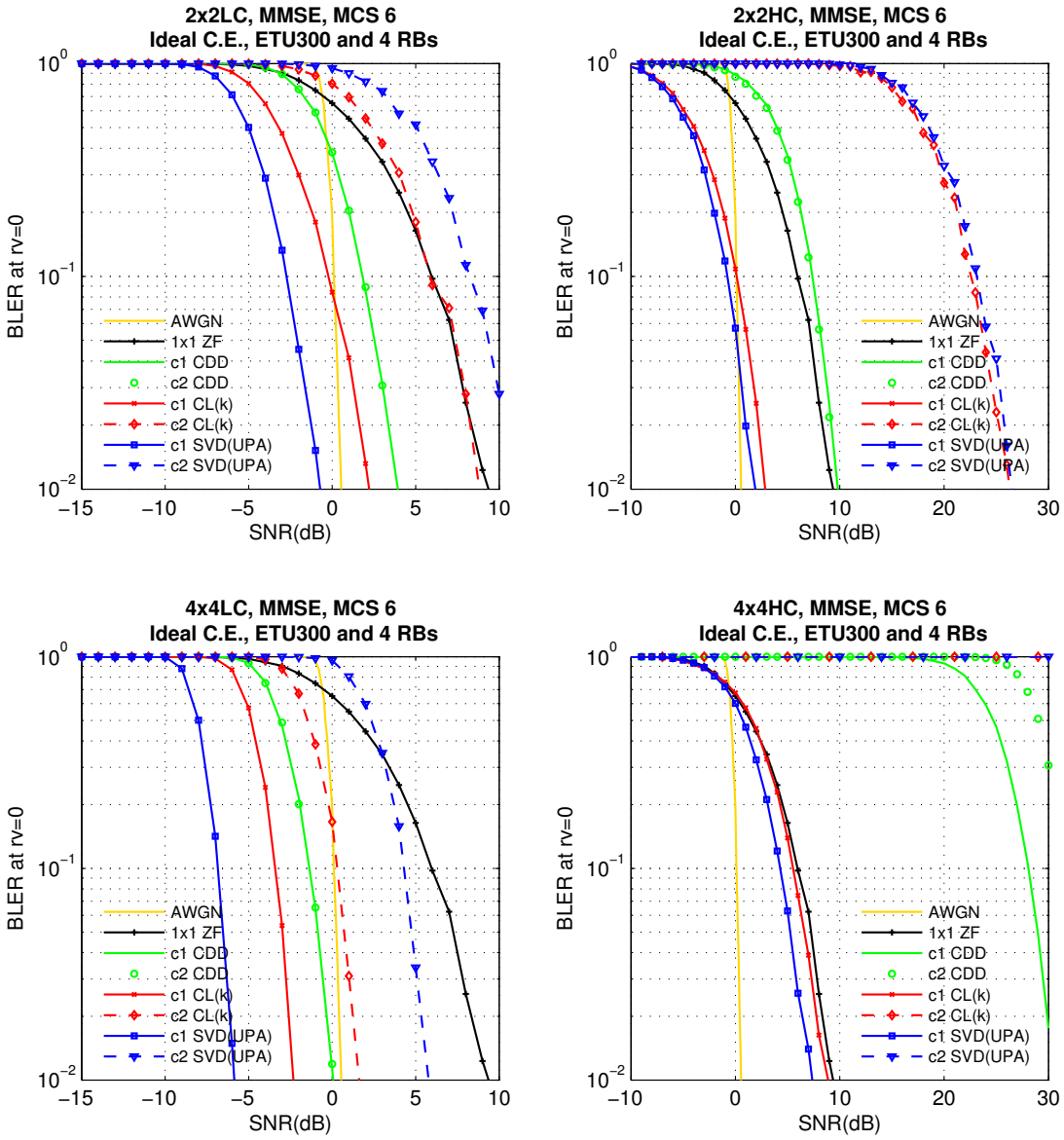

Figure 5.27: BLER (at rv= 0) vs. mean SNR for 2×2 and 4×4 MIMO-SM. MCS 6 in ETU300 with Ideal Channel Estimation in a bandwidth of 4 RBs. Antenna correlation LC (on the left) and HC (on the right). CL(k) vs. SVD(UPA), CL(k) vs. CDD precoding, MMSE detector.

BLER performance. For 2×2LC and MCS 17, the CL(k) BLER performance of codeword c1 is about 2 dB better and the SVD(UPA) BLER performance of codeword c1 is about 7.5 dB better than the CDD precoding BLER performance. In contrast, the BLER performance of the codeword c2 is worse than the CDD precoding BLER performance. For CL(k) and 2×2LC, the c2 BLER performance is quite similar to the SISO performance for MCS 6 and the c2 BLER performance is about 1 dB worse than the SISO performance for MCS 17. Notice that these results are based on assuming perfect channel estimation and low antenna correlation that is not a realistic scenario;

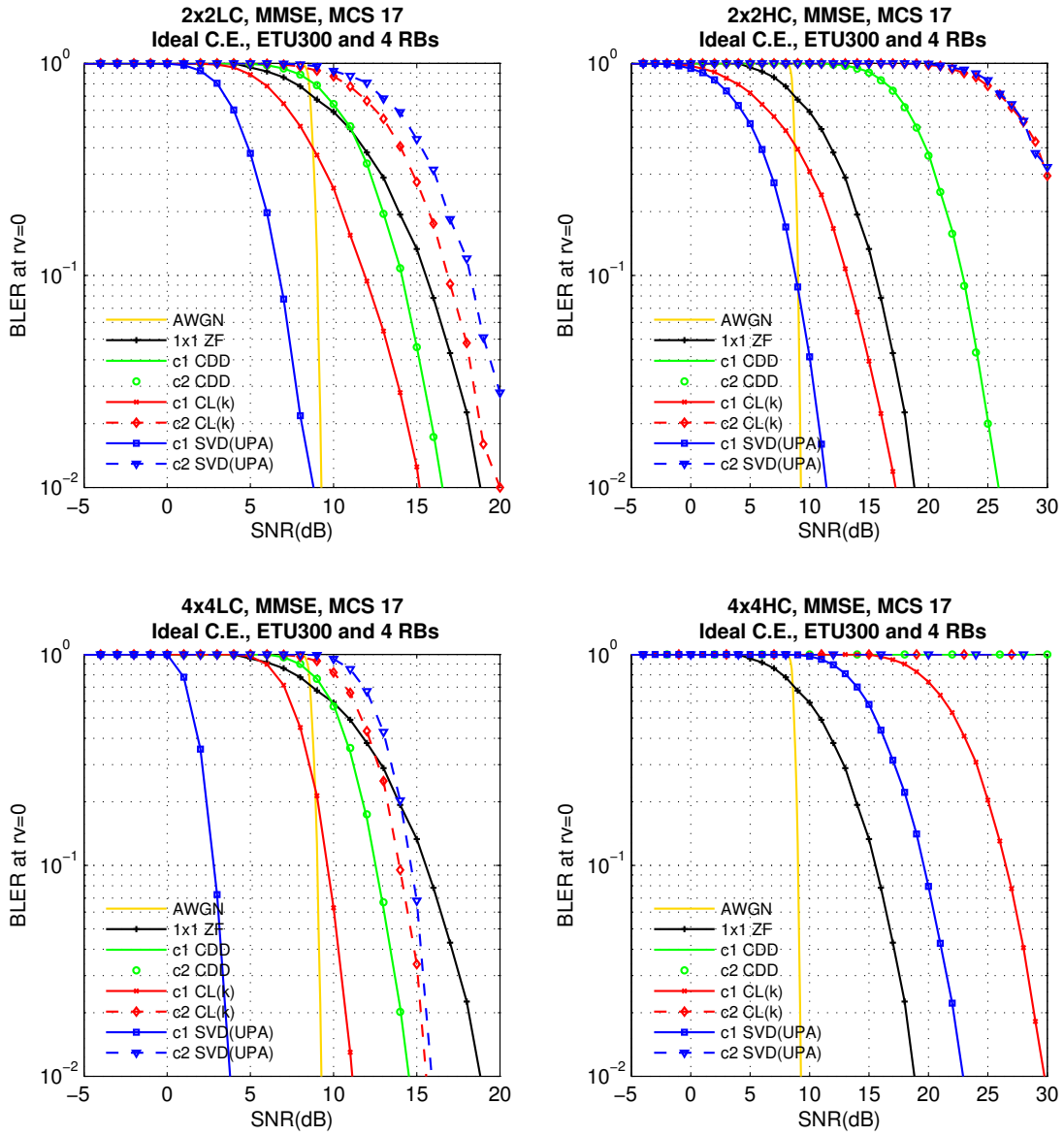

Figure 5.28: BLER (at rv= 0) vs. mean SNR for 2×2 and 4×4 MIMO-SM. MCS 17 in ETU300 with Ideal Channel Estimation in a bandwidth of 4 RBs. Antenna correlation LC (on the left) and HC (on the right). CL(k) vs. SVD(UPA), CL(k) vs. CDD precoding, MMSE detector.

turbo

however, we can observe the benefits of these CL techniques. The extreme case is the SVD(UPA) beamforming gain respect to SISO for 4×4LC that is observed in Figures 5.27 and 5.28 which is higher than 10 dB.

On the other hand, for 2×2HC, CL(k) and SVD(UPA) outperform CDD and SISO in terms of BLER for the priority codeword (c1). In contrast, there is a high BLER performance degradation

of the non-priority codeword (c2); for instance, more than 15 dB compared to SISO as shown in Figures 5.27 and 5.28. For 4 × 4HC and MCS 6, the CL(k) BLER performance of codeword c1 is about 0.5 dB better and the SVD(UPA) BLER performance of codeword c1 is about 1.5 dB better than the SISO BLER performance. In contrast, for 4 × 4HC and MCS 17, the CL(k) and SVD(UPA) detectors make a noise enhancement after equalization that their BLER performance is worst than the SISO BLER performance.

To sum up, the SVD(UPA) CL MIMO-SM scheme achieves better BLER performance than the CL(k) scheme for the codeword c1 (priority codeword). In contrast, the CL(k) scheme achieves better BLER performance than the SVD(UPA) scheme for the codeword c2 (non-priority codeword). For the obtained simulation results of CL MIMO-SM: CL(k) vs. SVD(UPA), Table 5.9 shows the mean SNR needed for a BLER (at rv= 0) of 10% where "x" denotes that the BLER of 10% is not achievable.

Table 5.9: SNR needed for a BLER (at rv= 0) of 10% for CL MIMO-SM: CL(k) vs. SVD(UPA) in a bandwidth of 4 RBs and Ideal Channel Estimation

MIMO	TM	ETU300 MCS 6 codeword 1	ETU300 MCS 6 codeword 2	ETU300 MCS 17 codeword 1	ETU300 MCS 17 codeword 2
1x1	SISO	5.95		15.54	
2x2LC	**MMSE CDD**	1.82	1.86	14.10	14.09
2x2LC	**MMSE CL(k)**	-0.23	5.86	11.87	16.86
2x2LC	**MMSE SVD(UPA)**	-2.74	8.25	6.73	18.21
2x2HC	**MMSE CDD**	7.37	7.26	22.88	22.80
2x2HC	**MMSE CL(k)**	0.12	22.58	13.15	x
2x2HC	**MMSE SVD(UPA)**	-0.77	23.14	8.81	x
4x4LC	**MMSE CDD**	-1.36	-1.38	12.52	12.58
4x4LC	**MMSE CL(k)**	-3.41	0.30	9.62	13.95
4x4LC	**MMSE SVD(UPA)**	-6.85	4.30	2.80	14.65
4x4HC	**MMSE CDD**	28.08	x	x	x
4x4HC	**MMSE CL(k)**	5.53	x	26.51	x
4x4HC	**MMSE SVD(UPA)**	4.29	x	19.60	x

5.2.2.3 Codeword-SIC Receiver

The simulation results for the codeword-SIC receiver, which is described in section 3.4.7, are presented using MMSE detection and applied to OL and CL MIMO-SM schemes. The performance of a MIMO MMSE linear receiver without SIC is also shown for the sake of comparison. Figures 5.29 and 5.30 show the BLER performance for MIMO-SM with and without codeword-SIC receiver for MCS 6 and 17, respectively. The MIMO-SM schemes which are shown in these figures are CDD precoding for OL MIMO-SM and CL(k) and CL(1) precoding for CL MIMO-SM. The CL(1) precoding consists of a coarse precoding matrix selection performed on the central subcarrier for each allocated RB which selects the same precoding matrix for the whole set of subcarriers within the same RB .

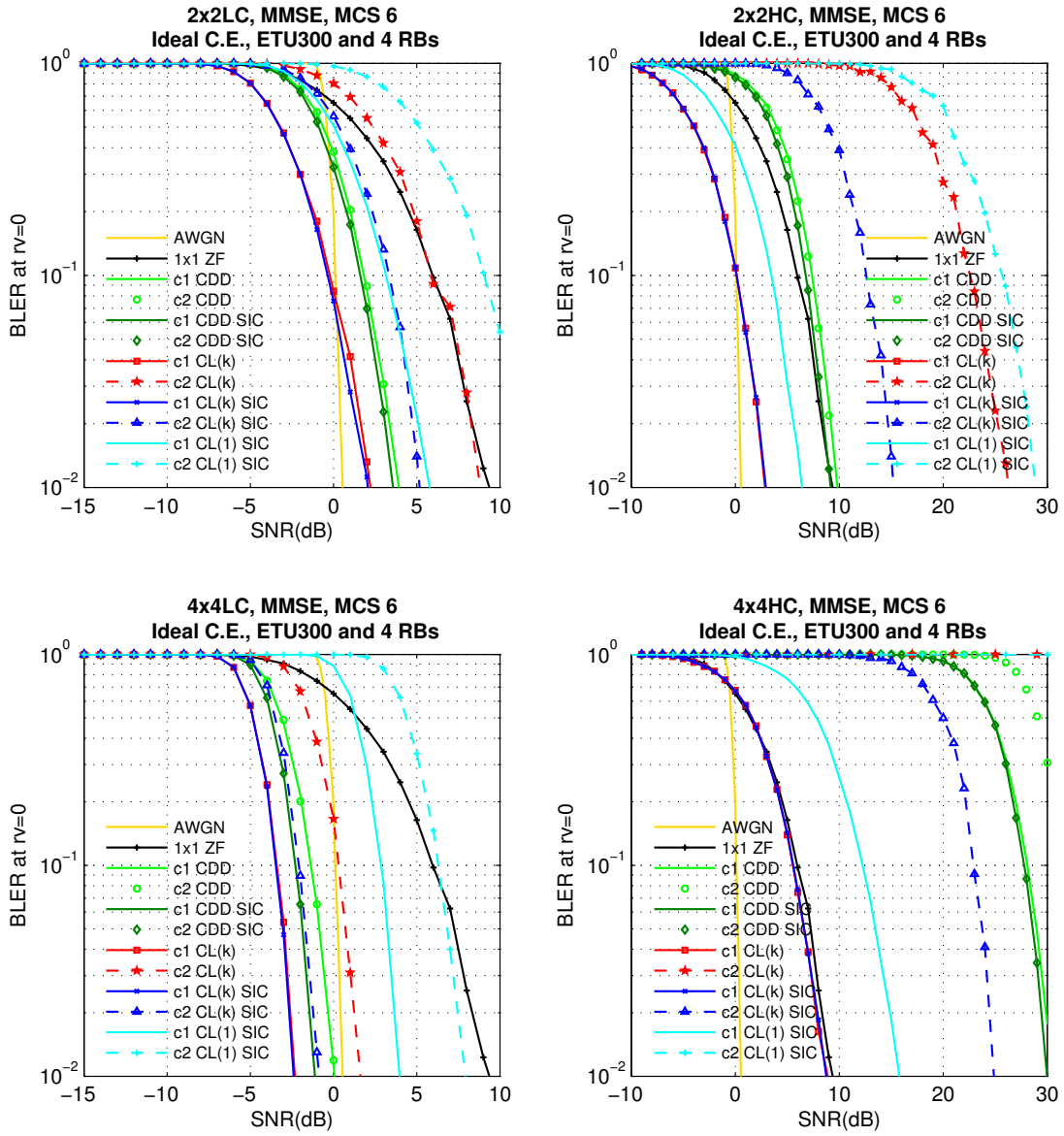

Figure 5.29: BLER (at rv= 0) vs. mean SNR for 2×2 and 4×4 MIMO-SM. MCS 6 in ETU300 with Ideal Channel Estimation in a bandwidth of 4 RBs. Antenna correlation LC (on the left) and HC (on the right). Codeword SIC vs. no SIC, MMSE detector.

Figures 5.29 and 5.30 shows that there is no significant gain with the usage of codeword-SIC in OL MIMO-SM with CDD precoding for 2×2LC and 2×2HC. For 4×4LC we observe a SIC gain around 1 dB for MCS 6 and 17 at a BLER of 10%. 4×4HC OL MIMO-SM presents a bad performance and this case is discarded. For CL MIMO-SM, since the interference cancellation is applied mainly to the non-priority codeword, codeword-SIC receiver enhances significantly the non-priority codeword BLER performance and a SIC gain, defined as the performance gain for the non-priority codeword (c2), is observed. In Figure 5.29, for non-priority codeword (c2) and MCS

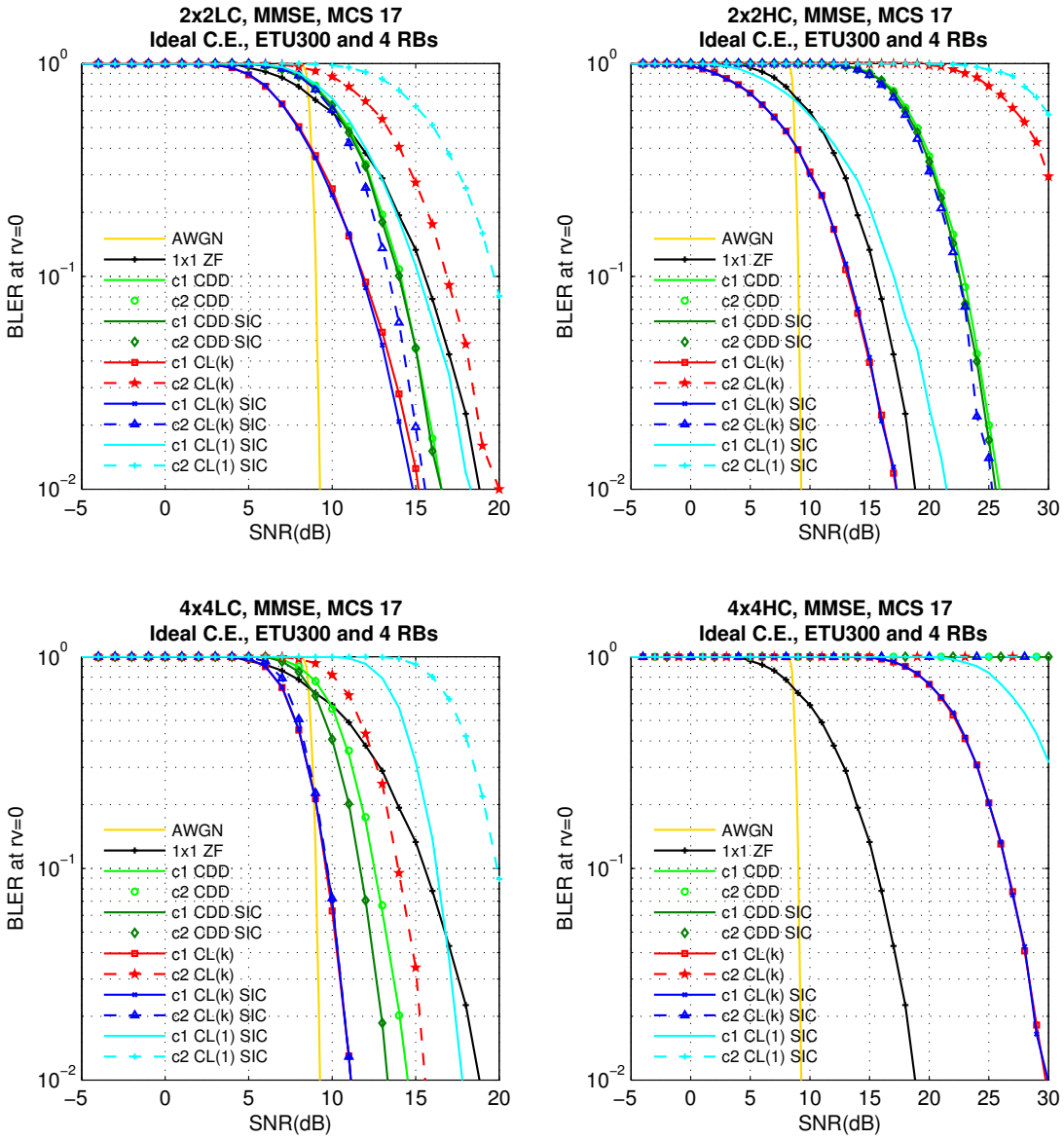

Figure 5.30: BLER (at rv= 0) vs. mean SNR for 2×2 and 4×4 MIMO-SM. MCS 17 in ETU300 with Ideal Channel Estimation in a bandwidth of 4 RBs. Antenna correlation LC (on the left) and HC (on the right). Codeword SIC vs. no SIC, MMSE detector.

6 we observe a SIC gain around 2.5 dB for 2×2LC, 10 dB for 2×2HC and 2.4 dB for 4×4LC; while for 4×4HC, codeword-SIC receiver makes possible a BLER of 10% around an SNR of 23 dB. In Figure 5.30, for non-priority codeword (c2) and MCS 17 we observe a SIC gain around 3.5 dB for 2×2LC and 4 dB for 4×4LC; while for high antenna correlation a BLER of 10% is not achieved.

In addition, Figures 5.29 and 5.30 show the BLER performance degradation when it is assumed CL(1) precoding combined with codeword-SIC compared to CL(k) precoding. For instance, for 2×2LC, we observe a degradation about 3.5 dB for c1 (priority codeword) and 6 dB for c2 (non-priority codeword). For 4×4LC, a degradation about 6 dB for c1 and 9.5 dB for c2. CL(1) precoding scheme is a basic method that does not achieve a good BLER performance due to the simplified precoding matrix selection procedure. It is only shown for the sake of comparison. For the obtained simulation results of CL MIMO-SM with/without codeword SIC, Table 5.10 shows the mean SNR needed for a BLER (at rv= 0) of 10% where "x" denotes that the BLER of 10% is not achievable.

Table 5.10: SNR needed for a BLER (at rv= 0) of 10% for MIMO-SM in a bandwidth of 4 RBs and Ideal Channel Estimation

MIMO	TM	ETU300 MCS 6 codeword 1	ETU300 MCS 6 codeword 2	ETU300 MCS 17 codeword 1	ETU300 MCS 17 codeword 2
1x1	**port 0**	5.95		15.54	
2x2LC	**MMSE CDD**	1.82	1.86	14.10	14.09
2x2LC	**MMSE CDD SIC**	1.61	1.60	14.01	14.01
2x2LC	**MMSE CL(k)**	-0.23	5.86	11.87	16.86
2x2LC	**MMSE CL(k) SIC**	-0.36	3.33	11.79	13.38
2x2LC	**MMSE CL(1) SIC**	3.15	9.05	15.19	19.69
2x2HC	**MMSE CDD**	7.37	7.26	22.88	22.80
2x2HC	**MMSE CDD SIC**	6.77	6.77	22.54	22.54
2x2HC	**MMSE CL(k)**	0.12	22.58	13.15	x
2x2HC	**MMSE CL(k) SIC**	0.13	12.60	13.28	22.44
2x2HC	**MMSE CL(1) SIC**	3.46	25.66	17.02	x
4x4LC	**MMSE CDD**	-1.36	-1.38	12.52	12.58
4x4LC	**MMSE CDD SIC**	-2.30	-2.30	11.67	11.67
4x4LC	**MMSE CL(k)**	-3.41	0.30	9.62	13.95
4x4LC	**MMSE CL(k) SIC**	-3.47	-2.08	9.68	9.72
4x4LC	**MMSE CL(1) SIC**	2.85	6.29	16.25	19.87
4x4HC	**MMSE CDD**	28.08	x	x	x
4x4HC	**MMSE CDD SIC**	27.78	27.78	x	x
4x4HC	**MMSE CL(k)**	5.53	x	26.51	x
4x4HC	**MMSE CL(k) SIC**	5.57	22.90	26.50	x
4x4HC	**MMSE CL(1) SIC**	12.24	x	x	x

5.2.3 Performance comparison

Figures 5.31, 5.32 and 5.33 show the BLER performance comparison of the different MIMO transmission modes for LC, MC and HC, respectively. It has been assumed ETU300 channel, ideal channel estimation, MMSE detector, a bandwidth of 4 RBs and MCS 6, 12, 17 and 27, In addition, AWGN BLER curves are depicted as reference and 1×2 SIMO BLER performance curves are depicted as the LTE baseline BLER performance. For MIMO-TD and MCS 27, we observe

a BLER error floor around 0.035 for an SNR higher than 25 dB for 2 × 2LC; around 0.15 and 0.25 for an SNR higher than 20 dB for 2 × 2MC and 4 × 4MC, respectively; and around 0.4 and 0.55 for an SNR higher than 20 dB for 2 × 2HC and 4 × 4HC, respectively. This is due to the assumption that the channel frequency response does not vary for the two consecutive subcarriers for which the SFBC has been applied at the transmitter side and the MRC gain is not enough to mitigate this effect. Table 5.10 shows, for the obtained simulation results, the mean SNR needed for a BLER (at rv= 0) of 10% where "x" denotes that the BLER of 10% is not achievable.

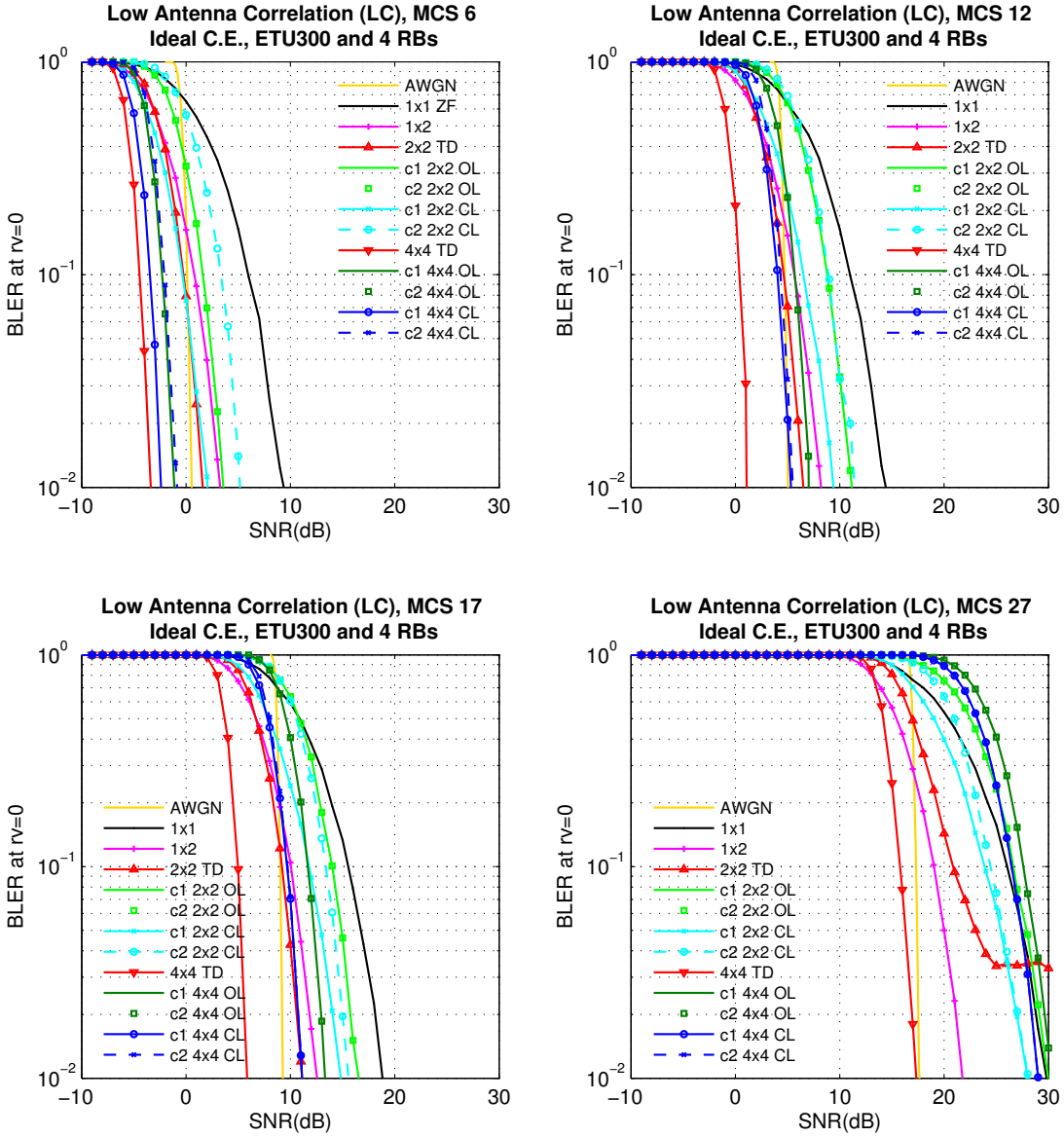

Figure 5.31: BLER (at rv= 0) vs. mean SNR for 2 × 2LC and 4 × 4LC MIMO. MCS 6, 12, 17 and 27 in ETU300 with Ideal Channel Estimation in a bandwidth of 4 RBs. SM vs. TD, OL with CDD Precoding, CL(k) Precoding and MMSE detector plus codeword-SIC.

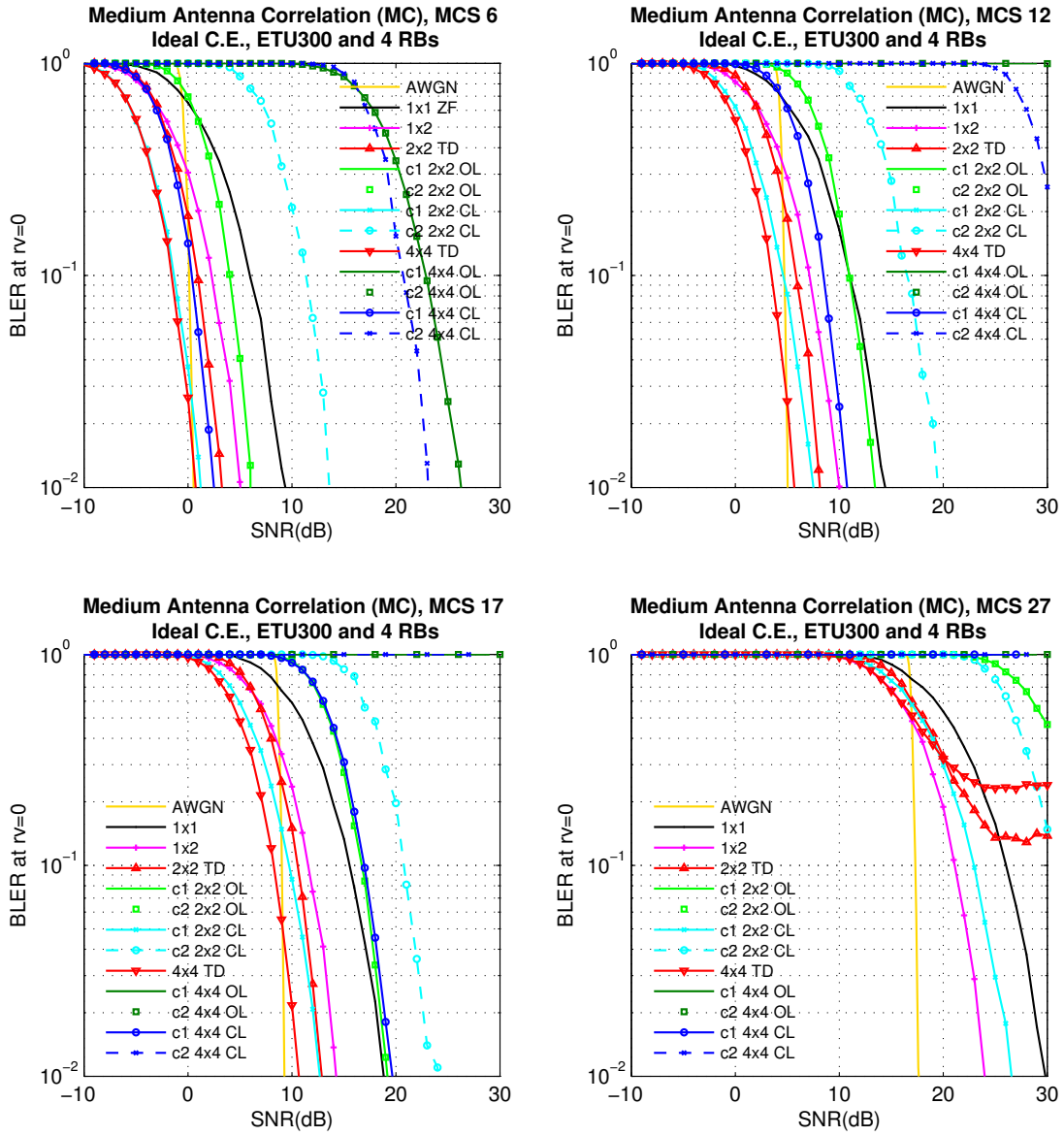

Figure 5.32: BLER (at rv= 0) vs. mean SNR for 2×2MC and 4×4MC MIMO. MCS 6, 12, 17 and 27 in ETU300 with Ideal Channel Estimation in a bandwidth of 4 RBs. SM vs. TD, OL with CDD Precoding, CL(k) Precoding and MMSE detector plus codeword-SIC.

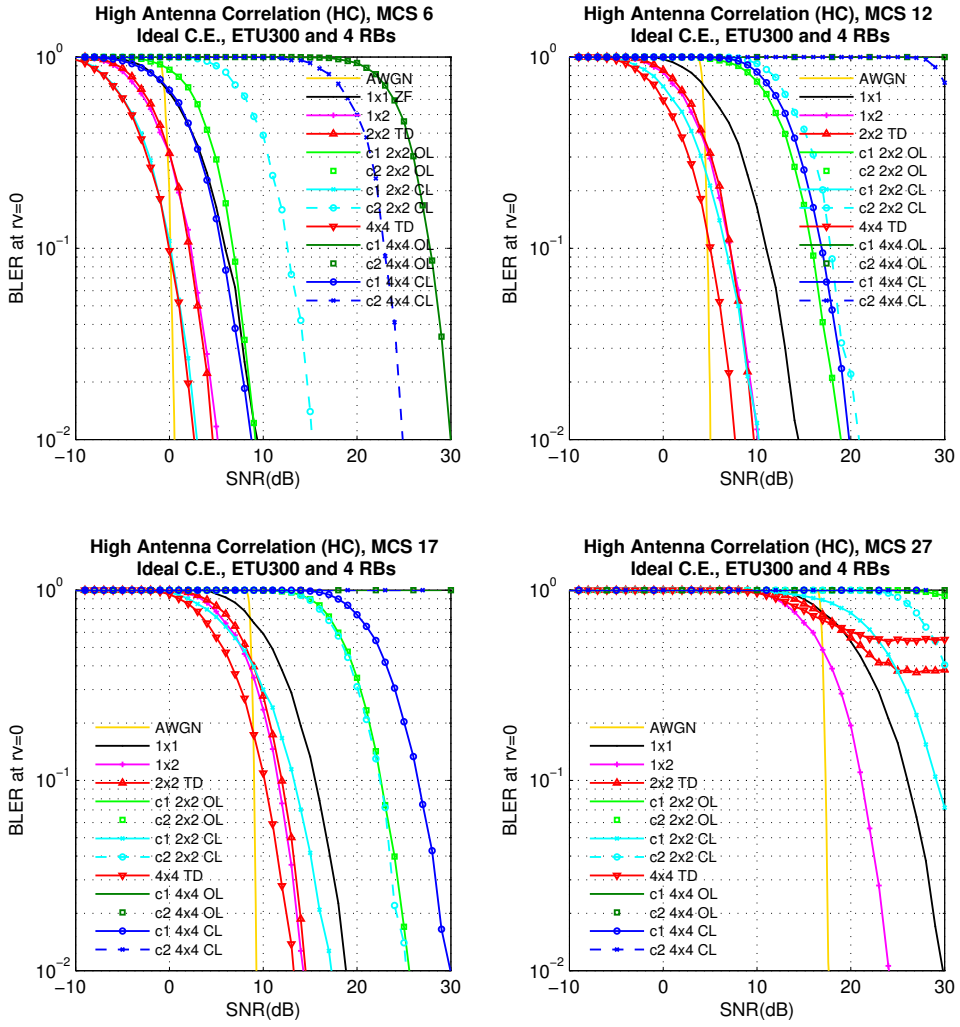

Figure 5.33: BLER (at rv= 0) vs. mean SNR for 2×2HC and 4×4HC MIMO. MCS 6, 12, 17 and 27 in ETU300 with Ideal Channel Estimation in a bandwidth of 4 RBs. SM vs. TD, OL with CDD Precoding, CL(k) Precoding and MMSE detector plus codeword-SIC.

Table 5.11: SNR needed for a BLER (at rv= 0) of 10% for MIMO-SM: OL vs. CL, in a bandwidth of 4 RBs and Ideal Channel Estimation

			ETU300							
			MCS 6		MCS 12		MCS 17		MCS 27	
MIMO	Loop	Scheme	c1	c2	c1	c2	c1	c2	c1	c2
1x1	Open	1x1 ZF	5.95		10.98		15.54		26.03	
1x2LC	Open	1x2	2.27		5.64		10.05		19.03	
2x2LC	Open	TD	-0.26		4.62		9.19		20.86	
2x2LC	Open	OL	1.61	1.60	8.80	8.80	14.01	14.01	26.63	26.63
2x2LC	Closed	CL	-0.36	3.33	6.51	8.93	11.79	13.38	23.88	24.45
4x4LC	Open	TD	-4.46		0.39		4.98		15.78	
4x4LC	Open	OL	-2.30	-2.30	5.69	5.69	11.67	11.67	27.59	27.59
4x4LC	Closed	CL	-3.47	-2.08	4.03	4.32	9.68	9.72	26.47	26.47
1x2MC	Open	1x2	2.27		7.12		11.55		21.10	
2x2MC	Open	TD	0.92		5.84		10.54		x	
2x2MC	Open	OL	4.00	4.01	10.95	10.96	16.72	16.72	x	x
2x2MC	Closed	CL	-1.35	11.35	4.60	16.52	9.72	20.76	22.95	x
4x4MC	Open	TD	-1.57		3.48		8.24		x	
4x4MC	Open	OL	22.88	22.88	x	x	x	x	x	x
4x4MC	Closed	CL	0.36	20.70	8.47	x	16.96	x	x	x
1x2HC	Open	1x2	2.29		7.12		11.58		21.14	
2x2HC	Open	TD	2.10		7.14		11.99		x	
2x2HC	Open	OL	6.77	6.77	15.85	15.85	22.54	22.54	x	x
2x2HC	Closed	CL	0.13	12.60	6.67	17.85	13.28	22.44	29.12	x
4x4HC	Open	TD	-0.05		5.02		10.14		x	
4x4HC	Open	OL	27.78	27.78	x	x	x	x	x	x
4x4HC	Closed	CL	5.57	22.90	16.90	x	26.50	x	x	x

5.3 E-UTRA DL Link Average Throughput

In this section we obtain the E-UTRA DL link average throughput taking into account ideal channel estimation and, on a more realistic scenario, considering the CEEM described in chapter 4. In order to obtain these results, the proposed CEEM channel estimation errors are simulated in the LTE link level simulator, that is described in chapter 3, by weighting MIMO channel matrix $\mathbf{H}$ with $\sqrt{1-\varepsilon^2}$ and adding a random complex Gaussian noise with a variance $\varepsilon^2 G$ according to Equation 4.10 which is rewritten below:

$$\hat{\mathbf{H}}_k = \sqrt{1-\varepsilon^2}\mathbf{H}_k + \varepsilon\mathbf{N} \tag{5.4}$$

By using CEEM in link level simulations, imperfect CSI at the receiver side as well as at the transmitter in the case of CL MIMO-SM is simulated. Figure 4.23 shows graphically the LUTs of ε for different combinations of SNR, the optimum channel estimators, the CRS pilot density and the channel models EPA5, EVA70 and ETU300. In the case of 4×4 MIMO we have two values for ε, $\varepsilon_{\text{Antennas}\,0,1}$ and $\varepsilon_{\text{Antennas}\,2,3}$, due to there are two pilot densities, one for APs 0 and 1 and another one for APs 2 and 3. Since the CEEM system model only considers one value for ε, we consider the mean value of $\varepsilon_{\text{Antennas}\,0,1}$ and $\varepsilon_{\text{Antennas}\,2,3}$ that is $\varepsilon = 0.5 \cdot (\varepsilon_{\text{Antennas}\,0,1} + \varepsilon_{\text{Antennas}\,2,3})$ for the 4×4 MIMO case.

For the simulations in this section we assume different AMC combinations and antenna configurations in different multipath fading channels with ideal and CEEM channel estimation. In addition, we assume that the MCS is not changed during the simulation. Hence, each AMC combination is simulated separately; this way the complexity of the link level simulator is reduced. In any case, the AMC performance is evaluated by analysing globally the simulation results for each MCS.

The link average throughput without HARQ is evaluated as the product of the modulation spectral efficiency (in *bits/s/Hz*) times the code rate and the probability of error free transmission (1 - BLER) at rv= 0 for a given mean SNR. As defined in section 3.4.3, the SNR is averaged over fast fading but not over shadowing fading. So the link average throughput in *bits/s/Hz* without HARQ is as follows:

$$\Gamma = Q_m \cdot r \cdot (1 - \text{BLER}) \tag{5.5}$$

where $Q_m = 2, 4, 6$ is the maximum spectral efficiency in *bits/s/Hz* of the modulation, r is the code rate and BLER is the mean BLER at rv= 0 for the given mean SNR. In the case of MIMO-SM, the computation of the link average throughput must take into account the spatial domain gain; thus the overall link average throughput is equal to the sum of the link average throughput of the two spatial codeword transmissions. Since the codeword is mapped onto N_L, that is the number of layers available per codeword, the link average throughput without HARQ for MIMO-SM is as follows:

$$\Gamma_{SM} = N_L \cdot \Gamma_{c1} + N_L \cdot \Gamma_{c2} \tag{5.6}$$

where Γ_{c1} and Γ_{c2} are the link average throughputs in *bits/s/Hz* without HARQ for codeword 1 and 2, respectively.

The link average throughput with HARQ is evaluated as the product of the modulation spectral efficiency (in *bits/s/Hz*) times the code rate and the HARQ retransmission efficiency, η_{HARQ} for a given mean SNR. The same mean SNR is assumed for each HARQ retransmission. η_{HARQ} is defined in Equation 3.11 and the link average throughput in *bits/s/Hz* with HARQ is as follows:

$$\Upsilon = Q_m \cdot r \cdot \eta_{HARQ} \tag{5.7}$$

In the case of MIMO-SM, the link average throughput in *bits/s/Hz* with HARQ also has to take into account the spatial domain gain as follows:

$$\Upsilon_{SM} = N_L \cdot \Upsilon_{c1} + N_L \cdot \Upsilon_{c2} \tag{5.8}$$

where Υ_{c1} and Υ_{c2} are the link average throughputs with HARQ for codeword 1 and 2, respectively. Table 5.12 summarizes the set of LTE DL link level simulator parameters used for the simulations presented in this section and Table 5.13 shows the acronyms used in the legends of the next figures to refer to the different combinations of the parameters of the different transmission modes.

Table 5.12: LTE DL link level simulator parameters

Parameter	**Value**
Carrier Frequency	2.14 GHz
Sub-carrier spacing	15 kHz
Number of sub-carriers per RB	12
Number of allocated RBs	4
TTI length	1 ms
Number of OFDM symbols per TTI	14 (11 PDSCH + 3 PDCCH)
Channel Model	ETU300, EVA70, EPA5 [19]
Channel Coding	Turbo code basic rate 1/3
Rate Matching and HARQ	According to [4] Maximum of 4 IR transmissions
AMC formats	According to [33] MCS 0, 3, 6, 9, 12, 15, 17, 21, 24, 27
Channel estimation	Ideal Channel Estimation, CEEM
Antenna scheme	SISO and MIMO: 1×2, 2×2 and 4×4 for SU-MIMO configuration
MIMO Correlation	According to [19] LC, MC and HC
SISO Detector	ZF one tap equalizer
SIMO Detector	ZF one tap equalizer with MRC
MIMO-SM Detector	MMSE (with and without codeword-SIC)
MIMO-TD Detector	Alamouti Detector with MRC

In the figures of this section, we present the MIMO-SM the link average throughput with/without HARQ. Notice that in the case of OL MIMO-SM the link average throughput for each codeword is approximately similar on average. In contrast, in the case of CL MIMO-SM the priority codeword

Table 5.13: Meaning of the acronyms in figure legends

Nomenclature	Description
$N_{RX} \times M_{TX} \times c$C	N_{RX} receive antennas, M_{TX} transmit antennas and cC is the MIMO correlation level (LC, MC, HC)
CDD	*Open-Loop* (OL) with Large Delay CDD Precoding
CL(k)	*Closed-Loop* (CL) with Codebook-based Precoding per subcarrier
TD	*Transmit Diversity* (TD)
MRC	MRC at the receiver
SIC	codeword-SIC
Ideal C.E.	Ideal Channel Estimation
CEEM	CEEM Channel Estimation
rv= 0	rv= 0
HARQ	*Hybrid ARQ* (HARQ)

(Codeword 0) presents better performance than the non priority (Codeword 1). Finally, the overall link average throughput is the sum of the individual link average throughput of each codeword. For instance, Figure 5.34 shows the E-UTRA DL link average throughput without HARQ for ideal channel estimation in ETU300 multipath fading channel for MCS 9, 2×2HC and CL MIMO-SM with CL(k) precoding.

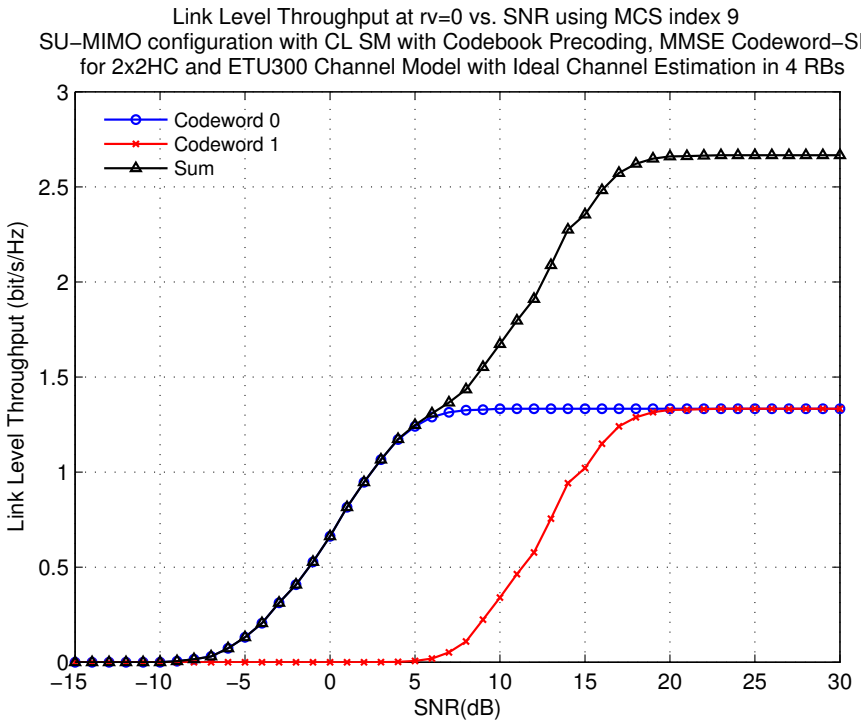

Figure 5.34: E-UTRA DL Link Average Throughput vs. mean SNR without HARQ for 2×2HC, CL MIMO-SM with CL(k) precoding and MCS 9 in ETU300 channel and 4 RBs

5.3.1 SISO

Figure 5.35 shows the E-UTRA DL link average throughput for ideal and CEEM channel estimation for MCS 0 to 27 in SISO channel with the following multipath channel models: EPA5, EVA70 and ETU300. In these Figures the maximum link average throughput is also depicted taking into account the best MCS format for each given SNR. We observe that the channel estimation error due to the CEEM leads to an SNR loss around 0.5 dB at a SNR of 20 dB in EPA5 and an SNR loss around 1 dB at a SNR of 25 dB in EVA70. So below these SNR bounds, the channel estimation error due to the CEEM is not significant. In contrast, we observe that the channel estimation error is noticeable in ETU300 from an SNR of 0 dB to 20 dB with a loss around 0.5 dB, from an SNR of 20 dB with a loss higher than 1 dB and an SNR loss around 2.5 dB at an SNR of 30 dB.

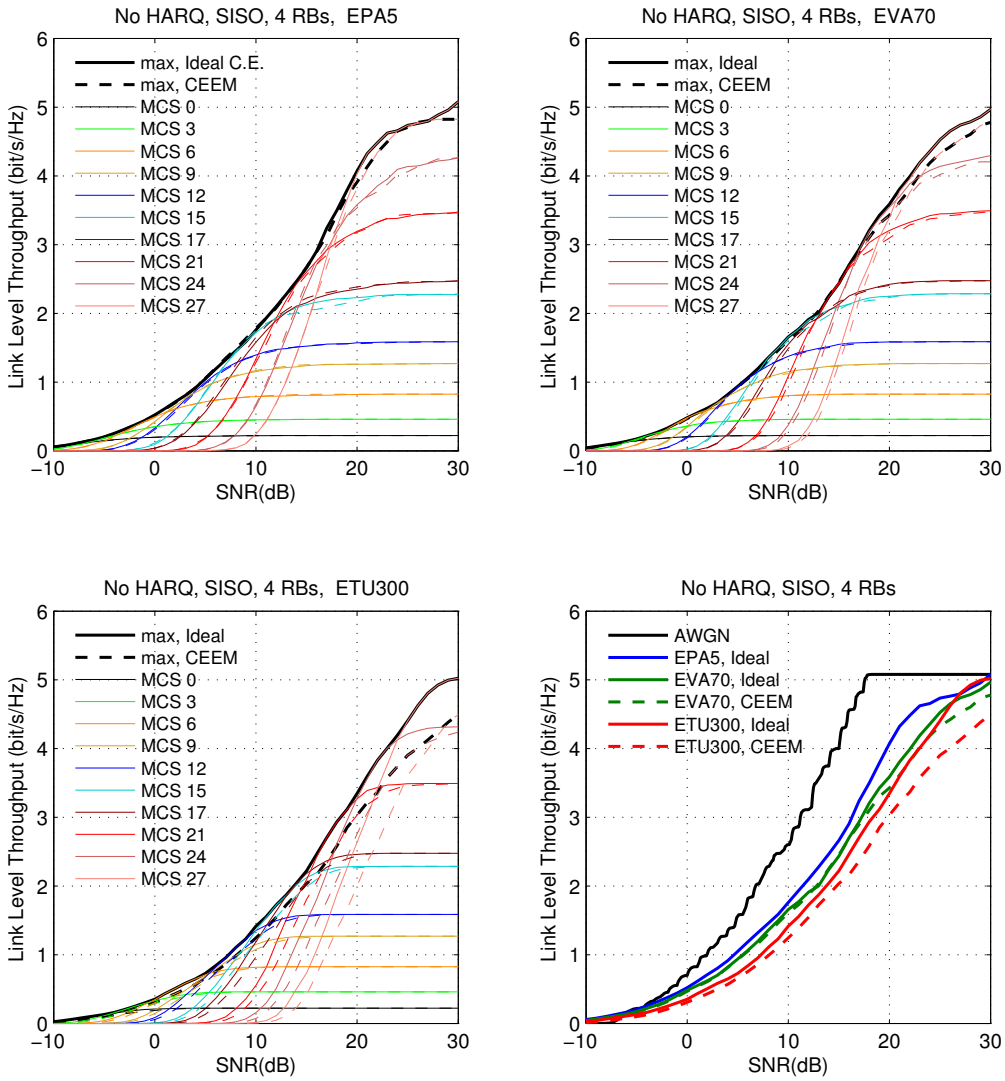

Figure 5.35: E-UTRA DL SISO Link Average Throughput vs. mean SNR without HARQ in EPA5, EVA70 and ETU300 multipath channels and a bandwidth of 4 RBs

5.3.2 MIMO

Figures 5.36 and 5.37 show the E-UTRA DL link average throughput for ideal and CEEM channel estimation without HARQ in EVA70 multipath fading channel for MCS 0, 9, 15 and 27 and 2×2LC and 2×2HC, respectively. For 2×2LC, the loss due to the CEEM channel estimation is significantly large for MCS 27 and MIMO-SM schemes: around 5 dB for OL MIMO-SM with CDD precoding and 2.5 dB for CL MIMO-SM at high SNRs where the error due to channel estimation is much more larger than the error due to AWGN noise that can be considered to be practically null. On the other hand, for MCS 27 and MIMO-TD at high SNRs, there is practically no difference between ideal and CEEM channel estimation thanks to the diversity gain. For 2×2HC, we observe that the loss due to CEEM is higher compared to 2×2LC case and that the CL MIMO-SM outperforms the OL MIMO-SM. However, for MCS 27 and CEEM channel estimation, the MIMO-TD outperforms the CL MIMO-SM; but 1×2 SIMO outperforms the MIMO-TD for SNRs lower than 29 dB.

Figures 5.38 and 5.39 show the E-UTRA DL link average throughput for ideal and CEEM channel estimation without HARQ in ETU300 multipath fading channel for MCS 0, 9, 15 and 27 and 2×2LC and 2×2HC, respectively. In this case, it can be verified that the loss due to CEEM is higher compared to the EVA70 case because the channel estimation error is also higher.

Figures 5.40 and 5.41 show the E-UTRA DL link average throughput for ideal and CEEM channel estimation without HARQ in EVA70 and ETU300 multipath fading channel for MCS 0, 9, 15 and 27 and 4×4LC, respectively. The number of layers per codeword for 4×4 MIMO-SM is $N_L = 2$; while for 2×2 MIMO-SM it is $N_L = 1$. Consequently, the spectrum efficiency of a spatial multiplexed codeword for 4×4 MIMO-SM is multiplied by 2 compared to a spatial multiplexed codeword for 2×2 MIMO-SM. The obtained simulation results verifies this feature for 4×4LC ; but we observe that 4×4 antenna correlation destroys the 4×4MC MIMO-SM link level performance for MCS 9, 15 and 27, as shown in Figure 5.42.

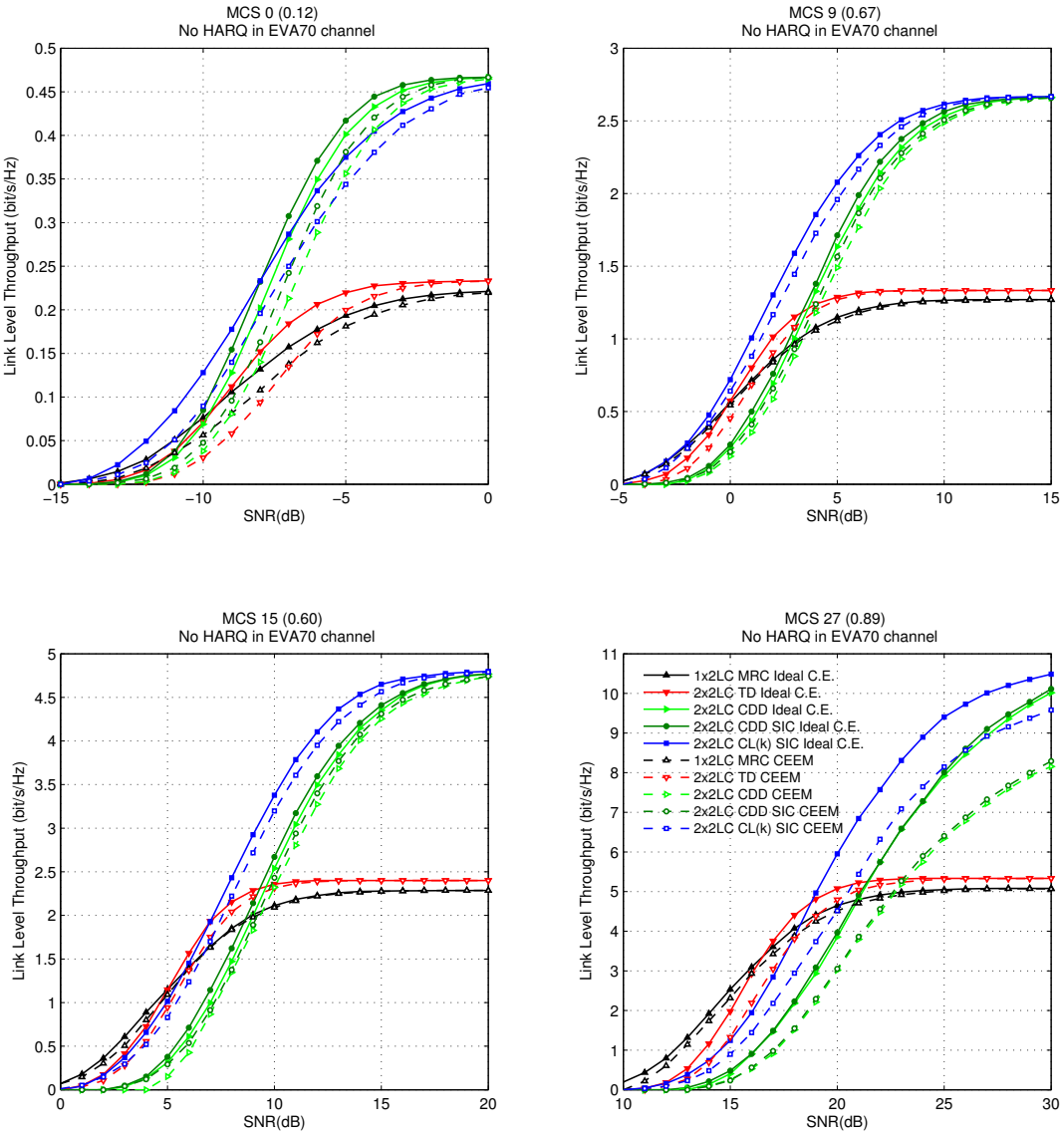

Figure 5.36: E-UTRA DL Link Average Throughput vs. mean SNR without HARQ for 2×2LC MIMO and MCS 0, 9, 15 and 27 in EVA70 channel and 4 RBs

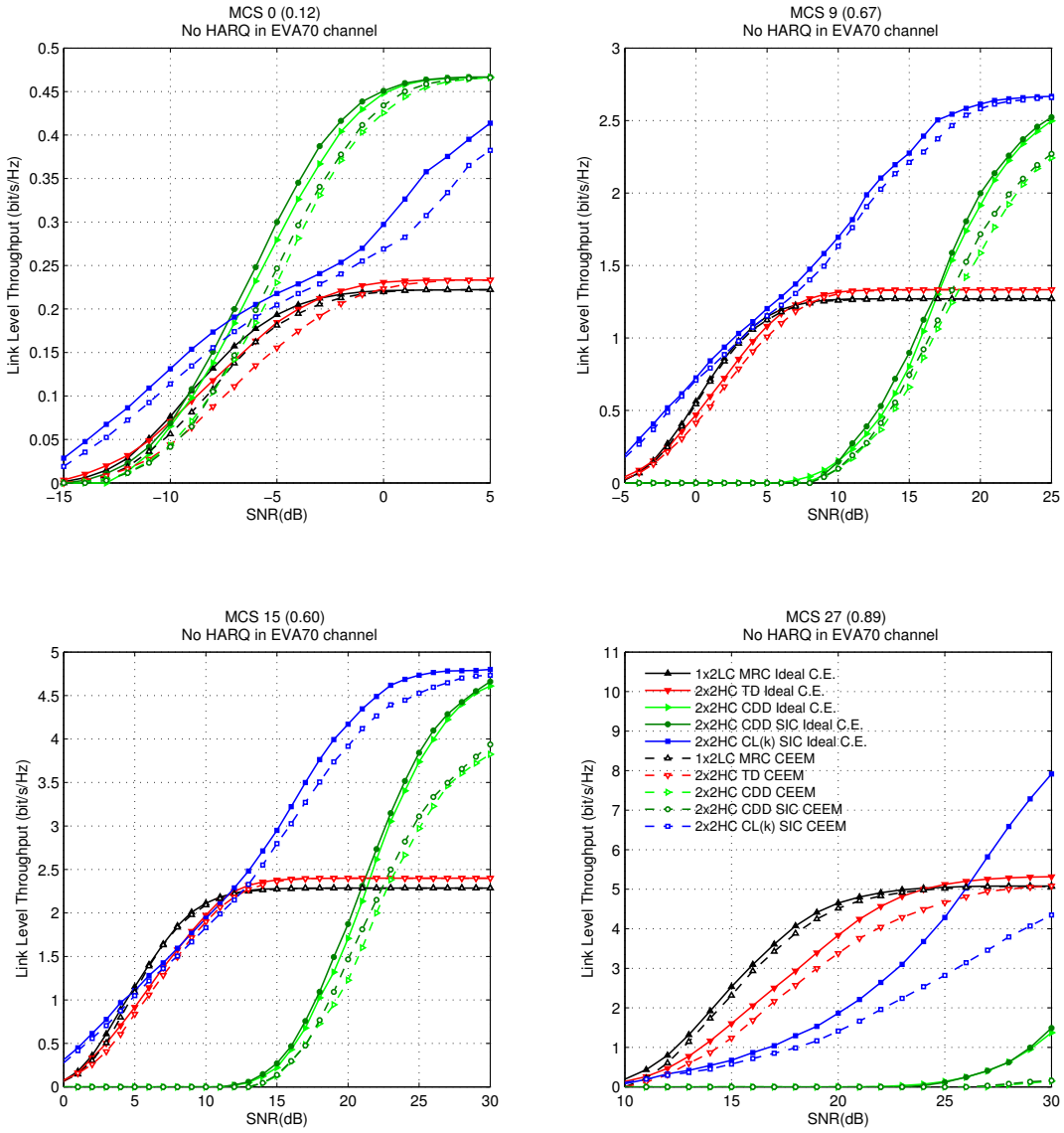

Figure 5.37: E-UTRA DL Link Average Throughput vs. mean SNR without HARQ for 2×2HC MIMO and MCS 0, 9, 15 and 27 in EVA70 channel and 4 RBs

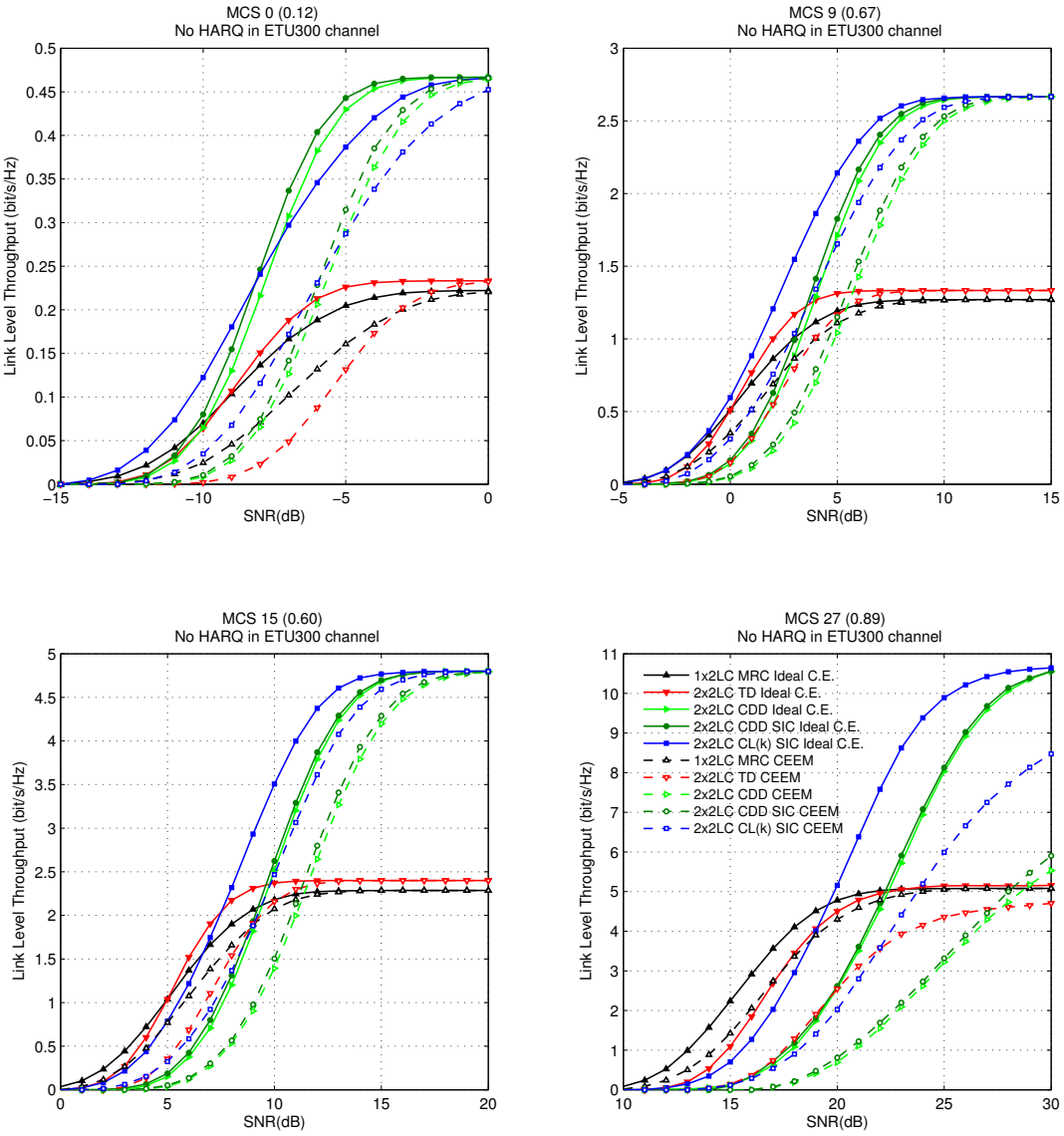

Figure 5.38: E-UTRA DL Link Average Throughput vs. mean SNR without HARQ for 2×2LC MIMO and MCS 0, 9, 15 and 27 in ETU300 channel and 4 RBs

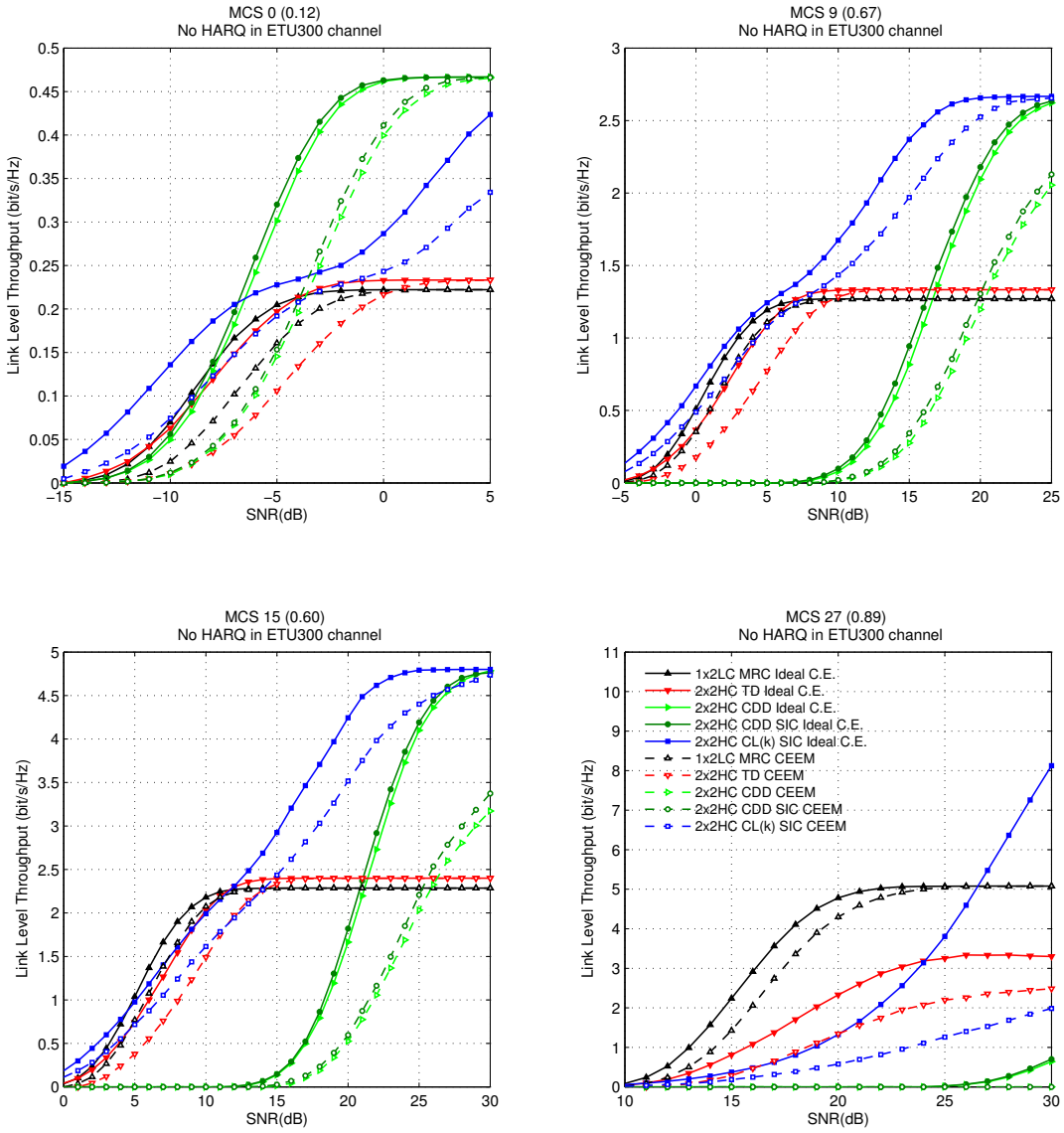

Figure 5.39: E-UTRA DL Link Average Throughput vs. mean SNR without HARQ for 2×2HC MIMO and MCS 0, 9, 15 and 27 in ETU300 channel and 4 RBs

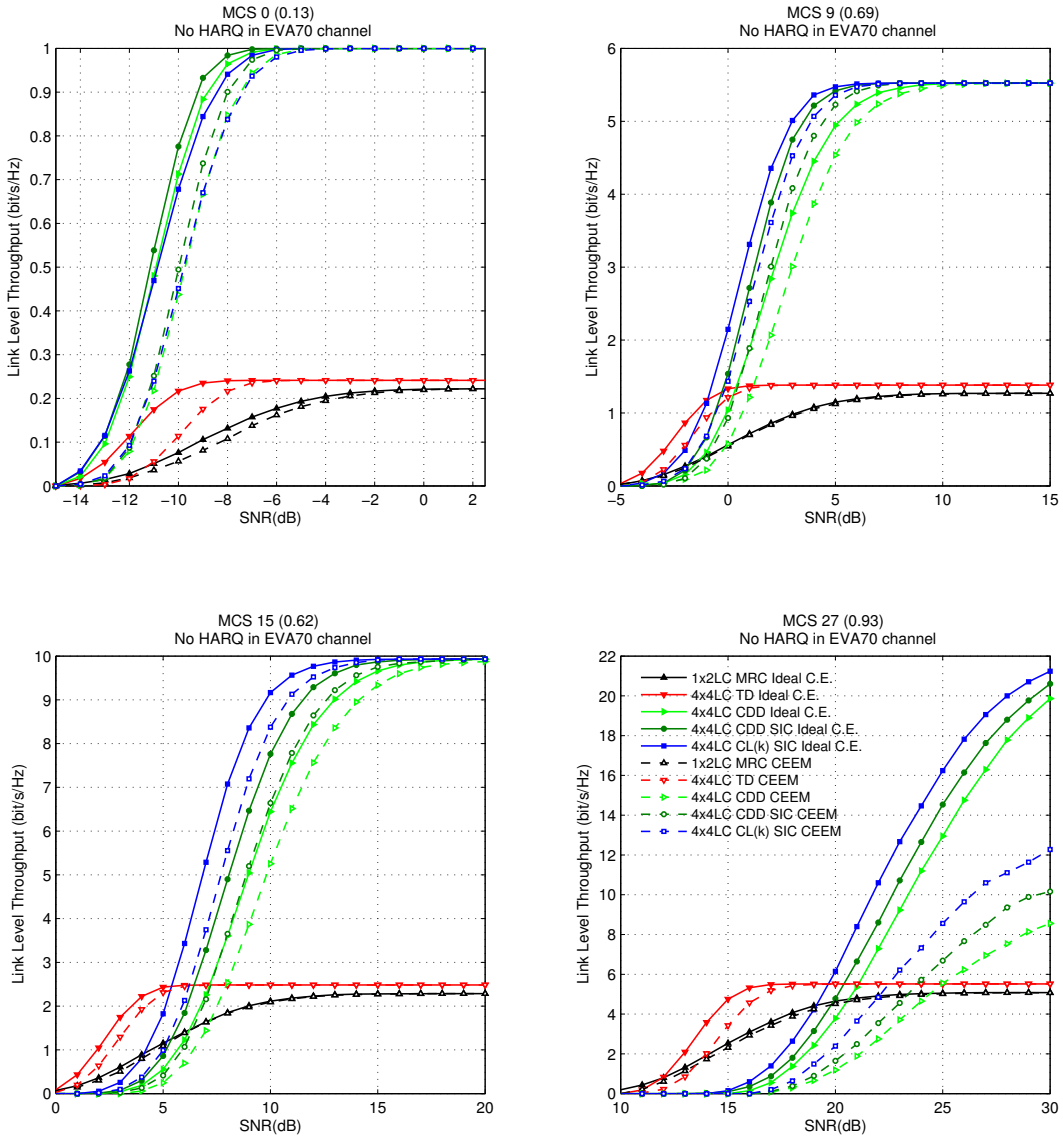

Figure 5.40: E-UTRA DL Link Average Throughput vs. mean SNR without HARQ for 4×4LC MIMO and MCS 0, 9, 15 and 27 in EVA70 channel and 4 RBs

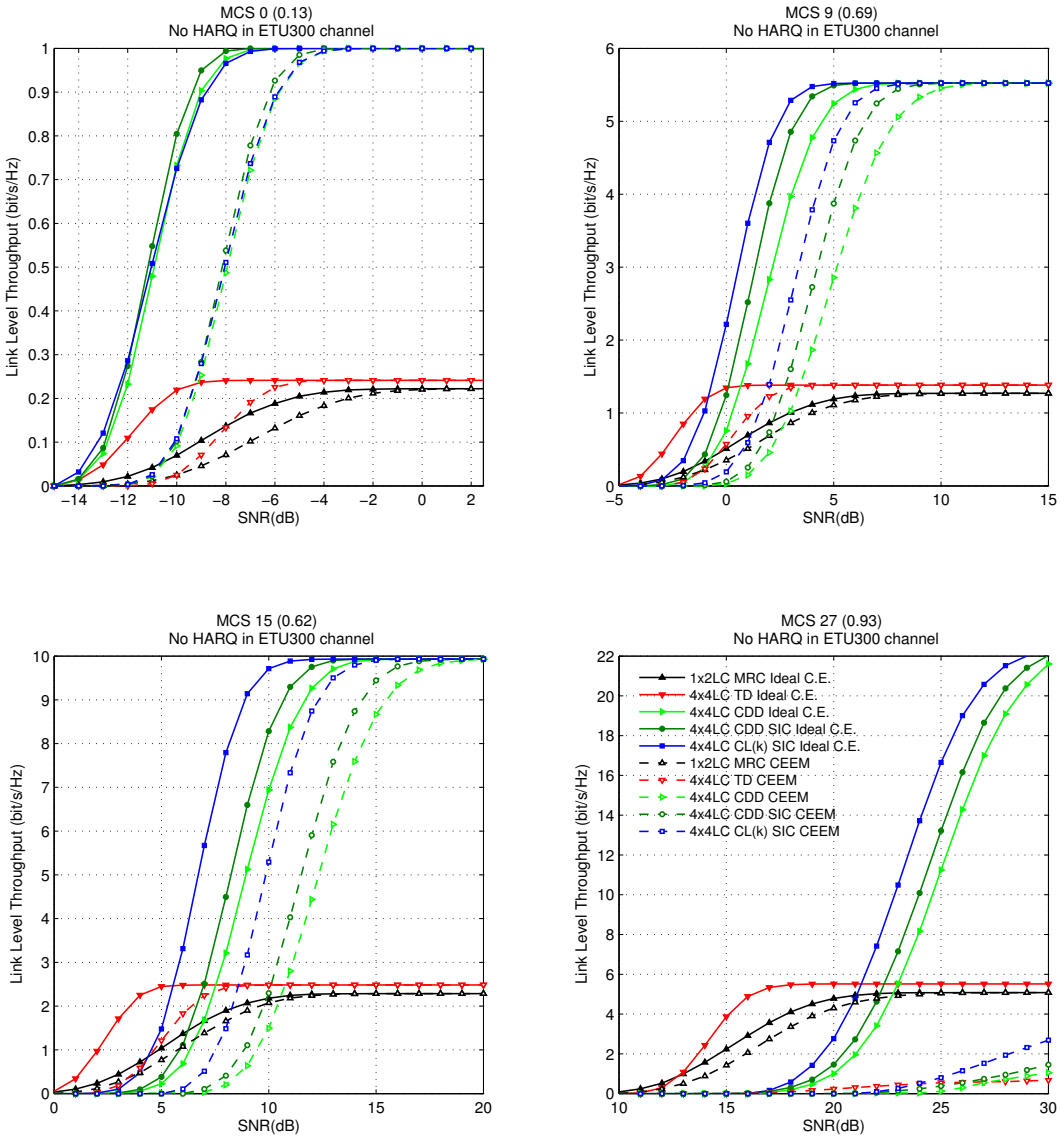

Figure 5.41: E-UTRA DL Link Average Throughput vs. mean SNR without HARQ for 4×4LC MIMO and MCS 0, 9, 15 and 27 in ETU300 channel and 4 RBs

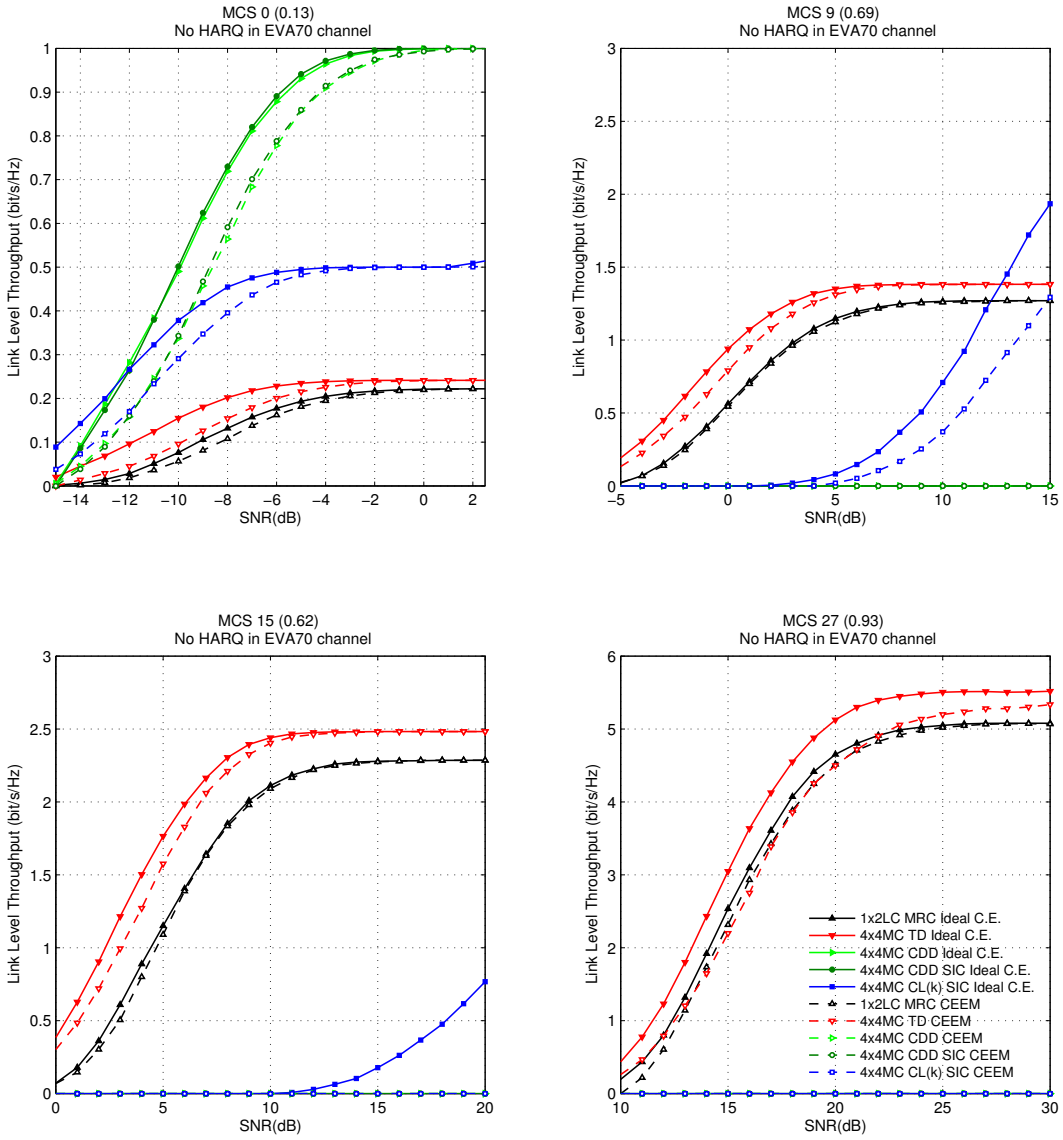

Figure 5.42: E-UTRA DL Link Average Throughput vs. mean SNR without HARQ for 4×4MC MIMO and MCS 0, 9, 15 and 27 in EVA70 channel and 4 RBs

5.3.3 AMC

In the figures of this section, we show the AMC E-UTRA DL link average throughput vs. mean SNR that results from overlapping the individual link average throughputs for MCS 0, 3, 6, 9, 12 ,15, 17, 21, 24 and 27. It has been assumed an ETU300 channel and a bandwidth of 4 RBs. MIMO-TD and MIMO-SM with codeword-SIC receiver and MMSE detector have been considered. In the case of MIMO-SM, the AMC E-UTRA DL link average throughput results from the sum of the link average throughputs of the two spatial multiplexed codewords.

For 2×2LC MIMO, Figures 5.43 and 5.44 show the AMC E-UTRA DL link average throughput with and without HARQ for ideal channel estimation and CEEM, respectively. Subfigures 5.43(a) and 5.44(a) show the simulation results for MIMO-TD, subfigures 5.43(b) and 5.44(b) show the simulation results for OL MIMO-SM with CDD precoding and subfigures 5.43(c) and 5.44(c) show the simulation results for CL MIMO-SM with CL(k) precoding.

For 2×2HC MIMO, Figures 5.45 and 5.46 show the AMC E-UTRA DL link average throughput with and without HARQ for ideal channel estimation and CEEM, respectively. Subfigures 5.45(a) and 5.46(a) show the simulation results for MIMO-TD, subfigures 5.45(b) and 5.46(b) show the simulation results for OL MIMO-SM with CDD precoding and subfigures 5.45(c) and 5.46(c) show the simulation results for CL MIMO-SM with CL(k) precoding.

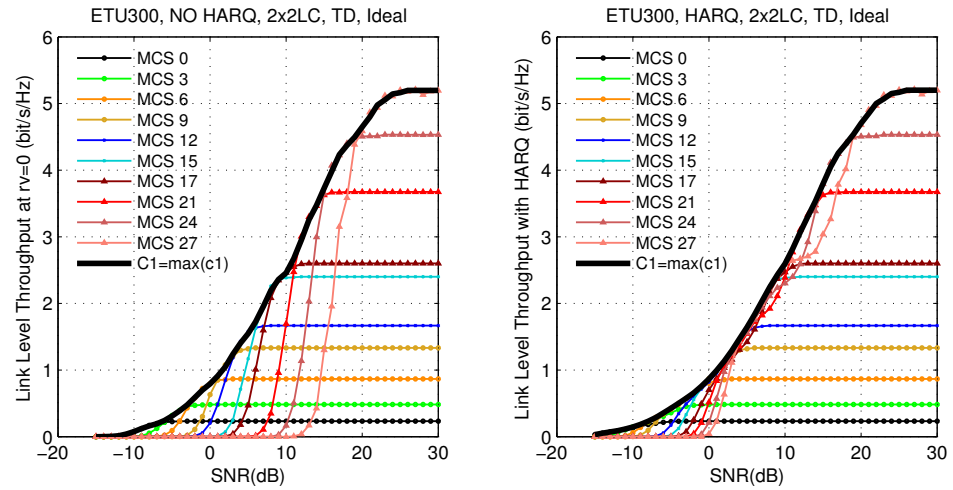

(a) MIMO-TD

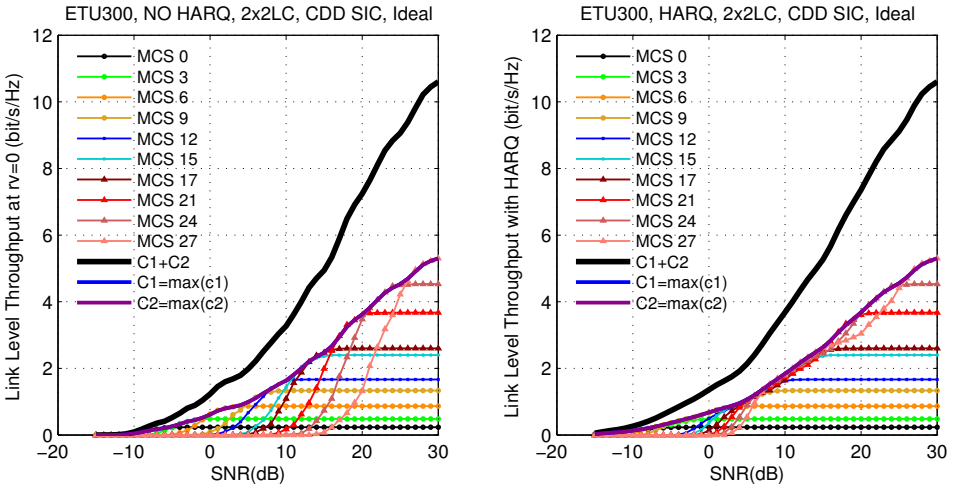

(b) OL MIMO-SM with CDD precoding

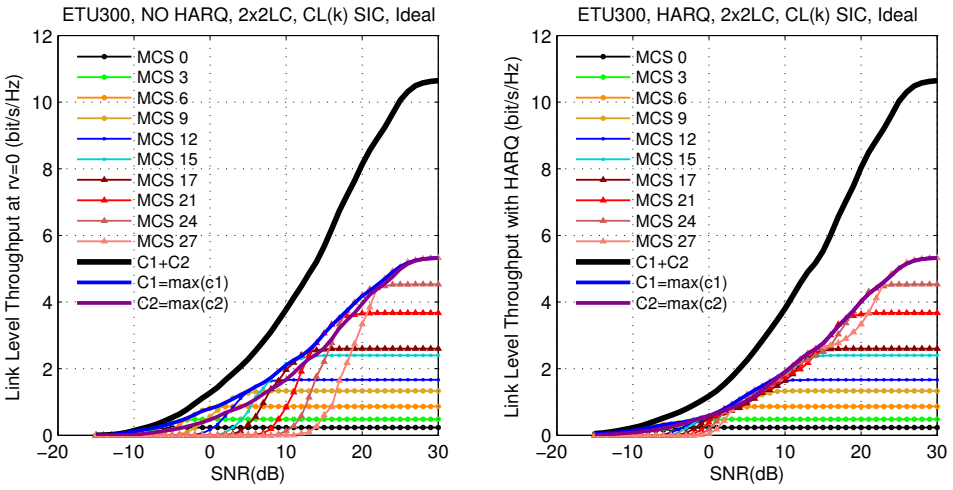

(c) CL MIMO-SM with CL(k) precoding

Figure 5.43: AMC E-UTRA DL Link Average Throughput vs. mean SNR without HARQ (on the left) and with HARQ (on the right) for 2×2LC MIMO and ideal channel estimation in ETU300 channel and a bandwidth of 4 RBs: (a) TD, (b) CDD precoding and (c) CL(k) precoding

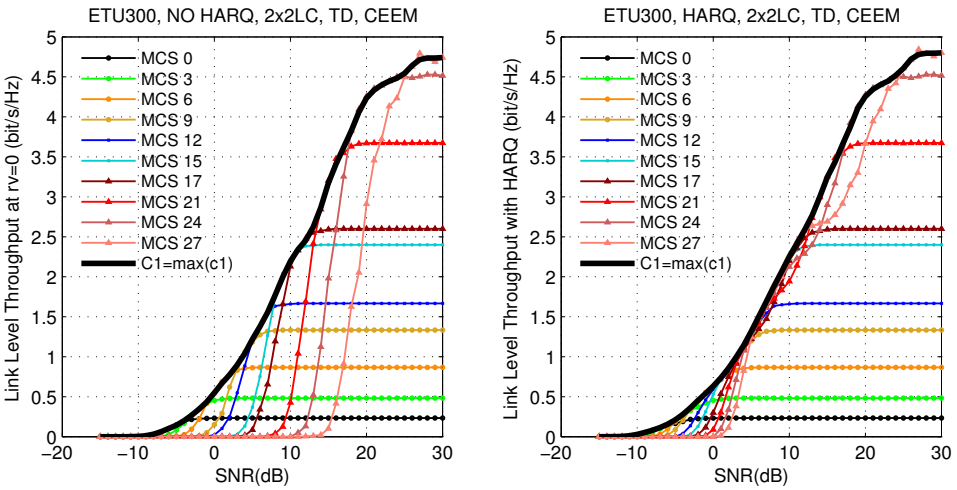

(a) TD

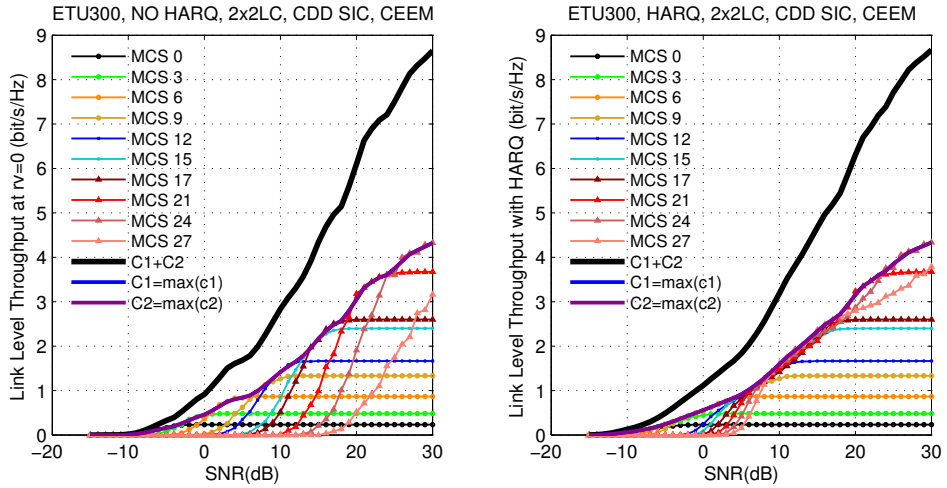

(b) CDD Precoding

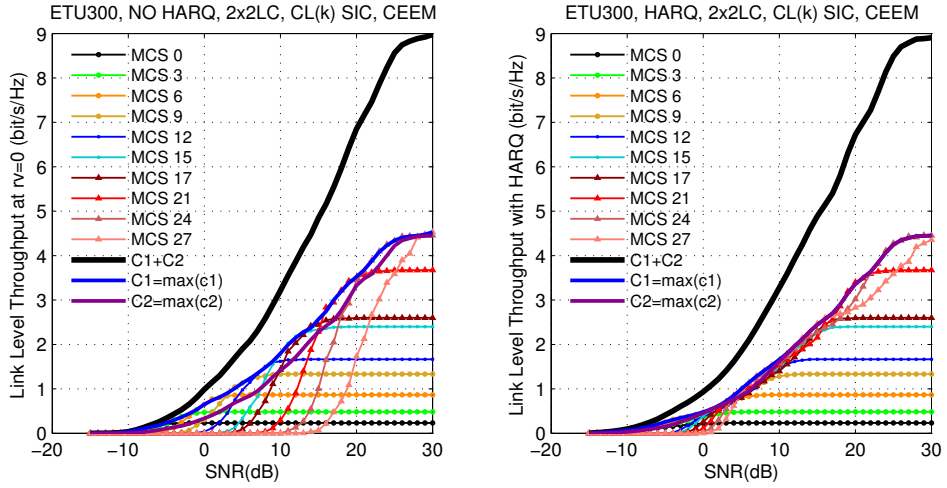

(c) CL(k) Precoding

Figure 5.44: AMC E-UTRA DL Link Average Throughput vs. mean SNR without HARQ (on the left) and with HARQ (on the right) for 2×2LC MIMO and CEEM channel estimation in ETU300 channel and a bandwidth of 4 RBs: (a) TD, (b) CDD precoding and (c) CL(k) precoding

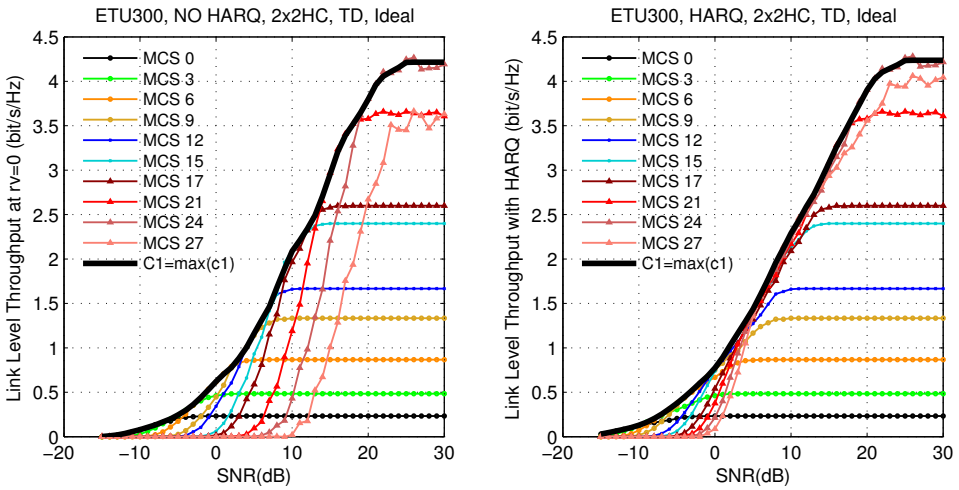

(a) MIMO-TD

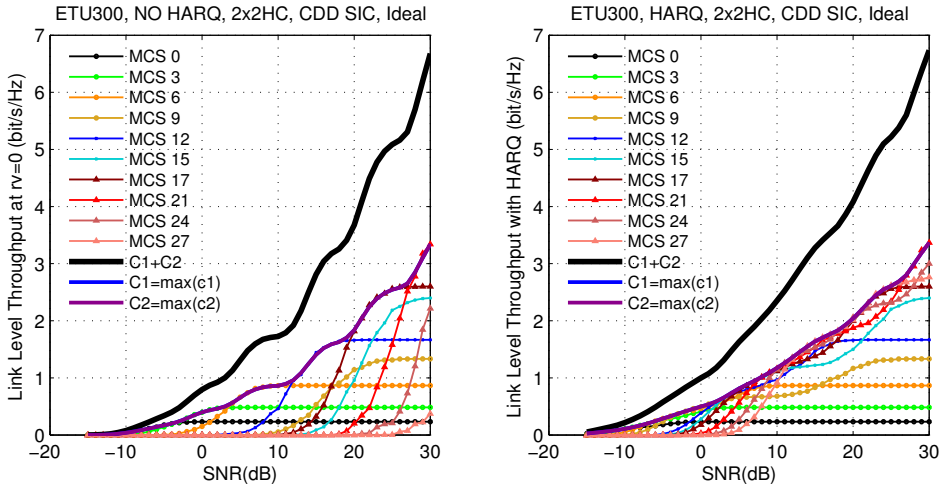

(b) OL MIMO-SM with CDD precoding

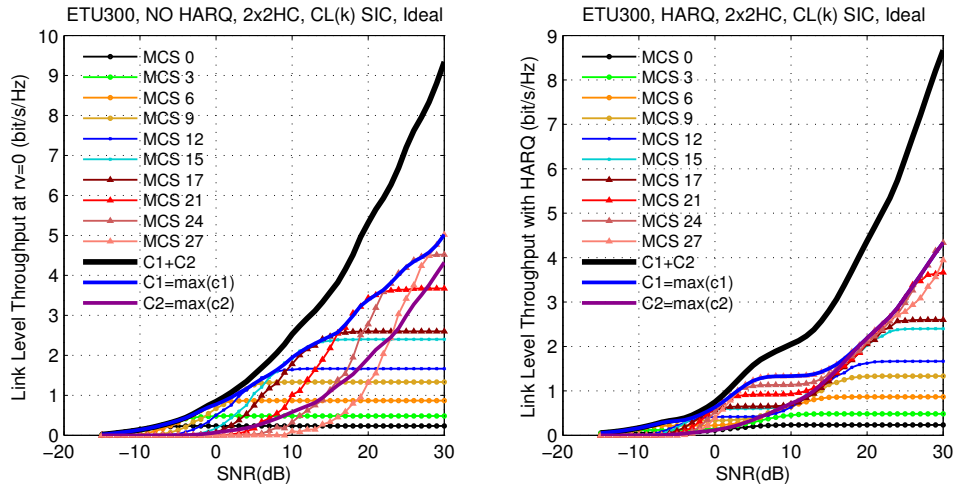

(c) CL MIMO-SM with CL(k) precoding

Figure 5.45: AMC E-UTRA DL Link Average Throughput vs. mean SNR without HARQ (on the left) and with HARQ (on the right) for 2×2HC MIMO and ideal channel estimation in ETU300 channel and a bandwidth of 4 RBs: (a) TD, (b) CDD precoding and (c) CL(k) precoding

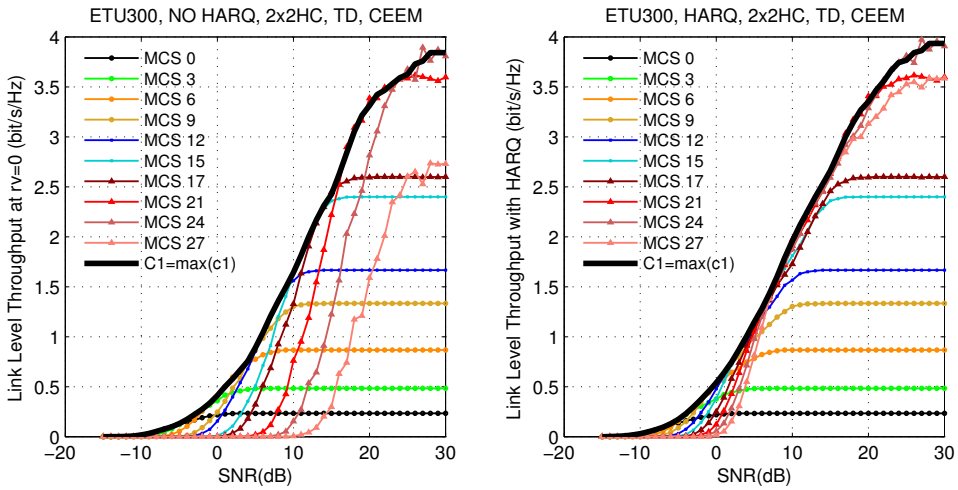

(a) TD

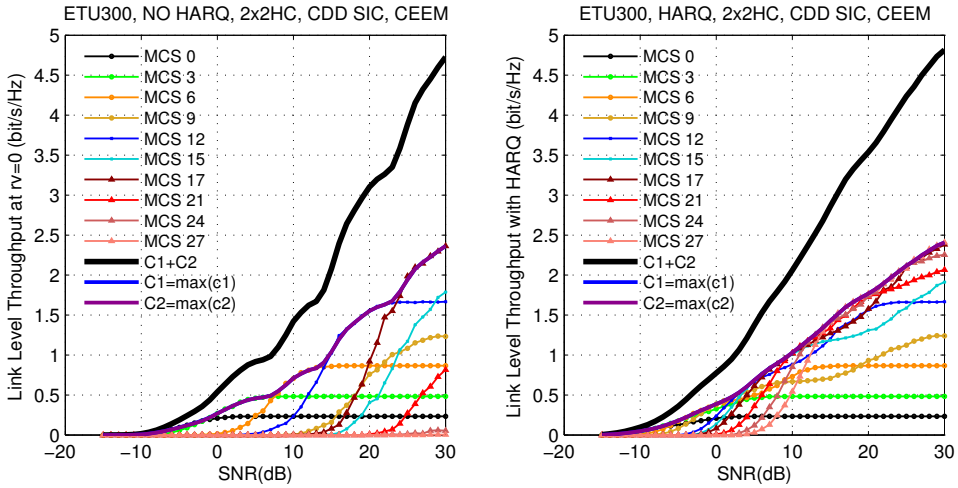

(b) CDD Precoding

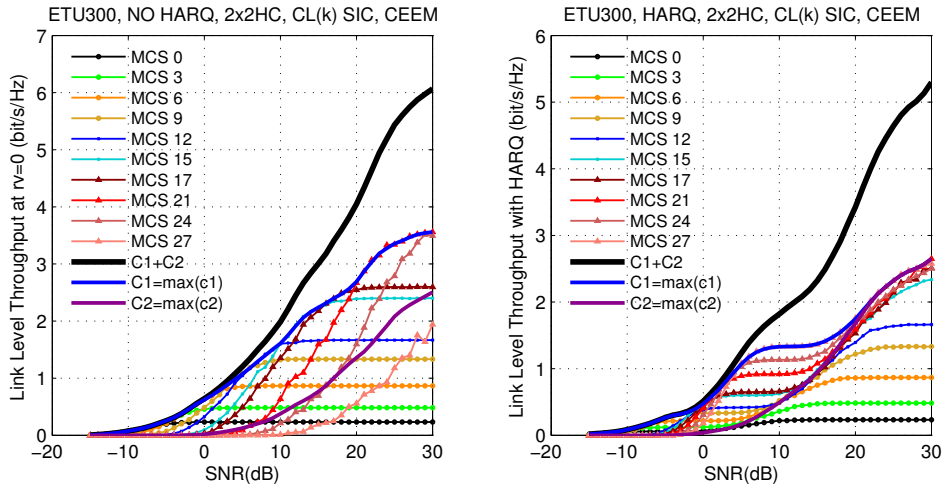

(c) CL(k) Precoding

Figure 5.46: AMC E-UTRA DL Link Average Throughput vs. mean SNR without HARQ (on the left) and with HARQ (on the right) for 2×2HC MIMO and CEEM channel estimation in ETU300 channel and a bandwidth of 4 RBs: (a) TD, (b) CDD precoding and (c) CL(k) precoding

5.3.4 MIMO-TD vs. MIMO-SM

5.3.4.1 TD and SM trade-off for SU-MIMO schemes without HARQ

Figures 5.47 and 5.48 show the AMC E-UTRA DL link average throughput vs. mean SNR without HARQ (i.e, at rv= 0) in EVA70 and ETU300 channels, respectively. It has been also considered ideal and CEEM channel estimation, 1×2, 2×2 and 4×4 MIMO with LC, MC and HC antenna correlations, codeword-SIC receiver with MMSE detector for MIMO-SM. The transmission modes which have been evaluated are listed below:

- TM 1: Single Antenna Port: 1×2 SIMO antenna configuration with MRC at reception.
- TM 2: MIMO-TD: 2×2 and 4×4 MIMO with SFBC (based on Alamouti Scheme) and MRC at reception.
- TM 3: OL MIMO-SM: Large Delay CDD Precoding.
- TM 4: CL MIMO-SM: Codebook-based precoding (CL(k) Precoding).

The obtained link average throughput for TM 1 is depicted as a reference. For 2×2LC and 4×4LC, MIMO-SM schemes get higher throughput than MIMO-TD for the whole range of SNR. On the other hand, it can be verified that the antenna correlation degrades the achievable throughput in MIMO-SM transmission modes. For 2×2MC and 2×2HC in EVA70 channel, the throughput obtained by MIMO-TD is slightly higher than the obtained by OL MIMO-SM below an SNR around 20 dB. For 4×4MC, CL MIMO-SM is the best option, while for 4×4HC, MIMO-TD is the best option except for high SNRs where the best option is CL MIMO-SM. As it can be observed by comparing the performance in EVA70 and ETU300 channels, the results for the TD vs. SM tradeoff are quite similar in both cases.

The E-UTRA requirement for the DL peak rate for the case of 2×2 MIMO, shown in Table 2.7, is 8.6 bits/s/Hz; therefore, without HARQ, it can be deduced from the DL link level simulations that this fact is feasible with low antenna correlation and MIMO-SM at high SNRs. For instance, the required throughput of 8.6 bits/s/Hz is achieved at around 21 dB in case of 2×2LC MIMO channel and ideal channel estimation. The required SNR is almost 30 dB in the case of CEEM. In the case of a 2×2MC MIMO channel, then the required throughput is achieved approximately at around 27 dB when ideal channel estimation when CL MIMO-SM is considered.

To sum up, when HARQ is not considered, SM throughput outperforms TD throughput for LC antenna correlation and CL MIMO-SM outperforms TD and OL MIMO-SM throughput for MC antenna correlation. For HC antenna correlation, it is only for high SNRs that CL MIMO-SM outperforms TD; however, it must be taken into account that it has been assumed perfect CL precoding. Lastly, in the case of correlated MIMO channels, TD gets better performance than OL MIMO-SM.

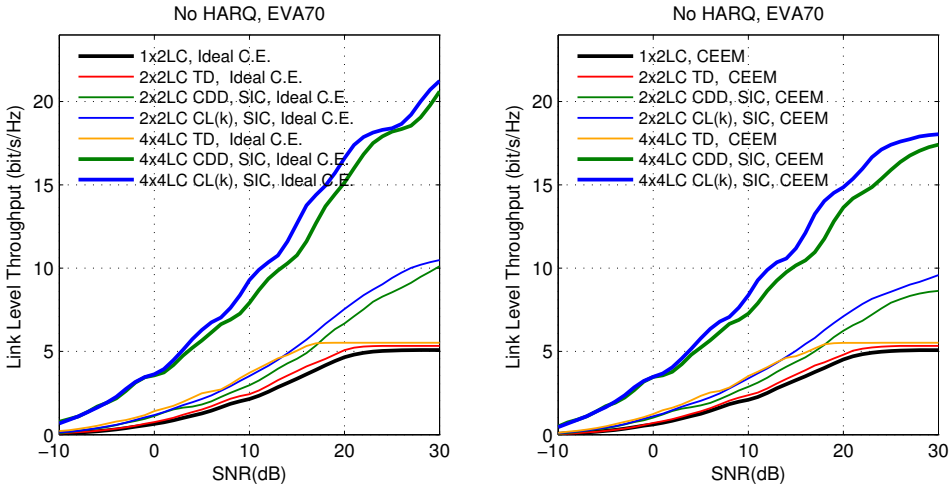

(a) Low Antenna Correlation

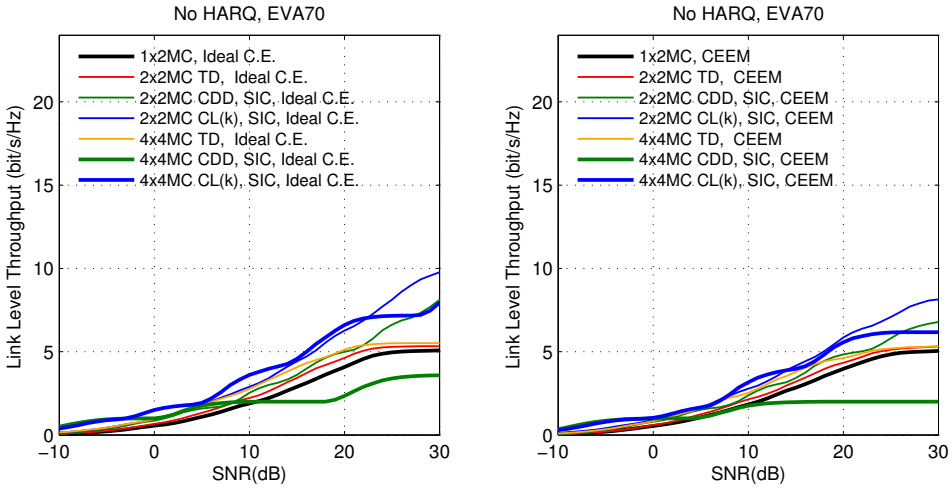

(b) Medium Antenna Correlation

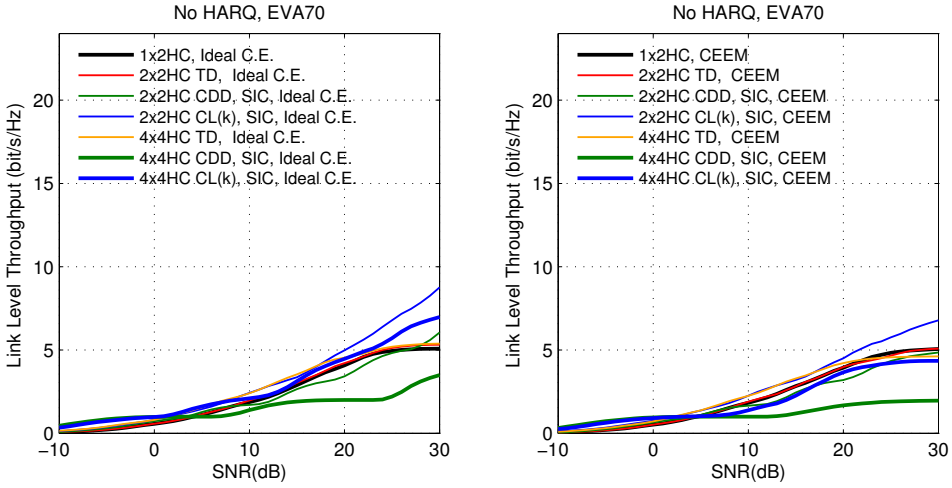

(c) High Antenna Correlation

Figure 5.47: AMC E-UTRA DL Link Average Throughput vs. mean SNR without HARQ in EVA70 channel with ideal (on the left) and CEEM (on the right) channel estimation and 4 RBs

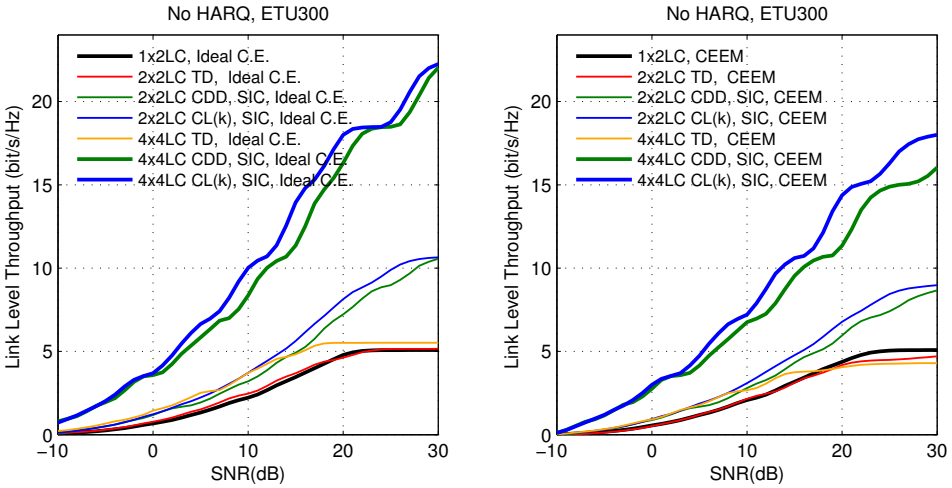

(a) Low Antenna Correlation

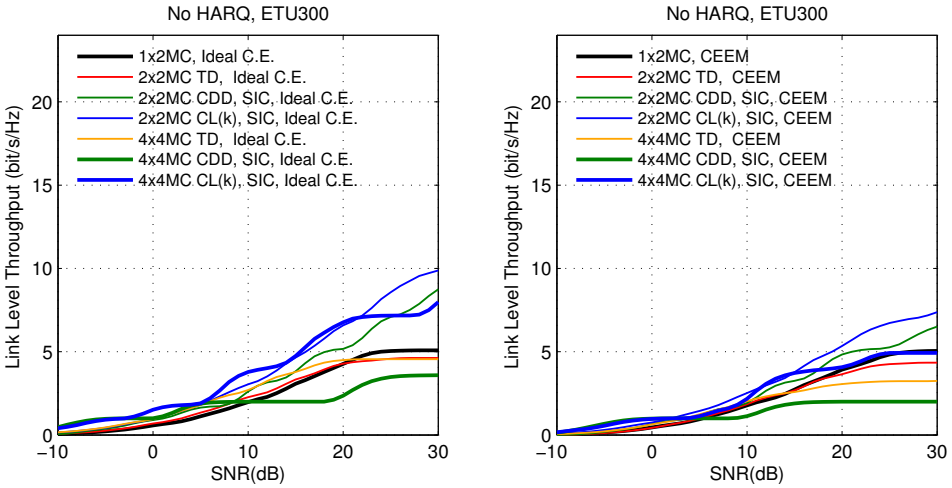

(b) Medium Antenna Correlation

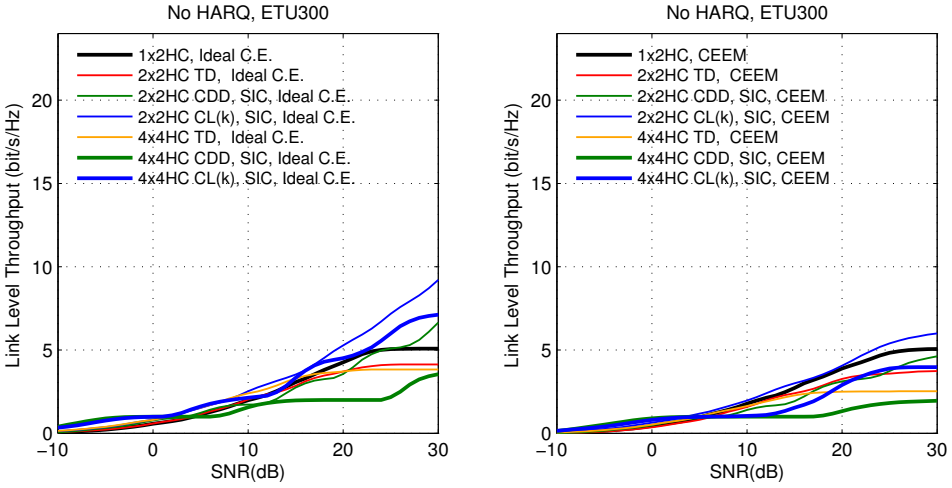

(c) High Antenna Correlation

Figure 5.48: AMC E-UTRA DL Link Average Throughput vs. mean SNR without HARQ in ETU300 channel with ideal (on the left) and CEEM (on the right) channel estimation and 4 RBs

5.3.4.2 TD and SM trade-off for SU-MIMO schemes with HARQ

Figures 5.49 and 5.50 show the AMC E-UTRA DL link average throughput vs. mean SNR with HARQ in EVA70 and ETU300 channels, respectively. We have considered 2×2LC, 2×2MC and 2×2HC and ideal and CEEM channel estimation. In addition, it has been assumed the same SNR for each HARQ retransmission. For 2×2LC, MIMO-SM gets higher average throughputs than MIMO-TD for the whole range of SNRs for both EVA70 and ETU300 channels and both ideal and CEEM channel estimation.

For 2×2MC, OL MIMO-SM outperforms MIMO-TD. Furthermore, CL MIMO-SM only gets higher throughputs than OL MIMO-SM for an average SNR higher than 22 dB for ideal channel estimation and 28 dB for CEEM in EVA70 channel. Considering ETU300, CL MIMO-SM only outperforms OL MIMO-SM with ideal channel estimation for an average SNR higher than 25 dB. For 2×2HC, at low SNRs, MIMO-SM and MIMO-TD obtain the same throughput approximately. However, CL and OL MIMO-SM outperform MIMO-TD for high SNRs only in the case of ideal channel estimation, an SNR higher than 21 dB and 25 dB in EVA70 and ETU300 channels, respectively. For CEEM and EVA70, only CL MIMO-SM gets higher throughputs than MIMO-TD for an average SNR higher than 23 dB. For CEEM and ETU300, 1×2 with MRC at the receiver gets similar throughputs than MIMO schemes for lower SNRs. For higher SNRs, MIMO-TD and OL MIMO-SM performance is lower than 1×2 with MRC at the receiver; a loss of 5 dB and 2.5 dB is observed, respectively.

The E-UTRA requirement for the DL peak rate for the case of 2×2 MIMO is 8.6 bits/s/Hz and this requirement is more feasible with HARQ. In particular, for LC antenna correlation, it is achieved for MIMO-SM schemes with ideal and CEEM channel estimation; while for MC and HC antenna correlations, it is achieved for MIMO-SM schemes with ideal channel estimation. For LC antenna correlation, ideal channel estimation and EVA70 or ETU300 channel, the DL peak rate of 8.6 bits/s/Hz for 2×2 MIMO is achieved approximately at an average SNR higher than 21 dB for CL MIMO-SM and at an average SNR higher than 23 dB for OL MIMO-SM. For CEEM channel estimation and EVA70 channel, this is achieved approximately at an average SNR higher than 24 dB for CL MIMO-SM and at an average SNR higher than 25 dB for OL MIMO-SM.

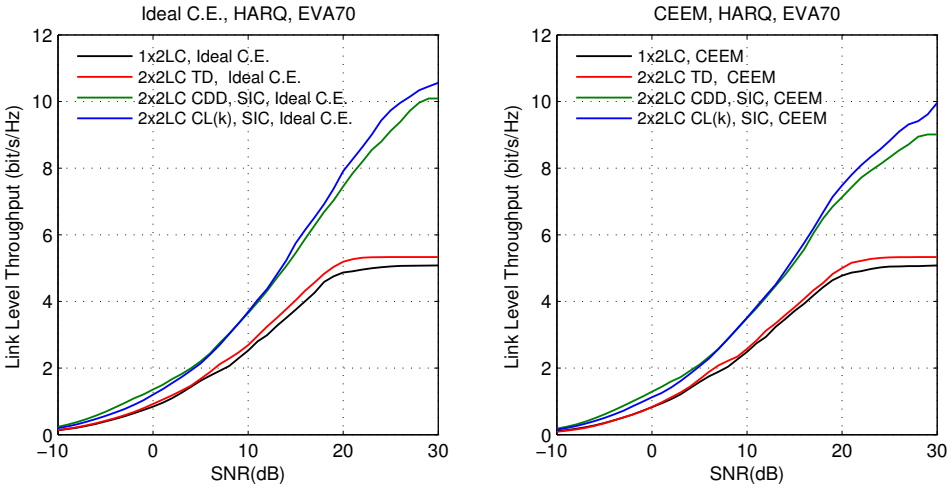

(a) Low Antenna Correlation

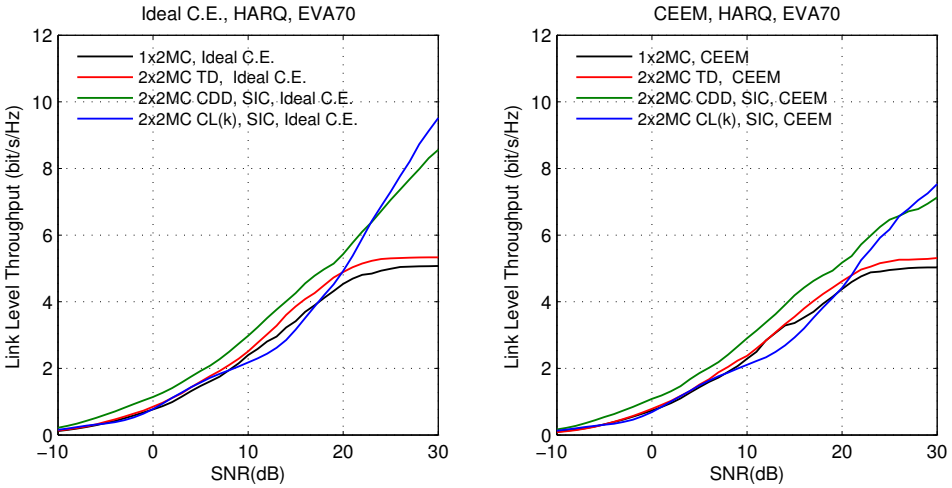

(b) Medium Antenna Correlation

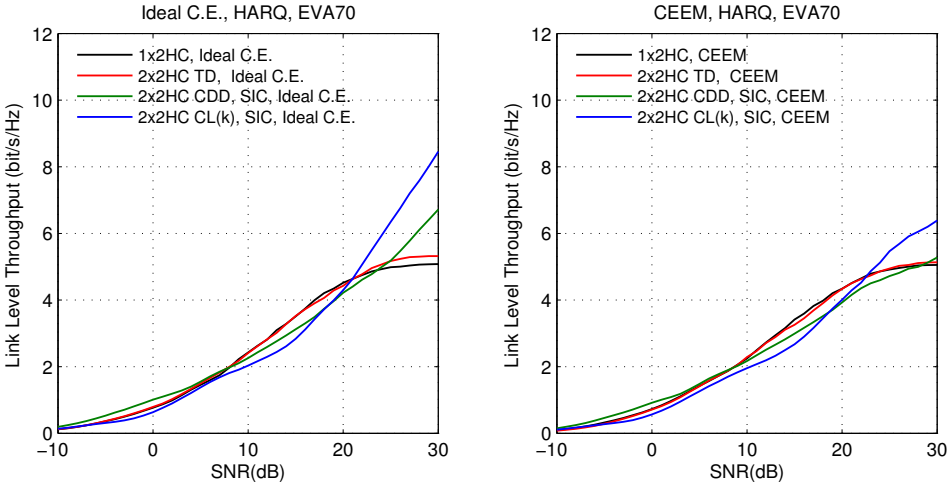

(c) High Antenna Correlation

Figure 5.49: AMC E-UTRA DL Link Average Throughput vs. mean SNR for OL vs. CL 2×2 MIMO schemes and different antenna correlations in EVA70 channel with ideal (on the left) vs. CEEM (on the right) channel estimation and 4 RBs

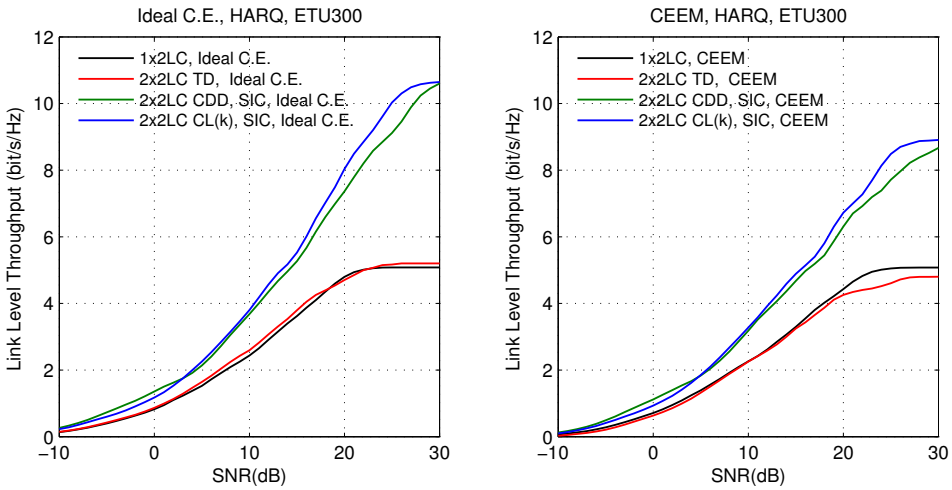

(a) Low Antenna Correlation

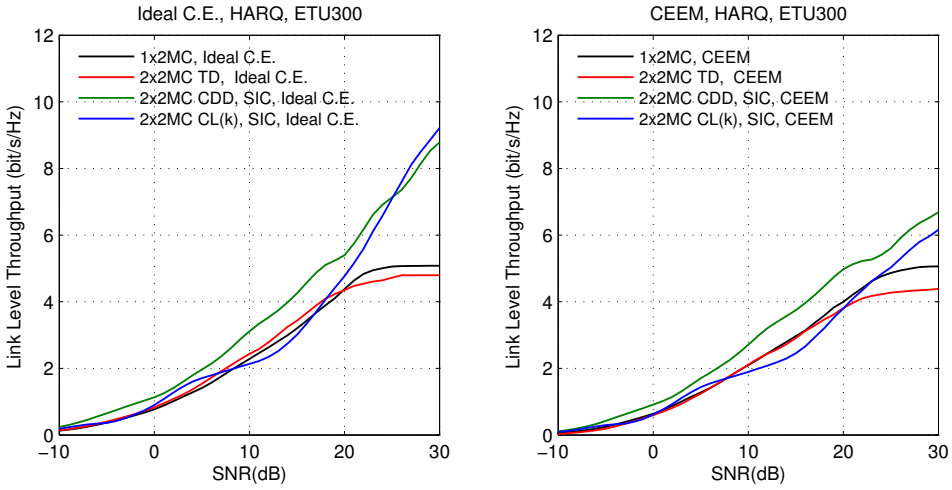

(b) Medium Antenna Correlation

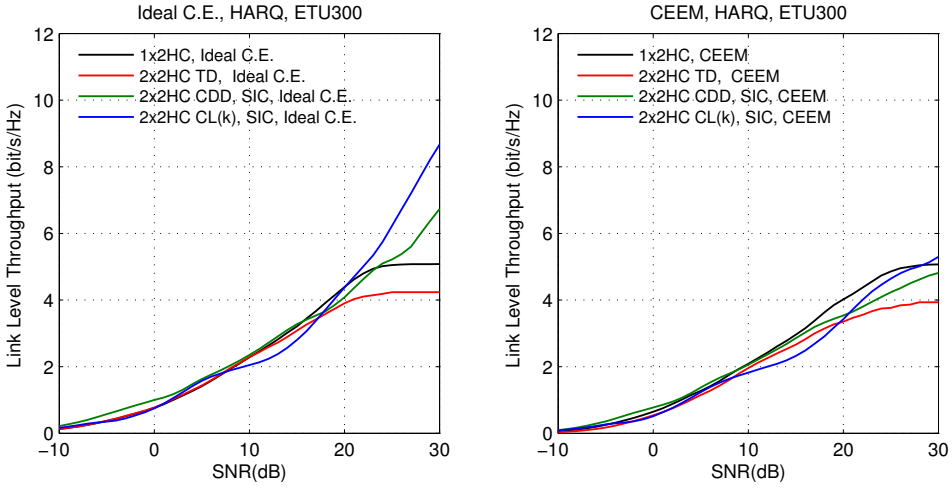

(c) High Antenna Correlation

Figure 5.50: AMC E-UTRA DL Link Average Throughput vs. mean SNR for OL vs. CL 2×2 MIMO schemes and different antenna correlations in ETU300 channel with ideal (on the left) vs. CEEM (on the right) channel estimation and 4 RBs

Chapter 6

Link Abstraction for E-UTRA

In this chapter, we propose a novel link abstraction method to predict the BLER with good accuracy in multipath fading and including the effects of HARQ retransmissions. The proposed method is based on estimating the MI between the transmitted bits and the received LLRs. We start introducing the link abstraction techniques. We then introduce two type of link abstraction methods, *Exponential ESNR* (EESNR) and MIESM. Next we show that, by working at bit level, the effect of unequal error protection in 16QAM and 64QAM modulations is properly captured without resorting to any set of calibration constants. Furthermore, we show how to reduce the set of reference BLER curves when working with multiple MCSs. Lastly we present the simulation results for LTE/LTE-Advanced DL taking into account SISO and 2×2 MIMO TMs.

6.1 Introduction to Link Abstraction

The classical approach for interfacing link level to system level simulators is to generate look-up tables of mean coded BER versus the mean SNR values. This approach is no longer valid for wideband packet mode systems like LTE/LTE-Advanced where one transport block, made up of one or more code blocks forming a codeword, is send in a TTI of 1 ms using a variable number of physical resource blocks, where each resource block occupies 12 OFDM subcarriers (180 kHz). In a wideband multipath channel environment, each OFDM subcarrier may suffer a different attenuation and this attenuation may undergo little variations in a TTI as shown in Figure 6.1 and, consequently, every subcarrier of each OFDM symbol that forms the codeword has a different SNR. The transmitted codeword are thus affected by a multistate channel.

A multistate channel arises when the received LLRs, within a given codeword, shows very different reliabilities. This is typically due to frequency selective fading, which may show important variations throughout the OFDM subcarriers. The LLR combination that happens before decoding when HARQ is in use also creates a multistate channel, and even the unequal error protection of high order modulations can be interpreted as a multistate channel. Considering all these effects together is a challenging (but necessary, [93]) task and Link abstraction techniques aim at obtaining LUTs to predict the BLER link performance for multistate channels, [94].

Link abstraction techniques take as input the SNR of each subcarrier (or group of subcarriers) and obtain a single scalar value, called the ESNR that can predict the BLER of the link. The reference BLER curves (BLER for the different AMC formats in AWGN channel) play an important role in this methodology. Depending of the desired accuracy, link abstraction techniques may become complex.

One popular choice for link abstraction is *Exponential Effective SNR Metric* (EESM), which derives from the union bound for the BLER performances of convolutional codes, [51], [10]. The advantage of EESM is that the weighting function that is used for averaging the SNR of the

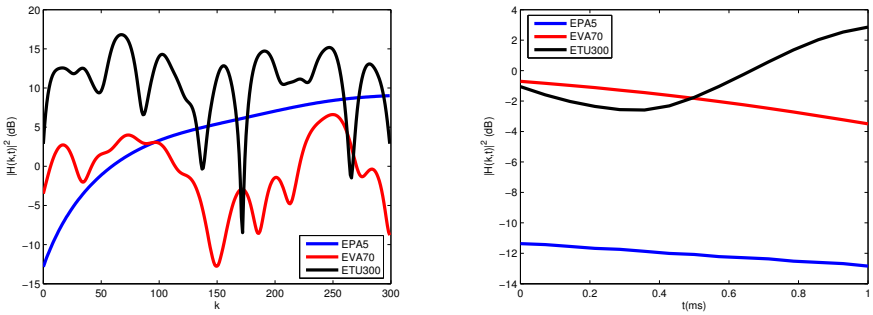

(a) Over 300 frequency subcarriers (b) Over 1 ms TTI time

Figure 6.1: Example of realizations of the EPA5, EVA70 and ETU300 multipath channel frequency response showing different frequency fading dynamic range. Bandwidth of 25 RBs and subcarrier spacing of 15 KHz

subcarriers has a closed form, but EESM requires training, i.e. to obtain good BLER predictions it is necessary to previously obtain a set of parameters which are dependent on the AMC format and on the transmission mode. Another possibility is the *Mutual Information based exponential SNR Mapping* (MIESM) which outperforms EESM in terms of BLER prediction accuracy and does not require training, [94], [34]. It is also interesting to predict the BLER after one or more IR retransmissions have happened in order to take into account HARQ, [11].

6.2 Link Abstraction Models: EESNR and MIESM

This section gives an overview of the two well-known types of link abstraction models: EESM and MIESM, which can be used for MIMO-OFDM systems, [95]. Link abstraction techniques are able to summarize the vector of channel parameters (the subcarrier SNRs for example) into a single scalar value, called the ESNR, which can be used to predict the BLER. Furthermore, link abstraction techniques should be as accurate and simple as possible, since they are used at system level simulators (which cannot cope with the complexity of simulating the link layer details for all system users) and also at the UE to obtain the CQIs that are periodically reported to the eNodeB.

The concept of finding an ESNR is the main idea behind link abstraction and this single scalar value summarizes the whole set of multistate channel quality measurements. In particular, the ESNR summarizes the information capacity limitations due to the applied modulation and code rate, plus the effects of all channel impairments experienced by a given TB transmitted inside one or more RBs, i.e.: propagation losses, shadowing fading, frequency selective fading and thermal plus interference noise power. Given an experimental BLER measured in a multistate channel with a specific MCS, the ESNR of that channel is defined as the SNR that would produce the same BLER, with the same MCS, in AWGN conditions. As explained in [94], for a given multistate channel with N different SNR measurements $\gamma_1, \gamma_2, \ldots \gamma_N$, the ESNR can be estimated as the value γ_{eff} that accomplishes the following equation:

$$I\left(\frac{\gamma_{eff}}{\alpha_1}\right) = \frac{1}{N}\sum_{k=1}^{N} I\left(\frac{\gamma_k}{\alpha_2}\right) \tag{6.1}$$

where N depends on the frequency resolution of the measurements available at the mobile node. Since one value of the ESNR for each group of resource blocks is required to report the CQIs according to the LTE specifications, the value of N should span a bandwidth equivalent to a *Resource Block Group* (RBG). A RBG is a set of 1, 2, 3 or 4 consecutive resource blocks (the actual value depends on the system bandwidth, see [33]). So the ESNR can be isolated from 6.1 as:

$$\gamma_{eff} = \alpha_1 \cdot I^{-1}\left(\frac{1}{N}\sum_{k=1}^{N} I\left(\frac{\gamma_k}{\alpha_2}\right)\right) \tag{6.2}$$

where the function $I(\cdot)$ is used to calculate a weighted average of the individual SNR measurements that allows to estimate the amount of information that can be delivered by a modulation symbol at a given SNR. The constants α_1 and α_2 are needed to adjust the obtained ESNR in a way that the MSE of the BLER prediction error given by Equation 6.3 is minimized.

$$MSE(\alpha_1, \alpha_2) = \frac{1}{M}\sum_{l=1}^{M}\left[\log 10\left(BLER_l\right) - \log 10\left(BLER_R\left(ESNR_l\left(\alpha_1, \alpha_2\right)\right)\right)\right]^2 \tag{6.3}$$

where it is assumed that an experiment, consisting in transmitting exactly N_{rv} rvs of the same codeword, has been repeated M times with different codewords and different SNR for each subcarrier and each rv. $BLER_l$ means the experimental (or simulated) BLER for realization l of the experiment, $ESNR_l(\alpha_1, \alpha_2)$ means ESNR for realization l and the function $BLER_R$ is the reference BLER curve. The reference BLER curve is obtained by simulating the experiment under AWGN conditions, i.e., assuming flat fading and the same SNR for each rv. Minimization of the MSE is performed over the logarithm of the BLER to achieve low error at low BLER, which is the region of interest, [34].

The function $I(\cdot)$ can take several forms. The EESM model uses the function $I(\cdot) = 1 - exp(-\frac{\gamma}{\beta})$ for all the modulation schemes where α_1 and α_2 are taken to be equal, i.e. $\alpha_1 = \alpha_2 = \beta$, in order to simplify the equation. The parameter β can be interpreted as a shift in the $I(\cdot)$ function to adapt the model to each MCS. So the EESNR, the ESNR for the EESM, is expressed as a function of the parameter β, [8]:

$$EESNR = -\beta \cdot ln\left(\frac{1}{N}\sum_{k=1}^{N}\exp\left(-\frac{\gamma_k}{\beta}\right)\right) \tag{6.4}$$

For the MIESM model, the function $I(\cdot)$ is obtained from the MMIB between the transmitted and received symbols vs. SNR in AWGN, [34]. MMIB is described in subsection 2.6.2.2.

The EESM was initially recommended in [21] for system evaluation; but several models are compared in [94] in terms of accuracy in the obtained BLER estimation and it is concluded that the MIESM outperforms EESM in terms of BLER prediction accuracy. On the other hand, the MIESM method has the drawback that, since there is not a closed form expression for the MI between transmitted and received modulation symbols, or between transmitted and received coded bits, it must be approximated or computed numerically. The EESM and MIESM models for LTE were described in [10] and [34] and, basically, the main drawbacks of these models were

that they needed to be trained in order to obtain the calibration parameters β or α_1 and α_2 for the modulation and coding scheme of all CQIs. Also those methods cannot consider the IR HARQ retransmissions. There is an additional complexity with IR HARQ, the BLER performance of a given rv depends on the SNR experienced by the receiver at current rv but also on the SNR of previously received rvs. In [11] the MIESM model was extended to consider all the LTE MCSs and HARQ redundancy versions 0 and 1, but maintaining the dependency with the parameters α_1 and α_2.

6.3 Accurate Link Abstraction Method in LTE with IR HARQ

So far several link abstraction techniques which work at modulation symbol level have been cited, like EESM [21] [51, 96, 97, 10] and MIESM [97, 94, 34, 11]; but they cannot properly capture the effect of the LLR combination when IR HARQ is in use. Since this combination happens at bit level, this dissertation proposes to use a novel link abstraction method which addresses the problem by modelling the system at bit level in order to predict the BLER with good accuracy in multipath fading and including the effects of HARQ retransmissions. This novel link abstraction method is based on the binary equivalent channel model shown in Figure 2.13, it is valid for any modulation scheme and it is characterized by means of the MI between the transmitted coded bits and the received LLR. This novel method is based on MIB and extends MIESM method to take into account the effects of the different *bit channels* of 16QAM and 64QAM when IR-HARQ is in use.

In this chapter the proposed link abstraction method for IR HARQ is described. Similar to other link abstraction methods, the proposed methodology is divided in two steps: the computation of the ESNR and the BLER prediction based on the computed ESNR and the reference BLER curves. Finally, the simulation results show a clear improvement with respect to previously proposed methods, obtaining good accuracy in the predicted BLER without resorting to any complex calibration process.

6.3.1 MRC and LLR combining

In LTE/LTE-Advanced when IR HARQ is applied, the receiver combines the LLRs for the coded bits that have been received more than once. Furthermore, for the MCSs with code rate $< 1/3$, some of the coded bits are repeated within the same redundancy version. This produces a combined LLR which is more reliable than any of the individual LLRs instances. Figure 6.2 shows graphically this combining where HARQ retransmissions are received with different SNRs $(\gamma_0, \gamma_1, \gamma_2, \gamma_3)$. Due to interleaving, the received coded bits with different SNRs are scrambled over the whole codeword. This combined LLR is then fed to the decoder to try to decode the codeword. Assuming independent realizations of the noise for each transmission of the same bit, it can be easily proved that adding together the LLRs instances of a given bit leads to a combined LLR equivalent to performing MRC on the individual decision variables.

Let's assume a narrowband SISO BPSK system with the equivalent AWGN channel of Figure 6.3. Assuming equal probability for the transmitted bits, the LLR is:

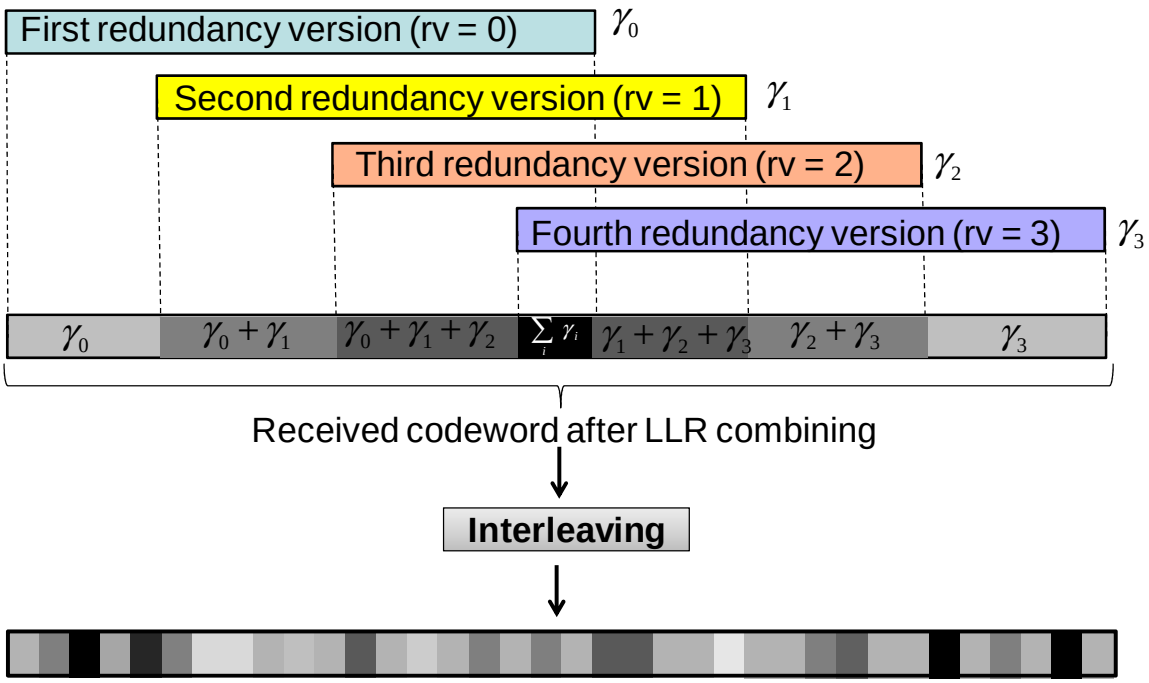

Figure 6.2: Graphical representation of the LLR combining with IR HARQ retransmissions

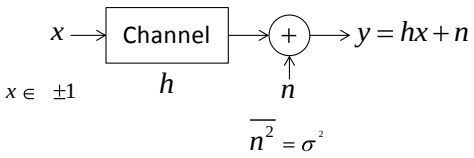

Figure 6.3: SISO BPSK equivalent channel

$$\Lambda = \ln\left(\frac{Prob\,(x=+1|y)}{Prob\,(x=-1|y)}\right) = \ln\left(\frac{Prob\,(y|x=+1)}{Prob\,(y|x=-1)}\right) = \ln\left(\frac{e^{-\frac{1}{2}\left(\frac{y-h}{\sigma}\right)^2}}{e^{-\frac{1}{2}\left(\frac{y+h}{\sigma}\right)^2}}\right) = \frac{2h}{\sigma^2}y = \frac{2h}{\sigma^2}x + \frac{2h}{\sigma^2}n \tag{6.5}$$

According to Equation 6.5 the LLR for BPSK is a Gaussian random variable with a variance equal to twice the average value (called a consistent Gaussian random variable). Also the BPSK LLR is equal to the decision variable times twice the channel gain over the noise variance.

Now let's consider two transmissions of the same bit, with independent channel and noise realizations, which are processed using MRC as it is depicted in Figure 6.4. The SNRs of the individual transmissions are expressed as $\gamma_1 = h_1^2/\sigma_1^2$ and $\gamma_2 = h_2^2/\sigma_2^2$. It can be shown that, after performing MRC of two transmissions of the same bit, the combined SNR is $\gamma_{MRC} = \gamma_1 + \gamma_2$ as well as the combined LLR is as follows:

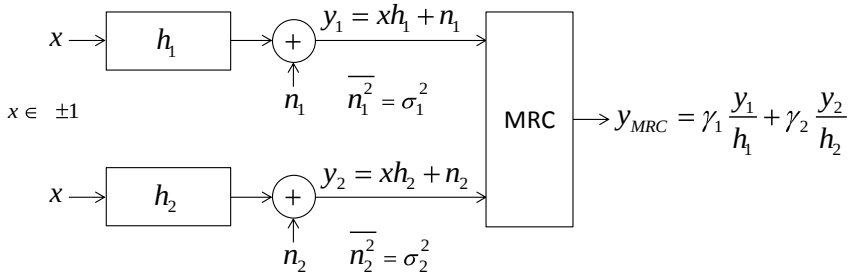

Figure 6.4: MRC processing of two independent BPSK transmission of the same bit

$$\Lambda_{MRC} = \ln\left(\frac{Prob\left(y_1, y_2|x=+1\right)}{Prob\left(y_1, y_2|x=-1\right)}\right) = \ln\left(\frac{e^{-\frac{1}{2}\left[\left(\frac{y_1-h_1}{\sigma_1}\right)^2+\left(\frac{y_2-h_2}{\sigma_2}\right)^2\right]}}{e^{-\frac{1}{2}\left[\left(\frac{y_1-h_1}{\sigma_1}\right)^2+\left(\frac{y_2-h_2}{\sigma_2}\right)^2\right]}}\right) = \frac{2h_1}{\sigma_1^2}y_1 + \frac{2h_2}{\sigma_2^2}y_2 = \Lambda_1 + \Lambda_2 \tag{6.6}$$

which is equivalent to compute the LLR of the MRC decision variable, Λ_{MRC}. As shown in Figure 6.4 y_{MRC} is defined as follows:

$$y_{MRC} = \gamma_1\frac{y_1}{h_1} + \gamma_2\frac{y_2}{h_2} = (\gamma_1+\gamma_2)\,x + \frac{\gamma_1}{h_1}n_1 + \frac{\gamma_2}{h_2}n_2 \tag{6.7}$$

and Λ_{MRC} is equal to y_{MRC} times twice the channel gain over the noise variance, i.e.:

$$\Lambda_{MRC} = \frac{2\left(\gamma_1+\gamma_2\right)}{\frac{\gamma_1^2}{h_1^2}\sigma_1^2 + \frac{\gamma_2^2}{h_2^2}\sigma_2^2}y_{MRC} = \Lambda_1 + \Lambda_2 \tag{6.8}$$

6.3.2 ESNR for OFDM with IR HARQ in multipath channel

The proposed method to compute the ESNR for an OFDM system with IR-HARQ in multipath channel is described in this section. SISO transmission mode is considered to formulate the ESNR equation. The proposed method can also be applied to MIMO transmission modes by substituting the SISO SNR by the MIMO post-processing SNR. The simulation results are shown in section 6.4.

In an OFDM system with multipath propagation, the process of bit interleaving jointly with the fact that each subcarrier shows a different SNR create a multistate channel. Even if the channel is flat fading, the unequal error protection of 16QAM and 64QAM jointly with the LLR combination process inherent to IR HARQ also lead to a multistate channel. In a multistate channel each received bit shows a different SNR. In this case the BLER depends on the received average bit information rate which is given by, [52]:

$$r^* = \frac{1}{N_{bits}}\sum_{i=1}^{N_{bits}}\chi_i \tag{6.9}$$

where N_{bits} is the size of the codeword and χ_i is the MI carried by bit i which depends on:

i) The number of times that bit i has been received considering all IR-HARQ transmissions that have taken place.

ii) The SNR of the different subcarriers where bit i has travelled (including all IR-HARQ transmissions).

iii) The weight (bit channel) that bit i has occupied within the modulation symbol throughout all IR-HARQ transmissions.

In case that there are not bit repetitions at all (no HARQ and code rate $> 1/3$) the received average bit information rate reduces to:

$$r^* = \frac{1}{N_{bits}} \sum_{i=1}^{N_{bits}} MIB_i(\gamma_i) \tag{6.10}$$

where γ_i is the SNR of the subcarrier where bit i has travelled and $MIB_i(x)$ is the MIB curve corresponding to the weight of bit i within the modulation symbol (see Figure 2.16).

Since r^* is a random variable, for a capacity approaching code the BLER can be approximated by the probability that $r^* < r$, [52], where r is the code rate applied at the current MCS:

$$\text{BLER} \approx \text{Prob}\left(r^* < r\right) = \text{Prob}\left(r^* < \overline{MIB}\left(\gamma_0\right)\right) = \text{Prob}\left(\underbrace{\overline{MIB}^{-1}\left(r^*\right)}_{ESNR} < \gamma_0\right) \tag{6.11}$$

where we have used the concept of the BICM threshold represented in Figure 2.17. Expression 6.11 leads to the definition of $ESNR = \overline{MIB}^{-1}(r^*)$ for a multistate channel. According to expression 6.11, for a capacity approaching code the BLER would be a step function switching from 1 to 0 at $ESNR = \gamma_0$ as shown in Figure 6.5. In practice the length of the codeword can be short and it cannot be assumed that a capacity approaching code is used. In this case, instead of having a sharp threshold, a smooth BLER curve as shown in Figure 6.5 is achieved and the BLER for a multistate channel is approximated as:

$$\text{BLER}\left(ESNR\right) \approx \text{BLER}_{\text{AWGN}}\left(ESNR, r\right) \tag{6.12}$$

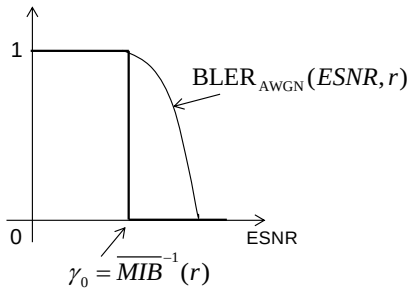

Figure 6.5: BICM threshold and realistic AWGN BLER curve

where $\text{BLER}_{AWGN}(ESNR, r)$ is the BLER curve for the current MCS in AWGN conditions. This curve starts to fall near the BICM threshold and depends on the modulation scheme, on the

code rate and on the size of the code block. The bigger the code block the steeper is the slope of the BLER curve.

Initially we consider only the computation of ESNR for BPSK modulation in subsection 6.3.2.1 and then, in subsection 6.3.2.2, we show that the cases of QPSK, 16QAM and 64QAM can be analysed based on BPSK equivalents .

6.3.2.1 ESNR for BPSK

With BPSK all bits have the same error probability. Let's proceed first with single transmission (redundancy version 0, rv= 0) and then we generalize. We aim at computing the received average bit information rate:

$$r^* = \frac{1}{\eta_0} \sum_{i \in U_0} MIB_{BPSK}(\gamma_i) \tag{6.13}$$

where U_0 is the set of coded bits that have been received (at least once) within rv= 0, η_0 is the cardinal of U_0, $MIB_{BPSK}(x)$ is the exact MIB for BPSK (see Figure 2.16) and γ_i is the SNR of the subcarrier for bit i. Since for $r < 1/3$ there is bit repetition and the same bit can be transmitted up to three times, U_0 can be decomposed into three disjoint subsets: U_1^0 , U_2^0 and U_3^0 where U_j^0 $(j = 1, 2, 3)$ means the set of bits that have been received exactly j times within rv= 0. According to this, Equation 6.13 can be rewritten as:

$$r^* = \frac{1}{\eta_0} \sum_{i \in U_1^0} MIB_{BPSK}(\gamma_{i,1}) + \frac{1}{\eta_0} \sum_{i \in U_2^0} MIB_{BPSK}(\gamma_{i,1} + \gamma_{i,2}) + \frac{1}{\eta_0} \sum_{i \in U_3^0} MIB_{BPSK}(\gamma_{i,1} + \gamma_{i,2} + \gamma_{i,3}) \tag{6.14}$$

where $\gamma_{i,j}$ $(j = 1, 2, 3)$ means the SNR of bit i during transmission j. Equation 6.14 relies on the fact that adding the LLRs is equivalent to performing MRC on the decision variables, which is equivalent to adding together the SNRs of the different transmissions of the same bit as described in subsection 6.3.1.

The computation of $\gamma_{i,j}$ $(j = 1, 2, 3)$ within a system level simulator would require tracking the subcarrier where bit i has travelled in transmission j for all i, j (all the coded bits in a codeword and all HARQ transmissions). Since this way is too complex we propose to approximate the summations in Equation 6.14 by their average values. Thanks to the interleaving, we can assume that the coded bits are uniformly spread through all the allocated subcarriers, or equivalently, that a given transmission of a coded bit has the same probability of travelling into any of the subcarriers. Then, using their average values, the summations in Equation 6.14 can be approximated as:

$$\frac{1}{\eta_1^0} \sum_{i \in U_1^0} MIB_{BPSK}(\gamma_{i,1}) \approx \frac{1}{N_{SC}} \sum_{k=1}^{N_{SC}} MIB_{BPSK}(\xi_k) = \langle MIB_{BPSK}(\xi_k) \rangle \tag{6.15}$$

$$\begin{aligned} \frac{1}{\eta_2^0} \sum_{i \in U_2^0} MIB_{BPSK}(\gamma_{i,1} + \gamma_{i,2}) &= \frac{1}{N_{SC}(N_{SC} - 1)} \sum_{k=1}^{N_{SC}} \sum_{\substack{l=1 \\ k \neq l}}^{N_{SC}} MIB_{BPSK}(\xi_k + \xi_l) \\ &\approx \frac{1}{N_{SC}^2} \sum_{k=1}^{N_{SC}} \sum_{l=1}^{N_{SC}} MIB_{BPSK}(\xi_k + \xi_l) = \langle MIB_{BPSK}(\xi_k + \xi_l) \rangle \end{aligned} \tag{6.16}$$

$$\frac{1}{\eta_3^0}\sum_{i\in U_3^0} MIB_{BPSK}\left(\gamma_{i,1}+\gamma_{i,2}+\gamma_{i,3}\right)$$
$$= \frac{1}{N_{SC}\left(N_{SC}-1\right)\left(N_{SC}-2\right)}\sum_{k=1}^{N_{SC}}\sum_{\substack{l=1\\k\neq l}}^{N_{SC}}\sum_{\substack{m=1\\m\neq l,k}}^{N_{SC}} MIB_{BPSK}\left(\xi_k+\xi_l+\xi_m\right) \tag{6.17}$$
$$\approx \frac{1}{N_{SC}^3}\sum_{k=1}^{N_{SC}}\sum_{l=1}^{N_{SC}}\sum_{m=1}^{N_{SC}} MIB_{BPSK}\left(\xi_k+\xi_l+\xi_m\right) = \left\langle MIB_{BPSK}\left(\xi_k+\xi_l+\xi_m\right)\right\rangle$$

where η_j^0 is the cardinal of U_j^0 $(j=1,2,3)$ $(\eta_1^0+\eta_2^0+\eta_3^0=\eta^0)$, N_{SC} is the number of subcarriers, ξ_k is the SNR of subcarrier k during rv$=0$ and $\langle x\rangle$ means the average of x.

Using Equations 6.15, 6.16 and 6.17 Equation 6.14 becomes:

$$r^* = \frac{\eta_1^0}{\eta^0}\left\langle MIB_{BPSK}\left(\xi_k\right)\right\rangle + \frac{\eta_2^0}{\eta^0}\left\langle MIB_{BPSK}\left(\xi_k+\xi_l\right)\right\rangle + \frac{\eta_3^0}{\eta^0}\left\langle MIB_{BPSK}\left(\xi_k+\xi_l+\xi_m\right)\right\rangle \tag{6.18}$$

where the ratios $\frac{\eta_j^0}{\eta^0}$ $(j=1,2,3)$ (called "repetition factors" from here on) can be computed by means of the rate matching algorithm.

For big number of subcarriers, the computation of Equations 6.16 and 6.17 can be complex. We propose a computation method that becomes practical even for a big number of subcarriers. By using Equation 2.23, the MIB for BPSK is approximated by the function $I\left(\gamma\right)$:

$$MIB_{BPSK}\left(\gamma\right) \approx I\left(\gamma\right) = 1-\exp\left(-\gamma/10^{-0.12}\right) \tag{6.19}$$

Although the function $I\left(\gamma\right)$ is non-linear, it can be decomposed into terms that can be independently averaged. It can be verified that:

$$I\left(x+y\right) = I\left(x\right)+I\left(y\right)-I\left(x\right)\cdot I\left(y\right) = I\left(y\right)+\left(1-I\left(y\right)\right)I\left(x\right) \tag{6.20}$$

and, if we define:

$$I_n\left(x_1,x_2,\cdots,x_n\right) \triangleq I\left(\sum_{i=1}^{n} x_i\right) \tag{6.21}$$

there is a simple recursive formula to compute $I_n\left(\cdot\right)$:

$$I_n\left(x_1,x_2,\cdots,x_n\right) = I\left(x_n\right)+\left[1-I\left(x_n\right)\right]I_{n-1}\left(x_1,x_2,\cdots,x_{n-1}\right) \tag{6.22}$$

By using Equation 6.22 the function $I\left(x\right)$ only has to be evaluated n times. For example, to compute the average $\left\langle MIB_{BPSK}\left(\xi_k+\xi_l\right)\right\rangle$ we use:

$$\left\langle MIB_{BPSK}\left(\xi_k+\xi_l\right)\right\rangle \approx \left\langle I\left(\xi_k+\xi_l\right)\right\rangle = \left\langle I_2\left(\xi_k,\xi_l\right)\right\rangle = \left\langle I\left(\xi_l\right)\right\rangle + \left(1-\left\langle I\left(\xi_l\right)\right\rangle\right)\cdot\left\langle I\left(\xi_k\right)\right\rangle \tag{6.23}$$

where we have assumed that the average of the product is the product of the averages thanks to the interleaving, which produces an independent fading on every transmission of every coded

bit. If this assumption holds, then Equation 6.23 (and so Equation 6.18) can be computed based on the average MIB of the individual subcarriers, $\langle I(\xi_k)\rangle$, which is computed as follows:

$$\langle I(\xi_k)\rangle = \frac{1}{N_{SC}} \sum_{k=1}^{N_{SC}} I(\xi_k) \tag{6.24}$$

The same method, but using $I_3(\cdot)$ instead of $I_2(\cdot)$ from Equation 6.22, can be used to compute $\langle MIB_{BPSK}(\xi_l + \xi_k + \xi_m)\rangle$.

6.3.2.2 ESNR for LTE modulation schemes

The considered modulation schemes for LTE/LTE-Advanced are QPSK, 16QAM and 64QAM. So we extend the computation of the received average bit information rate, r^*, to LTE/LTE-Advanced modulation schemes still assuming rv= 0. Notice that with 16QAM and 64QAM there is unequal error protection for the different bits within a modulation symbol.

For 16QAM and 64QAM one must consider two and three different MIB vs. SNR curves, respectively, as shown in Figure 2.16. Thus, it can be said that there are two different bit channels (called bit channel A and bit channel B) for 16QAM and three different bit channels (called bit channel A, bit channel B and bit channel C) for 64QAM, which can be characterized based on their MI. Each coded bit is transmitted through one of these channels, and due to the interleaving process, the probability of using each one of the possible bit channels can be considered uniform. If a coded bit is transmitted more than once, the receiver will sum up all the LLRs belonging to the same coded bit before decoding. Adding together the LLRs for the different transmissions of the same coded bit leads to an SNR gain equivalent to MRC diversity. Since the different transmissions may have used different bit channels in different subcarriers, we must compute the average MIB of the equivalent binary channel formed by the repeated transmissions of the same bit.

Figure 6.6 is a conceptual diagram of the equivalent binary channel that is formed when a single coded bit is transmitted twice using 16QAM in two subcarriers with $SNR_1 = \xi_1$ and $SNR_2 = \xi_2$. Now the transmission of a coded bit entails two independent random selections: the selection of the subcarrier and the selection of the binary channel within the modulation (the bit weight within the 16QAM symbol).

Assuming, for example, that the first transmission uses bit channel A and the second transmission uses bit channel B, the proposed procedure to characterize the equivalent binary channel of Figure 6.6 is:

1. Obtain the MIB of the relevant 16QAM bit channels (called $MIB_A(\xi_1)$ and $MIB_B(\xi_2)$) according to the plots of Figure 2.16 and the SNR of the subcarriers, ξ_1 and ξ_2.

2. Map $MIB_A(\xi_1)$ and $MIB_B(\xi_2)$ through the curve of MIB for BPSK, to obtain the equivalent BPSK SNR of the subcarriers (called $\gamma_{1A}(\xi_1)$ and $\gamma_{2B}(\xi_2)$), using the approximation of Equation 6.19:

$$\begin{aligned} \gamma_{1A}(\xi_1) &= I^{-1}(MIB_A(\xi_1)) \\ \gamma_{2B}(\xi_2) &= I^{-1}(MIB_B(\xi_2)) \end{aligned} \tag{6.25}$$

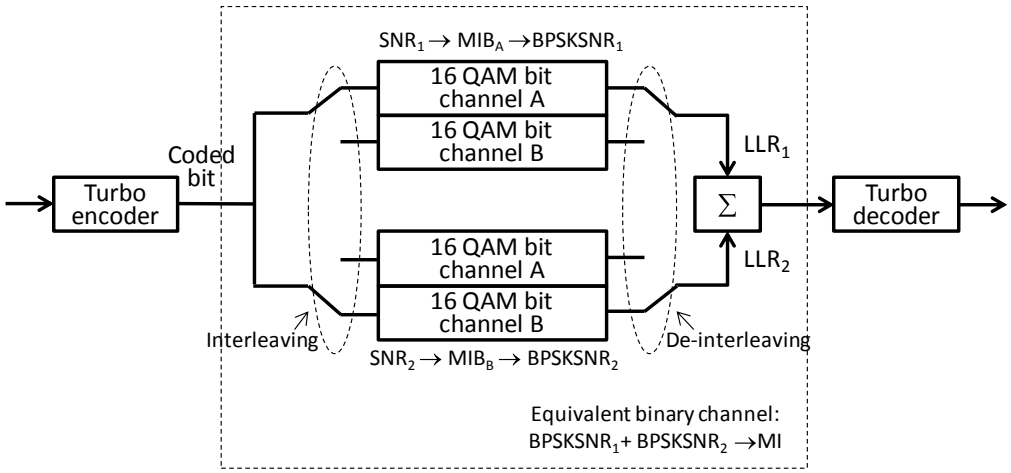

Figure 6.6: Concept of equivalent binary channel due to multiple transmissions of the same bit

3. Add the equivalent BPSK SNR of the subcarriers and map the result through the curve of MIB for BPSK to obtain the MIB of the equivalent binary channel:

$$MIB\left(\xi_1,\xi_2\right)=I\left[\gamma_{1A}\left(\xi_1\right)+\gamma_{2B}\left(\xi_2\right)\right]=I\left[I^{-1}\left(MIB_A\left(\xi_1\right)\right)+I^{-1}\left(MIB_B\left(\xi_1\right)\right)\right] \tag{6.26}$$

Equation 6.26 is a particular case, but since at system level simulation the bit channel and subcarrier for every coded bit are not tracked, we substitute the exact values by their average values. So Equation 6.26 must be averaged through all the possible combinations of bit channels of the modulation and through all the subcarriers:

$$\begin{aligned}\left\langle MIB\left(\xi_k,\xi_l\right)\right\rangle &= \frac{1}{4N_{SC}^2}\sum_{k=1}^{N_{NC}}\sum_{l=1}^{N_{NC}} I\left[\gamma_{kA}\left(\xi_k\right)+\gamma_{lA}\left(\xi_l\right)\right]+\frac{1}{4N_{SC}^2}\sum_{k=1}^{N_{NC}}\sum_{l=1}^{N_{NC}} I\left[\gamma_{kA}\left(\xi_k\right)+\gamma_{lB}\left(\xi_l\right)\right]+\\ &+\frac{1}{4N_{SC}^2}\sum_{k=1}^{N_{NC}}\sum_{l=1}^{N_{NC}} I\left[\gamma_{kB}\left(\xi_k\right)+\gamma_{lA}\left(\xi_l\right)\right]+\frac{1}{4N_{SC}^2}\sum_{k=1}^{N_{NC}}\sum_{l=1}^{N_{NC}} I\left[\gamma_{kB}\left(\xi_k\right)+\gamma_{lB}\left(\xi_l\right)\right]=\\ =\frac{1}{4}&\left(\left\langle I\left[\gamma_{kA}\left(\xi_k\right)+\gamma_{lA}\left(\xi_l\right)\right]\right\rangle+\left\langle I\left[\gamma_{kA}\left(\xi_k\right)+\gamma_{lB}\left(\xi_l\right)\right]\right\rangle+\left\langle I\left[\gamma_{kB}\left(\xi_k\right)+\gamma_{lA}\left(\xi_l\right)\right]\right\rangle+\left\langle I\left[\gamma_{kB}\left(\xi_k\right)+\gamma_{lB}\left(\xi_l\right)\right]\right\rangle\right)\end{aligned} \tag{6.27}$$

In order to compute Equation 6.27 the same procedure previously explained for BPSK is used. For instance, let's compute $\left\langle I\left[\gamma_{kA}(\xi_k)+\gamma_{lA}(\xi_l)\right]\right\rangle=\left\langle I_2\left[\gamma_{kA}(\xi_k),\gamma_{lA}(\xi_l)\right]\right\rangle$ based on Equation 6.23 but applied to 16QAM:

$$\left\langle I\left[\gamma_{kA}(\xi_k)+\gamma_{lA}(\xi_l)\right]\right\rangle=\left\langle I_2\left[\gamma_{kA}(\xi_k),\gamma_{lA}(\xi_l)\right]\right\rangle=\left\langle I\left(\gamma_{lA}(\xi_l)\right)\right\rangle+\left(1-\left\langle I\left(\gamma_{lA}(\xi_l)\right)\right\rangle\right)\cdot\left\langle I\left(\gamma_{kA}(\xi_k)\right)\right\rangle \tag{6.28}$$

In this way Equation 6.28 can be also computed based on the average MIB of the individual subcarriers. For example:

$$\langle I\left(\gamma_{kA}(\xi_k)\right)\rangle = \frac{1}{N_{SC}}\sum_{k=1}^{N_{SC}} I\left(\gamma_{kA}(\xi_k)\right) = \frac{1}{N_{SC}}\sum_{k=1}^{N_{SC}} I\left(I^{-1}\left(MIB_A(\xi_k)\right)\right) = \frac{1}{N_{SC}}\sum_{k=1}^{N_{SC}} MIB_A(\xi_k) = \langle MIB_A(\xi_k)\rangle \tag{6.29}$$

Notice that although according to 6.29, we don't need to evaluate the function $I(\gamma)$, since we apply the property of 6.22 we are still implicitly using the approximation of 6.19 .

Finally, for 16QAM or 64QAM Equation 6.18 must be substituted by:

$$r^* = \frac{\eta_1^0}{\eta_0}\langle MIB\left(\xi_k\right)\rangle + \frac{\eta_2^0}{\eta_0}\langle MIB\left(\xi_k,\xi_l\right)\rangle + \frac{\eta_3^0}{\eta_0}\langle MIB\left(\xi_k,\xi_l,\xi_m\right)\rangle \tag{6.30}$$

where for bits that have been transmitted only once:

$$\begin{aligned}\langle MIB\left(\xi_k\right)\rangle &= \frac{1}{2N_{SC}}\sum_{k=1}^{N_{SC}}\left[MIB_A(\xi_k) + MIB_B(\xi_k)\right] \quad \text{(16QAM)}\\ \langle MIB\left(\xi_k\right)\rangle &= \frac{1}{3N_{SC}}\sum_{k=1}^{N_{SC}}\left[MIB_A(\xi_k) + MIB_B(\xi_k) + MIB_C(\xi_k)\right] \quad \text{(64QAM)}\end{aligned} \tag{6.31}$$

For 64QAM there are three different bit channels (A, B and C) and so the second term in 6.30, $\langle MIB\left(\xi_k,\xi_l\right)\rangle$, contains 3^2 terms:

$$\langle MIB\left(\xi_k,\xi_l\right)\rangle = \frac{1}{9}\left[\langle I\left[\gamma_{kA}(\xi_k)+\gamma_{lA}(\xi_l)\right]\rangle + \langle I\left[\gamma_{kA}(\xi_k)+\gamma_{lB}(\xi_l)\right]\rangle + \langle I\left[\gamma_{kA}(\xi_k)+\gamma_{lC}(\xi_l)\right]\rangle + \cdots\cdots\right] \tag{6.32}$$

The third term in 6.30, $\langle MIB\left(\xi_k,\xi_l,\xi_m\right)\rangle$ contains 2^3 terms for 16QAM:

$$\langle MIB\left(\xi_k,\xi_l\right)\rangle = \frac{1}{8}\left[\langle I\left[\gamma_{kA}(\xi_k)+\gamma_{lA}(\xi_l)+\gamma_{mA}(\xi_m)\right]\rangle + \langle I\left[\gamma_{kA}(\xi_k)+\gamma_{lA}(\xi_l)+\gamma_{mB}(\xi_m)\right]\rangle + \cdots\cdots\right] \tag{6.33}$$

and 3^3 terms for 64QAM.

The computation of the received average bit information rate, r^* , for QPSK is similar as the computation for 16QAM with the simplification that bit channel B does not exist.

Now let's consider the received average bit information rate after the second round (rv= 1) of IR HARQ. Since the proposed model is valid regardless of the repeated bit transmissions taking place in the same HARQ round or in different rounds, it is sufficient to extrapolate the already explained method for rv= 0. Also the model can be easily extended for bits that are received more than twice and even for different retransmission formats (modulation and code rate).

We call U_1 the set of coded bits that have been received (at least once) after rv= 1 and η_1 is the cardinal of U_1. In principle U_1 can be decomposed into $4^2-1=15$ disjoint subsets:

$$\mathrm{U}^1_{0,1}, \mathrm{U}^1_{0,2}, \mathrm{U}^1_{0,3}, \mathrm{U}^1_{1,0}, \mathrm{U}^1_{2,0}, \mathrm{U}^1_{3,0}, \mathrm{U}^1_{1,1}, \mathrm{U}^1_{1,2}, \mathrm{U}^1_{1,3}, \mathrm{U}^1_{2,1}, \mathrm{U}^1_{2,2}, \mathrm{U}^1_{2,3}, \mathrm{U}^1_{3,1}, \mathrm{U}^1_{3,2} \text{ and } \mathrm{U}^1_{3,3}$$

where $\mathrm{U}^1_{j_0,j_1}$ $(j_0, j_1 = 0,1,2,3)$ means the set of bits that have been received exactly j_0 times within rv= 0 and exactly j_1 times within rv= 1. Depending of the MCS many of these subsets can be empty. The cardinal of $\mathrm{U}^1_{j_0,j_1}$ is $\eta^1_{j_0,j_1}$. Using this notation the received average bit information rate after rv= 1 may have a maximum of 15 terms. Those terms are:

$$\begin{aligned} r^* = &\frac{\eta^1_{1,0}}{\eta_1}\langle MIB(\xi_k)\rangle + \frac{\eta^1_{2,0}}{\eta_1}\langle MIB(\xi_k,\xi_l)\rangle + \frac{\eta^1_{3,0}}{\eta_1}\langle MIB(\xi_k,\xi_l,\xi_m)\rangle \\ &+\frac{\eta^1_{0,1}}{\eta_1}\langle MIB(\sigma_k)\rangle + \frac{\eta^1_{0,2}}{\eta_1}\langle MIB(\sigma_k,\sigma_l)\rangle + \frac{\eta^1_{0,3}}{\eta_1}\langle MIB(\sigma_k,\sigma_l,\sigma_m)\rangle \\ &+\frac{\eta^1_{1,1}}{\eta_1}\langle MIB(\xi_k,\sigma_l)\rangle + \frac{\eta^1_{1,2}}{\eta_1}\langle MIB(\xi_k,\sigma_l,\sigma_m)\rangle + \frac{\eta^1_{1,3}}{\eta_1}\langle MIB(\xi_k,\sigma_l,\sigma_m,\sigma_n)\rangle \\ &+\frac{\eta^1_{2,1}}{\eta_1}\langle MIB(\xi_k,\xi_l,\sigma_m)\rangle + \frac{\eta^1_{2,2}}{\eta_1}\langle MIB(\xi_k,\xi_l,\sigma_m,\sigma_n)\rangle + \frac{\eta^1_{2,3}}{\eta_1}\langle MIB(\xi_k,\xi_l,\sigma_m,\sigma_n,\sigma_t)\rangle \\ &+\frac{\eta^1_{3,1}}{\eta_1}\langle MIB(\xi_k,\xi_l,\xi_m,\sigma_n)\rangle + \frac{\eta^1_{3,2}}{\eta_1}\langle MIB(\xi_k,\xi_l,\xi_m,\sigma_n,\sigma_t)\rangle + \frac{\eta^1_{3,3}}{\eta_1}\langle MIB(\xi_k,\xi_l,\xi_m,\sigma_n,\sigma_t,\sigma_v)\rangle \end{aligned} \tag{6.34}$$

where σ_k is the SNR of subcarrier k during rv= 1. The last term in Equation 6.34, for bits that have been transmitted 3 times inside each round, contains 2^6 terms for 16QAM and $3^6=729$ terms for 64QAM. Despite the big number of terms their computation is fast thanks to Equation 6.22. In addition, the terms accounting for many repetitions of the same bits only appear if the MCS format uses a very low code rate.

It could seem that for rv= 2 or rv= 3 the received average bit information rate is even more complex to compute since the number of potential terms to check grows to $4^3-1=63$ and $4^4-1=255$ (respectively), but most of those terms are null. Obviously, there is no need to compute any term if its corresponding repetition factor is null. Figure 6.7 shows the repetition factors for the first transmission (rv= 0) for several MCSs in LTE assuming the code rate resulting from a bandwidth of 25 RBs, one transport block mapped onto one layer and 12 Reserved REs per RB (obtained by computing Equation 3.4). Furthermore Figures 6.8, 6.9, 6.10 shows the repetition factors for the second, third and fourth rounds (rv= 1, 2, 3) of HARQ retransmissions. Since the sum of all the repetition factors equals unity, they are interpreted as a pdf of a discrete random variable. Only the non-null repetition factors are plotted. The abscissa is labelled with a set of integer numbers which uniquely identify the repetition factor. For example label "332", in Figure 6.9, means those bits that have been received exactly twice at first round, third times at second round and third times at third round. As can be verified in Figure 6.10, even considering four HARQ transmissions, the number of non-null terms contributing to the computation is very low.

The final step, after obtaining the received average bit information rate, is to compute the ESNR as follows:

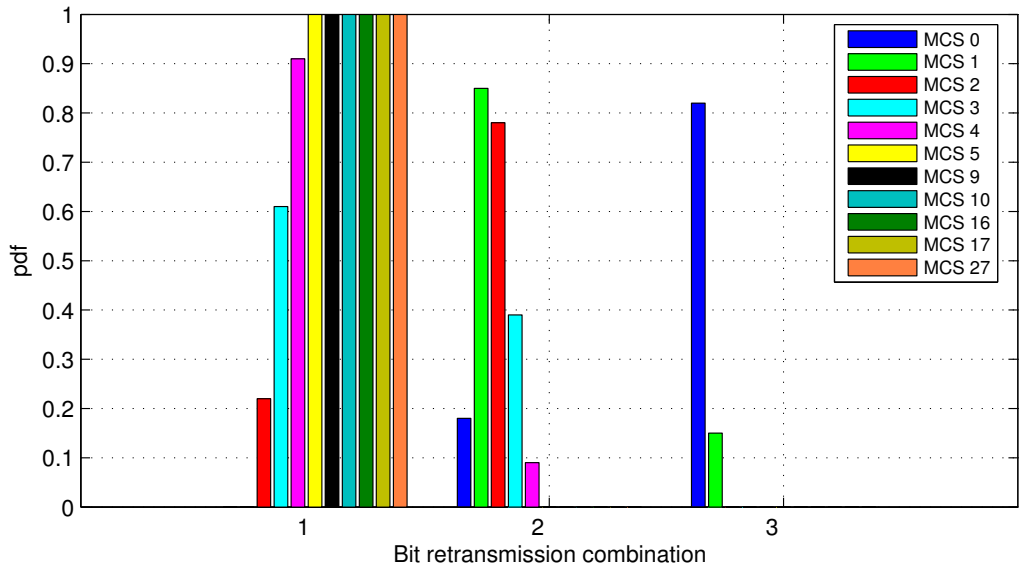

Figure 6.7: pdf of the repetition factors for the first round (rv= 0) of HARQ retransmission in LTE

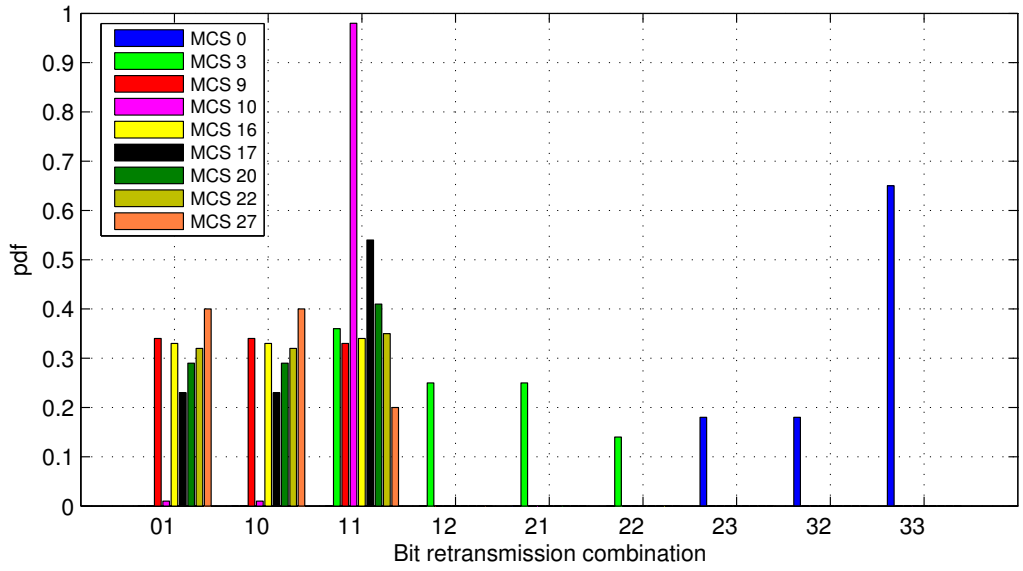

Figure 6.8: pdf of the repetition factors for the second round (rv= 1) of HARQ retransmission in LTE

$$ESNR = \overline{MIB}^{-1}(r^*) \tag{6.35}$$

where $\overline{MIB}(\cdot)$ is the average MIB curve of the modulation in use shown in Figure 2.16.

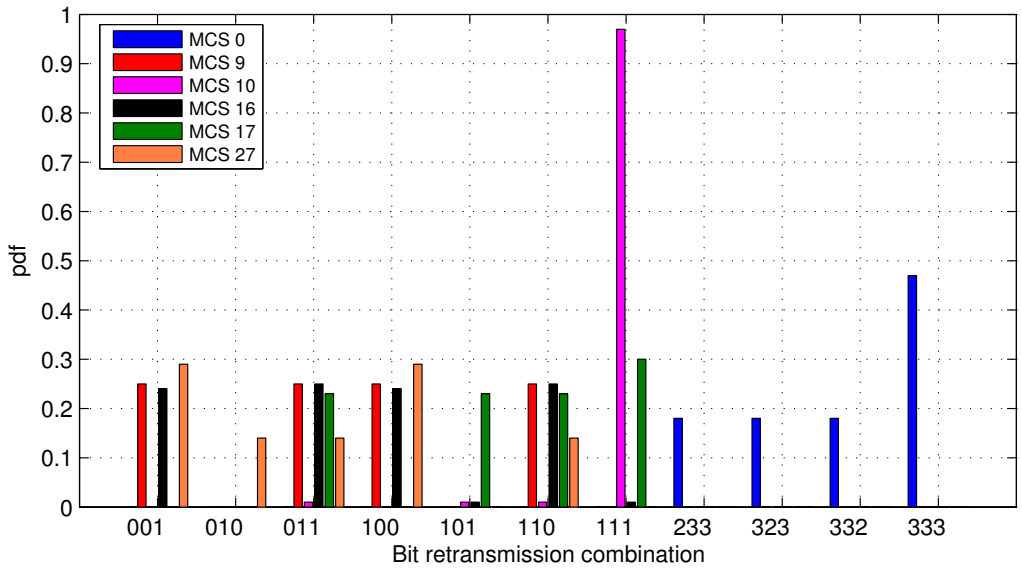

Figure 6.9: pdf of the repetition factors for the third round (rv= 2) of HARQ retransmission in LTE

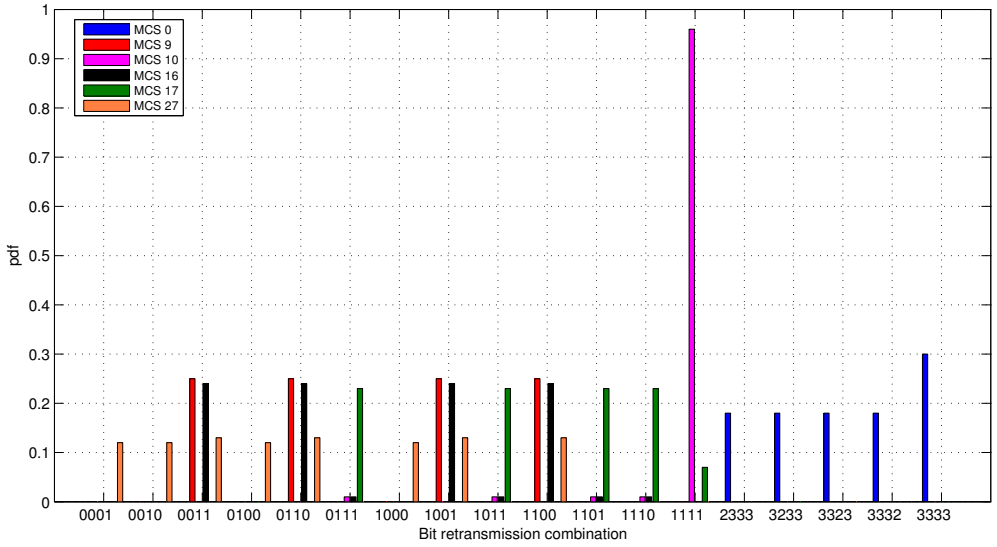

Figure 6.10: pdf of the repetition factors for the fourth round (rv= 3) of HARQ retransmission in LTE

6.3.3 Reference BLER curves for Link Abstraction

6.3.3.1 Mother code rate BLER curves

Figure 6.11 shows the BLER curves for the full range of valid turbo code block sizes in AWGN channel with BPSK modulation and rate 1/3. In practice, the BLER curve for the LTE turbo

codes (in AWGN channel) begins to fall down for a SNR slightly higher than the BICM threshold. So knowing that threshold is useful to check the validity of the obtained BLER curves in AWGN channel and to have a rough estimation of the minimum SNR needed for the particular AMC format. The offset of the BLER curve with respect to the BICM threshold, as well as the slope of the curve, depends on the size of the turbo code block.

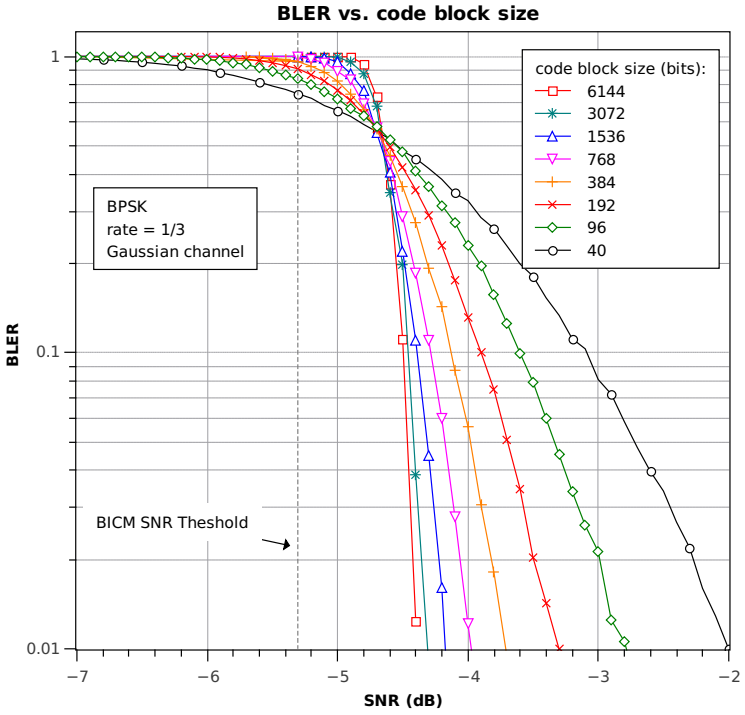

Figure 6.11: AWGN Reference BLER for BPSK modulation and different code block sizes

Figure 6.12 shows the reference BLER curves which are proposed for each of the considered LTE modulation schemes: QPSK, 16QAM and 64QAM, assuming 1 and 25 RBs of bandwidth and taking into account AWGN channel, the mother code rate 1/3 and rv= 0. In addition, Figure 6.12 also shows the BICM thresholds and it can be also observed the impact of the size of the code block on the slope of the BLER curves. The selected size of the code block is approximately an average size for each of the modulations. These BLER curves can be used to predict the BLER after any of the HARQ retransmissions. For instance, Table 6.1 lists all the possible code block sizes for the LTE modulations jointly with the selected code block size of 2368 for QPSK, 4288 for 16QAM and 5056 for 64QAM for a bandwidth of 25 RBs, as already proposed in [12]. Table 6.1 shows the details of the MCS considered in the link level simulator: the modulation, the number of code blocks per TB, the turbo code block size, the code rate and the BICM SNR threshold assuming a bandwidth of 25 RBs, rv= 0, only one antenna port and the use of CRSs.

Table 6.1: Details of the MCS considered in the link level simulator for a bandwidth of 25 RBs

MCS Index	Modulation Modulation	Number of Code Blocks	Turbo code block size	Code Rate	BICM SNR threshold [dB]	Proposed code block size, [12]
0	QPSK	1	704	0,11	-7,80	
1	QPSK	1	928	0,15	-6,48	
2	QPSK	1	1120	0,18	-5,56	
3	QPSK	1	1440	0,23	-4,30	
4	QPSK	1	1824	0,29	-3,06	
5	QPSK	1	2240	0,36	-1,93	QPSK: 2368
6	QPSK	1	2624	0,42	-0,99	
7	QPSK	1	3136	0,50	0,12	
8	QPSK	1	3520	0,56	0,91	
9	QPSK	1	4032	0,64	1,94	
10	16QAM	1	4032	0,32	2,07	
11	16QAM	1	4416	0,35	2,66	
12	16QAM	1	4992	0,40	3,49	16QAM: 4288
13	16QAM	1	5760	0,46	4,54	
14	16QAM	2	3264	0,52	5,54	
15	16QAM	2	3648	0,58	6,52	
16	16QAM	2	3904	0,62	7,17	
17	64QAM	2	3904	0,41	7,61	
18	64QAM	2	4032	0,43	7,91	
19	64QAM	2	4608	0,49	9,16	
20	64QAM	2	4992	0,53	9,98	
21	64QAM	2	5376	0,57	10,78	64QAM: 5056
22	64QAM	2	5760	0,61	11,57	
23	64QAM	3	4224	0,67	12,76	
24	64QAM	3	4544	0,72	13,77	
25	64QAM	3	4736	0,75	14,39	
26	64QAM	3	5120	0,81	15,66	
27	64QAM	3	5312	0,84	16,33	

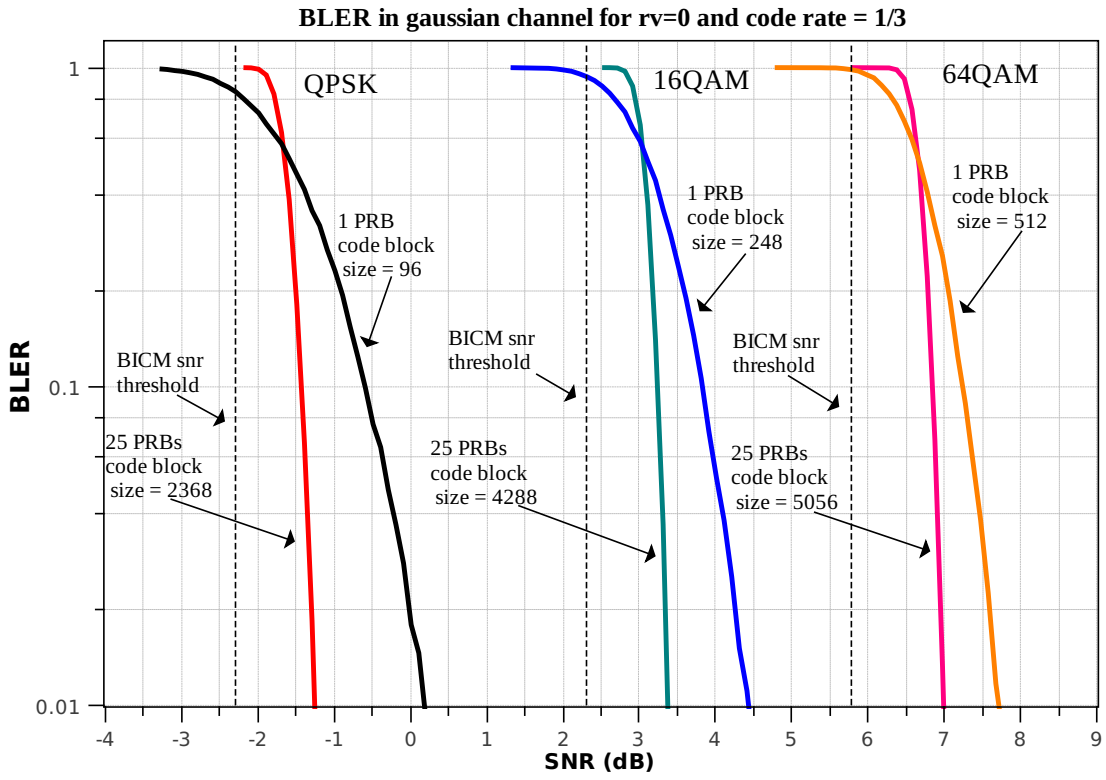

Figure 6.12: AWGN Reference BLER curves (code rate = 1/3) for LTE and a bandwidth of 1 and 25 RB.

6.3.3.2 Effects of TB fragmentation on the BLER curves

It can be observed in Table 6.1 that from MCS 14 to 27 the TB is fragmented in two or three code blocks. This happens when the PHY capacity exceeds the maximum turbo code block size of 6144 bits, [4]. If the TB is fragmented in two code blocks the BLER (defined as the TB error probability) for a given ESNR is slightly higher. Since the BLER curves have been obtained with a single code block this translates into a small offset in the reference BLER curves which can be considered to improve accuracy. Figure 6.13 shows the effects of code block fragmentation on the BLER curves for AWGN channel. It can be verified that the BLER with fragmentation fits quite well with a model of independent errors per code block as shown in Figure 6.13 where "ncb" is the number of code blocks, i.e, number of fragments, and "P_e" means the BLER for "ncb = 1". Assuming a model of independent errors the overall TB error probability can be expressed as BLER$= 1 - (1 - P_e)^{ncb}$.

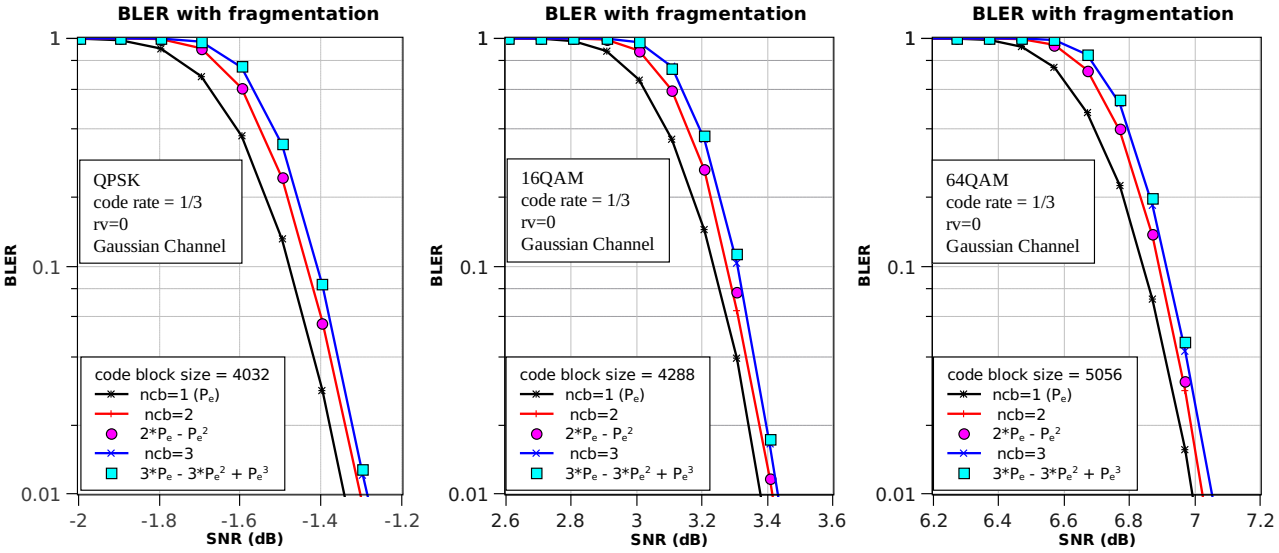

Figure 6.13: Effect of transport code block fragmentation in Reference BLER curves

Figure 6.14 shows the effect of the code block size, which depends on the allocated bandwidth, assuming one antenna port for transmission (AP=0) in AWGN SISO channel. Notice the different slopes of BLER curves in function of the assigned RBs. At BLER= 0.1, it can be observed that for MCS 15, 22 and 27 the BLER performance gain for 25 RBs is approximately equal or lower than 0.5 dB with respect to 1 RB; while for MCS 9 is about 0.7 dB, for MCS 5 is about 1 dB and for MCS 0 is about 2.5 dB.

Figure 6.15 shows the effect of different reserved REs on the BLER performance due to the differences in the ECRs shown in Tables 3.1, 3.2 and 3.3. In particular, it is assumed 25 RBs assigned to the UE and the use of CRSs. If only AP=0 is used, there are 8 reserved REs per RB, if APs=$0, 1$ are used, there are 16 reserved REs per RB; and if APs=$2, 3$ are used, there are 24 reserved REs per RB.

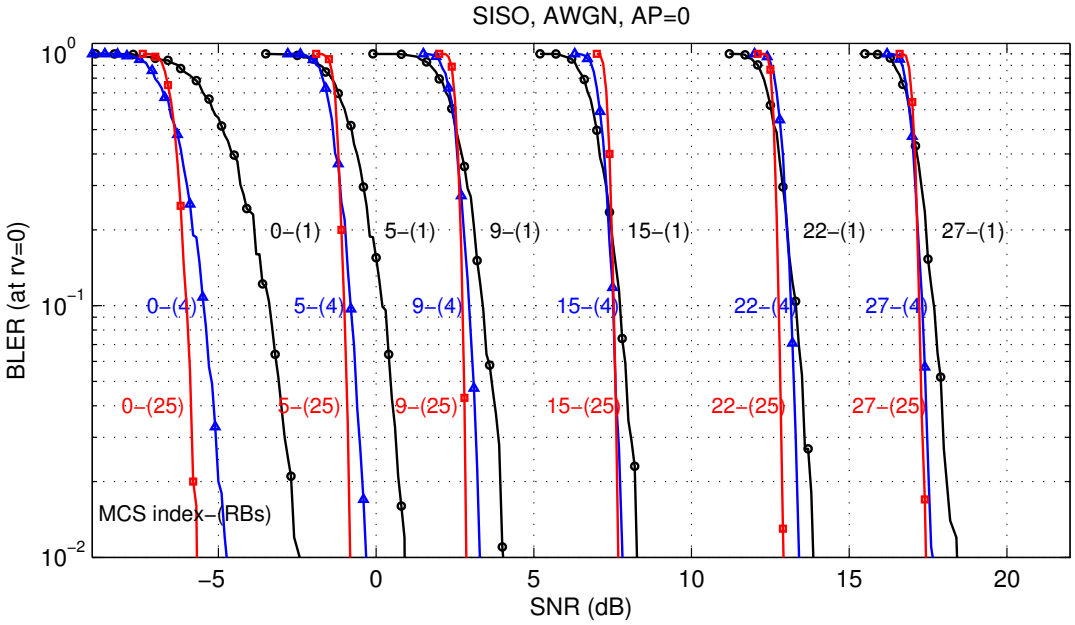

Figure 6.14: BLER curves at rv=0 for 1, 4 and 25 RBs allocations and AP=0 (8 Reserved REs per RB) in AWGN SISO channel

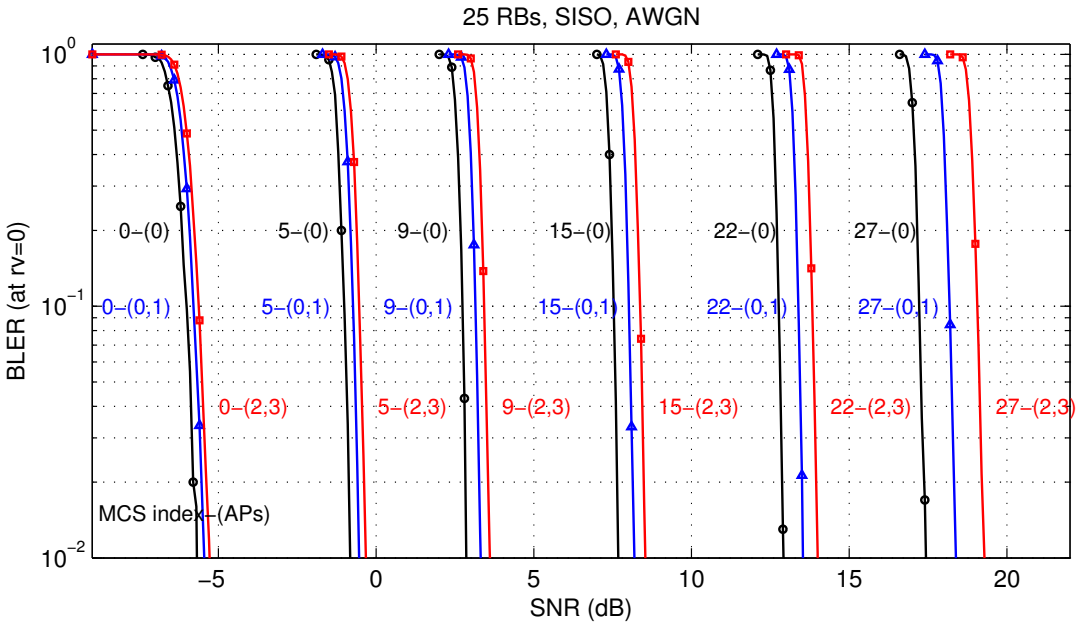

Figure 6.15: BLER curves at rv=0 for different APs (25 RBs) in AWGN SISO channel

The BLER curves depend on multiple factors as shown in Figures 6.14 and 6.15 and, in practice, a simplification is needed to calculate approximately the BLER with link abstraction methods. Thus, we propose to take as a reference the mother code rate BLER curves for QPSK, 16QAM and 64QAM shown in Figure 6.12 and the curve for any code rate $r > 1/3$ can be approximated

by shifting the mother code rate curve as described in next section.

6.3.4 BLER prediction

The ESNR of the multistate channel is used to predict the BLER using Equation 6.12 which is rewritten below:

$$\mathrm{BLER}\left(ESNR\right) \approx \mathrm{BLER}_{\mathrm{AWGN}}\left(ESNR, r\right) \tag{6.36}$$

where $\mathrm{BLER}_{\mathrm{AWGN}}(\cdot)$ is the reference BLER curve in AWGN conditions and r is the code rate. This curve depends on the MCS format (modulation scheme and code rate) and on the size of the code block, so in principle we need as many reference curves as the number of possible combinations of MCS formats and code block sizes. In practice the reference BLER curves of the different MCSs mainly differ on an offset on the SNR axis, as shown in Figures 5.4 and 5.5. So the proposed method shows how to reduce the set of reference BLER curves taking as a reference a single BLER curve: the BLER for the mother code rate ($r = 1/3$).

Taking as a reference the BLER for the mother code rate, the curve for any code rate $r > 1/3$ can be approximated by shifting the mother code rate curve to the right hand side by an amount Δ[dB] that depends on the distance from r to 1/3. This offset accounts for the reduction in the coding gain due to an increase of the code rate from 1/3 to r. For ease of reference, in Figure 6.16 we draw the MMIB curves for QPSK, 16QAM and 64QAM already shown in Figure 2.16. Figure 6.16 also shows the BICM thresholds (γ_0) for the different MCSs along with the SNR needed to achieve a BLER= 0.1. Since the code rate increases with the increasing MCS index, the size of the code block also increases (in order to occupy all the available physical layer capacity); for that reason the code performance is kept close to the theoretical capacity. From Figure 6.16 it is clear that we may approximate the reduction in the coding gain by:

$$\Delta[\mathrm{dB}] = \gamma_0 - \overline{\mathrm{MIB}}^{-1}(1/3) = \overline{\mathrm{MIB}}^{-1}(r) - \overline{\mathrm{MIB}}^{-1}(1/3) \tag{6.37}$$

for any $r > 1/3$. For any MCS with $r \leqslant 1/3$ the same mother code rate BLER curve can be used, i.e., Δ[dB] = 0 dB. This is because for $r \leqslant 1/3$ the rate matching procedure introduces bit repetition, which translates into an energy gain but there is not any additional coding gain with respect to rate 1/3. The energy gain is properly captured by the proposed method of computing the received average bit information rate and the ESNR (Equation 6.35), so that in practice, when there is bit repetition the ESNR is higher than the physical layer SNR. For example, for $r = 1/6$ all the bits are repeated twice and the ESNR is 3 dB higher than the physical SNR. For this reason it is taken Δ[dB] = 0 dB for any MCS with $r \leqslant 1/3$.

When IR HARQ is applied, after the reception of a new rv the receiver combines the LLRs of all the available rvs. Assuming that the rate matching has punctured the codeword ($r > 1/3$), the codeword seen by the decoder has less punctured bits than any of the individual rvs. That is, although from the point of view of the rate matching at the transmitter side all the rvs exhibit the same code rate, from the point of view of the turbo decoder the effective code rate decreases with every new received rv. This reduction of the effective code rate increases the coding gain and so the probability of correct decoding. Thus, it is defined the effective code rate after each rv (r_{eff}) as the size of the information code block over the number of non-zero LLRs in the codeword at the input of the decoder (assuming that LLR= 0 means that the bit has not been received). With

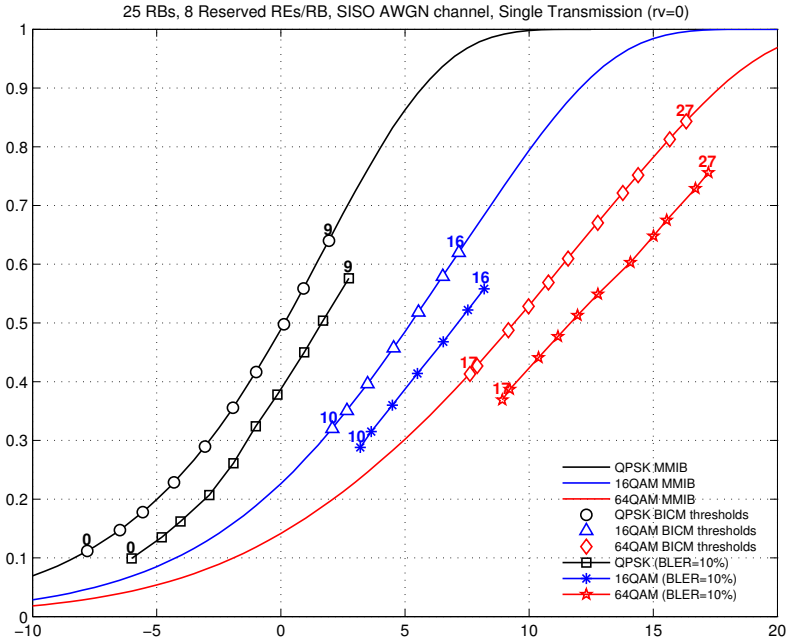

Figure 6.16: BICM thresholds and SNR needed for BLER= 0.1 for the first round (rv= 0) of HARQ transmissions in LTE (assuming a bandwidth of 25 RBs)

this definition r_{eff} is always higher than 1/3 ($r_{eff} > 1/3$) and $r_{eff} = 1/3$ only when all the bits in the codeword have been received at least once. For any MCS, for the first HARQ round, we have $r_{eff} = r$ (where $r = \eta_{ECR}$ is the code rate given by Equation 3.4) and after 4 IR transmissions the decoder always sees $r_{eff} = 1/3$. In other words, r_{eff} measures the effective code rate from the point of view of the decoder and it is convenient to obtain the coding gain reduction (Δ[dB]) after any of the IR HARQ rounds with Equation 6.38.

$$\Delta[\text{dB}] = \overline{\text{MIB}}^{-1}(r_{eff}) - \overline{\text{MIB}}^{-1}(1/3) \ \ (\geq 0) \tag{6.38}$$

The advantage of separating the coding gain (captured with Equation (6.38)) and the energy gain (captured with the ESNR, Equation 6.35)) is that the same reference BLER curves of Figure 6.12 can be used to predict the BLER after any of the HARQ rounds, [98]. It is sufficient to compute r_{eff} for the current HARQ round and then use Equation 6.38 to find the offset Δ[dB] (to the right hand side) to apply to the reference BLER curve. Depending on the MCS and HARQ round we may have $\Delta[\text{dB}] = 0$ dB.

In conclusion, by using the proposed methodology the BLER in multipath channel conditions and with IR HARQ can be predicted without resorting to complex calibration steps.

6.4 Simulation Results

In this section some simulation results are presented based on the proposed link abstraction method for SISO and 2×2 MIMO with low and high antenna correlation. For 2×2LC and

2×2HC, two transmission modes have been considered: OL MIMO-SM with CDD precoding and MIMO-TD. These simulations are performed with the link level simulator described in this dissertation. It is assumed ideal channel estimation and ETU300 as multipath channel model. For MIMO-SM, it has been considered MMSE receiver without SIC. Figure 6.12 shows the reference BLER curves for a bandwidth of 1 and 25 RBs which have been used for the BLER prediction. In addition the effect of TB fragmentation is also considered as shown in Figure 6.13. Although the procedure is general, only some relevant MCS have been studied.

The results are obtained by generating many channel snapshots with different ESNR. In addition, when HARQ is simulated the program generates an independent channel snapshot for each of the HARQ rounds. A global ESNR (including all the received HARQ rounds) is computed according to 6.35. As the target BLER is $\text{BLER}_{target} = 0.1$, then the simulator processes $100/\text{BLER}_{target} = 1000$ TBs through the LTE link layer and measures the BLER. During the processing of the TBs the multipath channel remains static. The measured BLER is plotted vs. the ESNR in order to compare with the reference BLER curve.

In general, the proposed link abstraction method leads to a good match between the simulated and predicted BLER as shown in the figures presented in this section. The analysis of the simulation results is done by comparing the simulated BLER (dots and labelled as "sim.") with the predicted BLER (solid lines and labelled as "pred.") for different MCS after the first, second, third and fourth HARQ round for 1 and 25 RBs. Let's have a look to the simulation results for the two considered cases, SISO and 2×2 MIMO.

The BLER prediction for SISO shows a good accuracy for the first HARQ round (rv= 0), as shown in Figure Figures 6.17. For the second round (rv= 1) (Figure 6.18), the results are quite good and it has to be noticed only that from MCS 10 to 27 there is a small deviation of the simulated BLER compared to the predicted BLER, specially for MCS 10. The same comments also apply for third and fourth HARQ rounds (Figure 6.19 and 6.20) including that the deviation for MCS 17 is also remarkable as in the case of MCS 10. The difference between the predicted and the simulated BLER is approximately lower than 1 dB for all the studied cases. In particular the results are very accurate for MCS 9 as shown in these figures. However, for MCS 10 and rv= $1, 2, 3$ and MCS 17 and rv= $2, 3$, a systematic error is observed which can reach 1.5 dB. The arrows in Figures 6.17, 6.18, 6.19 and 6.20 show the coding gain reduction in dB that results from the selection of the highest MCS or the lowest MCS for the same modulation scheme after each HARQ round for 25 RBs. Additionally, the values of the effective code rate (r_{eff}) for each MCS are also shown in the figure.

For 2×2LC and 2×2HC, it can be observed that for the first HARQ round the results are quite accurate except for a small systematic error for MCS 27 and TD, as shown in Figures 6.21 and 6.22. As shown in Figures 6.23, 6.24, 6.25, 6.26, 6.27 and 6.28, for the rest of HARQ rounds the BLER prediction works pretty well except for a small systematic error at MCS 16 to 27. Obviously one cause of this error can be due to the different size of the real and the reference code block. Similarly to SISO, the results are very accurate for MCS 9 for the considered MIMO schemes. In any case, considering the overall simulation results, the accuracy of the proposed method is generally better than 1 dB (although from MCS 16 to 27, this error can reach 2 dB for some specific cases). As a result, the proposed link abstraction methodology has been proven to work for the MIMO transmission modes CDD precoding and TD independently of the antenna

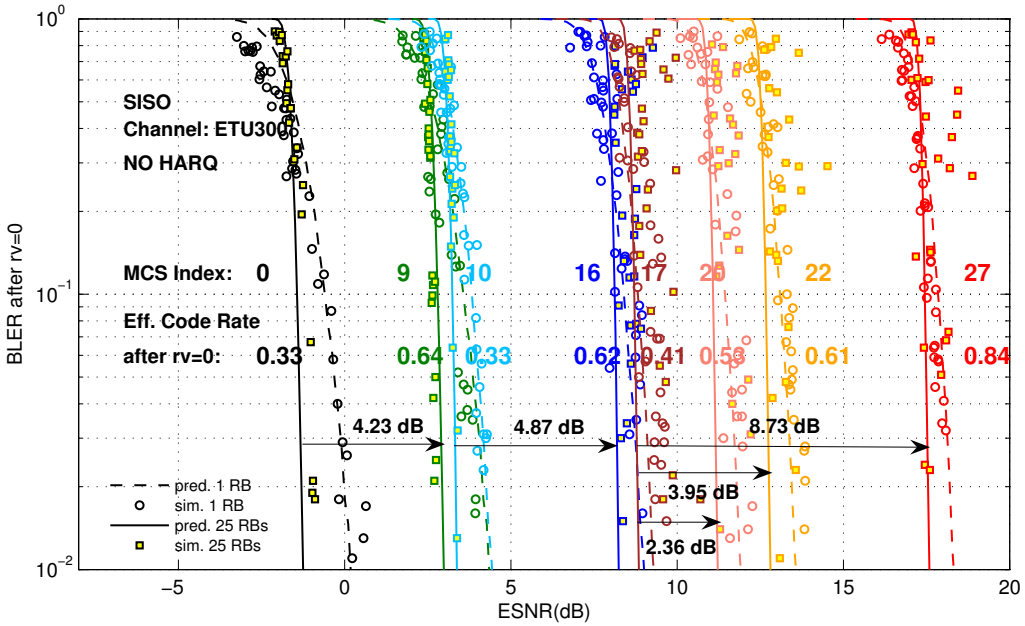

Figure 6.17: Predicted and Simulated BLER after the first HARQ round in LTE for SISO case and bandwidth of 1 and 25 RBs

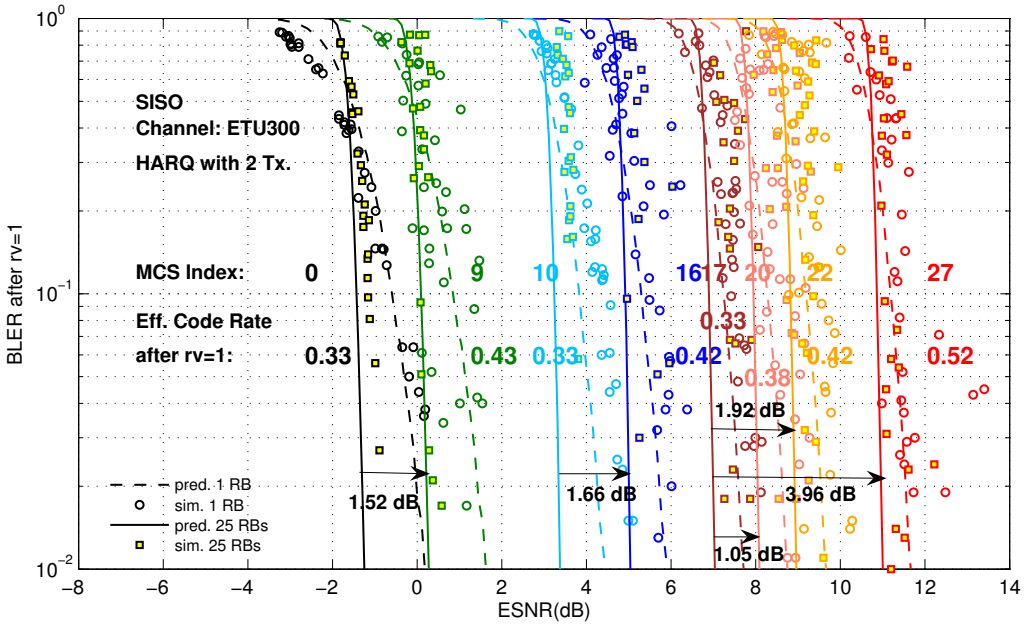

Figure 6.18: Predicted and Simulated BLER after the second HARQ round in LTE for SISO case and bandwidth of 1 and 25 RBs

correlation. Furthermore, more simulation results of the proposed link abstraction method are provided in Appendix C.

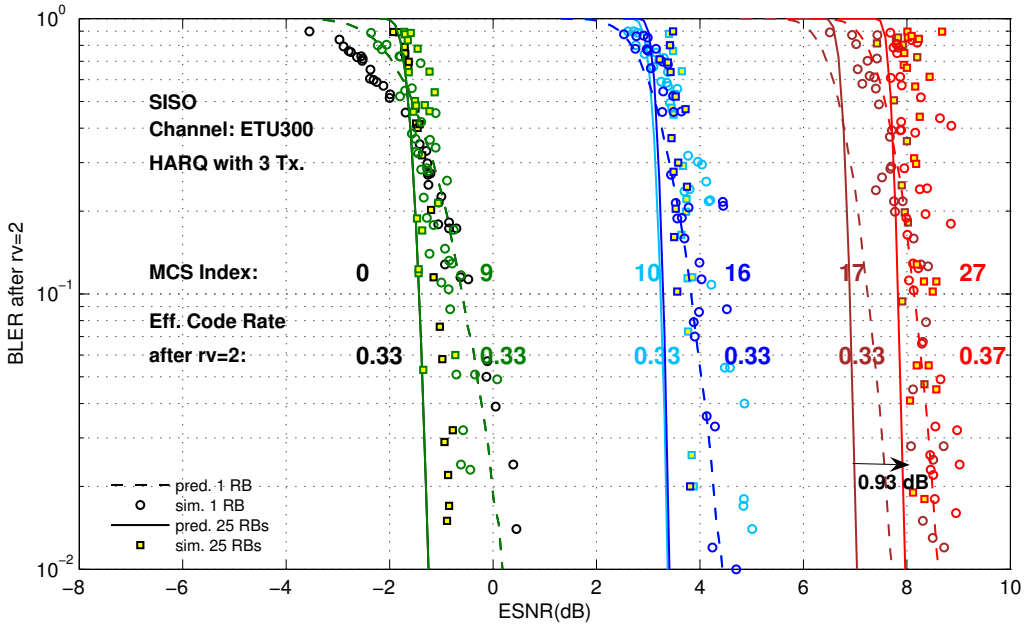

Figure 6.19: Predicted and Simulated BLER after the third HARQ round in LTE for SISO case and bandwidth of 1 and 25 RBs

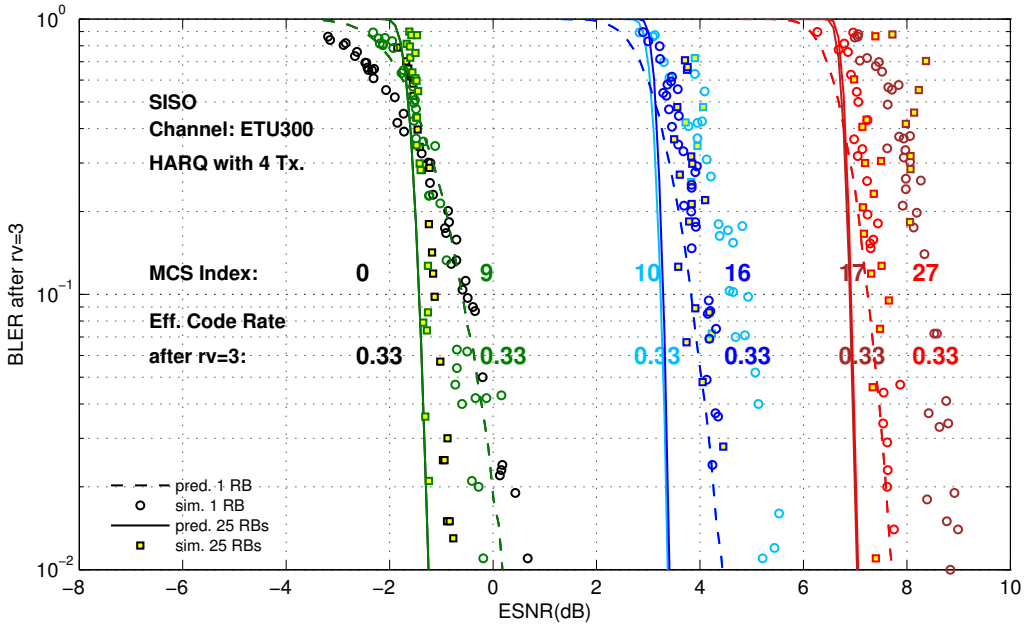

Figure 6.20: Predicted and Simulated BLER after the fourth HARQ round in LTE for SISO case and bandwidth of 1 and 25 RBs

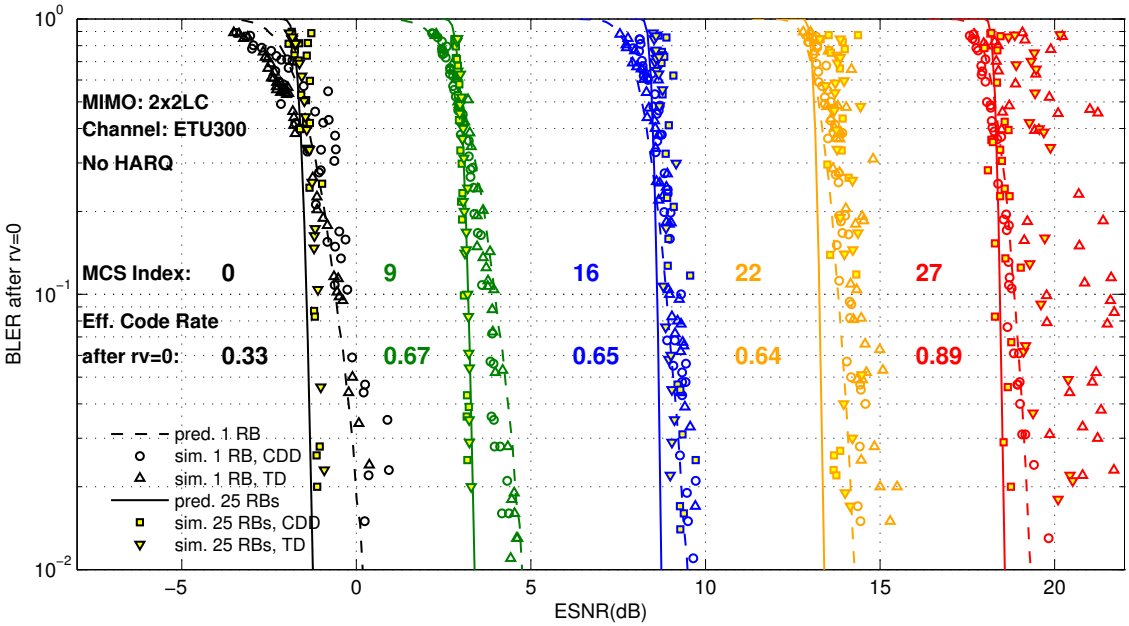

Figure 6.21: Predicted and Simulated BLER after the first HARQ round in LTE for 2 × 2LC MIMO case and bandwidth of 1 and 25 RBs

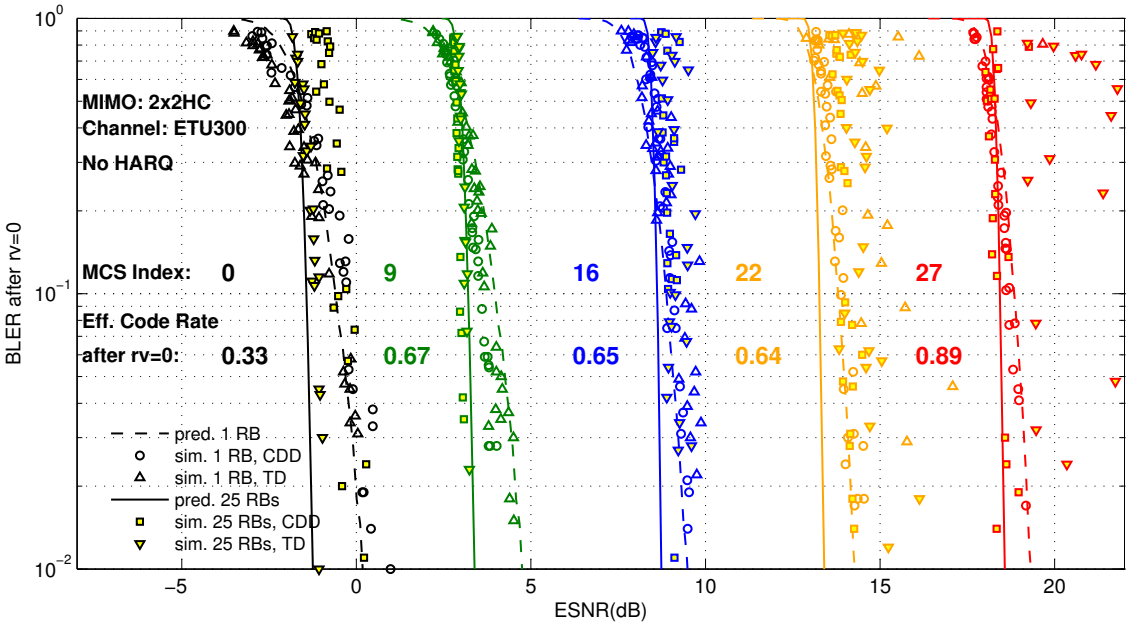

Figure 6.22: Predicted and Simulated BLER after the first HARQ round in LTE for 2 × 2HC MIMO case and bandwidth of 1 and 25 RBs

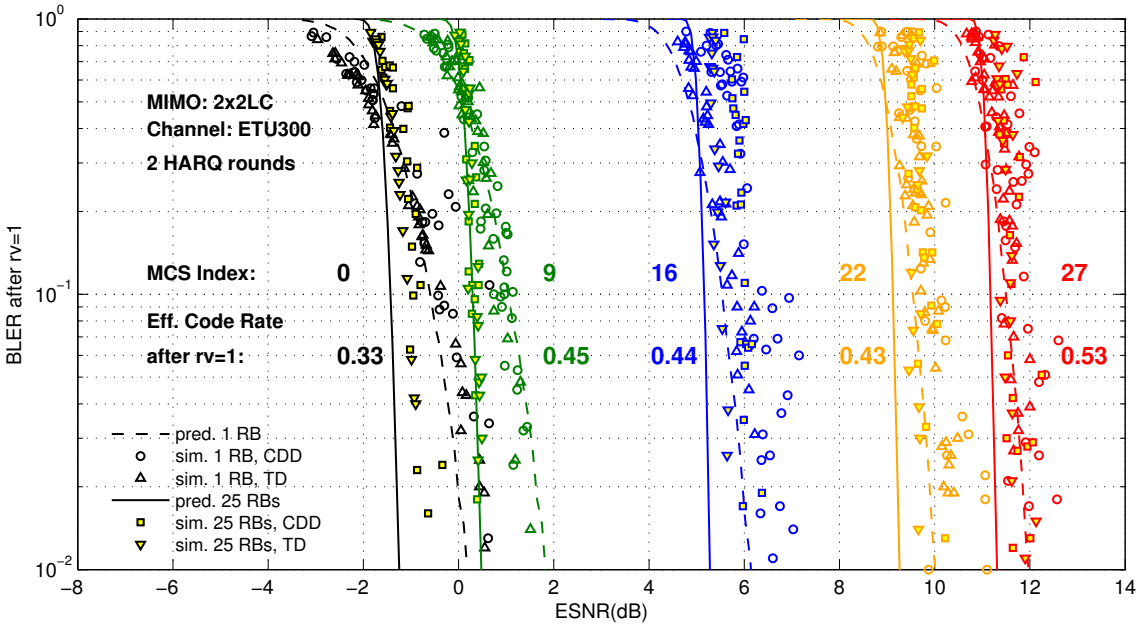

Figure 6.23: Predicted and Simulated BLER after the second HARQ round in LTE for 2×2LC MIMO case and bandwidth of 1 and 25 RBs

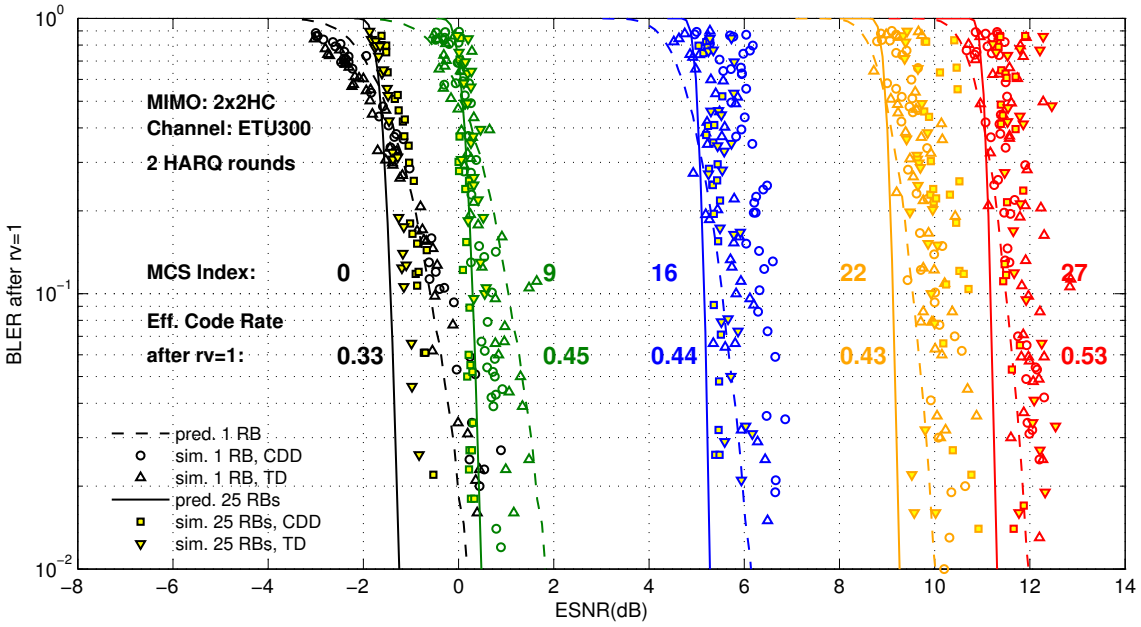

Figure 6.24: Predicted and Simulated BLER after the second HARQ round in LTE for 2×2HC MIMO case and bandwidth of 1 and 25 RBs

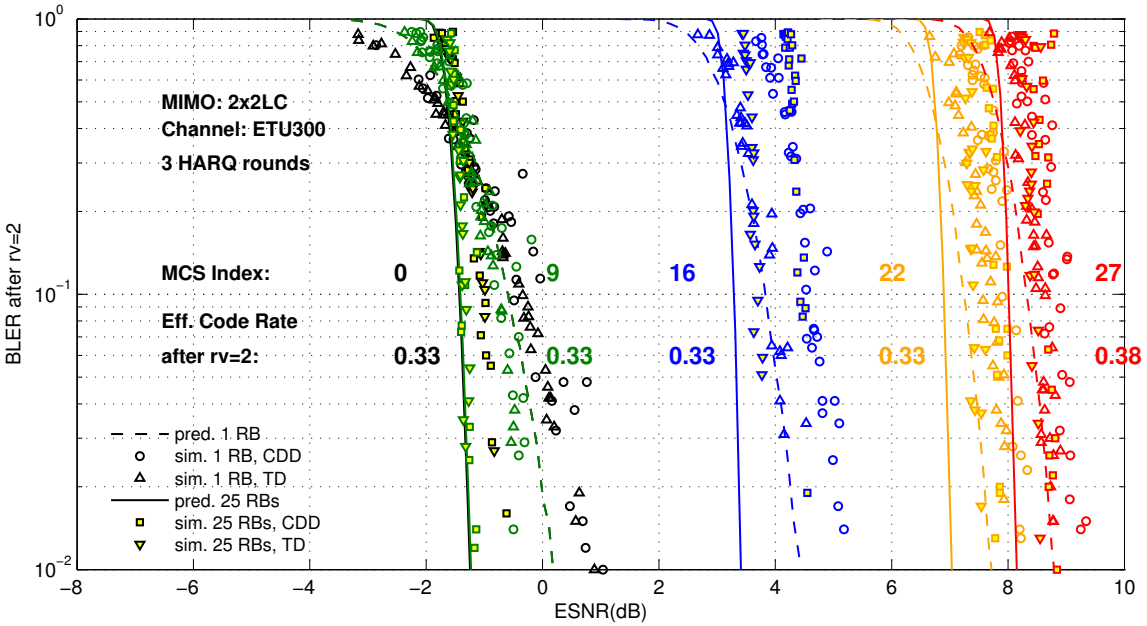

Figure 6.25: Predicted and Simulated BLER after the third HARQ round in LTE for 2×2LC MIMO case and bandwidth of 1 and 25 RBs

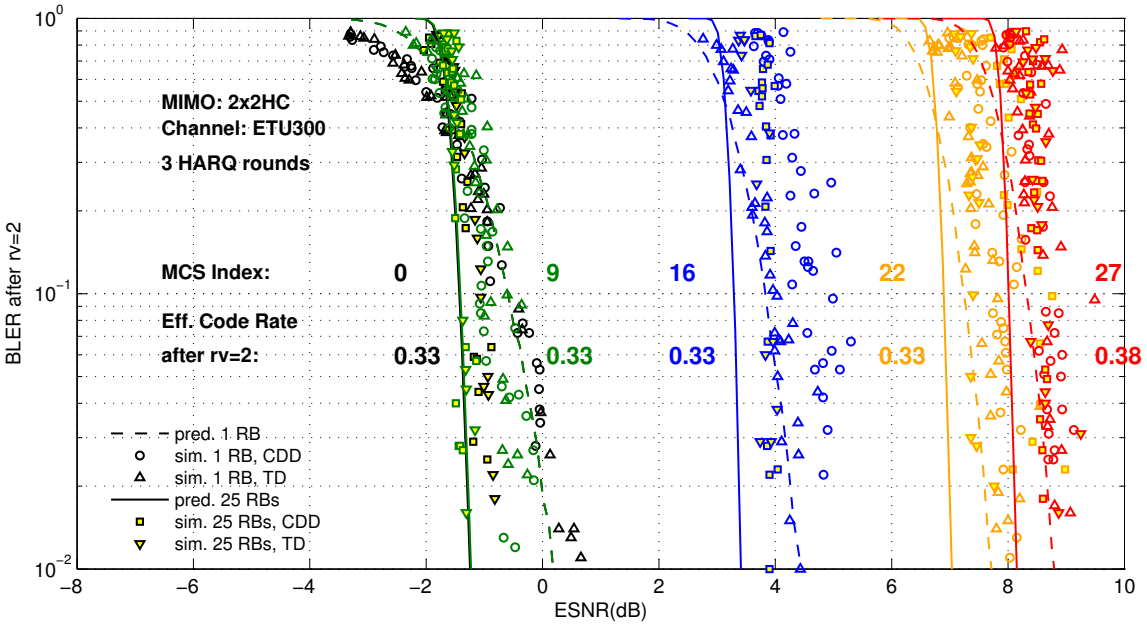

Figure 6.26: Predicted and Simulated BLER after the third HARQ round in LTE for 2×2HC MIMO case and bandwidth of 1 and 25 RBs

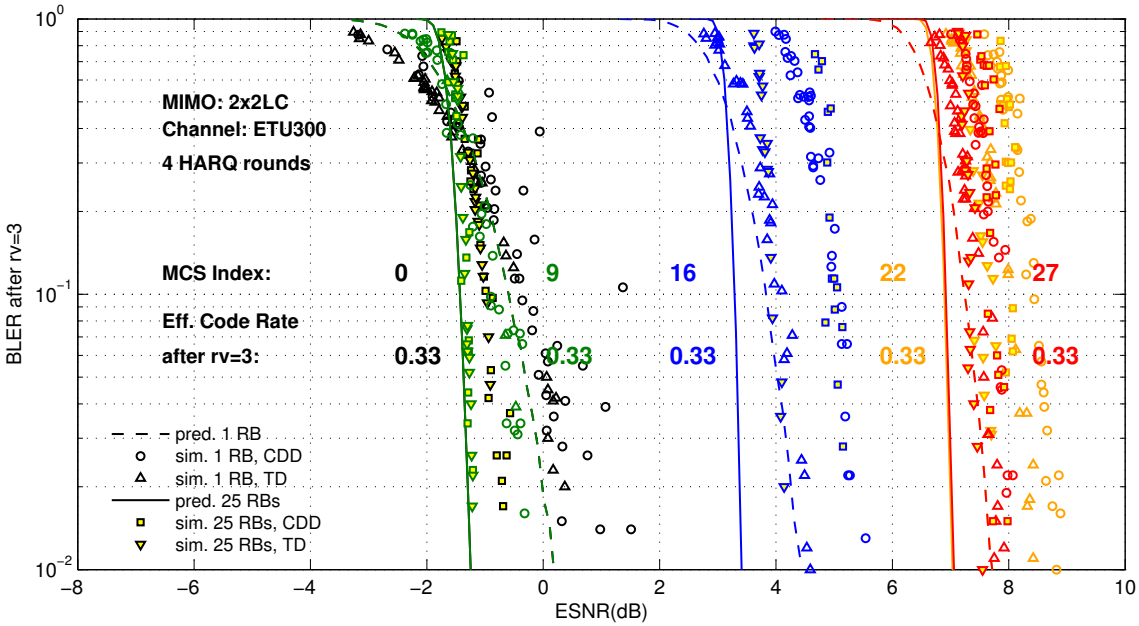

Figure 6.27: Predicted and Simulated BLER after the fourth HARQ round in LTE for 2×2LC MIMO case and bandwidth of 1 and 25 RBs

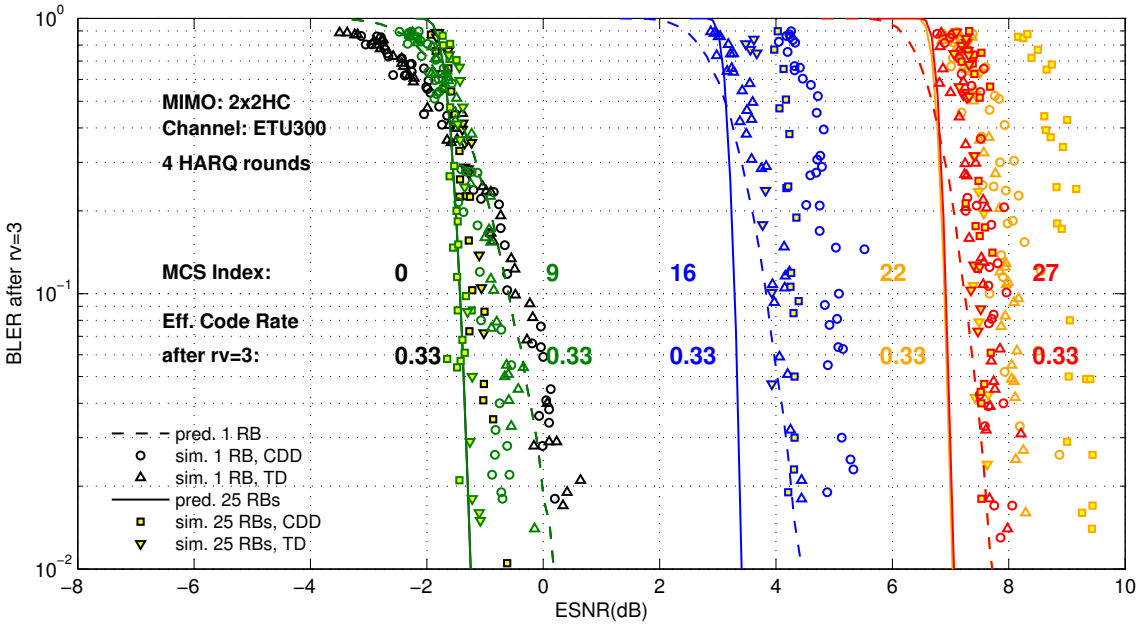

Figure 6.28: Predicted and Simulated BLER after the fourth HARQ round in LTE for 2×2HC MIMO case and bandwidth of 1 and 25 RBs

Chapter 7

Conclusions

7.1 Conclusions

7.1.1 Main Conclusions and Summary of Objectives

The LTE/LTE-Advanced standard defines an extremely flexible radio interface, which it is based on OFDM technology with MIMO antenna processing and an all-IP flat network architecture where all the user plane radio functionalities are terminated at the eNodeB, and all services are conveyed over packed based shared transport channels. These innovations open important research challenges related to the optimization of the PHY and MAC layers. The main objectives of this dissertation are the link level performance evaluation and the link abstraction for LTE/LTE-Advanced-DL. In particular, DL SU-MIMO transmission modes have been evaluated taking into account perfect and imperfect channel estimation and a novel link abstraction method with application to wideband OFDM systems in multipath fading has been presented and assessed.

The link level simulation of LTE/LTE-Advanced is a key aspect in order to study the radio link with full details and establish simplified LUTs for system level simulators. So an E-UTRA link level simulator in order to accomplish the objective of the link level performance evaluation has been developed. Previously, we have reviewed the main aspects to consider when designing a link level simulator with the objective to point out the parameters and configuration options that must be agreed in order to obtain results that can be compared.

The effects of imperfect channel estimation on LTE/LTE-Advanced DL link level performance have been studied. Practical estimation methods have been assessed and a Gaussian channel estimation error model, which is called CEEM, has been validated in different propagation conditions. The proposed model allows simulating the LTE/LTE-Advanced link level without the need to process the pilot symbols or assuming ideal channel estimation. The Wiener filter in the frequency domain, when fed with the right channel covariance matrices, leads to a low channel estimation error.

It has been presented a novel method of link abstraction with application to wideband OFDM systems in multipath fading including the effects of IR HARQ retransmissions. It has been shown that, by working at bit level, the proposed method can capture properly the effect of the LLR combination of different IR HARQ transmissions. Simulation results for LTE/LTE-Advanced DL with SISO and 2×2 MIMO TMs have been presented and it has been shown that the proposed link abstraction method can predict the BLER with good accuracy.

The achieved goals of this dissertation can be summarized in four highlights listed below:

- Development of a E-UTRA DL link level simulator.

- Proposal of a *Channel Estimation Error Model* (CEEM) and study of the effect of imperfect channel estimation on the link level performance.
- Evaluation of the E-UTRA DL link level performance for SISO and MIMO TMs with perfect and imperfect channel estimation.
- Proposal of a novel link abstraction method for E-UTRA including the effects of IR HARQ retransmissions.

More detailed conclusions and what was achieved in this dissertation with respect to each of these objectives are presented in next subsections.

7.1.2 E-UTRA link level simulator

In Chapter 3 we have reviewed the main aspects to consider when designing an E-UTRA link level simulator with the objective to point out the parameters and configuration options that must be agreed in order to obtain results that can be compared. It has been shown that there are many options to consider, an so the emphasis and the simulation efforts have been put on the most interesting transmission modes from a research point of view.

In order to evaluate the baseline DL link level performance of LTE/LTE-Advanced and study different link abstraction methods, it has been developed an E-UTRA DL link level simulator which features the SISO-OFDM and the MIMO-OFDM physical channels, the channel coding, the rate matching and the HARQ processes based on the 3GPP LTE specifications defined in [3, 4]. More specifically, we have studied the transport and physical channel processing for E-UTRA; it has been shown how to compute the transport channel capacity and the ECR for E-UTRA; it has been described how to simulate the MIMO wideband mobile channel taking into account the correlation-based MIMO radio mobile stochastic model defined in LTE/LTE-Advanced standard and it has been analysed the MIMO precoding and the MIMO processing for OL MIMO-SM, CL MIMO-SM and MIMO-TD.

Regarding MIMO processing, the ZF and MMSE MIMO linear detectors have been described. Additionally, a codeword-SIC receiver over MIMO linear receivers that takes also into account the HARQ transmissions has been proposed.

7.1.3 CEEM

In Chapter 4 the RSs (pilot symbols) for LTE/LTE-Advanced have been reviewed and it has been studied the effect of pilot-based channel estimation for E-UTRA DL based on CRS. CEEM has been proposed in order to simulate the LTE/LTE-Advanced link level without the need to process any pilot symbol, i.e, any RS. The simulation results for pilot-based channel estimation have been used to calibrate and validate the CEEM.

The Wiener filter in the frequency domain, when fed with the right channel covariance matrices, leads to low channel estimation error and outperforms the LS method. In addition, it has been assessed the effect of imperfect knowledge of channel statistics on the Wiener filter performances. Thus UE needs to have proper knowledge of the channel statistics in order to decode the received data by using pilots and to apply different channel estimation techniques like interpolation, extrapolation, Wiener filtering or sliding window averaging. Averaging can be done over multiple pilots

in time/frequency to obtain a better channel estimate as long as the sliding window size is lower than the 50% coherence time and coherence bandwidth. So depending on the channel conditions, averaging is useful or destroys channel time/frequency correlation properties.

The 2D-Wiener filter in frequency and time domain is the optimum channel estimator, but it introduces too much complexity on the channel estimation procedure to obtain a limited performance gain. In order to obtain a trade-off between complexity and performance, the channel estimation procedure is split into time and frequency domain. We have studied practical estimation methods where Wiener filtering in the frequency domain precedes and follows time domain linear interpolation. It has been shown that the 1D Wiener filter in the frequency domain is a channel estimation technique that enhances the channel estimation error performance with respect to LS channel estimator making the data transmission more robust. It has been found that the best results are achieved if linear interpolation is applied in the time domain and, afterwards, 1D Wiener filtering is applied in the frequency domain. It has been found that the optimum scheme for channel estimation is LS+SVT+LT+WF(C), where V is size of the sliding window average in the time domain and V=9 TTIs for EPA5 and V=3 TTIs for EVA70. For ETU300 is not recommended to use a sliding window average in the time domain. With respect to the Wiener filtering matrix size (called C in Chapter 4), it has been obtained that taking 36 subcarriers, i.e. 3 RBs, achieves a good channel estimation error performance compared to using more subcarriers, so for a low complexity channel estimator $C = 36$ is proposed.

7.1.4 E-UTRA DL link level performance

In Chapter 5 the AWGN link level performance has been studied and the reference BLER curves, the capacity and the net throughput that can be achieved and the AMC spectral efficiency for E-UTRA DL have been obtained. It has been observed that in order to maximize the average throughput in AWGN channel without HARQ, the transport format must be changed within a SNR range of a few dB, while HARQ allows the use of the same transport format in a wider range of SNR.

Different MIMO detectors for E-UTRA DL and 2×2 and 4×4 MIMO under ideal channel estimation have been assessed. For MIMO-SM it has been found that the MMSE receiver outperforms the ZF receiver. There have been also shown the benefits of the precoding defined in LTE specifications. It has been observed that OL MIMO-SM is very sensitive to antenna correlation making leading to the conclusion that it is more suitable for this scenario the use CL MIMO-SM, MIMO-TD or SIMO with MRC. It has been evaluated the performance of the proposed codeword-SIC receiver and, although for OL MIMO-SM it is also useful, it shows a significant gain in CL MIMO-SM for the non-priority codeword.

It has been evaluated the E-UTRA DL link average throughput taking into account ideal and CEEM channel estimation. CEEM simulation results provides a more realistic achievable average throughput. Without HARQ it has been found that, for low antenna correlation OL and CL MIMO-SM throughput overperfoms TD. For medium and high antenna correlation, TD scheme gets better performance than OL MIMO-SM scheme. However, CL MIMO-SM scheme outperforms TD scheme for medium antenna correlation while, for HC antenna correlation, TD is more suitable.

It has been observed that HARQ is useful in order to achieve more easily the E-UTRA DL peak rate requirement which in the case of 2×2 MIMO is 8.6 bits/s/Hz. For low antenna correlation there is no problem to achieve this requirement under CEEM; but for medium and high antenna correlation it is only achieved with ideal channel estimation. Particularly, for all the cases where the E-UTRA DL peak rate requirement is achieved, the required average SNR is higher than 20 dB assuming that all the HARQ transmissions take place with the same average SNR.

7.1.5 Link Abstraction for E-UTRA

A novel method of link abstraction to simulate the LTE/LTE-Advanced with IR HARQ at system level has been described and assessed. Since the proposed method is based on estimating the MI between the transmitted bits and the received LLRs, we have computed and plotted the MIB vs. SNR curves for QPSK, 16QAM and 64QAM applied in LTE/LTE-Advanced and also for BPSK in AWGN channel. Thanks to the MIB the three effects that contribute to the multistate channel, i.e, frequency selective fading, IR HARQ and unequal error protection of the modulation scheme are properly captured without resorting to any set of calibration constants. Furthermore, it has been shown how to reduce the set of reference BLER curves when working with multiple MCSs.

We have shown the simulation results for LTE/LTE-Advanced DL with SISO and 2×2 MIMO TMs with low and high antenna correlation, highly-selective ETU channel and 5 MHz bandwidth (i.e. 25 RBs). It has been observed that there is a good match between the predicted and simulated BLER.

To sum up, the advantages of the proposed method are listed below:

- It doesn't need calibration.
- It can work with only three reference BLER curves.
- It captures all the effects of the multistate channel in highly selective fading.
- It can even be applied when the MCS format changes at every HARQ round.

7.2 Open issues and future work

As a result of the work of this dissertation, we present some open issues and future work for further research:

- The E-UTRA link level simulator presented in Chapter 3 can be extended to include more LTE/LTE-Advanced features such as:
  - UL
  - The full set of LTE/LTE-Advanced *Transmission Mode*s (TMs) for both DL and UL, including SU-MIMO, MU-MIMO, beamforming.
  - Optimization of the CL precoding selection without assuming perfect selection per sub-carrier.

Table 7.1: New CQIs table in LTE-Advanced Release 12

CQI index	Mod.	Mod. Order Q_m	Code Rate
1	QPSK	2	0.076
2	QPSK	2	0.188
3	QPSK	2	0.438
4	16QAM	4	0.369
5	16QAM	4	0.479
6	16QAM	4	0.602
7	64QAM	6	0.455
8	64QAM	6	0.554
9	64QAM	6	0.650
10	64QAM	6	0.754
11	64QAM	6	0.853
12	256QAM	8	0.694
13	256QAM	8	0.778
14	256QAM	8	0.864
15	256QAM	8	0.926

Table 7.2: New MCS indexes table in LTE-Advanced Release 12

MCS Index	Modulation	Modulation Order	MCS Index	Modulation	Modulation Order
0	QPSK	2	**14**	64QAM	6
1	QPSK	2	**15**	64QAM	6
2	QPSK	2	**16**	64QAM	6
3	QPSK	2	**17**	64QAM	6
4	QPSK	2	**18**	64QAM	6
5	16QAM	4	**19**	64QAM	6
6	16QAM	4	**20**	256QAM	8
7	16QAM	4	**21**	256QAM	8
8	16QAM	4	**22**	256QAM	8
9	16QAM	4	**23**	256QAM	8
10	16QAM	4	**24**	256QAM	8
11	64QAM	6	**25**	256QAM	8
12	64QAM	6	**26**	256QAM	8
13	64QAM	6	**27**	256QAM	8

- Regarding the E-UTRA link level simulator, instead of implementing the wideband MIMO channel model that comes from applying the simplified stochastic model based on correlation matrices in order to generate channel coefficients proposed in [67, 68]; it can be programmed the more complex method, proposed in [66, 67, 68], which takes into account the per-path power azimuth spectrum at the eNodeB and at the UE, so it models the geometry of the scattering in a stochastic way.

- Regarding the proposed CEEM, the channel estimation LUTs can be extended to other type of reference signals than the CRSs.

- An open issue is to extend the proposed CEEM to take different values of ε for the MIMO channel matrix in function of the reference signals density for each antenna port.

- Regarding the AMC, an open issue is to extend the the AWGN link level performance to the new CQI indices (Table 7.1) and MCS indices (Table 7.2), which are introduced by LTE-Advanced Release 12, that consider a higher order modulation, 256QAM.

- The proposed link abstraction model can be extended to other DL transmission modes, such as MU-MIMO, and UL transmission modes.

Appendix A

MMSE Formulation

A.1 MIMO MMSE Linear Detector

In this appendix the formulation of the MMSE solution for the MIMO receiver processing introduced in section 3.4.5.1. Using linear processing, the estimate of the transmitted symbol vector $\mathbf{s}_k$ at subcarrier k can be found by:

$$\hat{\mathbf{s}}_k = \mathbf{W}_k \mathbf{r}_k \tag{A.1}$$

where $\mathbf{W}_k$ is the equalization receiver matrix which is a $N \times M$ complex matrix since a MIMO system of M receive antennas and N transmit antennas is considered. In order to simplify the notation of next equations, we omit the subcarrier index k and Equation A.2 is rewritten as:

$$\hat{\mathbf{s}} = \mathbf{W}\mathbf{r} \tag{A.2}$$

where $\mathbf{r}$ is $M \times 1$ complex vector whose elements correspond to the detected complex symbols at each receive antenna.

$$\mathbf{r} = \mathbf{H} \cdot \mathbf{s} + \sigma\mathbf{n} = \begin{bmatrix} \mathbf{H}_1 & \mathbf{H}_2 & \dots & \mathbf{H}_N \end{bmatrix} \begin{bmatrix} s_1 \\ s_2 \\ \vdots \\ s_N \end{bmatrix} + \sigma \begin{bmatrix} n_1 \\ n_2 \\ \vdots \\ n_M \end{bmatrix} \tag{A.3}$$

where $\mathbf{s}$ is $N \times 1$ complex vector whose elements correspond to the transmitted complex symbols, $\mathbf{H}$ is the $M \times N$ MIMO channel complex matrix at subcarrier, $\mathbf{H}_j$ denotes the channel column vector j and $\mathbf{n}$ is a $N \times 1$ vector containing iid complex Gaussian noise, σ^2 is the noise variance and each element of the noise vector n_i satisfies $E\left\{|n_i|^2\right\} = \overline{\left(|n_i|^2\right)} = 1$, where $E\{x\} = \overline{(x)}$ denotes the expectation of x.

As described in section 3.4.5.1, the MMSE receiver is an alternative to the ZF receiver which attempts to strike a balance between spatial-interference suppression and noise enhancement by simply minimizing the distortion by finding $\mathbf{W}$ that minimizes the MSE as follows:

$$\mathbf{W} = \arg\min_{\mathbf{W}} E\left\{\|\mathbf{s} - \hat{\mathbf{s}}\|^2\right\} = \arg\min_{\mathbf{W}} E\left\{\|\mathbf{s} - \mathbf{W}\mathbf{r}\|^2\right\} \tag{A.4}$$

Now we define the MSE vector $\mathbf{e}$ as:

$$\mathbf{e} = E\left\{\|\mathbf{s}-\hat{\mathbf{s}}\|^2\right\} = \begin{pmatrix} \overline{|s_1-\hat{s}_1|^2} \\ \vdots \\ \overline{|s_j-\hat{s}_j|^2} \\ \vdots \\ \overline{|s_N-\hat{s}_N|^2} \end{pmatrix} = \begin{pmatrix} \overline{\left|s_1-\mathbf{w}_1^{\mathrm{T}}\mathbf{r}\right|^2} \\ \vdots \\ \overline{\left|s_j-\mathbf{w}_j^{\mathrm{T}}\mathbf{r}\right|^2} \\ \vdots \\ \overline{\left|s_N-\mathbf{w}_N^{\mathrm{T}}\mathbf{r}\right|^2} \end{pmatrix} = \begin{pmatrix} e_1 \\ \vdots \\ e_j \\ \vdots \\ e_N \end{pmatrix} \tag{A.5}$$

and $\mathbf{W}$ is defined as:

$$\mathbf{W} = \begin{pmatrix} w_{1,1} & \dots & w_{1,M} \\ \dots & \dots & \dots \\ w_{N,1} & \dots & w_{N,M} \end{pmatrix} = \begin{pmatrix} \mathbf{w}_1^{\mathrm{T}} \\ \vdots \\ \mathbf{w}_N^{\mathrm{T}} \end{pmatrix} \tag{A.6}$$

where $(\cdot)^{\mathbf{T}}$ is the transpose.

In order to obtain the linear MMSE solution, $\mathbf{W}$ must be chosen such that the MSE vector $\mathbf{e}$, Equation A.5, is at its minimum possible value. To minimize Equation A.5, we can equate

$$\bigtriangledown \mathbf{e} = \begin{bmatrix} \bigtriangledown \mathbf{e}_1^{\mathrm{T}} \\ \bigtriangledown \mathbf{e}_2^{\mathrm{T}} \\ \dots \\ \bigtriangledown \mathbf{e}_M^{\mathrm{T}} \end{bmatrix} = \begin{bmatrix} \frac{\partial e_1}{\partial w_{1,1}} & \frac{\partial e_1}{\partial w_{1,2}} & \cdots & \frac{\partial e_1}{\partial w_{1,N}} \\ \frac{\partial e_2}{\partial w_{2,1}} & \frac{\partial e_2}{\partial w_{2,2}} & \cdots & \frac{\partial e_2}{\partial w_{2,N}} \\ \vdots & \vdots & \vdots & \vdots \\ \frac{\partial e_M}{\partial w_{M,1}} & \frac{\partial e_M}{\partial w_{M,2}} & \cdots & \frac{\partial e_M}{\partial w_{M,N}} \end{bmatrix} = \begin{bmatrix} 0 & 0 & \dots & 0 \\ 0 & 0 & \dots & 0 \\ \vdots & \vdots & \vdots & \vdots \\ 0 & 0 & \dots & 0 \end{bmatrix} \tag{A.7}$$

where e_j is the j^{th} element of the MSE vector $\mathbf{e}$:

$$\begin{aligned} e_j = \overline{\left|s_j - \mathbf{w}_j^{\mathrm{T}}\mathbf{r}\right|^2} = \overline{|s_j - (w_{j,1}r_1 + w_{j,2}r_2 + \ldots + w_{j,N}r_N)|^2} = \\ = \overline{\left(s_j^{RE} - \left(w_{j,1}^{RE}r_1^{RE} - w_{j,1}^{IM}r_1^{IM} + \kappa^{RE}\right)\right)^2} + \overline{\left(s_j^{RE} - \left(w_{j,1}^{RE}r_1^{IM} + w_{j,1}^{IM}r_1^{RE} + \kappa^{IM}\right)\right)^2} \end{aligned} \tag{A.8}$$

for instance, this gives for the first element of $\mathbf{e}$ the following expression:

$$\begin{aligned} \frac{\partial e_1}{\partial w_{j,1}} = \frac{\partial e_1}{\partial w_{j,1}^{RE}} + \frac{\partial e_1}{\partial w_{j,1}^{IM}} = \overline{2w_{j,1}\left|r_1\right|^2 + 2r_1^*\left(\kappa - s_j\right)} = \\ = \overline{2w_{j,1}\left|r_1\right|^2 + 2r_1^*\left(\mathbf{w}_j^{\mathrm{T}}\mathbf{r} - w_{j,1}r_1 - s_j\right)} = \overline{2r_1^*\mathbf{w}_j^{\mathrm{T}}\mathbf{r} - 2r_1^*s_j} = 0 \end{aligned} \tag{A.9}$$

where

$$\frac{\partial e_1}{\partial w_{j,1}^{RE}} = \overline{2w_{j,1}^{RE}\left|r_1\right|^2 + 2r_1^{RE}\left(\kappa^{RE} - s_j^{RE}\right) + 2r_1^{IM}\left(\kappa^{IM} - s_j^{IM}\right)} \tag{A.10}$$

$$\frac{\partial e_1}{\partial w_{j,1}^{IM}} = \overline{2w_{j,1}^{IM}\left|r_1\right|^2 + 2r_1^{RE}\left(\kappa^{IM} - s_j^{IM}\right) - 2r_1^{IM}\left(\kappa^{RE} - s_j^{RE}\right)} \tag{A.11}$$

Based on Equation A.9, we may write $\bigtriangledown \mathbf{e}_j$ as follows:

$$\bigtriangledown \mathbf{e}_j = \begin{bmatrix} \frac{\partial e_1}{\partial w_{1,1}} \\ \frac{\partial e_1}{\partial w_{1,2}} \\ \vdots \\ \frac{\partial e_1}{\partial w_{1,N}} \end{bmatrix} = 2\overline{\mathbf{r}^* \mathbf{w}_j^{\mathrm{T}} \mathbf{r}} - 2\overline{s_j \mathbf{r}^*} = 2\overline{\mathbf{r}^* \mathbf{r}^{\mathrm{T}}} \mathbf{w}_j - 2\overline{s_j \mathbf{r}^*} = \mathbf{0} \tag{A.12}$$

Then from Equation A.12, we get

$$\overline{\mathbf{r}^* \mathbf{r}^{\mathrm{T}}} \mathbf{w}_j = \overline{s_j \mathbf{r}^*} \tag{A.13}$$

where

$$\overline{s_j \mathbf{r}^*} = \overline{s_j \left(s_1^* \mathbf{H}_1^* + \ldots + s_N^* \mathbf{H}_N^* \right)} + \overline{s_j \sigma \mathbf{n}^*} = \overline{|s_j|^2} \mathbf{H}_j^* \tag{A.14}$$

$$\begin{aligned} \overline{\mathbf{r}^* \mathbf{r}^{\mathrm{T}}} &= \overline{\left(s_1^* \mathbf{H}_1^* + \ldots + s_N^* \mathbf{H}_N^* + \sigma \mathbf{n}^* \right) \left(s_1 \mathbf{H}_1^T + \ldots + s_N \mathbf{H}_N^T + \sigma \mathbf{n}^{\mathrm{T}} \right)} = \\ &= \sigma^2 \overline{\mathbf{n}^* \mathbf{n}^{\mathrm{T}}} + \sum_{i=1}^{N} \overline{|s_i|^2} \mathbf{H}_i^* \mathbf{H}_i^T = \sigma^2 \mathbf{I}_M + \sum_{i=1}^{N} \overline{|s_i|^2} \mathbf{H}_i^* \mathbf{H}_i^T \end{aligned} \tag{A.15}$$

where $\mathbf{I}_M$ is a $M \times M$ identity matrix.

Using Equations A.14 and A.15 in Equation A.13, we get how to obtain $\mathbf{w}_j$:

$$\mathbf{w}_j = \left(\overline{\mathbf{r}^* \mathbf{r}} \right)^{-1} \overline{s_j \mathbf{r}^*} = \overline{|s_j|^2} \left(\sigma^2 \mathbf{I}_M + \sum_{i=1}^{N} \overline{|s_i|^2} \mathbf{H}_i^* \mathbf{H}_i^T \right)^{-1} \mathbf{H}_j^* \tag{A.16}$$

Equation A.16 can be rewritten as:

$$\mathbf{w}_j = \left(\mathbf{\Sigma}^* + \mathbf{H}_j^* \mathbf{H}_j^{\mathrm{T}} \right)^{-1} \mathbf{H}_j^* \tag{A.17}$$

where $\mathbf{\Sigma}$ is defined as:

$$\mathbf{\Sigma} = \frac{\sigma^2}{\overline{|s_j|^2}} \mathbf{I}_M + \sum_{\substack{i=1 \\ i \neq j}}^{N} \frac{\overline{|s_i|^2}}{\overline{|s_j|^2}} \mathbf{H}_i \mathbf{H}_i^H \tag{A.18}$$

where $(\cdot)^{\mathbf{H}}$ is the complex conjugate transpose.

Then Equation A.8 is rewritten as:

$$
\begin{aligned}
e_j = \overline{\left|s_j - \mathbf{w}_j^{\mathrm{T}}\mathbf{r}\right|^2} = \overline{\left(s_j - \mathbf{w}_j^{\mathrm{T}}\mathbf{r}\right)\left(s_j - \mathbf{w}_j^{\mathrm{T}}\mathbf{r}\right)^*} = \\
= \overline{|s_j|^2} + \overline{\mathbf{w}_j^{\mathrm{T}}\mathbf{r}\mathbf{r}^{\mathrm{H}}\mathbf{w}_j^*} - \overline{s_j\mathbf{w}_j^{\mathrm{H}}\mathbf{r}^*} - \overline{s_j^*\mathbf{w}_j^{\mathrm{T}}\mathbf{r}} = \\
= \overline{|s_j|^2} + \mathbf{w}_j^{\mathrm{T}}\overline{\mathbf{r}\mathbf{r}^{\mathrm{H}}}\left(\overline{\mathbf{r}\mathbf{r}^{\mathrm{H}}}\right)^{-1}\overline{s_j^*\mathbf{r}} - \overline{s_j^*\mathbf{w}_j^{\mathrm{T}}\mathbf{r}} - \overline{s_j\mathbf{w}_j^{\mathrm{H}}\mathbf{r}^*} = \\
= \overline{|s_j|^2} - \overline{s_j\mathbf{w}_j^{\mathrm{H}}\mathbf{r}^*} = \overline{|s_j|^2} - \overline{s_j\mathbf{r}^{\mathrm{H}}}\mathbf{w}_j^* = \\
= \overline{|s_j|^2} - \overline{s_j\mathbf{r}^{\mathrm{H}}}\left(\overline{\mathbf{r}\mathbf{r}^{\mathrm{H}}}\right)^{-1}\overline{s_j^*\mathbf{r}} = \\
= \overline{|s_j|^2} - \overline{|s_j|^2}\mathbf{H}_j^H\left(\sigma^2\mathbf{I}_M + \sum_{i=1}^{N}\overline{|s_i|^2}\mathbf{H}_i\mathbf{H}_i^H\right)^{-1}\overline{|s_j|^2}\mathbf{H}_j = \\
= \overline{|s_j|^2}\left[1 - \mathbf{H}_j^H\left(\frac{\sigma^2}{\overline{|s_j|^2}}\mathbf{I}_M + \sum_{i=1}^{N}\frac{\overline{|s_i|^2}}{\overline{|s_j|^2}}\mathbf{H}_i\mathbf{H}_i^H\right)^{-1}\mathbf{H}_j\right] = \\
= \overline{|s_j|^2}\left[1 - \mathbf{H}_j^H\left(\mathbf{\Sigma} + \mathbf{H}_j\mathbf{H}_j^{\mathrm{H}}\right)^{-1}\mathbf{H}_j\right]
\end{aligned}
\tag{A.19}
$$

When we have an inverse of a matrix with the form $\mathbf{A}+\mathbf{BCD}$, we can apply the matrix inversion lemma which is given by $(\mathbf{A}+\mathbf{BCD})^{-1} = \mathbf{A}^{-1} - \mathbf{A}^{-1}\mathbf{B}\left(\mathbf{C}^{-1} + \mathbf{DA}^{-1}\mathbf{B}\right)\mathbf{DA}^{-1}$. Thus, we use the matrix inversion lemma in the matrix $\mathbf{\Sigma} + \mathbf{H}_j\mathbf{H}_j^{\mathrm{H}}$ as follows:

$$
\left(\mathbf{\Sigma} + \mathbf{H}_j\mathbf{H}_j^{\mathrm{H}}\right)^{-1}\mathbf{H}_j = \left[\mathbf{\Sigma}^{-1} - \mathbf{\Sigma}^{-1}\mathbf{H}_j\left[1 + \mathbf{H}_j^{\mathrm{H}}\mathbf{\Sigma}^{-1}\mathbf{H}_j\right]^{-1}\mathbf{H}_j^{\mathrm{H}}\mathbf{\Sigma}^{-1}\right]\mathbf{H}_j = \frac{\mathbf{\Sigma}^{-1}\mathbf{H}_j}{1 + \mathbf{H}_j^{\mathrm{H}}\mathbf{\Sigma}^{-1}\mathbf{H}_j} \tag{A.20}
$$

Thus, substituting Equation A.20 into Equation A.19 leads to

$$
e_j = \overline{|s_j|^2}\left[1 - \frac{\mathbf{H}_j^H\mathbf{\Sigma}^{-1}\mathbf{H}_j}{1 + \mathbf{H}_j^{\mathrm{H}}\mathbf{\Sigma}^{-1}\mathbf{H}_j}\right] = \frac{\overline{|s_j|^2}}{1 + \mathbf{H}_j^{\mathrm{H}}\mathbf{\Sigma}^{-1}\mathbf{H}_j} \tag{A.21}
$$

and substituting Equation A.20 into Equation A.17 leads to the following equations:

$$
\mathbf{w}_j^* = \frac{\mathbf{\Sigma}^{-1}\mathbf{H}_j}{1 + \mathbf{H}_j^{\mathrm{H}}\mathbf{\Sigma}^{-1}\mathbf{H}_j} \tag{A.22}
$$

$$
\mathbf{w}_j = \frac{\left(\mathbf{\Sigma}^*\right)^{-1}\mathbf{H}_j^*}{1 + \mathbf{H}_j^{\mathrm{H}}\mathbf{\Sigma}^{-1}\mathbf{H}_j} \tag{A.23}
$$

$$
\mathbf{w}_j^{\mathrm{T}} = \frac{\mathbf{H}_j^{\mathrm{H}}\left(\mathbf{\Sigma}^{\mathrm{H}}\right)^{-1}}{1 + \mathbf{H}_j^{\mathrm{H}}\mathbf{\Sigma}^{-1}\mathbf{H}_j} \tag{A.24}
$$

The post-equalization SNR on each of the spatial components of $\hat{\mathbf{s}}_k$, j, is defined as follows:

$$\mathbf{SNR}_j = \frac{\overline{\left|s_1 \mathbf{w}_j^{\mathrm{T}} \mathbf{H}_j\right|^2}}{\left|\left(\mathbf{r}^{\mathrm{T}} - s_1 \mathbf{H}_j^{\mathrm{T}}\right) \mathbf{w}_j\right|^2} = \frac{\overline{|s_1|^2}\left(\mathbf{w}_j^{\mathrm{T}} \mathbf{H}_j\right)\left(\mathbf{w}_j^{\mathrm{T}} \mathbf{H}_j\right)^*}{\mathbf{w}_j^{\mathrm{H}} \overline{\left(\mathbf{r}^* - s_j^* \mathbf{H}_j^*\right)\left(\mathbf{r}^{\mathrm{T}} - s_j \mathbf{H}_j^{\mathrm{T}}\right)} \mathbf{w}_j} = \\ = \frac{\mathbf{w}_j^{\mathrm{T}} \mathbf{H}_j \left(\mathbf{w}_j^{\mathrm{T}} \mathbf{H}_j\right)^*}{\mathbf{w}_j^{\mathrm{H}} \boldsymbol{\Sigma}^* \mathbf{w}_j} = \mathbf{H}_j^{\mathrm{H}} \left(\boldsymbol{\Sigma}^{\mathrm{H}}\right)^{-1} \mathbf{H}_j \tag{A.25}$$

where

$$\overline{\left(\mathbf{r}^* - s_j^* \mathbf{H}_j^*\right)\left(\mathbf{r}^{\mathrm{T}} - s_j \mathbf{H}_j^{\mathrm{T}}\right)} = \overline{\mathbf{r}^* \mathbf{r}^{\mathrm{T}}} + \overline{|s_j|^2} \mathbf{H}_j^* \mathbf{H}_j^{\mathrm{T}} - \overline{s_j^* \mathbf{H}_j^* \mathbf{r}^{\mathrm{T}}} - \overline{s_j \mathbf{r}^* \mathbf{H}_j^{\mathrm{T}}} = \\ = \sigma^2 \mathbf{I}_M + \sum_{i=1}^{N} |s_j|^2 \mathbf{H}_i^* \mathbf{H}_i^{\mathrm{T}} - |s_j|^2 \mathbf{H}_j^* \mathbf{H}_j^{\mathrm{T}} = \overline{|s_j|^2} \boldsymbol{\Sigma}^* \tag{A.26}$$

From Equations A.21 and A.25, the MSE and the post-equalization SNR of the spatial component j is given by the following Equations, respectively:

$$e_j = \frac{\overline{|s_j|^2}}{1 + \mathbf{SNR}_j} \tag{A.27}$$

$$\mathbf{SNR}_j = \frac{\overline{|s_j|^2}}{e_j} - 1 \tag{A.28}$$

In matrix notation, the received signal vector is given by:

$$\mathbf{r} = \mathbf{H}\mathbf{s} + \sigma \mathbf{n} \tag{A.29}$$

and $\boldsymbol{\Sigma}$ may be written as:

$$\boldsymbol{\Sigma} = \left(\overline{\mathbf{r}^* \mathbf{r}^{\mathrm{T}}} - \overline{|s_j|^2} \mathbf{H}_j^* \mathbf{H}_j^{\mathrm{T}}\right)^* \frac{1}{\overline{|s_j|^2}} = \frac{\overline{\mathbf{r}\mathbf{r}^{\mathrm{H}}}}{\overline{|s_j|^2}} - \mathbf{H}_j \mathbf{H}_j^{\mathrm{H}} = \frac{1}{\overline{|s_j|^2}} \overline{(\mathbf{H}\mathbf{s} + \sigma \mathbf{n})\left(\mathbf{H}^{\mathrm{H}} \mathbf{s}^{\mathrm{H}} + \sigma \mathbf{n}^{\mathrm{H}}\right)} - \mathbf{H}_j \mathbf{H}_j^{\mathrm{H}} = \\ = \frac{1}{\overline{|s_j|^2}} \left[\mathbf{H} \overline{\mathbf{s}\mathbf{s}^{\mathrm{H}}} \mathbf{H}^{\mathrm{H}} + \sigma^2 \overline{\mathbf{n}\mathbf{n}^{\mathrm{H}}}\right] - \mathbf{H}_j \mathbf{H}_j^{\mathrm{H}} = \frac{\mathbf{H}\mathbf{Q}_s \mathbf{H}^{\mathrm{H}}}{\overline{|s_j|^2}} + \frac{\sigma^2 \mathbf{I}_M}{\overline{|s_j|^2}} - \mathbf{H}_j \mathbf{H}_j^{\mathrm{H}} \tag{A.30}$$

where $\mathbf{Q}_s = \overline{\mathbf{s}\mathbf{s}^{\mathrm{H}}}$.

The hermitian matrix of the MMSE filter matrix $\mathbf{W}$ is given by

$$\mathbf{W}^{\mathrm{H}} = \begin{bmatrix} \mathbf{w}_1^* & \mathbf{w}_2^* & \dots & \mathbf{w}_N^* \end{bmatrix} = \left[\sigma^2 \mathbf{I}_M + \mathbf{H}\mathbf{Q}_s \mathbf{H}^{\mathrm{H}}\right]^{-1} \begin{bmatrix} \overline{|s_1|^2} \mathbf{H}_1 & \overline{|s_2|^2} \mathbf{H}_2 & \dots & \overline{|s_N|^2} \mathbf{H}_N \end{bmatrix} = \\ = \left[\sigma^2 \mathbf{I}_M + \mathbf{H}\mathbf{Q}_s \mathbf{H}^{\mathrm{H}}\right]^{-1} \mathbf{H}\mathbf{Q}_s \tag{A.31}$$

where from Equation A.17 $\mathbf{w}^*$ is defined as follows:

$$\mathbf{w}^* = \left[\boldsymbol{\Sigma} + \mathbf{H}_j \mathbf{H}_j^{\mathrm{H}}\right]^{-1} \mathbf{H}_j = \overline{|s_j|^2} \left[\sigma^2 \mathbf{I}_M + \mathbf{H}\mathbf{Q}_s \mathbf{H}^{\mathrm{H}}\right]^{-1} \mathbf{H}_j \tag{A.32}$$

Thus, $\mathbf{W}$ is written as follows:

$$\mathbf{W} = \begin{bmatrix} \mathbf{w}_1^* & \mathbf{w}_2^* & \dots & \mathbf{w}_N^* \end{bmatrix} = \mathbf{Q}_s \mathbf{H}^{\mathrm{H}} \left[\sigma^2 \mathbf{I}_M + \mathbf{H} \mathbf{Q}_s \mathbf{H}^{\mathrm{H}} \right]^{-1} \tag{A.33}$$

The MMSE estimates of the transmitted symbol vector is given by:

$$\hat{\mathbf{s}} = \mathbf{W}\mathbf{r} = \mathbf{W}\mathbf{H}\mathbf{s} + \sigma \mathbf{W}\mathbf{n} \tag{A.34}$$

Applying the matrix inversion lemma to the matrix $\sigma^2 \mathbf{I}_M + \mathbf{H}\mathbf{Q}_s\mathbf{H}^{\mathrm{H}}$ leads to

$$\left[\sigma^2 \mathbf{I}_M + \mathbf{H} \mathbf{Q}_s \mathbf{H}^{\mathrm{H}} \right]^{-1} = \frac{1}{\sigma^2} \left[\mathbf{I}_M - \mathbf{H} \left[\sigma^2 \mathbf{Q}_s^{-1} + \mathbf{H}^{\mathrm{H}} \mathbf{H} \right]^{-1} \mathbf{H}^{\mathrm{H}} \right] \tag{A.35}$$

Using Equations A.36 and A.35 in Equation A.34, we get

$$\begin{aligned} \mathbf{W} &= \frac{1}{\sigma^2} \left(\mathbf{Q}_s \mathbf{H}^{\mathrm{H}} - \mathbf{Q}_s \mathbf{H}^{\mathrm{H}} \mathbf{H} \left(\sigma^2 \mathbf{Q}_s^{-1} + \mathbf{H}^{\mathrm{H}} \mathbf{H} \right)^{-1} \mathbf{H}^{\mathrm{H}} \right) = \\ &= \frac{1}{\sigma^2} \mathbf{Q}_s \left(\sigma^2 \mathbf{Q}_s^{-1} + \mathbf{H}^{\mathrm{H}} \mathbf{H} - \mathbf{H}^{\mathrm{H}} \mathbf{H} \right) \left(\sigma^2 \mathbf{Q}_s^{-1} + \mathbf{H}^{\mathrm{H}} \mathbf{H} \right)^{-1} \mathbf{H}^{\mathrm{H}} = \left(\sigma^2 \mathbf{Q}_s^{-1} + \mathbf{H}^{\mathrm{H}} \mathbf{H} \right)^{-1} \mathbf{H}^{\mathrm{H}} \end{aligned} \tag{A.36}$$

Thus, the MMSE estimates of the transmitted symbol vector from Equation A.34 are given by

$$\hat{\mathbf{s}} = \mathbf{W}\mathbf{r} = \left(\sigma^2 \mathbf{Q}_s^{-1} + \mathbf{H}^{\mathrm{H}} \mathbf{H} \right)^{-1} \mathbf{H}^{\mathrm{H}} \mathbf{r} = \left(\sigma^2 \mathbf{Q}_s^{-1} + \mathbf{H}^{\mathrm{H}} \mathbf{H} \right)^{-1} \mathbf{H}^{\mathrm{H}} \mathbf{H}\mathbf{s} + \sigma \left(\sigma^2 \mathbf{Q}_s^{-1} + \mathbf{H}^{\mathrm{H}} \mathbf{H} \right)^{-1} \mathbf{H}^{\mathrm{H}} \mathbf{n} \tag{A.37}$$

Since we consider the all the symbols are transmitted with the same power σ_s^2, this gives

$$\mathbf{W} = \left(\frac{\sigma^2}{\overline{|s_j|^2}} \mathbf{I}_N + \mathbf{H}^{\mathrm{H}} \mathbf{H} \right)^{-1} \mathbf{H}^{\mathrm{H}} = \left(\frac{\sigma^2}{\sigma_s^2} \mathbf{I}_N + \mathbf{H}^{\mathrm{H}} \mathbf{H} \right)^{-1} \mathbf{H}^{\mathrm{H}} = \left(\alpha \mathbf{I}_N + \mathbf{H}^{\mathrm{H}} \mathbf{H} \right)^{-1} \mathbf{H}^{\mathrm{H}} \tag{A.38}$$

The MMSE matrix can also be calculated from the following extended channel matrix:

$$\mathbf{Z} = \begin{bmatrix} \mathbf{H} \\ \sqrt{\alpha} \mathbf{I}_N \end{bmatrix} \tag{A.39}$$

where $\alpha = \frac{\sigma^2}{\sigma_s^2}$. This gives

$$\hat{\mathbf{s}} = \mathbf{W}\mathbf{r} = \left[\alpha \mathbf{I}_N + \mathbf{H}^{\mathrm{H}} \mathbf{H} \right]^{-1} \mathbf{H}^{\mathrm{H}} \mathbf{r} = \left[\alpha \mathbf{I}_N + \mathbf{H}^{\mathrm{H}} \mathbf{H} \right]^{-1} \begin{bmatrix} \mathbf{H}^{\mathrm{H}} & \sqrt{\alpha} \mathbf{I}_N \end{bmatrix} \begin{bmatrix} \mathbf{r} \\ \mathbf{0} \end{bmatrix} = \left(\mathbf{Z}^H \mathbf{Z} \right)^{-1} \mathbf{Z}^{\mathrm{H}} \mathbf{y} \tag{A.40}$$

where $\mathbf{y} = \begin{bmatrix} \mathbf{r} \\ \mathbf{0} \end{bmatrix}$ and $\mathbf{Z}^{\mathrm{H}}\mathbf{Z}$ is given by

$$\mathbf{Z}^{\mathrm{H}} \mathbf{Z} = \begin{bmatrix} \mathbf{H}^{\mathrm{H}} & \sqrt{\alpha} \mathbf{I}_N \end{bmatrix} \begin{bmatrix} \mathbf{H} \\ \sqrt{\alpha} \mathbf{I}_N \end{bmatrix} = \mathbf{H}^{\mathrm{H}} \mathbf{H} + \alpha \mathbf{I}_N \tag{A.41}$$

In this way ZF processing ($\hat{\mathbf{s}} = \left(\mathbf{Z}^H\mathbf{Z}\right)^{-1}\mathbf{Z}^{\mathrm{H}}\mathbf{y}$) can be applied in order to find the MMSE estimates of the transmitted symbol vector. Thus, the MSE and the post-equalization SNR of the spatial component j are given by the following Equations, respectively:

$$e_j = \sigma^2(\mathbf{Z}^{\mathrm{H}}\mathbf{Z})^{-1}_{j,j} \tag{A.42}$$

where $(\cdot)_{j,j}$ denotes the entry in the j^{th} row and the j^{th} column of a matrix.

$$\mathrm{SNR}_j = \frac{\overline{|s_j|^2}}{e_j} - 1 = \frac{\sigma_s^2}{e_j} - 1 \tag{A.43}$$

The covariance matrix of the estimation error $\mathbf{s} - \hat{\mathbf{s}}$ for MMSE can be shown to be

$$\begin{aligned}
\mathbf{Q}_e = \overline{(\mathbf{s}-\hat{\mathbf{s}})(\mathbf{s}-\hat{\mathbf{s}})^{\mathrm{H}}} &= \overline{(\mathbf{s}-\mathbf{W}(\mathbf{H}\mathbf{s}+\sigma\mathbf{n}))(\mathbf{s}-\mathbf{W}(\mathbf{H}\mathbf{s}+\sigma\mathbf{n}))^{\mathrm{H}}} = \\
&= \overline{((\mathbf{I}_N-\mathbf{W}\mathbf{H})\mathbf{s}-\sigma\mathbf{W}\mathbf{n}))((\mathbf{I}_N-\mathbf{W}\mathbf{H})\mathbf{s}-\sigma\mathbf{W}\mathbf{n}))^{\mathrm{H}}} = \\
&= (\mathbf{I}_N-\mathbf{W}\mathbf{H})\,\overline{\mathbf{s}\mathbf{s}^H}\left(\mathbf{I}_N-\mathbf{H}^{\mathrm{H}}\mathbf{W}^{\mathrm{H}}\right) + \sigma^2\mathbf{W}\overline{\mathbf{n}\mathbf{n}^{\mathrm{H}}}\mathbf{W}^{\mathrm{H}} = \\
&= (\mathbf{I}_N-\mathbf{W}\mathbf{H})\left(\mathbf{Q}_s-\mathbf{H}^{\mathrm{H}}\mathbf{W}^{\mathrm{H}}\right) + \sigma^2\mathbf{W}\mathbf{W}^{\mathrm{H}} = \\
= \mathbf{Q}_s - \mathbf{Q}_s\mathbf{H}^{\mathrm{H}}\mathbf{W}^{\mathrm{H}} - \mathbf{W}\mathbf{H}\mathbf{Q}_s + \mathbf{W}\mathbf{H}\mathbf{Q}_s\mathbf{H}^{\mathrm{H}}\mathbf{W}^{\mathrm{H}} + \sigma^2\mathbf{W}\mathbf{W}^{\mathrm{H}} &= \\
&= \sigma^2\left(\sigma^2\mathbf{Q}_s^{-1}+\mathbf{H}^{\mathrm{H}}\mathbf{H}\right)^{-1} = \\
&= \sigma^2\left(\frac{\sigma^2}{\sigma_s^2}\mathbf{I}_N+\mathbf{H}^{\mathrm{H}}\mathbf{H}\right)^{-1}
\end{aligned} \tag{A.44}$$

where $\mathbf{W} = \left(\sigma^2\mathbf{Q}_s^{-1}+\mathbf{H}^{\mathrm{H}}\mathbf{H}\right)^{-1}\mathbf{H}^{\mathrm{H}}$ and $\mathbf{Q}_s = \sigma^2\mathbf{I}_N$. Thus, the MSE and the post-equalization SNR of the spatial component j are rewritten as follows:

$$e_j = \overline{|s_j - \hat{s}_j|^2} = \sigma^2\left(\frac{\sigma^2}{\sigma_s^2}\mathbf{I}_N+\mathbf{H}^{\mathrm{H}}\mathbf{H}\right)^{-1}_{j,j} \tag{A.45}$$

$$\mathrm{SNR}_j = \frac{\sigma_s^2}{\sigma^2\left(\frac{\sigma^2}{\sigma_s^2}\mathbf{I}_N+\mathbf{H}^{\mathrm{H}}\mathbf{H}\right)^{-1}_{j,j}} - 1 \tag{A.46}$$

A.2 1D-LMMSE channel estimator by Wiener filtering

This appendix provides the detailed formulation of the 1D-LMMSE estimator by applying Wiener filtering in the frequency domain. This channel estimator is used in the practical channel estimation algorithm presented in section 4.6 for LTE/LTE-Advanced DL. The 1D-LMMSE channel estimator is presented in [85, 86, 87] as well as low complexity channel estimators based on 1D-LMMSE are presented in [88, 92, 99].

The expression of the 1D-LMMSE estimator in the frequency domain is given in Equation 4.9 as follows:

$$\hat{\mathbf{H}}_{\mathrm{W}} = \mathbf{R}_{\mathrm{h}} \left[\mathbf{R}_{\mathrm{H}} + \frac{\sigma^2}{B} \mathbf{I}_{N_p} \right]^{-1} \cdot \hat{\mathbf{H}}_{LS} = \hat{\mathbf{R}}_{\mathrm{W}} \cdot \hat{\mathbf{H}}_{LS} \tag{A.47}$$

where $\hat{\mathbf{H}}_{LS}$ is the $(N_p \times 1)$ LS channel estimation vector; $\hat{\mathbf{H}}_{\mathrm{W}}$ is the Wiener filtered channel estimation vector; $\mathbf{R}_{\mathrm{h}} = \overline{\mathbf{h}\mathbf{H}^{\mathrm{H}}}$ is the $(12N_{RB} \times N_p)$ correlation matrix of the $(12N_{RB} \times 1)$ full channel response vector $\mathbf{h}$ with $\mathbf{H}$; $\mathbf{H}$ being the $(N_p \times 1)$ complex vector that contains the channel frequency response at the pilot subcarriers; $\mathbf{R}_{\mathrm{H}} = \overline{\mathbf{H}\mathbf{H}^{\mathrm{H}}}$ is the $(N_p \times N_p)$ covariance matrix of the channel with all the diagonal elements of $\mathbf{R}_{\mathrm{H}}$ equal to the average channel gain G; B is the power of the pilot symbol; σ^2 is the variance of the complex Gaussian noise at the pilot subcarriers and $\gamma = G \cdot B/\sigma^2$ is the mean SNR of the received pilots.

We consider a multipath propagation channel based on the GWSSUS model and the impulse response of the channel is treated as a time-limited pulse train with L channel paths or taps:

$$h(t) = \sum_{l=1}^{L} \alpha_l \delta(t - \tau_l) \tag{A.48}$$

where α_l is the complex coefficient and τ_l is the excess tap delay of each of the L propagation paths of the channel in time domain. Then, the channel frequency response is the Fourier transform of the impulse response which is defined as:

$$H(f) = \sum_{l=1}^{L} \alpha_l e^{-j2\pi f \tau_l} \tag{A.49}$$

and the channel frequency response at subcarrier i is:

$$H_i = H(f_i) = H(i \cdot \Delta f) = \sum_{l=1}^{L} \alpha_l e^{-j2\pi \Delta f \tau_l i} \tag{A.50}$$

where Δf is the subcarrier spacing.

The $(N_p \times N_p)$ covariance matrix of the channel $\mathbf{R}_{\mathrm{H}}$ at the pilot subcarriers is defined as:

$$\mathbf{R}_{\mathrm{H}} = E\left\{\mathbf{H}\mathbf{H}^{\mathrm{H}}\right\} = \overline{\mathbf{H}\mathbf{H}^{\mathrm{H}}} = \begin{bmatrix} \overline{H_{i_1} \cdot H_{i_1}^*} & \cdots & \overline{H_{i_1} \cdot H_{i_{N_p}}^*} \\ \vdots & \ddots & \vdots \\ \overline{H_{i_{N_p}} \cdot H_{i_1}^*} & \cdots & \overline{H_{i_{N_p}} \cdot H_{i_{N_p}}^*} \end{bmatrix}_{(N_p \times N_p)} \tag{A.51}$$

and the $(12N_{RB} \times N_p)$ correlation matrix of the full channel response vector $\mathbf{h}$ with $\mathbf{H}$ is defined as:

$$\mathbf{R}_{\mathrm{h}} = E\left\{\mathbf{h}\mathbf{H}^{\mathrm{H}}\right\} = \overline{\mathbf{h}\mathbf{H}^{\mathrm{H}}} = \begin{bmatrix} \overline{H_0 \cdot H_{i_1}^*} & \cdots & \overline{H_0 \cdot H_{i_{N_p}}^*} \\ \vdots & \ddots & \vdots \\ \overline{(H_{(12N_{RB}-1)} \cdot H_{i_1}^*} & \cdots & \overline{H_{(12N_{RB}-1)} \cdot H_{i_{N_p}}^*} \end{bmatrix}_{(12N_{RB} \times N_p)} \tag{A.52}$$

where $E\{x\}$ and $\overline{x}$ denote the operator of expectation of x, N_{RB} is the number of allocated *Physical Resource Block*s (PRBs), $N_p = 2N_{RB}$ and i_p is the subcarrier index of the pilot location p. Since expectation is linear operator, the only random variable is the channel amplitude α_l and channel taps are independent $E\{\alpha_l \cdot \alpha_q\} = 0$ for $l \neq q$, [87], the frequency correlation function of the channel between the subcarrier i and k is defined as:

$$R_H(i,k) = \overline{H_i \cdot H_k^*} = \sum_{l=1}^{L} \overline{|\alpha_l|^2} e^{-j2\pi(i-k)\tau_l \Delta f} \tag{A.53}$$

Assuming the 3GPP standardized channel models, the values of $\overline{|\alpha_l|^2}$ and τ_l are shown in Table A.1 for EPA, EVA and ETU and the PDPs of these channel models are depicted in Figure A.1.

Table A.1: Delay profiles for E-UTRA channel models

	EPA model		**EVA model**		**ETU model**	
tap l	**Excess tap delay [ns]** τ_l	**Relative power [dB]** $\overline{\lvert\alpha_l\rvert^2}$	**Excess tap delay [ns]** τ_l	**Relative power [dB]** $\overline{\lvert\alpha_l\rvert^2}$	**Excess tap delay [ns]** τ_l	**Relative power [dB]** $\overline{\lvert\alpha_l\rvert^2}$
1	0	0.0	0	0.0	0	-1.0
2	30	-1.0	30	-1.5	50	-1.0
3	70	-2.0	150	-1.4	120	-1.0
4	90	-3.0	310	-3.6	200	0.0
5	110	-8.0	370	-0.6	230	0.0
6	190	-17.2	710	-9.1	500	0.0
7	410	-20.8	1090	-7.0	1600	-3.0
8			1730	-12.0	2300	-5.0
9			2510	-16.9	5000	-7.0

Since pilot transmissions from different antennas are orthogonal, we consider a SISO-OFDM system model. Equation 4.2 gives the vector expression of the received OFDM pilot vector, at one of the receiver antennas, as $\mathbf{Y} = \mathbf{C} \cdot \mathbf{H} + \mathbf{n}$. Then, at each pilot subcarrier k, the received complex symbol is given by:

$$Y_k = C_k H_k + N_k \tag{A.54}$$

where C_k is the transmitted complex pilot symbol, H_k is the actual complex coefficient of the channel frequency response and N_k is the *iid* complex, zero-mean, Gaussian noise with variance σ^2.

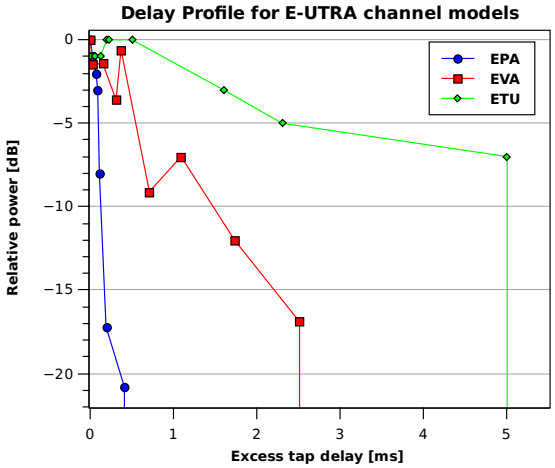

Figure A.1: Delay profiles for E-UTRA channel models

The baseline channel estimation is the LS estimate which is obtained by dividing Y_k by the known pilot C_k at pilot subcarrier k:

$$\hat{H}_k = \frac{Y_k}{C_k} = H_k + \frac{N_k}{C_k} = H_k + N'_k \tag{A.55}$$

Notice that in the case of the LS estimator, the remaining channel coefficients at the data subcarriers have to be obtained by interpolation.

We consider the Wiener filter in order to reduce the LS estimation error by exploiting the correlation of the channel in the frequency domain, [84]. The Wiener filter is a LMMSE estimator which tries to minimize the MSE between the actual and the estimated channel, so the LMMSE estimate of the channel coefficient H_k at subcarrier k taking into account the LS estimates of the channel at pilot subcarrier locations p is defined as:

$$\hat{H}_{\mathrm{w},k} \triangleq \sum_{p=0}^{N_p-1} w_{i_p,k} \hat{H}_{i_p} \tag{A.56}$$

We can rewrite Equation A.56 in terms of a product of vectors:

$$\hat{\mathbf{H}}_{\mathrm{w},k} = \mathbf{w}_k^{\mathrm{T}} \cdot \hat{\mathbf{H}}_{LS} = \mathbf{w}_k^{\mathrm{T}} \cdot \hat{\mathbf{H}} \tag{A.57}$$

where

$$\hat{\mathbf{H}}_{LS} = \hat{\mathbf{H}} = \begin{bmatrix} \hat{H}_{i_1} \\ \vdots \\ \hat{H}_{i_p} \\ \vdots \\ \hat{H}_{i_{N_p}} \end{bmatrix} \quad , \quad \mathbf{w}_k = \begin{bmatrix} w_{i_1,k} \\ \vdots \\ w_{i_p,k} \\ \vdots \\ w_{i_{N_p},k} \end{bmatrix} \tag{A.58}$$

where $(\mathbf{w}_k)^{\mathrm{T}}$ denotes the transpose of the vector $\mathbf{w}_k$.

In order to find the Wiener filter coefficients $w_{i_p,k}$, the MSE defined as

$$\varepsilon \triangleq \overline{\left|H_k - \hat{H}_{w,k}\right|^2} = \overline{\left|H_k - \mathbf{w}_k^{\mathrm{T}} \cdot \hat{\mathbf{H}}_{LS}\right|^2} \tag{A.59}$$

has to be minimized and, according to the MMSE proof, minimizing the MSE over $\mathbf{w}_k$, $\min_{\mathbf{w}_k}(\varepsilon)$, leads to differentiate ε with respect to each component of $\mathbf{w}_k$ and the minimum is found when $\mathbf{w}_k$ satisfies the next equation:

$$\bigtriangledown \varepsilon = \begin{bmatrix} \frac{\partial \varepsilon}{\partial w_{i_1,k}} \\ \frac{\partial \varepsilon}{\partial w_{i_2,k}} \\ \vdots \\ \frac{\partial \varepsilon}{\partial w_{i_{N_p},k}} \end{bmatrix} = 2\overline{\hat{\mathbf{H}}^* \mathbf{w}_k^{\mathrm{T}} \hat{\mathbf{H}}} - 2\overline{\hat{\mathbf{H}}^* H_k} = \overline{\hat{\mathbf{H}}^* \hat{\mathbf{H}}^{\mathrm{T}}} \mathbf{w}_k - \overline{H_k \hat{\mathbf{H}}^*} = \begin{bmatrix} 0 \\ 0 \\ \vdots \\ 0 \end{bmatrix} \tag{A.60}$$

so we get

$$\mathbf{w}_k = \left(\overline{\hat{\mathbf{H}}^* \hat{\mathbf{H}}^{\mathrm{T}}}\right)^{-1} \cdot \left(\overline{H_k \hat{\mathbf{H}}^*}\right) \tag{A.61}$$

and conjugating $\mathbf{w}_k^*$, we get

$$\mathbf{w}_k^* = \left(\overline{\hat{\mathbf{H}} \hat{\mathbf{H}}^{\mathrm{H}}}\right)^{-1} \cdot \left(\overline{H_k^* \hat{\mathbf{H}}}\right) \tag{A.62}$$

From Equation A.55, Equation A.57 can be rewritten as:

$$\hat{\mathbf{H}}_{\mathrm{w},k} = \mathbf{w}_k^{\mathrm{T}} \cdot \hat{\mathbf{H}} = (\mathbf{w}_k^*)^{\mathrm{H}} \cdot \hat{\mathbf{H}} = \left[\left(\overline{\hat{\mathbf{H}} \hat{\mathbf{H}}^{\mathrm{H}}}\right)^{-1} \cdot \left(\overline{H_k^* \hat{\mathbf{H}}}\right)\right]^{\mathrm{H}} \cdot \hat{\mathbf{H}} = \overline{H_k \hat{\mathbf{H}}^{\mathrm{H}}} \cdot \left(\overline{\hat{\mathbf{H}} \hat{\mathbf{H}}^{\mathrm{H}}}\right)^{-1} \cdot \hat{\mathbf{H}} \tag{A.63}$$

then, introducing matrix formulation, the LMMSE channel estimate of the full bandwidth can be written as:

$$\hat{\mathbf{H}}_{\mathrm{w}} = \begin{bmatrix} \hat{H}_{\mathrm{w},0} \\ \vdots \\ \hat{H}_{\mathrm{w},k} \\ \vdots \\ \hat{H}_{\mathrm{w},12N_{RB}-1} \end{bmatrix} = \overline{\mathbf{h} \hat{\mathbf{H}}^{\mathrm{H}}} \cdot \left(\overline{\hat{\mathbf{H}} \hat{\mathbf{H}}^{\mathrm{H}}}\right)^{-1} \cdot \hat{\mathbf{H}} \tag{A.64}$$

where $\mathbf{h}$ is the $(12N_{RB} \times 1)$ full channel response vector:

$$\mathbf{h} = \begin{bmatrix} H_0 \\ \vdots \\ H_k \\ \vdots \\ H_{12N_{RB}-1} \end{bmatrix} \tag{A.65}$$

From Equation A.54, Equation A.58 can be rewritten as:

$$\hat{\mathbf{H}}_{LS} = \hat{\mathbf{H}} = \mathbf{H} + \begin{pmatrix} C_{i_1} & 0 & \dots & 0 \\ 0 & C_{i_2} & \dots & 0 \\ \vdots & \vdots & \dots & 0 \\ 0 & 0 & \dots & C_{i_{N_p}} \end{pmatrix}^{-1} \begin{pmatrix} N_{i_1} \\ N_{i_2} \\ \vdots \\ N_{i_{N_p}} \end{pmatrix} = \mathbf{H} + \mathbf{C}^{-1}\mathbf{n} = \mathbf{H} + \mathbf{N}' \tag{A.66}$$

By substituting $\hat{\mathbf{H}}$ by Equation A.66 in Equation A.64, $\hat{\mathbf{H}}_{\mathrm{w}}$ can be rewritten in matrix formulation as:

$$\hat{\mathbf{H}}_{\mathrm{w}} = \overline{\mathbf{h}\mathbf{H}^{\mathrm{H}}} \cdot \left(\overline{\mathbf{H}\mathbf{H}^{\mathrm{H}}} + \sigma^2 \left(\mathbf{C}\mathbf{C}^{\mathrm{H}} \right)^{-1} \right)^{-1} \cdot \hat{\mathbf{H}} \tag{A.67}$$

since the elements of the noise vector $\mathbf{N}'$ are independent of each other and are also independent of the elements of the channel coefficients H_k, i.e., $\overline{N_i' N_j'} = 0$ when $i \neq j$ and $\overline{\mathbf{h}\mathbf{N}'} = 0$, $\overline{H_k N_i'} = 0$; then

$$\overline{\mathbf{h}\hat{\mathbf{H}}^{\mathrm{H}}} = \overline{\mathbf{h}\left(\mathbf{H} + \mathbf{N}'\right)^{\mathrm{H}}} = \overline{\mathbf{h}\mathbf{H}^{\mathrm{H}}} = \mathbf{R}_{\mathrm{h}} \tag{A.68}$$

$$\begin{aligned} \overline{\hat{\mathbf{H}}\hat{\mathbf{H}}^{\mathrm{H}}} = \overline{\left(\mathbf{H} + \mathbf{C^{-1}n}\right)\left(\mathbf{H} + \mathbf{C^{-1}n}\right)^{\mathrm{H}}} = \overline{\mathbf{H}\mathbf{H}^{\mathrm{H}}} + \mathbf{C}^{-1}\overline{\mathbf{n}\mathbf{n}^{\mathrm{H}}} \left(\mathbf{C}^{\mathrm{H}}\right)^{-1} = \\ = \overline{\mathbf{H}\mathbf{H}^{\mathrm{H}}} + \sigma^2 \mathbf{I}_{N_p} \left(\mathbf{C}\mathbf{C}^{\mathrm{H}}\right)^{-1} = \mathbf{R}_{\mathrm{H}} + \frac{\sigma^2}{B}\mathbf{I}_{N_p} \end{aligned} \tag{A.69}$$

where

$$\begin{aligned} \left(\mathbf{C}\mathbf{C}^{\mathrm{H}}\right)^{-1} = \left[\begin{pmatrix} C_{i_1} & 0 & \dots & 0 \\ 0 & C_{i_2} & \dots & 0 \\ \vdots & \vdots & \dots & 0 \\ 0 & 0 & \dots & C_{i_{N_p}} \end{pmatrix} \begin{pmatrix} C_{i_1}^* & 0 & \dots & 0 \\ 0 & C_{i_2}^* & \dots & 0 \\ \vdots & \vdots & \dots & 0 \\ 0 & 0 & \dots & C_{i_{N_p}}^* \end{pmatrix} \right]^{-1} = \\ = \begin{pmatrix} \frac{1}{\left|C_{i_1}\right|^2} & 0 & \dots & 0 \\ 0 & \frac{1}{\left|C_{i_2}\right|^2} & \dots & 0 \\ \vdots & \vdots & \dots & 0 \\ 0 & 0 & \dots & \frac{1}{\left|C_{i_{N_p}}\right|^2} \end{pmatrix} = \frac{1}{B}\mathbf{I}_{N_p} \end{aligned} \tag{A.70}$$

and the LMMSE channel estimate vector $\hat{\mathbf{H}}_{\mathrm{w}}$ given by Equation A.67 can be rewritten as

$$\hat{\mathbf{H}}_{\mathrm{w}} = \mathbf{R}_{\mathrm{h}} \left[\mathbf{R}_{\mathrm{H}} + \frac{\sigma^2}{B}\mathbf{I}_{N_p} \right]^{-1} \cdot \hat{\mathbf{H}} \tag{A.71}$$

which proves Equation A.47.

Figures A.2, A.3 and A.4 show snapshots of the channel estimation performance in frequency domain at a given time t and SNR= 15 dB for the channel estimation procedure described in section 4.6 taking into account the proposed optimum channel estimators which considers Wiener filtering vs. using LS and linear interpolation in the frequency domain. In Figures A.2, A.3 and A.4, the figures on the left hand side show snapshots of the channel estimation performance for the optimum channel estimators proposed in section 4.7.4 which are rewritten below:

- LS+S9T+LT+WF(36) for EPA5
- LS+S3T+LT+WF(36) for EVA70
- LS+LT+WF(36) for ETU300

and the figures on the right hand side show snapshots of the channel estimation performance using only LS estimates and linear interpolation (labelled as LF) in frequency domain, i.e. the following channel estimation algorithm combinations are considered:

- LS+S9T+LT+LF for EPA5
- LS+S3T+LT+LF for EVA70
- LS+LT+LF for ETU300

Notice that, only looking at the $|H(t,k)|^2\,(dB)$ snapshots shown in Figures A.2, A.3 and A.4, Wiener filtering outperforms LF method for all cases shown in these figures.

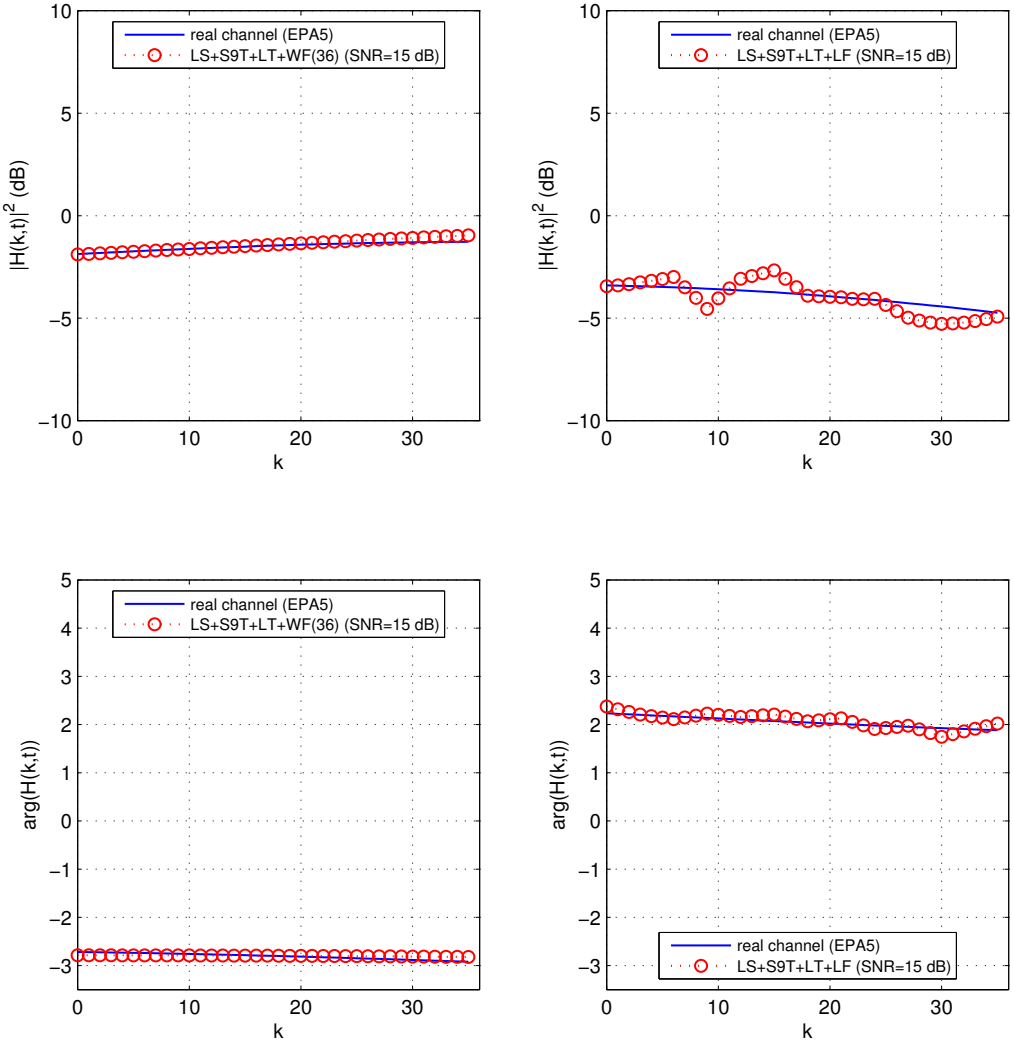

Figure A.2: Channel estimation performance snapshots of $|H(t,k)|^2\ (dB)$ and $\arg(H(l,k)$ for EPA5 in frequency domain at a given time t and SNR= 15 dB

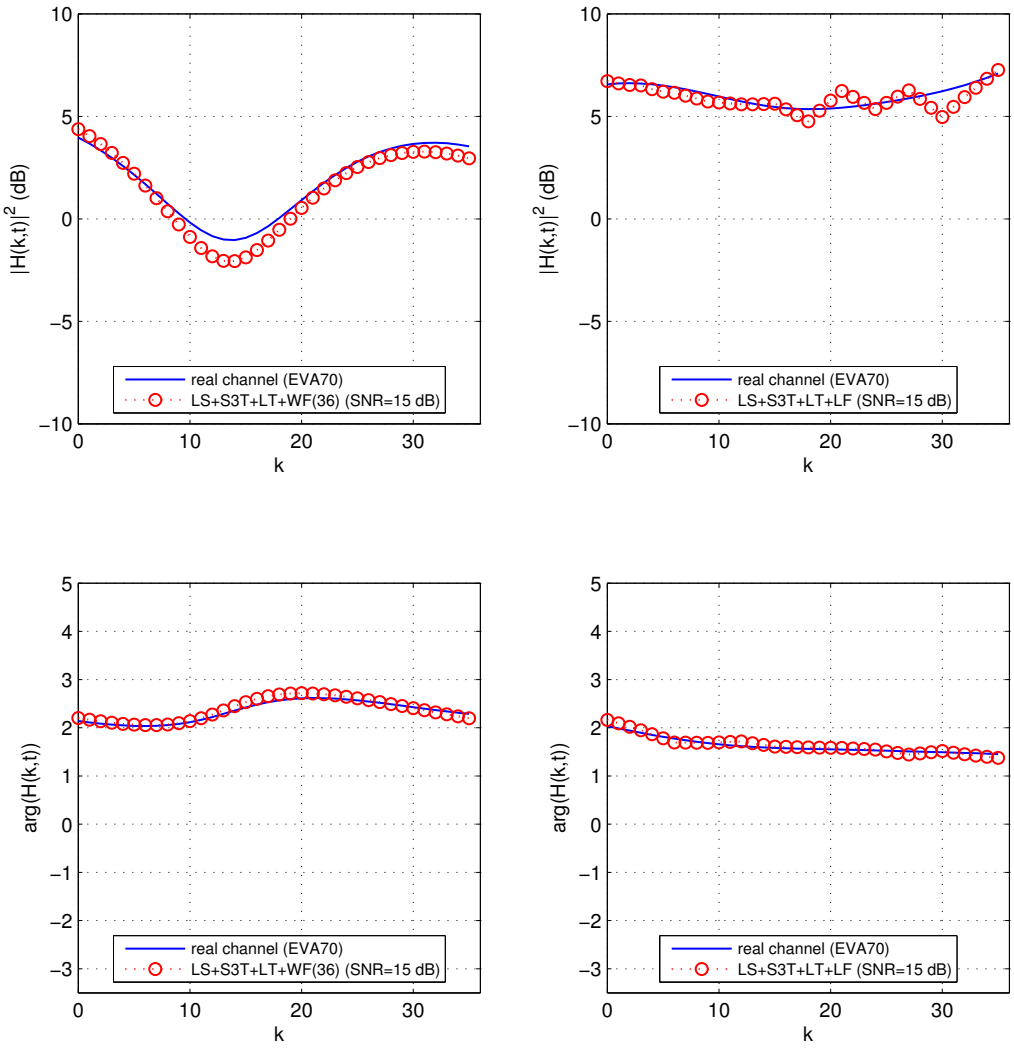

Figure A.3: Channel estimation performance snapshots of $|H(t,k)|^2\,(dB)$ and $\arg(H(l,k)$ for EVA70 in frequency domain (where k is the index in frequency domain and l is the index in time domain) and SNR= 15 dB

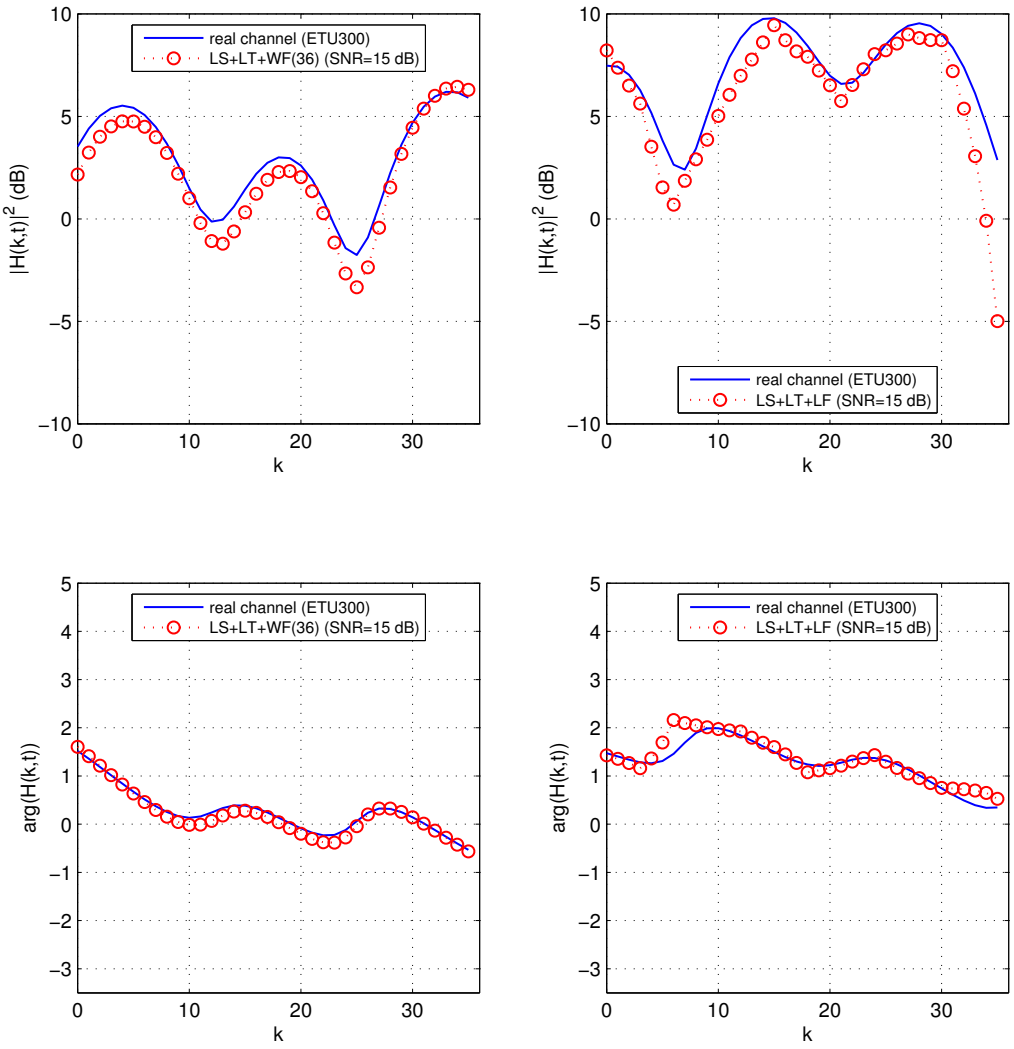

Figure A.4: Channel estimation performance snapshots of $|H(t,k)|^2\,(dB)$ and $\arg(H(l,k)$ for ETU300 in frequency domain (where k is the index in frequency domain and l is the index in time domain) and SNR= 15 dB

Appendix B

EESNR formulation from Union Bound

B.1 Union Bound and EESNR

We want to transmit $k = 2$ bits of information and we chose $2^2 = 4$ different waveforms of a set of eight possible waveforms formed each one by the possible binary combinations of three symbols: x, y, z $\in \{\pm 1\}$ that are BPSK modulated. These combinations can be viewed as the vertices of a cube. Since we have to choose one subset of 4 combinations, we select those that are more distant; for instance, the combination depicted with a red square in Figure B.1.

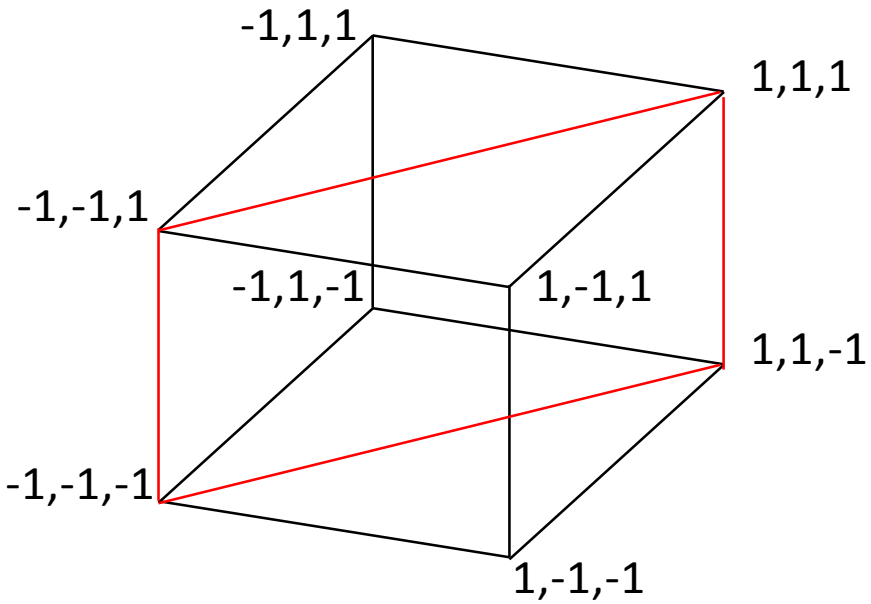

Figure B.1: Possible combinations of 3 binary symbols

We consider ML detector and BPSK with noise power $\sigma^2 = \overline{n_x^2} = \sigma^2 = \overline{n_y^2} = \sigma^2 = \overline{n_z^2}$ and $SNR_x = \gamma_x = E_x/(2\sigma^2)$, if we convey the waveform $\mathrm{x}_1, \mathrm{y}_1, z_1$, then the output of the 4 correlators of an optimum receiver is given by:

$$C_1 = \left(\sqrt{E_x}x_1 + n_x\right) \cdot \sqrt{E_x}x_1 + \left(\sqrt{E_y}y_1 + n_y\right) \cdot \sqrt{E_y}y_1 + \left(\sqrt{E_z}z_1 + n_z\right) \cdot \sqrt{E_z}z_1 = \\ = \left(E_x x_1^2 + E_y y_1^2 + E_z z_1^2\right) + \sqrt{E_x}x_1 n_x + \sqrt{E_y}y_1 n_y + \sqrt{E_z}z_1 n_z = \mathbf{S}_1^{\mathrm{T}} \cdot \mathbf{S}_1 + n_1 = \|\mathbf{S}_1\| + n_1 \tag{B.1}$$

$$C_2 = \left(\sqrt{E_x}x_1 + n_x\right) \cdot \sqrt{E_x}x_2 + \left(\sqrt{E_y}y_1 + n_y\right) \cdot \sqrt{E_y}y_2 + \left(\sqrt{E_z}z_1 + n_z\right) \cdot \sqrt{E_z}z_2 = \\ = \left(E_x x_1 x_2 + E_y y_1 y_2 + E_y z_1 z_2\right) + \sqrt{E_x}x_2 n_x + \sqrt{E_y}y_2 n_y + \sqrt{E_z}z_2 n_z = \mathbf{S}_1^{\mathrm{T}} \cdot \mathbf{S}_2 + n_2 \tag{B.2}$$

$$\begin{aligned} C_3 &= \left(\sqrt{E_x}x_1 + n_x\right)\cdot\sqrt{E_x}x_3 + \left(\sqrt{E_y}y_1 + n_y\right)\cdot\sqrt{E_y}y_3 + \left(\sqrt{E_z}z_1 + n_z\right)\cdot\sqrt{E_z}z_3 = \\ &= (E_x x_1 x_3 + E_y y_1 y_3 + E_y z_1 z_3) + \sqrt{E_x}x_3 n_x + \sqrt{E_y}y_3 n_y + \sqrt{E_z}z_3 n_z = \mathbf{S}_1^{\mathrm{T}}\cdot\mathbf{S}_3 + n_3 \end{aligned} \tag{B.3}$$

$$\begin{aligned} C_4 &= \left(\sqrt{E_x}x_1 + n_x\right)\cdot\sqrt{E_x}x_4 + \left(\sqrt{E_y}y_1 + n_y\right)\cdot\sqrt{E_y}y_4 + \left(\sqrt{E_z}z_1 + n_z\right)\cdot\sqrt{E_z}z_4 = \\ &= (E_x x_1 x_4 + E_y y_1 y_4 + E_y z_1 z_4) + \sqrt{E_x}x_4 n_x + \sqrt{E_y}y_4 n_y + \sqrt{E_z}z_4 n_z = \mathbf{S}_1^{\mathrm{T}}\cdot\mathbf{S}_4 + n_4 \end{aligned} \tag{B.4}$$

where the waveforms are represented as vectors: $\mathbf{S}_1 = \left[\sqrt{E_x}x_1, \sqrt{E_y}y_1, \sqrt{E_z}z_1\right]^{\mathrm{T}}, \cdots, \mathbf{S}_4 = \left[\sqrt{E_x}x_4, \sqrt{E_y}y_4, \sqrt{E_z}z_4\right]^{\mathrm{T}}$. The noise power at the output of the correlators is the same: $\overline{n_1^2} = \overline{n_2^2} = \overline{n_3^2} = \overline{n_4^2} = (E_x + E_y + E_z)\sigma^2$ and the noises n_1, n_2, n_3, n_4 are correlated. If we define the received noise vector as $N = [n_x, n_y, n_z]^{\mathrm{T}}$, then the noise at the output of the correlators is given by:

$$n_1 = \mathbf{S}_1^{\mathrm{T}}\cdot\mathbf{N} \qquad n_2 = \mathbf{S}_2^{\mathrm{T}}\cdot\mathbf{N} \qquad n_3 = \mathbf{S}_3^{\mathrm{T}}\cdot\mathbf{N} \qquad n_4 = \mathbf{S}_4^{\mathrm{T}}\cdot\mathbf{N} \tag{B.5}$$

We decide that the binary combination of two bits that has been transmitted is the one that corresponds to the correlator that gives the maximum output. Thus, the BLER conditioned to that waveform 1 has been transmitted is bounded according to the following expression:

$$P_{\varepsilon,1} < \mathrm{Prob}(C_2 > C_1) + \mathrm{Prob}(C_3 > C_1) + \mathrm{Prob}(C_4 > C_1) < 3\cdot\mathrm{Prob}(C_m > C_1) \tag{B.6}$$

where C_m is the waveform which is more similar to C_1. For instance, the squared euclidean distance between waveforms 3 and 1,$\left(d_{3,1}^E\right)^2$, is given by:

$$\begin{aligned} \left(d_{3,1}^E\right)^2 &= E_x(x_3 - x_1)^2 + E_y(y_3 - y_1)^2 + E_z(z_3 - z_1)^2 = \\ &= E_x x_3^2 + E_x x_1^2 + E_y y_3^2 + E_y y_1^2 + E_z z_3^2 + E_z z_1^2 - 2E_x x_3 x_1 - 2E_y y_3 y_1 - 2E_z z_3 z_1 = \\ &= \|\mathbf{S}_3\|^2 + \|\mathbf{S}_1\|^2 - 2\cdot\mathbf{S}_1^{\mathrm{T}}\cdot\mathbf{S}_3 = 2\left(\|\mathbf{S}_1\|^2 - \mathbf{S}_1^{\mathrm{T}}\cdot\mathbf{S}_3\right) \end{aligned} \tag{B.7}$$

From Equation B.7, we have

$$\mathbf{S}_1^{\mathrm{T}}\cdot\mathbf{S}_3 = \|\mathbf{S}_1\|^2 - \frac{\left(d_{3,1}^E\right)^2}{2} \tag{B.8}$$

Therefore, the decoding error probability, conditioned to that waveform 1 has been transmitted, is bounded by:

$$\begin{aligned} P_{\varepsilon,1} &< 3\cdot\mathrm{Prob}(C_m > C_1) = 3\cdot\mathrm{Prob}\left(\mathbf{S}_1^{\mathrm{T}}\cdot\mathbf{S}_m + n_m > \|\mathbf{S}_1\|^2 + n_1\right) = \\ &= 3\cdot\mathrm{Prob}\left(\|\mathbf{S}_1\|^2 - \frac{\left(d_{m,1}^E\right)^2}{2} + n_m > \|\mathbf{S}_1\|^2 + n_1\right) = 3\cdot\mathrm{Prob}\left(n_m - n_1 > \frac{\left(d_{m,1}^E\right)^2}{2}\right) = \\ &= 3\cdot\frac{1}{\sqrt{2}}\int_{\frac{(d_{m,1}^E)^2}{2}}^{\infty} e^{-\frac{1}{2}\left(\frac{x}{\nu}\right)^2} d\left(\frac{x}{\nu}\right) = \\ &= 3\cdot\frac{1}{\sqrt{2}}\int_{\frac{(d_{m,1}^E)^2}{2\nu}}^{\infty} e^{-\frac{t^2}{2}} dt = 3\cdot Q\left(\frac{(d_{m,1}^E)^2}{2\nu}\right) \end{aligned} \tag{B.9}$$

where $Q(\cdot)$ is the Q-function that it is the tail probability of the standard normal (Gaussian) distribution and it is defined as follows:

$$Q(x) = \frac{1}{\sqrt{2\pi}} \int_x^\infty \exp\left(-\frac{u^2}{2}\right) du \tag{B.10}$$

and the variance of the noise difference is defined as follows:

$$\nu^2 = \overline{(n_m - n_1)^2} = \overline{\left(\mathbf{S}_m^{\mathrm{T}} \cdot \mathbf{N} - \mathbf{S}_1^{\mathrm{T}} \cdot \mathbf{N}\right)} = (\mathbf{S}_m - \mathbf{S}_1)^{\mathrm{T}} \cdot \overline{\mathbf{N} \cdot \mathbf{N}^{\mathrm{T}}} \cdot (\mathbf{S}_m - \mathbf{S}_1) \tag{B.11}$$

Assuming that

$$\mathbf{N}^{\mathrm{T}} = \overline{\begin{bmatrix} n_x \\ n_y \\ n_z \end{bmatrix} \begin{bmatrix} n_x & n_y & n_z \end{bmatrix}} = \begin{bmatrix} \overline{n_x^2} & 0 & 0 \\ 0 & \overline{n_y^2} & 0 \\ 0 & 0 & \overline{n_z^2} \end{bmatrix} = \sigma^2 \mathbf{I}_3 \tag{B.12}$$

we have

$$\nu^2 = \sigma^2 \left\|\mathbf{S}_m - \mathbf{S}_1\right\|^2 = \sigma^2 \left(E_x(x_m - x_1)^2 + (E_y(y_m - y_1)^2 + (E_z(z_m - z_1)^2\right) \tag{B.13}$$

there are thus as many contributions of $4E\sigma^2$ (with $E \in \{E_x, E_y, E_z\}$) as the hamming distance (number of different components) between the waveforms 1 and m. If $d_{1,m}^H = 3$, then we have $\nu^2 = 4\sigma^2 \cdot (E_x + E_y + E_z)$. If $d_{1,m}^H = 2$, then there are $\binom{3}{2} = 3$ possibilities (depending on how the waveforms are): $\nu^2 = 4\sigma^2 \cdot (E_x + E_y)$; or $\nu^2 = 4\sigma^2 \cdot (E_x + E_z)$; or $\nu^2 = 4\sigma^2 \cdot (E_y + E_z)$. If $d_{1,m}^H = 1$, then there are also 3 possibilities: $\nu^2 = 4\sigma^2\ E_x$; or $\nu^2 = 4\sigma^2\ E_y$; or $\nu^2 = 4\sigma^2\ E_z$.

Now we consider that all the components of the received waveforms have the same SNR which is $\nu^2 = 4E\sigma^2 d_{m,1}^H$. Additionally, in this case it holds that

$$\left(d_{m,1}^E\right)^2 = E\left((x_m - x_1)^2 + (y_m - y_1)^2 + (z_m - z_1)^2\right) = 4E d_{m,1}^H \tag{B.14}$$

This gives

$$P_{\varepsilon,1} < 3 \cdot Q\left(\frac{2E \cdot d_{m,1}^H}{\sqrt{4E\sigma^2 d_{m,1}^H}}\right) = 3 \cdot Q\left(\sqrt{\frac{E \cdot d_{m,1}^H}{\sigma^2}}\right) = 3 \cdot Q\left(\sqrt{2 \cdot SNR \cdot d_{m,1}^H}\right) \tag{B.15}$$

Defining E_b as the energy per information bit, we have $E_b/N_0 = (3E_b^{'}/2)/N_0 = r^{-1} \cdot E_b^{'}/N_0 = r^{-1} \cdot SNR$ (where $E_b^{'}/N_0 = SNR$ is the SNR for BPSK and $r = 2/3$ is the code rate). This gives:

$$P_{\varepsilon,1} < 3 \cdot Q\left(\sqrt{2 \cdot \frac{E_b}{N_0} \cdot r \cdot d_{m,1}^H}\right) < 2^k \cdot Q\left(\sqrt{2 \cdot \frac{E_b}{N_0} \cdot r \cdot d_{m,1}^H}\right) \leq \frac{2^k}{2} e^{-\frac{E_b}{N_0} \cdot r \cdot d_{m,1}^H} = \frac{2^k}{2} e^{-SNR \cdot d_{m,1}^H} \tag{B.16}$$

where the function Q has been approximated by the Chernoff bound.

$Prob(C_m > c_1)$ is the probability of mistaking waveform 1 for m; however, in general, there can be other waveforms that when considered pairwise, the Hamming distance between any of these pairs is equal to $d = d^H_{m,1}$. The probability of mistaking between any of these waveforms is called *Pairwise Error Probability* (PEP) and is equal to $P_2(d,\gamma) = Q(\sqrt{2d\gamma})$ (where $\gamma = SNR$). The number of waveforms that, when considered pairwise, have a Hamming distance equal to d, is called the multiplicity of this Hamming distance and it is denoted by a_d. The code free distance, d^H_{min}, is the minimum Hamming distance between any different encoded sequences. In the absence of more information about the code, we can approximate the unconditioned decoding error probability to:

$$P_\varepsilon < 2^k \cdot Q\left(\sqrt{2 \cdot SNR \cdot d^H_{min}}\right) = 2^k \cdot Q\left(\sqrt{2 \cdot \frac{E_b}{N_0} \cdot r \cdot d^H_{min}}\right) \tag{B.17}$$

Although this is very pessimistic since we assume that the probability of mistaking a pair of waveforms is equal to the probability of mistaking in the worst case. This is like considering that the Hamming distance between any of the 2^k possible waveforms is equal to the minimum distance (the worst case), i.e, the multiplicity of the free-code distance is $a_d = 2^k$. Thus, without coding and assuming BPSK, Equation B.19 is rewritten as $P_\varepsilon < 2^k \cdot Q\left(\sqrt{2 \cdot \frac{E_b}{N_0}}\right)$ and the asymptotic code gain is $r \cdot d^H_{min}$.

A bound closer to the real case can be obtained by classifying all possible valid waveforms in subsets (disjoint and with cardinal a_d) formed by all the waveforms that, considered pairwise, all of them have the same Hamming distance (equal to d). Following this criteria the BLER (unconditioned) is bounded by:

$$BLER(\gamma) = P_\varepsilon(\gamma) \leq \sum_{d=d^H_{min}}^{\infty} a_d \cdot Q(\sqrt{2d\gamma}) \leq \sum_{d=d^H_{min}}^{\infty} a_d \frac{1}{2} e^{-\gamma \cdot d} \tag{B.18}$$

If we consider that all the components of the waveforms do not have the same SNR and practical codes (long waveforms with $m = k/r$ length), then, the Hamming distance of the waveforms (d), considered pairwise, is the same and the variance of the noise difference at the correlator output takes a value of $\nu^2 = 4\sigma^2 \sum_{i=1}^{d} E_{f(i)} = \sigma^2 \left(4 \sum_{i=1}^{d} E_{f(i)}\right) = \sigma^2 \left(d^E\right)^2$ (where $f(i)$ selects which components contributes to ν^2). If each component of all the received waveforms can take a different value of SNR, then there can be m possible different values of E and, among these values, function $f(i)$, from $\left(\sum_{i=1}^{d} E_{f(i)}\right)$, selects the values of d that contribute to the noise. Since we do not know which of the $\binom{m}{d}$ possible combinations occurs in practice, we assume that the amplitude of the components of the received waveforms (which are coded bits) can take only two possible values, i.e., $E \in \{E_1, E_2\}$ (like having only two subcarriers). The first value takes a probability of p_1 and the second one a probability of p_2; thus, there are mp_1 components with amplitude E_1 and mp_2 components with amplitude E_2 on average. Since we analyse the waveforms with Hamming distance equal to d, there are only d noise contributions. If we take i contributions of E_1, then there are d_1 contributions of E_2. Therefore, the average PEP can be written as follows:

$$P_2(d,\gamma_1,\gamma_2) = \overline{Q\left(\frac{(d^E)^2}{2\nu}\right)} = \sum_{i=0}^{d}\binom{d}{i}p_1^i\cdot p_2^{d-i}\cdot Q\left(\frac{4i\cdot E_1+4(d-i)\cdot E_2}{4\sigma\sqrt{i\cdot E_1+(d-1)\cdot E_2}}\right) =$$
$$= \sum_{i=0}^{d}\binom{d}{i}p_1^i\cdot p_2^{d-i}\cdot Q\left(\sqrt{i\cdot\frac{E_1}{\sigma^2}+(d-i)\cdot\frac{E_2}{\sigma^2}}\right) = \sum_{i=0}^{d}\binom{d}{i}p_1^i\cdot p_2^{d-i}\cdot Q\left(\sqrt{2(i\cdot\gamma_1+(d-i)\cdot\gamma_2)}\right) \tag{B.19}$$

If there are three possible values of SNR, then we have:

$$P_2(d,\gamma_1,\gamma_2,\gamma_3)) = \sum_{i=0}^{d}\binom{d}{i}\left[\sum_{j=0}^{d-i}\binom{d-i}{j}p_1^i\cdot p_2^j\cdot p_3^{d-i-j}\cdot Q\left(\sqrt{2(i\cdot\gamma_1+j\cdot\gamma_2+(d-i-j)\cdot\gamma_3)}\right)\right] \tag{B.20}$$

The function Q(x) can be written as follows:

$$Q(x) = \frac{1}{\pi}\int_0^{\pi/2} e^{-\frac{x^2}{2\sin(\theta)}}d\theta \tag{B.21}$$

This gives for two possible values of SNR

$$\begin{aligned} P_2(d,\gamma_1,\gamma_2) &= \sum_{i=0}^{d}\binom{d}{i}p_1^i\cdot p_2^{d-i}\cdot\frac{1}{\pi}\int_0^{\pi/2} e^{-\frac{i\cdot\gamma_1+(d-i)\cdot\gamma_2}{\sin(\theta)}}d\theta = \\ &= \frac{1}{\pi}\int_0^{\pi/2}\left\{\sum_{i=0}^{d}\binom{d}{i}\left(p_1\cdot e^{-\frac{\gamma_1}{\sin^2(\theta)}}\right)^i\cdot\left(p_2\cdot e^{-\frac{\gamma_2}{\sin^2(\theta)}}\right)^{d-i}\right\}d\theta = \\ &= \frac{1}{\pi}\int_0^{\pi/2}\left(p_1\cdot e^{-\frac{\gamma_1}{\sin^2(\theta)}}+p_2\cdot e^{-\frac{\gamma_2}{\sin^2(\theta)}}\right)^d d\theta \end{aligned} \tag{B.22}$$

This gives for three possible values of SNR

$$\begin{aligned} P_2(d,\gamma_1,\gamma_2,\gamma_3) &= \sum_{i=0}^{d}\binom{d}{i}\left[\sum_{j=0}^{d-i}\binom{d-i}{j}p_1^i\cdot p_2^j\cdot p_3^{d-i-j}\cdot\int_0^{\pi/2} e^{-\frac{i\cdot\gamma_1+j\cdot\gamma_2+(d-i-j)\cdot\gamma_3}{\sin^2(\theta)}}\right] = \\ &= \frac{1}{\pi}\int_0^{\pi/2}\left\{\sum_{i=0}^{d}\binom{d}{i}p_1^i\cdot e^{-\frac{i\cdot\gamma_1}{\sin^2(\theta)}}\left[\sum_{j=0}^{d-i}\binom{d-i}{j}\cdot p_2^j\cdot p_3^{d-i-j}\cdot e^{-\frac{j\gamma_2+(d-i-j)\cdot\gamma_3)}{\sin^2(\theta)}}\right]\right\}d\theta = \\ &= \frac{1}{\pi}\int_0^{\pi/2}\left\{\sum_{i=0}^{d}\binom{d}{i}\left(p_1\cdot e^{-\frac{\gamma_1}{\sin^2(\theta)}}\right)^i\left[\sum_{j=0}^{d-i}\binom{d-i}{j}\cdot\left(p_2\cdot e^{-\frac{\gamma_2}{\sin^2(\theta)}}\right)^j\cdot\left(p_3\cdot e^{-\frac{\gamma_3}{\sin^2(\theta)}}\right)^{d-i-j}\right]\right\}d\theta = \\ &= \frac{1}{\pi}\int_0^{\pi/2}\left\{\sum_{i=0}^{d}\binom{d}{i}\left(p_1\cdot e^{-\frac{\gamma_1}{\sin^2(\theta)}}\right)^i\left(p_2\cdot e^{-\frac{\gamma_2}{\sin^2(\theta)}}+p_3\cdot e^{-\frac{\gamma_3}{\sin^2(\theta)}}\right)^{d-i}\right\}d\theta = \\ &= \frac{1}{\pi}\int_0^{\pi/2}\left(p_1\cdot e^{-\frac{\gamma_1}{\sin^2(\theta)}}+p_2\cdot e^{-\frac{\gamma_2}{\sin^2(\theta)}}+p_3\cdot e^{-\frac{\gamma_3}{\sin^2(\theta)}}\right)^d d\theta \end{aligned} \tag{B.23}$$

Thus, this equation can be generalized to any number of different values of SNR. The goal is to find a value of SNR, which is called ESNR, such that this value satisfies the following Equation:

$$P_2(d,\gamma_{eff}) = P_2(d,\gamma_1,\gamma_2) \Rightarrow \frac{1}{\pi}\int_0^{\pi/2}\left(e^{-\frac{\gamma_{eff}}{\sin^2(\theta)}}\right)^d d\theta = \frac{1}{\pi}\int_0^{\pi/2}\left(p_1\cdot e^{-\frac{\gamma_1}{\sin^2(\theta)}} + p_2\cdot e^{-\frac{\gamma_2}{\sin^2(\theta)}}\right)^d d\theta \tag{B.24}$$

Since this equation does not have an exact solution, we can make an approximation.

$$e^{-\frac{\gamma}{\sin^2(\theta)}} \leq e^{-\gamma} \quad \left(\gamma \geq 0; 0 \leq \theta \leq \frac{\pi}{2}\right) \tag{B.25}$$

Substituting the exact equation by the approximated equation, i.e., instead of equating the original integrals, we equal the upper bounds:

$$\frac{1}{\pi}\int_0^{\pi/2}\left(e^{-\gamma_{eff}}\right)^d d\theta = \frac{1}{\pi}\int_0^{\pi/2}\left(p_1\cdot e^{-\gamma_1} + p_2\cdot e^{-\gamma_2}\right)^d d\theta \tag{B.26}$$

This gives the *Exponential ESNR* (EESNR)

$$e^{-\gamma_{eff}} = p_1\cdot e^{-\gamma_1} + p_2\cdot e^{-\gamma_2} \tag{B.27}$$

Thus, in the general case of m different values of SNR (m subcarriers), we have:

$$\gamma_{eff} = -\ln\left(\sum_{i=1}^{m} p_i\cdot e^{-\gamma_i}\right) \tag{B.28}$$

It is also true that:

$$e^{-\gamma_{eff}} = \sum_{i=1}^{m} p_i\cdot e^{-\gamma_i} \Rightarrow 1 - e^{-\gamma_{eff}} = 1 - \sum_{i=1}^{m} p_i\cdot e^{-\gamma_i} = \sum_{i=1}^{m} p_i - \sum_{i=1}^{m} p_i\cdot e^{-\gamma_i} = \sum_{i=1}^{m} p_i\cdot\left(1-e^{-\gamma_i}\right) \tag{B.29}$$

If we define the function $I(\gamma) = 1 - e^{-\gamma}$, then we can write the EESNR as :

$$I(\gamma_{eff}) = \sum_{i=1}^{m} p_i\cdot I(\gamma_i) \Rightarrow \gamma_{eff} = I^{-1}\left(\sum_{i=1}^{m} p_i\cdot I(\gamma_i)\right) \tag{B.30}$$

The EESNR is the SNR that causes the same PEP (and consequently the same BLER) in AWGN channel than in a multistate channel. The EESNR is a weighted average of the different SNRs that models the effects of the channel into a single scalar value; where the weighting function is $I(\gamma)$ which is not lineal.

Appendix C

Link Abstraction Simulation Results

C.1 SISO and 1 RB

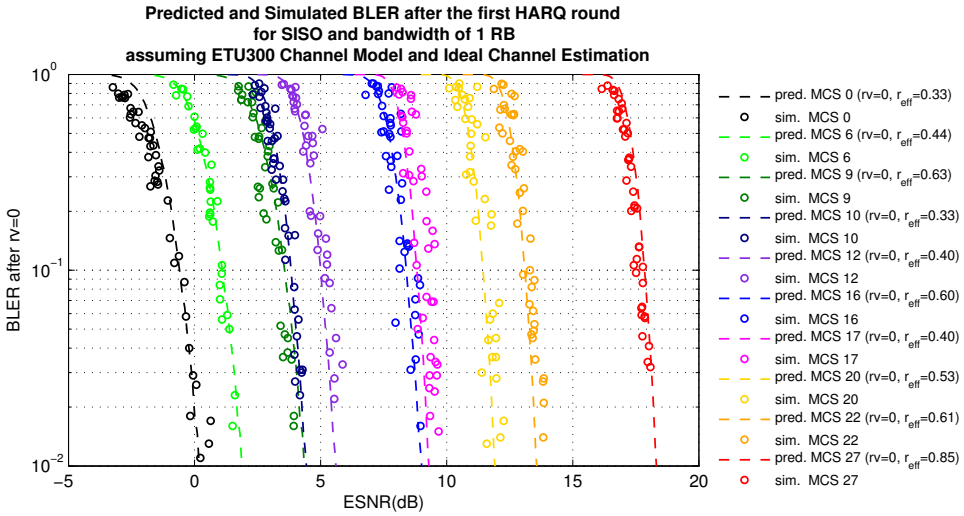

Figure C.1: Predicted vs. Simulated BLER after the first HARQ round in LTE for SISO and bandwidth of 1 RB in ETU300 with ideal channel estimation

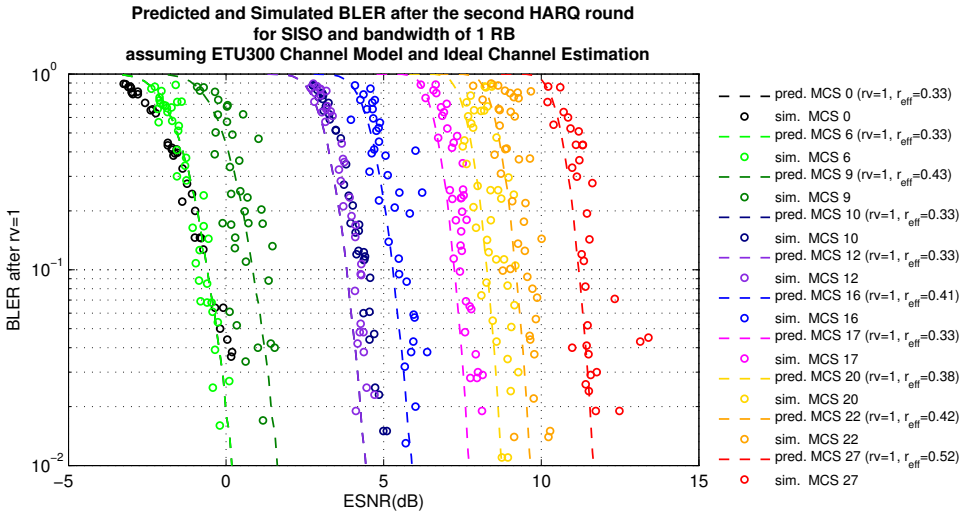

Figure C.2: Predicted vs. Simulated BLER after the second HARQ round in LTE for SISO and bandwidth of 1 RB in ETU300 with ideal channel estimation

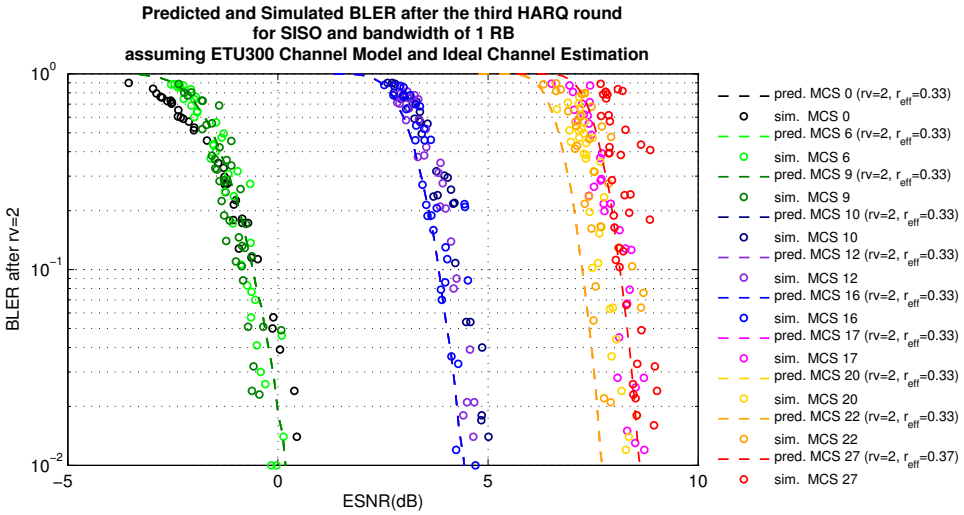

Figure C.3: Predicted vs. Simulated BLER after the third HARQ round in LTE for SISO and bandwidth of 1 RB in ETU300 with ideal channel estimation

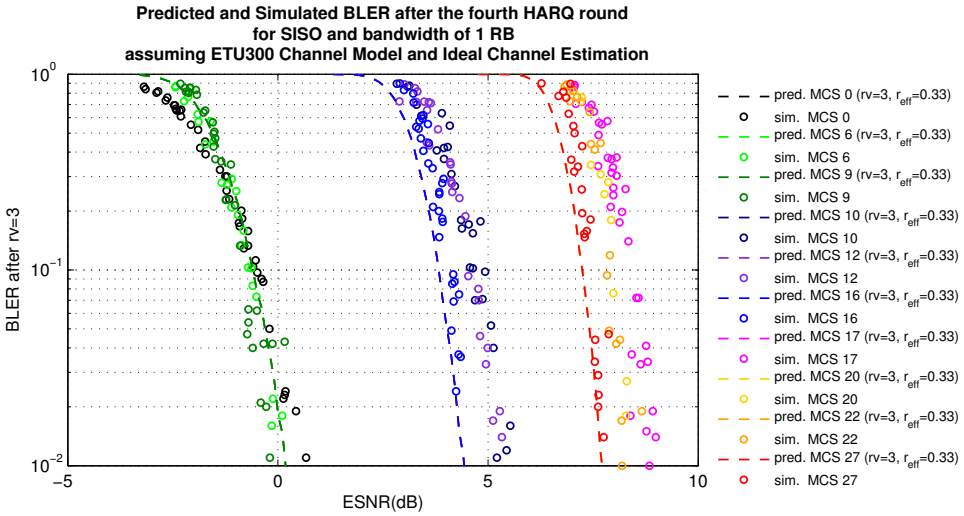

Figure C.4: Predicted vs. Simulated BLER after the fourth HARQ round in LTE for SISO and bandwidth of 1 RB in ETU300 with ideal channel estimation

C.2 2×2 MIMO-SM without precoding, ZF receiver and 1 RB

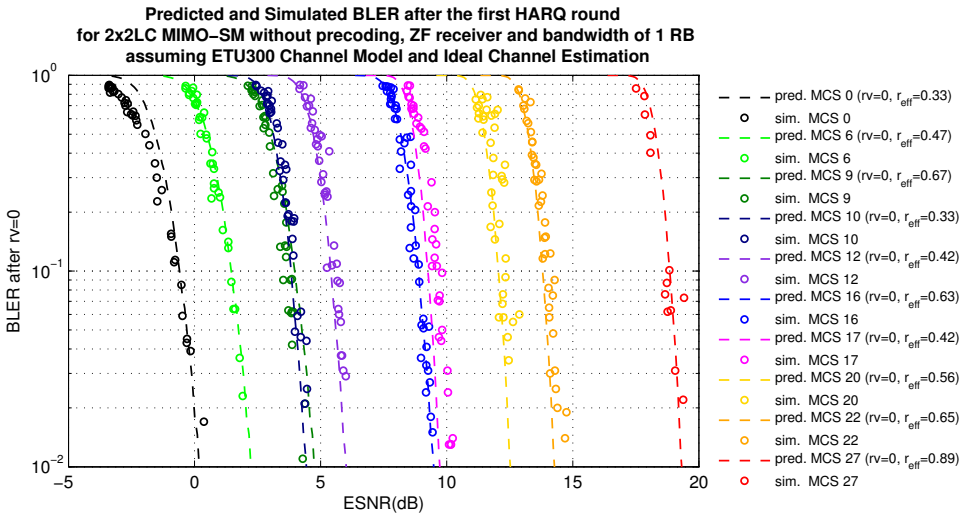

Figure C.5: Predicted vs. Simulated BLER after the first HARQ round in LTE for 2×2LC MIMO-SM without precoding, ZF receiver and bandwidth of 1 RB in ETU300 with ideal channel estimation

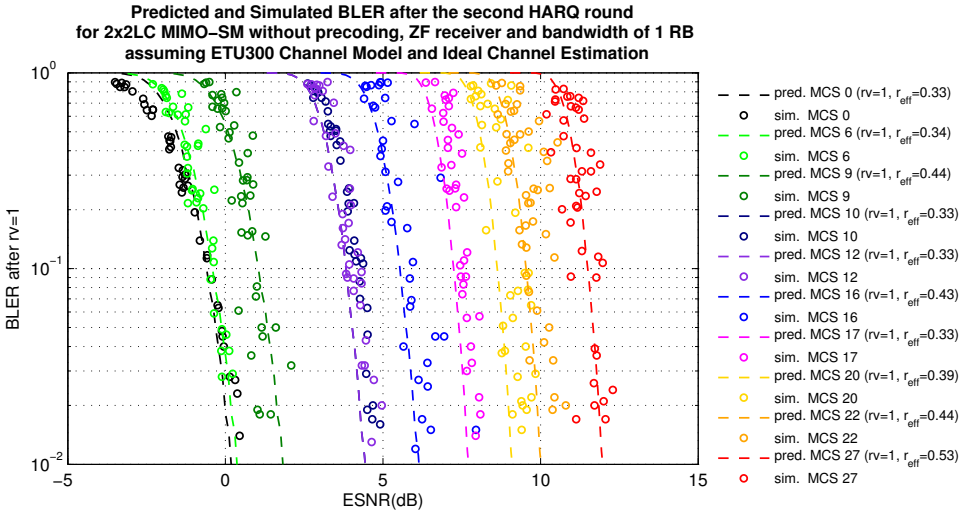

Figure C.6: Predicted vs. Simulated BLER after the second HARQ round in LTE for 2×2LC MIMO-SM without precoding, ZF receiver and bandwidth of 1 RB in ETU300 with ideal channel estimation

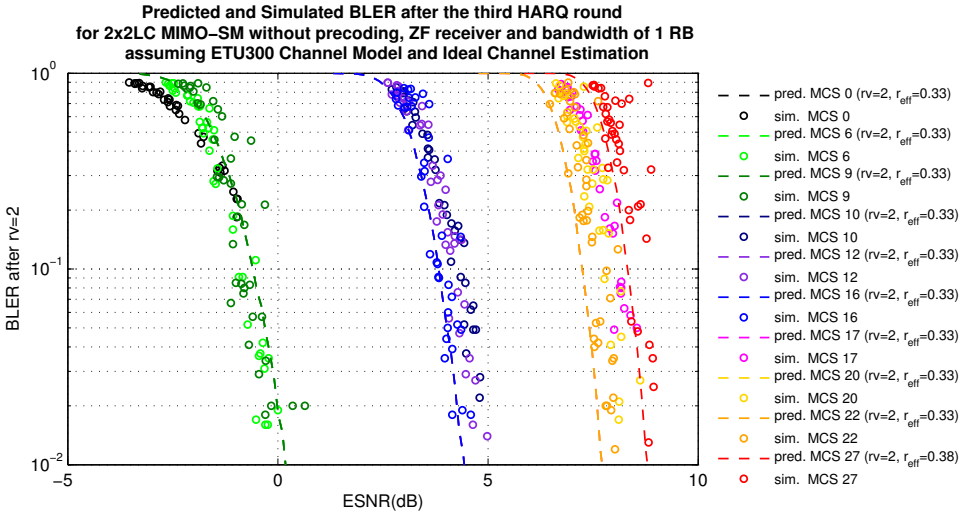

Figure C.7: Predicted vs. Simulated BLER after the third HARQ round in LTE for 2×2LC MIMO-SM without precoding, ZF receiver and bandwidth of 1 RB in ETU300 with ideal channel estimation

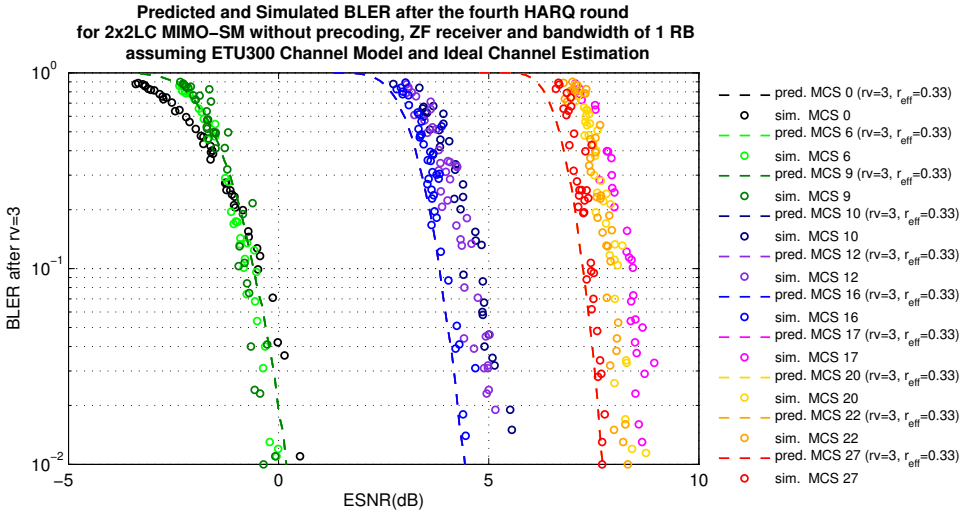

Figure C.8: Predicted vs. Simulated BLER after the fourth HARQ round in LTE for 2×2LC MIMO-SM without precoding, ZF receiver and bandwidth of 1 RB in ETU300 with ideal channel estimation

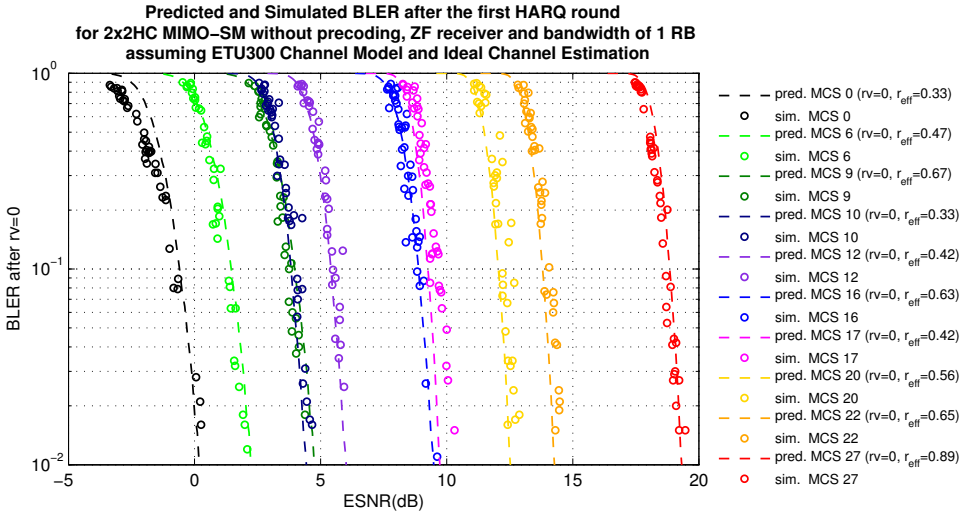

Figure C.9: Predicted vs. Simulated BLER after the first HARQ round in LTE for 2×2HC MIMO-SM without precoding, ZF receiver and bandwidth of 1 RB in ETU300 with ideal channel estimation

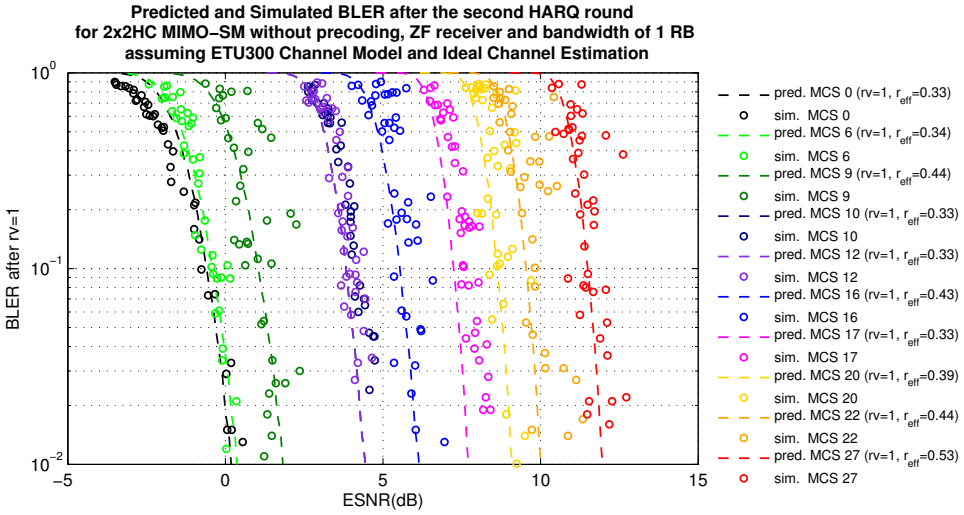

Figure C.10: Predicted vs. Simulated BLER after the second HARQ round in LTE for 2×2HC MIMO-SM without precoding, ZF receiver and bandwidth of 1 RB in ETU300 with ideal channel estimation

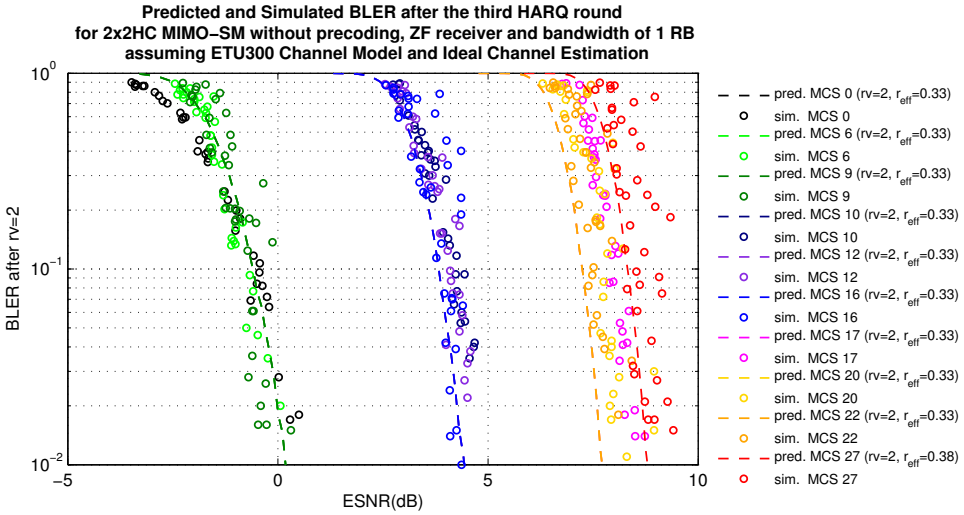

Figure C.11: Predicted vs. Simulated BLER after the third HARQ round in LTE for 2×2HC MIMO-SM without precoding, ZF receiver and bandwidth of 1 RB in ETU300 with ideal channel estimation

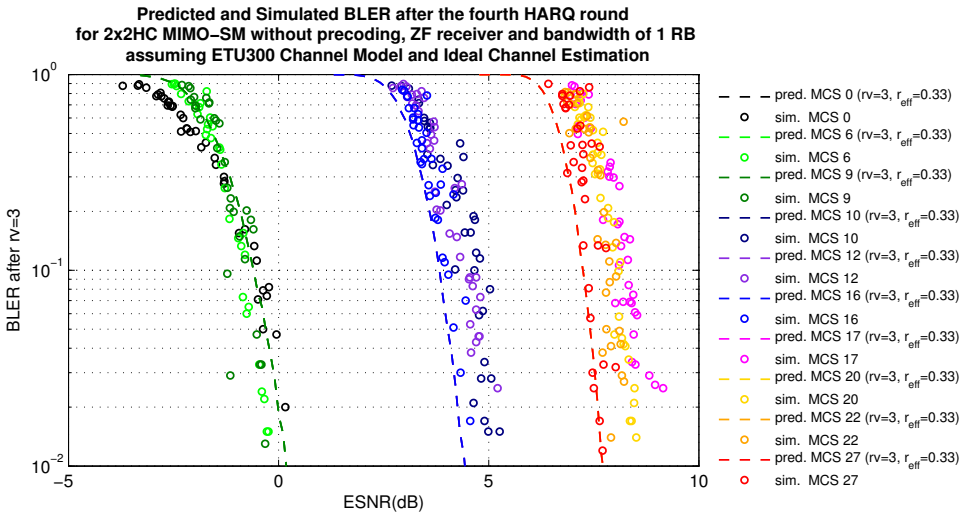

Figure C.12: Predicted vs. Simulated BLER after the fourth HARQ round in LTE for 2×2HC MIMO-SM without precoding, ZF receiver and bandwidth of 1 RB in ETU300 with ideal channel estimation

C.3 2×2 MIMO-SM with CDD precoding, MMSE receiver and 1 RB

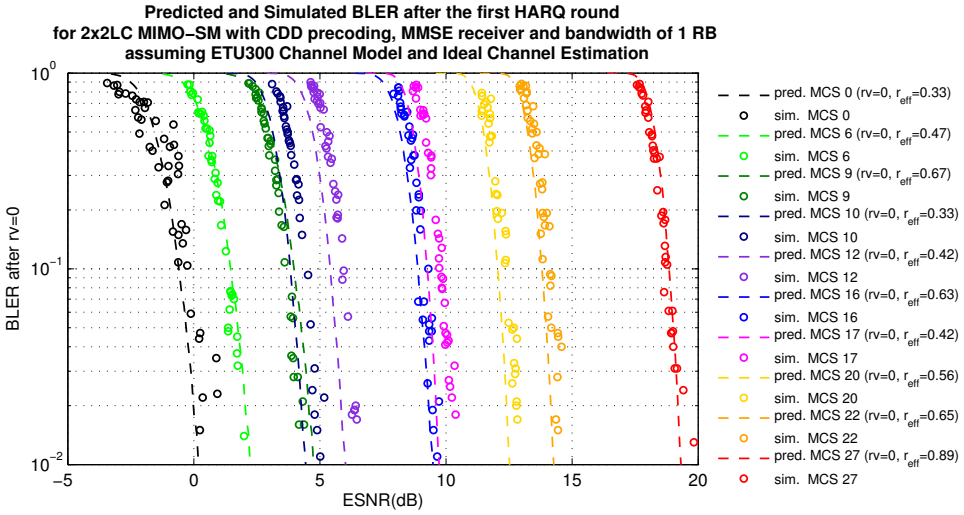

Figure C.13: Predicted vs. Simulated BLER after the first HARQ round in LTE for 2×2LC MIMO-SM with CDD precoding, MMSE receiver and bandwidth of 1 RB in ETU300 with ideal channel estimation

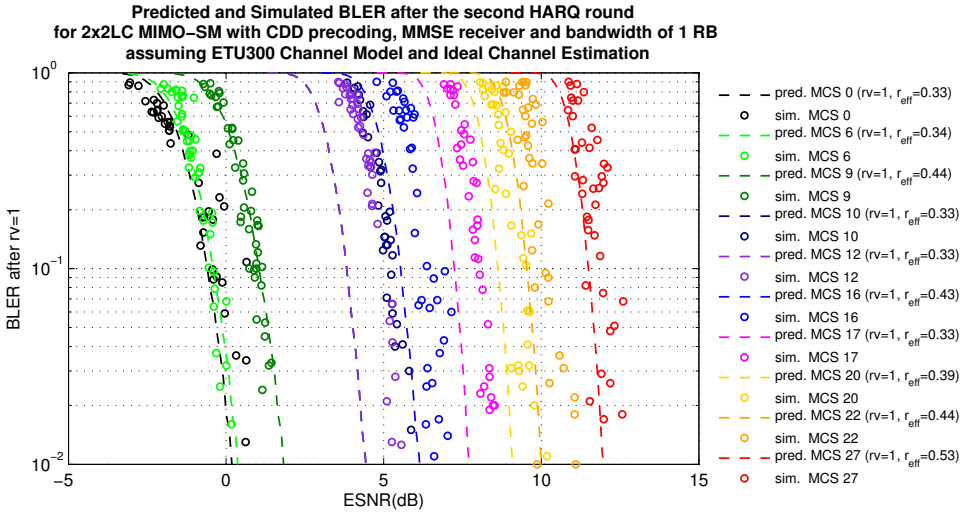

Figure C.14: Predicted vs. Simulated BLER after the second HARQ round in LTE for 2×2LC MIMO-SM with CDD precoding, MMSE receiver and bandwidth of 1 RB in ETU300 with ideal channel estimation

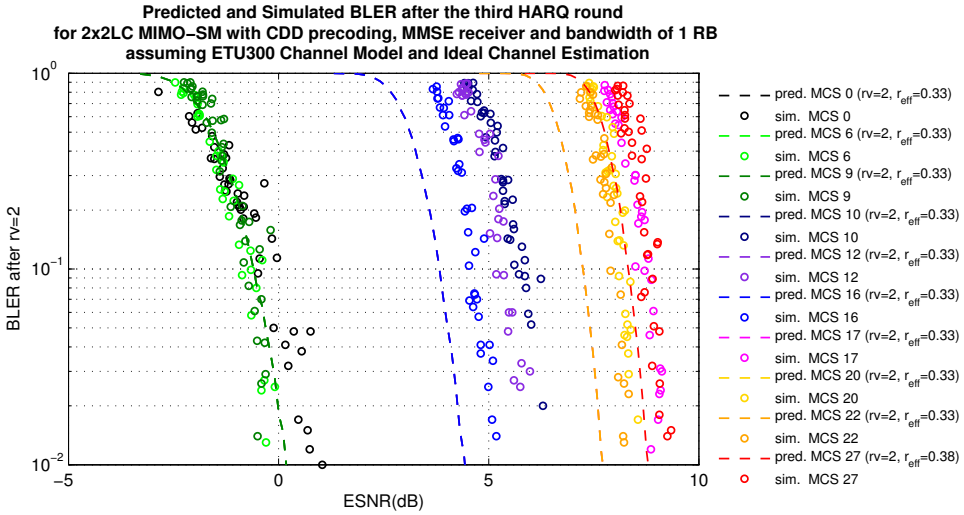

Figure C.15: Predicted vs. Simulated BLER after the third HARQ round in LTE for 2×2LC MIMO-SM with CDD precoding, MMSE receiver and bandwidth of 1 RB in ETU300 with ideal channel estimation

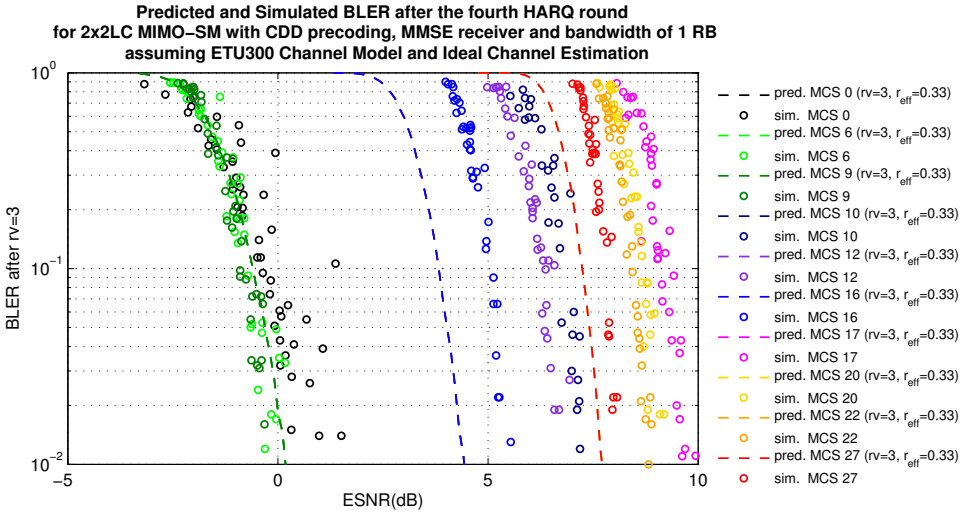

Figure C.16: Predicted vs. Simulated BLER after the fourth HARQ round in LTE for 2×2LC MIMO-SM with CDD precoding, MMSE receiver and bandwidth of 1 RB in ETU300 with ideal channel estimation

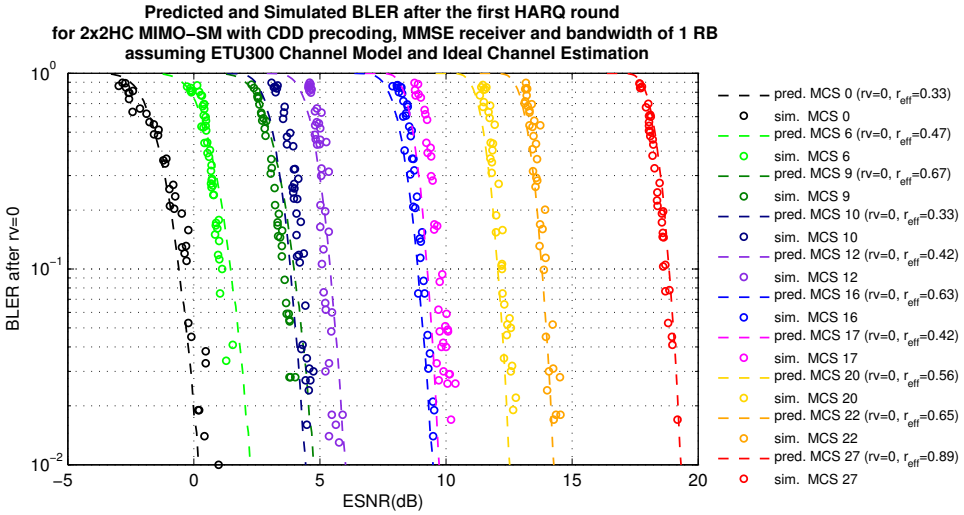

Figure C.17: Predicted vs. Simulated BLER after the first HARQ round in LTE for 2×2HC MIMO-SM with CDD precoding, MMSE receiver and bandwidth of 1 RB in ETU300 with ideal channel estimation

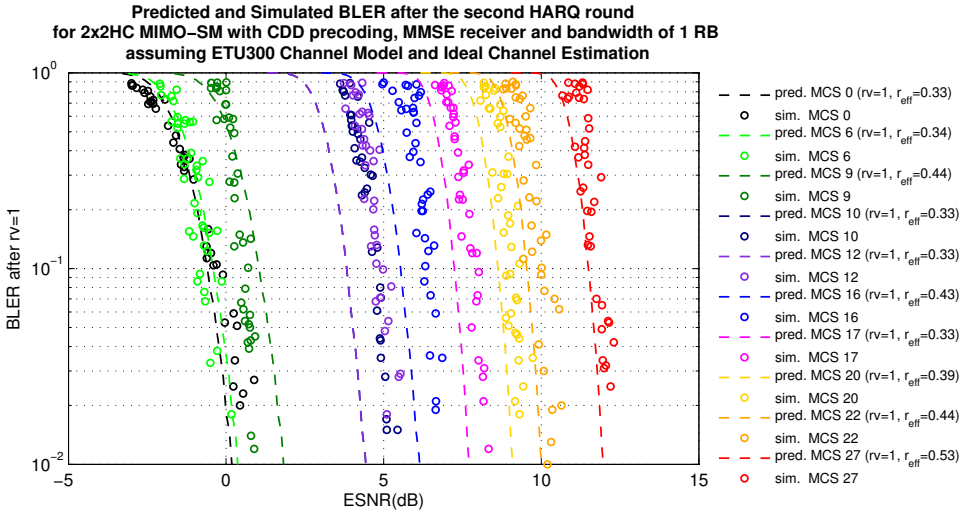

Figure C.18: Predicted vs. Simulated BLER after the second HARQ round in LTE for 2×2HC MIMO-SM with CDD precoding, MMSE receiver and bandwidth of 1 RB in ETU300 with ideal channel estimation

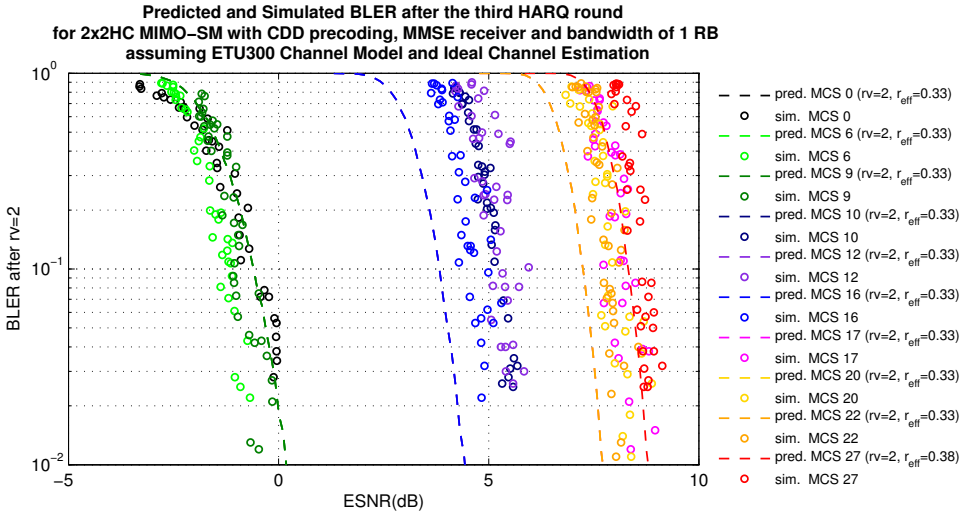

Figure C.19: Predicted vs. Simulated BLER after the third HARQ round in LTE for 2×2HC MIMO-SM with CDD precoding, MMSE receiver and bandwidth of 1 RB in ETU300 with ideal channel estimation

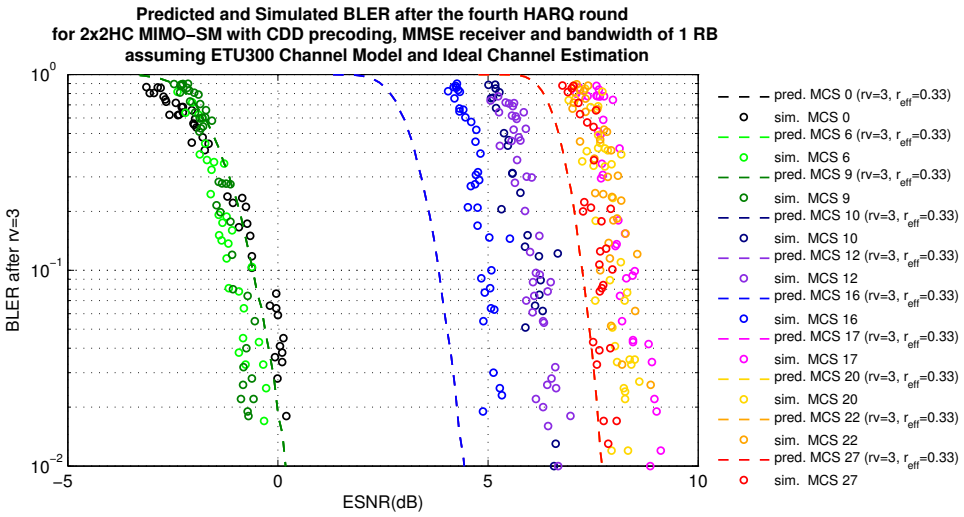

Figure C.20: Predicted vs. Simulated BLER after the fourth HARQ round in LTE for 2×2HC MIMO-SM with CDD precoding, MMSE receiver and bandwidth of 1 RB in ETU300 with ideal channel estimation

C.4 2 × 2 MIMO-TD and 1 RB

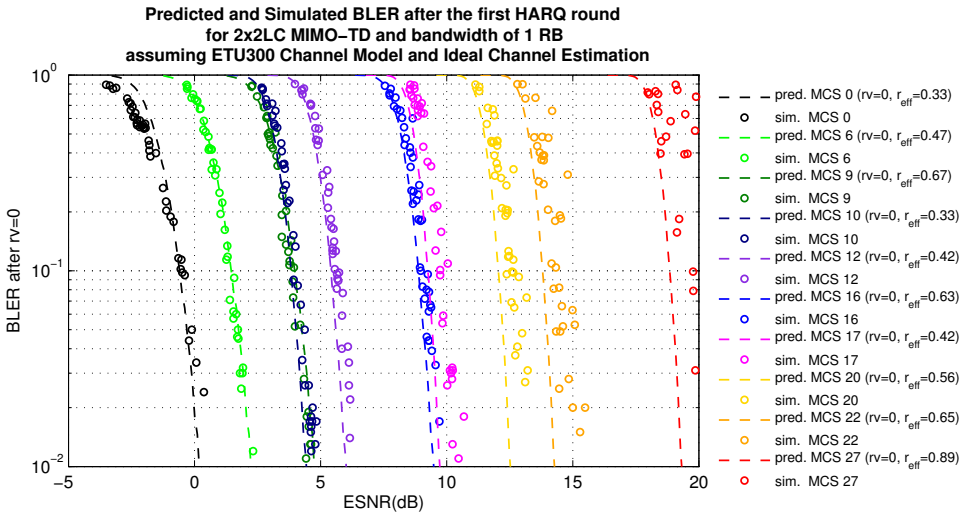

Figure C.21: Predicted vs. Simulated BLER after the first HARQ round in LTE for 2 × 2LC MIMO-TD and bandwidth of 1 RB in ETU300 with ideal channel estimation

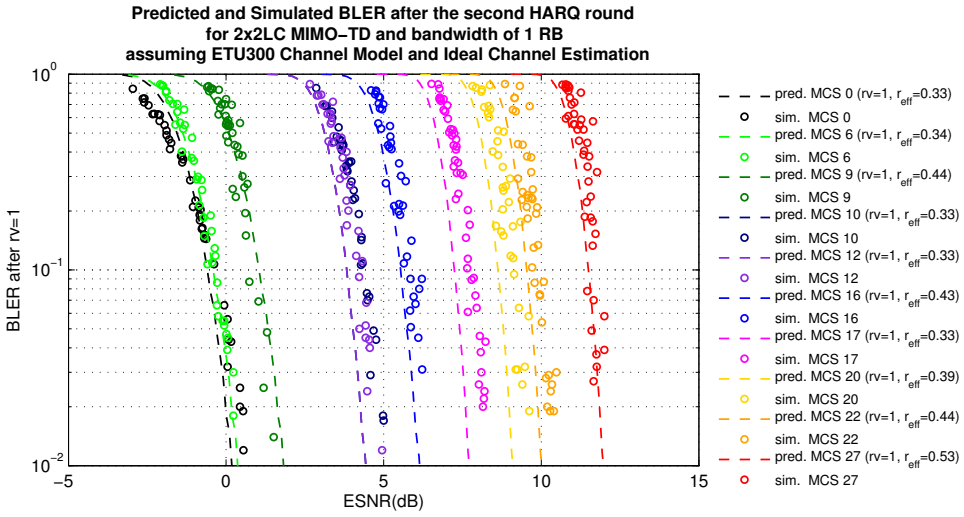

Figure C.22: Predicted vs. Simulated BLER after the second HARQ round in LTE for 2 × 2LC MIMO-TD and bandwidth of 1 RB in ETU300 with ideal channel estimation

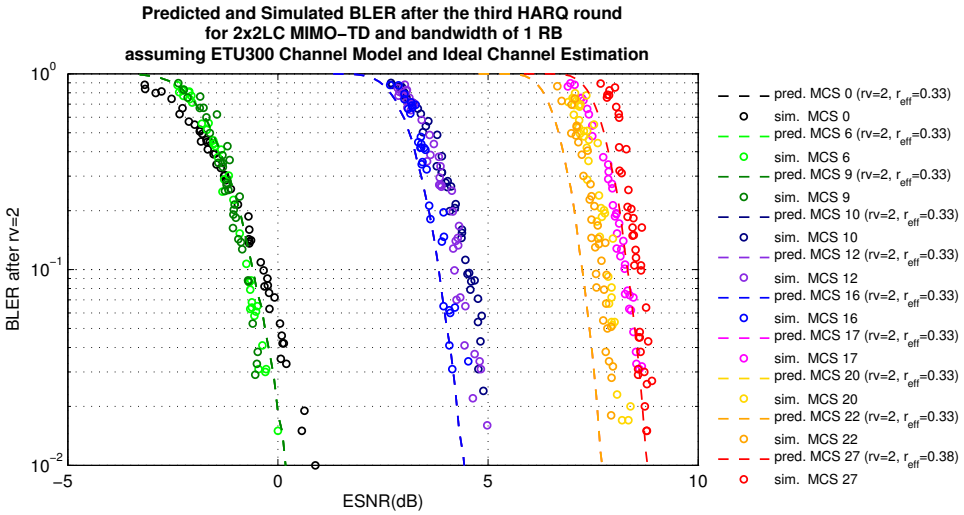

Figure C.23: Predicted vs. Simulated BLER after the third HARQ round in LTE for 2 × 2LC MIMO-TD and bandwidth of 1 RB in ETU300 with ideal channel estimation

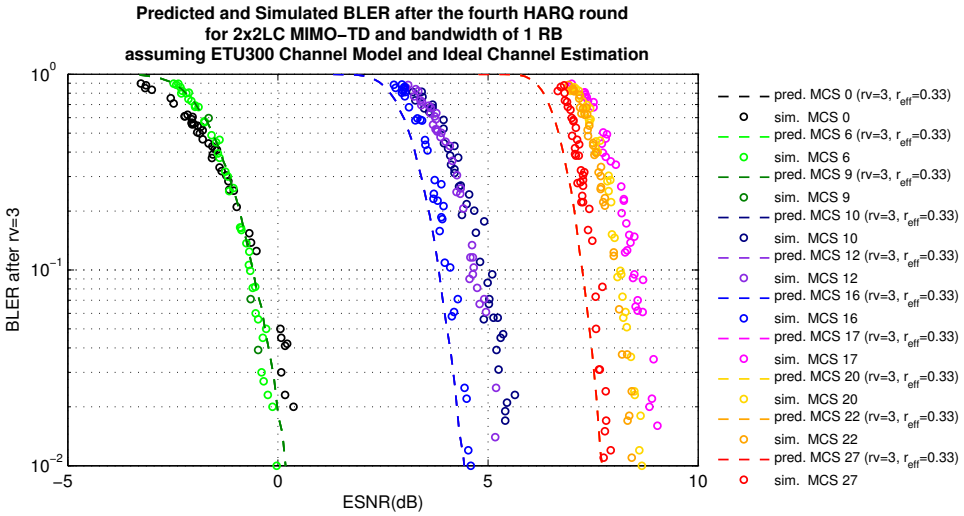

Figure C.24: Predicted vs. Simulated BLER after the fourth HARQ round in LTE for 2 × 2LC MIMO-TD and bandwidth of 1 RB in ETU300 with ideal channel estimation

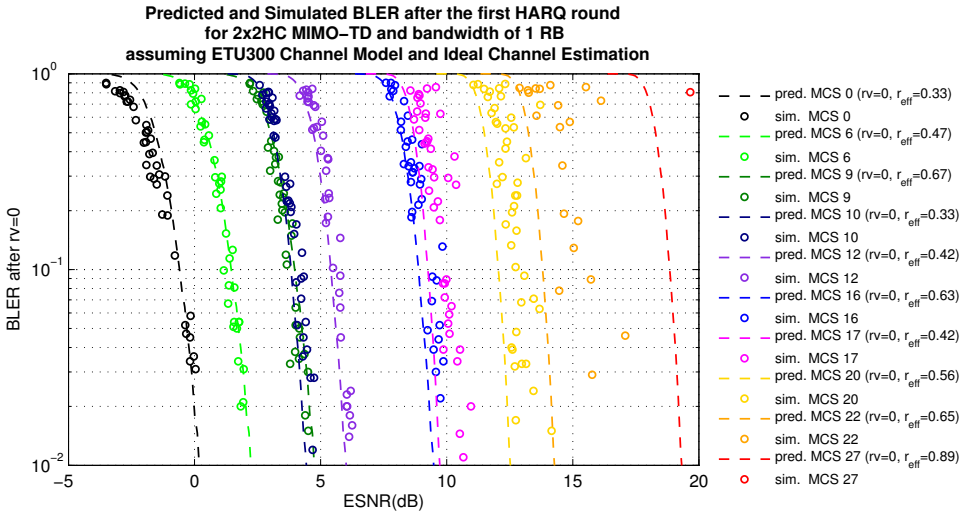

Figure C.25: Predicted vs. Simulated BLER after the first HARQ round in LTE for 2×2HC MIMO-TD and bandwidth of 1 RB in ETU300 with ideal channel estimation

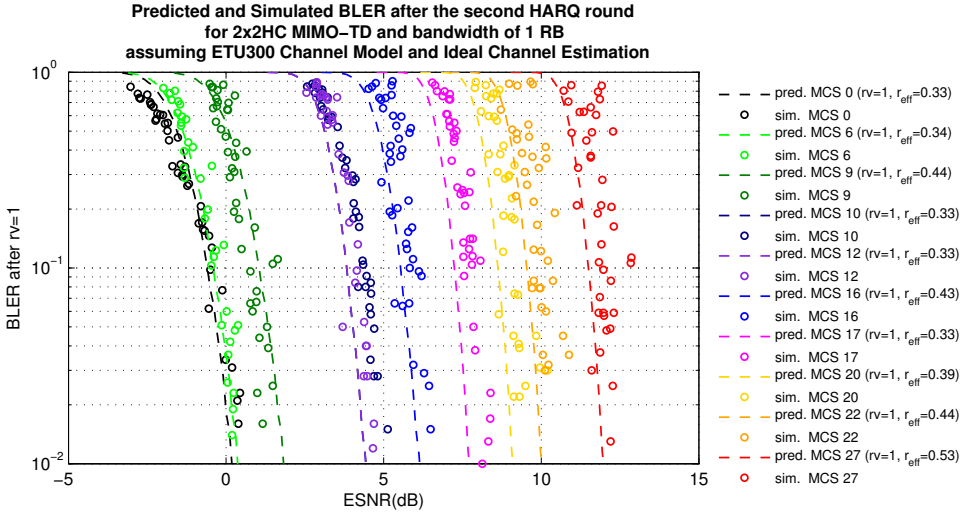

Figure C.26: Predicted vs. Simulated BLER after the second HARQ round in LTE for 2×2HC MIMO-TD and bandwidth of 1 RB in ETU300 with ideal channel estimation

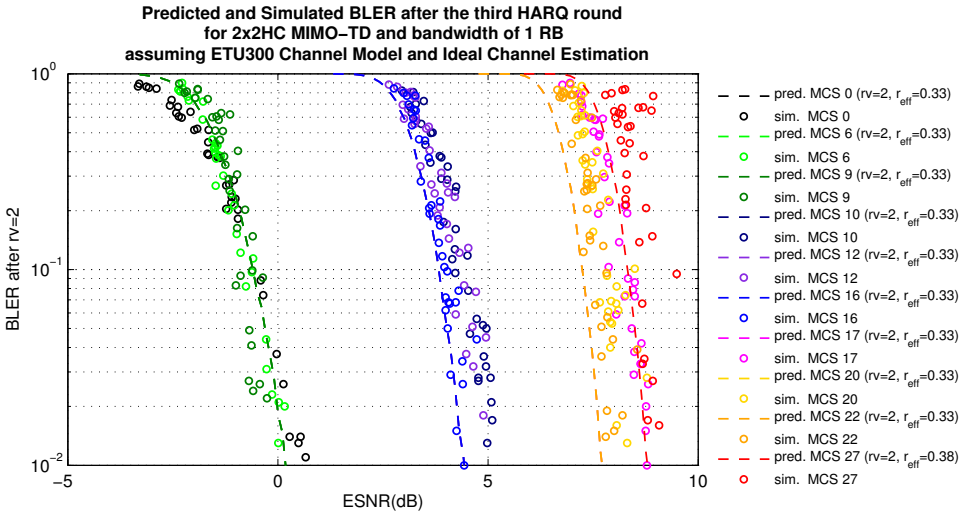

Figure C.27: Predicted vs. Simulated BLER after the third HARQ round in LTE for 2×2HC MIMO-TD and bandwidth of 1 RB in ETU300 with ideal channel estimation

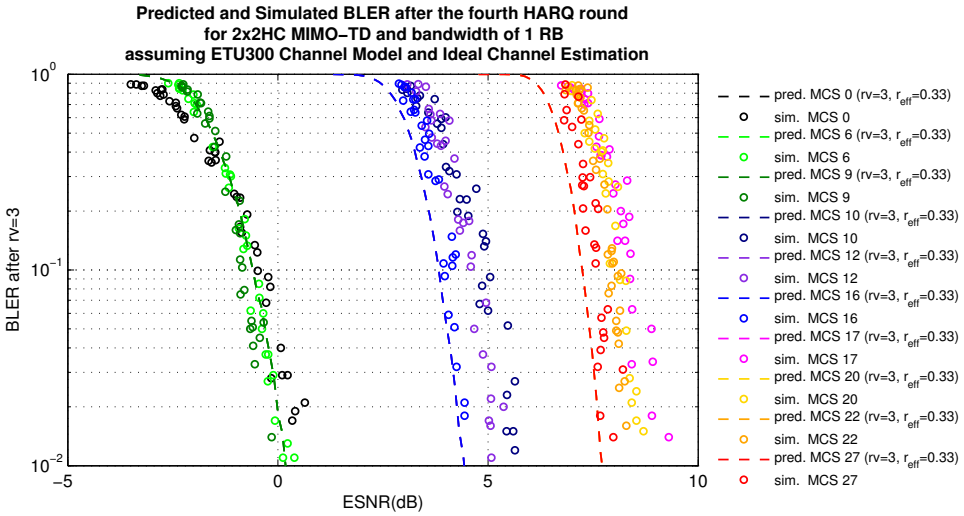

Figure C.28: Predicted vs. Simulated BLER after the fourth HARQ round in LTE for 2×2HC MIMO-TD and bandwidth of 1 RB in ETU300 with ideal channel estimation

C.5 SISO and 25 RBs

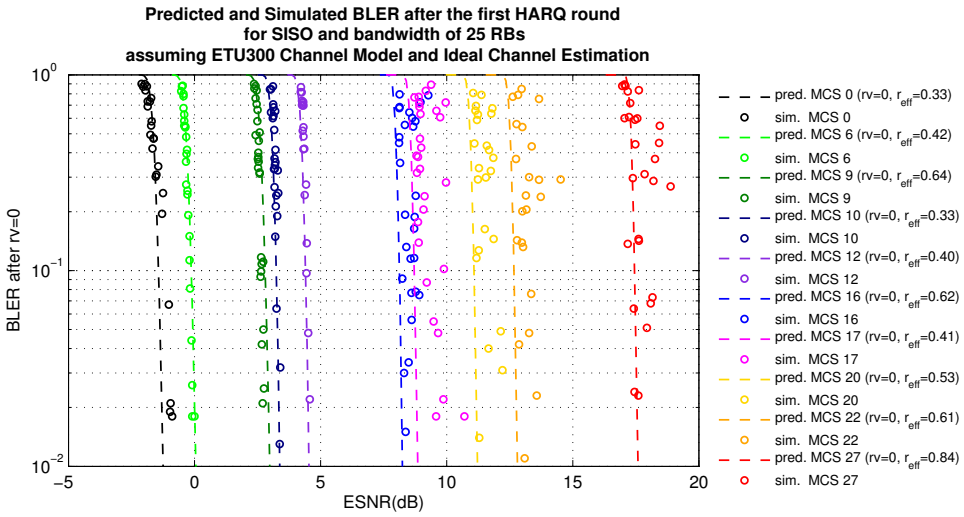

Figure C.29: Predicted vs. Simulated BLER after the first HARQ round in LTE for SISO and bandwidth of 25 RBs in ETU300 with ideal channel estimation

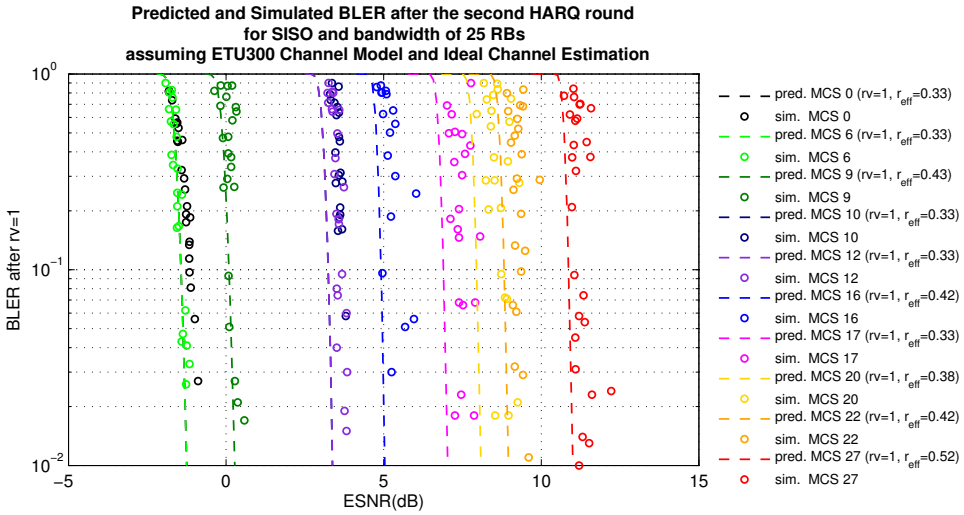

Figure C.30: Predicted vs. Simulated BLER after the second HARQ round in LTE for SISO and bandwidth of 25 RBs in ETU300 with ideal channel estimation

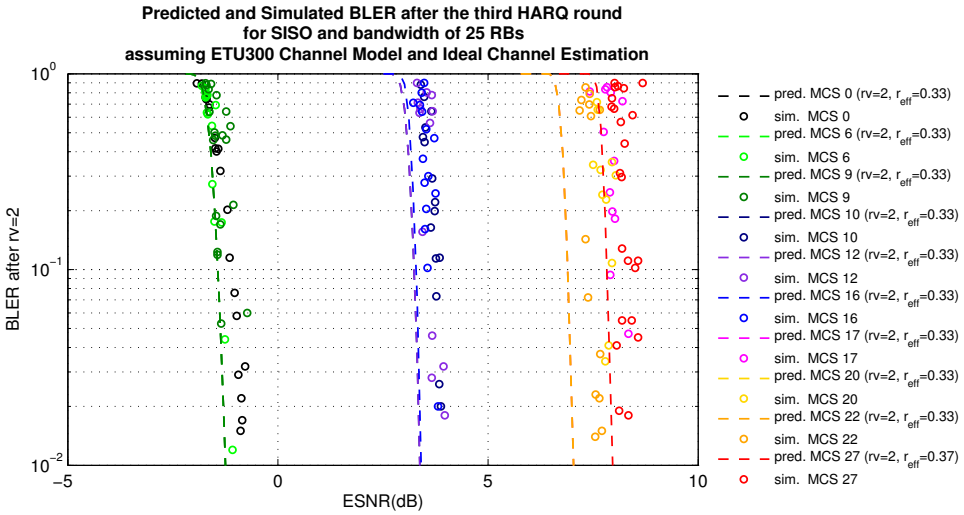

Figure C.31: Predicted vs. Simulated BLER after the third HARQ round in LTE for SISO and bandwidth of 25 RBs in ETU300 with ideal channel estimation

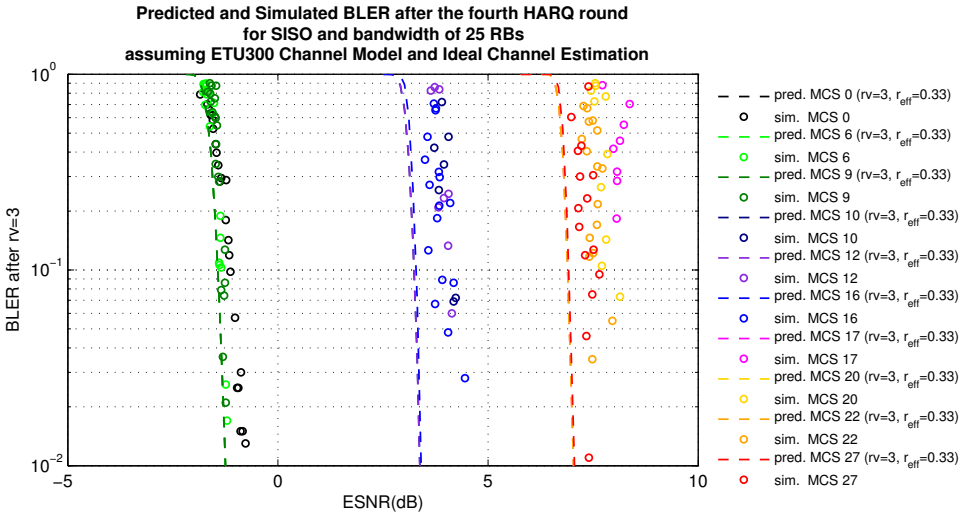

Figure C.32: Predicted vs. Simulated BLER after the fourth HARQ round in LTE for SISO and bandwidth of 25 RBs in ETU300 with ideal channel estimation

C.6 2 × 2 MIMO-SM with CDD precoding, MMSE receiver and 25 RBs

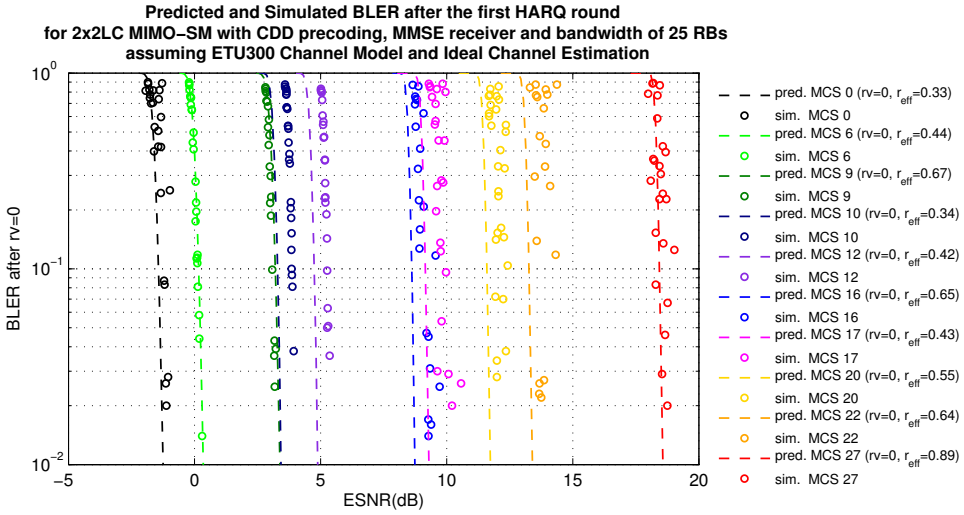

Figure C.33: Predicted vs. Simulated BLER after the first HARQ round in LTE for 2 × 2LC MIMO-SM with CDD precoding, MMSE receiver and bandwidth of 25 RBs in ETU300 with ideal channel estimation

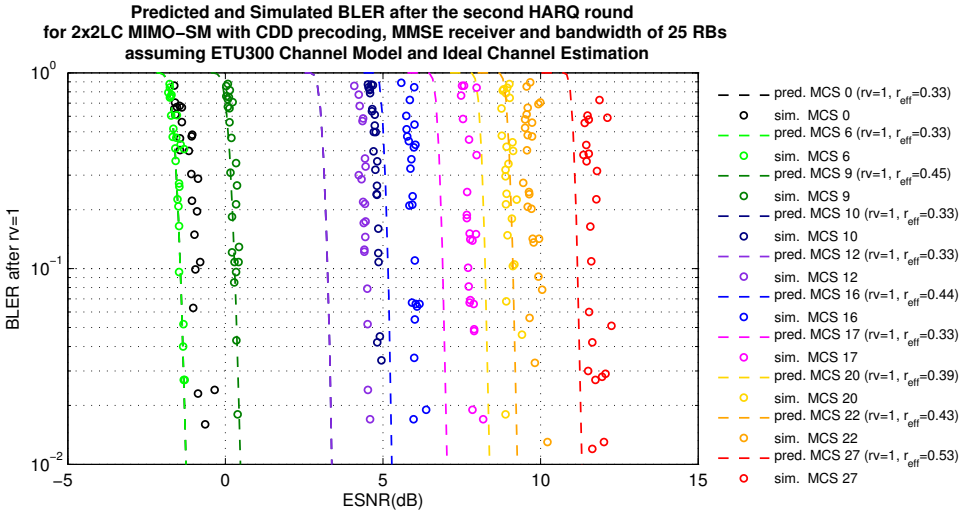

Figure C.34: Predicted vs. Simulated BLER after the second HARQ round in LTE for 2×2LC MIMO-SM with CDD precoding, MMSE receiver and bandwidth of 25 RBs in ETU300 with ideal channel estimation

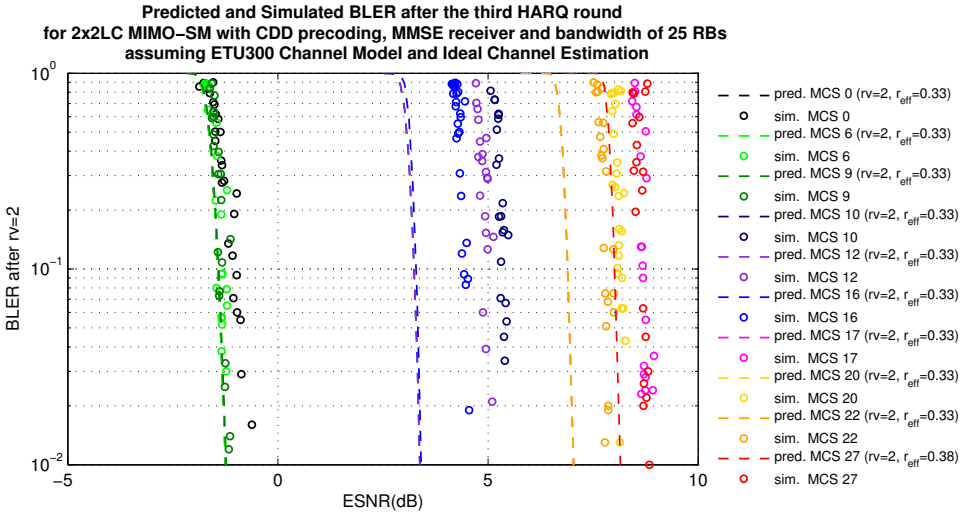

Figure C.35: Predicted vs. Simulated BLER after the third HARQ round in LTE for 2×2LC MIMO-SM with CDD precoding, MMSE receiver and bandwidth of 25 RBs in ETU300 with ideal channel estimation

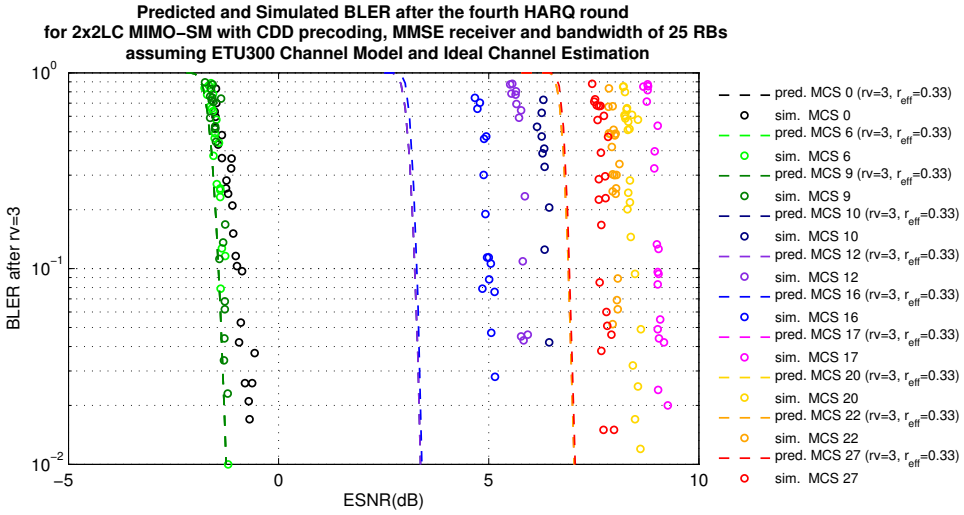

Figure C.36: Predicted vs. Simulated BLER after the fourth HARQ round in LTE for 2×2LC MIMO-SM with CDD precoding, MMSE receiver and bandwidth of 25 RBs in ETU300 with ideal channel estimation

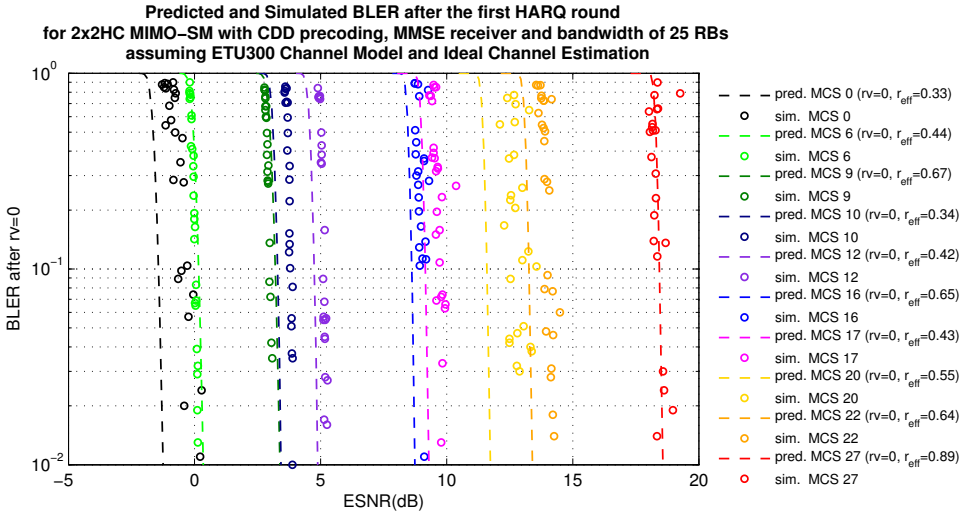

Figure C.37: Predicted vs. Simulated BLER after the first HARQ round in LTE for 2×2HC MIMO-SM with CDD precoding, MMSE receiver and bandwidth of 25 RBs in ETU300 with ideal channel estimation

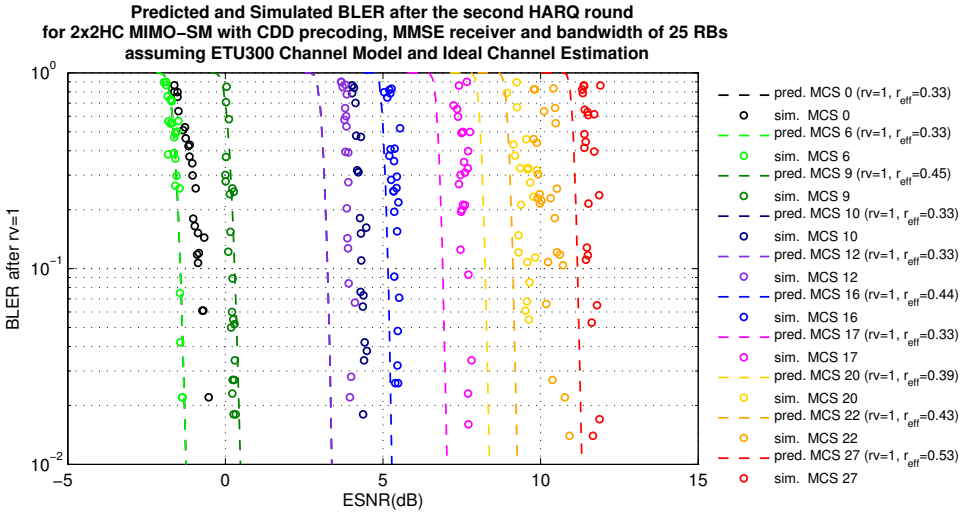

Figure C.38: Predicted vs. Simulated BLER after the second HARQ round in LTE for 2×2HC MIMO-SM with CDD precoding, MMSE receiver and bandwidth of 25 RBs in ETU300 with ideal channel estimation

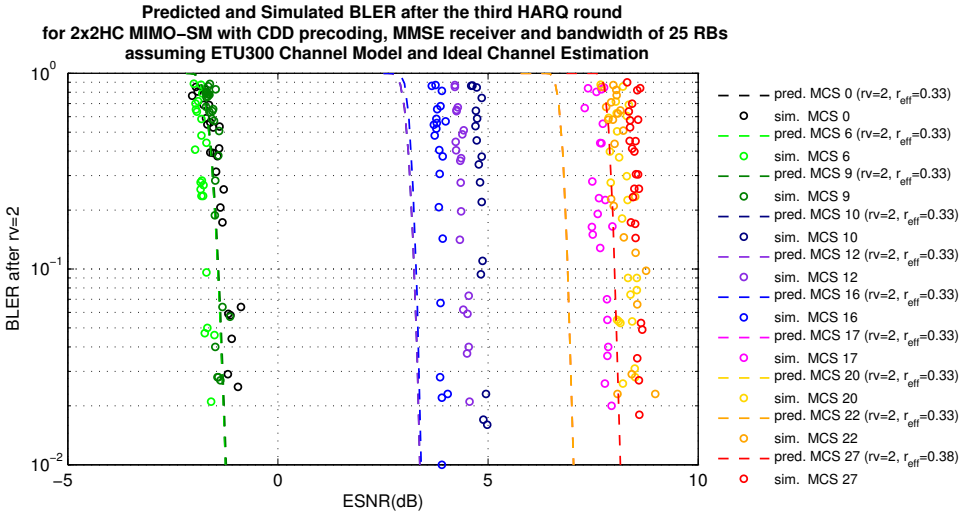

Figure C.39: Predicted vs. Simulated BLER after the third HARQ round in LTE for 2×2HC MIMO-SM with CDD precoding, MMSE receiver and bandwidth of 25 RBs in ETU300 with ideal channel estimation

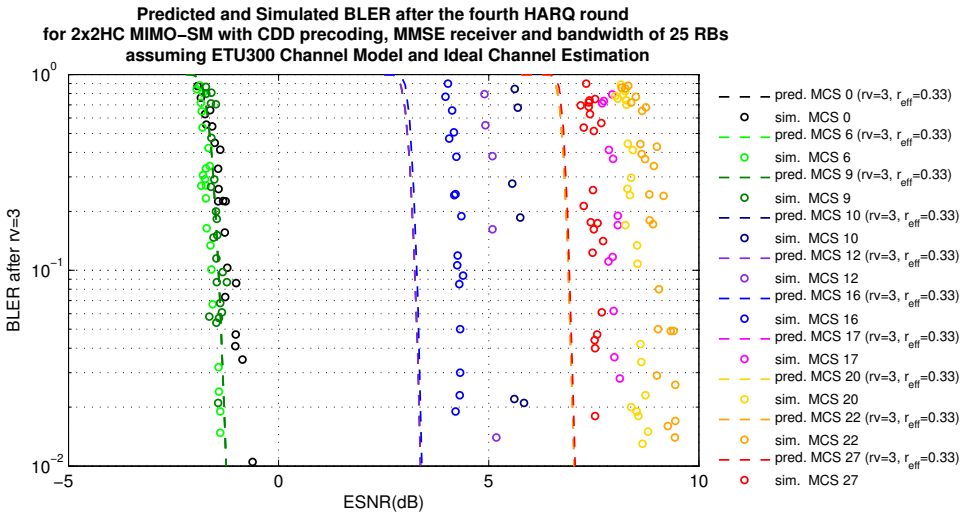

Figure C.40: Predicted vs. Simulated BLER after the fourth HARQ round in LTE for 2×2HC MIMO-SM with CDD precoding, MMSE receiver and bandwidth of 25 RBs in ETU300 with ideal channel estimation

C.7 2×2 MIMO-TD and 25 RBs

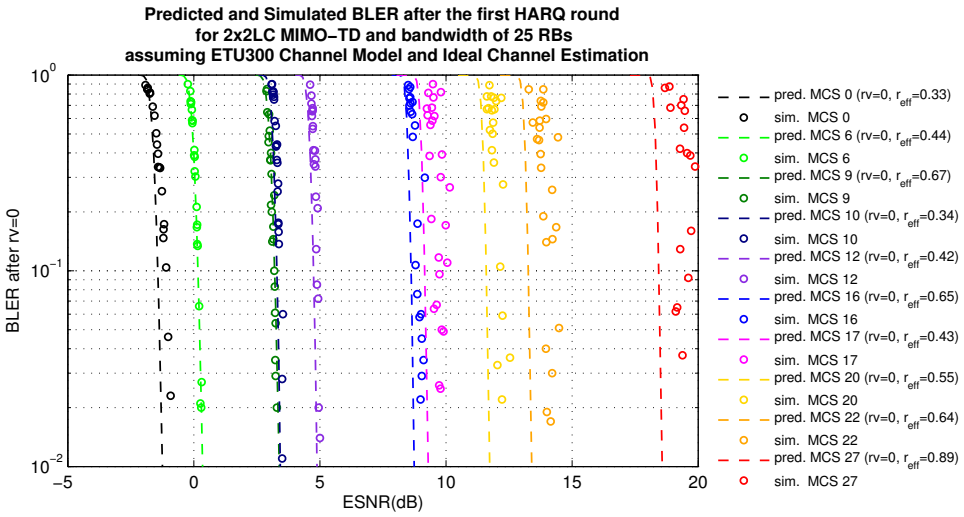

Figure C.41: Predicted vs. Simulated BLER after the first HARQ round in LTE for 2×2LC MIMO-TD and bandwidth of 25 RBs in ETU300 with ideal channel estimation

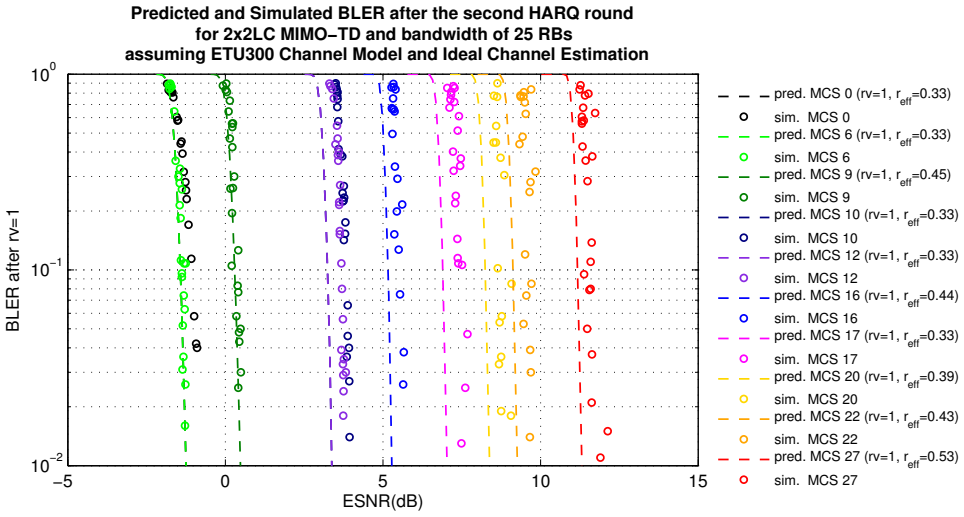

Figure C.42: Predicted vs. Simulated BLER after the second HARQ round in LTE for 2×2LC MIMO-TD and bandwidth of 25 RBs in ETU300 with ideal channel estimation

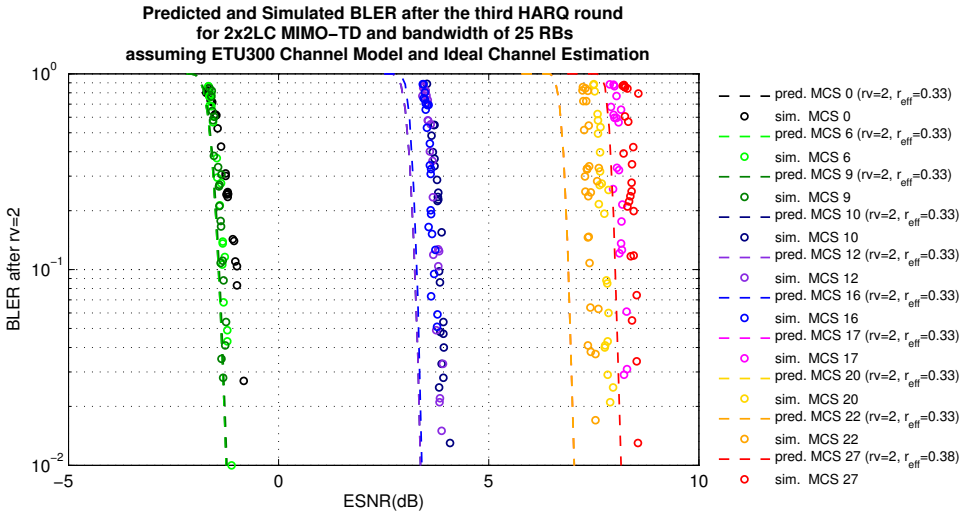

Figure C.43: Predicted vs. Simulated BLER after the third HARQ round in LTE for 2×2LC MIMO-TD and bandwidth of 25 RBs in ETU300 with ideal channel estimation

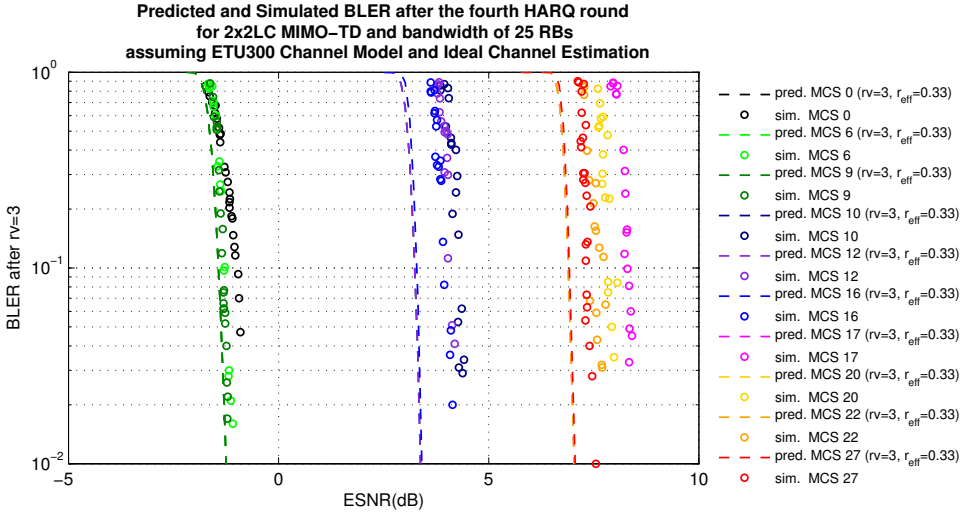

Figure C.44: Predicted vs. Simulated BLER after the fourth HARQ round in LTE for 2×2LC MIMO-TD and bandwidth of 25 RBs in ETU300 with ideal channel estimation

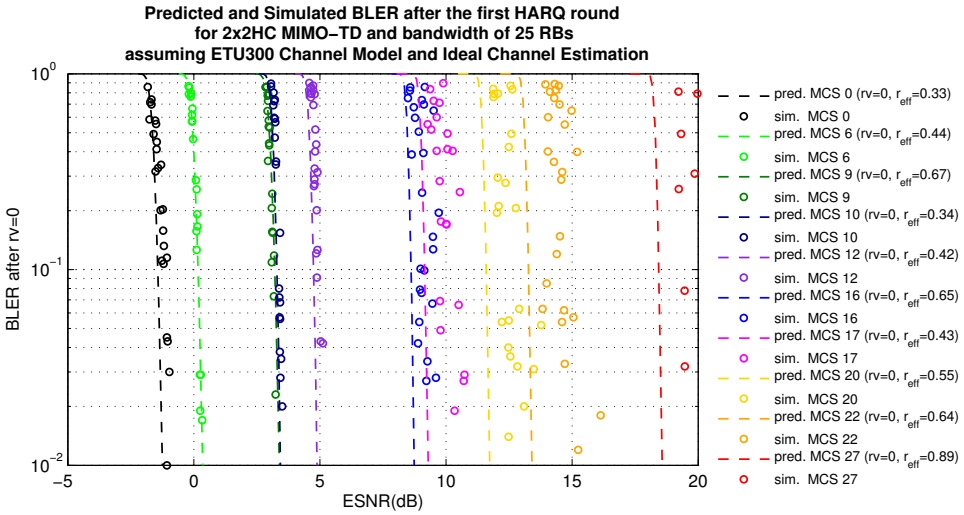

Figure C.45: Predicted vs. Simulated BLER after the first HARQ round in LTE for 2×2HC MIMO-TD and bandwidth of 25 RBs in ETU300 with ideal channel estimation

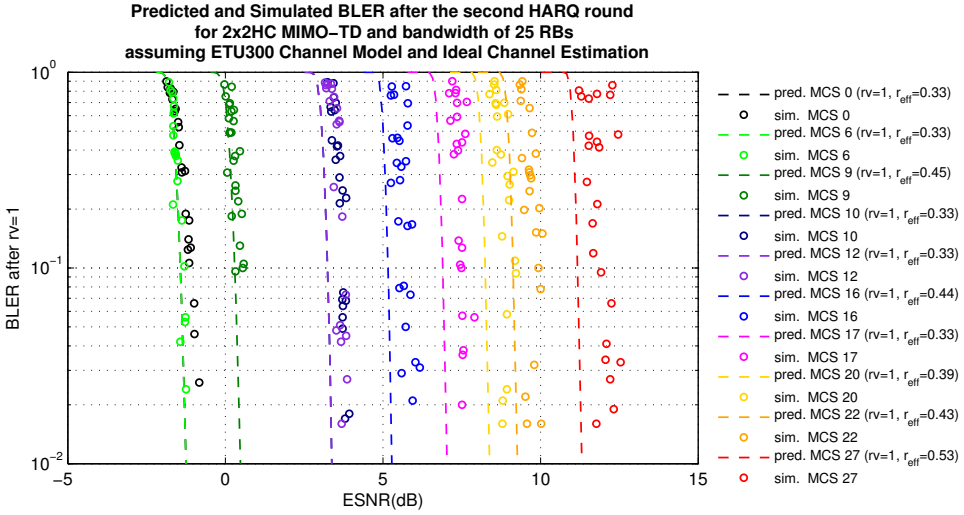

Figure C.46: Predicted vs. Simulated BLER after the second HARQ round in LTE for 2×2HC MIMO-TD and bandwidth of 25 RBs in ETU300 with ideal channel estimation

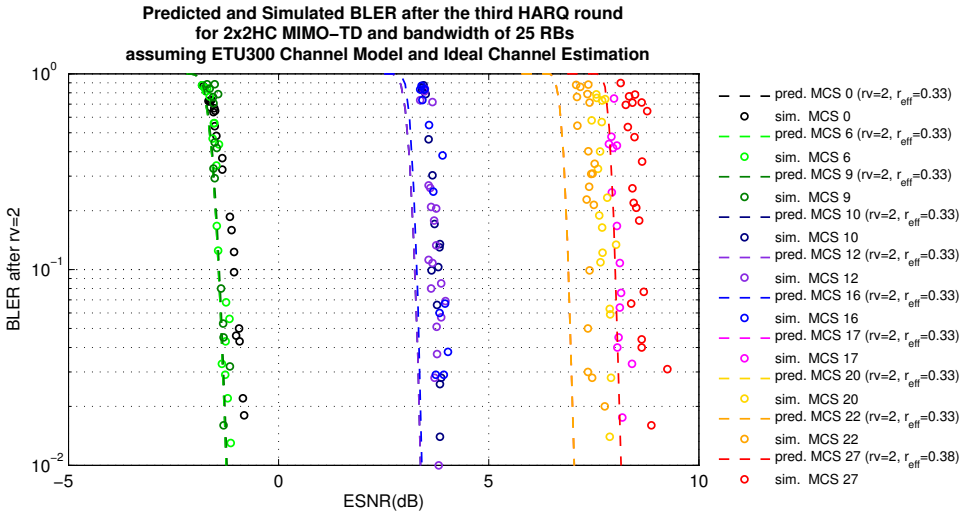

Figure C.47: Predicted vs. Simulated BLER after the third HARQ round in LTE for 2×2HC MIMO-TD and bandwidth of 25 RBs in ETU300 with ideal channel estimation

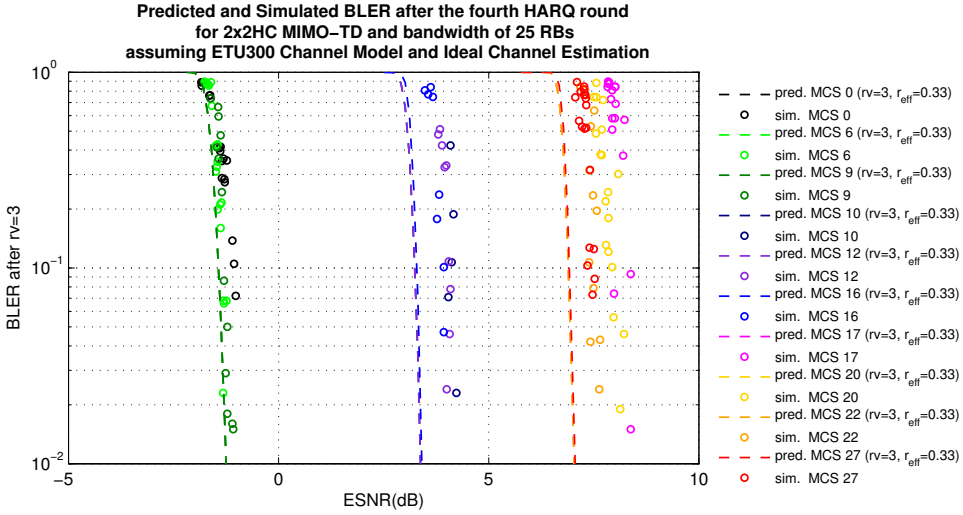

Figure C.48: Predicted vs. Simulated BLER after the fourth HARQ round in LTE for 2×2HC MIMO-TD and bandwidth of 25 RBs in ETU300 with ideal channel estimation

Bibliography

[1] 3GPP TR 25.912. Feasibility study for evolved Universal Terrestrial Radio Access (UTRA) and Universal Terrestrial Radio Access Network (UTRAN) (Release 7). (Release 7), 2007. (Cited on pages xiii, xxiii, 5, 6 and 22.)

[2] 3GPP TS 36.201. LTE physical layer; General description. 2012. (Cited on pages xiii and 17.)

[3] 3GPP TS 36.211. Physical Channels and Modulation. 2012. (Cited on pages xiii, 17, 19, 21, 39, 64, 65, 82, 85, 87, 89, 104, 105, 158, 163 and 228.)

[4] 3GPP TS 36.212. Multiplexing and channel coding. 2012. (Cited on pages xiii, 17, 39, 43, 44, 45, 52, 53, 55, 130, 138, 156, 175, 215 and 228.)

[5] 3GPP TR 36.912. Feasibility study for Further Advancements for E-UTRA (LTE-Advanced). (Release 10), 2011. (Cited on pages xxiii, 12, 16 and 22.)

[6] 3GPP TR 25.913. Requirements for Evolved UTRA (E-UTRA) and Evolved UTRAN (E-UTRAN) (Release 9). (Release 9), 2009. (Cited on pages 1, 5, 16 and 20.)

[7] REPORT ITU-R M.2134. Requirements related to technical performance for IMT-Advanced radio interface (s). 2008. (Cited on pages 1, 16 and 107.)

[8] Joan Olmos, Albert Serra, Silvia Ruiz, Mario García-lozano, and David Gonzalez. Link Level Simulator for LTE Downlink. In *COST 2100 TD(09)779*, 2009. (Cited on pages 3, 39 and 199.)

[9] Joan Olmos, Albert Serra, Silvia Ruiz, Mario García-lozano, and David Gonzalez. Exponential Effective SIR Link Performance Model for LTE Downlink. *COST 2100 TD09)874*, 2009. (Cited on page 3.)

[10] Joan Olmos, Albert Serra, Silvia Ruiz, Mario García-lozano, and David Gonzalez. Exponential Effective SIR Metric for LTE Downlink. *20th IEEE International Symposium On Personal, Indoor and Mobile Radio Communications*, pages 900–904, 2009. (Cited on pages 3, 197, 199 and 200.)

[11] Joan Olmos, Albert Serra, Mario García-lozano, Silvia Ruiz, and David Pérez Díaz De Cerio. Simulation of LTE IR H-ARQ at System Level Using MIESM Error Prediction. *IC1004 TD(11)02072*, 2011. (Cited on pages 3, 138, 198 and 200.)

[12] Joan Olmos, Albert Serra, Silvia Ruiz, and Imran Latif. On the Use of Mutual Information at Bit Level for Accurate Link Abstraction in LTE with Incremental Redundancy H-ARQ. In *IC1004 TD(12)05046*, 2012. (Cited on pages 4, 29, 212 and 213.)

[13] Albert Serra, Joan Olmos, and Maria Lema. Modelling Channel Estimation Error in LTE Link Level Simulations. *IC1004 TD(12)03067*, 2012. (Cited on page 4.)

[14] David González, Silvia Ruiz, Joan Olmos, and Albert Serra. System Level Evaluation of LTE Networks with Semidistributed Intercell Interference Coordination. In *IEEE 20th International Symposium on Personal, Indoor and Mobile Radio Communications*, 2009. (Cited on page 4.)

[15] David Gonzalez, Joan Olmos, Silvia Ruiz, and Albert Serra. Downlink Inter-Cell Interference Coordination and Scheduling for LTE Featuring HARQ over Multipath Fading Channel. pages 1–5, 2009. (Cited on page 4.)

[16] David Gonzalez, Silvia Ruiz, Joan Olmos, and Albert Serra. Link and System Level Simulation of Downlink LTE. In *COST 2100 TD(09)734*, 2009. (Cited on page 4.)

[17] Joan Olmos, Albert Serra, and Silvia Ruiz. On the Definition of Reference Scenarios for LTE-A Link Level Simulations within COST IC1004. In *IC1004 TD(13)06043*, 2013. (Cited on pages 4, 45 and 58.)

[18] 3GPP TR 25.814. Physical layer aspects for evolved Universal Terrestrial Radio Access (UTRA) (Release 7). (Release 7), 2006. (Cited on page 5.)

[19] 3GPP TS 36.101. User Equipment (UE) radio transmission and reception. 2012. (Cited on pages 7, 19, 64, 65, 67, 118, 130, 156 and 175.)

[20] 3GPP TS 36.104. Base Station (BS) radio transmission and reception. 2012. (Cited on pages 7 and 19.)

[21] 3GPP TR 25.892. Feasibility Study for Orthogonal Frequency Division Multiplexing (OFDM) for UTRAN enhancement, (Release 6), v6.0.0). 2004. (Cited on pages 7, 199 and 200.)

[22] Ramjee Prasad. *OFDM for Wireless Communications Systems*. Artech House, Inc., 2004. (Cited on page 8.)

[23] 3GPP TR 25.943. Deployment Aspects (Release 7). (Release 7), 2007. (Cited on page 8.)

[24] Narcís Cardona, Mario García, Jose F Monserrat, and Juan José Olmos. *3GPP LTE: Hacia la 4G móvil*. marcombo, 2011. (Cited on pages 9, 12, 76, 77, 79 and 81.)

[25] Erik Dahlman, Anders Furuskär, Ylva Jading, Magnus Lindström, and Stefan Parkvall. Key features of the LTE radio interface. *Ericsson Review No. 2*, pages 77–80, 2008. (Cited on page 10.)

[26] Ltd.) Yang, Hongwei (Alcatel Shngai Bell Co. A Road to Future Broadband Wireless Access : MIMO-OFDM-Based Air Interface. *IEEE Communications Magazine*, (January):53–60, 2005. (Cited on page 10.)

[27] Arogyaswami J Paulraj, Dhananjay A Gore, Rohit U Nabar, Helmut Bölcskei, and Senior Member. An Overview of MIMO Communications - A Key to Gigabit Wireless. *Proceedings of the IEEE*, 92(2):198–218, 2004. (Cited on page 10.)

[28] Gordon L Stüber, John R Barry, Steve W Mclaughlin, Senior Member, Y E Geoffrey Li, Mary A N N Ingram, and Thomas G Pratt. Broadband MIMO-OFDM Wireless Communications. In *PROCEEDINGS OF THE IEEE*, volume 92, pages 271–294, 2004. (Cited on page 10.)

[29] Albert Van Zelst. *MIMO OFDM for Wireless LANs*. PhD thesis, Technische Universiteit Eindhoven, 2004. (Cited on pages 10, 79 and 82.)

[30] The Univerity of Texas at Austin) Andrews, Jeffrey G. (Department of Electrical and Computer Engineering, Arunabha (AT&T Labs Inc.) Ghosh, and Rias (AT&T Labs Inc.) Muhamed. *Fundamentals of WiMAX Understanding Broadband Wireless Networking*. Prentice Hall, 2007. (Cited on pages 10 and 79.)

[31] Siavash M Alamouti. A Simple Transmit Diversity Technique for Wireless Communications. *IEEE Communications Magazine*, 16(8):1451–1458, 1998. (Cited on pages 10 and 82.)

[32] Erik Dhalman, Stefan Parkvall, Johan Sköld, and Per Berming. *3G Evolution: HSPA and LTE for Mobile Broadband*. Elsevier B.V., 2007. (Cited on page 11.)

[33] 3GPP TS 36.213. Physical layer procedures. 2012. (Cited on pages 13, 17, 23, 42, 44, 133, 138, 156, 175 and 199.)

[34] Joan Olmos, Silvia Ruiz, Mario García-lozano, and David Martín-sacristán. Link Abstraction Models Based on Mutual Information for LTE Downlink. In *COST 2100 TD(10)11052*, pages 1–18, 2010. (Cited on pages 13, 27, 138, 198, 199 and 200.)

[35] Stefania Sesia, Issam Toufik, and Matthew Baker. *LTE the UMTS Long Term Evolution, From Theory to Practice*. John Wiley & Sons Ltd., 2009. (Cited on pages 14 and 44.)

[36] 3GPP. Overview of 3GPP Release 1999 V0.1.1 (2010-02). 2010. (Cited on page 15.)

[37] 3GPP. Overview of 3GPP Release 4 V1.1.2 (2010-02). 2010. (Cited on page 15.)

[38] 3GPP. Overview of 3GPP Release 5 V0.1.1 (2010-02). 2010. (Cited on page 15.)

[39] 3GPP. http://www.3gpp.org/technologies. (Cited on page 15.)

[40] 3GPP TR 36.913. Eveolved Universal Terrestrial Radio Access (E-UTRA) (LTE-Advanced). (Release 10), 2011. (Cited on pages 16 and 20.)

[41] Takehiro Nakamura. LTE Release 12 and Beyond 3GPP. pages 1–17, 2013. (Cited on page 16.)

[42] 3GPP. Overview of 3GPP Release 12 V0.1.4 (2014-09). 2014. (Cited on page 17.)

[43] Eiko Seidel and Chief Technical Officer. 3GPP LTE-A Standardisation in Release 12 and Beyond. (January):1–9, 2013. (Cited on page 17.)

[44] Rohde & Schwarz. LTE-Advanced (3GPP Rel.12) Technology Introduction. 2014. (Cited on page 17.)

[45] 3GPP TR 36.872. Physical Layer Aspects (Release 12). (Release 12), 2013. (Cited on page 17.)

[46] Yan Li, Xiaodong Ji, Dong Liang, and Yuan Li. Dynamic beamforming for three-dimensional MIMO technique in LTE-advanced networks. *International Journal of Antennas and Propagation*, 2013, 2013. (Cited on page 17.)

[47] 3GPP TS 36.321. Medium Acces Control (MAC) protocol specification. (Release 11), 2013. (Cited on pages 17 and 42.)

[48] David Tse and Pramod Viswanath. *Fundamentals of Wireless Communications*. Cambridge University Press, 2005. (Cited on page 24.)

[49] John G. Proakis. Digital Communications. 2001. (Cited on page 24.)

[50] Giuseppe Caire, Giorgio Taricco, and Ezio Biglieri. Bit-Interleaved Coded Modulation. *IEEE Transactions on Information Theory*, 44(3):927–946, 1998. (Cited on pages 33, 43 and 57.)

[51] S. Shawn Tsai and Anthony C. K. Soong. 3GPP2-C30-20030429-010 - Effective SNR-Mapping for Modelling Frame Error Rates in Multiple-state Channels. 2003. (Cited on pages 33, 197 and 200.)

[52] J.-F. Cheng. Coding Performance of Hybrid ARQ Schemes. *IEEE Transactions on Communications*, 54(6):1017–1029, 2006. (Cited on pages 33, 202 and 203.)

[53] Albert Serra Pagès. A Long Term Evolution Link Level Simulator. Master's thesis, Universitat Politècnica de Catalunya, 2009. (Cited on pages 39 and 79.)

[54] Stefan H Müller-weinfurtner. Coding Approaches for Multiple Antenna Transmission in Fast Fading and OFDM. *IEEE Transactions on Signal Processing*, 50(10):2442–2450, 2002. (Cited on page 43.)

[55] Peter Fertl, Joakim Jaldén, Gerald Matz, Senior Member, and A Background. Performance Assessment of MIMO-BICM Demodulators Based on Mutual Information. *IEEE Transactions on Signal Processing*, 60(3):1366–1382, 2012. (Cited on page 43.)

[56] Jelena Nikolic-popovic. Implementing a MAP Decoder for cdma2000 Turbo Codes on a TMS320C62x DSP Device. (May):1–38, 2000. (Cited on page 53.)

[57] Jordi Pérez, Juan J. Olmos, and Silvia Ruiz. IST-2000-25133 : ARROWS D08 UTRA-FDD Simulators. 2000. (Cited on page 53.)

[58] R1-0061050 3GPP TSG RAN WG1#44bis. EUTRA FEC Enhancement. 2006. (Cited on page 55.)

[59] R1-072137 3GPP TSG RAN #49. Turbo rate-matching in LTE. 2007. (Cited on page 55.)

[60] 3GPP TR 36.815. LTE-Advanced feasibility studies in RAN WG4. (Release 9), 2010. (Cited on page 64.)

[61] 3GPPTSG RAN WG4 R4-070141. Radio Propagation Modelling for E-UTRA performance requirement definition. 2007. (Cited on page 64.)

[62] Jean Philippe Kermoal, Laurent Schumacher, Klaus Ingemann Pedersen, Preben Elgaard Mogensen, and Frank Frederiksen. A Stochastic MIMO Radio Channel Model With Experimental Validation. *IEEE Journal On Selected Areas in Communications*, 20(6):1211–1226, 2002. (Cited on page 64.)

[63] Jean-philippe Kermoal. *Measurement , Modelling and Performance Evaluation of the MIMO Radio Channel*. PhD thesis, Aalborg University, 2002. (Cited on page 64.)

[64] Klaus I Pedersen, Jorgen Bach, Jean Philippe Kennoa, and Preben Mogensen. A Stochastic Multiple-Input-Multiple-Output Radio Channel Model for Evaluation of Space-Time Coding Algorithms. In *IEEE 51st Vehicular Technology Conference Proceedings*, pages 893–897, 2000. (Cited on page 64.)

[65] Jean Philippe Kermoal, Laurent Schumacher, and Preben Mogensen. IST-2000-30148 I-METRA D2: Channel Characterisation. 2002. (Cited on page 64.)

[66] 3GPP TR 25.996. Spatial channel model for Multiple Input Multiple Output (MIMO) simulations. (Release 10), 2011. (Cited on pages 64 and 231.)

[67] 3GPP TR 36.814. Further advancements for E-UTRA physical layer aspects. (Release 9), 2010. (Cited on pages 64 and 231.)

[68] REPORT ITU-R M.2135. Guidelines for evaluation of radio interface technologies for IMT-Advanced. 2008. (Cited on pages 64 and 231.)

[69] 3GPPTSG RAN WG4 R4-070572. Proposal for LTE Channel Models. 4, 2007. (Cited on page 64.)

[70] H. Sari, G. Karam, and I. Jeanclaude. Transmission techniques for digital terrestrial TV broadcasting. *IEEE Communications Magazine*, 33(February):100–109, 1995. (Cited on page 72.)

[71] Emre Telatar. Capacity of Multi-antenna Gaussian Channels. *European Transactions on Telecommunications*, 10:585–595, 1999. (Cited on page 76.)

[72] Jørgen Bach Andersen. Array Gain and Capacity for Known Random Channels with Multiple Element Arrays at Both Ends. *IEEE Journal On Selected Areas in Communications*, 18(11):2172–2178, 2000. (Cited on page 76.)

[73] Sergio Verdú. *Multiuser Detection*. Cambridge University Press, 1998. (Cited on page 81.)

[74] Carles Navarro Manch, Luc Deneire, Preben Mogensen, and Troels B. Sorensen. On the Design of a MIMO-SIC Receiver for LTE Downlink. *IEEE 68th Vehicular Technology Conference, VTC 2008-Fall.*, pages 1–5, 2008. (Cited on page 94.)

[75] Michael Ohm. SIC receiver in a mobile MIMO-OFDM system with optimization for HARQ operation. *International OFDM Workshop*, 2008. (Cited on page 94.)

[76] Young-Han Nam, Yosuke Akimoto, Younsun Kim, Moon-il Lee, Kapil Bhattad, and Anthony Ekpenyong. Evolution of Reference Signals for LTE-Advanced Systems. *IEEE Communications Magazine*, 50(February):132–138, 2012. (Cited on page 104.)

[77] Jonathan Duplicy, Biljana Badic, Rajarajan Balraj, Rizwan Ghaffar, Florian Kaltenberger, Raymond Knopp, Z Kov, Hung T Nguyen, Deepaknath Tandur, and Guillaume Vivier. MU-MIMO in LTE Systems. *EURASIP Journal on Wireless Communications and Networking*, 2011. (Cited on page 106.)

[78] Lingjia Liu, Runhua Chen, S. Geirhofer, K. Sayana, Zhihua Shi, and Yongxing Zhou. Downlink MIMO in LTE-Advanced: SU-MIMO vs. MU-MIMO. *IEEE Communications Magazine*, 50(February):140–147, 2012. (Cited on page 106.)

[79] Dongwoon Bai, Cheolhee Park, Jungwon Lee, Hoang Nguyen, J. Singh, A.; Gupta, Zhouyue Pi, Taeyoon Kim, Chaiman Lim, Min-Goo Kim, and Inyup Kang. LTE-Advanced Modem Design : Challenges and Perspectives. *IEEE Communications Magazine*, 50(February):178–186, 2012. (Cited on pages 107 and 111.)

[80] F. Boccardi, B. Clerckx, A. Ghosh, E. Hardouin, G. Jongren, K. Kusume, E. Onggosanusi, and Yang Tang. Multiple-Antenna Techniques in LTE-Advanced. *IEEE Communications Magazine*, 50(March):114–121, 2012. (Cited on page 107.)

[81] 3GPP TS 36.141. Base Station (BS) conformance testing. 2012. (Cited on pages 109, 115, 116, 119 and 122.)

[82] Jaeho Chung, Se-jun Park, and Seong-choon Lee. Effect of Channel Estimation Errors on the Performance of MIMO-OFDM Systems in Correlated Fading Channels. *IEEE Canadian Conference on Electrical and Computer Engineering*, 2006. (Cited on page 109.)

[83] Peter Hoeher, Stefan Kaiser, and Patrick Robertson. Two-dimensional pilot-symbol-aided channel estimation by wiener filtering. *IEEE International Conference on Acoustics, Speech, and Signal Processing*, pages 1845–1848, 1997. (Cited on pages 111, 121 and 122.)

[84] Moritz Schack, Jörg Nuckelt, and Thomas Kürner. Performance Evaluation of Wiener Filter Designs for Channel Estimation in Vehicular Environments. In *COST IC1004 TD(11)02031*, 2011. (Cited on pages 111 and 242.)

[85] J-J de Beek, Ove Edfors, Magnus Sandell, Sarah Kate Wilson, and Per Ola Borjesson. On channel estimation in OFDM systems. *Vehicular Technology Conference, 1995 IEEE 45th*, 2(1):815–819, 1995. (Cited on pages 111 and 240.)

[86] Ove Edfors, Magnus Sandell, Jan-jaap Van De Beek, Sarah Kate Wilson, and Per Ola Börjesson. Ofdm channel estimation by singular value decomposition. *IEEE Communications Magazine*, pages 1–5, 1998. (Cited on pages 111 and 240.)

[87] Muhammad Saad Akram. Pilot-based Channel Estimation in OFDM Systems. 1(80):6–8, 2007. (Cited on pages 111, 240 and 241.)

[88] Michal Simko, Di Wu, Christian Mehlführer, and Dake Liu. Implementation Aspects of Channel Estimation for 3GPP LTE Terminals. In *17th European Wireless Conference*, 2011. (Cited on pages 117 and 240.)

[89] David Martín-sacristán, Jorge Cabrejas, Daniel Calabuig, and Jose F Monserrat. MAC Layer Performance of Different Channel Estimation Techniques in UTRAN LTE Downlink. *IEEE 69th Vehicular Technology Conference, VTC Spring*, pages 4–8, 2009. (Cited on pages 117, 122 and 124.)

[90] Theodore S. Rappaport. *Wireless Communications*. Prentice Hall, 2002. (Cited on page 118.)

[91] Magnus Sandell and Ove Edfors. A Comparative Study of Pilot based Channel Estimatros for Wireless OFDM. 1996. (Cited on pages 118 and 121.)

[92] M Noh, Y Lee, and H Park. Low complexity LMMSE channel estimation for OFDM. *IEEE Proceedings Communications,*, 153(6):645–650, 2006. (Cited on pages 123 and 240.)

[93] Jeff Zhuang, Louay Jalloul, Robert Novak, and Jeongho Park. IEEE 802.16m Evaluation Methodology Document (EMD). pages 1–195, 2008. (Cited on page 197.)

[94] Karsten Brueninghauss, David Astély, Thomas Sälzer, Samuli Visuri, Angeliki Alexiou, Stephan Karger, and Gholam-ali Seraji. Link Performance Models for System Level Simulations of Broadband Radio Access Systems. In *International Symposium on Personal, Indoor and Mobile Radio Communications*, pages 2306–2311, 2005. (Cited on pages 197, 198, 199 and 200.)

[95] Xin He, Kai Niu, Zhiqiang He, and Jiaru Lin. Link Layer Abstraction in MIMO-OFDM System. *International Workshop on Cross Layer Design*, 2007. (Cited on page 198.)

[96] Brian Classon, Philippe Sartori, Yufei Blankenship, and Kevin Baum. Efficient OFDM-HARQ System Evaluation Using a Recursive EESM Link Error Prediction. In *IEEE Wireless Communications and Networking Conference*, volume 00, 2006. (Cited on page 200.)

[97] Xiang Chen, Lei Wan, Zhenyuan Gao, Zesong Fei, and Jingming Kuang. The Application of EESM and MI-based Link Quality Models for Rate Compatibble LDPC Codes. *IEEE 66th Vehicular Technology Conference*, 2007. (Cited on page 200.)

[98] Imran Latif, Florian Kaltenberger, Raymond Knopp, and Joan Olmos. Low Complexity Link Abstraction for Retransmission in LTE / LTE-Advanced with. In *COST IC1004 TD(12)05060*, number 12, 2012. (Cited on page 218.)

[99] Yushi Shen and Ed Martinez. Channel Estimation in OFDM Systems. *Freescale Semiconductor Application Note*, pages 1–16, 2006. (Cited on page 240.)